

AGARD

ADVISORY GROUP FOR AEROSPACE RESEARCH & DEVELOPMENT
7 RUE ANCELLE, 92200 NEUILLY-SUR-SEINE, FRANCE

AGARD CONFERENCE PROCEEDINGS 601

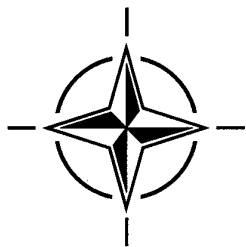
Advanced Aerodynamic Measurement Technology

(Technologies avancées de mesure aérodynamique)

*Papers presented and discussions recorded at the 81st Fluid Dynamics Panel Symposium held in
Seattle, United States, 22-25 September 1997.*

DISTRIBUTION STATEMENT A

Approved for public release;
Distribution Unlimited



NORTH ATLANTIC TREATY ORGANIZATION

Published May 1998

Distribution and Availability on Back Cover

19980626 034

AGARD

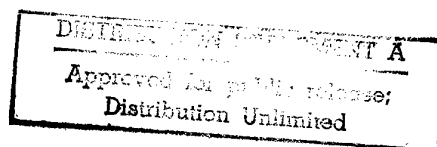
ADVISORY GROUP FOR AEROSPACE RESEARCH & DEVELOPMENT

7 RUE ANCELLE, 92200 NEUILLY-SUR-SEINE, FRANCE

AGARD CONFERENCE PROCEEDINGS 601

Advanced Aerodynamic Measurement Technology

(Technologies avancées de mesure aérodynamique)



Papers presented and discussions recorded at the 81st Fluid Dynamics Panel Symposium held in Seattle, United States, 22-25 September 1997.



North Atlantic Treaty Organization
Organisation du Traité de l'Atlantique Nord

REPRODUCTION QUALITY NOTICE

This document is the best quality available. The copy furnished to DTIC contained pages that may have the following quality problems:

- **Pages smaller or larger than normal.**
- **Pages with background color or light colored printing.**
- **Pages with small type or poor printing; and or**
- **Pages with continuous tone material or color photographs.**

Due to various output media available these conditions may or may not cause poor legibility in the microfiche or hardcopy output you receive.



If this block is checked, the copy furnished to DTIC contained pages with color printing, that when reproduced in Black and White, may change detail of the original copy.

The Mission of AGARD*

According to its Charter, the mission of AGARD is to bring together the leading personalities of the NATO nations in the fields of science and technology relating to aerospace for the following purposes:

- Recommending effective ways for the member nations to use their research and development capabilities for the common benefit of the NATO community;
- Providing scientific and technical advice and assistance to the Military Committee in the field of aerospace research and development (with particular regard to its military application);
- Continuously stimulating advances in the aerospace sciences relevant to strengthening the common defence posture;
- Improving the co-operation among member nations in aerospace research and development;
- Exchange of scientific and technical information;
- Providing assistance to member nations for the purpose of increasing their scientific and technical potential;
- Rendering scientific and technical assistance, as requested, to other NATO bodies and to member nations in connection with research and development problems in the aerospace field.

The highest authority within AGARD is the National Delegates Board consisting of officially appointed senior representatives from each member nation. The mission of AGARD is carried out through the Panels which are composed of experts appointed by the National Delegates, the Consultant and Exchange Programme and the Aerospace Applications Studies Programme. The results of AGARD work are reported to the member nations and the NATO Authorities through the AGARD series of publications of which this is one.

Participation in AGARD activities is by invitation only and is normally limited to citizens of the NATO nations.

* AGARD merged with the Defence Research Group of NATO (DRG) on 1 January 1998 to form the Research and Technology Organization (RTO) of NATO. However, both AGARD and DRG will continue to issue publications under their own names in respect of work performed in 1997.

The content of this publication has been reproduced
directly from material supplied by AGARD or the authors.



Printed on recycled paper

Published May 1998

Copyright © AGARD 1998
All Rights Reserved

ISBN 92-836-0056-8



*Printed by Canada Communication Group Inc.
(A St. Joseph Corporation Company)
45 Sacré-Cœur Blvd., Hull (Québec), Canada K1A 0S7*

Advanced Aerodynamic Measurement Technology

(AGARD CP-601)

Executive Summary

The demands for higher performance for modern aircraft have led the wind tunnel community, which is an integral link in the design process, to develop more refined and cost effective measuring techniques. These technologies have gradually matured from laboratory novelties into instruments regularly used in aerodynamic testing. The development of these modern measurement techniques has greatly extended the capability and accuracy of the classical methods for measurement techniques and provided better insight into flow physics. This Symposium provided a forum for active researchers to address the state-of-the-art, to exchange experiences and ideas, and for the practitioners to obtain an overview of the technology and learn how to apply it.

Measurement techniques were presented for flows from subsonic to hypersonic Mach numbers and environments from cryogenic to high-enthalpy reacting flows. Flow measurements have traditionally been limited to optical transmission methods and pressure or hot wire probe traversing. In recent years, there have been many developments using optical scattering from small particles carried with the flow. These methods raise the prospects for practical wind tunnels systems for mapping of 3-D flow field velocity components. In addition, the optical scattering techniques have the advantage of being non-intrusive, in that there is no physical object in the flow, and in some cases, the complete velocity field can be captured in an instant. The utility of this category of measurement is still being demonstrated.

An other broad category of methods, model surface measurements, includes methods of measuring skin friction, boundary layer transition, and pressure. Traditionally, arrays of thermocouples and pressure taps have been used to obtain surface temperature and pressure distributions. These techniques are very labor intensive and model preparation costs are high when detailed maps of temperature and pressure are desired. Measurements obtained utilizing Pressure Sensitive Paint and Temperature Sensitive Paint have the potential to be of extreme value to airplane design programs. These techniques provide a way to obtain simple, inexpensive, measurements of temperature and pressure with high spatial resolution.

Technologies avancées de mesure aérodynamique

(AGARD CP-601)

Synthèse

La recherche d'amélioration des performances des aéronefs modernes a amené la communauté des experts en soufflerie, qui constituent un maillon intégral de la chaîne de conception, à développer des techniques de mesure plus rentables et plus sophistiquées. Ces technologies, considérées autrefois comme des simples curiosités de laboratoire, ont évolué vers une utilisation quotidienne en tant qu'outils d'essais aérodynamiques. Le développement des techniques modernes de mesure a permis une amélioration considérable des possibilités et de la précision des méthodes classiques, ainsi qu'une meilleure compréhension de la physique des écoulements. Ce symposium a servi de forum sur ce sujet, où les chercheurs dans le domaine ont pu faire le point de l'état actuel des connaissances des techniques de mesure, tout en échangeant des idées et des expériences. Les exploitants ont aussi eu un aperçu de ces technologies et des moyens de leur mise en œuvre.

Des techniques de mesure ont été présentées pour une gamme d'écoulements ayant des nombres de Mach allant du subsonique à l'hypersonique et pour des environnements allant du cryogénique aux écoulements réactifs à haute enthalpie. Traditionnellement, la mesure des écoulements s'est limitée à la mesure au fil chaud et aux méthodes de transmission optique ou à la sonde de pression. Cependant, ces dernières années ont vu bon nombre de développements faisant appel à la diffusion optique à partir de petites particulesensemencées dans l'écoulement. Ces méthodes laissent prévoir la réalisation de systèmes pratiques pour la cartographie des composantes de vitesse des champs d'écoulement en trois dimensions. En outre, les techniques de diffusion optique ont l'avantage d'être non intrusifs, dans la mesure où aucun objet physique n'est présent dans l'écoulement, et dans certains cas, la totalité du champ de vitesse peut être capturée dans un seul instant. L'utilité de cette catégorie de mesure continue d'être démontrée.

Une autre grande catégorie de méthodes, la mesure de la surface de la maquette, comprend des techniques pour la mesure de la résistance de frottement, la transition de la couche limite, et la pression. Traditionnellement, des bancs de thermocouples et des robinets manométriques ont été utilisés pour obtenir la répartition des températures et des pressions surfaciques. Cependant, il s'agit de techniques à forte concentration de main-d'œuvre et si des cartes détaillées de température et de pression sont demandées, les coûts de fabrication des maquettes sont élevés. Les mesures obtenues à l'aide de peintures sensibles à la pression et à la température peuvent être très précieuses pour les programmes d'études des aéronefs. Ces techniques permettent d'obtenir, à coût réduit, des mesures de température et de pression à résolution spatiale élevée.

Contents

	Page
Executive Summary	iii
Synthèse	iv
Recent Publications of the Fluid Dynamics Panel	viii
Fluid Dynamics Panel	x
	Reference
Technical Evaluation Report by J.P. Crowder	T
Review of Optical Methods for Fluid Dynamics by A.L. Heyes and J.H. Whitelaw	1
Advanced Measurement Technology at NASA Langley Research Center by R.R. Antcliff	2
Measurement Techniques Developed for Cryogenic Field in T2 Transonic Wind Tunnel by A. Seraudie, J.P. Archambaud and A. Mignosi	3
Development of PIV for Two and Three Component Velocity Measurements in a Large Low Speed Wind Tunnel by P.W. Bearman, J.K. Harvey and J.N. Stewart	4
Application of PIV in the Large Low Speed Facility of DNW by J.W. Kooi, K. Pengel, M. Raffel, C. Willert and J. Kompenhans	5
Analysis of Complex Flow Fields by Animation of PIV and High Resolution Unsteady Pressure Data by F. Coton, R. Galbraith, I. Grant and D. Hurst	6
Recent Advances in Particle Image Velocimetry by L. Lourenco, A. Krothapalli and C.A. Smith	7
Recent Developments in Doppler Global Velocimetry by T.J. Beutner and H.D. Baust	8
Planar Doppler Velocimetry for Large-Scale Wind Tunnel Applications by R.L. McKenzie	9
Intérêt de l'Utilisation d'une Source Laser Accordable en Vélocimétrie Doppler Globale by B. Leporcq, J.-F. Le Roy, B. Pinchemel and S. Hostyn	10

Surface Integral Method to Quantify the Droplet Non-Sphericity Effect on Rainbow Thermometry	11
by J.P.A.J. van Beeck and M.L. Riethmuller	
Airplane Flow-Field Measurements and the Flying Strut	12
by J.P. Crowder	
Molecular Diagnostics for Rarefied Flows	13
by J.P. Taran	
Rotational and Vibrational Temperatures and Density Measurements by Coherent Anti-Stokes Raman Scattering in a Nonequilibrium Shock Layer Flow	14
by F. Grisch, P. Bouchardy, U. Koch and A. Gülhan	
Rotational and Vibrational Temperature and Density Measurements by Planar Laser Induced NO-Fluorescence Spectroscopy in a Nonequilibrium High Enthalpy Flow	15
by U. Koch, A. Gülhan, B. Esser, F. Grisch and P. Bouchardy	
Time Resolved Measurements of the Energy Separation Process in a Transonic Turbine Vane Wake Flow	16
by W.E. Carscallen, S.I. Hogg, J.P. Gostelow and D.R. Buttsworth	
Application of Optical and Interference Methods in Experimental Aerodynamics	17
by V.P. Koulech, S.D. Fonov and V.A. Yakovlev	
Enregistrement et Traitement des interférogrammes par Caractérisation Spectrale de la Chaîne Optique	18
by J.M. Dese	
Advances in Aerodynamic Holography	19
by J.D. Trolinger, J. Millerd, D. Weber and M. Brown	
Holographic and Tomographic Interferometry for the Study of Unsteady Compressible Flows	20
by B.H. Timmerman and P.G. Bakker	
Development of High Speed Interferometry Imaging and Analysis Techniques for Compressible Dynamic Stall	21
by M.S. Chandrasekhara, L.W. Carr and M.C. Wilder	
Wall-Shear Stress Measurement with Quantitative IR-Thermography	22
by R. Mayer, R.A. Henkes and J.L. van Ingen	
Skin Friction Measurement and Transition Detection Techniques for the Ludwig-Tubes at DLR	23
by E. Schüle, S. Koch and H. Rosemann	
Surface Forces Measurements with High Spatial and Temporal Resolution by Means of Liquid Crystal Foils, Piezofolios and Surface Hot-Film Arrays	24
by W. Nitsche, J. Suttan, F. Haselbach and D. Sturzebecher	
Application of Oil Film Interferometry Skin-Friction to Large Wind Tunnels	25
by D.M. Driver	
Visualization and Measurement of Surface Shear Stress Vector Distributions Using Liquid Crystal Coatings	26
by D.C. Reda and M.C. Wilder	

Shear Sensitive Liquid Crystals in Subsonic and Transonic Wind Tunnel Testing by G. Lombardi, M. Morelli and D. Waller	27
Applications of Temperature and Pressure Sensitive Paints by T. Liu and J.P. Sullivan	28
Study Result for the Application of Two-Component PSP Technology to Aerodynamic Experiment by A. Bykov, S. Fonov, V. Mosharov, A. Orlov, V. Pesetsky and V. Radchenko	29
The Two-Component PSP Investigation on a Civil Aircraft Model in S2MA Wind Tunnel by M. Lyonnet, B. Deléglise, G. Grenat, A. Bykov, V. Mosharov, A. Orlov and S. Fonov	30
Low-Speed Flow Studies Using the Pressure Sensitive Paint Technique by O.C. Brown, R.D. Mehta and B.J. Cantwell	31
The Status of Internal Strain Gage Balance Development for Conventional and for Cryogenic Wind Tunnels by B. Ewald	32
Summary Report of the First International Symposium on Strain Gauge Balances and Workshop on AoA/Model Deformation Measurement Techniques by J.S. Tripp, P. Tchong, A.W. Burner and T.D. Finley	33
Model Deformation Measurements at NASA Langley Research Center by A.W. Burner	34
MEMS Applications in Aerodynamic Measurement Technology by E. Reshotko, M. Mehregany and C. Bang	35
General Discussion	GD

Recent Publications of the Fluid Dynamics Panel

AGARDOGRAPHS (AG)

Turbulent Boundary Layers in Subsonic and Supersonic Flow

AGARD AG-335, July 1996

Computational Aerodynamics Based on the Euler Equations

AGARD AG-325, September 1994

Scale Effects on Aircraft and Weapon Aerodynamics

AGARD AG-323 (E), July 1994

Design and Testing of High-Performance Parachutes

AGARD AG-319, November 1991

Experimental Techniques in the Field of Low Density Aerodynamics

AGARD AG-318 (E), April 1991

Techniques Expérimentales Liées à l'Aérodynamique à Basse Densité

AGARD AG-318 (FR), April 1990

A Survey of Measurements and Measuring Techniques in Rapidly Distorted Compressible Turbulent Boundary Layers

AGARD AG-315, May 1989

REPORTS (R)

High Speed Body Motion in Water

AGARD R-827, February 1998

Turbulence in Compressible Flows

AGARD R-819, Special Course Notes, June 1997

Advances in Cryogenic Wind Tunnel Technology

AGARD R-812, Special Course Notes, January 1997

Aerothermodynamics and Propulsion Integration for Hypersonic Vehicles

AGARD R-813, Special Course Notes, October 1996

Parallel Computing in CFD

AGARD R-807, Special Course Notes, October 1995

Optimum Design Methods for Aerodynamics

AGARD R-803, Special Course Notes, November 1994

Missile Aerodynamics

AGARD R-804, Special Course Notes, May 1994

Progress in Transition Modelling

AGARD R-793, Special Course Notes, April 1994

Shock-Wave/Boundary-Layer Interactions in Supersonic and Hypersonic Flows

AGARD R-792, Special Course Notes, August 1993

Unstructured Grid Methods for Advection Dominated Flows

AGARD R-787, Special Course Notes, May 1992

Skin Friction Drag Reduction

AGARD R-786, Special Course Notes, March 1992

Engineering Methods in Aerodynamic Analysis and Design of Aircraft

AGARD R-783, Special Course Notes, January 1992

ADVISORY REPORTS (AR)

Ice Accretion Simulation

AGARD AR-344, Report of WG-20, December 1997

Sonic Nozzles for Mass Flow Measurement and Reference Nozzles for Thrust Verification

AGARD AR-321, Report of WG-19, June 1997

Cooperative Programme on Dynamic Wind Tunnel Experiments for Manoeuvring Aircraft

AGARD AR-305, Report of WG-16, October 1996

Hypersonic Experimental and Computational Capability, Improvement and Validation

AGARD AR-319, Vol. I, Report of WG-18, May 1996

Aerodynamics of 3-D Aircraft Afterbodies

AGARD AR-318, Report of WG-17, September 1995

A Selection of Experimental Test Cases for the Validation of CFD Codes

AGARD AR-303, Vols. I and II, Report of WG-14, August 1994

Quality Assessment for Wind Tunnel Testing

AGARD AR-304, Report of WG-15, July 1994

Air Intakes of High Speed Vehicles

AGARD AR-270, Report of WG-13, September 1991

Appraisal of the Suitability of Turbulence Models in Flow Calculations

AGARD AR-291, Technical Status Review, July 1991

Rotary-Balance Testing for Aircraft Dynamics

AGARD AR-265, Report of WG11, December 1990

Calculation of 3D Separated Turbulent Flows in Boundary Layer Limit

AGARD AR-255, Report of WG10, May 1990

CONFERENCE PROCEEDINGS (CP)

Aerodynamics of Wind Tunnel Circuits and Their Components

AGARD CP-585, June 1997

The Characterization & Modification of Wakes from Lifting Vehicles in Fluids

AGARD CP-584, November 1996

Progress and Challenges in CFD Methods and Algorithms

AGARD CP-578, April 1996

Aerodynamics of Store Integration and Separation

AGARD CP-570, February 1996

Aerodynamics and Aeroacoustics of Rotorcraft

AGARD CP-552, August 1995

Application of Direct and Large Eddy Simulation to Transition and Turbulence

AGARD CP-551, December 1994

Wall Interference, Support Interference, and Flow Field Measurements

AGARD CP-535, July 1994

Computational and Experimental Assessment of Jets in Cross Flow

AGARD CP-534, November 1993

High-Lift System Aerodynamics

AGARD CP-515, September 1993

Theoretical and Experimental Methods in Hypersonic Flows

AGARD CP-514, April 1993

Aerodynamic Engine/Airframe Integration for High Performance Aircraft and Missiles

AGARD CP-498, September 1992

Effects of Adverse Weather on Aerodynamics

AGARD CP-496, December 1991

Manoeuvring Aerodynamics

AGARD CP-497, November 1991

Vortex Flow Aerodynamics

AGARD CP-494, July 1991

Missile Aerodynamics

AGARD CP-493, October 1990

Aerodynamics of Combat Aircraft Controls and of Ground Effects

AGARD CP-465, April 1990

Computational Methods for Aerodynamic Design (Inverse) and Optimization

AGARD CP-463, March 1990

Applications of Mesh Generation to Complex 3-D Configurations

AGARD CP-464, March 1990

Fluid Dynamics of Three-Dimensional Turbulent Shear Flows and Transition

AGARD CP-438, April 1989

Fluid Dynamics Panel

Chairman: Prof. Dr. C. ÇIRAY
Aeronautical Eng. Department
Middle East Technical University
Inonu Bulvari PK: 06531
Ankara, Turkey

Deputy Chairman: Prof. B. CANTWELL
Stanford University
Dept. of Aeronautics & Astronautics
Stanford, CA 94305
United States

PROGRAMME COMMITTEE

Dr. Louis CHAN (Chairman)
High Speed Aerodyn.Lab. - U66
Institute for Aerospace Research
National Research Council Canada
Montreal Road
Ottawa, Ontario K1A 0R6 - CANADA

Prof. Dr. Roland DECUYPERE
Ecole Royale Militaire
Avenue de la Renaissance 30
B-1040 Brussels - BELGIUM

Ing. en Chef Xavier BOUIS
Directeur des Grands Moyens d'Essais
ONERA - BP 72
92322 Chatillon Cedex - FRANCE

Prof. Dr. Gerd E.A. MEIER
Direktor des Institutes für
Stromungsmechanik der DLR
Bunsenstrasse 10
D-37073 Göttingen - GERMANY

Assoc. Professor S. TSANGARIS
Dept. of Mechanical Engineering
National Technical University of Athens
P.O. Box 64070
15710 Zografou-Athens - GREECE

Prof. Michele ONORATO
Dipartimento di Ingegneria
Aeronautica e Spaziale
Politecnico di Torino
C. so Duca degli Abruzzi 24
10129 Torino - ITALY

Ir Bram ELSENAAR
National Aerospace Laboratory NLR
Anthony Fokkerweg 2
1059 CM Amsterdam - NETHERLANDS

Mr. Oyvind GRANDUM
Division for Weapons and Materiel
Norwegian Defence Research Establ.
P.O. Box 25
N-2007 Kjeller - NORWAY

Dr. Roque CORRAL
Departamento de Mecanica de Fluidos
Industria de Turbopropulsores (ITP)
Carretera Torrejon Ajalvir, Km 3.5
28850 Torrejon de Ardoz (Madrid) - SPAIN

Col. Dr. Mehmet AKCAY
Armament and Defence Research
Dept of Turkish General Staff
06100 Ankara - TURKEY

Dr. David. WOODWARD
Research Manager - Low Speed & Basic
Aerodynamics Dept.
X80 Building
Defence Research Agency
Farnborough Hants GU14 6TD - U.K.

Dr. Yung H. YU
Chief, Fluid Mechanics Division
Aeroflightdynamics Directorate
Mail Stop 215-1
NASA Ames Research Center
Moffett Field, CA 94035-1099 - U.S.A.

PANEL EXECUTIVE

Mr. J.K. MOLLOY

Mail from Europe:
AGARD-OTAN
Attn: FDP Executive
7, rue Ancelle
92200 Neuilly-sur-Seine
France

Mail from USA and Canada:
AGARD-NATO
Attn: FDP Executive
Unit PSC 116
APO AE 0977

Tel: 33 (1) 55 61 22 75

TECHNICAL EVALUATOR REPORT

Fluid Dynamic Panel Symposium on ADVANCED AERODYNAMIC MEASUREMENT TECHNOLOGY

James P. Crowder
Boeing Aerodynamics Laboratory
Mail Stop IW-82, P.O. Box 3707
Seattle, WA 98124, USA

Wind tunnel testing and much of the associated measurement techniques have been practiced for many decades and are sometimes regarded as a mature technology. Those of us working in this arena, however, realize that there is continuous pressure for improvement and innovation, if not revolution, in experimental aerodynamic methods for wind tunnel testing. This recognition is largely responsible for this 81st Fluid Dynamics Panel Meeting and Symposium on Advanced Aerodynamic Measurement Technology.

The scope of the Symposium was narrow in the sense that the topic was limited to experimental methods for wind tunnel testing, but broad in the range of applications. Measurement techniques for all types of aerodynamic reactions and phenomena were presented for flows from subsonic to hypersonic Mach numbers and environments from cryogenic to high-enthalpy reacting flows.

The meeting was held in Seattle, Washington, USA during September 22 to 25, 1997. During the 3.5 days of the Symposium, a total of 35 papers were presented in a single session format. Of these, 3 papers were invited reviews of selected topics. For the remaining 32 papers two broad categories emerged: flow field measurements and model surface measurements. These two categories were responsible for 28 of the 32 papers.

Flow field measurements have traditionally been limited to optical transmission methods, (schlieren, interferometer, etc), and pressure or hot wire probe traversing. In recent years there have been many developments using optical scattering from small particles carried with the flow. These methods raise the prospects for practical wind tunnel systems for mapping of 3-D flow field velocity components. In addition, the optical scattering techniques have the advantage of being non-intrusive, in that they have no physical object in the flow, and in some cases, the complete velocity field can be captured in an instant. The utility of this category of measurement is still being demonstrated. Since the flow field contains all the reactions produced by the aerodynamics on the model surface, it may be possible that the flow field data can provide more than general documentation of the flow field, and yield model forces.

The other broad category of methods, model surface measurements, include methods of measuring skin friction, boundary layer transition, and pressure. The latter, known as Pressure Sensitive Paint (PSP), has the potential to be of extreme value to commercial airplane programs because of the impact of conventional surface pressure taps on wind tunnel test cycle time.

The Symposium was organized into 11 separate sessions of generally 3 to 4 papers. This allowed good opportunity for discussion and reflection. The following tables summarize these facts.

Session No.	No. Papers	Session Title [paper no.]
1	3	Overview Papers [1][2][3]
2	4	PIV [4][5][6][7]
3	3	DGV [8][9][10]
4	2	Special Topics (1) [11][12]
5	3	Molecular Diagnostics [13][14][15]
6	1	Special Topics (2) [16]
7	5	Holographic Interf [17][18][19][20][21]
8	6	Skin Friction [22][23][24][25][26][27]
9	4	PSP [28][29][30][31]
10	3	Balance & Model Defl [32][33][34]
11	1	Special Topics (3), MEMS [35]

No. Papers	No. Sessions	Session Numbers
1	2	6,11
2	1	4
3	4	1,3,5,10
4	2	2,9
5	1	1
6	1	8

Comments and observations pertaining to the individual papers are presented below in the order of the sessions in which the papers were presented.

SESSION 1, OVERVIEW PAPERS.

Three invited papers were presented in this first session. The first Paper 1, "Review of Optical Methods for Fluid Dynamics" presents a good and complete description of optical velocimeters (LDV, PIV, DGV) and a useful summary of surface reacting paints for pressure and temperature measurements.

Paper 2 is an informative summary of many varied activities underway at NASA Langley Research Center, including focusing schlieren for wind tunnel installations and a unique long distance in-flight application, various laser sheet visualization reactions, velocimeters such as PIV and DGV, acoustic measurements with microphone arrays and wind tunnel model deflections using Projected Moiré Interferometry. The ultimate schlieren application, surely, must be the startling result of Weinstein in capturing the shock wave system of a supersonic T-38 airplane at long distance in flight.

The third paper, "Measurement Techniques Developed for Cryogenic Field in T2 Transonic Wind Tunnel," is not so much a review paper on cryogenic methods as a report of a few specific applications in the T2 wind tunnel. These are not necessarily of general importance, as the T2 wind tunnel is rather unique, but they are interesting, nonetheless. It is fascinating to learn that naturally occurring ice particles in the cryogenic flow can be useful as laser velocimeter scattering seeds.

The next two sessions, 2, 3 are devoted to flow field measurements using Particle Image Velocimetry (PIV) [4][5][6][7] and Doppler Global Velocimetry (DGV) [8][9][10], respectively. Session 4, labeled Special Topics, includes one paper on flow field measurements with a fast traversing pressure probe[12].

SESSION 2. PARTICLE IMAGE VELOCIMETRY

Paper 4, "Development of PIV for Two and Three Component Velocity Measurements in a Large Low Speed Wind Tunnel," and paper 5, "Application of PIV in the Large Low Speed Facility of DNW," are similar in that they both focus on the practical aspects of applying PIV to large industrial wind tunnels which is no small feat. Paper 4 provides a lucid explanation of parallax error for 3-D measurements in a perpendicular cross-plane and the process of Stereo-PIV correction. Both papers discuss the importance of instantaneous flow field data capture in the context of unsteady flow properties. Examples of turbulent separated flow are shown to illustrate the velocity field variability.

In paper 5 velocity data are presented showing large variability in the position of trailing vortex features behind a high-lift flapped wing at a distance of 2 spans. In the experience of this reviewer, such differences are unexpected. This behavior may be indicative of a critical stability condition or vortex meander induced by unsteady onset flow rather than ordinary turbulence.

Paper 6, "Analysis of Complex Flow Fields by Animation of PIV and High Resolution Unsteady Pressure Data," describes a welcome attempt to develop useful data presentation and visualization tools to accommodate the vast amount of flow field data produced by these techniques.

Paper 7, "Recent Advances in Particle Image Velocimetry," is a interesting and informative account of many of the detailed problems and techniques required in implementing PIV in industrial wind tunnels. Sample data from a low speed 7-by-10-foot wind tunnel are presented.

SESSION 3. DOPPLER GLOBAL VELOCIMETRY

It appears that DGV is somewhat of a competitor to PIV in that it is the only other recognized technique in which an entire flow field is captured in one instant. It is also sometimes claimed to be better suited for 3-D measurements.

Paper 8, "Recent Developments in Doppler Global Velocimetry," includes a frank discussion of the problems and limitations of applying DGV in a large industrial wind tunnel. The statement "... the [DGV] instrument described here is qualitative in nature." is telling. As a qualitative flow field survey system, it is rather ineffective, in terms of the great effort to achieve such modest results. Time will tell how practical the quantitative potential of the method is in such wind tunnel settings.

Paper 9, "Planar Doppler Velocimetry for Large-Scale Wind Tunnel Testing," makes a serious effort to estimate the potential performance of the method based on careful analysis and small laboratory experiments. Many details of possible system refinements are discussed.

The final paper in the DGV session, paper 10, unfortunately, was not available in an English version nor is there an English abstract. The Symposium does provide simultaneous French-English translation, but it is sometimes difficult to remain focused on a technical presentation with the additional effort of listening to a translation. Apparently the paper presents a discussion of the suitability of various laser wavelengths for DGV.

SESSION 4. SPECIAL TOPICS (1)

Paper 11 on "Rainbow Thermometry", a technique to determine the temperature of individual aerosols particles in a spray, examines the error effects of non-sphericity of the particles.

One additional paper on flow field measurements, paper 12, "Airplane Flow Field Measurements and the Flying Strut Traverser," was presented in this session. This is a two-part report where the first relates recent experience in the use of fast traversing pressure probe systems for quantitative measurements of airplane model wake properties in industrial wind tunnels. The measurements provide detailed spatial distributions of airplane model lift and drag with excellent agreement to the overall balance force measurements. In addition to the total drag, the system can decompose the drag into profile and induced drag components. The second part of the report describes the Flying Strut Traverser, an aerodynamically trimmed and actuated system with the potential to greatly simplify the application of pressure probe surveys to very large wind tunnels and to in-flight settings.

SESSION 5. MOLECULAR DIAGNOSTIC TECHNIQUES

The three papers included in this session are all concerned with optical techniques for high enthalpy, hypersonic flows and combustion. These typically have extremely short run times and are very hostile to intrusive instrumentation.

Paper 13, "Molecular Diagnostics for Rarefied Flows," is an extensive review of point, line-of-sight and imaging measurements using, 1. Rayleigh and Raman scattering, 2. Electron Beam Fluorescence and 3. Coherent Anti-Stokes Raman Scattering. Application examples from the ONERA F4 hot shot facility are presented.

Paper 14, "Rotational and Vibrational Temperatures and Density Measurements by Coherent Anti-Stokes Raman Scattering in a Nonequilibrium Shock Layer Flow," relates CARS results in a nonequilibrium shock layer air flow induced by a two-dimensional body. Results are compared to theoretical Navier-Stokes results with good agreement.

Paper 15, describes Planar Laser Induced NO-Fluorescence Spectroscopy experiments in the L2K arc-heated high enthalpy facility.

SESSION 6. SPECIAL TOPICS (2)

This session includes only one paper, number 16, "Time Resolved Temperature Measurements in Transonic Turbine Vane Wake Flows." The report describes use of a special temperature and pressure sensor traversed through the wake of a transonic cascade vane in a continuously running facility. The sensor response permits identification of

high frequency periodic behavior associated with vortex shedding and unusual temperature redistribution effects in the wake of cascade vanes.

SESSION 7. HOLOGRAPHIC INTERFEROMETRY

Paper 17, "Application of Optical and Interferometric Methods in Experimental Aerodynamics," describes many different techniques developed and employed at TsAGI, Moscow in a range of aeronautical applications. These include clever adaptations of classical shadowgraph, schlieren, and interferometer techniques and methods of video photogrammetry for measuring shape and displacement of solid surfaces including a system for measuring the aeroelastic deformation of a full scale helicopter rotor in a large wind tunnel. The paper contains many images showing typical results.

Paper 18, "Recording and Processing of Interferograms by Spectral Characterization of the Interferometric Chain," did not appear with English text nor abstract. Without having participated in the presentation and simultaneous translation, this reviewer is hard pressed to comment on the paper. It appears to present a study of circular cylinder wake shedding by high-frame-rate photography of using a color coded interferometer readout system.

Paper 19, "Advances in Aerodynamic Holography," is an review of holographic systems for a wide variety of applications. These include long-range holography, tomography, resonance and real-time holography, and four wave mixing. These examples are largely based on work performed at MetroLaser.

Paper 20, "Holographic and Tomographic Interferometry for the Study of Unsteady Compressible Flows," is an account of 2-D projection holographic interferometer results from a small supersonic wind tunnel and a nine-view 3-D tomographic interferometer studying a small round jet with screech. The system employs a pulsed ruby laser illumination system to freeze high frequency unsteady motion.

Paper 21, "Development of High Speed Interferometry Imaging and Analysis Techniques for Compressible Dynamic Stall," describes a specialized apparatus to produce multiple high quality interferograms for 2-D airfoil undergoing dynamic pitch motion in a air stream at $M=0.3$. A unique optical configuration called Point Diffraction Imaging (PDI), employs a pinhole as an optical mask which is produced in place by the illuminating laser. A time series of up to 224 sequential images can be captured by film photography at rates up to 40,000 frames per second. The results are impressive.

It is apparent from these papers that methods sometimes considered "classical" are far from static and undergo continuous innovation and evolution. It is also apparent that many of these developments applied to hypersonic, for example, might not be recognized by persons working in low speed flow. The opportunity to expose all the Symposium attendees to the entire range of applications may lead to serendipitous discovery.

SESSION 8. SKIN FRICTION MEASUREMENTS

The seven papers in this session constitute the most populous in the Symposium. That is welcome, as one sometimes has the impression that skin friction is the forgotten stepchild of aerodynamic parameters of interest, at least in the commercial airplane business. We

have never had a good way to measure it, so we learned to live without that information. The results presented below suggest that may change soon.

Paper 22, "Wall-Shear Stress Measurement with IR-Thermography," provides a useful summary of the skin friction problem and describes two new skin friction measurement methods. The first is a small sensor built into the model surface with a heater and a directional array of thermocouples. The other method employs a laser to momentarily heat a spot on the model surface. An IR camera then images the heated spot from which the time history of the temperature decay can be extracted. The advantage of the later system is that nothing is installed in the model itself.

Paper 23, "Skin Friction Measurement and Transition Detection Techniques for the Ludweig-Tubes at DLR," describes three different systems for facilities with short run times, very high unit Reynolds number and cryogenic temperatures. The three basic methods are oil film interferometer, heated thin films and thermocouples.

Paper 24, "Surface Forces Measurement of High Spatial and Temporal Resolution by Means of Liquid Crystal Foils and Piezofuels," describes experience with sensors intended for in-flight use at low speeds. The systems are: temperature responsive liquid crystal material on an electrically heated graphite film, piezofuel sensor arrays and surface hot film arrays. Despite the word "forces" in the title, the results presented are practically limited to use as transition detectors. The liquid crystal foil technique employs a layer of temperature sensitive encapsulated liquid crystal material applied over a thin sheet of graphite which is electrically heated. Results from an in-flight experiments with a large foil of 0.4-by-1.2-m dimensions on a laminar glove appear very effective. The visible patterns sometimes include high spatial resolution details of crossflow transition streaks. The piezofuel sensor is said to be very effective at responding to high frequency boundary layer disturbances in natural transition and forces excitation.

Paper 25, "Application of Oil Film Interferometry Skin-Friction to Large Wind Tunnels," is an engaging account of several demonstrations in production wind tunnels of this very simple technique. A frank discussion of the productivity limitations due to the one-shot nature of the measurements is presented.

Paper 26, "Visualization and Measurement of Surface Shear Stress Vector Distributions Using Liquid Crystal Coating," demonstrates the possibility of quantitative areal shear stress distribution measurements. The demonstration is limited to the case of circular jet impinging on a flat plate at a non-perpendicular angle. The discussion includes a useful review of the illumination and viewing requirements for detecting the color shift parameters related to the shear stress.

Paper 27, "Shear Sensitive Liquid Crystals in Subsonic and Transonic Wind Tunnel Testing," relates experience with liquid crystal coatings over a wide range of Mach numbers in a typical industrial wind tunnel setting to observe multiple surface features such as boundary layer transition, separation and reattachment, and shock wave position. Satisfactory results were demonstrated in qualitative visualization of transition and separation. Investigation of the prospects for quantitative measurement of boundary layer

parameters by analysis of color concluded that the problem was too complex for industrial wind tunnel applications.

SESSION 9. PRESSURE PAINT TECHNIQUES

The four papers presented in this session represent a good cross-section of the efforts underway around the world in this important technology.

Paper 28, "Applications of Temperature- and Pressure-Sensitive Paints in Aerodynamics," is a very effective review of most of the possible applications of this important technology so far identified. The potential advantages of lifetime or phase-shift measurements schemes are highlighted. The possibility of pressure paint application in a cryogenic flow is mentioned with extremely low concentrations of oxygen.

Paper 29, "Study Result for the Application of Two-Component PSP Technology to Aerodynamic Experiment," presents results of improved PSP technology to eliminate one of the most troublesome aspects of the method, the need for static reference images. In addition it was interesting to hear of this work from one of the originators of the basic technology, Prof. A. Orlov. Results of an application to a large helicopter rotor at forward speed are presented.

Paper 30, "Two-Component PSP Investigation on a Civil Aircraft Model in S2MA Wind Tunnel,," presents very high quality results of a production PSP application in the ONERA S2MA wind tunnel. A careful comparison with conventional pressure instrumentation suggests that the technology is fully suitable for routine use in an industrial production wind tunnel environment.

Paper 31, "Low-Speed Flow Studies Using the Pressure Sensitive Paint Technique," is an attempt to document the suitability of PSP for flow speed applications and to identify the limiting factors in such applications. Acceptable results at speeds as low as 20m/s were possible, but the potential source of errors are strongly dependent on so many environmental factors that these findings are not generally applicable.

SESSION 10. BALANCE AND MODEL DEFORMATION MEASUREMENTS

These three papers return to the more mundane (but no less important) concerns of wind tunnel testing technology. They are a useful reminder that incremental progress in conventional technology is equally important as technology breakthroughs.

Paper 32, "Status of Internal Strain Gage Balance Development for Conventional and for Cryogenic Wind Tunnels," relates the results of 12 years of improvement effort in Germany for the design, fabrication and calibration of internal balances for cryogenic wind tunnels. These efforts have relied on electron beam welding methods and the development of automatic calibration apparatus. Application of these results to conventional wind tunnel testing environments is an important outcome.

Paper 33, "Summary Report of the First International Symposium on Strain Gauge Balances and Workshop on AoA/Model Deformation Measurement Techniques," is a account of the symposium sponsored by NASA in October, 1996. The views of the nine panel members are summarized and a short discussion of the papers presented are given

in the separate topics of balance design and automatic calibration, mathematical modeling and uncertainty analysis. A workshop on AoA and model deformation, immediately following the balance symposium is briefly discussed. A list of paper titles and authors is presented.

Paper 34, "Model Deformation Measurements at NASA Langley Research Center," describes the rationale for and the development of a video-photogrammetry system being used in several NASA wind tunnel facilities. Examples from the 16-foot, UPWT 12-foot, NTF, TDT, and 12-foot semi-span facilities are described. Another technology, Projection Moiré Interferometry is briefly described.

SESSION XI, SPECIAL TOPICS (3)

The single paper in this session, and the final event of the Symposium, paper 35, "MEMS Applications in Aerodynamic Measurements Technology," offers a fascinating, if not teasing, view of future sensor technology using Micro-Electro-Mechanical-Sensor methods. It is apparent that much of the promise of this technology is still far from routinely practical.

OBSERVATIONS ON FLOW FIELD MEASUREMENTS

It is appropriate to make a few observations about the trends in industrial flow field surveys, as exemplified by the papers in sessions 2 and 3. There is increasing recognition that the flow field contains useful information that has not heretofore been properly exploited. There may still be a poorly developed sense of what actual benefit can be realized from the flow field data, however. There is also an almost universal presumption that a measurement system offering instantaneous data capture with no physical probe in the flow enjoys an obvious, if not overwhelming, advantage compared to a system requiring data acquisition over a long time using a physical probe in the flow.

Clearly, for flows having a significant variability in time, and which might be critically unstable to small disturbances, the above attributes might be essential. However, there are a large class of aerodynamic flows, with significant economic importance, that do not fall in that category. The productivity of an apparently conventional probe traverse system can be vastly improved over past conventional practice. The results reported in paper 12 show that a complete airplane wake survey has been accomplished in less than 20 minutes with the potential for further reductions by a factor of 2 or more. The data acquired in such a survey, comprising nearly 50,000 individual measurement points, can provide incredible detail of the spatial distributions of lift and drag and can provide a separate measure of induced drag, which has never before been accomplished.

In almost all cases these flow fields are stationary and can be accurately characterized by long time average measurements. Even though a physical probe located in the flow field may produce a disturbance, our experience shows convincingly that the disturbance can be nearly insignificant. In fact the traversing machinery is, by far, a more significant disturbance than the actual probe. By careful design and integration with the wind tunnel facility, minimal overall disturbance is possible.

Furthermore, on the issue of intrusiveness, there are many ways to characterize it, besides a physical presence in the flow. Cost and complexity are, in some cases, far more important to the success of an experiment, than a small probe positioned in the flow.

A final point: velocimeters measure velocity. An aerodynamic flow field in the wake of a vehicle cannot be completely characterized by distributions of velocity components alone. The local total pressure in the wake must also be measured if there is to be a determination of the profile drag. In addition to quantitative measurements, the size, shape and character of the wake, defined as the area of reduced total pressure behind an airplane, can be an extremely graphic qualitative indicator of many important aspects of aerodynamic flows.

Review of optical methods for fluid dynamics

A L Heyes and J H Whitelaw
 Department of Mechanical Engineering
 Imperial College of Science Technology and Medicine
 Exhibition Road
 London
 England
 SW7 2BX

ABSTRACT

There are many methods for measuring the velocity, pressure and temperature characteristics of the flows around solid bodies and this paper considers their relative advantages with special consideration of the needs of wind tunnels. The emphasis is on optical techniques for which brief descriptions of the principles and requirements are provided together with an indication of applications and their findings.

1. INTRODUCTION

The descriptions and discussion which follow apply to all forms of external aerodynamics though they focus more closely on the requirements of aircraft and, in particular, of model testing. It can be difficult and expensive to make accurate measurements in flight so that improvements in drag performance are often judged on fuel consumption over a very long flight and in high-lift performance by flight tests with angle of attack close to stall and consequent risk. Exceptions include the use of tufts and dyes, as described for example in references 27 and 49, and the more recent use of laser-Doppler velocimetry, reference 51; the former are necessarily qualitative and the latter still at the development stage though with excellent possibilities. In both cases, a priori knowledge of the flow region of importance is essential and may be acquired from computations or from model tests or some combination of the two.

Models are manufactured to scales which allow more convenient examination than the real vehicle which, in the case of aircraft and flight, invariably means smaller and within a wind tunnel. The related problems of scaling are well known though solutions are less readily available. Transition occurs at a similar physical distance in model and reality but the corresponding chord Reynolds number may be different by factors of more than ten so that physical knowledge is required and is not always sufficiently accurate to ensure proper scaling. Further information is available in many previous contributions including those of references 84 and 85.

In general, it is much easier to measure the flow around a model in a wind tunnel than over a vehicle in flight. Thus, for example, the Pitot tubes of flight are generally stationary whereas those in a wind tunnel are usually readily translated; and the laser-Doppler anemometer of reference 51 had to measure in a predetermined region whereas those of wind tunnels are, at least in principle, limited only by optical access. The extrapolation from wind tunnel to flight is not, however, a simple matter with implications for tunnel and model arrangements and for the ability to correctly simulate transition and separation. This topic is not considered here but remains of fundamental importance and with imperfect resolution so that skill is often required to interpret wind-tunnel measurements. It is important to remember that static pressure holes, thermocouples, Pitot tubes and even hot-wire systems are much cheaper to obtain or fabricate, and easier to use, than the optical techniques considered here.

The methods considered here for the measurement of pressure and temperature require that the surface be coated with material which is sensitive to the property to be measured and that it can be viewed conveniently by a camera or cameras. This is likely to be easier to achieve in small wind tunnels. Also, it is desirable that the measurements be achieved at the same time as other measurements so that interference with other techniques, for example, the use of a pressure-tube rake, erosion or chemical interactions as a consequence of the flow, the tunnel pressure, droplets or particles have to be avoided.

It is useful to consider the requirements and possible advantages of the optical methods for the measurement of local velocity, namely laser-Doppler, particle-image and Doppler-global velocimetry, in a general way prior to the more detailed discussions of the chapters. Optical access is required for all optical methods and, for velocity measurements, this means for transmitted light beams and the observation of a measuring volume which may be a local region as for the first or a light sheet for the second and third. The lasers involve sufficient power to require the imposition of safety requirements as does the seeding material which the three techniques require to scatter light. The first method is in contrast with the second and third in that it measures on-line and discontinuous signals as a function of time at one local region with a measurement duration which depends on the concentration of droplets or particles; measurements at additional locations require that the measuring volume be moved. Particle-imaging and Doppler-global velocimetry observe a region of a light sheet which may be small or large, and is generally large for application to wind tunnels where an overview of the flow is required; as a consequence, the requirements of signal-processing instrumentation may be expected to be more extensive in terms of storage and speed of data transfer so that real-time information is more difficult to obtain. These light-sheet techniques are themselves different in that the former is based on observation of the movement of discrete droplets or particles and the latter on the movement of an ensemble of particles in the measurement region associated with each of an array of detectors, so that, the discrete phase for the second method may consist of higher concentrations of smaller sizes.

The purposes of the paper are to describe and appraise methods for the measurement of the important characteristics of external aerodynamic flows. The emphasis is on optical methods and comments on non-optical methods are included for completeness and to provide a more traditional base against which to evaluate the more modern optical methods. The descriptions and discussions have been prepared with reference to the application of the techniques on and around models in wind tunnels. It should be remembered, however, that wind tunnels have been in operation for many years and with instrumentation other than that based on optical methods. The measurement of drag still remains a main purpose of many wind-tunnel experiments so that the improvement of

drag-count accuracy has priority in many cases. Similarly, information from flow visualisation together with velocities from total-head probes and wall static pressure taps, are often sufficient for the aerodynamic designer

Of course, measurements are also required in liquid and in internal flows and the techniques reviewed here may also be applicable though with some different requirements. Optical access is required for the successful application of optical methods and may present special difficulties for some internal flows. Similarly, their application in liquid flows requires a transparent liquid and may involve problems associated with liquid and solid materials with different refractive indices. Also, the requirement for seeding is likely to be different since the number density of naturally-occurring particles may be larger in liquid than in air and the frequency range of turbulent fluctuations may be smaller by an order of magnitude or more.

Review papers reflect the experience and interests of the authors and are invariably conducted with a background of other reviews. Some of these previous reviews are introduced in the later sections of this paper. In addition, the reader is referred to the references 5,33,40 and 67 for recent reviews which encompass some of the topics considered here.

The paper has been prepared in two main sections, following this introduction. These sections consider surface methods for pressure and temperature and velocimetry techniques for local and free stream velocity characteristics. In each case, these chapters include brief descriptions of the techniques, a review of their application in wind tunnels and, where appropriate, comments on non-optical alternatives. The paper ends with a summary of the more important conclusions.

2. SURFACE TECHNIQUES

2.1 Surface pressure

The simplest way to measure surface pressure is to make use of holes normal to the surface and connected to pressure transducers. The design of the holes has been considered, for example, in Livesey et al (1962) to which the reader is referred for further information and it should be noted that there can be uncertainties associated with the holes, the orientation of the flow with respect to the body, the transmission of the pressure information, the transducer and the instrumentation which follows. It is also possible to measure surface pressure by observation of pressure-sensitive paint (PSP) and this topic is considered in the following paragraphs.

The method is based on the relationship between the intensity of the fluorescence signal from a coated surface or on the rate of decay of the fluorescence signal, to the static pressure at the surface and can be measured by photosensitive devices. The surface or model under investigation is usually coated with a layer of a photoluminescent medium suspended in a permeable adhesive binder, illuminated at a wavelength which causes fluorescence and observed by a camera. The potential advantage is that the pressure distribution over the surface can be recorded without the need for holes in the model whilst limitations may include the sensitivity of the method, optical access within wind tunnels and interference from other techniques including the particle or droplet-based Doppler methods for velocity measurement. Nevertheless, the method has been applied with success to wind tunnel models by Dowgwillo (1996) and to flight tests, Abbitt et al (1996). In most cases, steady state pressure has been measured but the response of the PSP to pressure fluctuations has also been examined, for example by Baron et al (1993) and Carroll et al (1996). The majority of the work reported has been carried out

in the aircraft industry and hence is concerned with the study of pressure distributions on aircraft models. Applications to the automotive and power industries have been considered by Burns and Sullivan (1995).

Basic principles

The sensitivity of luminescent materials to pressure has been known for many years, for example Kautsky (1939), and an early application to flow visualisation has been described by Peterson and Fitzgerald (1980). More quantitative measurements have been described by Ardasheva et al (1985) and Bukov et al (1992) and applications to aerodynamics have followed with emphasis on the measurement of intensity, the so-called radiometric method, and more recently on the fluorescence lifetime method. The two approaches are considered briefly in the following paragraphs and both depend on the Stern-Volmer relationship between intensity and pressure, that is:

$$\frac{I_0}{I} = \frac{\tau_0}{\tau} = 1 + Kc$$

where I is the luminescent intensity of the paint, I_0 is the luminescent intensity in the absence of oxygen quenching, τ is the time constant of the emission decay, τ_0 is the time constant in the absence of oxygen, K is the Stern Volmer quenching constant and c is the concentration of the quenching material.

Radiometric mode

An experimental arrangement for the measurement of intensity is shown in figure 1 and comprises a light source to illuminate the surface, an arrangement of lenses and a camera to record an image of the surface and a computer to process the results. If the concentration, c , is linearly dependent on pressure, then the Stern-Volmer relation for the radiative mode can be written as:

$$\frac{I_0}{I} = 1 + Kp$$

where p is the local pressure. I_0 is not known but using an image recorded at a known reference pressure, it can be cancelled out and the pressure field can be determined. In wind-tunnel applications, the reference image is usually obtained in the absence of the airflow and is referred to as the wind-off image.

The illumination source depends on the experimental conditions and on the particular form of PSP but is usually blue or ultra-violet and examples include a low voltage tungsten halogen lamp by Dowgwillo et al (1996), a mercury vapour lamp by McLachlan et al (1995), a CW argon ion laser by Morris et al (1993) and a pulsed Nd:YAG laser by Davis et al (1997). It should also be noted that that PSP can undergo photodegradation at a rate which is proportional to illumination intensity so that high energy lasers sources must be used with caution, McLachlan and Bell (1995). The image recording system usually includes a filter to ensure that only the PSP emission is recorded and CCD cameras are usual, with best precision achieved by using a scientific grade, cooled CCD camera with a slow readout rate and 16 bit resolution.

Limitations of the radiometric technique in wind tunnels include model movement and distortion, temperature variations, interference from other measuring methods and the response of the PSP's to pressure fluctuations. The normalising procedure used to cancel I_0 requires an intensity

ratio to be formed for each point on the model surface using the wind-off and wind-on images. Movement and distortion of the model under wind-on conditions therefore leads to errors and the problem is compounded by variations in the illumination intensity across the model surface. The extent of this movement/distortion may be measured precisely using optical methods. Care must also be taken to align the images prior to normalisation and registration techniques have been reviewed by Bell and McLachlan (1996) where it is claimed that image alignment to between 0.1 and 0.2 pixel widths can be achieved. Methods of transforming the two-dimensional image to the three-dimensional model surface were also considered by this author. The emission characteristics of PSP's vary with temperature and, according to Schanze et al (1997), temperature dependence of the diffusion of oxygen into the binder is also a factor. Temperature variations between calibration and measurement can be dealt with but spatial variations across the surface of a model present a greater problem and require that the surface temperature distribution be measured. This might be achieved using paints sensitive to both temperature and pressure (Gallery (1994)) and multi-layered coatings, alternative stripes or painting half a symmetrical model with PSP and the other half with TSP are all possibilities McLachlan (1995). Davis et al (1997) measured temperature variation by covering a PSP with an impermeable PVA coating thereby rendering it sensitive to temperature only. The possible problems associated with the seed material used in relation to optical methods of measuring velocity are unknown but it should be noted that measurement precision can be impaired by flow borne dirt and oil from skin excretions so that careful handling practices are required, and may auger badly for simultaneous velocity and pressure measurements. Carroll et al (1996) studied the response of various PSP's to a step change in pressure from 0.7kPa to atmospheric. It was found that the response was limited by the rate of diffusion of oxygen into the binder and response times of 0.05 to 2.5 seconds were observed.

Applications of the PSP technique in the radiometric mode include the measurement of the pressure distribution on aircraft models in wind tunnels and McLachlan and Bell (1995) have provided a comprehensive review. McLachlan et al (1995) examined the pressure on a highly swept wing in supersonic flow. With in-situ calibration, the precision of pressure measurements was reported to be 0.6 kPa whilst using a-priori calibration and known surface temperature, precision of the order of 10% was obtained. Dowgwillo et al (1996) reported measurements on a model of an F-15E fighter at a range of transonic Mach numbers. A-priori calibration was carried out and in-situ pressure tappings were used to make temperature compensation. Images were recorded with exposure times between 1 and 3 seconds and high speed image processing enabled the pressure distributions to be observed on-line. The precision of the pressure measurements was reported to be better than 3 kPa based on a 95% confidence interval. Cler and Lamb (1996) used the PSP technique to study the pressure distribution in a supersonic nozzle. The nozzle was equipped with a number of pressure tappings so that in-situ calibration could be employed. As the nozzle pressure ratio was varied from 2 to 10 and the pressure range seen by the paint varied from 7.3-15.5psi to 18.5-50.5psi the mean error in the PSP data varied from 2.13% to 3.33 %. The increase in error was due to the decreased SNR ratio observed at the higher pressures.

Lifetime mode

When excited by a pulsed light source, the fluorescence from a

PSP decays rapidly. A simple model of the time dependent intensity is given by the expression :

$$I = I' e^{-t/\tau}$$

where I is the luminescent intensity, I' is the maximum intensity and τ is the decay time constant which is a function of pressure according to the Stern Volmer relation. Two detectors are used to integrate the fluorescence signal over two contiguous time intervals, as shown in figure 2 and the ratio of the signals from the two detectors can then be shown to be :

$$\frac{S_2}{S_1} = \frac{\int_t^{2t} I dt}{\int_0^t I dt} = \text{EXP}\left(-\frac{(1 + Kp)t}{\tau_0}\right)$$

This signal ratio is sensitive to pressure changes but is independent of illumination intensity so that there is no need for uniform illumination over the model surface or for a reference image. The technique can also be implemented using a modulated light source with the paint fluorescing with a sinusoidal oscillation with modulation a function of the phase difference which is in turn a function of the decay time constant and of pressure.

Holmes (1997) has shown that the lifetime method can give rise to small uncertainties at high pressures, in contrast to the radiometric technique, and this, coupled the insensitivity to variations in illumination and, therefore, model movement makes it attractive for wind tunnel use. Davies et al (1997) have constructed a system based on a modulated light source in the form of a diode pumped Nd:YAG laser able to scan a surface at a rate of 10,000 points per second with precision better than 1% provided temperature effects are correctly represented.

2.2 Surface temperature

Temperature distributions can be measured in a number of ways including the use of paints and liquid crystals, and with excellent sensitivity in limited ranges. The temperature can then be determined remotely with the aid of CCD cameras and the results transferred to computers in the same way, and with many of the same potential problems, as with corresponding signals for pressure.

Temperature sensitive paints

In the previous section it was pointed out that luminescent paint formulations used for pressure sensing also show sensitivity to temperature. This was regarded as a source of uncertainty in the measurement of pressure but it may provide a convenient method for surface temperature measurement, or luminescent thermometry as it was called by Gallery et al (1994). The physics of the process is similar to that for pressure measurement so that an active molecule may fluoresce with appropriate lighting. Molecular collisions may cause non-radiative de-excitation, Crites and Morris (1997), and this thermal quenching is temperature dependent affecting both the lifetime and intensity of the fluorescence either of which may be used to measure temperature. Under ideal circumstances, the luminescent material would be sensitive to temperature alone but some pressure sensitivity may be unavoidable. Davis et al (1997) overcame this possible limitation by over-painting a pressure sensitive paint with an impermeable PVA coating preventing diffusion of oxygen in

and out of the paint layer thereby rendering it sensitive to temperature changes only. Gallery et al (1994) used rhodamine B base as the active ingredient in a temperature sensitive paint and reported that it shows no sensitivity to pressure over a range from vacuum to ambient conditions and allowed temperature measurements in the range 10 to 70°C. The system was demonstrated by measuring the temperature distribution on an airfoil in a wind tunnel at Mach numbers from 0.32 to 0.56 and with results within 1°C of those measured by thermocouples. These applications aimed to provide simultaneous measurements of pressure and temperature and Gallery and Buck (1995) discussed the possibility of dual and triple sensor paints to measure pressure, temperature and illumination intensity.

The implementation of luminescence thermometry using thermographic phosphors has been considered by Allison and Gillies (1997) and a wide range of phosphors are known to offer temperature sensitivity over a very wide range of temperature. An early implementation of the technique is that by Bradley (1953) where the temperature distribution on a flat plate in a supersonic flow was measured in the range 8-25°C with an uncertainty of $\pm 0.2^\circ\text{C}$. Certain phosphors have a range of fluorescence emission lines, some insensitive to temperature change, and this property can be used to reduce effects of non-uniform illumination, as by Goss (1989). Micol (1995) has also used this two-colour technique to study surface temperatures on a model of a space shuttle orbiter model in a hypersonic wind tunnel and was able to determine heat transfer coefficients with an uncertainty of $\pm 15\%$. Bizzak and Chyu (1995) used the same approach to examine hot jet impingement

Liquid crystals

Liquid crystals have molecular structure similar to that of a crystalline solid and an isotropic liquid and this variable structure enables them to be used to sense temperature. A review of the process is provided by Jones (1992). When white light is incident upon a liquid crystal, interference effects cause light of wavelength equivalent to the pitch of a characteristic helical molecular arrangement to be selectively reflected and, temperature differences are revealed as colour changes. A dynamic range of up to 20°C can be achieved at temperatures from -30 to 130°C and with accuracy's of up to $\pm 0.2^\circ\text{C}$. Roberts and East (1996) review the application of liquid crystals to hypersonic flows and include consideration of image-processing methods. The method has been used successfully in many laboratory applications, including small wind tunnels as by Martinez-Botas (1995) and in a stirred reactor by Yianneskis et al (1994). Klein and Margozi (1969) demonstrated that liquid crystals are also sensitive to shear stress. Reda and Aeschliman (1992) used them for this purpose in the laboratory and Holmes et al (1986) in flight tests. Reda and Muratore (1994) developed a more quantitative approach to measure the shear stress angle to within $\pm 1^\circ$ and magnitude to within $\pm 5\%$. The possibilities are encouraging but far from application in production wind tunnels.

3. LOCAL VELOCITY CHARACTERISTICS

3.1 Flow Seeding

All of the velocimetry techniques reviewed in this section require the flow under investigation to be seeded with particles or droplets and it is the velocity of these seeds which is subsequently measured. In this section, overall seeding requirements as they apply to all the velocimetry technique will be considered. Requirements specific to individual

techniques are also discussed.

Simply stated the requirements of flow seeding are that they faithfully follow the flow in which they are suspended, that they scatter sufficient light to be detected and that they are present in appropriate quantities.

There have been a number of theoretical and experimental investigations of particle response including the response of particles to turbulent flows (Bachalo et al (1987) and to the flow through shock waves (Feller and Meyers (1975), Nichols (1985) and D'Humieres et al (1991). As an example, droplets or particles of the order of $2\mu\text{m}$ in diameter are required to follow the turbulent fluctuations of a 20 m/s turbulent flow and one tenth of this size is required to resolve the rapid change in velocity across a shock wave shock wave with an upstream velocity slightly above supersonic.

Light scattering by particles in the above size range is described by the Mie theory (Van De Hulst (1957)). The scattered intensity is dependent on direction with the light scattered in the forward direction (i.e. in the same direction as the illuminating radiation) being the most intense by a factor of as much as 1000 over the light scattered in the backscatter direction. LDV and PIV are techniques that require individual seeding particles to be detected. With LDV scattered light can be collected in any direction so that forward scatter should always be preferred where optical access permits. With PIV the collection optics are placed in a side scatter configuration to record an image of the seeding particles suspended in the light sheet. This is the weakest scattering direction so that illuminating intensity must be high if particles are to be detected. This limits the area of the flow which can be investigated. Adrian and Yao (1985) have shown that $1\mu\text{m}$ glass spheres in air require a minimum of about 150 mJ of laser light per 100 mm^2 of light sheet cross sectional area for successful imaging. With DGV it is not necessary to resolve individual seeding particles, but to record the intensity of light scattered from a particular region of the flow. If many particles pass through this region during the data collection period then the signal obtained represents the ensemble average of the velocities of these particles. In supersonic wind tunnels this offers the interesting possibility of using condensation droplets as seeding. These droplets are an order of magnitude smaller than the wavelength of visible light (Wegner and Stein (1968)) and hence scatter too little light for use with LDV or PIV. However, they are present in such quantities that a strong DGV signal can still be obtained. Meyers (1995) has successfully used this method to study the flow over a delta wing at Mach 2.8.

Generating seeding particles and injecting them into the flow presents a number of difficulties. First it is important to recognise that particles are potentially harmful to health either because they are made of toxic material or because they are ingested and remain attached to lung tissue. Also, it is desirable that wind tunnels and the models within them remain clean and without coatings of liquid or solid material which may alter the aerodynamic characteristics and add to the problem of general cleanliness. Equally, liquid or solid materials are unwelcome coatings to walls, rotating machinery, screens and honeycombs and perfect filters to do not exist. Thus, droplets and particles are generally unwelcome within wind tunnels and it would be advantageous to select droplets or particles that exist in the region of interest and evaporate or sublimate else where. More practically, it is desirable to seed locally so as to minimise the quantity of seed material and to run the test for a short a period as possible, with subsequent cleaning of surfaces. However, with this

approach care must be taken to ensure that the region of interest is uniformly seeded to avoid problems associated with velocity biasing.

Some examples of the seeding methods reported in the literature and the difficulties encountered are as follows: Towers et al (1991) used polystyrene microspheres in monodisperse sizes from 0.3 to 2.7 μm to study flow in a transonic wind tunnel using PIV. The particles were suspended in a liquid and injected into the flow using sixteen nebulisers placed 9m upstream of the measurement area to form a plume with a seeding density of only 3 particles per cm^2 in the image plane. Meyers (1996) used smoke locally injected upstream of an aircraft model to study flow using DGV in a large scale subsonic wind tunnel. He reports that at the edges of the seeding plume data quality was degraded resulting in large uncertainties. Lienhart (1996) used LDV to study the boundary layer over a wing in flight. Here, natural seeding was utilised so that in clouds or haze data rates of several kilohertz could be achieved but in clear skies rates of only 150 to 200 Hz were observed. Elena (1987) reported that in a supersonic wind tunnel the wake of a local seeding injector can significantly effect the flow even if the velocities at the injector outlet and in the flow are matched and the injector is placed upstream of the tunnel throat. Heyes (1994) overcame this in the study of the flow over a delta wing in a small-scale supersonic wind tunnel using LDV, by seeding the entire flow in the plenum chamber using 0.6 μm polyethylene glycol droplets injected by a commercial seeding generator. Data rates of up to 20kHz were achieved but the wind tunnel windows and the model surface were quickly coated with seeding liquid and regular cleaning was necessary. Supersonic condensation as discussed above and used by Meyers (1995) enables the entire flow in a supersonic wind tunnel to be seeded regardless of scale and the particles are automatically dissipated downstream of the terminating shock by re-evaporation. This may prove to be a convenient method of seeding supersonic tunnels for the purposes of DGV.

3.2 Laser-Doppler velocimetry

The technique of laser-Doppler velocimetry is well established and the books of Dust, Melling and Whitelaw (1981) and Drain (1980) provide useful descriptions. It is based on light scattered from particles or droplets so that the results are representative of the flow provided the discrete phase follows the flow.

Laser-Doppler velocimeters can operate with light scattered from droplets or particles in any direction but with consequences for the amplitude of the scattered signal. Near-forward scattered light provides the largest signal and a typical optical arrangement is shown on figure 3; an alternative operating with back-scattered light is also shown. In a 5 m working section, it is necessary for the transmission lens to have a focal length of around 3 m and for the beam separation to be hundreds of mm. Thus, the transmission lens has to be large and, since the throw of light is long, of good quality. The use of the same lens to collect light implies a collection cone which is comparatively small so that single-to-noise ratios are likely to require high efficiency photodetectors and signal-processing instrumentation with the ability to separate signal from noise. Rejection of signals from some droplets or particles also causes reduced data rates.

It is usually required that the measurement of a velocity at one location be followed by measurement at subsequent locations and this involves traversing the measuring volume which can be achieved by moving the instrumentation usually along a

line and with measured points separated by predetermined distances. This is likely to be acceptable for one traverse, say normal or near normal to the surface of a model but it does require time; perhaps one minute per point to acquire sufficient acceptable signals to form a single-point measurement with acceptable statistical accuracy, and thirty minutes for a traverse. The same information can be obtained with greater efficiency by sweeping the measuring volume, for example by reflecting the transmitting light beams from a rotating mirror. Equally, the transmitted light beams may be divided to form several measuring volumes which allows information to be acquired simultaneously from each measuring volume or, more realistically, in rapid sequence but, of course, with reduction in the data rate from each measuring volume as a consequence of the reduced light intensity. The movement of the instrumentation to allow measurements in a different axial plane requires more effort and this applies also to PIV and DGV as described below.

The above discussion was based on the measurement of a single component of velocity and with direction known from the geometry of the optical component so that the transform equation,

$$V' = \Delta v \frac{\lambda}{2 \sin(\alpha/2)}$$

allows a direct link between the velocity (V') orthogonal to the bisector of the angle between the two incident light beams (α), the measured frequency shift (Δv) and the laser wavelength (λ) each of which can be measured to high precision. Thus the relationship between the measured frequency and the required velocity is linear whereas the measurement is as discontinuous as the combination of the particle number density, the optical components and the signal-processing system allow. In contrast, hot wires have a non-linear transform equation with calibration essential and a continuous signal, though with inaccuracy increasing with turbulence intensities around 15 %.

The measurement of velocities which are negative, either mean or instantaneous, is comparatively easy with laser-Doppler velocimetry since the frequency of one or both of the transmitted light beams can readily be altered by rotating gratings or Bragg cells. In contrast, hot-wire anemometry requires that the wire be moved at a known velocity as, for example by Thompson and Whitelaw (1984).

The measurement of two components of velocity can be achieved by two sets of orthogonal incident light beams, usually with wavelength different from each other. The two beams may be obtained from the same laser with a prism to separate the colours and with reduction of the light available to scatter light for each component. The measurement of three components is possible in principle but always implies a compromise in the accuracy of measurement of one component and further reduction in the light available to scatter light for each component.

3.3 Phase- and Shadow-Doppler velocimetry

The measurement of the dimensions of droplets or particles simultaneously with velocity can be achieved by variants of laser-Doppler velocimetry and these techniques have some importance to wind tunnels which make use of all scattered light since they provide information which determines the extent to which the droplets or particles follow the flow. Thus, they are described briefly below.

An arrangement of optical components for a phase-Doppler

system is shown on figure 4 and is similar to that for velocity measurements except for the three photomultipliers which receive signals at different times and with the phase difference proportional to the diameter of the droplet or particle from which the signal is received. The successful operation of phase-Doppler velocimetry requires careful selection of the angle at which the signals are received so that the diffracted light is responsible for the scattered signal. Thus, it is common for the receiving optical components to be located off the axis of the transmitting components in both planes and this can, on occasions, restrict the usefulness of the method. It does not work well with back-scattered light.

The consequence of the proper observation, recording and processing of a phase-Doppler signal is a number directly proportional to the curvature of the surface of the discrete phase. Thus, a spherical droplet or particle gives rise to a radius which uniquely describes the size. If the discrete phase comprises droplets or particles which are not spherical, the methods will still provide one number. Thus, misinterpretations are possible, for example, when an ellipsoidal particle or other shape passes through the intersection of the two light beams and the magnitude of the consequent uncertainty can be large. Similarly, particles with surface irregularities, for example glass beads with scratched surfaces, can result in erroneous results. Shadow-Doppler velocimetry is an alternative technique which can help to avoid the related errors.

Figure 5 shows an arrangement of a shadow-Doppler velocimeter. Using an Ar⁺ laser, a control volume is created as for a laser-Doppler velocimeter and the control volume imaged onto a photodiode array together with the images of any droplets or particles passing through the volume.

The receiving optics collect transmitting light so that an image of the measuring volume is formed, magnified by a microscope objective and projected onto a 32-element linear photodiode array. A particle passing through the measuring volume generates an image of its shadow on the linear array and the size and shape of the droplet or particle is determined from the size and shape of the shadow of the particle on the array. Since the presence or absence of the shadow is a binary phenomenon, the method is not based on signal intensity. Alignment is accomplished easily due to the width of the linear array and measurement is not sensitive to minor displacement caused by displacement of the windows or beam motion due to gradients of refractive index. The outputs of the diode array are digitised, stored and passed to a PC computer for display and processing. The processing includes compensating the measurement for the Gaussian light distribution in the control volume and the generation of a two-dimensional shadow from the temporal output of a one-dimensional array. The size of the irregular particle can be registered as a single number, corresponding to the diameter of a sphere and in common with phase-Doppler velocimetry, this has the same area as that measured from the projected area. Alternatively, and with precision depending on the number of diodes per particle image, the shape of the droplet or particle can be identified. More details of the instrument, the data acquisition and processing and the validation criteria can be found in Hardalupas et al (1994) and Morikita et al (1997). It should be noted that the sampling rate per photodiode implies a limit between precision and the maximum velocity of the droplet or particle and that the measurable size has a dynamic range of around 10:1 in a range from 10 μ m to a few hundred microns.

To date this technique has been used mainly to measure coal

particles in swirl-stabilised flames as for example by Prassas, Taylor and Whitelaw (1997a&b).

3.4 Particle-image velocimetry

Particle image velocimetry (PIV) allows near-instantaneous velocity vectors to be obtained throughout an illuminated and usually planar region of a flow and this is achieved by tracking the positions of seeding particles, naturally occurring or artificially introduced. Thus, images of the particles are recorded at discrete time intervals and successive images of the same particle identify a velocity vector. If particles are well distributed throughout the region of interest, a near-instantaneous map of velocity vectors can be obtained. The development of PIV owes much to the early contributions of Adrian (1984) and Pickering and Halliwell (1985).

A typical configuration is as shown in figure 6 with a laser creating a light sheet and a camera viewing particles illuminated by it and in a direction normal to the plane of the sheet so that the object plane of the camera and the light sheet are coplanar. Multiple exposure images or a rapid sequence of single exposure images are then recorded. Variable exposure separation has been reported by Ferrugia (1995), two colour illumination and observation by Stefanini (1992) and single exposure frame sequences recorded on cine by Lin and Rockwell (1994) or on video by Willert and Gharib (1991). The method by which to extract velocity information from the images depends on the number density of observed particles. If it is small, the images can be paired to generate velocity vectors and this approach is usually referred to as particle tracking; if it is large, the images are divided into interrogation regions each containing a number of particle images. Within each interrogation region it is assumed that the velocity is constant, and spatial correlation is used to identify periodicity of the images and to determine a single spatially averaged velocity vector.

Velocity vectors can be determined simultaneously throughout a large region of flow and yield parameters such as vorticity and circulation, but time-dependent properties require a number of images to be recorded so that an ensemble average can be calculated. Additionally, a series of images may be used to observe the development of time dependent flows, as for example, by Willert and Gharib (1991) who recorded images at a frame rate of 30Hz to determine velocity changes in a water flow. Much higher frequencies are likely to be required in air flows particularly if small scales are to be identified and this, in turn, requires high speed image acquisition and an efficient processing algorithm.

The components of a PIV are considered in the following paragraphs and examples of PIV are described with emphasis on wind-tunnel applications.

The light sheet

The light source must be focussed to a well defined sheet of constant thickness and allow light to be scattered by particles and detected by the image collection system. Where multiple exposure images are required, rapid and short pulses must be generated with speed and length appropriate to the flow conditions. CW lasers are appropriate to low speed flows whereas pulsed lasers, such as the ruby, Nd:YAG or copper vapour lasers, are suitable for air flows and higher speed flows. These lasers offer a combination of short (of the order 10ns) pulse duration capable of freezing the motion of high speed aerodynamic flows at several hundred metres per second and high pulse energy suitable for imaging particles of sub-micron diameter.

The frequency doubled Nd:YAG laser offers particular benefits in that it can produce pulses of visible light (532nm) with energies of up to 500mJ and pulse duration's of around 10ns. The pulse repetition rate of a single laser is typically 20Hz and it is customary to operate two lasers in tandem thereby producing a train of double pulses at a frequency of 20Hz with an almost infinite range of pulse separations. This approach is well suited to situations where a single double exposure image or a series of un-correlated double exposure images is required. If transient-flow phenomena are to be characterised, a rapid sequence of frames is required and a copper-vapour laser can be preferable since it has a repetition rate of the order of 20 kHz, but with a pulse energy of the order of 10mJ so that larger seeding particles may be required.

Image Capture

Photographic emulsion and CCD arrays can both be used to capture images. CCD's have much to commend them: they can be sensitive and so enable the light scattered from very small particles to be detected and they allow direct transfer to a computer for processing. Their spatial resolution is, however, limited with 512 x 512 elements a common matrix and the area investigated is less than that which can be viewed using high resolution photographic emulsions.

Photographic emulsion is favoured in many investigations and has the advantages of wide dynamic range and good spatial resolution with 200 lines per millimetre common in commercial film. This approach is comparatively cheap and sequences of images can be recorded with high-speed cine cameras as by Lin and Rockwell (1994) and Oakley et al (1996). The major drawback is the time taken for film processing and the subsequent interpretation.

Signal processing

PIV data consists of either multiple exposure images or a sequence of single exposure images. If these are recorded using a CCD camera they may be down loaded directly to a PC in digital format for processing. If the images are recorded photographically they must be interrogated by some means, dependent on the processing technique, to extract particle image data and vectors.

The processing depends on the number density of droplets or particles achieved. For very low seeding densities particle tracking may be used with images paired to form velocity vectors as by Cenedese and Pagliarunga (1990), Hassan and Canaan (1991), Heyes and Turner (1992), Okamoto et al (1995), Siu, Taylor and Whitelaw (1996) and Gui and Merzkirch (1996). With increasing particle number density, this approach becomes time consuming and the alternative is to divide the image into a number of sub images referred to as interrogation regions sized so that it may be assumed that the velocity within each region is constant (see figure 7). A spatial correlation of each interrogation region can then be used to detect the particle image displacement. The correlation may be an auto-correlation, used for multiple exposure images, or a cross-correlation, used for frame sequence images. The maximum peak in the correlation indicates the most commonly occurring particle image displacement and therefore describes the velocity vector associated with the interrogation region. This correlation procedure is repeated for each interrogation region so that velocity vectors may be obtained throughout the image plane.

The reliability of the auto-correlation method is dependent on the number of particle image pairs per interrogation region, the size of the particle images and of interrogation region and

the velocity gradient within each interrogation region and these factors have been investigated, for example by Keane and Adrian (1990) and Lawson (1994). The amplitude of the maximum in the auto-correlation depends on the number of particle image pairs and, by defining a minimum acceptable signal to noise ratio, Keane (1990) showed that a minimum of 10 vectors are required in each interrogation region. Between exposures particles may move into or out of the interrogation region in both the in-plane and out-of-plane directions. This results in unpaired particle images generating noise in the correlation plane and impeding detection of the signal peak. The interval between exposures, the thickness of the light sheet and the size of the interrogation region may all be used to control this source of error. Keane has suggested that these variables should be chosen to ensure that the particle displacement represents no more than 30% of the dimensions of the interrogation region in the in-plane direction and no more than 30% of the thickness of the light sheet in the out-of-plane direction. It should also be noted that there is a lower limit on the displacement that can be measured due to the zero displacement peak in the auto-correlation plane. Velocity gradients within the interrogation region reduce the height and increase the width of the correlation peak. To combat this Keane has suggested that the particle displacements should vary by no more than one particle image diameter across the interrogation region.

A number of ways of implementing the auto-correlation processing technique have been developed. The earliest is the Young's fringe method. Here a photographic multiple exposure image is interrogated with an un-expanded laser beam each interrogation region being illuminated in turn. Pairs of particle images behave like double slits and a fringe pattern is generated the spacing and orientation of the fringes corresponding to the magnitude and orientation of the particle displacement in the interrogation region.

It is normal practice to record an image of the fringe pattern using a video camera and to process this image by taking a 2-D Fourier transform of the fringes thereby revealing the auto-correlation function. In the early days of PIV low speed computers made this approach time consuming and to combat this, an entirely optical processing technique of interrogating the fringe pattern was developed (Mao et al (1996) and Jakobson et al (1992). However, today, with the advent of high speed desktop computers, a direct imaging method has become the most common way of processing multiple exposure PIV images. Here, either, the PIV image is illuminated with an incoherent white light source and an image of each interrogation region recorded in sequence using a scanning CCD video camera or, the entire image is digitised using a frame scanner and interrogation regions defined digitally thereafter. In both methods the image data is passed to a computer for processing. A two dimensional auto-correlation is calculated by means of FFT's. This process is computationally intensive but relatively speedy due to modern computer power enabling an image which would have previously taken several hours to process to be processed in several minutes. A similar approach can also be used for processing if images of the flow are directly recorded by a CCD camera. This removes the wet processing and image scanning stages and thereby offers the potential for high speed and perhaps even on-line data processing.

Some of the performance limitations of the auto-correlation technique, discussed above, can be relaxed if single exposure images are to be processed since, here, the cross-correlation approach can be adopted.

Cross-correlation does not generate a zero order peak in the correlation plane. This has a number of advantages. It allows lower velocities to be measured and hence, adhering to the 30% displacement rule, enables smaller interrogation regions with commensurately greater spatial resolution to be used. By similar reasoning processing also becomes less sensitive to out-of-plane motion and velocity gradients.

Directional ambiguity

Two images of a particle can provide a two-dimensional vector and the direction of flow provided that the time order of the images is known. Image coding techniques can enable time order to be established and various methods have been suggested. Marko and Rimai (1985) used variable pulse duration's to create images as a series of dots and dashes but processing is problematic. Gharib et al (1985) used phosphorescent particles which produced a bright images followed by decaying streaks but, again, post-processing was required to determine direction. Farrugia et al (1995) preferred a three-pulse sequence which also required specialised processing but here a triple-correlation algorithm was developed to extract vectors and direction automatically.

Reeves et al (1995) described a polarisation sensitive mask which enabled the light scattered by particles from each pulse to be distinguished. A pockel cell was used to give successive laser pulses orthogonal polarisation. The mask enabled the scattered light from each pulse to be differently spatially filtered so that orthogonal fringes were superimposed on the particle images. Digital filtering then separated the exposures to allow cross correlation processing. Successive images may also be colour coded as by Stefanini (1992) with a combination of a CW argon ion laser and a ruby pulsed laser. Copper vapour lasers with their dual wavelength output can be used to achieve the same result.

Where the time-record of images is not known, it is necessary to make use of shifting methods similar to those described earlier in connection with laser-Doppler velocimetry. In the case of PIV, it is necessary to shift the image as described, for example by Adrian (1986) and shown in figure 8. A shift is applied to the particle images so that the vectors are in the same direction and the known shift is subtracted by the computer to provide the true vectors complete with their direction. The size of the shift applied must be greater than the maximum reverse flow velocity and sufficient to ensure a non-zero vectors.

Methods of image shifting have been reported by several authors. Wormell and Sopchak (1993) developed a system with a high resolution CCD camera to record double exposure PIV images and electronically moved the first image across the CCD chip by up to 16 pixels in a time interval of less than 150 ms. Landreth and Adrian (1988), Lourenco (1993) and Molezzi and Dutton (1993) makes use of the beam-steering characteristics of bi-refracting crystals so that successive laser pulses experienced different deflections as they passes through the crystal. Raffel and Kompenhans (1995) preferred the use of a rotating mirror in front of the camera which was able to apply image shifts up to 500 m/s.

Applications

Many applications of PIV have been described and most seem to be demonstrations of the method rather than its use to determine new information of fluid mechanics and this reflects the relative newness of the method. Recent examples include those of Liu et al (1996) who used a stereoscopic PIV to investigate a turbulent boundary layer, Bryanston-Cross et al

(1991) who applied PIV to the flow in a transonic annular turbine cascade, Reeves et al (1996) who reported measurements in a firing internal combustion engine and Lawson et al (1994) who examined the flow through a normal shockwave in a de Laval nozzle. An excellent review has been provided by Adrian (1991) and, together with co-authors, he has made useful contributions to fluid mechanics. In the comments which follow, applications of PIV to aerodynamic studies primarily in wind tunnels are described and it should be noted that they also tend to be demonstrative with little new knowledge of fluid mechanics. There is also a tendency to provide limited information of seeding densities, and few substantiated estimates of the ability of seeding material to follow the flow.

Shih et al (1995) report the study of leading and trailing edge flows on a pitching airfoil (NACA 0012) in a water filled towing tank. Towing speed was varied from 5-25cm/s giving chord Reynolds numbers in the range 5000 to 25000. Seeding particles were commercial metallic coated particles of diameter 11µm and a specific gravity of 2.6, illumination was provided by a CW argon ion laser beam reflected from a rotating polygonal mirror. Images were recorded photographically with image shifting being employed to resolve directional ambiguity. Processing was by the Young's fringe method and calibration showed that an uncertainty of 1.5% was present in the velocity measurements. Instantaneous velocity and vorticity fields were obtained but no cycle resolved data was recorded. At the leading edge primary separation, interaction of the primary vortex with the reversed boundary layer and subsequent secondary separation were observed.

Wernet et al (1996) describe an investigation of the dynamic stall vortex on a pitching airfoil placed in a low speed wind tunnel with a freestream velocity of 28m/s and pitched up and down at a frequency of 6.67 Hz. The tunnel was locally seeded with olive oil droplets of diameter 1µm using several Laskin nozzles. Double exposure PIV images were recorded photographically, illumination was provided by a dual oscillator Nd:YAG laser and a rotating mirror image shifting mechanism was employed. Image processing was by the Young's fringe method and typically 3000 vectors were extracted per image. Images were recorded at a rate of about 1Hz so that a cycle resolved image sequence could not be obtained. Good agreement was seen between experimental data and a numerical prediction of the flow field although cycle to cycle variations of the flow were observed.

Horner et al (1996) investigated blade vortex interaction to simulate the interaction of a rotorcraft blade with the tip vortex from a preceding blade. A rotating NACA 0015 airfoil section of chord 0.149m and radius 0.94m was placed in a low speed wind tunnel with a free stream velocity of 47 m/s and rotated to give a tip speed of 59m/s. A vortex generator was placed upstream of the rotor to generate a vortex whose axis coincided with that of the tunnel. PIV measurements were made in a cross sectional plane at 90° to the free stream. The tunnel was seeded with 20µm micro-balloons with an average specific gravity of 0.06 and illumination was provided by a pulsed ruby laser. Images were recorded photographically using a 35mm camera and a triple pulse sequence with varying pulse separation was used to code the images and provide directional information. Processing appears to have been by a particle tracking method since actual particle image pairs were identified. The processing technique used took up to two hours per image and hence only selected images were processed. This study provided quantified flow visualisation of the

splitting of the imposed vortex for head on collisions and enabled secondary vortex generation to be observed and its effect studied.

Willert et al (1996) reported the use of high speed video and high resolution CCD imaging systems. Both systems allowed single exposure image pairs to be recorded and hence cross-correlation processing. The purpose built high speed system allowed a minimum exposure time of 0.8 ms and a minimum image separation of 0.8 ms and was demonstrated in a free jet at some 60 m/s with seeding by olive-oil droplets of 1 μ m diameter, an imaged area of 45 mm by 30 mm and velocity uncertainties of around 0.4 m/s. The high resolution system included a 1000 by 1000 pixel interline transfer camera which allowed image separation to 1 μ s and a continuous sequence of images to be recorded at a frame rate of 15 Hz. It was used to study tip vortices from helicopter rotor blades in a wind tunnel with free stream velocities of up to 31 m/s, a working section of 6 x 8 m and an imaged area of 65 x 65 mm. The freestream velocity was nearly perpendicular to the light sheet and uncertainties in the in-plane velocities were large. In this study vectors were observed within 30 seconds of image capture so that during the test the camera could be relocated to view several areas and concentrate of regions of particular interest.

Stewart et al (1996) examined the wake behind a 1/8th scale model car and the flow over a swept wing in a 3 x 1.5 m low speed wind tunnel with a pulsed ruby laser and seeding by an oil smoke generator. Double exposure photographic images were recorded and image shifting by a rotating mirror allowed the determination of the flow direction. A two camera stereoscopic imaging system was developed primarily to remove parallax errors but which also enabled through-plane velocity components to be measured. In both studies the light sheet was oriented at 90° to the freestream but the out-of-plane motion was less than 30%. Significant differences were noted between the instantaneous car wake flow and that obtained by point measurement using a split film probe. The instantaneous flow consisted of a random series of vortices whilst the flow field obtained with the probe showed a single large scale vortex. However, by averaging 10 instantaneous PIV vector fields qualitative agreement between the PIV and probe measurements was observed.

Bryanston-Cross et al (1995) examined transonic flow in the wing-pylon region of a 5.7% scale model of a wing and engine combination in a 2.74 x 2.44 m transonic tunnel. Seeding was with polystyrene spheres of 0.5 μ m diameter and a CCD camera was used to collect double exposure images without image shifting. The imaged area was 25 x 25 mm and 16 coplanar images were summed so that an area of 0.1 x 0.1 m was examined. The light sheet was oriented parallel to the freestream, the seeding was sparse so that a particle-tracking algorithm was used, and velocities in excess of 300 m/s were measured with an uncertainty of $\pm 2\%$ and the existence of a cross flow shock was detected.

3.5 Doppler global velocimetry

Doppler global velocimetry (DGV) allows flow velocities to be obtained by measuring the Doppler shift in the frequency of light scattered by seeding particles suspended in a flow and illuminated by a laser light sheet. The principle is similar to that of LDV technique and one of the common features is that the frequency shifts generated by the flow velocities are usually too small to be measured directly. With LDV, this problem can be overcome by heterodyning the Doppler shifted scattered light with unshifted light or with light scattered

through a different angle and with DGV, the Doppler shifted, scattered light is collected through a spectroscopic cell. If the laser frequency is centred on an absorption line of the material in the cell and has a bandwidth less than the width of the absorption line, changes in frequency due to Doppler shift will cause a change in transmission. Therefore, if an image is formed of the light sheet, frequency variations will be manifest as variations in the intensity of the image so that, with appropriate calibration information, velocity may be calculated throughout the illuminated region.

There are many substances with absorption lines in the visible part of the electromagnetic spectrum and that chosen for DGV has usually been iodine vapour, partly because its absorption spectrum is well known, see for example, Gerstenkorn and Luc (1979). Iodine vapour has also been used to stabilise the frequency of lasers including the Argon-ion laser, as by Camy (1977) and Chebotayev (1990), and the Nd:YAG laser, as by Arie (1993) and both are suitable lasers for DGV.

The layout of a simple DGV measuring system is shown in figure 9 with a CCD video camera to record an image of the light sheet. In theory the image should exhibit intensity variations which correspond to velocity variations in the flow but the intensity of the image also varies as a result of local variations in the seeding density and in intensity across the light sheet. Thus, a second unfiltered image of the light sheet is recorded by a separate camera and is used to normalise the filtered image so that, in the absence of extraneous scattered light from nearby surfaces, the intensity variations are a function of velocity only.

The magnitude of the Doppler shift depends on the flow velocity and on the scattering and illumination directions according to the following expression:

$$\Delta \nu = \frac{\nu_0 (\hat{o} - \hat{i}) \cdot V}{c}$$

where \hat{o} and \hat{i} are unit vectors in the scattering and illumination directions respectively, V is the velocity vector, c is the speed of light and ν_0 is the frequency of the illuminating radiation. With this arrangement a single characteristic velocity component V' in a direction at ninety degrees to the bisector of the scattering and illuminating directions is measured. Figure 10 shows the relative orientation of the illumination, scattering and measured velocity vectors respectively, it can be considered as a plan view of the system in figure 9. From this it is clear that the technique may be extended to measure three velocity components with a single collector and three differently oriented light sheets or, more probably, with a single light sheet and three collectors arranged to measure different velocity component.

The main features of the method and the potential advantages include simultaneous measurements of velocities throughout the illuminated plane. The absorption line filter can discriminate between increases and decreases in frequency so that flow direction is automatically detected. Even with low resolution cameras, each image might typically contain 250,000 velocity vectors. There is no need to resolve the individual particle images so that, provided the density of the discrete phase is sufficient, large areas of the flow can be imaged and object distances of the order of 10 m can be used. Also, extension to measure of three velocity components is comparatively simple in principle although problems associated with equal precision of the three components remain, as mentioned in connection with laser-Doppler

velocimetry.

In the remainder of this section, the components of an instrument are considered together with the important choices. Previous applications are then considered and relative advantages highlighted. The section concludes with a brief discussion of the prospects for DGV for commercial wind tunnels.

Absorption Line Filter

The arrangement of a typical iodine vapour filter consists of iodine crystals in a glass cell that has been evacuated and sealed. Sublimation results in the formation of iodine vapour whilst solid crystals form in the coldest region of the cell. By providing a cold finger at a temperature below that of the main body of the cell, it can be ensured that no crystals form in the main body and particularly on the windows. The vapour pressure within the cell, and hence the level of absorption, are controlled by varying the temperature of the cold finger and the accuracy of measured velocities depends on this control. Large variations in the body temperature can also change the absorption characteristics by Doppler broadening and, again, temperature control is required. The transmission characteristics are a functions of the optical depth defined as the product of the path length through the cell and the number density of the iodine vapour. Increase in the optical depth increases the slope of the absorption line and hence resolution is improved, although the level of non-resonant background absorption also increases with number density which decreases dynamic range. Hence choice of cell design and operating parameters is a compromise for a particular optical depth; a large cell with a long path length provides good dynamic range or alternatively a cell with high number density can be compact but with reduced dynamic range. Most researchers have adopted the latter approach with a typical cell length of 50mm though McKenzie (1996) recommended a cell length of 150mm and a stem temperature of 40°C.

The light sheet is imaged through the cell and the windows should be of good optical quality. They may be diffusion bonded onto the tube forming the cell body although Morrison (1995) suggested that this can lead to distortion. A better approach may be to glue the windows to the ends of the tube. Care is required to ensure that the iodine vapour does not break down the seal material and Morrison has recommended the use of silicon-based adhesives. An additional advantage of this approach is that anti-reflection coatings may be applied. A more detailed review of the features and properties of iodine vapour can be found in Chan et al (1995).

Laser Light Source

By considering the features and potential advantages discussed above, it is clear that the light source should meet particular requirements. It should operate at a frequency corresponding to the absorption line of the absorber, usually iodine, and should provide sufficient power to enable the light scattered from small seeding particles to be detected. Also, it should enable very short duration exposures so that near-instantaneous velocities can be measured and provide a rapid sequence of images to be recorded so that time-varying flows can be characterised.

The argon ion CW laser and the Nd:YAG pulsed laser have been used for most applications, in part due to availability. Neither offers all the features listed above and the choice is, again, a compromise. The 514.5nm line of an Argon ion laser lies conveniently close to the P(13)/R(15) line of iodine and single-frequency operation can be achieved readily by an

intra-cavity etalon which restricts the output to a single longitudinal cavity mode with a line width of about 2MHz. This does not guarantee absolute frequency stability since both the etalon and the laser cavity are susceptible to thermal expansion but the possible consequences of frequency drift and mode hopping can be overcome by feedback control of the length of the laser cavity using iodine vapour as an absolute frequency reference, Chebotayev (1990). The main drawback of argon ion lasers is their limited power output with maximum values around 4W in single-mode operation, and this limits the dimensions of flow areas to be investigated.

The pulsed, frequency doubled, Nd:YAG laser produces pulses with duration of around 10ns so that a frozen, near-instantaneous image of high-speed flows is possible with pulse energies up to 500mJ so that very small seeding particles can be imaged. One drawback is the pulse repetition rate which is usually less than 100Hz and implies that many unsteady flows cannot be resolved.

Single frequency operation is achieved by injection seeding using a diode pumped CW Nd:YAG with its beam introduced into the cavity of the host pulsed laser. The high reflector of the host is mounted on a piezoelectric drive and the cavity length is tuned to match the frequency of the seed laser to provide a single frequency corresponding to that of the seed laser. Although it is claimed that this system produces single frequency output for >99% of the output pulses, McKenzie (1996) has reported that the output frequency is randomly modulated by approximately ± 10 MHz and that frequency drift of up to 10MHz/min can occur. Thus frequency stability cannot be guaranteed and it is necessary to monitor the laser output frequency of each pulse if accurate velocity measurements are to be made. Hence four signals have to be measured corresponding to the filtered and unfiltered Doppler shifted light to detect frequency variations due to flow velocity and filtered and unfiltered unshifted light to enable a laser frequency datum to be obtained and allow velocities to be calculated.

Data recording and processing

Scattered light is collected by means of a CCD video camera. Such cameras have a response to changes in light intensity that is intrinsically linear and high quantum efficiency to allow faint images to be detected. A typical camera contains 512 by 512 individual CCD elements making it possible to obtain 262144 vectors from a single exposure. Furthermore, a wide range of relatively cheap CCD-based cameras are available. Dark-current noise and photon statistics can limit the accuracy of measurement. The use of a scientific grade cooled chip can improve matters and McKenzie has also suggested the use of a 16 bit CCD camera to improve resolution. He estimates that a Doppler shift resolution of 2MHz, corresponding to 1.5m/s (for a typical set-up) can realistically be expected.

Processing a DGV image involves calculating a transmission level for each element and using this to calculate a velocity vector for the corresponding region of the flow using the known iodine vapour transmission characteristics. This requires comparison of the filter and unfiltered images on a pixel-by-pixel basis, a process known as image normalising. It is important that the two images are recorded at the same magnification by both cameras and that correct alignment be established between an element containing a given part of the image on each camera. The problems of this alignment are exacerbated by non-orthogonal viewing angles. The steps required to overcome such problems and achieve accurate image registration, as discussed by Meyers (1996).

Principle sources of uncertainty

In addition to the CCD noise sources discussed above the principal source of error to which the DGV technique is susceptible is surface scatter. Nearby surfaces either windows, walls or model surfaces will scatter light which will contribute to both the filtered and unfiltered images. Since this light will not undergo any frequency shift it will produce a bias in the velocity data obtained. The effect can be minimised by taking a reference image of only surface scatter and subtracting it from all subsequent data images. However, this approach can never be wholly effective since in the presence of seeding different surface scatter conditions will exist. This problem is likely to be greatest for measurements close to model surfaces and to date the authors are unaware of any attempt to quantify the accuracy of the DGV in the vicinity of a surface.

Applications

The technique is relatively new and most research has been concerned with developments and laboratory demonstrations, for example Komine et al (1991), Thorpe et al (1994, 1995 & 1996) Ford and Tatum (1996), Chan et al (1995 & 1995) and McKenzie (1996).

Wind tunnel applications have been reported by Meyers et al (1991, 1993, 1994 & 1996) although these too have been demonstrative. Nevertheless Meyers (1991) has examined vortical flow over a delta wing in a wind tunnel setting and the results reveal unsteady surging of the vortical flow, although the accuracy of the measurements is not discussed. Thus, at worst, the technique provides useful semi-quantitative visualisation in the plane orthogonal to the flow. The laboratory investigations of McKenzie (1996) suggest that quantitative velocities can be measured within $\pm 2\text{m/s}$ in many cases.

Meyers (1996) reported measurements of three components of velocity in a high temperature jet at 500m/s, in a wing tip vortex on a model in a 30 x 60 ft wind tunnel and in the entry flow for a helicopter tail rotor on a model within a 14 x 22 ft low speed wind tunnel. The object distances extended to 18m and velocities were measured with uncertainty of better than $\pm 2\text{m/s}$. Difficulties included misalignment of the receiving optics for the three components, uncertainties in sparsely seeded regions and temperature instability of the iodine cell. Replacement of the argon laser by a pulsed Nd:YAG laser and the use of a 10 bit video camera is expected to improve resolution and the temperature stabilisation of the iodine cell can and will be improved.

4. SUMMARY

Wind tunnels have been in operation for many years and have provided valuable information to aircraft designers in the absence of optical methods so that if these methods are to be adopted in commercial wind tunnels, they must achieve one of two goals. Either they must replace conventional instrumentation and allow the same measurements to be made with greater accuracy, over extended regions, in less time or at lower cost or, alternatively, they must enable new and greater insight into flow physics thereby providing previously unavailable information. Wind tunnel testing can be expensive, hence, techniques falling into the first category will quickly find favour in industry although those in the second category are most likely to improve the design process. Of the techniques reviewed, the use of parameter sensitive paints complies most closely with the first requirement.

Conventional pressure measurement is achieved by discrete pressure tappings at the model surface and requires advance consideration of the locations at which pressure data will be

most valuable. Optical measurement offers the possibility of a continuous pressure distribution regardless of internal model structure so that combined force and surface pressure measurements can be made with the same model. Limitations may be introduced by model displacement, temperature and illumination intensity variations and restricted optical access on complex geometry and the radiometric mode resolution is limited to around 300Pa so that the technique is best suited to flows with large pressure variations, for example compressible flows at moderate to high Mach numbers. The lifetime mode is relatively new and its characteristics have yet to be fully investigated but, initial reports suggest that it is independent of intensity variations, may operate at higher overall pressures than the radiometric mode and may offer improved resolution.

The other techniques can enhance knowledge of flow physics and particularly of local velocities. They may be used to provide immediate information of flow and turbulence characteristics and to calibrate computational methods.

The velocimetry techniques require the flow to be seeded and this provides a major challenge. Particles and droplets may be toxic, may stick to surfaces and obscure windows and yet must be present in large quantities. They may also contaminate parameter sensitive paint precluding combined use of both methods. No universal seeding scheme exists and tunnel specific solutions must be sought.

Laser Doppler velocimetry is reliable, robust and accurate and two and three-dimensional measurements may be made, where optical access permits, and close to surfaces with mean and turbulence information readily available. It may encompass a range of velocities from zero to supersonic recognising the increasing difficulty of flow seeding as velocity increases. It provides velocity information at discrete locations which can be advantageous but also implies a need to traverse the measurement volume if measurements are required at more than one location.

Particle image velocimetry enables velocities to be measured throughout a light sheet and spatial characteristics may be derived with mean and turbulence obtained if images are recorded over a period of time. A rapid sequence of images may also be used to characterise transient flow phenomena.

Doppler global velocimetry is a relatively new technique, which, like PIV, enables velocity to be measured throughout an illuminated plane although it is sensitive to out-of-plane velocity components. The technique is directionally sensitive and data processing is relatively simple so that on-line processing is a realistic option and processing multiple frames for time dependent properties can be achieved. Some seeding restrictions may be removed in that individual seeding particles need not be resolved and imaging large flow areas or large object distances are theoretically possible.

As a final comment on the velocimetry techniques, a large number of demonstrative laboratory experiments have taken place and a gradually increasing number of wind tunnel applications have been reported. The techniques offer a range of capabilities and are becoming increasingly reliable and robust. Further developments will require more applications in the industrial setting and it is incumbent on researchers and industry to pursue this next stage.

5. REFERENCES

- 1 Arie A, Byer R L, 1993, "Frequency stabilisation of the 1064nm Nd:YAG lasers to Doppler broadened lines of iodine", *Applied Optics* Vol.32, No.36, pp. 7382-7386
- 2 Abbit J D, Fuentes C A, Carroll B F, 1996, "Film based pressure sensitive paint measurement", *Optics Letters*, Vol. 21, No. 22, pp.1797-1799.
- 3 Adrian R.J. 1984, "Scattering particle characteristics and their effect on pulsed laser measurements of fluid flow : speckle velocimetry vs particle image velocimetry", *Applied Optics* Vol. 23, pp. 1690-1691.
- 4 Adrian R J, Yao C S, 1985, "Pulsed laser technique application to liquid and gaseous flows and the scattering power of seed materials", *Applied Optics* Vol. 24, No. 1, pp. 44-52.
- 5 Adrian R J, 1991, "Particle imaging techniques for experimental fluid mechanics", *Annual Revue of Fluid Mechanics*, 23, pp. 261-304, 1991.
- 6 Allison S W, Gillies G T, 1997, "Remote thermometry with thermographic phosphors: instrumentation and applications", *Rev. Sci. Instrum.* Vol. 68, pp. 2615-2650.
- 7 Ardasheva M M, Nevskii L B, Pervushin G E, 1985, "Measurement of pressure distribution by means of indicator coatings", *J. Appl. Mech. Tech. Phys.* Vol. 26, pp. 469-474.
- 8 Bachalo W D, Rudoff R C, Houser M J, 1987, "Laser Velocimetry In Turbulent Flow Fields : Particle Response", *AIAA Paper* 87-0118.
- 9 Baron A E, Danielson D S, Gouterman M, Wan J R, Callis J B, McLachlan B, 1993, "Submillisecond response times of oxygen quenched luminescent coatings", *Rev. Sci. Instrum.* Vol. 64, No. 12, pp. 3394-3402.
- 10 Bell J H, McLachlan B G, 1996, "Image registration for pressure sensitive paint applications", *Experiments in Fluids*, Vol. 22, pp. 78-86.
- 11 Bizzak D J, Chyu M K, 1995, "Use of a laser induced fluorescence thermal imaging system for local jet impingement heat transfer measurement", *Int. J. Heat Mass Transfer*, Vol. 38, pp. 267-274.
- 12 Bokov A P, Orlov A A, Masharov V E, Radchenko V N, Pesetsky V A, 1992, "Application of luminescence quenching for pressure field measurements on the model surface in a wind tunnel", *Proc. of RAe Soc, 1992 Forum - Wind Tunnel and Wind Tunnel Test Techniques*.
- 13 Bradley L C, 1953, "A temperature sensitive phosphor used to measure surface temperatures in aerodynamics", *Rev. Sci. Instrum.* Vol. 24, pp. 219-220.
- 14 Bryanston-Cross P.J., Harasgama S.P., Towers C.E., Judge T.R., Towers D.P., Hopwood S.T. 1991, "The application of particle image velocimetry in a short duration transonic annular turbine cascade", *Optics and Laser Technology* Vol.23 No.5.
- 15 Bryanston-Cross P.J., Judge T.R., Quan C, Pugh G. 1995, "The application of digital particle image velocimetry (DPIV) to transonic flows", *Progress in Aerospace Sciences*, Vol. 31, pp. 273-290.
- 16 Buck G M, 1995, "Simultaneous luminescence pressure and temperature measurement system for hypersonic wind tunnels", *Journal of Spacecraft and Rockets*, Vol. 32, No.5 pp.791-794.
- 17 Burns S P, Sullivan J P, 1995, "The use of pressure sensitive paints in rotating machinery", *Proc. Int. Cong. on Instrumen. in Aerospace Simulation Facilities*, IEEE Publication 95CH3482-7.
- 18 Camy G, Decomps B, Gardissat J L, Borde C J, 1977, "Frequency stabilisation of argon lasers at 582.49 THz using saturated absorption in $^{127}\text{I}_2$ ", *Metrologia* Vol.13 pp.145-148.
- 19 Carroll B F, Abbit J D, Lukas E W, 1996, "Step response of pressure sensitive paints", *AIAA Journal*, Vol. 34, No. 3, pp. 521-526.
- 20 Cenedese A, Paglialunga A, 1990, "Digital direct analysis of a multiexposed photograph in PIV", *Experiments in Fluids* Vol. 8, pp. 273-280.
- 21 Chan V S S, Heyes A L, Robinson D I, Turner J T, 1995, "Iodine absorption filters for Doppler global velocimetry", *Meas. Sci. Technol.* Vol. 6, pp.784-794.
- 22 Chan V S S, Heyes A L, Robinson D I, Turner J T, 1995, "A simplified Doppler global velocimeter", *Proc. ASME/ EALA 6th Int Conference on Laser Anemometry, Advances and Applications*.
- 23 Chebotayev V P, Goldort V G, Goncharov A N, Ohm A E, Skvortsov, 1990, "Argon ion laser with high frequency stability", *Metrologia*, Vol.27 pp. 61-64.
- 24 Cler D, Lamb M, Farokhi S, Taghavi R, Hazlewood R, 1996, "Application of pressure sensitive paint in supersonic nozzle research", *Journal of Aircraft*, Vol.33, No.6, pp.1109-1114.
- 25 Crites R, Morris M, 1997, "Parameter sensing paints – current capabilities and future potential", *Proc. of RAe Soc, 1997 Forum - Wind Tunnel and Wind Tunnel Test Techniques*.
- 26 Davies A G, Bedwell D, Dunleavy M, Brownjohn N, 1997, "Recent developments in pressure sensitive paint measurements using the BAe system", *Proc. of RAe Soc, 1997 Forum - Wind Tunnel and Wind Tunnel Test Techniques*.
- 27 Del Frate J H, 1992, "In-flight visualisation results from high angle of attack tests on a forward swept wing aircraft with comparisons to water tunnel tests", In *Flow Visualisation VI*, 267-269. Springer.
- 28 D'Humieres C, Micheli F, Papirnyk O, 1991, "Aerosol Behaviour In Supersonic Flows", *Proc. 4th Int. Conf. on Laser Anemometry*, Cleveland, August 5-9.
- 29 Dowgwillo R M, Morris M J, Donovan J F, Benne M E, 1996, "Pressure sensitive paint in transonic wind tunnel testing of the F15", *Journal of Aircraft*, Vol. 33 No. 1, pp.109-116.
- 30 Drain L E 1980, "The Laser Doppler Technique", John Wiley & Sons, Chichester.
- 31 Durst F, Melling A, Whitelaw J H, 1981, "Principles and Practice of Laser Doppler Anemometry", Academic Press, London.
- 32 Elenar M, 1987, "Laser Doppler anemometry in supersonic flows: problems of seeding and angular bias", *Agard AG* 315.
- 33 Erbland P J, Bogue R K, McKenzie R L, Hanson R K, Eckbreth A C, Trolinger J D, Havener G, Crowder J P, Crooks R S, Owen F K, Miles R B, Menon R. 1992, "Taking the measure of aerodynamic testing", *Aerospace America*, November 1992. pp. 17-39.
- 34 Farrugia N, Kanne S, Greenhalgh D.A. 1995, "3-pulse digital particle image velocimetry", *Optics Letters*, Vol. 20, pp. 1827-1829.
- 35 Feller W V, Meyers J F, 1975, "Development of a controllable particle generator for laser velocimetry seeding in

- hypersonic wind tunnels", Proc. Minnesota Symp. on Laser Anemometry, Oct 22-24, pp. 343-357.
- 36 Ford H D, Tatum R P, 1996, "Development of Doppler global velocimetry for turbomachinery applications", Proc. 8th Int. Symp. on Applications of Laser Techniques to Fluid Mechanics, Lisbon, Portugal.
 - 37 Gallery J, Gouterman M, Callis J, Khalil G, McLachlan B, Bell J, 1994, "Luminescent thermometry for aerodynamic measurements", Rev. Sci. Instrum. Vol. 65, pp. 712-720.
 - 38 Gerstenkorn S., Luc P. 1979, "Assignments of several groups of iodine lines in the B-X system", Journal of Molecular Spectroscopy, 77, pp310-321.
 - 39 Goss L P, Smith A A, Post M E, 1989, "Surface thermometry by laser induced fluorescence", Rev. Sci. Instrum. Vol. 60, pp. 3702-3706.
 - 40 Gui L C, Merzkirch W, 1996, "A method of tracking ensembles of particle images", Experiments in Fluids Vol. 21 pp. 465-468.
 - 41 Grant I, 1997, "Particle image velocimetry: A review", Journ. Mech. Eng. Sci. Vol. 211 No. 1, pp. 55-76.
 - 42 Hardalupas, Y., Hishida, K., Maeda, M., Morikita, H., Taylor, A. M. K. P. and Whitelaw, J. H. (1994), "Shadow Doppler technique for sizing particles of arbitrary shape", Applied Optics, 33, no. 36, pp. 8417-8426.
 - 43 Hassan Y A, Canaan R E, 1991, "Full field bubbly flow velocity measurement using a multi-frame particle tracking technique", Experiments in Fluids Vol. 12, pp. 49-60.
 - 44 Heyes A L, Turner J T 1992., "PIV vector extraction by direct particle image pairing", Proc. Optical Methods and Data Processing in Heat and Fluid Flow, City University, London, April 2-3 1992
 - 45 Heyes A L, Turner J T 1994., "Three-Dimensional LDA In The Vortical Flow Around A Lifting Delta Wing At Mach 2.3", Proc. Fifth Int. Conference on Laser Anemometry - Advances and Applications, 23-27 August 1993, Koningshof, Veldhoven, The Netherlands
 - 46 Holmes J W, 1997, "Analysis of radiometric lifetime and fluorescent lifetime imaging for pressure sensitive paint", Proc. RAe Soc, 1997 Forum - Wind Tunnel and Wind Tunnel Test Techniques.
 - 47 Holmes B J, Gall P D Croom C C, Manuel G S, Kelliher W C, 1986, "A new method for laminar boundary layer transition visualisation in flight: colour changes in liquid crystal coatings", NASA TM-87666
 - 48 Horner M B, Galbraith R A M, Coton F N, Stewart J N, Grant I, 1996, "Examination of vortex deformation during blade vortex interaction", AIAA Journal, Vol. 34, No. 6, pp. 1188-1194.
 - 49 Hughes J P, Brumby J E, Belevtsov N, 1983, "Flow visualisation from the ground up", AIAA paper 83-2691.
 - 50 Jakobson M L, Hossack W J, Greated C A, Easson W J, 1992., "PIV analysis using an optically addressed spatial light modulator", Proc. Applied Optics and Opto-Electronics, Leeds, Sept. 14-17 1992.
 - 51 Jentink H W, Stieglmeier M, Tropea C, 1993, "In-flight velocity measurements by laser-Doppler anemometry", J Aircraft, Vol. 31, pp.444-446.
 - 52 Jones T V, 1992, "The use of liquid crystals in aerodynamic and heat transfer testing", Proc. 4th Int. Symp. On Transport Phenomena in Heat and Mass Transfer, Elsevier, Amsterdam, pp. 1242-1273.
 - 53 Kautsky H, 1939, "Quenching of luminescence by oxygen", Trans. Faraday Soc. Vol. 35.
 - 54 Keane R.D, Adrian R.J. 1990, "Optimisation of particle image velocimeters. Part I: double pulsed systems.", Meas. Sci. Technol. 1, pp. 1202-1215.
 - 55 Klein E J, Margozi A P, 1969, "Exploratory investigation on the measurement of skin friction by means of liquid crystals", NASA TM-X-1774.
 - 56 Komine H., Brosnan S.J. 1991, "Instantaneous three-component Doppler global velocimetry", Proc. 4th International Conference on Laser Anemometry Advances and Applications, Cleveland Ohio, August 5-9, 1991.
 - 57 Lading L, Wigley G, Buchhave P, 1993, "Optical diagnostics for flow processes", Plenum Press, New York, London.
 - 58 Landreth C.C, Adrian R.J, 1988, "Electro-optic image shifting for particle image velocimetry", Applied Optics Vol. 27. pp. 4216-4220.
 - 59 Lawson N.J, Coupland J.M, Halliwell N A, Christodoulou M.S, Hancox J. 1994, "Application of particle image velocimetry to a normal shock in a supersonic De Laval nozzle", Proc. Optical Methods and Data Processing in Heat and Fluid Flow, City University, London, April 14-15 1994.
 - 60 Lawson N.J. 1994, "The application of particle image velocimetry to high speed flows", PhD Thesis, University Of Loughborough, UK.
 - 61 Lin J.C, Rockwell D. 1994, "Cinematographic system for high image density particle image velocimetry", Experiments in Fluids, Vol. 17 pp. 110-118.
 - 62 Liu Z.C, Adrian R.J, Meinhardt C.D, Lai W. 1996, "Visualisation of structure in a turbulent boundary layer using stereoscopic particle image velocimetry", Proc. 8th Int.Symp. on App. of Laser Tech. to Fluid Mech. Lisbon.
 - 63 Livesey J L, Jackson J D, Southern C J, 1962, "The static hole error problem", Aircraft Engineering, Vol. 34, p.43.
 - 64 Lourenco L.M. 1993, "Velocity bias technique for particle image velocimetry measurements of high speed flows.", Applied Optics, Vol. 32 pp. 2159-2162.
 - 65 Mao Z.Q, Halliwell N.A, Coupland J.M. 1996, "High speed analogue autocorrelation for PIV transparency analysis using a ferroelectric liquid crystal spatial light modulator", Optics and Laser in Engineering, Vol. 24, pp. 301-317.
 - 66 Martinez-Botas R F, Lock G D, Jones T V, 1995, "Heat transfer measurement in an annular cascade of transonic gas turbine blades using the transient liquid crystal technique", Journal of Turbomachinery, Vol. 117, No.3 pp. 425-431.
 - 67 McKenzie R L, 1996, "Measurement capabilities of planar Doppler velocimetry using pulsed lasers", Applied Optics, Vol.35, No.6 pp.948-964.
 - 68 McLachlan B G, Bell J H, Park H, Kennelly R A, Schreiner J A, Smith S C, Strong J M, Gallery J, Gouterman M. 1995, "Pressure sensitive paint measurements on a supersonic high sweep oblique wing model", Journal of Aircraft, Vol. 32, No. 5, pp. 217-227.
 - 69 McLachlan B G, Bell J H, 1995, "Pressure sensitive paint in aerodynamic testing", Expt. Therm. and Fluid Science, Vol.10, pp. 470-485.
 - 70 Meyers J.F., Komine H. 1991, "Doppler global velocimetry: a new way to look at velocity", 4th Int. Conference On Laser Anemometry Advances And Applications, Cleveland Ohio, August 5-9, 1991.

- 71 Meyers J F, Lee F W, Cavone A A, (1993), "Three component Doppler global velocimetry measurements of the flow above a delta wing", *Laser Techniques and Applications in Fluid Mechanics*, Springer, pp. 345-363.
- 72 Meyers J F, (1994), "Development of Doppler global velocimetry for wind tunnel testing", AIAA paper 94-2582.
- 73 Meyers J F, 1996, "Evolution of Doppler global velocimetry data processing", *Proc. 8th Int. Symp. on Applications of Laser Techniques to Fluid Mechanics*, Lisbon, Portugal.
- 74 Micol J R, 1995, "Aerothermodynamic measurement and prediction for modified orbiter at Mach 6 and 10", *Journal of Spacecraft and Rockets*, Vol.32, pp.737-748.
- 75 Molezzi M.J, Dutton J.C. 1993, "Application of particle image velocimetry in high speed separated flows", *AIAA Journal*. Vol. 31. pp. 438-446.
- 76 Maeda, M., Morikita, H., Prassas, I., Taylor, A.M.K. P. and Whitelaw, J. H. (1997), "Shadow Doppler Velocimetry for Simultaneous Size and Velocity Measurements of Irregular Particles in Confined Reacting Flows", *Particle and Particle Systems Characterization*, Vol. 14, pp. 79-87.
- 77 Morris M J, Donovan J F, Kegelman J T, Schwab S D, Levy R L, Crites R C, 1993, "Aerodynamic applications of pressure sensitive paint", *AIAA Journal*, Vol. 31, No. 3, pp. 419-425.
- 78 Morrison G L, Charles G A, Deotte R E, 1995, "Doppler global velocimetry: problems and pitfalls", *Flow Meas. Instrum.* Vol.6 No.2 pp. 83-91.
- 79 Nichols R H, 1985, "Calculation of particle dynamics effects on laser velocimetry data", *NASA Conference Publication 2393*
- 80 Oakley T.R, Loth E, Adrain R.J. 1996, "Cinematic particle image velocimetry of high Reynolds number turbulent free sheat layer", *AIAA Journal*, Vol. 34, pp. 299-308
- 81 Okamoto K, Hassan Y A, Schmidl W D, 1995, "New tracking algorithm for particle image velocimetry", *Experiments in Fluids* Vol. 19 No.5 pp. 342-347.
- 82 Peterson J I, Fitzgerald R V, 1980, "New technique of surface flow visualisation based on oxygen quenching of fluorescence", *Rev. Sci. Instrum.* Vol. 51, pp.670-671.
- 83 Pickering C J D, Halliwell N A, 1985., "Particle image velocimetry: fringe visibility and pedestal removal" *Applied Optics* Vol.24, No. 16, pp. 2474-2476.
- 84 Pope A, Goin K L, 1965, "High speed wind tunnel testing", John Wiley & Sons, New York, London, Sydney
- 85 Pope A, Harper J J, 1966, "Low speed wind tunnel testing", John Wiley & Sons, New York, London, Sydney
- 86 Prassas, I, Taylor, A. M. K. P. and Whitelaw, J. H. (1997a)., "Simultaneous particle velocity, size and temperature measurement in a swirl-stabilised gas-supported pulverised coal flame", *4th International Conference on Technologies and Combustion for a Clean Environment*, 7-10 July, Lisbon, Portugal.
- 87 Prassas, I, Taylor, A. M. K. P. and Whitelaw, J. H. (1997b)., "Simultaneous measurement of velocity, size and temperature of burning coal particles in swirl-stabilised vitiated air flames", *ASME IMEC&E, Symposium on Combustion, Fire, Explosion and Alternative Fuels*, 16-21 November, Dallas, USA.
- 88 Raffel M, Kompenhans K. 1995, "Theoretical and experimental aspects of image shifting by means of a rotating mirror system for particle image velocimetry.", *Meas. Sci. Technol.* Vol. 6 pp. 795-808.
- 89 Reda D C, Aeschliman D P, 1992, "Liquid crystal coatings for surface shear stress visualisation in hypersonic flows", *Journal of Spacecraft and Rockets*, Vol. 29, No.2 pp.155-158.
- 90 Reda D C, Muratore J J, 1994, "Measurement of surface shear stress vectors using liquid crystal coatings", *AIAA Journal* Vol. 32, No.8 pp. 1576-1582.
- 91 Reeves M, Garner C.P, Dent J.C, Halliwell N.A. 1996, "Full field IC engine flow measurement using particle image velocimetry", *Journal of Optical Engineering*, Vol. 35, pp.579-587.
- 92 Reeves M, Lawson N.J, Halliwell N.A, Coupland J.M. 1995, "Particle image velocimetry - image labeling using encoding of the point spread function by application of a polarization sensitive mask", *Applied Optics*, Vol. 34, pp. 194-200.
- 93 Roberts G T, East R A, 1996, "Liquid crystal thermography for heat transfer measurement in hypersonic flows: a review", *Journal of Spacecraft and Rockets*, Vol. 33, No.6 pp.761-768.
- 94 Sajben M, 1993, "Uncertainty estimates for pressure sensitive paint measurements", *AIAA Journal*, Vol. 31, No. 11, pp.2105-2110.
- 95 Schanze K S, Carroll B F, Korotkevitch S, Morris M, 1997, "Temperature dependence of pressure sensitive paints", *AIAA Journal*, Vol. 35, No. 2, pp.306-310.
- 96 Shih C, Lourenco L M, Krothapalli A, 1995, "Investigation of flow at the leading and trailing edges of pitching-up airfoil", *AIAA Journal*, Vol. 33, No.8, pp. 1369-1376.
- 97 Stefanini J, Cognet G, Vila J C, Brenier Y, 1992., "The use of a CCD video camera for a coloured PIV technique", *Proc. Optical Methods and Data Processing in Heat and Fluid Flow*, City University, London, April 2-3 1992.
- 98 Stewart J.N, Wang Q, Moseley P, Bearman P.W, Harvey J.K. 1996, "Measurement of vortical flows in a low speed wind tunnel using particle image velocimetry", *Proc. 8th Int. Symp. on App. of Laser Tech. to Fluid Mech.* Lisbon.
- 99 Thompson B E, Whitelaw J H, 1984, "Flying hot wire anemometry", *Experiments in Fluids*, Vol.2 No.1, pp. 47-55.
- 100 Thorpe S J, Ainsworth R W, 1994, "The development of a Doppler global velocimeter for transonic turbine applications", *ASME 94-GT-146*.
- 101 Thorpe S J, Ainsworth R W, Manners R J, 1995, "The development of Doppler global velocimetry and its application to a free jet", *Proc. ASME/ EALA 6th Int Conference on Laser Anemometry, Advances and Applications*, pp.131-138.
- 102 Thorpe S J, Ainsworth R W, Manners R J, 1996, "Time averaged free-jet measurements using Doppler global velocimetry", *Proc. ASME Symp. on Laser Anemometry and Experimental and Numerical Flow Visualisation*
- 103 Towers C E, Bryanston-Cross P J, Judge T R, 1991, "Application of particle image velocimetry to large scale transonic wind tunnels", *Optics & Laser Technology* Vol. 23, No. 5, 1991.
- 104 Van De Hulst H C, 1957, "Light Scattering By Small Particles", John Wiley & Sons/Chapman & Hall
- 105 Wegner P, Stein G, 1968, "Light scattering experiments and the theory of homogeneous nucleation in condensing

supersonic flow", Proc. 12th International Symposium on Combustion, pp. 1183-1191.

106 Wernet P, Geissler W, Raffel M, Kompenhans J, 1996, "Experimental and numerical investigations of dynamic stall on a pitching airfoil", AIAA Journal, Vol. 34 No. 5 pp. 982-989.

107 Willert C.E., Gharib M. 1991, "Digital particle image velocimetry", Experiments In Fluids 10, pp. 181-193. 1991.

108 Willert C, Stasicki B, Raffel M, Kompenhans J. 1996, "High speed digital camera systems and related software for applications PIV in wind tunnel flows", Proc. 8th Int. Symp. on App. of Laser Tech. to Fluid Mech. Lisbon.

109 Wormell D, Sopchak J, 1993, "A particle image velocimetry system using a high resolution CCD camera", Diagnostics in Fluid and Thermal Flow. Proc. SPIE 2005 pp. 648-654.

110 Yianneskis M, Lee K C, 1994, "Mixing characteristics of a stirred reactor with an axial flow impeller", Proc. Of 8th Int. Conf. On Mixing, Cambridge, September 21-23, 1994.

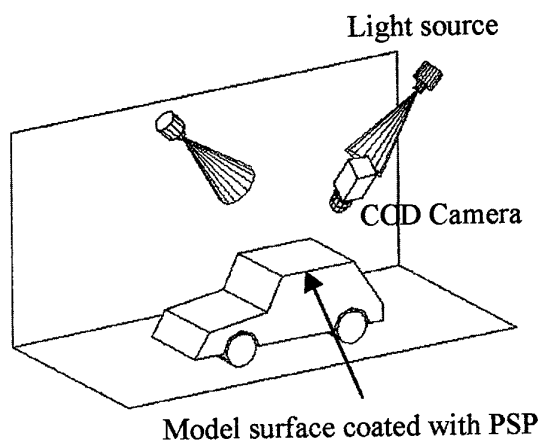


Figure 1 Experimental arrangement for PSP's

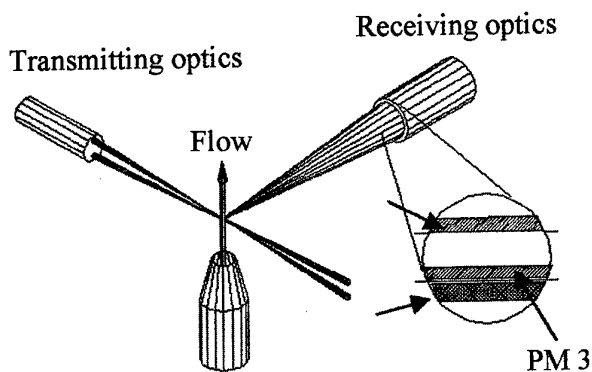


Figure 4 PDA optics configuration

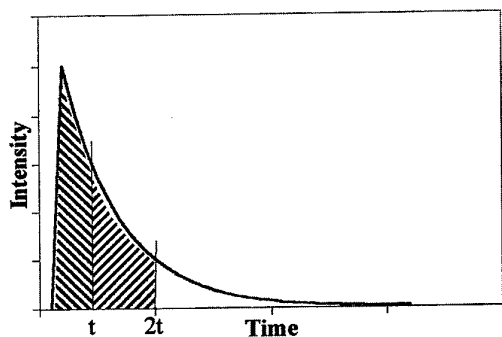


Figure 2 Exponential decay of emission from a PSP following pulsed illumination

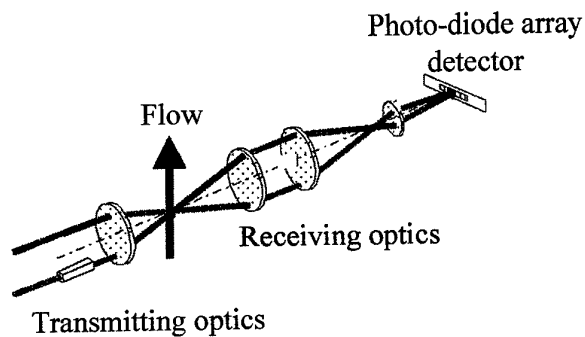


Figure 5 Shadow Doppler optics configuration

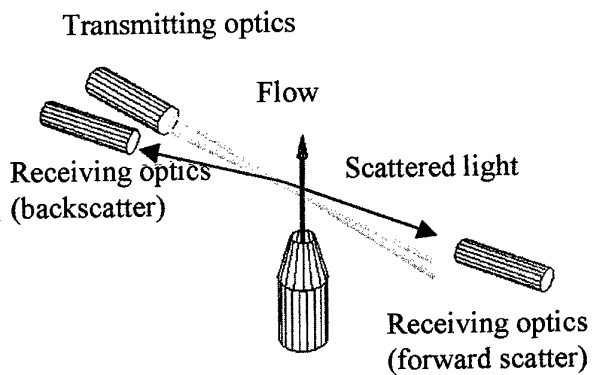


Figure 3 LDV Optics configuration

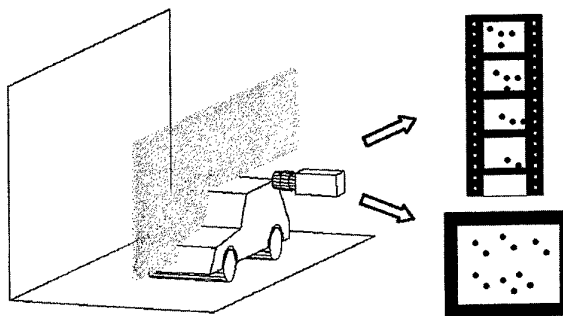


Figure 6 PIV experimental arrangement

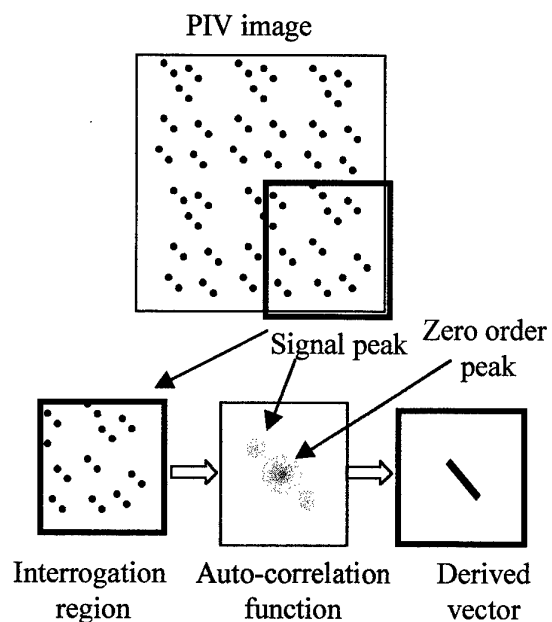


Figure 7 PIV- the auto correlation technique

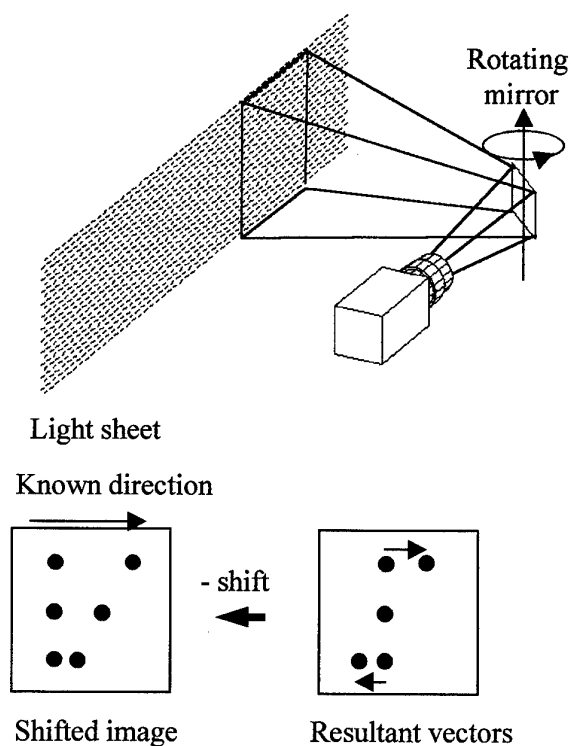


Figure 8 Image shifting in PIV

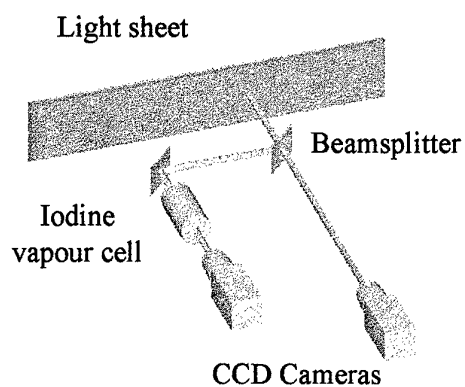


Figure 9 DGV optics configuration

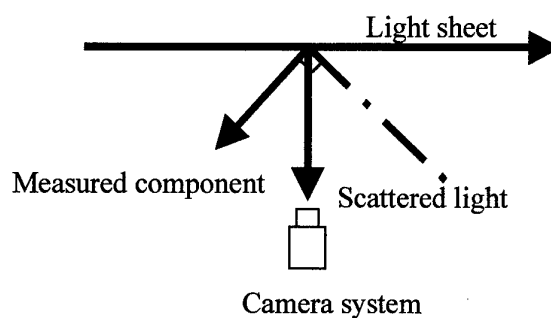


Figure 10 DGV - measured component for a 1-D system

Advanced Measurement Technology at NASA Langley Research Center

Richard R. Antcliff
 NASA Langley Research Center
 MS 493
 Hampton, VA 23681-0001, USA
 r.r.antcliff@larc.nasa.gov

1. Summary

Instrumentation systems have always been essential components of world class wind tunnels and laboratories. Langley continues to be on the forefront of the development of advanced systems for aerospace applications. This paper will describe recent advances in selected measurement systems which have had significant impact on aerospace testing. To fully understand the aerodynamics and aerothermodynamics influencing aerospace vehicles, highly accurate and repeatable measurements need to be made of critical phenomena. However, to maintain leadership in a highly competitive world market, productivity enhancement and the development of new capabilities must also be addressed aggressively. The accomplishment of these sometimes conflicting requirements has been the challenge of advanced measurement developers. However, several new technologies have recently matured to the point where they have enabled the achievement of these goals. One of the critical areas where advanced measurement systems are required is flow field velocity measurements. These measurements are required to correctly characterize the flowfield under study, to quantify the aerodynamic performance of test articles and to assess the effect of aerodynamic vehicles on their environment.

Advanced measurement systems are also making great strides in obtaining planar measurements of other important thermodynamic quantities, including species concentration, temperature, pressure and the speed of sound. Langley has been on the

forefront of applying these technologies to practical wind tunnel environments. New capabilities in Projection Moiré Interferometry and Acoustics Array Measurement systems have extended our capabilities into the model deformation, vibration and noise measurement arenas.

An overview of the status of these techniques and recent applications in practical environments will be presented in this paper.

2. Flow Visualization

2.1 Focusing Schlieren

Focusing Schlieren is a technique that has long historical roots but only recent fruit. This technique has the unique advantage of being able to focus in on a particular plane in the flow to image. Normal Schlieren only obtains an integrated image. Focusing Schlieren systems have been developed and used since the late 1940's.¹ However, these systems were limited by the small size of their field of view and their optical complexity requiring tedious set-up and stability. A breakthrough in the utility of this tool came in 1991 with the introduction of a Fresnel lens and a simplified optical system.² Since this time Focusing Schlieren has been utilized to investigate a wide range of aerospace and nonaerospace applications.³

An example of the application of this technology includes work performed in the 0.3 meter Transonic Cryogenic Tunnel. This facility is a recirculating facility which typically operates at 100°K. This type of facility poses challenges for any optical technique due to the thermal gradients and the

side effects which include tunnel movement and condensation. This problems highlighted the unique advantages of the focusing schlieren system for ignoring the parts of the flowfield which were unimportant. An example of a shuttle system imaged in this facility is displayed in figure 1. This type of image would have been severely distorted in a normal Schlieren system.

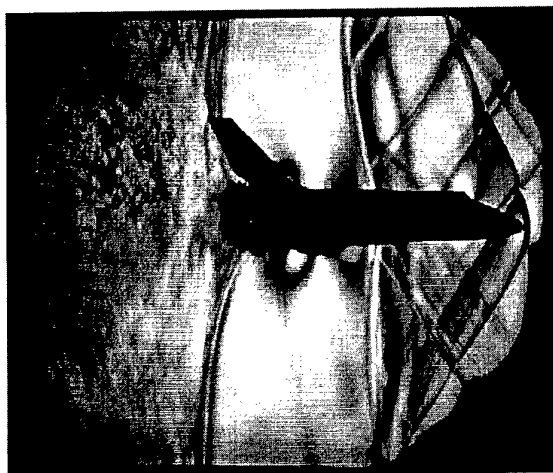


Figure 1. Focusing Schlieren image in the 0.3 meter Transonic Cryogenic Tunnel.

A recent extension to focusing Schlieren technology has allowed flow field images of aircraft in free flight to be obtained.⁴ In these experiments a sliver of the sun is used as the light source. The aircraft is required to pass through the field between the imaging system and the sun to obtain the image. Dramatic images of supersonic aircraft have been obtained. An example of these is shown in figure 2. Currently, this technique is being improved to better track the movement of the sun and is also being expanded to devise an air to air system, such that a follower aircraft can interrogate the test aircraft in flight.

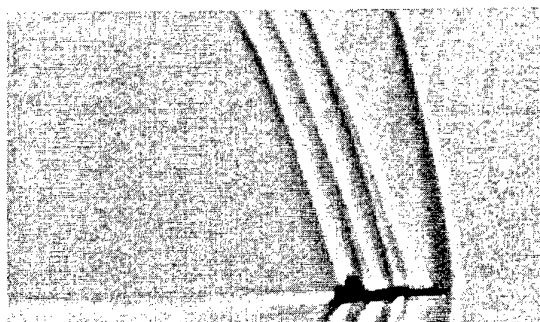


Figure 2. Focusing Schlieren image of a T-38 in flight. Supersonic shock waves are clearly seen.

2.2 Rayleigh Scattering

Both Rayleigh scattering and laser induced fluorescence have unique capabilities to obtain quantitative information from the flow field. However, we have also successfully utilized these techniques to meet challenging flow visualization requirements. These laser based systems allow us to surgically select planes of interest for visualization.

Rayleigh scattering has been utilized to characterize the mixing of "fuel" into a supersonic combustor.⁵ In this experiment, helium was utilized to simulate combustible hydrogen injected into a Mach 6 air flow. The experimental setup is illustrated in the upper left of figure 3. The helium was injected through three ports, parallel to the flow. The Rayleigh data was taken downstream of the injectors and in a plane perpendicular to the flow, creating a cross section of the mixing. As discussed in reference 5, the scattering medium in these studies were molecular clusters formed by the expansion cooling. A UV excimer laser provided high power light energy. The detection system was based on a single-intensified CCD camera. Considerable effort was placed on reducing the scattering in the experimental setup and compensating for detection challenges (camera field variability, perspective distortion, calibration, laser fluctuations, e.g.).

A sample of the data from this experiment is shown in the bottom right of figure 3. These data were taken 10 injector heights

downstream of the injectors. The dark area is actually an absence of signal. This absence of signal is attributable to the presence of helium because of the low scattering efficiency of this gas. The bright area reflects the air flow, in this case filled with molecular clusters. These data provided unique insight into the turbulent nature of this mixing. Comparisons were made with 5 hole probe and CFD calculations which led to a better understanding of the three techniques and the flow itself.

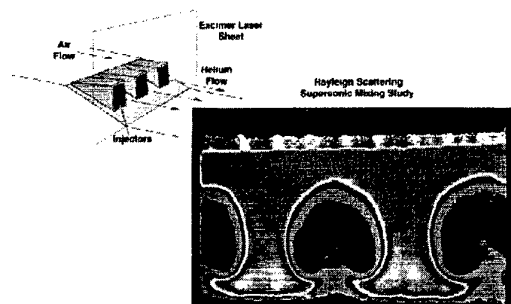


Figure 3. Rayleigh mixing visualization study. Experimental setup and sample data.

2.3 Laser Induced Fluorescence

In addition to the benefit of using a laser sheet based technique for flow visualization, LIF allows us to select a particular molecule to visualize, giving us a species specific visualization. Obviously, this is constrained to molecules that are fluorescent. This benefit was exploited in a recent study of a hot, Mach 2 annular air jet.⁶ In this study both Rayleigh scattering and laser induced fluorescence were utilized. The system being studied was a supersonic hydrogen air combustor. This device injects supersonic hydrogen into a flow of supersonic air producing sustained external combustion. This external combustion field was then studied with these techniques. In particular, the hydroxyl radical (OH) is probed because it is an intermediate in the combustion process and is easily accessible spectroscopically with current laser technology. The laser system employed here is a xenon chloride excimer laser operating near 308 nm with a 96 mJ per pulse output.

This laser was spread into a sheet and passed through the flow in the same plane as the flow axis. Figure 4 shows an example of the data obtained in this study. The instantaneous LIF images show that the spatial and temporal OH signal profiles in the vitiated airstream were not uniform as portrayed in the average images. The instantaneous images showed striation patterns or alternating regions of high and low signal levels along the axis perpendicular to the flow. These striation patterns were unexpected and are the focus of future studies of this combustion system.

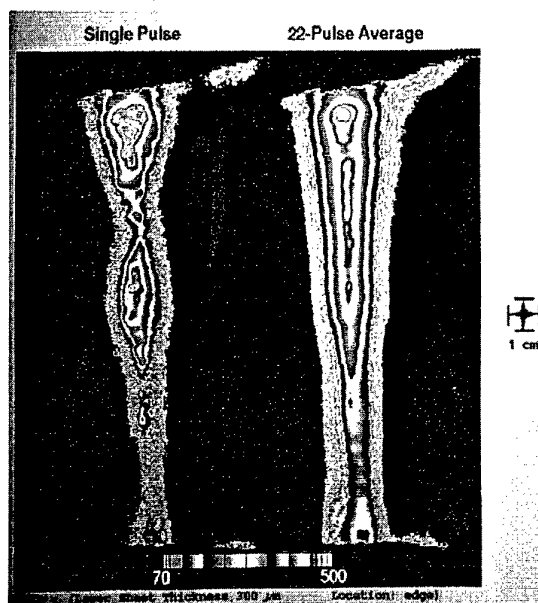


Figure 4. LIF images above a Mach 2 combustor.

A recent variant of this technique has utilized locally seeded iodine to visualize the flow in the wake of simple aerodynamic models.⁷ In these studies localized seeding is performed by painting a small area of a porous ceramic model with a tincture of iodine. When the model is injected into the flow, the adsorbed iodine is entrained into the boundary layer, follows the model contour, and ultimately mixes into the wake region. Planar "snapshots" of the wake flow are taken by exciting the iodine with an ArF excimer laser sheet at 193 nm and observing the

fluorescence in the 210-600 nm region with an intensified CCD camera.

3. Velocity

3.1 Laser Velocimetry

Laser Doppler Velocimetry has been utilized extensively at NASA LaRC to investigate flow field velocities. There are currently operating systems in the Basic Aerodynamic Research Tunnel and the 14' x 22' Wind Tunnel. These systems provide routine measurements on a customer demand basis. In addition there are several mobile systems which are used for unique measurements. Currently a considerable amount of work has been done in conjunction with Ford Motor company. In this effort, measurements have been made of air flow through blower ducts, circulation within the vehicle and of course velocity profiles of the air flow over the vehicle.⁸

3.2 Particle Image Velocimetry

Particle Image Velocimetry has been used on a wide variety of application to obtain velocity measurements across a planer field of view. This technique relies on imaging individual particles which are typically injected into the flow field being studied. Two images are obtained separated in time. The two images are then compared to obtain the distance through which the particle has traveled and hence its velocity. A recent publication provided an overview of several applications of this technology⁹. PIV has been successfully utilized to obtain velocity measurements in the LaRC High Reynold's Number Mach 6 Tunnel, the Counter Flow Diffusion Flame Laboratory, the Jet Noise Laboratory and the Chemical Vapor Deposition Reactor laboratory in addition to several traditional low speed wind tunnels.

Figure 5 shows an example of the data obtained over a wedge in the High Reynold's number Mach 6 Tunnel. The individual vectors represent particle velocity in that region. The front edge shock can be clearly seen as a velocity change above the model. This instrument was then utilized to obtain data on sensitive supersonic models.

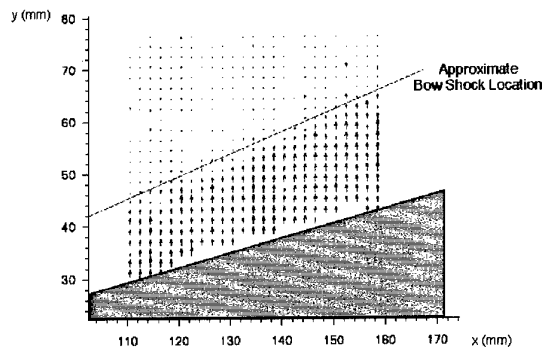


Figure 5. PIV data obtained above a wedge in a Mach 6 flowfield.

A combustion study utilized PIV in the Counter Flow Diffusion Flame Laboratory. The flame system is composed of two opposing tubes which contain the fuel and air respectively to produce a disk shaped flame. The nature of flame formation and extinction is studied in this facility. The PIV was utilized to quantify the flow velocity of the fuel and air up to and through the flame zone. Figure 6 shows an example of this data. The figure shows the incoming air flow and the spreading of the flow as it combines with the fuel flow and produces combustion.

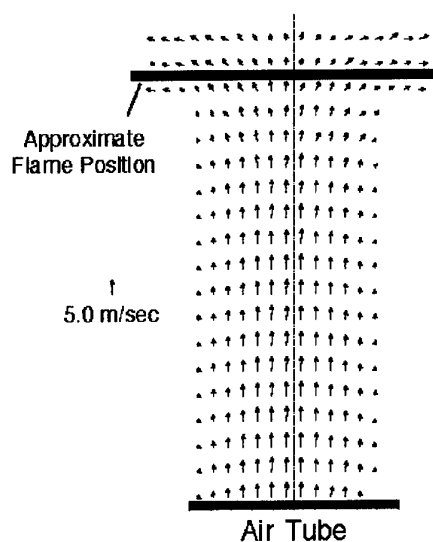


Figure 6. PIV data obtained at the exit of an opposed jet burner.

3.3 Doppler Global Velocimetry

A relatively new technology, Doppler Global Velocimetry, has experienced a rapid rise in popularity among wind tunnel researchers.¹⁰ The reason for this popularity is the unique capabilities of this system coupled with simplicity of the optical design. The unique capabilities include the ability to obtain quantitative measurement of flow velocity across a plane in the flow, instantaneously (within a laser shot or camera cycle). Relative to PIV, this technique does not require the identification of individual particles in the flow, but rather relies of the scattering of any media in the flow. The light scattered from these particles is Doppler shifted due to the motion of the particles. The shifted light is "filtered" using a molecular absorption line filter. This filter essentially transforms the change in frequency due to the Doppler shift to a change in intensity due to the molecular absorption. Therefore, a measure of intensity of the light is directly related to the frequency shift and thereby the velocity of the flow. Both cw and pulsed laser sources have been used with molecular optical cells and off-the-shelf CCD cameras to produce exceptional instrumentation systems.

Several exciting applications have already been performed with this type of system. A few will be highlighted here. Some of the early work concentrated on repeating measurements that had been quantified by laser velocimetry years before. To this end, a study of vortical flow over a delta wing was undertaken¹¹ In this study DGV images were compared with data obtained from traditional LDV experiments on the same model. An example of this data is displayed in figure 7. Although the data is early in the development process, it was still possible to obtain instantaneous quantitative measurements which compared favorably with the measurements which were obtained over an eight hour period!

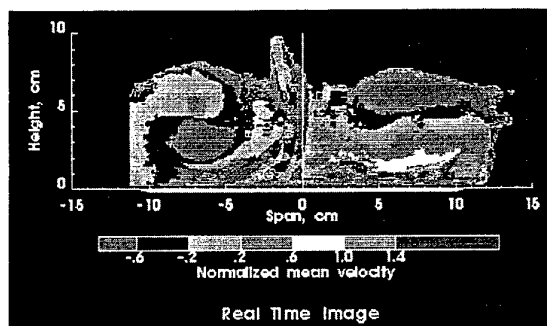


Figure 7. DGV images of vortex above a delta wing.

Recently, some work has been done to assess the applicability of DGV to supersonic flow fields¹² This study included experimental studies of particle lag and its effect on these type of measurements. Figure 8 shows an example of the data obtained. These data display the velocities in a vortical flow above a delta wing set a 24 degrees angle-of-attack and at Mach 2.8. The expected flow structure is clearly delineated with a grid density sufficient for comparison with computational fluid dynamics.

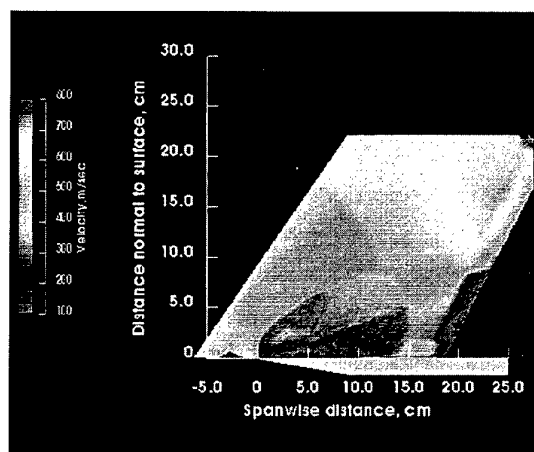


Figure 8. DGV images of a vortex in a supersonic flow above a delta wing.

A variant of DGV called Planar Doppler Velocimetry has also been explored at Langley.¹³ This technique utilizes a pulsed Nd:YAG laser to study turbulent environments. In this study the system was utilized to study the instantaneous velocity structure of a round, Mach 0.85, high

Reynolds number, compressible air jet in the LaRC Small Anechoic Jet Facility. Figure 9 shows an example of these data. The reference and Doppler images are combined to produce the velocity image which is quantitative in intensity.

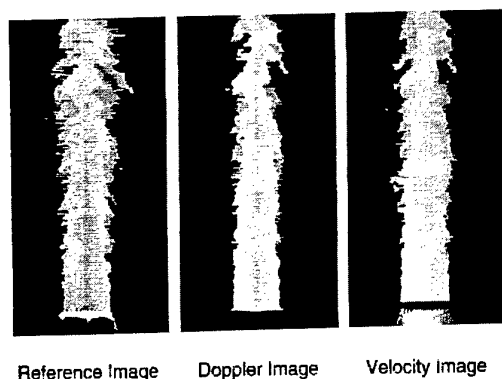


Figure 9. PDV images of a combustor jet.

4.4 RELIEF

Raman Excited Laser Induced Excitation Fluorescence is a relatively new technology which has been developed to measure velocity. In this technique molecular species in the flow are "tagged" electronically with a laser system and then interrogated later to see where they have gone. Knowing the time between tagging and interrogation the velocity can be deduced. Recent work at Langley has focused on the details of the RELIEF technique, including flow tagging improvement, fraction of the molecules tagged, vibrational deactivation by water vapor, vibrational up-pumping in oxygen and modeling of the oxygen Schumann-Runge LIF process.¹⁴

4. State Properties

4.1 Absorption

A rugged, easy to implement, line-of-sight absorption instrument has been developed to make simultaneous measurements of the OH concentration and temperature at ten spatial positions.¹⁵ The system utilizes a low pressure water vapor microwave discharge

cell as the light source. Fiber optic coupling of the light source to the investigated region and back to the detector is employed. The signal is spread over a number of spectral channels to obtain the frequency distribution and thereby the temperature. The absolute magnitude of the signals is measured to calculate the OH concentration. The system has been tested on a flat flame burner and used to make measurements in a scramjet combustor.

4.2 Rayleigh Scattering

Quantitative Rayleigh scattering in supersonic tunnels has been the area of considerable debate for the past several years. Although all of the factors are not well understood, it is clearly true that molecular clustering can cause considerable interference with Rayleigh data at low temperatures. A recent study at elevated temperatures obtained excellent Rayleigh results in a supersonic facility.¹⁶ These studies were performed in the LaRC Mach 6 High Temperature wind tunnel. This tunnel can achieve stagnation temperatures up to 700 °K. The high temperature capability eliminates the clustering effects observed earlier.

Model flow field measurements were obtained on a 38.1 mm diameter cylinder. Measurements were made in the free stream, in the region behind the bow shock in front of the model and the region behind the model, including the wake. An ArF excimer laser was focused into a sheet to interrogate the regions of interest. The Rayleigh scattering was collected with a single intensified CCD. Figure 10 displays a collage of some of these data overlaid on CFD calculations for the model. The correlation's are remarkably good. In fact, the discrepancy in the spreading of the wake has been attributed to incompleteness of the CFD calculations. Obviously a broader light sheet will be investigated so that we can obtain data over a larger field.

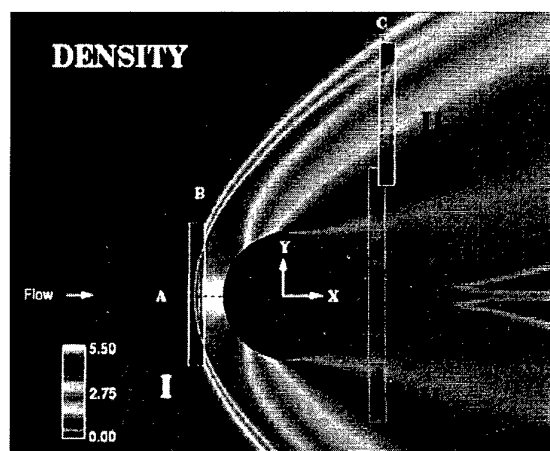


Figure 10. Rayleigh data obtained in 15" Mach 6 high temperature tunnel compared with computational fluid dynamics calculations.

4.3 Laser-Induced-Grating Spectroscopy

Degenerate Four Wave Mixing (DFWM) and Two-Color Laser-Induced-Grating Spectroscopy (TC-LIGS) have been investigated to determine their applicability to combustion diagnostics at NASA LaRC.¹⁷ We have been specifically interested in utilizing these techniques to investigate water, since it is an important end product in the combustion of hydrogen containing fuels. These techniques offer coherent output, good spatial and temporal resolution and easy extension to linear and planar imaging. Although laser-induced population gratings do not appear feasible in practical flame environments, laser induced thermal gratings have been observed and utilized to study water. Measurements were obtained at 266 nm and spectra were obtained in a flame system. A line image was also obtained by spreading the beams with a cylindrical lens. Figure 11 shows the optical alignment for these studies. These studies were only proof of concept, follow-on work will quantify these results.

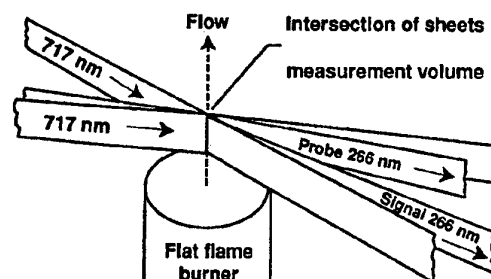


Figure 11. Optical alignment for LIGS.

5. Physical Deflection

5.1 Projection Moiré Interferometry

Projection Moiré Interferometry (PMI), a method for measuring wind tunnel model deformation, has been under development at NASA - LaRC. PMI is a simple, yet powerful technique that has been used since the early 1900's for surface topology and shape characterization. Past efforts to use PMI for wind tunnel model deformation measurements revealed limitations in the technique - particularly directional ambiguity. Recent advances in electronic image acquisition and image processing have overcome these limitations, and have made PMI a viable instrument capable of measuring whole field, 3-component displacement vectors of any visible point on the model surface.

A single component PMI system consists of an illumination source, Ronchi ruling, CCD camera, and frame grabber. Using the illumination source and ruling, a series of equi-spaced, parallel lines are projected onto the object surface. A reference image is acquired in a non-deformed (or wind off) condition to digitally record the projected line pattern. Under load, the model will have moved, and the projected lines will appear to lie in different spatial locations. When subsequent images of the deformed state are acquired and subtracted from the reference image, Moiré fringes are formed. The

geometric configuration of the instrument and projected line pitch dictate the Moiré fringe spacing. Using this relation and fringe counting via image processing, the displacement field can be determined. With commercial hardware and generic RS-170 video cameras, fringe sensitivities of 0.5 mm are common. Advanced image processing and fringe interpolation techniques can extend this resolution to 1/10 to 1/20 of a fringe.

PMI requires no surface preparation or registration targets to be placed on the model. Moiré fringes can be observed in real time providing the test engineer immediate video feedback regarding model position. If desired, this capability allows the engineer to reposition the model before acquiring aerodynamic data, thus minimizing deformation effects. At LaRC, PMI systems are being designed with high power, 800-810 nm laser diodes as the illumination source.

PMI is currently being investigated for measuring dynamic rotor blade deflection, and for unification with other instrumentation systems. Towards these goals, two proof-of-concept tests have been planned: (1) a combined PMI/DGV rotor craft test in the Langley 14- x 22- foot tunnel to investigate rotor blade / wake vortex interaction, and (2) a unified instrumentation test in the Langley Unitary Plan Wind Tunnel comprised of PMI, video photogrammetry, DGV, and PSP. Long term PMI applications include measuring deformation profiles of active feedback controlled rotor blades in simulated flight conditions.

5.2 Electro-Optical Holography

Electro-Optic Holography (EOH) is a laser based, full field diagnostic technique used to measure micron sized deformations in statically displaced or vibrating structures. Using CCD cameras and video framegrabbers, EOH acquires digital holograms of an object under load. When these holograms are computationally interfered with a reference hologram, fringes indicative of the object displacement are formed. For a normal incidence configuration, each fringe represents 1 laser

wavelength of displacement. Using this relation and fringe counting via image processing, the displacement field can be determined. In contrast to scanning vibrometers, the deformation of the entire surface is measured simultaneously, at video rates.

EOH research at Langley has been directed toward the development of an instrument for routine use in studying aircraft fuselage vibration and active noise control. Recently, EOH testing was conducted on an aircraft sidewall model for finite element model (FEM) enhancement and validation. Example results from this test are shown in Figure 12, which compare experimentally measured and computationally predicted mode shapes. Other EOH applications currently being pursued are (a) the measurement of hysteresis and fatigue induced disbands in Rainbow and Thunder piezo-electric actuators, and (b) methods to extract the complex-valued velocity and power flow from EOH measurements.

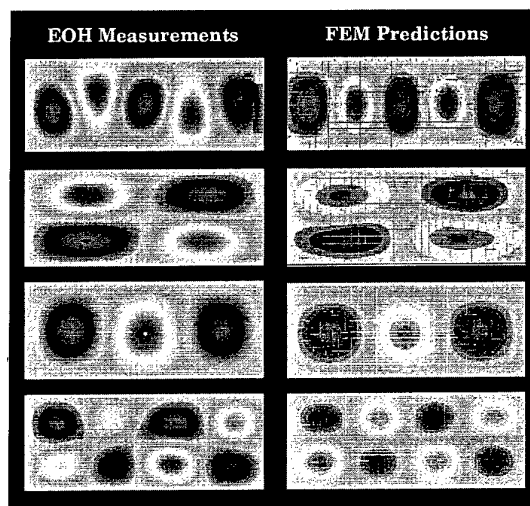


Figure 12: Comparison of EOH measurements vs. FEM predictions for the aircraft sidewall model. Field-of-view is 7.5 x 18.5 inches.

6. Acoustics

6.1 Acoustic Array

There is an increasing demand to measure aircraft noise to meet strict regulations. This has required an increased emphasis on the development of technologies to measure noise. One of the areas which has received considerable emphasis recently is microphone-based directional acoustic array technology. Unique data processing algorithms have been developed to allow noise spectra and noise source image maps to be obtained. An acoustic array consisting of 35 individual microphones arranged in logarithmic spirals has been designed and built at Langley (figure 13).¹⁸ The necessary software was also developed in-house and utilized in a series of test to study airframe noise. In particular, the noise associated with the edge of a wing flap was interrogated. A model wing was placed in the Langley Quiet Flow Facility and the acoustic images were obtained under typical flight conditions.

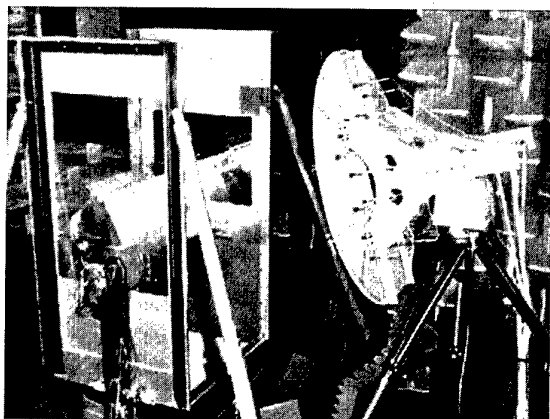


Figure 13. LaRC Acoustic Array in the Quiet Flow Facility, investigating wing flap edge noise.

6.2 Particle Image Velocimetry

One of the more unique applications of particle image velocimetry involved the study of acoustic particle displacements and velocities in a normal incidence impedance tube used to test nacelle liner structures. The PIV system utilized high energy pulsed

Nd:YAG lasers to illuminate particles introduced into the tube. Images of the oscillatory particle motions were captured using a high resolution digital camera and analyzed using classical spatial autocorrelation techniques. For this work, the flow field consisted of a zero-mean, acoustically driven flow induced in a closed impedance tube having a square 2- by 2-inch interior cross section. The acoustic source was capable of generating pure tones over a frequency range of 500-3000 Hz at sound pressure levels from 90 dB to 120 dB. For each test frequency and sound pressure level, a series of 20 separate PIV images were acquired. Autocorrelation analysis of these images generated a mean velocity field containing 285 vectors. To obtain a highly accurate mean particle displacement over the entire field of view of the acquisition camera (approximately 42 mm²), the 285 vectors were averaged to give one particle displacement and hence velocity for each acquired image. The 20 individual particle displacements, one for each image, were further averaged to yield a single particle displacement for the test condition. Different sets of particle displacement measurements were made for a variety of frequencies, sound pressure levels, and synchronization phases between the acoustic driver and the laser system. The results, which were in good agreement with theoretical predictions, indicated an excellent ability of the instrument to measure submicron particle displacements in a zero-mean flow. These measurements were the first of their kind obtained with PIV techniques.

7. Micro-electro-mechanical Systems

Several investigative studies have been performed on MEMs devices to ascertain their usefulness in aerodynamic environments. We have recently placed an optical based skin friction sensor developed at MIT¹⁹ in the Langley 0.3M cryogenic tunnel to assess its characteristics. These initial studies have shown the great potential

of these devices and indicated some areas for improvement.

Acknowledgments

This paper represents the work of a large number of talented scientists, engineers and technicians. Following is a list of contacts for the described techniques.

Focusing Schlieren

Leonard Weinstein

Rayleigh Scattering

Behrooz Shirinzadeh

Laser Induced Fluorescence

R. Jeff Balla

Laser Velocimetry

Luther Gartrell

Particle Image Velocimetry

Tony Humphreys

Doppler Global Velocimetry

Jim Meyers

Planar Doppler Velocimetry

Mike Smith

RELIEF

Glenn Diskin

Absorption

Behrooz Shirinzadeh

Laser-Induced-Grating Spec.

R. Jeff Balla

Projection Moiré

Gary Fleming

Electro-Optical Holography

Gary Fleming

Acoustic Array

Bill Hunter

MEMs

Ken Tedjojuwono

¹ Fish, R. W. and Parnham, K., "Focusing Schlieren Systems," Aeronautical Research Council, CP54(13.865), ARC Technical Report, TN IAP999, London, Nov. 1950.

² Weinstein, L.W., "Large-Field High-Brightness Focusing Schlieren System", presented as paper 91-0567 at the AIAA 29th Aerospace Sciences Meeting, Reno, NV, Jan. 7-10, 1991.

³ Settles, G.S., Hackett, E.E., Miller, J.D., Garg, S., Weinstein, L.M., "Full-Scale Schlieren Flow-Visualization", presented as a plenary paper at the 7th

International Symposium on Flow Visualization, Seattle, Sept. 11-14, 1995.

⁴ Weinstein, L.M., Stacy, K., Viera, G.J., Haering, E.A., Jr., Bowers, A.H., "Visualization and Image Processing of Aircraft Shock Wave Structures", presented at the 1st Pacific Symposium on Flow Visualization and Image Processing, paper 23, Honolulu, Hawaii, Feb. 23-26, 1997.

⁵ Shirinzadeh, B., Hillard, M.E., Balla, R.J., Waitz, I.A., Anders, J.B., Exton, R.J., "Planar Rayleigh scattering results in helium-air mixing experiments in a Mach-6 wind tunnel," Applied Optics, 31(30), pp. 6529, October, 20, 1992.

⁶ Balla, R.J., "Planar Rayleigh Scattering and Laser-Induced Fluorescence for Visualization of Hot, Mach 2 Annular Air Jet, NASA TM 4576, October 1994.

⁷ Exton, R.J., Balla, R.J., Shirinzadeh, B., Hillard, B., Braukman, G., "Flow visualization using fluorescence from locally seeded iodine by ArF excimer laser", submitted to Experiments in Fluids, 1997.

⁸ Hepner, T.E., NASA LaRC, private communications, paper in progress.

⁹ Humphreys, W.M. and Bartram, S.M., "Using Particle Image Velocimetry in Difficult Facilities", AIAA 96-2267, presented at the 19th AIAA Advanced Measurement and Ground Testing Technology Conference, New Orleans, LA, June 17-20, 1996.

¹⁰ Meyers, J.F., "Development of Doppler global velocimetry as a flow diagnostic tool", Meas. Sci. Technol., Vol. 6, p. 769-783, 1995.

¹¹ Meyers, J.F., Usry, J.W., Miller, L.S., "Assessing the capability of Doppler global velocimetry to measure vortical flow fields", presented at a seminar on "Optical methods and data processing in heat and fluid flow" held in London on 2-3 April, 1992. published in Proc. Instn. Mech. Engrs., Part G: Journal of Aerospace Engineering. Vol 208, p.99-105, 1993.

¹² Meyers, J.F., "Application of Doppler Global Velocimetry to Supersonic Flows", AIAA 96-2188, presented at the 19th AIAA Advanced Measurement and Ground Testing Technology Conference, New Orleans, LA, June 17-20, 1996.

¹³ Smith, M.W., "Application of a Planar Doppler Velocimetry System to a High Reynolds Number Compressible Jet", submitted to the 1998 AIAA Aerospace Science Conference, Reno, NV.

¹⁴ Diskin, G.S., "Experimental and Theoretical Investigation of the Physical Processes Important to the RELIEF Flow Tagging Technique," Ph.D. Dissertation, Princeton University, June 1997.

¹⁵ Shirinzadeh, B., Gregory, R.W., "Resonance lamp absorption technique for simultaneous determination of the OH concentration and temperature at 10 spatial positions in combustion environments.", *Laser Application in Combustion and Combustion Diagnostics II*, SPIE, V. 2122, p.29-48, 1994.

¹⁶ Shirinzadeh, B., Balla, R.J. and Hillard, M.E., "Rayleigh Scattering Measurements in Supersonic Facilities", AIAA 96-2187, presented at the 19th AIAA Advanced Measurement and Ground Testing Technology Conference, New Orleans, LA, June 17-20, 1996.

¹⁷ Hart, R.C., Balla, R.J. and Herring, G.C., "Observation of H₂O in a Flame by Two-Color Laser-Induced-Grating Spectroscopy", accepted for publication by *Measurement Science and Technology*, 1997.

¹⁸ Humphreys, W.M, Jr., Brooks, T.F., Hunter, W.W., Jr., Meadows, K. R., "Design and Use of Microphone Directional Arrays for Aeroacoustic Measurements", submitted for presentation at the 36th AIAA Aerospace Sciences Meeting and Exhibit, Reno, NV, Jan. 12-15, 1998.

¹⁹ Brauer, K., MIT, private communication.

Measurement techniques developed for cryogenic field in T2 transonic wind tunnel

A. Seraudie - J.P. Archambaud - A. Mignosi

ONERA/CERT

Department of Aerothermodynamics
2 avenue E. Belin - 31055 TOULOUSE Cedex (FRANCE)

ABSTRACT

T2 is an induction driven wind tunnel (fig. 1) in which Reynolds number variations are obtained by increasing the total pressure ($P_t = 1,4$ to 3bar) and reducing the total temperature ($T_t = 300$ to 110K). The flow is driven by an injection of dry air at ambient temperature and cooled by another injection of liquid nitrogen.

Advanced development of conventional techniques and modern measurement techniques have been performed for low-temperature cryogenic flows.

This paper presents the evolution of the specific tools sometimes developed, always tested and mainly used for different 2D or 3D flows at ambient and cryogenic conditions.

Firstly it gives the developments performed in the field of anemometer and pressure probes to measure the flow quality of the cryogenic wind tunnel. Secondly it describes the use of infrared technique for the qualification of the boundary layer transition on 2D and 3D models. Finally this paper presents some L.D.A. typical 2D and 3D measurements at ambient condition and the adaptation of this velocity measurement device to work in cryogenic condition.

NOMENCLATURE

A_{film}/A_{wire} : amplitude ratio (film / wire probes)

C : model chord

C_h : station number

d : distance from the wall

M_l : local Mach number

M_v : free stream Mach number

P : static pressure (bar)

P_t : total pressure (bar)

$(p)'$: static pressure fluctuations

Re_c : Reynolds number based on model chord length

t : time (seconds)

T : static temperature (K)

T_t : total temperature (K)

T_w : wall temperature (K)

$(Tat)'$: stagnation temperature fluctuation

$(pu)'$: mass flow fluctuations

α : model angle of attack ($^\circ$)

ϵ : emissivity coefficient

λ : wavelength

INTRODUCTION

The use of cryogenic technology has produced real progress in wind tunnel testings, permitting the attainment in high Reynolds numbers and so the good simulation of aerodynamic phenomena existing on aircraft in flight.

In the T2 wind tunnel, an induction system using ambient temperature air and driving the flow in the circuit at pressure up to 3 bar is combined to a cryogenic operation, cooling the flow by liquid nitrogen injection. The T2 wind tunnel operated at ambient temperature under pressurized conditions from 1975 until its cryogenic adaptation in 1981. The increase in Reynolds number provided more aerodynamic studies in a wide range of transonic flows for basic research and industrial applications. During the same time period, instrumentation and new models, well adapted to low temperatures, were developed to analyse the flow characteristics connected with Reynolds number variations.

After a brief presentation of the main features of the wind tunnel we will describe the tools mainly used on different 2D or 3D models : anemometer and pressure probes for flow quality measurement, infrared technique for the qualification of the boundary layer transition and L.D.A. for flow velocity measurement.

1. THE T2 WIND TUNNEL

1.1. Different Parts of the Circuit

The diagram presented in figure 2 gives a good idea of the main parts of the pressurized transonic cryogenic wind tunnel T2 (Ref. 1).

The settling chamber of square section ($1,8 \times 1,8 m^2$) is followed by the convergent part with a contraction ratio of 22. The test section is 0,39m wide, 0,37m high and 1,32m long and is equipped with 2-D adaptive walls to avoid transonic blockage and to reduce wall interference effects. In the downstream section, a sonic throat regulates the test Mach number between 0,6 and 1. Flow is produced by the high pressure dry air injected through the trailing edges of the turning vanes in the first corner downstream of the test section (fig. 2). The liquid nitrogen injection, necessary to cool the flow, is located in the driven air mixing chamber, which is immediately after the injector corner. The exhaust of the air-nitrogen mixture takes place in the first diffuser between the test section and the injector corner. A

compressor supplies, at a pressure of 80 bar, a 45 m³ tank with the injection compressed air. The cooling liquid nitrogen is moved from the 20 m³ storage tank to the pressurized test tank, for the run.

1.2. Test Section

The T2 test section is equipped with flexible top and bottom walls made of *INVAR* plates, 1.3 mm thick, each one controlled by 16 hydraulic jacks (fig. 3). This is the 2-D adaptive wall part of the tunnel (Ref. 2).

Wall adaptation is performed in real time by an iterative strategy which converges in about 3 or 4 iterations (4 seconds/iteration) during the run (Ref. 3). For 2D flows, a 2D adaptation method allows to cancel wall interferences around 2D airfoils ; for 3D flows, a 3D method designed for 2D wall deformations minimizes wall interferences around various types of 3D models (bodies of revolution, aircrafts, half fuselage-wing).

Sidewalls of the test section are equipped with round and rectangular windows. Some of them are made of a special glass and are used for optic measurements in the test section (infrared, laser).

1.3. Operating mode for cryogenic runs

During the short duration of the run (60 to 120 s), good conditions are obtained through the use of two mini computers to control the flow (Ref. 4), the adaptation of the walls and the measurements (fig. 4). The first computer is devoted to the control of the parameters (M_v , P_t , T_t), the second one handles the control of the measurements and exploring system, data acquisition and wall adaptation.

We present, in figure 4, a typical run at $M_v = 0.750$, $T_t = 120$ K, $P_t = 3$ bar, with the evolution of the main flow parameters versus time during the time.

The operating chart of the T2 wind tunnel is presented in figure 5 for two stagnation temperature levels ($T_{at} = 290$ K and 120 K). The usual operating domain of T2 covers the range of Mach number from 0,3 to 1, stagnation pressure from 1 to 3 bar, temperature from 120 to 300 K, Reynolds number from 3 to 29 million (chord ≈ 0.18 m) and testing time from 30 to 120 s (Ref. 5).

2. FLOW QUALITIES MEASUREMENTS

The wind tunnel fluctuation level (mass flow and pressure), is an important parameter for the laminar studies. When the transition location is freely moving with the test conditions (the Mach number, the angle of attack, the Reynolds number, the wall temperature,...) the fluctuation level becomes very influential (Ref. 6); so it has to be known in all the range of the wind tunnel conditions.

2.1. Instrumentation to Measure Flow Quality

To qualify the flow disturbances in T2, an unsteady type instrumentation was developed measuring the fluctuations of the static pressure (p'), the mass flow (\dot{m}'), and the stagnation temperature (T_{at}') in the test section at transonic speeds (Ref. 6 and 7).

A probe, equipped with a small cryogenic pressure transducer, measured the static pressure fluctuations (fig. 6). This transducer (Kulite XCQL-7A-093-4D) was calibrated at different temperature levels ; the frequency range is from 0 to 10 kHz. A complete calibration of the probes has been performed before the T2 measurements (Ref. 9) to determine the right calibration coefficients applied for the tests.

The mass flow fluctuations were measured with a hot film probe (Dantec 55R71), likewise calibrated with temperature ; the probe was kept at constant temperature by the anemometer and the frequency range was from 0 to 10 kHz (fig. 6). Other probes (Dantec 55R31 and 55R41) were recently compared in T2 test section to a wire probe with measurements performed at low pressure into the turbulent boundary layer developing on the side wall of T2 test section (6mm from the wall for a boundary layer thickness $\delta=15$ mm). An example of the spectra is given in figure 7. The agreement is good at very low frequency ($f < 1$ Hz) but a systematic shift depending on the Mach number exist for $f > 100$ Hz (fig. 7). This problem is connected to the fact that the heat fluxes between the hot film and the silica support are much more important compare to those in the wire probe. At low Mach number this conduction effect is crucial for the film probe and so the difference is greater. Moreover for low frequencies (D.C or $F < 1$ HZ) the conduction of the backing material dominate the dynamic property, at high frequency ($f > 100$ Hz) the penetration depth of the thermal waves is small and the attenuation coefficient seems constant (fig. 8). The wedge probe 55R31, with a smaller damping coefficient (fig. 8), can easily be used for transonic cryogenic measurement with small corrections. This probe has been used in ETW, to measure the flow qualities in the test section.

For total temperature fluctuations a special probe has been designed around a cold wire of 2.5 μ m diameter (Ref. 8). This probe measures the temperature of the flow at a constant speed of 50 m/s, fixed by a sonic throat located just upstream of a vacuum pump (fig. 11). The temperature of the wire is nearly equal to the total temperature of the flow, its bandwidth is 0 to 600 Hz. After a calibration using the time response of the wire to a heating pulse produced by a laser, the measures are corrected up to 3 kHz by the experimental transfer function.

2.2. Flow quality measurements in T2

The fluctuation measurements are presented in figures 9, 10 and 11 in a dimensionless form versus the total temperature of the flow, from 140 K to 300 K. Several Mach numbers (from 0.7 to 0.77), were experimented here for different temperature levels ; these conditions correspond to a laminar airfoil test.

The static pressure is reduced by the total pressure P_t of the flow. The rms. level of p/P_t seems quite constant with temperature (fig. 9), the 0.28% value is nearly independent of the flow conditions, only a small change is observed with the bandwidth analysis.

The relative mass flow fluctuations versus test section Mach number, measured at different stagnation temperatures, are presented in the figure 10. They are roughly constant around an average value of 1.10^{-3} .

The relative temperature fluctuations (T'/T_{at}) increase when the temperature decreases : from 0.02% (T_{at}' rms. = 0.06K) at ambient temperature to 0.12% (T_{at}' rms. = 0.17K) at 140K (fig. 11). Most of the energy corresponds to the low frequencies ; the fluctuations are attributed to the temperature regulation process, the liquid nitrogen spraying, the imperfect mixing of the driving-air (at room temperature) with the driven cryogenic flow, and the wall heat fluxes.

3. INFRARED THERMOGRAPHY

It is essential to know experimentally the transition location on a model as the transition location greatly modifies the airfoil characteristics. Connected to laminar studies, some different techniques have been developed and used to qualify the transition front location. Up to now, the principle often used in T2 wind tunnel is based on the wall temperature measurement, giving a local information with thermocouples or global information with liquid crystal or infrared visualizations. In our case the best adapted system for both ambient temperature and cryogenic condition is the infrared thermographic device giving a map of wall temperature.

The different key points for the use of such a system in cryogenic condition are the infrared camera, the traversing window, and the coating material of the metallic models working at low temperatures, necessary to avoid the mirror effect.

3.1. Infrared equipment

We use a classical high wavelength camera INFRAMETRICS 600 (8-12 μ m), which observes the model upper side through a lateral ZnSe glass window (fig. 12 and 13). As we can see on figure 12 the angle between the camera and the normal to the model surface is close to 65° which is close to a limit for the emissivity performance. In spite of this observation angle we can see a great part of the model upper side in good condition, without any lens.

This device can be used by two different ways :

- for model global visualizations in order to oversee the boundary layer state during the tests (Ref. 12 and 13)
- to determine more accurately the transition front location. Before the tests some reference marks are put on the model and we perform some pictures without wind to have good references of the model. After the

tests the infrared measurement files are treated on a P.C. computer, achieving temperature distributions along the model chord to determine the transition front location. Moreover this classical infrared camera works correctly only down to 200K.

E T W team asked for different researches in order to find solutions for transition qualification in cryogenic condition : the Physic Division of ONERA had in charge the development of a new long wavelength camera working well down to 100K ; our department had developed some coating materials for metallic models working at low temperatures.

3.2. Metallic model preparation

For our applications of infrared measurements we chose the solution of metallic model coated with painting for different reasons:

- first for the manufacturing accuracy and the surface finish of the model (better results with metallic support),
- secondly for the mechanical behavior of the structure during the tests in cryogenic and pressurized conditions,
- for the equipment with thermocouples and pressure taps, easier to be installed in metallic models,
- finally for the use of existing models.

During the first phase of the work we chose usable materials, well adapted for the test conditions and easy to install on different types of models without alteration of the shape and the roughness (Ref. 14).

In the second phase of the study tests have been performed on selected materials : mechanical, thermal and optical tests have been carried out to qualify the coating materials. So we selected 3 to 4 aeronautic paintings with the requirement of spraying in 2 layers : the first one sticking to the metallic wall and the second one achieving a good infrared response and a nice surface finish necessary for laminar flows.

Optical and mechanical tests have been performed on the different coating painting.

The optical tests are relative to the emissivity measurement as a function of the observation angle (fig. 14), in a large wavelength (fig. 15). To measure the emissivity for different view angles, the different samples were fixed on a heating support ($T=60^{\circ}\text{C}$: the emissivity coefficient is no dependent of the temperature level), close to a black body reference. The support could rotate and made possible directional emissivity measurements between 0 to 70° (fig. 14). The emissivity coefficient is higher than 90% (3-12 μ m) up to 70° view angle.

To measure the emissivity evolution with wavelength for different thicknesses of the coating material (fig. 15) another method was used ; tests were performed in an integrating sphere. In the first step the integrating sphere is empty and the incident light is sent in the sphere and the detector measures the intensity versus the wavelength. In the second step the sample is put in the center of the sphere with 15° angle with the incident light. The detector records the flux reflected by the

sample for different wavelength. The emissivity is given by the KIRCHOFF's law $\epsilon = 1 - R$ (R is the ratio of the 2 records). In the wavelength less than $20\mu\text{m}$ the emissivity level is greater than 90% for painting thickness greater than $10 - 15\mu\text{m}$; for the metallic surface alone, without coating, the emissivity is very low (close to 10%).

During cryogenic, pressurized tests the model is submitted to severe conditions like thermal gradients, forces due to the flow, thermal cycles, moisture,.... Mechanical and thermal tests have been performed on the tests samples trying to reproduce the wind tunnel conditions. Figure 16 gives the envelope of the mechanical and thermal tests performed, and a picture of the result of adherence test. After 5 thermal cycles ($300\text{K} \rightarrow 77\text{K}$) the sample was notched with a blade. An adhesive tape was strongly glued on the coating and pull out, then the surface was observed. Concerning the adherence, the best results were obtained with the use of wash primer under the painting.

For laminar studies it's necessary to achieve a very good surface finish of the model, mainly in the leading edge region in order to keep laminar the boundary layer. The surface roughness of the painting was not sufficient and a large improvement was achieved by polishing. Very good values, between 0.2 to $0.5\mu\text{m}$ were reached, very close to the surface finish of the metallic walls. Finally the thickness of the coating is very close to $60 - 70\mu\text{m}$ on the tested samples and we use the same thickness order on the models.

In the third part of the study we have performed different tests in wind tunnel (down to 170K) to verify the good behavior of the paintings on different models, using our classical infrared camera (Ref. 16 and 17). Up to now, these coating paintings are currently used for all the laminar studies needing infrared visualization. This technique is interesting because we can perform infrared measurements on existing models. All these tests are completely reported in (Ref. 15).

3.3. Transition detection principle

The first technique based on the temperature equilibrium level is difficult to achieve due to :

- the time needed to obtain a perfect temperature equilibrium on laminar models,
- the laminar/turbulent temperature difference which decreases when the total temperature of the flow decreases,
- and the pressure gradients inducing adiabatic wall temperature gradients which can mask the difference when the transition occurs.

We prefer the second technique based on a small temperature step of the flow ; the observation of how the model comes back to the equilibrium indicates the nature of the boundary layer. The easiest way, applied in T2, is to stop the cooling phase of the model (fig.4) few degrees before reaching the nominal temperature. In this case the measurements begin when the model is 5 to 6K warmer than the flow and its wall temperature is decreasing slowly during the time, to the adiabatic condition ; the total temperature of the flow is kept constant. The heat fluxes between the model and the

flow are calculated considering a monodimensional sheet of metal. In fact the thin skin of the model, 3mm thick, is used as a flux meter, and the conduction heat fluxes are neglected. The strong difference in the Stanton number evolution along the chord indicates the transition location. Figure 17 shows a good example of this determination : distributions of Mach number, measured temperature and Stanton coefficient along the model chord for a typical test are given. The transition location is well defined in this configuration (Ref. 12 and 13).

3.4. Infrared Visualizations

Figure 18 shows a typical visualization with a natural transition from laminar (clear region) to turbulent (dark region) on a 2D model close to 240K . Because the temperature equilibrium is not yet reached (model warmer than flow), heat fluxes are greater on turbulent region than on laminar one. So the temperature on turbulent region is lower than on laminar one as indicated by the infrared visualization which is an instantaneous temperature map of the model surface. At high Reynolds number the inspection of the infrared image gives information about the possible appearance of turbulent cones during the test around critical temperature condition ($T_{at} \approx$ flow dew point temperature) as behind local roughness (in the background of the figure 18). Another colored infrared picture is given (fig. 19) for a test close to 240K on an axisymmetric body. In this configuration the transition location is well defined by the rapid color change in the middle of the picture ; the left part corresponds to the laminar part with higher temperature level. In addition temperature distribution along the model equatorial line can be drawn from the infrared image file, to define accurately the beginning of the transition front (fig. 19).

4. LASER DOPPLER ANEMOMETRY

4.1. Laser Doppler Anemometer

The last important device developed for T2 wind tunnel is the 3D laser Doppler anemometer ; it is used since 1990 at ambient condition for aerodynamic 2D or 3D measurements for boundary layer and wake survey. The different main parts of the bench are given (fig. 20) : the three displacement axes with computer controlled motors, the laser source (15 watts) and optical couplers, 2 emitting optics and their monomode optical fibers, the 2 receiving optics and the 3 real time Doppler F.F.T. processors (Burst Spectrum Analyser). The main characteristics of the mechanical, optical and electronic parts are given in figure 21. The flow is seeded with oil droplets of $1\mu\text{m}$ in average diameter in the return leg of the circuit (Ref. 18, 19 and 20), the diameter of the measuring volume is close to $130\mu\text{m}$.

Up to now aerodynamic measurements have been performed only at ambient condition, to qualify the lateral boundary layer effect, the steady and unsteady shock waves, the shock wave - boundary layer interaction on a 2D model, or the 3D flow downstream of the model of a modern transport aircraft, in the T2 test section. First there is a typical result obtained

through the steady shock wave on the upper side of a OAT15A 2D model (fig. 22). The horizontal probings performed at 10, 30 and 60 mm above the model wall give a good idea of the intensity variation, the area and the shape of the shock wave. For the probing near the wall, the length of the shock wave step is given by the drag of the seeded particles.

A great problem for the laser velocimetry measurements is the wall approach which determines the part of the boundary layer we can measure. Among the different boundary layer probings that we performed on several models, we have observed important differences on the minimum distance from the wall where the measurements were not valid (fig. 23). The forward scattering configuration is the most favorable case : the distance is close to 0.5mm. On the other hand this distance becomes important with great angles between the emitting light and the wall (back scattering configuration). A typical example of 2D velocity measurements gives the secondary field in the wake of a 3D model (fig. 24) ; we can see the different vortices generated by the upsweep of the rear part of a modern aircraft model.

4.2. Adaptation For Cryogenic condition

The key points of laser velocimetry in cryogenic condition are the glass window well designed for important temperature gradients (without frosting of the external surface and allowing a good transmission of the beams into the test section) and the seeding of the flow. The first point was studied by the use of 2 thick (60mm) silica windows (fig. 25). The important thickness solves the problem of pressure (mechanical behavior) and temperature during the short T2 run time. A computation of the temperature front propagation in the silica material have been done for the definition of the window size (fig. 25). The result is in good agreement with the temperature measurement on the external surface of the window : during the run this part of the glass remains effectively at ambient temperature. In addition the expansion coefficient of the silica material is very low, so the window accepts a great temperature gradient without breaking the glass.

The 2D velocity measurements have been performed in the center of the empty T2 test section at $M_v = 0.77$, $P_t = 1.7b$ for different temperature levels, with and without seeding. The forward scattering configuration was chosen with a yaw angle (20°) to simulate future 3D measurements (fig. 26).

When T_{at} is decreasing, it achieves successively the H_2O dew point (210K) and the CO_2 condensation point (135K) of the flow ; for these two levels a lot of small icicles appear in the flow and the frequency acquisition of the velocimeter becomes greater than at ambient temperature (fig. 27). Moreover the validation rate is decreasing due to the saturation of the photo-multiplier : in fact there are a lot of small particles in the flow and it's necessary to decrease the electric supply of the photo-multipliers. So below the dew point it's not necessary to inject oil particles in the wind tunnel, ice particles of the flow are sufficient to measure correctly the velocity (fig. 27). From a quality point of

view, there is a good agreement between the velocimeter information (with and without seeding) and the velocity coming from the wall pressure measurements (fig. 28).

This investigation is encouraging for future tests concerning laser aerodynamic measurements in cryogenic condition.

CONCLUSION

T2 is an induction, pressurized, transonic wind tunnel, converted since 1981 for cryogenic operation. It is an internal insulated facility, equipped with a high performance automatic control system and a test section with a 2D flexible wall system for adaptation.

We present the evolution of the specific tools sometimes developed, always used for different 2D or 3D flows at ambient and cryogenic conditions.

The developments concern the anemometer and pressure probes to measure the flow quality of the cryogenic wind tunnel. The goal of the different studies was to know as better as possible the tools we used to perform the measurements : the static and dynamic bandwidth of the different probes. In laminarity studies the use of infrared technique for the experimental qualification of the boundary layer transition on 2D and 3D models is a very good tool for tests at ambient and cryogenic condition. We have developed the coating painting working well at low temperatures, to improve the infrared pictures and the accuracy of the transition front determination.

The last device developed around T2 is the 3D laser velocimeter, very useful at ambient condition and now able to measure in cryogenic condition.

The association of research and industrial activities allowed to analyze various subjects in an extended Reynolds number range : model performances, transition, laminar flow (low turbulence level), buffeting and 2D or 3D wall adaptation performances, drag reduction technique.

REFERENCES

- /1/ Michel R., Quemard C., Mignosi A., March 1979, "The induction driven tunnel T2 of O.N.E.R.A./C.E.R.T." *Journal of Aircraft*, Vol.16,n° 3.
- /2/ Archambaud J.P., Mignosi A., May 18-20, 1988, "Two-dimensional and three-dimensional adaptation at T2 transonic wind tunnel of O.N.E.R.A./C.E.R.T." *A.I.A.A., 15th Aerodynamic Testing Conference*, San Diego, California (U.S.A.).
- /3/ Archambaud J.P. September, 1992, "Use of flexible walls to minimize interferences at T2 wind tunnel" *European forum on wind tunnels and wind tunnel test techniques*. Southampton.
- /4/ Gobert J.L., Mignosi A., September 15-17, 1982, "Studies of the cryogenic induction driven wind tunnel T2." *E.T.W. Cryogenic Technology*

Review Meeting, N.L.R., Amsterdam (Netherlands).

- /5/ Séraudie A., Archambaud J.P., Mai 20-24, 1996, "T2 Transonic Cryogenic Wind Tunnel at Toulouse" *Special course on advances in cryogenic wind tunnel technology*, D.L.R. Research Center, Köln (Germany).
- /6/ Mignosi A, Arnal D, Prudhomme S, Reneaux J March 1992, "Problems connected with laminar flows in a cryogenic wind tunnel." First European forum on laminar flow technology. Hamburg
- /7/ Mignosi A., Archambaud J.P., Prudhomme S., Plazanet M., Payry M.J., June 28-30, 1988, "T2 ability concerning model design and instrumentation in short run processing." *Second Cryogenic Technology Review Meeting*, Köln/Porz (R.F.A.).
- /8/ Blanchard A, Dor J B, Séraudie A, Breil J F. June, 1988, "Flow quality in the T2 cryogenic wind tunnel-problems and solutions." Second cryogenic technology review meeting Köln Germany
- /9/ Mignosi A., Archambaud J.P., Caruana D., Séraudie A, Sept - Oct., 1997, "Measurement Techniques Developed for Cryogenic Environment in T2 Transonic Windtunnel." 17th ICIASF Monterey California USA
- /10/ Séraudie A. et Al Septembre 1994. "Analyse fine de la transition en écoulement 2D". R.T.S. DERAT N°65/5006.47
- /11/ Bize D., Lempereur Ch., Mathé J.M., Mignosi A., Séraudie A., Serrot G. Sept - Oct 1997 "Surface temperature mapping using liquid crystals applied to identifying the laminar-turbulent transition". 17th ICIASF Monterey California USA.
- /12/ Blanchard A, Dor J B, Séraudie A. September 14-17, 1992, "New testing techniques in the T2 cryogenic wind tunnel." European forum on wind tunnels. Southampton University (U.K.)
- /13/ Séraudie A, Dor J B, Archambaud J P, Blanchard A. March 16-18 1982, "Laminar flow testing in the T2 cryogenic wind tunnel." 1st European forum on laminar flow technology. Hamburg (Germany)
- /14/ Blanchard A, Petitniot J.L., Septembre 1992 "Investigation about the use of model coating materials in conjunction with infrared camera systems at cryogenic temperature. Phase 1 : Survey of candidate materials and possible alternative models " RT DERAT N° 51/5006.37 (ETW contract)
- /15/ Mignosi A, Bize D, Janvier 1993 "Investigation of the use of model coating materials in conjunction with infrared camera systems at cryogenic temperature. Phase 2 - The selection of coating materials : realisation, mechanical, thermal and optic tests." RF DERAT N° 56/5006.37 (ETW contract)
- /16/ Caruana D. et Al, January 1994 "Investigation about the use of model coating materials for infrared camera systems. Phase 3 : Verification testing. " RT DERAT N° 61/5006.45 (ETW contract)
- /17/ Caruana D. et Al, Decembre 1996 "Tests of the ETW Laminar Reference model at T2 Windtunnel" RF DERAT N° 75/5006.62 (ETW contract)
- /18/ Prudhomme S., Séraudie A. September 18-21 1989, "Design of a three-dimensional Laser Doppler anemometer for T2 transonic wind tunnel." ICIASF'89 DLR Göttingen Germany
- /19/ Prudhomme S., Séraudie A, Mignosi A. August 5-9 1991, "A recent three-dimensional Laser Doppler applications at the T2 transonic wind tunnel : optimisation, experimental results, measurement accuracy." 4th international conference on laser anemometry advances and applications Cleveland OHIO (U.S.A.)
- /20/ Séraudie A, Mignosi A, Dor J B , Prudhomme S. October 4-7 1993, "Technique expérimentale de mesure en écoulement transsonique avec un système de vélocimétrie laser tridimensionnel. Application à la détermination de la traînée d'un fuselage." AGARD meeting Brussels (Belgium)

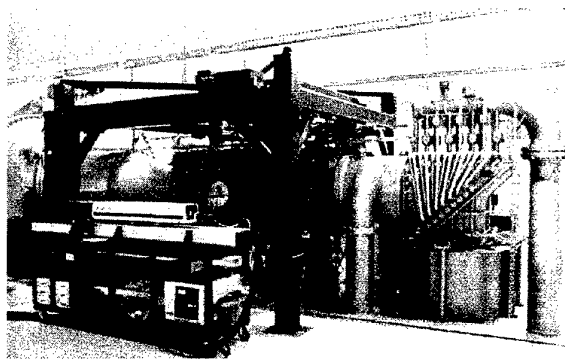


Figure 1 - T2 Wind tunnel

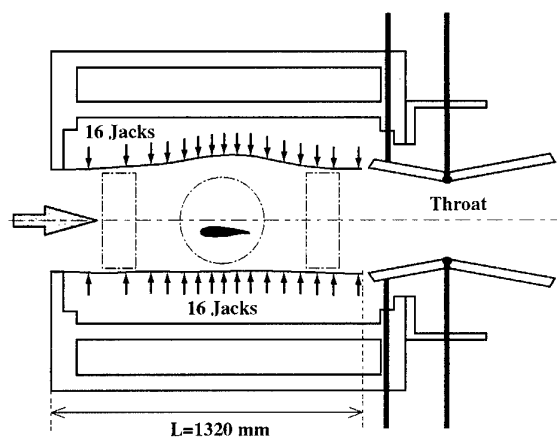


Figure 3 - T2 Test section and cryogenic adaptive walls

$120 \text{ K} < T_t < T_a$ $0,6 < M < 0,9$ $3 \text{ million} < Re_c < 30 \text{ million}$
 $100 \text{ mm} < C < 250 \text{ mm}$ $1,6 \text{ b} < P_t < 3 \text{ b}$ Run time : 60 s to 120 s

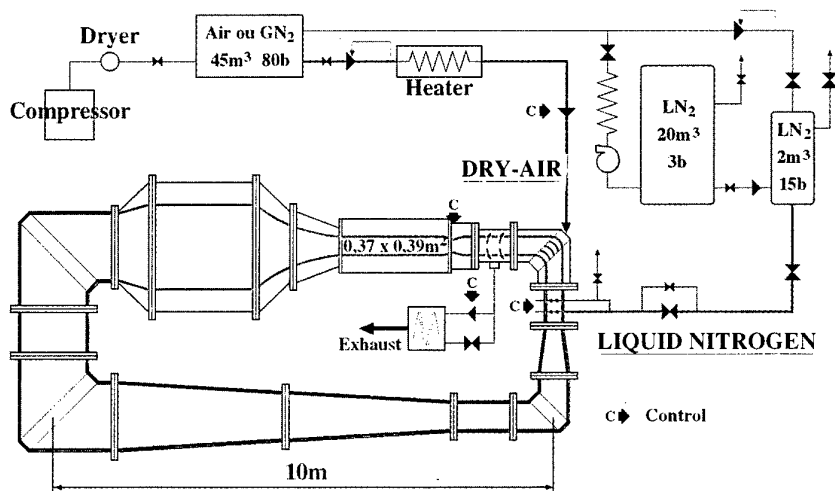


Figure 2 - T2 Wind tunnel layout

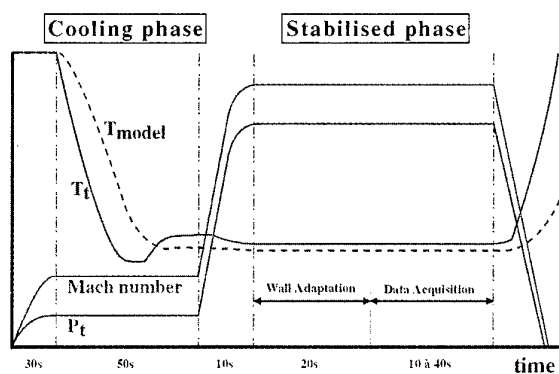


Figure 4 - Typical cryogenic run
 $M_o = 0,75$ $P_t = 3 \text{ bars}$ $T_i = 120 \text{ K}$

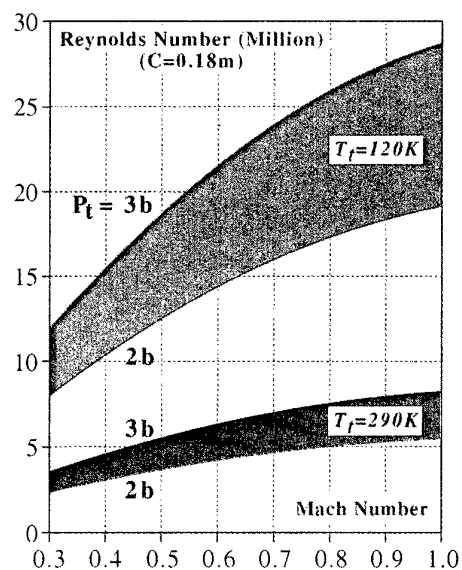


Figure 5 - T2 operating envelope

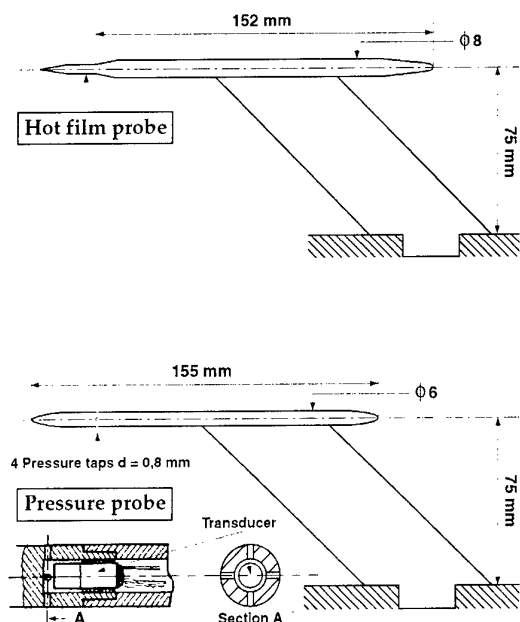


Figure 6 - Hot film and pressure probes

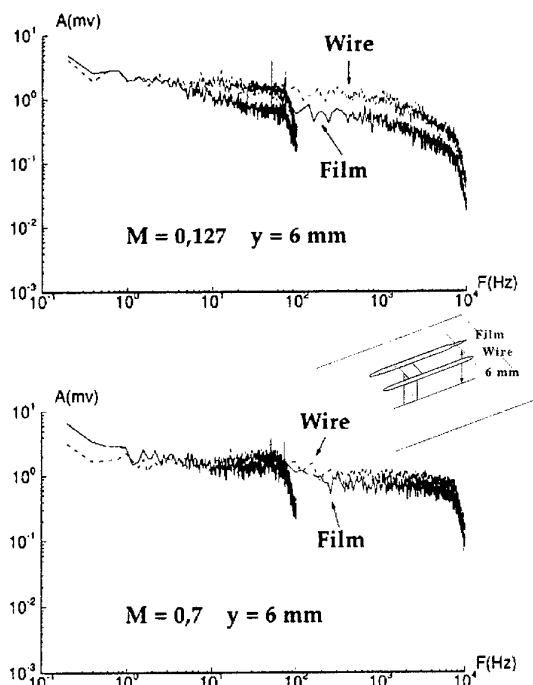


Figure 7 - Comparison hot wire/hot film Spectra in a boundary layer

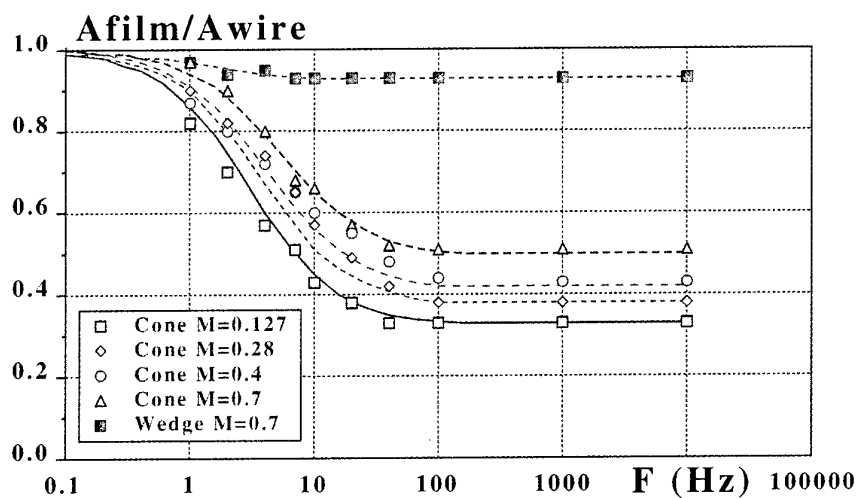
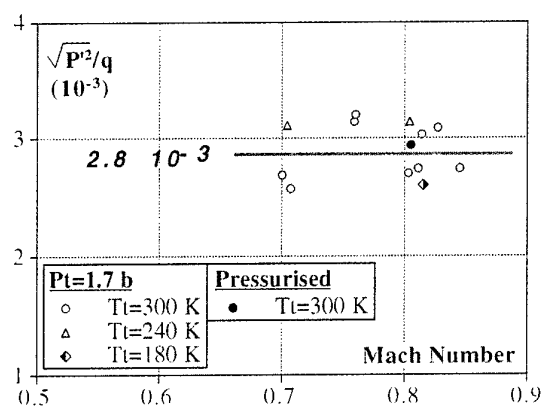
Figure 8 - Amplitude ratio : $A_{\text{film}}/A_{\text{wire}}$ 

Figure 9 - T2 result : pressure fluctuation level in the test section

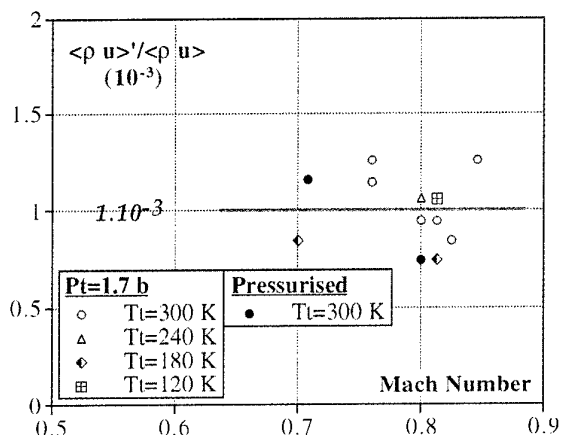


Figure 10 - T2 result : massflow fluctuation level in the test section

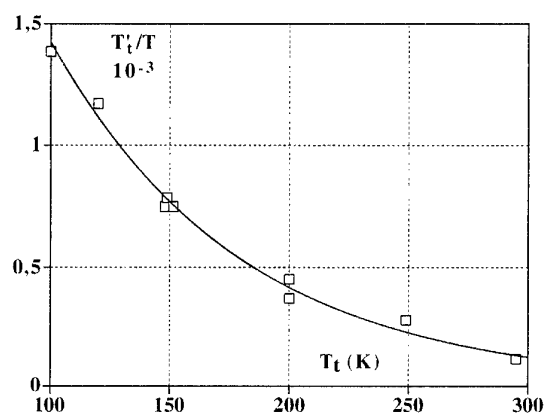
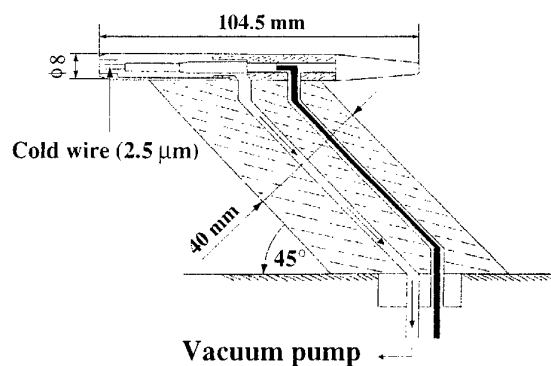


Figure 11 - T2 result : temperature fluctuation level in the test section

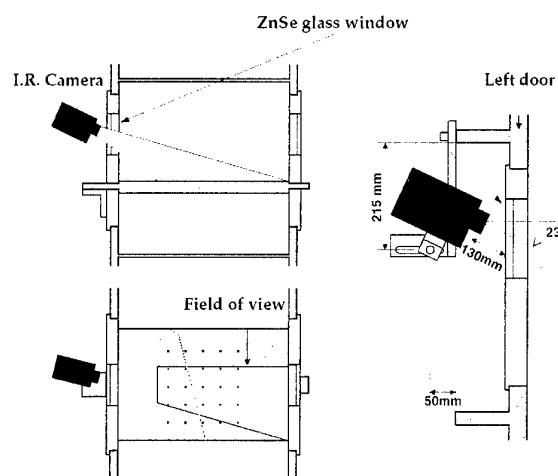


Figure 12 - Infrared camera set up - View field

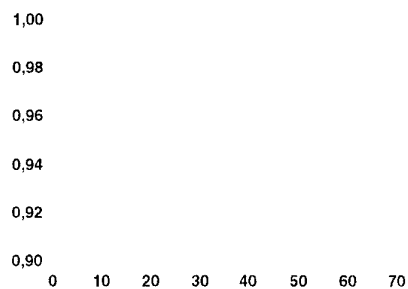


Figure 14 - Painting emissivity : evolution with view angle

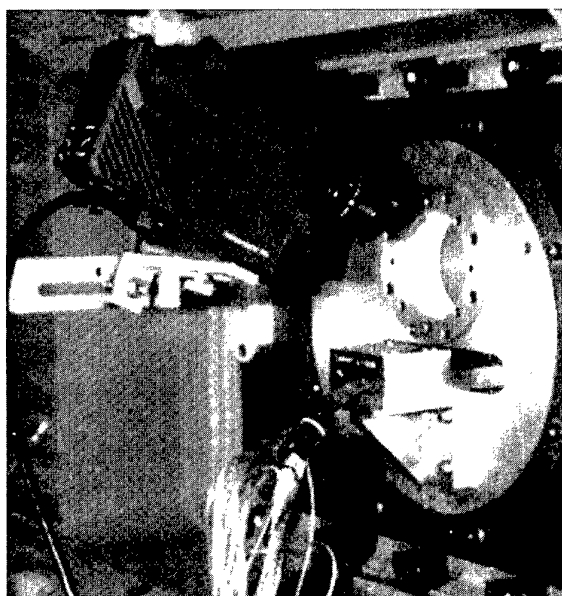


Figure 13 - Infrared camera - ZnSe glass window

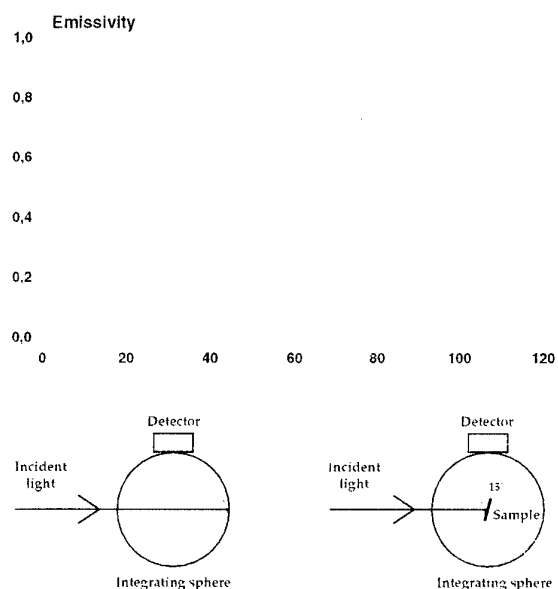


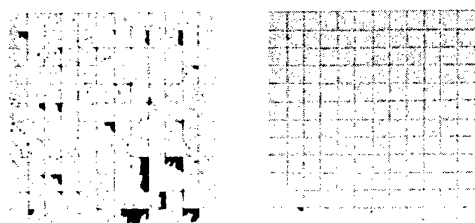
Figure 15 - Painting emissivity : evolution with the wavelength

● Mechanical and thermal tests

- Soaking and bending tests
 - $T_a \leftrightarrow 77\text{ K}$
 - Deformation 3 mm
- Adherence tests
 - Tests with an air jet
 - Tests with an adhesive tape (*)
- Surface roughness and hardness

● Optical tests : emissivity measurements

- Variation of view angle
 - comparison with a black body
- Variation of the light wavelength
 - comparison to the reference beam



(*) Adherence test

Figure 16 - Samples tests

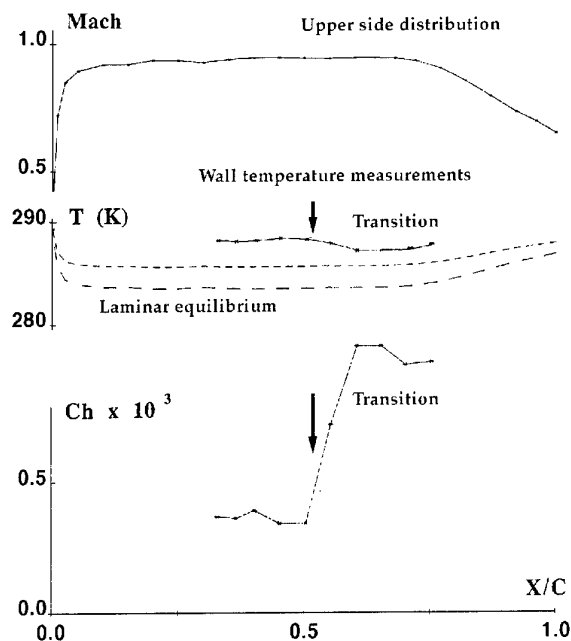


Figure 17 - Transition detection principle with wall temperature measurements

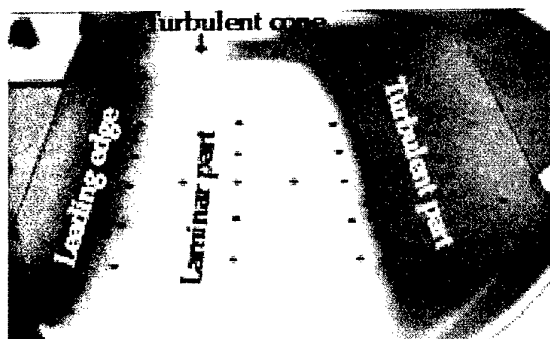


Figure 18 - Infrared imaging on a 2D model

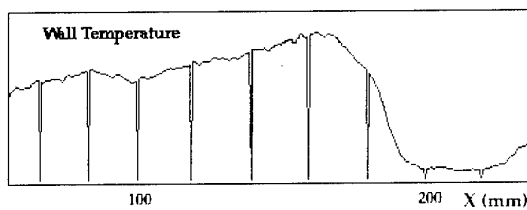
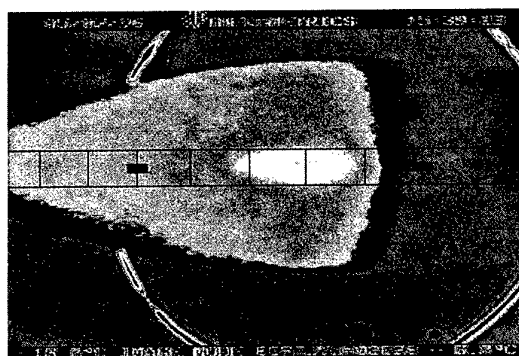


Figure 19 - Infrared imaging on a 3D model at 240 K

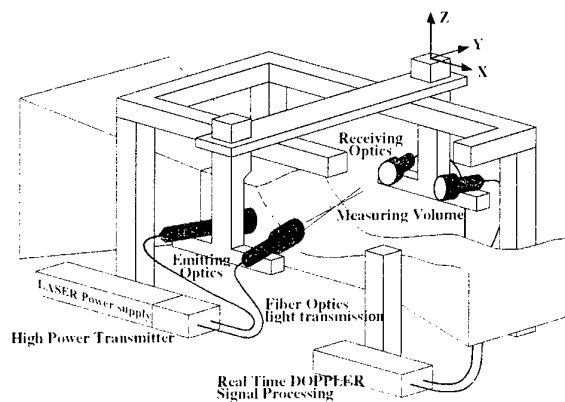


Figure 20 - 3D laser doppler anemometer bench

REQUIREMENTS :

- Velocity range : 100 to 450 m/s
- Data acquisition : 60 to 90 s for 30 to 50 points
- Measurement accuracy : 1 m/s

TRAVERSING DEVICE :

- Displacements : $X = 1.7$ m, $Y = 0.4$ m, $Z = 0.6$ m
- Positioning accuracy : ± 0.03 mm
- Displacement speed : 12 mm/s
(+ 0.2 s for the starting and stopping phases)

OPTIC DEVICES :

- Argon laser source : power ligh 15 Watts
- High power transmitter :
6 beams (3 colors), 6 Bragg cells,
6 monomode optic fibers 10 m length
- 2 emitting optics and 2 receiving optics
3 photodetectors
Focal length : 800 and 600 mm
- Measuring volume diameter : 130 μ m
Interfringe : $d = 5$ μ m

ELECTRONIC DEVICE : 3 B.S.A.

- 16 frequency bandwidth : Δf from 977 Hz to 32 MHz
- 12 central frequency : F_c from 610 Hz to 64 MHz
- Samples number : $N = 8, 16, 32, 64$
- Accuracy on F_d : $64 \times 10^{-3} \times \Delta f / N$
- Synchronisation : measurement of arrival and transit times of each particule

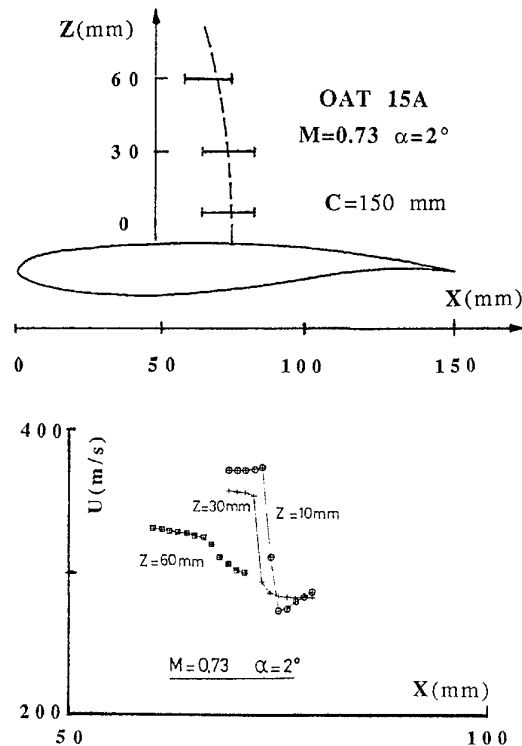


Figure 21 - 3D laser doppler anemometer characteristics

Figure 22 - Velocity measurements through a steady shock wave

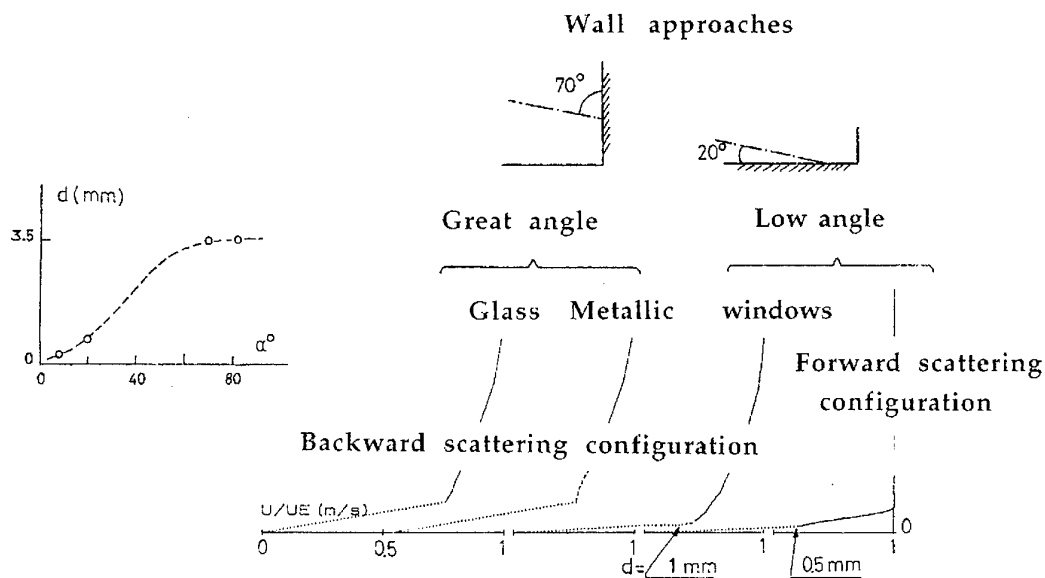


Figure 23 - Wall approaches for different configurations

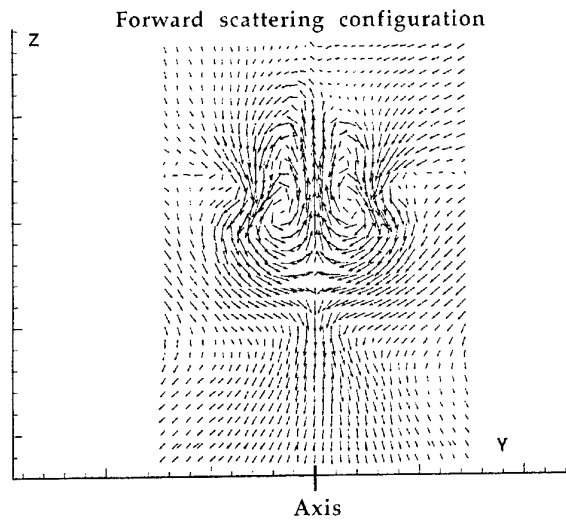


Figure 24 - Secondary field in a 3D wake flow

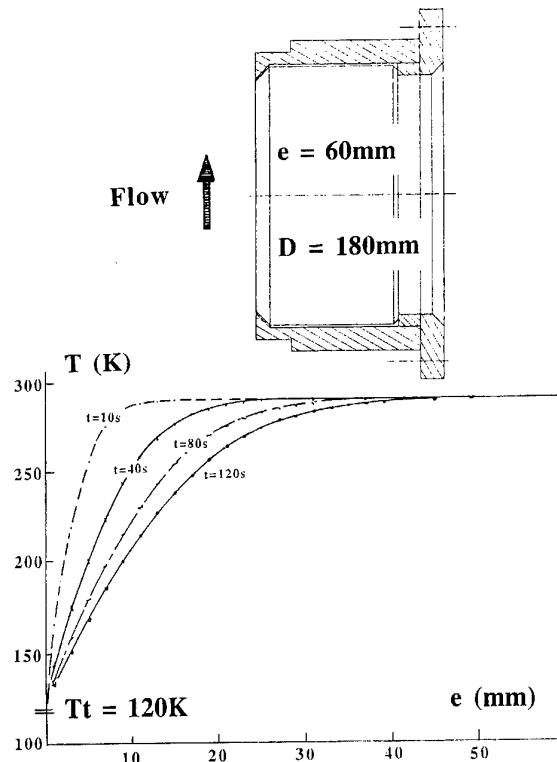


Figure 25 - Silica window design for cryogenic operation

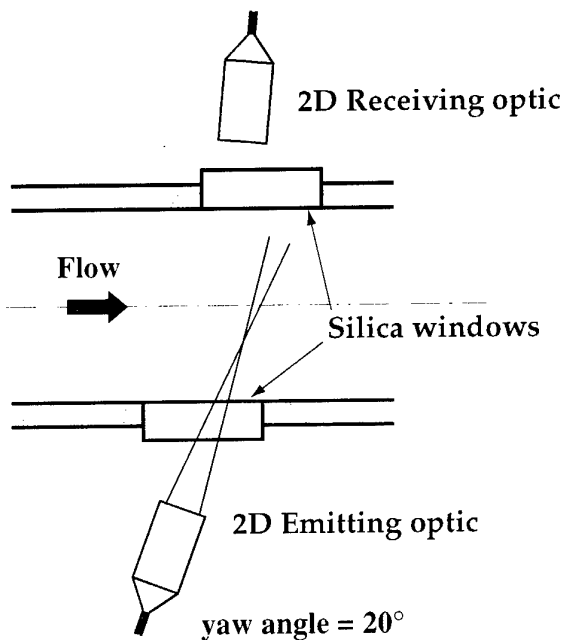


Figure 26 - Laser configuration used for cryogenic tests

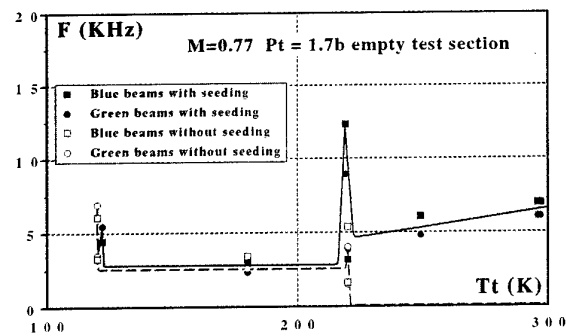


Figure 27 - Data acquisition rate evolution with temperature

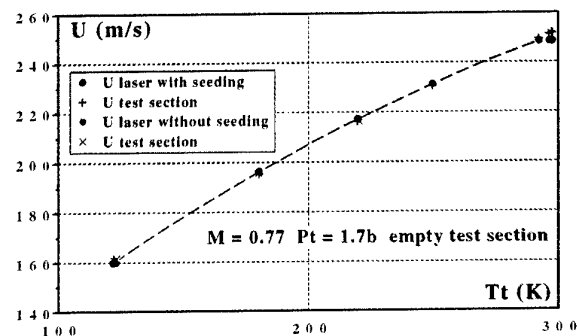


Figure 28 - Velocity measurement results

DEVELOPMENT OF PIV FOR TWO AND THREE COMPONENT VELOCITY MEASUREMENTS IN A LARGE LOW SPEED WIND TUNNEL

P.W.Bearman, J.K.Harvey and J.N.Stewart*

Department of Aeronautics

Imperial College of Science, Technology and Medicine
London, SW7 2BY, UK

SUMMARY

The use of particle image velocimetry, PIV, to make measurements in flows generated around models in a low speed wind tunnel is described. The tunnel test section employed is 3m wide by 1.5m high. The problems associated with using PIV in air at large scale, and how they can be overcome, are discussed. Stereoscopic PIV is used to measure all three components of velocity in planes across a flow. Errors due to parallax that are present in velocity components measured in the plane of a light sheet when there is an accompanying flow through the sheet, are corrected. The flows studied are generated by a 1/8th scale passenger car model and a 1/8th scale model of an aircraft with a wing sweep of 70°. It is found that a reasonable estimate of a mean flow field can be obtained by averaging as few as ten instantaneous spatial distributions of velocity.

LIST OF SYMBOLS

- d distance between light sheet and camera lens
- M Magnification
- s distance between optical axes of cameras
- u through-plane velocity
- v_a apparent velocity due to parallax
- x distance of particle from optical axis

1. INTRODUCTION

A number of recent developments in experimental aerodynamics have been associated with obtaining simultaneous multi-point measurements of flow quantities. There are several reasons why multi-point measurements are attractive and perhaps the most obvious is that their use can drastically cut wind tunnel running times. For example, traversing a flow field with a single probe can be very time consuming and while the probe

is in one position no information is being gained from the rest of the flow. From a more fundamental viewpoint, multi-point measurements have the potential to provide new information about complex flows. At most practical Reynolds numbers many flows are unsteady, either resulting from the generation of turbulence or due to the motion of organised vortex structures. Multi-point measurements can provide unique information about the spatial structure of the unsteadiness. This paper is about the implementation of one such technique, particle image velocimetry (PIV), for measuring the instantaneous spatial distribution of velocity in a low speed wind tunnel.

Techniques such as hot-wire anemometry and laser Doppler velocimetry are used to measure velocity at a given location in a flow. The resulting signals can be analysed to produce time-averaged quantities such as mean velocity, r.m.s. velocity and power spectra. Further information about flow structure can be obtained by measuring more than one component at a location, or by measuring simultaneously the velocity at two locations. However, it is difficult to obtain much more from two-point measurements than time-averaged information about the size of eddy structures in the flow. Investigators have used extensive arrays of hot wires to obtain more detailed spatial information but then there may be concerns about the interference these arrays cause to the flow. Also such arrays are rarely able to cover the whole flow area of interest with a sufficiently fine resolution. LDV has the advantage of being non-intrusive but the conventional technique is not suited to making measurements at many points simultaneously. However, it should be noted that single point techniques are very effective for studying certain aspects of flows and, working within the framework of the Reynolds-Averaged Navier Stokes equations, they are a useful tool

*Now at Sira Technology Centre

for helping to validate CFD codes and for providing information to assist in the development of turbulence models. Their main limitations are that they are time consuming and they are unable to provide information on the instantaneous structure of flows.

When investigating a complex flow it can be very instructive to carry out flow visualisation studies. Particle image velocimetry (PIV), which provides measurements of instantaneous velocity fields, is related to visualisation but has the added advantage of being a quantitative method for determining flow structure. Also valuable additional physical insight can be obtained by calculating the vorticity field from the velocity estimates. PIV is now a widely used technique (Adrian¹) and one which is undergoing continuous development. The goal is to have a quick, reliable and easy to use method that can be employed in a large scale wind tunnel, as a matter of routine, to measure all three components of velocity over extensive planes of the flow. Much of the early development work on PIV was carried out in water at small scale and with low flow velocities. Many of the problems associated with its use are minimised in such flows because relatively large seeding particles can be used, say of order 50 μ m, and less stringent requirements are placed on both the illumination and the particle image recording medium. For example, in small scale water flows it is possible to make use of relatively low power continuous lasers and to record particle positions directly using a standard video system.

In air much smaller particles have to be used to ensure that they will follow the flow closely, and in the work to be described here oil droplets with diameters of the order of 1 μ m have been used. A pulsed, 10 Joule, ruby laser is employed as the light source and this can provide sufficient illumination to record particle positions over areas roughly 20cm square. To obtain estimates of velocity, the laser is pulsed twice and images of the particles are recorded for each pulse on a common medium. If the light sheet is directed normal to the main flow then the combination of pulse separation and light sheet thickness has to be chosen such that the majority of the particles remain within the sheet during the

time between pulses. Otherwise an excessive number of unpaired particles will contaminate the records. To ensure that about 75% of particles remain within the light sheet requires a thickness equal to roughly four times the distance particles move between pulses. In the present work the particles move of the order of 0.5mm and hence the light sheet thickness used was 2mm. Increasing the thickness of the light sheet, while keeping the illuminated area constant, reduces the level of illumination and hence, for a given PIV system, the sheet thickness used effectively fixes the maximum flow area that can be investigated.

When working at large scale in air the device used to record particle positions needs to have a very high spatial resolution. While CCD cameras might seem an attractive choice, they do not yet match the high degree of resolution that can be obtained from a conventional film camera. Hence, in order to maximise the flow interrogation area, film cameras have been used as the recording medium in this study. Clearly one of the main disadvantages of this is that the film has to be processed before the images can be interrogated. In order to analyse the films they are mounted in a PC controlled traverse and a CCD camera is used to view small areas. Data from these areas is then transferred to the computer for analysis. Considerable effort was directed towards developing a fast and accurate interrogation method and 128 x 128 pixel areas are analysed using an autocorrelation method based on direct fast Fourier transforms. A DSP32C digital signal processing card was installed in the PC to speed up this interrogation process. Experience has shown that the main difficulty with PIV is obtaining good quality records of particle images and, relatively, the interrogation of these images is fairly straightforward.

A familiar difficulty associated with the interrogation of particle positions is the uncertainty of $\pm 180^\circ$ in the determination of flow direction if the sequence of image recording is unknown. In this study a rotating mirror is placed between the flow plane and the camera, in common with a number of other PIV systems, to impose an artificial shift on particle images between pulses. This shift, which has to be larger than any shift due to

the flow, is removed in the interrogation stage to reveal the true flow direction and speed.

An error that may arise in velocity estimates obtained from PIV when working at large scale is associated with perspective or parallax. In any flow field illuminated with a thin light sheet, where seeding particles possess a component of velocity normal to the sheet, parallax gives rise to an apparent velocity which is added to the true velocity in the plane of the sheet. The magnitude of this error is related to the flow velocity through the sheet and the distance the measurement point is away from the optical axis of the recording device. By using two cameras to take stereoscopic pictures of the area under investigation, the flow velocity through the sheet can be estimated and the velocities in the plane of the sheet corrected. Although the velocities through the sheet are not measured to as high an accuracy as those in the plane of the sheet, the technique to be described here provides a means of measuring all three components instantaneously. Examples of other studies using stereoscopic PIV are reported by Prasad and Adrian² and Liu et al³.

The aims of the present paper are to: (a) demonstrate the use of PIV in a wind tunnel with a test section 3m x 1.5m and to present two component velocity measurements made in the wake of a 1/8th scale vehicle model and a 1/8th scale swept wing aircraft; (b) to discuss the problem associated with parallax and to present a method for removing the error it introduces into velocity measurements; (c) to describe the use of stereoscopic PIV to measure all three components of velocity within a flow plane and to present results obtained with the swept wing model.

2. EXPERIMENTAL ARRANGEMENT

2.1 The General Arrangement

A PIV system has been developed for use in a low speed wind tunnel with a test section 3m wide by 1.5 m high, located in the Department of Aeronautics at Imperial College. The majority of the work carried out has been at flows speeds of 15 to 20m/s. These are convenient speeds to use in this

tunnel but in principle there is nothing to prevent the technique being used at higher speeds. A diagram illustrating the general arrangement of the PIV system is shown in Figure 1. Many of the features have already been introduced in the previous section and will not be repeated here. One of the most

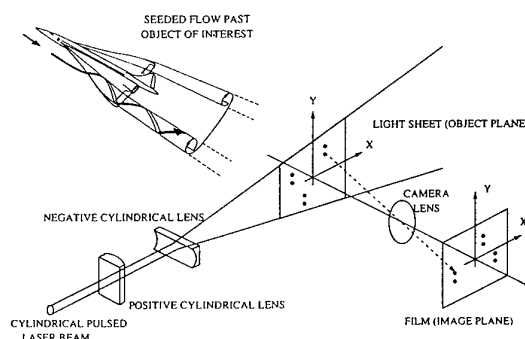


Figure 1 General arrangement of a PIV measurement system

challenging aspects of PIV is to supply seeding particles, in sufficient concentration, that will both follow the flow and scatter enough light to be observed by the recording device. The seeding used was smoke from a Concept Comet smoke generator which was introduced some distance upstream of models. A substantial number of seeding sources were investigated but this proved to be the most suitable.

Single photographs and stereoscopic photographs were taken with Bronica SQ-Am, 120 format, motorised cameras. The main film employed in the investigation was Kodak Technical Pan 2415. Flat field lenses with focal lengths of 110mm are used and it has been found, with the particular arrangement employed, that to obtain successful PIV photographs magnifications of at least 0.15 have to be used. This is in order to be able to resolve the images of 1 μ m seeding particles; even when using the very high quality, near diffraction limited lenses that were employed in this investigation. For stereo operation the cameras were mounted one above the other and a single mirror provided the image shifting for both cameras. The mirror for single and double camera operation was fixed on a turntable rotating at constant velocity. The laser was fired using a signal from the

turntable indicating when the mirror was in the correct position. Illumination was supplied by a Lumonics HLS4, Q-switched, double pulsed, holographic ruby laser. This provides two spatially uniform pulses of light, each with a duration of 25ns and a maximum energy of 5 Joules, which can be separated by between 1 and 500 μ s. The choice of 694nm wavelength red light is not ideal because films are substantially more sensitive to green, but at the time the laser was purchased high power Nd:Yag lasers proved unable to match the beam quality of holographic ruby lasers. Now there are high power dual Nd:Yag lasers available that have been specially developed for PIV.

Experiments have been carried out using this system to measure velocities in the flow generated by a range of wind tunnel models (Stewart et al⁴, Bearman et al⁵). In this paper we describe the results of measurements made in the wakes of a 1/8th scale passenger car model and 1/8th scale half model of a variable sweep aircraft, donated to the Department by British Aerospace.

2.2 Parallax Removal and the Measurement of Three Components

The origin of the parallax or perspective error introduced by particle motion normal to the light sheet is illustrated in figure 2 where, for

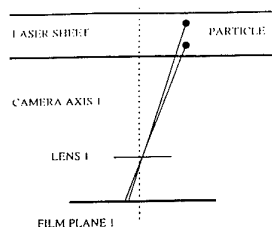


Figure 2 Origin of the perspective or parallax error

the particular flow shown, the particle velocity in the plane of the sheet is zero. On the film plane a displacement arises between consecutive images which is related to the through-plane velocity, u , the distance the particle is away from the optical axis of the camera, x , and the distance, d , between the sheet and the camera lens. In the interrogation process an apparent velocity, v_a , is predicted

in the plane of the light sheet, given by $v_a = u x / d$. Clearly, for a given flow, this error can be reduced by using a longer focal length lens. However, high quality, long focal length, lenses are expensive and even with such a lens the error cannot be completely eliminated. An alternative approach, which is the one followed here, is to photograph simultaneously the same area of flow using a second camera. The arrangement is sketched in figure 3 where it can be seen that a different velocity in the plane of the light sheet will be predicted from the analysis of each photograph. From this information, and knowing the distance between the optical axes of the cameras, it is possible to evaluate u and to correct the velocity in the plane of the light sheet to its true value of zero. In the general case, the particle will have components of velocity in all three directions and this will generate appropriate displacements on the films of the two cameras. The equations relating the true in-plane velocity components and the through-plane velocity to the components measured in the plane of the light sheet are straightforward and easily incorporated into a data processing programme (see for example Gauthier and Riethmuller⁶).

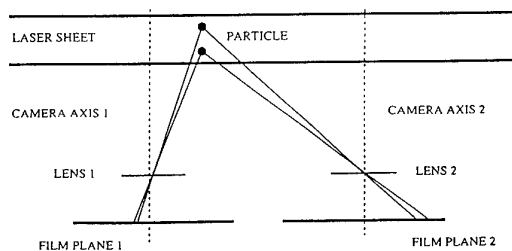


Figure 3 Set up for stereoscopic PIV

In this study stereoscopic PIV has been used both to remove parallax errors and to obtain estimates of through plane velocities. It should be noted that using this technique these velocities can only be recovered from the areas of the flow where the focal areas of the two cameras overlap. Using conventional cameras side by side this means that the flow area over which it is possible to obtain velocities is less than that for single camera PIV. During the data analysis stage for stereoscopic PIV the position of a point in the flow and its corresponding positions on the

two negatives have to be known accurately. This was achieved by arranging for a very thin wire to pass through the light sheet, close to a corner of the area being photographed. The image of the wire appears as a dot in each negative and is used as the reference point.

From an analysis of the errors in estimating velocity components it can easily be shown that, for a given error in measuring the displacement between images on a negative, the error in the resulting in-plane velocity components is inversely proportional to the magnification, M ; which is the ratio of a length in the film plane to a length in the flow plane. However, the corresponding error for the through-plane component can be substantially higher and the ratio of this error to the error on the in-plane components is given by $2d / S$, where S is the distance between the optical axes of the two cameras. Employing the values used in this investigation the ratio of errors is around 10. Hence we can expect significantly more scatter in the estimates of the through-plane component of velocity than for the in-plane ones.

While discussing errors it should be noted that an inaccuracy is introduced by the rotating mirror used to generate image shifting. As discussed by Raffel and Kompenhans⁷, the mirror rotates through a small interval during the time between laser pulses and this has the effect of rotating the focal plane of the camera. This produces an apparent through-plane component of velocity which gives rise to an error in the object plane which is similar to that caused by parallax. In stereoscopic PIV it is seen from the discussion above that it is important to have accurate estimates of the displacements in the object plane in order to calculate the through-plane component. Hence this error has been removed in the post processing stage using equations given by Oschwald et al⁸.

2.3 Data Processing

An outline of the data processing has already been given and it has been noted that particle displacements between laser pulses are found by using a direct autocorrelation method. This involves searching for the position of the

highest peak in the autocorrelation function, after the peak at zero displacement which corresponds to particles correlating with themselves and which must always be the highest one. Without using any special processing technique the accuracy with which the position of a peak can be detected is limited to the pixel resolution used to record the particular segment of a negative. Since estimates of the through-plane component of velocity are very sensitive to errors in measuring displacements on the film, it is important to try to keep these errors as small as possible. Sub pixel accuracy in locating a peak can be achieved by assuming some form for the correlation function in the vicinity of a peak and fitting this to the available data. The effectiveness of various peak searching routines has been investigated by Lourenco and Krothapalli⁹ and they conclude that simple curve fitting methods are not necessarily the most accurate. Their recommendation is to use a multi-grid interpolation procedure known as Whitaker's reconstruction. This involves first locating the maximum from the original measured grid of points and then constructing a sub-grid around this at half the original spacing using an interpolation routine based on an $n \times n$ array of points. The process is repeated p times and in theory should provide the peak location to an accuracy of 2^{-p} th of a pixel. Lourenco and Krothapalli, working with synthetic data, recommend using a 5×5 array of points but with our real data we found that an 11×11 array was needed to obtain the same accuracy. Using such a large array introduces a very considerable increase in the analysis time for a data set. However, we found that using a bicubic spline fit to a peak its location could be identified to almost the same accuracy as employing Whitaker's reconstruction. Hence, in order to keep analysis times to a minimum we have used the spline fitting method.

The ideal result from a PIV experiment is to have reliable estimates of velocity at every mesh point over a regular grid. In practice there will often be points where the analysis procedure either cannot determine a velocity or returns an incorrect estimate. The most common reason for this is that the seeding is not sufficiently concentrated. In many cases this results in the correct peak being lower than one or more other spurious peaks in the

autocorrelation function and hence the interrogation algorithm returns the wrong velocity. Fortunately an incorrect estimate is usually quite different to the true value and hence can be easily detected by comparing its value with that of its near neighbours. An automatic checking routine is built into the software and if a suspect velocity is identified then it is replaced by the estimate obtained by using the next lowest peak. The revised estimate is checked and is either accepted or rejected. If after checking a number of peaks a realistic velocity cannot be found then a zero is returned for that mesh point.

Within a turbulent flow no two instantaneous velocity fields measured using PIV will be the same. Measuring a large ensemble of velocity fields it would be possible to recover the kind of time-average statistical data on turbulence that is routinely obtained using hot-wire anemometry and LDV. However, assuming velocity is normally distributed, it can be expected that to obtain r.m.s. values to an acceptable accuracy might require upwards of 10,000 estimates. Presently this is impractical and, until there are significant further advances, PIV should be viewed as a complementary technique and not one which replaces single point measurement methods. However, when averaging across a number of instantaneous velocity fields, very few seem to be required to generate an acceptable estimate of the mean velocity field. Averages across ten sets of PIV data will be shown.

3. EXPERIMENTAL RESULTS

3.1 Two Component Velocity Measurements Behind a Car Model

The wake of a three-dimensional body like a car is complex and dominated by streamwise vortex structures. These vortices originate from various features of the upstream body and may interact with each other both around the body and in the near wake. Until relatively recently the instantaneous structure of such wake flows has been very difficult to measure but with the advent of techniques such as PIV much more detailed information can now be obtained.

A typical measurement (for further details see Wang et al¹⁰), obtained using PIV, of the

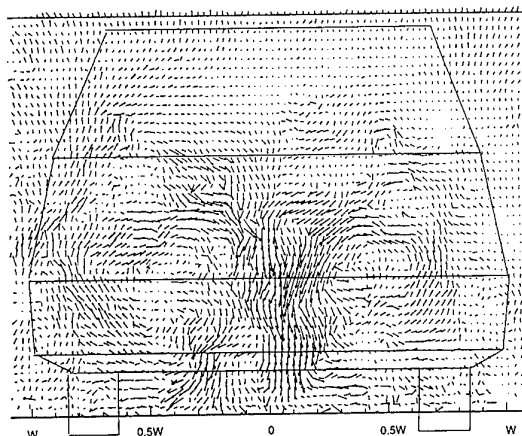


Figure 4 Instantaneous cross flow velocities in the wake of a car model

instantaneous velocity field in a cross flow plane in the wake of a car model is shown in figure 4. This plane is situated 23% of the car's length downstream of the car. It is seen that the wake is composed of a substantial number of coherent vortex structures and they move apparently randomly in time and space.

If the velocity fields obtained from a small number of PIV measurements are averaged then the fine detail of the multiple vortex structures is lost and the twin vortex structures seen in time-average measurements appear. This is illustrated in figure 5 where the outcome of averaging only 10 sets of

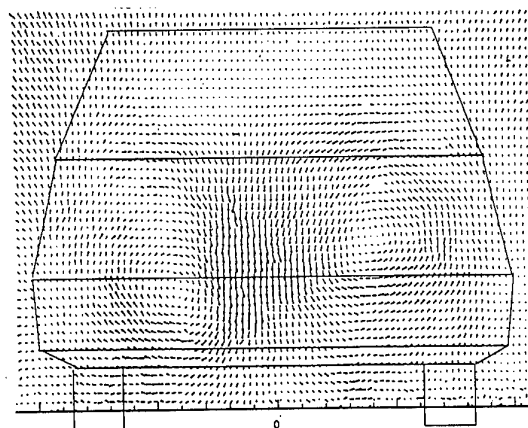


Figure 5 The average of ten velocity distributions

instantaneous velocity measurements is presented. The apparent asymmetry in the

resulting vortex structures may be due to averaging too few a number of instantaneous fields. The many longitudinal vortex structures observed in the instantaneous flow will have originated from various features of the complex car body. On the basis of these measurements, the concept of a car wake consisting mainly of a pair of contra-rotating turbulent vortices would appear to be wrong.

A surprising feature of Figure 5 is how smooth the resulting plot appears, bearing in mind that each velocity estimate is based on so few data values. However, this average is not the same as that obtained by traversing a hot wire or an LDV and taking the mean of ten velocity readings at each point. Presumably this would be much more scattered. Using PIV any spatial correlation within the flow is preserved and it is the average of a small number of complete fields that is calculated whereas with single point measurements each data point is obtained for a separate realisation of the flow. To date this powerful feature of PIV does not seem to have been fully exploited.

The data presented in this section are subject to two important limitations. One is that only the components in the plane of the sheet are measured and, secondly, these components are subject to a parallax error which becomes significant towards the edges of the measurement area. In the following section these restrictions are removed through the use of stereoscopic PIV.

3.2 Two and Three Component Velocity Measurements behind a Swept Wing

The 1/8th scale, half model of a generic aircraft, incorporating the swept port wing, is 1.75m long and was mounted on a base plate 7cm above the floor of the 3m x 1.5m wind tunnel. By slightly elevating the model any interference effect from the floor boundary layer was minimised. The model is shown in figure 6. Measurements were carried out for a variety of sweep angles and for various angles of incidence. For the results to be presented in this section the laser sheet entered normal to the free stream direction and was placed 3cm, which is a distance equal to 28% of the tip chord, downstream of the wing, as shown in figure 7. The wing sweep was 70° and in the



Figure 6 1/8th scale aircraft model

results to be presented the incidence of the model was 8°.

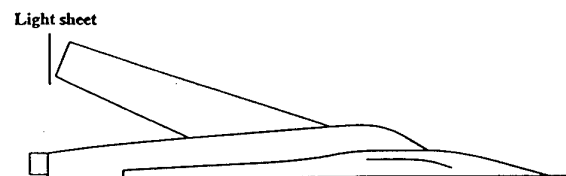


Figure 7 Position of the light sheet

A typical set of velocity measurements for the in-plane component obtained from one negative, and hence including the parallax error, is illustrated in figure 8. The profile of the wing at the tip, as seen from downstream, is also pictured. The leading edge is at the origin of the co-ordinate system and it should be recalled that the measurement plane is a little way downstream of the tip. The corresponding plot using data from both negatives to remove the parallax error is shown in figure 9.

Differences are most obvious around the edges of the plots, for example in figure 8 there is an unrealistic out flow measured along the boundary above the upper surface of the wing. The plot of true cross flow velocities shows a number of interesting features, the most obvious one being a large clockwise vortex above the wing. Near the origin there is evidence of a smaller anticlockwise vortex,

50% of freestream

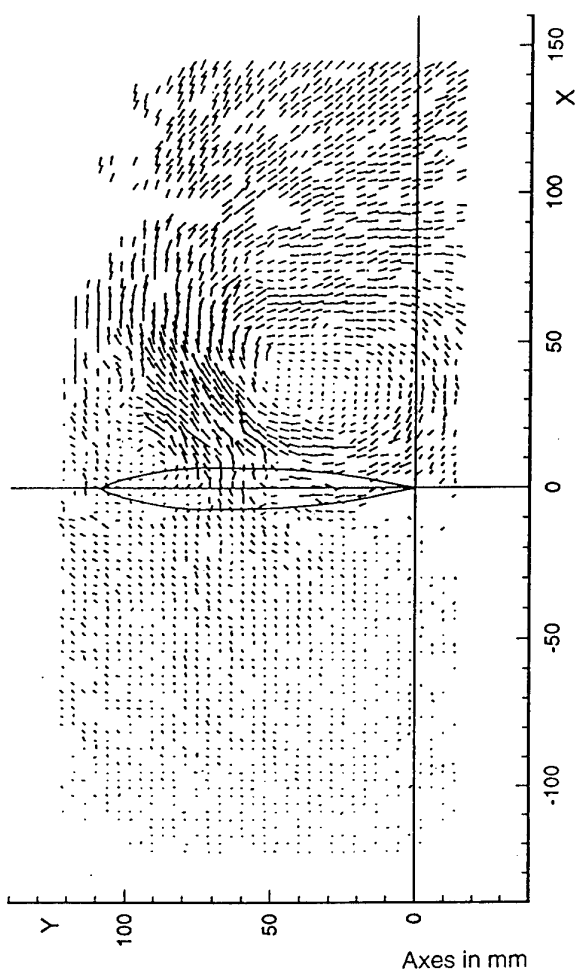


Figure 8 Velocities without parallax correction

with a relatively high velocity flow between the vortices. Below the wing the cross flow velocities are small. By tracing back along the vortices it was found that, as expected, the large vortex originates at the wing leading edge. The second vortex is shed from the wing tip at its inboard edge. Under the influence of the stronger leading edge vortex it is rapidly convected outwards from the fuselage and in the figures appears in a position near the leading edge of the wing.

with a relatively high velocity flow between the vortices. Below the wing the cross flow velocities are small. By tracing back along the vortices it was found that, as expected, the large vortex originates at the wing leading edge. The second vortex is shed from the wing tip at its inboard edge. Under the influence of the stronger leading edge vortex it is rapidly convected outwards from the

50% of freestream

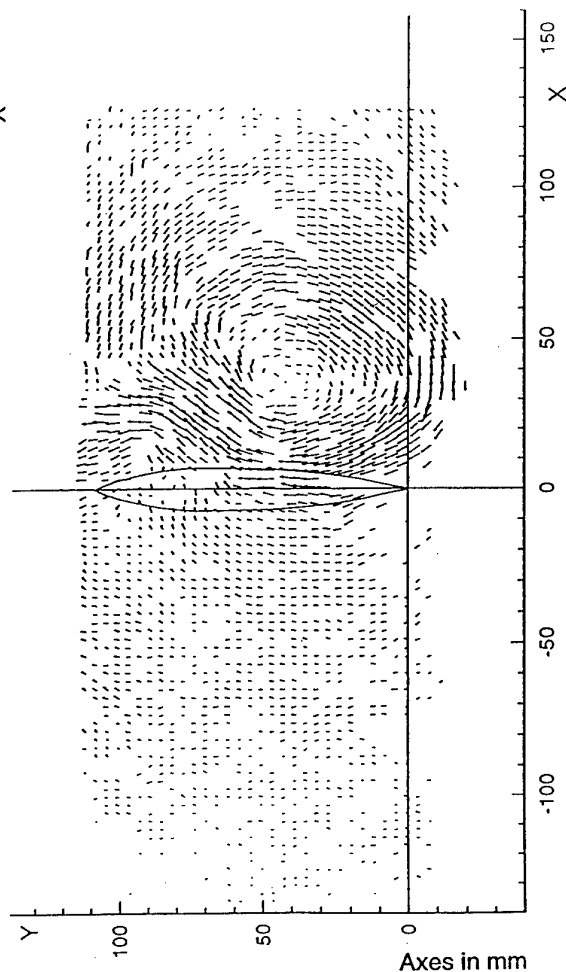


Figure 9 Velocities with parallax correction

fuselage and in the figures appears in a position near the leading edge of the wing.

A series of plots of the velocity field for this flow were obtained and in each the positions of the main vortices and their strengths were slightly different. The flow is turbulent in the vortices and so the fine structure was quite different between plots. In order to obtain a rough estimate of the mean flow, data from ten instantaneous velocity fields was averaged and the result is shown in figure 10. As with the measurements in the car wake, it is surprising how smooth the resulting plot appears.

The vorticity field corresponding to the velocity field plotted in figure 10 is shown in figure 11. The main leading edge vortex and the vortex shed from the trailing edge are the dominant features. The small patch of

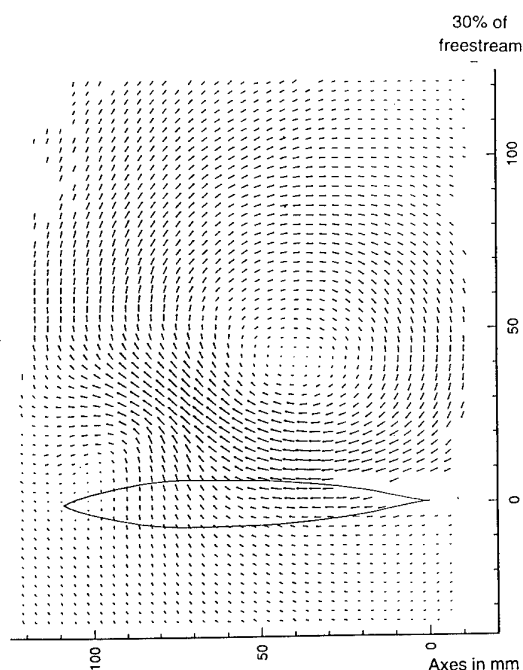


Figure 10 The average of ten velocity distributions

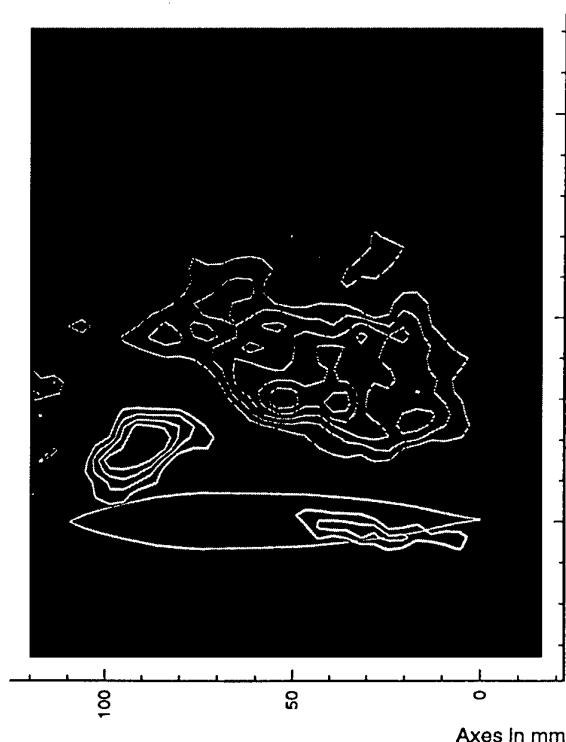


Figure 11 Distribution of vorticity: brighter contours +ve vorticity

anticlockwise vorticity at about the three quarter chord point is thought to be spurious

and due to there being insufficient correct data in this area.

Being restricted in this paper to black and white plots it is difficult to show all three components of velocity together. In figure 12,

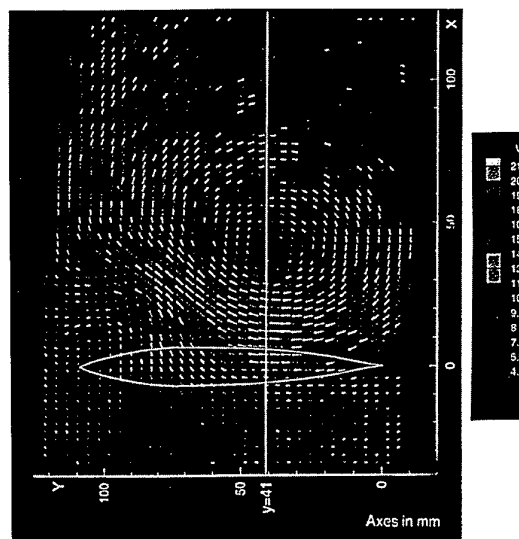


Figure 12 Plot of all three velocity components. The scale gives the range of velocities through the plane.

taken from a colour plot, the magnitudes of the in-plane component are given by the lengths of the lines and the through-plane component is related to the brightness of the lines, but not in a consistent manner. In the darker areas of the plot above the main vortex and below the wing the velocity is near the free stream velocity. For the particularly bright lines the velocity is roughly 90% of the free stream and near the centre of the main vortical region it is between 60 and 70%. It should be noted that in this plot the origin of the co-ordinate system has been moved to the trailing edge.

4. CONCLUSIONS

Stereoscopic PIV has been shown to be suitable for use in a large, low speed wind tunnel. It has been used to correct for the parallax error that occurs while measuring velocity components in the plane of a light sheet when there is a through-plane velocity component present. The technique has also been used to measure all three components of

velocity simultaneously across a flow plane. However, it was noted that the error in the through-plane component is likely to be substantially greater than that for the other two components. The PIV measurements reveal interesting features of the instantaneous spatial structure of the wakes of a car and a swept wing flow. An interesting finding is that a surprisingly good estimate of the mean flow field in the wakes of these models can be obtained by averaging as few as ten instantaneous velocity fields.

ACKNOWLEDGEMENTS

The authors gratefully acknowledge the support of British Aerospace, Military Aircraft Division, who funded the research on stereoscopic PIV. The data related to the car wake and presented in figures 4 and 5, was obtained by Q.Wang (see Wang et al¹⁰).

REFERENCES

- 1 Adrian, R.J., Particle-imaging techniques for experimental fluid mechanics, *Ann. Rev. Fluid Mech.*, Vol 23, 1991, pp 261-304.
- 2 Prasad, A.K. and Adrian, R.J., Stereoscopic particle image velocimetry applied to liquid flows, *Exp. in Fluids*, Vol 15, 1993, pp 49-60.
- 3 Lui, Z.C., Adrian, R.J., Meinhart, C.D. and Lai, W., Visualisation of structure in a turbulent boundary layer using a stereoscopic particle image velocimeter, *Proc. 8th Int. Sym. on Applications of Laser Techniques to Fluid Mechanics*, Lisbon, 1996.
- 4 Stewart, J.N., Wang, Q., Moseley, R.P., Bearman, P.W. and Harvey, J.K., Measurement of vortical flows in a low speed wind tunnel using particle image velocimetry, *Proc. 8th Int. Sym. on Applications of Laser Techniques to Fluid Mechanics*, Lisbon, 1996.
- 5 Bearman, P.W., Harvey, J.K. and Stewart, J.N., Two and three component velocity measurements in a wind tunnel using PIV, *Proc. Wind Tunnels and Wind Tunnel Test Techniques*, The Royal Aeronautical Society, Cambridge, April 1997.
- 6 Gauthier, V and Riethmuller, M.L., Application of PIDV to complex flows: measurement of the third component, VKI - LS 1988-06, Particle Image Displacement Velocimetry, 1988.
- 7 Raffel, M. and Kompenhans, J., Theoretical and experimental aspects of image shifting by means of a rotating mirror system for particle image velocimetry, *Measurement Science and Technology*, Vol 6, 1994, pp 795-808.
- 8 Oschwald, M., Bechle, S. and Welke, S., Systematic errors in PIV by realising velocity offsets with the rotating mirror method, *Exp. in Fluids*, Vol 18, 1995, pp 329-334.
- 9 Lourenco, L. and Krothapalli, A., On the accuracy of velocity and vorticity measurements with PIV, *Exp. in Fluids*, Vol 18, 1995, pp 421-428.
- 10 Wang, Q., Bearman, P.W. & Harvey, J.K., A study of instantaneous flow structure behind a car by particle image velocimetry, *Int. Conf. Optical Methods and Data Processing in Heat and Fluid Flow*, 18-19 April, IMechE Conf. Transaction 3, 1996.

APPLICATION OF PIV IN THE LARGE LOW SPEED FACILITY OF DNW

J.W. Kooi

K. Pengel

German-Dutch Wind Tunnel (DNW)

Postbus 175, 8300 AD Emmeloord, The Netherlands

M. Raffel

C. Willert

J. Kompenhans

Deutsche Forschungsanstalt für Luft- und Raumfahrt (DLR)

Bunsenstrabe 10, D-37073 Göttingen, Germany

SUMMARY

Particle Image Velocimetry (PIV) is a non-intrusive measurement technique capable to measure the instantaneous velocity field in a two-dimensional plane. This technique has matured to a state that it now can be employed on a routine base in large industrial wind tunnels. For that reason, the German Dutch Wind Tunnel has acquired a two-component PIV system for its Large Low Speed Facility. The main components of the system are a high speed video camera, a powerful pulsed Nd:YAG laser and for evaluation of the recordings a software system. The tracer particles are introduced in the flow by means of a rake mounted in the wind-tunnel settling chamber.

A first application of the PIV system was the measurement of the trailing wake of transport type aircraft model. The measurement plane was positioned perpendicular to the main flow direction and the video camera was mounted on a traversing system installed inside the test section far downstream the model. One of the important results was that in the individual velocity plots an unsteady vortex was found almost absent in the time averaged results.

The PIV system cannot only be used in the closed wall test section of the DNW-LLF, but also in the Open Jet test section. Because of the large size of the facility the set-up requires both for the video camera and the pulse laser a stable support. This could be realised by using existing support systems.

LIST OF SYMBOLS

M	magnification factor of PIV recording: pixels/mm
V_y	flow velocity in y-direction
V_z	flow velocity in z-direction

V_F cross flow velocity $V_F = \sqrt{V_y^2 + V_z^2}$
 τ laser pulse delay

1. INTRODUCTION

Non-intrusive measurement techniques are not only applied because they lack the interference with the flow and hence the possible introduction of measurement errors, but also because there are many applications where direct probing of the flow is prohibitive. Clear examples of this are measurements in high temperature or aggressive fluids or gases and the measurement of the flow field around rotating systems like helicopter rotors, aircraft propellers and the rotating parts of gas turbine engines. Additionally flow fields generated by rotating systems have in common that they are periodical which requires a fast responding system even to obtain a true averaged value. Such a capability is offered by a hot wire or a hot film measuring system, but the time consuming, intrusive and delicate character of the probes limits application in industrial wind-tunnel environment.

For subsonic to supersonic flow two non-intrusive velocity measurement techniques, Laser Doppler Anemometry (LDA) and Particle Image Velocimetry (PIV), have emerged over the past fifteen years as reliable systems and have proven their capabilities in a number of applications (Ref. 1,2). As far as wind tunnel testing is concerned the applications were mostly limited to small or moderate sized facilities. This is not surprising as use of LDA or PIV in large low speed facilities like the German-Dutch Wind Tunnel (DNW-LLF)¹ requires powerful lasers and high quality long range optics and it was not until recently that this equipment became available.

¹ Since 1996 the foundation DNW includes three low speed wind tunnels. To identify uniquely the large wind tunnel, formerly known as the DNW, this facility is now called DNW-LLF.

In 1995 a program was started to upgrade the measurement capabilities of the DNW-LLF and in this framework DNW decided to buy a PIV-system. That PIV was favoured over LDA had to do firstly with the expected interest from customers in general and secondly with the expected higher productivity of the PIV system. Although the LDA and PIV have overlapping capabilities, one of the well-accepted advantages of the PIV over LDA is its capability to map two-dimensional velocity vectors over a certain area instantaneously. Compared to the LDA which measures the velocity vector on a point by point base, measuring over an area at once allows to capture coherent structures. This feature makes PIV very attractive for measuring velocity distributions in vortices such as found in the wake behind a wing or the in the vortex system shed by a helicopter rotor. Testing of helicopter rotors forms an important market for DNW-LLF. Mapping a complete area at once contributes also to the high productivity of the PIV system. For a large facility like DNW-LLF productivity is a prime factor.

Although PIV has matured to a tool applicable in the industrial wind tunnel environment, it is not possible to buy off the shelf systems. Therefore, the DNW ordered the DLR Institute of Fluid Mechanics to design and build a PIV system for use both in the closed test sections of the DNW-LLF and in the Open Jet. The latter is mostly used for helicopter rotor testing.

To validate the system concept and to build up experience it was decided to use the PIV system in two different types of tests. The first case selected was the measurement of the development of the vortex system downstream of an aircraft model (Ref. 3). During landing and take-off the trailing vortices from preceding aircraft can be dangerous to the following aircraft. The air safety regulations require a minimum separation based on the expected intensity of these vortices. Because the flow field of interest extends in stream wise direction over a distance of many wing spans, in a wind tunnel test recourse has to be made to relative small scale models installed in the test section as far upstream as possible.

The second case in the validation process not yet completed but planned in the very near future is the measurement of the velocities in the vortices from a helicopter rotor model. The sting-supported model will be placed in the Open Jet of the DNW-LLF.

The paper describes the components of the newly acquired DNW PIV-system and presents the results from the first application of the system. Following this the set up for the measurement of a rotor will be discussed.

2. THE PIV SYSTEM

2.1 The Image Recording System

Detailed descriptions of the various implementations of PIV can be found in Ref. 4 and 5. The most wide spread method is to take at least two consecutive images from small particles suspended in the flow under investigation. When the camera shutter is fully opened the particles are illuminated twice during a short time period by a thin laser light sheet carefully positioned perpendicular to the camera axis (see Fig 1). By measuring the particle image displacement, either by particle tracking or locally applying statistical methods, the two dimensional projection of the local velocity vector can be calculated using the image magnification factor, M , and the time between the two pulses from the laser.

Since 1986 the DLR Fluid Mechanics Division has been developing PIV systems with the emphasis on systems applicable in the DLR wind tunnels. This imposes a number of additional requirements not present in a typical laboratory environment. The PIV system has to be easily portable and its components need to be modular to adapt to the unique features of each wind tunnel. For large facilities with high operating costs reliability is of principle concern. Another set of requirements arises from the fact that nearly all applications of PIV take place in air at moderate to high speed and some times with high centrifugal force: small seeding particles are needed to accurately follow the flow which in turn requires the use of high powered lasers in conjunction with high quality imaging equipment. This holds in particular in large facilities where distances between observation area and recording equipment can be considerable (for DNW-LLF up to eight meters).

The current existing PIV systems and systems under development at DLR are outlined in Fig 2. To the left of the figure the classical two-dimensional PIV systems are given whereas at the right side the systems capable to record the third, out of plane velocity component are indicated. These three-dimensional systems are still under development and have not matured to a state that they can be used in an industrial wind tunnel. It was therefore from the start of the development of the system for DNW clear that it should be a system capable to measure two velocity components at once.

Of the three two-component systems, the photographic, single frame/ double-exposure recording set-up is the oldest (Ref. 6). To remove directional ambiguity which may occur for example in areas of reversed flow, a rotating mirror has been used (Ref. 7) and recently also through the use of a birefringent crystal plate. Improvements in the spatial resolution of a factor of two of this system have been achieved by replacing the Young's fringe method of interrogation of the photograph by a digital interrogation method based on high resolution scans of the recording (Ref. 8)

The digital approach significantly reduces processing time because there is no longer need to produce a high contrast contact copy prior to interrogation. This has resulted in turn around times of about an hour. From a point of view of productivity for a large facility an hour is still too long. This has to do with the fact that changing to the next observation area takes rather long because of the time needed for alignment of the laser light sheet and the calibration of the image. In general the decision to move to the next position is only taken after the processed data have been approved as valid data. Therefore, it was decided that for the DNW-system the photographic recording would not become the prime recording system, but would only be used as a kind of back-up system.

To speed up the processing of PIV data video based approaches have been developed and successfully applied (Ref. 9). In the video approach two separate recordings are taken with the results that the directional ambiguity is completely removed. Initially use of video based systems were limited to low speed application in water. This is a direct consequence of the low frame rate of conventional video, typical 25 Hz (CCIR video standard) or 30 Hz (RS-170 video standard). Later on the video technique has been improved and the speed range increased considerably. Despite the improvements the standard video camera still has one major disadvantage, its triggering is not fast enough to capture asynchronous, rapidly changing flows like the ones generated by rotor and propeller blades or flapping airfoils.

In an effort to provide a video based PIV system suitable of capturing unsteady flow phenomena, a special camera has been designed by DLR. The PIV-camera is based on a high-speed video camera containing eight CCD sensors with a burst rate of 1 million frames per second (Ref. 10). Instead of eight the PIV-camera has only two sensors, which increases the light sensitivity of the camera by a factor of four compared to the eight-sensor design. The minimum exposure time, τ , for this camera is 0.8 μ s.

How attractive the video system might look from a point of turn around time, the draw back is its much lower resolution. The dual sensor camera provides approximately 23 by 18 discrete velocity vectors, whereas the standard 35-mm photographic film, digitised at 100 pixels per millimetre, yields about 56 by 37 discrete vectors at comparable measurement uncertainty. Due to the low resolution mapping a certain area would require a multiple displacement of the camera. Although the images could be merged to together, coherent structures larger than the viewed area cannot be covered. This low resolution was therefore not acceptable for the DNW.

As a compromise between the high resolution of photographic recording and the high speed of the video system a third camera was developed and selected for the

DNW PIV-system. In this case the camera incorporates full-frame interline CCD technology. The difference between this technology and the technology used in the above described high speed video camera is that full-frame interline design allows the shuttering (exposing) and the storage of entire array of pixels and not just every other line. A direct consequence of this is that the vertical resolution is doubled. The camera has a 15 Hz frame rate and a 1000 by 1000 pixel array, which results in a spatial resolution of 31 by 31 velocity vectors. Because the camera has a build-in digitiser and memory to store the picture, direct viewing of the recording is not possible. But via an interface the digitised data is transferred at a rate of about 20 Mbyte/s to the memory of a PC and presented on the monitor. This allows almost online viewing of the unprocessed recordings.

To permit the recording of two full frames at short interval the camera had to be exactly synchronised with the laser. To this end the timing for the pulsed laser is coming from the camera. A special frequency divider/multiplexer was designed to synchronise the 15 Hz frame rate of the camera with the 10 Hz rate of the pulsed laser. This allows a recording speed of pairs of PIV images of 5 Hz. The phase of the timing signals is set such that the first laser light pulse occurs shortly before the interline transfer in the sensor is started, while the second laser light pulse follows shortly thereafter. This procedure is similar to those described in Ref. 11 and 12. The minimal delay time, τ , between two pulses have been found to be for low light levels as low as 1 μ s, but for high saturation levels of the exposed pixels the delay time increases to 5 - 10 μ s.

2.2 Particle Illumination

The light source for illumination of the particles is a pulsed Nd:YAG laser with a dual oscillator and a second harmonic generator supplying two consecutive pulses at a maximum rate of 10 Hz, each pulse has an energy of 320 mJ and the pulse width is 3 ns. Nd:YAG lasers produce light with a wavelength of $\lambda = 1064$, but the harmonic generator changes this to $\lambda = 532$ nm (green) and the interval between the two pulses can be set between 1 μ s and 1 s. Note that photographic film is more sensitive to green than to for example red light as produced by ruby lasers. PIV measurements over long distances not only require powerful lasers but also excellent characteristic like the spatial intensity distribution, co-linearity, beam pointing stability ($< 100 \mu$ rad) and energy stability.

To obtain a thin light sheet, typical thickness in the order of 0.5 mm, the round light beam emitted by the pulse laser goes through a set of spherical and cylindrical lenses.

2.3 Seeding Generator

It is clear from the principle of PIV that it can be said to be a 'direct' velocity measurement technique, because - in contrast to hot wire or pressure probe techniques - it is based on the direct determination of the two fundamental dimension of the velocity length and time. On the other hand, the technique measures indirectly, because it is the tracer particle velocity, which is determined instead of fluid velocity. Therefore, fluid mechanical properties of the particles have to be checked in order to avoid large discrepancies between fluid and particle motion. First applications of PIV have already shown that it is much more difficult to provide high quality seeding in high speed gas flows compared to applications in liquid flows (Ref. 13-17). The problems are similar to those, which are faced when applying LDA. It is clear that the diameter of the particles must be very small in order to assure a good tracking of the fluid motion. But the fact that the light scattering properties reduce with decreasing particle diameter has also to be taken into account and a compromise has to be found. This problem is discussed in literature intensively (Ref. 18-20).

The most common seeding particles for PIV investigation of gaseous flows are oil particles, which are generated by means of Laskin nozzles. Pressurised air, injected in olive oil, leads to the formation of small oil droplets. The aerodynamic diameter of the olive oil particles is about $1\mu\text{m}$. In wind tunnel flows the supply of tracers is very often difficult. The particles, which are mostly used, are not easy to handle because many droplets formed from liquids tend to evaporate rather quickly and solid particles are difficult to disperse and very often agglomerate. Therefore, the particles cannot simply be fed preceding the measurement, but must be injected during the test into the flow just upstream of the test section. The injection has to be done without significantly disturbing the flow, but also in a way and at a location that guarantees homogenous distribution of the tracers. Since the existing turbulence in many test facilities is not strong enough to mix the fluid with particles which were added at one position sufficiently, the particles have to be supplied out of a large number of openings. Distributors like rakes consisting of many small pipes with a large number of tiny holes are often used. This requires particles, which can be transported inside small pipes. Below a description of an atomiser is given which generates suitable particles and has been used for most PIV measurements in airflows. The particles generated by this device are non toxic, stay in air at rest for hours, and don't change in size significantly under various conditions. In closed circuit wind tunnels these particles can be used for a global seeding of the complete volume or for a local seeding of a stream tube by a seeding rake with a few hundred tiny holes like the rake used at DNW-LLF. This rake is relatively large and measures $2.5\text{ m} \times 2\text{ m}$. It is mounted

on a traversing mechanism in the settling chamber upstream the cooler, the grids and screens. Because of the size of the rake three aerosol generators containing 40 Laskin nozzles each are used.

Each generator (Fig 3) consists of a closed cylindrical container with two air inlets and one aerosol outlet. Four air supply pipes mounted at the top dip into vegetable oil inside the container. They are connected to one air inlet by a tube and a valve each. The pipes are closed at their lower ends. Four Laskin nozzles, 1 mm in diameter, are equally spaced radially in each pipe. A horizontal circular impactor plate is placed inside the container, so that a small gap of about 2 mm is formed by the plate and the inner wall of the container. The second air inlet and the aerosol outlet are directly connected to the top. Two gauges measure the pressure on the inlet of the nozzles and inside the container, respectively. Compressed air with 0.5 to 1.5 bar pressure difference against the outlet pressure is applied to the Laskin nozzles and creates air bubbles within the liquid. Due to the shear stress induced by the tiny sonic jets small droplets are generated and carried inside the bubbles towards the oil surface. Big particles are retained by the impactor plate; small particles escape through the gap and reach the aerosol outlet. The amount of particles can be controlled by switching the four valves at the nozzle inlet. The particle concentration can be decreased by an additional air supply via the second air inlet. The mean size of the particles generally depends on the type of liquids being atomised but is only slightly dependent on the operating pressure of the nozzles. Vegetable oil is the most commonly used liquid since it is said to be less unhealthy than many other liquids. However, any kind of seeding particles, which can not be dissolved in water, should not be inhaled. Most vegetable oils (except cholesterol-free oils) lead to polydisperse distributions with mean diameters of approximately $1\mu\text{m}$.

2.4 Data Processing

After transfer of the recordings from the video camera to the PC memory, the recordings are next temporarily stored on the hard disk of the PC. For a first inspection, the data is processed on the PC and thereafter as soon as possible transferred over a link to a workstation for final processing.

The core of the evaluation software is based on cross-correlation analysis using small, 32^2 pixel, interrogation windows similar to that described in Ref. 9. The interrogation windows have an overlap of 50 percent (16 pixels). This cross-correlation analysis program includes a multiple pass algorithm in which a number of passes (typical three) are used to off set the interrogation window with respect to each other in accordance with the local displacement vector. This procedure as described in Ref. 21 has the advantage of significantly

reducing the measurement uncertainty and improving the signal to noise ratio (i.e. higher data yield). Between each of the interrogation passes an outlier search algorithm eliminates vectors which deviate significantly from their neighbours to prevent the following interrogation to lock onto the suspect displacement data. In the final pass, the peak detection algorithm is limited to a smaller search region within the correlation plane to recover displacement data, which may not otherwise be found. No outlier detection and replacement is performed after the last pass of the interrogation. Since the interrogation windows can only be shifted by integer amounts the multiple pass algorithm converges after typically three passes and generally requires approximately twice the interrogation time as the standard, single pass interrogation.

Once the displacement data has been calculated, the data is converted to velocity using the known magnification factor, M , and the exposure delay τ . Further on the co-ordinates of the measurement plane are inputted in the program to relate the measured velocities to the model bound co-ordinate system.

3 PIV MEASUREMENTS OF THE TRAILING VORTEX BEHIND A WING

3.1 Wind Tunnel and Model

For this test a half model of a twin-engined aircraft model in high lift configuration was mounted at the up stream end of the closed test section of the DNW-LLF. The DNW-LLF is an atmospheric, single return wind tunnel with two exchangeable test sections, of which the smaller one has a convertible cross section. Of these two sections the largest one has a cross section of 9.5 by 9.5 m² and the convertible either 8 by 6 m² or 6 by 6 m². The length of the 9.5 by 9.5 m² and the 8 by 6 m² configuration is 20 meters but due to the longer transition needed the 6 by 6 m² test section is just 15 m long. All test sections have at the downstream end breathers which purpose is to keep the static pressure in the test section at ambient. The maximum speed in the largest test section is 62 m/s, in the medium size a speed of 117 m/s can be achieved, whereas the maximum velocity in the smallest test section is 153 m/s. Most of aircraft related testing is executed in the 8 by 6 m² test section and so was the test described in this paper.

The half model tested represented a typical medium range, 150 passenger aircraft at a scale of 1:13.6 which resulted in a span of the half model of 1.25 m. Before, the same model was tested in the low-speed wind tunnel of Daimler-Benz Aerospace Airbus in Bremen, Germany (Ref. 3). Of the two available high lift configurations, the one with the double slotted type was selected for the PIV test. The aircraft engine was represented by a through-flow nacelle, which simulates the flight idle condition.

The half model was firmly attached to the bottom of the test section with an angle of attack of seven degrees. A 143-mm high peniche ensured that the fuselage was well outside in the test section boundary layer. Fig 4 gives a picture of the model in the test section. Because the model was mounted at the very upstream end of the test section, it was possible to follow the wake development over a long distance, up to seven wing spans. All tests were executed at a free stream velocity of 60 m/s, which equals a Mach number of 0.18.

3.2 Set-up of the PIV system

With the two-component PIV-system a choice had to be made whether the stream wise or the cross flow velocities should be measured. The vorticity in the wake of a wing is proportional to the lift of the wing and is the most significant parameter for describing the wake development. This vorticity is calculated from the cross flow velocities V_y and V_z . Therefore, it was decided to measure the cross flow velocities. As a consequence the camera must be put inside the flow; viewing in upstream direction and the light sheet had to be projected perpendicular to the main flow direction. The PIV set up is schematically shown in Fig 5. An arrangement with the camera inside the flow with the observation area perpendicular to the main flow direction is very demanding in a number of respects. The camera and the camera support are directly exposed to the flow and are subjected to flow-induced vibrations. An additional critical condition is the short residence time of seeding particles in the light sheet. Previous 5-hole probe results (Ref. 3) showed the maximum cross flow velocity V_F is only in the order of half the free flow velocity. This requires the delay time τ between two pulses to be as short as possible and to increase the light sheet thickness to its maximum in order to record enough particle pairs. However increasing the light sheet is limited while otherwise the light intensity and hence the light scattered by the 1 μ m oil droplet particles falls below the minimum level needed for exposure of the video camera. Finally, to capture an as large as possible part of a vortex, a large observation area is required which translates to a reduction of the displacement in the image plane. This cannot be compensated because of the fixed thickness of light sheet does not permit the pulse delay τ to be increased accordingly.

In the final configuration the parameters were optimised with respect to each other such that a pulse delay of $\tau = 20 \mu$ s resulted in a particle displacement of 1.2 mm normal to the light sheet which had a thickness of about 3 mm. With a particle displacement of 3 mm the related in-plane displacement is 0.6 mm. Given an observation area of 0.2 by 0.2 m, this gives a displacement of one to two pixels on the CCD sensor. A one to two pixel displacement results in a dynamic range of 20, because the noise level in the recovered displacement data is in the order of $1/10^{\text{th}}$ to $1/20^{\text{th}}$ of a pixel.

As a further measure to increase the change that a particle is illuminated twice the second-pulse-light sheet was shifted in flow direction by a small amount (1 mm).

The video camera was mounted on a remotely controllable traversing system. It was decided to place the traversing system as far downstream as possible to avoid any interaction of the traversing system with the flow at the observation position. Practical limitations resulted in a distance between the model and the traversing system of eight meter. A careful alignment of traversing plane with the laser light sheet guaranteed that once the magnification factor M and the spatial position of the observation area was measured, the camera could be moved to scan the flow field. The traversing system has a vertical range of about two meters and in the horizontal direction it can move 1.9 meters. Two planes have been scanned: one plane 0.93 m or 0.37 span widths behind the tip, the other one 5.0 m or 2.0 span widths downstream of the origin. At both locations, also data obtained from scans with a 5-hole probe rake were available.

As shown in Fig 5 the Nd:YAG pulse laser (see section 2.2) was mounted at the outside of the sidewall of the test section. The whole set up was build up on an optical bank using standard available X-95 elements. This results in a stable but still very flexible set up. The transmitting optics included a mirror to turn the laser beam over 90 degrees. Two spherical and two cylindrical lenses have been used to generate a light sheet with a thickness given above and a height of approximately 0.4 m at the observation area.

3.3 Results

A typical result obtained 5 m downstream of the model is represented in Fig 6. The figure shows a vector map as a result of one double-frame analysis. Structures of two vortices, the tip vortex and the flap vortex can be easily recognised. The averaged velocity vector maps were compared with the results from the five-hole probe measurements, published in Ref. 3 and the overall agreement was very good. The location of the aerodynamic centre of the model within all represented vector maps is zero in vertical and horizontal direction.

Fig 7 shows composed vector maps of the main part of the observation plane at 0.93m downstream of the wing tip. One video frame area of $0.2 \times 0.2 \text{ m}^2$ is too small to represent the main two vortices. The partly superimposed single frames cover the area of the stronger flap vortex and the tip vortex. In addition, the area between the two vortices where the cross velocities compensate each other is perceptible. The individual PIV results (before being averaged, i.e. instantaneous flow fields) showed an unsteady vortex (Fig 8), which was almost absent in the five-hole probe results and in the averaged

PIV results as well (Fig 9). The mean induced drag, for example, calculated from this data would be too small.

The location of the centre of the flap vortex in Fig 6 and Fig 7 are only marginally different. The vortex is almost stable in his position. However, the less strong tip vortex changes its position by rotating around the stronger flap vortex. Results from the five-hole probe measurements, which were also made at several positions in-between 0.93m and 5m emphasize that it is about half a revolution of the tip vortex around the flap vortex. Thus for the investigated wing configuration the roll-up center of this particular wake is the region of the flap vortex.

An estimate of the accuracy of each individual velocity vector can be made based on the pixel diameter. In the present recordings the particle image diameters are of the order of two pixels such that a conservative estimate for a 32^2 pixel interrogation window is 0.1 pixel, which translates approximately 3 per cent of the free stream velocity.

4 TEST SET UP FOR ROTOR TESTING IN THE OPEN JET

Measurements of velocity distributions in the down wash of a helicopter rotor require a more complex test set-up. The laser pulse has to be synchronised with the rotor in order to get instantaneous velocity distributions of one particular azimuthal rotor angle. In addition the laser sheet has to be oriented and traversed remote controlled to make images of tip vortex cross-sections at different locations and of different blades. In order to keep the same seeding particles focused within two successive images (requirement for the data analysis, in particular for the cross-correlation) the dynamic behaviour of the traverse and support facilities have to be of small amplitudes in the secondary flow of the open jet configuration of the DNW-LLF. The depth of field of the applied video camera lenses is about 2 mm, the thickness of the laser-sheet is in the same order of magnitude. Thus the distance fluctuation between the camera and the laser light-sheet may not exceed 1mm. Fig 10 is a top-view of the test set-up in the Open Jet of the DNW-LLF for rotor testing. The laser system (Laser head and light-sheet optics) is built up on an already existing traversing support mechanism, which moves the laser-sheet in wind direction. The PIV-camera is installed on a two-dimensional traversing system, which is located on top of a tower so that the camera is on the same height as the rotor plane. This two-dimensional traversing system is the same as used for the PIV measurements in the closed test section (see section 3). Fig 11 is a three-dimensional view on the set-up in the Open Jet.

However, the most critical component is the seeding of the flow. The particle size, the seeding concentration

5 CONCLUSIONS

A Particle Image Velocimetry system for the measurement of two velocity components has been developed for the Large Low Speed Facility of the German Dutch Wind Tunnel. A flexible system set-up allows to use it both in the closed and the Open Jet test sections. The main components of the system are a full-frame interline CCD video camera with a 1000 by 1000 pixel array, a pulsed Nd:YAG laser of which each pulse has an energy of 320 mJ, a seeding generator installed in the settling chamber of the wind tunnel and a software package for analysis of the PIV recordings.

The first application of the system was the measurement of wake of a transport aircraft model at two different streamwise locations. Because the objective of the experiment was to trace the streamwise development of the vortices in the wake, the 0.2 by 0.2 m² measurement plane was set perpendicular to the main flow direction. Although there was a strong out-of-plane velocity component, excellent PIV recordings have been made. One of the established advantages of PIV is its capability to measure the instantaneous velocity field and the recordings taken showed a vortex which position changed from recording to recording. By taking the mean value over a large number of recordings this randomly moving vortex averages out. This underlines that PIV is very suitable to map flows containing large unsteady coherent structures.

The next application of the PIV system are measurements of the flow field of a scaled helicopter rotor in the Open Jet test section of the DNW-LLF. This requires a special set up of the PIV system. Using existing support structures the requirements could be met. In the near future the stability of the system will be tested.

6 ACKNOWLEDGEMENT

The financial support of the German Bundes Ministerium für Bildung, Forschung und Technologie for the development and acquisition of the PIV system is gratefully acknowledged. The authors would like to thank Daimler-Benz Aerospace Airbus for the permission to make use of their wind tunnel model.

7 REFERENCES

1. Seelhorst, U., Bütefisch, K.A., Sauerland, K.H., "Three Component Laser-Doppler-Velocimetry Development for Large Wind Tunnel", in ICI-ASF Record, 1993, p. 33.1-33.7.
2. Adrian, R.J et al. (eds.), "Applications of Laser Techniques to Fluid Mechanics", Proc. of Eighth Int. and the seeding traverse mechanism have to be arranged, so that the entire tip vortex including the vortex core of the rotating blade is provided by particles at the location of investigation. Experiences made during flow visualisation at helicopter rotors in the DNW-LLF by means of smoke and laser light-sheet are very helpful for this purposes. Symposium, Lisbon, July 8-11, 1996.
3. Huenecke, K., "Structure of a Transport Aircraft-Type Near Field Wake", in The Characterisation & Modification of Wakes from Lifting Vehicles in Fluids, AGARD-CP-584, May 1996, Paper 5.
4. Adrian, R.J. "Particle-image Techniques for Experimental Fluid Mechanics", Ann. Rev. Fluid Mech. 23, 1991, pp. 261-304.
5. Hinsch, K.D. "Particle Image Velocimetry", in Speckle Metrology, Sihoro, R. S. (ed.), New York, USA, Marcel Dekker, 1993, pp. 235-323.
6. Kompenhans, J. and Höcker, R., "Application of Particle Image Velocimetry to High Speed Flows", in von Karman Institute for Fluid Dynamics, Lecture Series 1988-06, Particle Image Displacement Velocimetry, March 21-25, pp. 67-83.
7. Raffel, M. and Kompenhans, J., "Theoretical and Experimental Aspects of Image Shifting by means of a Rotating Mirror System for Particle Image Velocimetry", Meas. Sci. Tech. 6, 1995, pp. 795-808.
8. Willert, C., "The Fully Digital Evaluation of Photographic PIV Recordings", Appl. Sci. Res., to appear.
9. Hornung, H., Willert, C. and Turner, S., "The Flow Field Downstream a Hydraulic Jump", J. Fluid Mech. 287, 1995, pp. 229-316.
10. Stasicki, B. and Meier, G.E.A., "A Computer Controlled Ultra High-Speed Video Camera System", in SPIE Proceedings. 21 Intl. Congress, High-Speed Photography and Photonics, Teajon, Korea, 29-Aug.- 2 Sep. 1994, SPIE Vol. 2513, pp. 196-208.
11. Lecordier, B., Mouqualid, M., Vottier, S., Rouland, E., Allano, D. and Trinity, M., "CCD Recording Method for Cross-Correlation PIV Development in Unsteady High-Speed Flows", Exps. Fluids, 18, No 3, 1994, pp. 205-208.
12. Huang, H.T. and Fiedler, H.E., "Reducing the Time Interval Between Successive Exposures in Video-PIV", Exps. Fluids, 17, No 5, 1994, pp. 356-357.
13. Höcker, R. and Kompenhans, J. "Application of Particle Image Velocimetry to Transonic Flows," Application of Laser Techniques to Fluid Mechanics, Springer-Verlag, Berlin, 1991, pp. 415-434.
14. Bryanston-Cross, P.J. and Epstein, A., "The Application of Sub-Micron Particle Visualisation for PIV (Particle Image Velocimetry) at Transonic and Supersonic Speeds," Prog. Aerospace Sci., Vol. 27, 1990, pp. 237-265.
15. Towers, C.E., Bryanston-Cross, P. J. Judge, T.R., "Application of Particle Image Velocimetry to Large-Scale Transonic Wind Tunnels," Optics & Laser Technology, Vol. 23, No 5, 1991, pp. 289-295.
16. Humphreys, W.M., Bartram, S.M. and Blackshire, J.L., "A Survey of Particle Image Velocimetry Applications in Langley Aerospace Facilities," 31st

- Aerospace Sciences Meeting, January 11-14, 1993, Reno, AIAA paper 93-041.
17. Molezzi, M.J. and Dutton, J.C., "Application of Particle Image Velocimetry in High-Speed Separated Flows," AIAA Journal, Vol. 31, No 3, 1993, pp. 438- 446.
 18. Hunter, W.W. and Nichols, C.E. (eds.), "Wind Tunnel Seeding Systems for Laser Velocimeters," NASA Conference Publication 2393, Workshop, March 19-20, 1985, NASA Langley Research.
 19. Meyers, J.F. "Generation of Particles and Seeding," Von Kármán Institute for Fluid Dynamics, Lecture Series 1991-05, Laser Velocimetry, Brussels, June 10-14, 1991.
 20. Melling, A. "Seeding Gas Flows for Laser Anemometry", in AGARD Conference on Advanced Instrumentation for Aero Engine Components, AGARD-CP 399, May 1986.
 21. Willert, C. and Gharib, M., "Digital Particle Image Velocimetry", Exps. Fluids, 10,1991, pp.181-183.

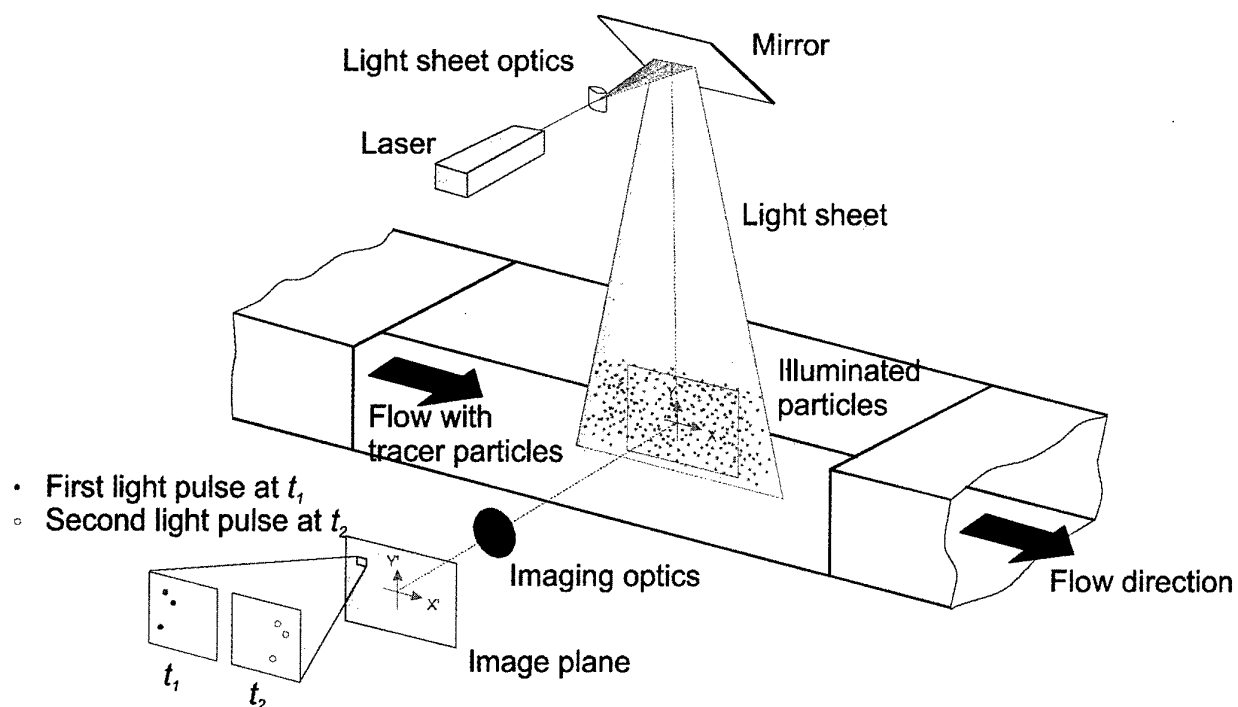


Fig 1: Experimental set-up for PIV in a wind tunnel.

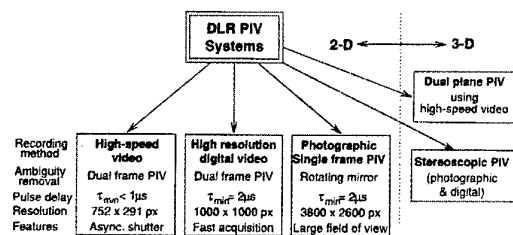


Fig 2: PIV systems available at DLR for use in wind tunnels.

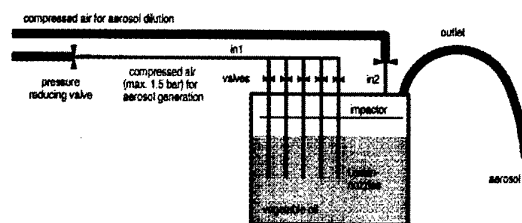


Fig 3: Seeding generator.

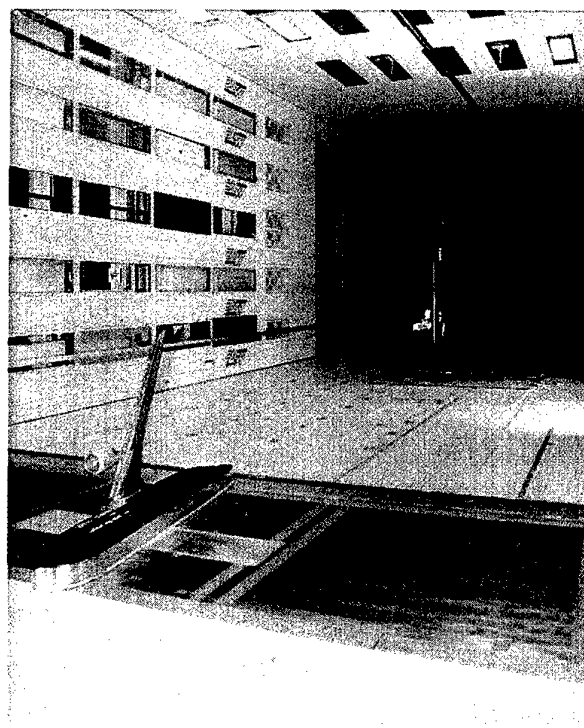


Fig 4: Picture of model in test section.

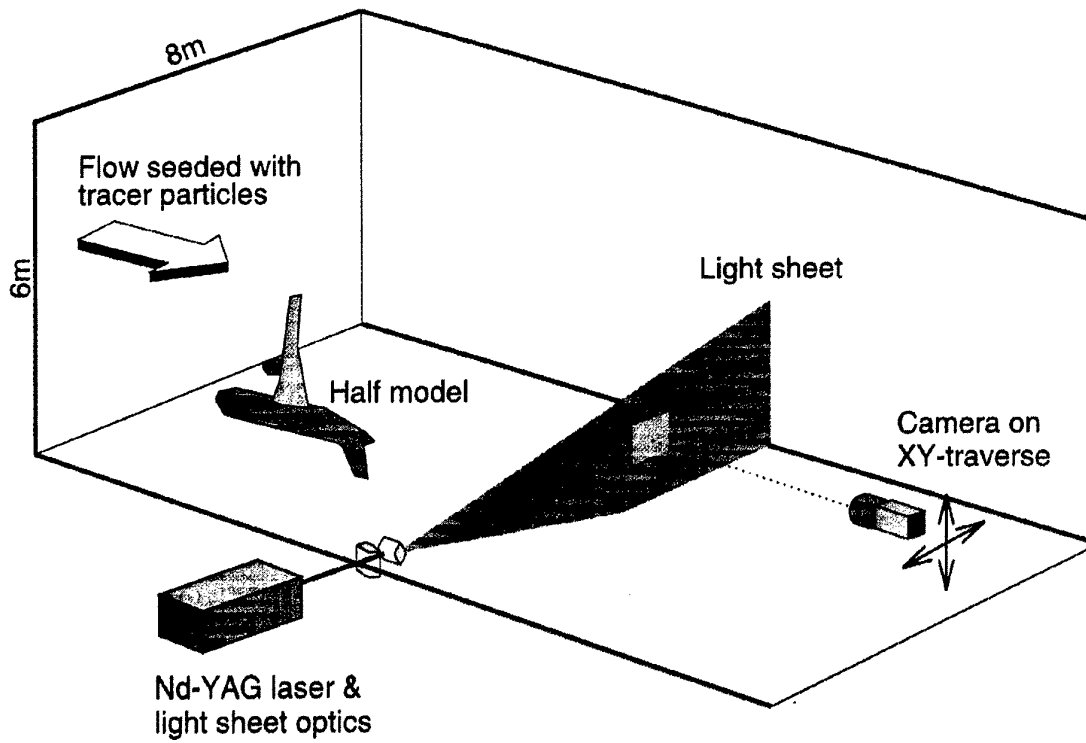


Fig 5: Sketch of set-up of PIV in DNW-LLF

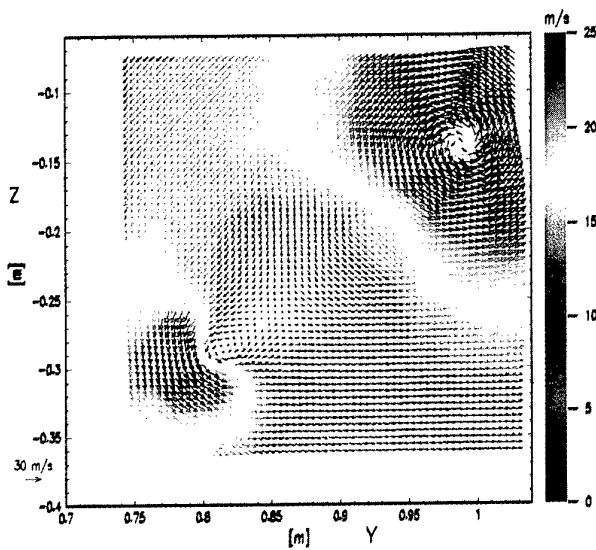


Fig 6: Averaged cross velocity distribution 2 span widths downstream of the wing tip of the half model. Wind velocity $V_\infty = 60$ m/s.

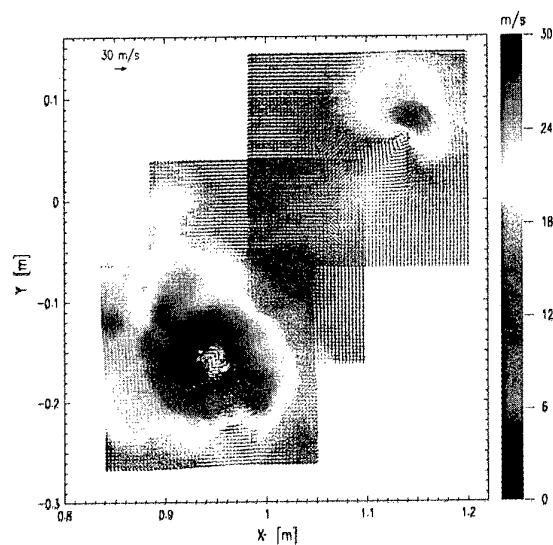


Fig 7: Composite of three vector maps measured 0.93m downstream of the wing tip.

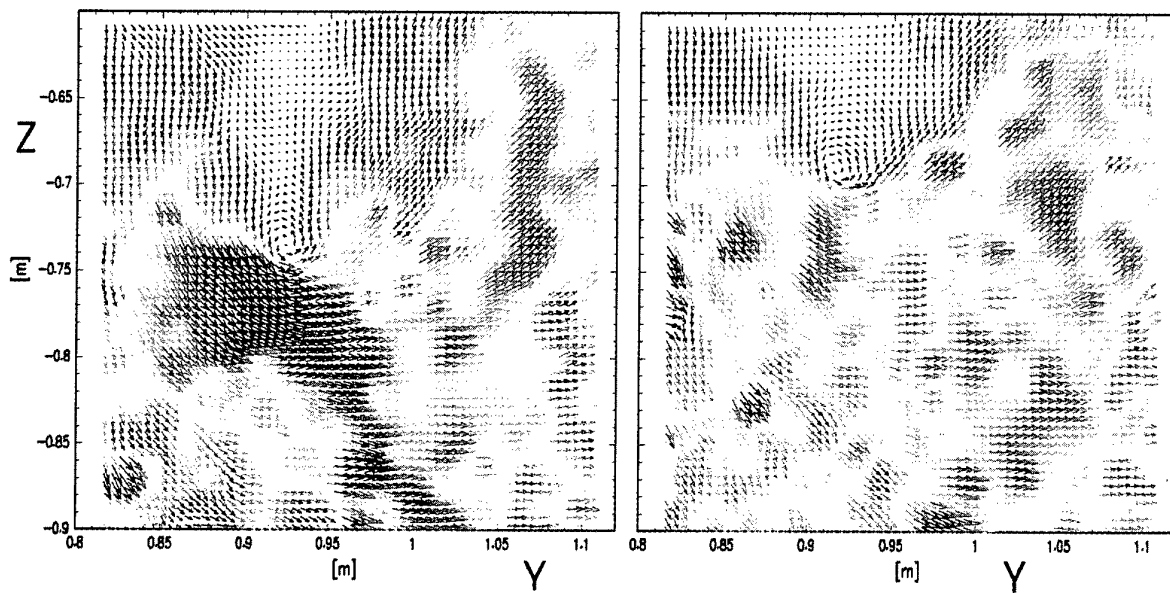


Fig 8: Two instantaneous cross velocity distribution at different times 2 span widths down stream of the wing tip in an area underneath of the two main vortices. The locations of the shown vortex center are different .

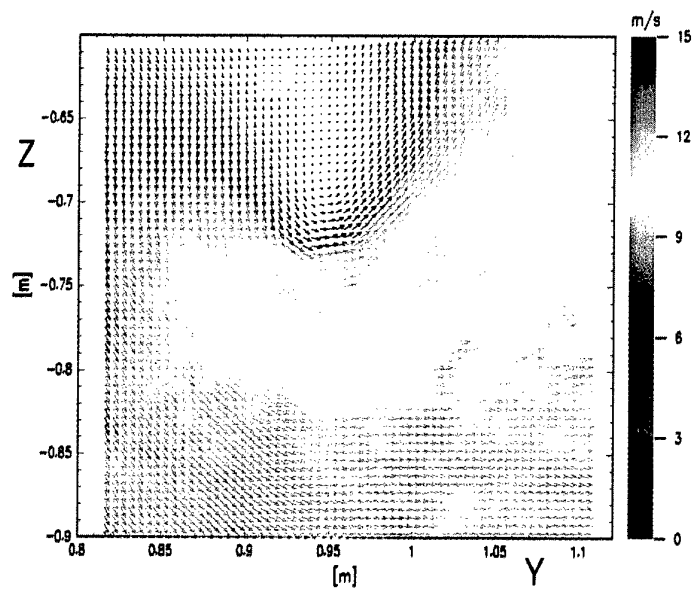


Fig 9: Averaged cross velocity distribution of the same vortex as shown in Fig 8.

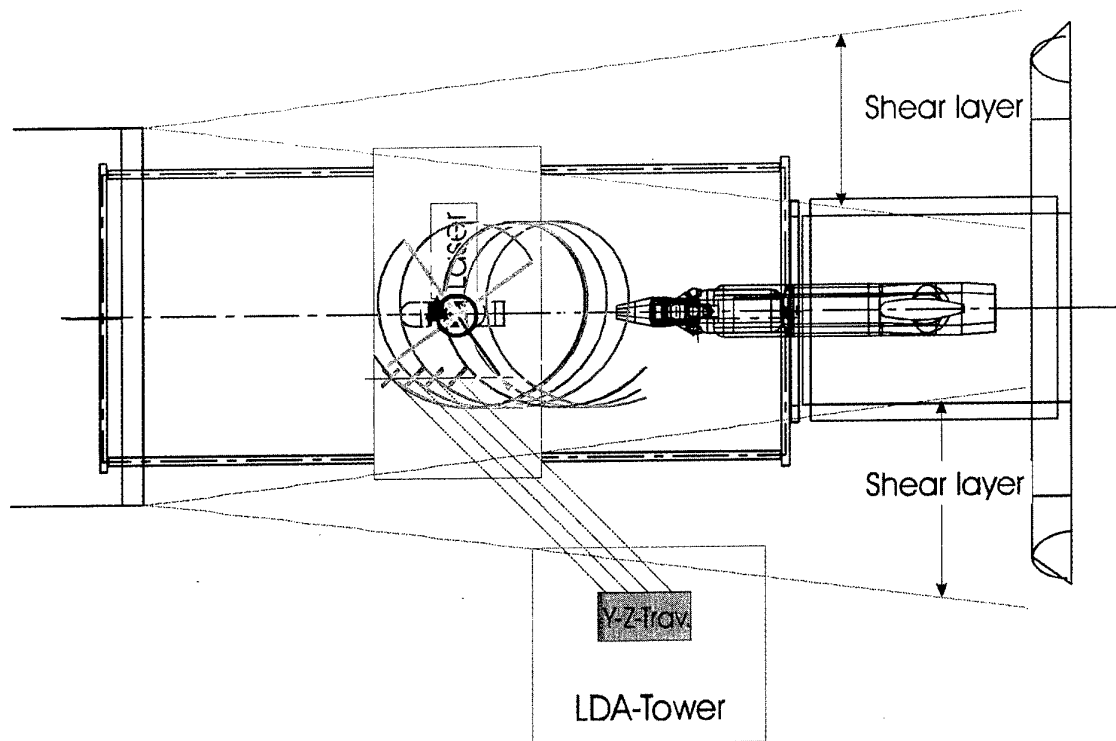


Fig 10: Top-view of test set-up for rotor testing.

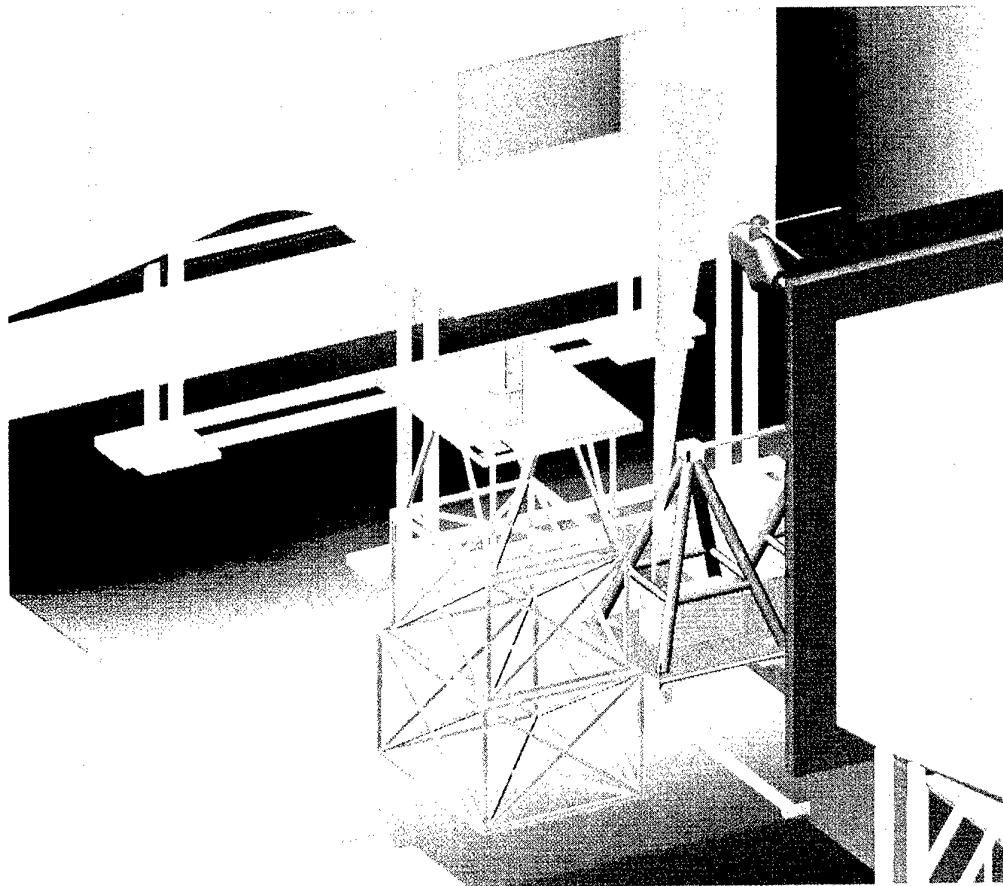


Fig 11: Perspective view of the test set-up for rotor testing.

Analysis of Complex Flow Fields by Animation of PIV and High Resolution Unsteady Pressure Data

F.Coton⁺
R. Galbraith⁺
I.Grant*
D. Hurst⁺

⁺Department of Aerospace Engineering
University of Glasgow
Glasgow, G12 8QQ, U.K.

*Department of Civil and Offshore Engineering
Heriot-Watt University
Edinburgh, EH14 2AS, U.K.

SUMMARY

This paper describes the use of animation in the analysis of data from unsteady aerodynamic tests where the phenomena of interest vary both temporally and spatially. Particular emphasis is given to results from an investigation of blade vortex interaction (BVI) where both flow field and surface pressure data were recorded. It is shown that animation can be used, in a manner akin to basic flow visualisation, to identify the interesting features of such a flow and to, thus, guide more detailed conventional analysis techniques. The method adopted in this study involved the acquisition of a series of PIV images which were then processed and subsequently interpolated onto a regular grid. The temporal variation in velocity at each grid point was then established by a further interpolation between PIV frames. Finally, particles were placed in the initial velocity field and their subsequent trajectory during the interaction process calculated using a multi-step integration method.

LIST OF SYMBOLS

c	blade chord
C_p	pressure coefficient
\vec{r}	position vector
x	distance along chord
\vec{V}	velocity vector
t	time
Ψ	azimuth angle

INTRODUCTION

Many of the most significant advances in the understanding of complex fluid dynamic phenomena have occurred through some form of flow visualisation (Ref. 1). The principal reason for the success of visualisation as an interrogative tool lies in the ability of humans to observe and, therefore, document flow features which evolve over both time and space. One major drawback, however, of this form of experimentation is the lack of quantitative information which can be obtained from a simple visualisation test. As a consequence of this, flow visualisation has traditionally been used to provide an initial description of the flow which is then subsequently enhanced by other forms of quantitative measurement.

In recent years considerable attention has been focused on the role of high quality experiments in the validation of Computational Fluid Dynamics (CFD) codes. In particular, much effort has been directed towards the acquisition, by non-intrusive technologies, of quantitative off-body flow field data. In this respect, Particle Image Velocimetry (PIV), has successfully provided global flow field information for a wide range of test cases. At the same time, advances in other areas of measurement, such as pressure transducer manufacturing technology and PC based data acquisition capabilities, have significantly reduced the cost of interrogating complex flow fields in great detail. These benefits have been exploited by researchers at Glasgow University and Heriot-Watt University, in the development of a facility which has the capability to provide simultaneous surface and flow field data for unsteady flows (Ref. 2). The elements of this facility were developed as separate entities at the respective Universities but have been used effectively together in a variety of projects during a long-standing collaboration.

As with any major data acquisition facility, the volume of data collected by this combined facility can be immense. This is, of course, generally advantageous and reduces the risk of non-measurement of important flow phenomena. On the other hand, it can be very difficult to identify the key features of a very large data set without considerable effort on the part of the researcher. Even then, the particular analysis technique or domain can have a considerable bearing on the outcome of the investigation and often important phenomena are overlooked. Ideally, it would be beneficial to conduct flow visualisation tests to gain a superficial understanding of the flow behaviour in advance of analysis. Often, however, the actual test conditions cannot be reproduced with enough confidence in a low speed flow visualisation facility and this option is, therefore, not possible. PIV helps to bridge the gap between the 'quick look' superficial type of analysis and more detailed quantitative investigations. Nevertheless, when the flow is temporally varying it is often still difficult to evolve a clear mental picture of the flow development simply from a series of PIV vector plots. One solution to this problem is to use the information contained in the vector plots as the basis for an

animation of the flow field over a given time period. This approach, which in many ways may be considered as numerically reconstructing the original flow field, allows key features to be easily identified. When combined with animated surface pressure data, the technique is even more powerful.

In the past, analysis of time varying pressure data was relatively straightforward since generally, as a result of limitations in measurement technology, only a small number of measurement points were used. This is no longer the case and the current system at Glasgow University has the capability to measure two hundred channels of data at 50kHz per channel. This system has recently been applied to the measurement of unsteady surface pressures on a variety of wing planforms subject to pitching motions (Refs. 3,4). Animation has played an important role in the interrogation of the resulting data by identifying both spatially and temporally varying phenomena at the early stages of the analysis process.

In the present study, PIV and surface pressure data from a wind tunnel based blade vortex interaction experiment (Refs. 5,6) have been used to develop an animated representation of the flow field and blade surface loading patterns as a single vortex interacts in a nominally parallel manner with a rotating blade. The animation can be configured either as an animated series of vector plots or as a particle field. In each case, the information obtained is subtly different and provides valuable insight into the interaction phenomenon.

EXPERIMENTAL FACILITIES

Particle Image Velocimetry

The PIV system used in the present study has been developed at the Fluid Loading and Instrumentation Centre of Heriot Watt University over a number of years. Unlike many commercial systems, it provides a great degree of flexibility allowing image capture both digitally and using a variety of wet film formats. Processing can then be carried out either using auto-correlation or via in-house particle tracking algorithms. Processing times depend on the method of image capture used but, with a digital camera, quasi-real-time PIV is possible. The PIV system has been used extensively in a range of wind tunnel projects at speeds up to 50m/s; this has been the maximum speed of the wind tunnels used to date.

Particle Image Velocimetry is a technique which allows the velocity of a fluid to be simultaneously measured throughout a region illuminated by a two-dimensional light sheet (Refs. 7,8). 'Seeding', flow following particles are introduced into the airstream and their motion used to determine the kinematics of the local fluid. The particles are chosen to be near neutrally buoyant and to efficiently scatter light.

The motion of the particles is recorded via multiple exposure photographic methods either using conventional wet-film or using a digital camera. From a knowledge of the time between recording the position of consecutive images, together with the camera magnification, and allowing for lens distortion and perspective effects, the velocity of the particles is

obtained. The recording parameters are chosen to obtain good spatial separation of the images, ensuring accurate and reliable velocity measurements.

The illumination is most commonly provided by a laser, shaped into a planar 'sheet' using cylindrical lenses. An advantage of using a laser source is that many lasers have a pulsed output with a pulse duration and a repetition rate making them suitable as a stroboscopic illumination source. In the present system, there are various laser configurations available for illumination purposes depending on the particular application and on the size of the viewing area under consideration. The illumination method used for the particular case presented in this paper, is outlined below.

Various strategies exist for image analysis in the present system (Ref. 9,10), these are accessed via menus on a PC based software suite. Depending on the density of the particle images a choice can be made between tracking and correlation approaches. Tracking is selected when the discrete particle image groups can be distinguished. This technique was used in the BVI study described below.

During analysis, the flow image transparency is searched using a custom built scanner offering high magnification. The interrogation window is illuminated by an incoherent light source, and the image region then digitised and subjected to processing and filtering algorithms to improve image quality as a precursor to the evaluation of particle velocity. The velocity measurement procedure usually consists of a statistical algorithm to establish the global distribution of displacements of the particle images. This information is then used in identifying the particle image pairs or groups using a windowing method. Where significant changes in the flow characteristics take place, an adaptive processing algorithm based on a neural net strategy significantly improves successful grouping. Where appropriate, directional ambiguity can be resolved using image coding or 'tagging' (Ref. 11).

Unsteady Pressure Measurement System

In the system developed at Glasgow University, the signals from a large number of miniature pressure transducers are input to a specially designed signal conditioning unit of modular construction with each module containing its own control board. On instruction from the computer, the control board automatically removes all offsets to below the A-D converter resolution and adjusts all gains as necessary. In fact, during a test, the computer samples the maximum and minimum of each transducer output and adjusts the gains accordingly to improve the data acquisition resolution. The data acquisition is carried out by a PC microcomputer interfaced with proprietary Bakker Electronics BE256 modules which provide the necessary analogue to digital conversion. The software used for data acquisition is TEAM 256. At present, the system has 200 channels, each of which is capable of sampling to a maximum rate of 50KHz, giving an overall sampling rate of 10MHz. For most applications, the system utilises Kulite differential pressure transducers of type CJQH-187 with one side of the pressure diaphragm

open to the ambient pressure outside the wind-tunnel via tubing.

BLADE VORTEX INTERACTION INVESTIGATION

Blade vortex interaction, can occur on helicopter rotors under conditions of powered descent or vigorous manoeuvring. This interaction has been identified as a significant source of noise and vibration in rotorcraft and, as such, has been the subject of many experimental and computational studies (Refs. 12,13,14). Experiments were conducted in the University of Glasgow Handley Page wind tunnel on an untwisted, non-lifting, single blade rotor which interacted in a parallel or oblique manner with an oncoming vortex generated upstream of the rotor disk by a stationary wing (Refs. 15,16). In this study, particle image velocimetry was used to document flows about the rotor blade during interactions and the blade was instrumented with a chordal array of ultra miniature pressure transducers which could be moved to a variety of span locations. The experimental set-up is illustrated in Fig. 1.

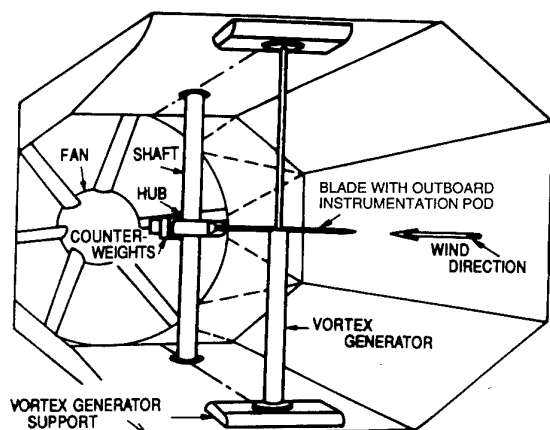


Fig. 1. Glasgow University Blade-Vortex Interaction Facility

The aluminium rotor blade had a NACA 0015 aerofoil section, with a 0.149 m chord and a 0.9426 m radius. The vortex generator comprised of two adjoining NACA 0015 aerofoil sections spanning the height of the test section 2.1 rotor radii upstream of the rotor hub. During the test sequence, conducted in the 1.61m x 2.13m octagonal test section, the tunnel speed was 47.0 m/s while that of the rotor tip was 59.25 m/s. The vortex strength was controlled by setting the two sections of the vortex generator at equal but opposite incidence. The horizontal position of the vortex generator was altered to control the angle of intersection between the interaction vortex and the blade, resulting in either a nominally parallel or oblique BVI. The vertical position of the aerofoil junction on the vortex generator was varied to allow an examination of interactions for different blade-vortex separation heights.

The outer portion of the rotating blade was constructed in a modular fashion which allowed an instrumentation

pod to be positioned at a variety of span locations. Using this pod, which contained twenty eight ultra-miniature pressure transducers distributed around the blade chord, it was possible to obtain a series of high temporal resolution chordwise pressure distributions throughout the interaction. PIV data were collected in two planes oriented perpendicularly to the tunnel free stream, one plane at 0.78 rotor radii upstream of the rotor hub, and the second at 0.94 rotor radii. In this paper, pressure and PIV data collected at the 0.78 span position are presented for a head-on interaction case.

During testing, the flow in the closed-return wind tunnel was seeded with Expancel DE20 micro-balloon particles which were illuminated by a pulsed sheet of laser light. This form of seeding produced average particle density levels which were sufficient for particle tracking but were too low for correlation methods. The particles had an average diameter of 20 microns and an average specific gravity of 0.06. To minimise flow field disturbances, an upstream facing 35 mm camera (Nikon F801) was mounted five chord lengths downstream of the measurement plane below the rotor hub. Images were collected on Kodak Recording Film 2475 using a 55 mm flat field lens. The camera mount was constructed of 49 mm box section mild steel, attached directly to the floor of the wind tunnel bay, thus isolated from the vibration of the tunnel and rotor system. A fairing covering the camera mount and the lower half of the rotor shaft was also employed to shield the camera mount from any aerodynamic buffeting. An accelerometer attached to the top of the camera mount indicated that errors in velocity measurement due to camera vibration were less than 0.3% of the maximum velocities recorded in the measurement plane.

The laser light was provided by a Lumonics HLS4 ruby laser. The laser beam was formed into a light sheet of using a bi-concave lens and a convex lens in an appropriate configuration. In this case, the thickness of the light sheet was around 10mm which was necessarily high due to the strong three-dimensionality of the flow. Triple pulses of laser light were used to generate multiple images of each seed particle on the photographic film, thus allowing later calculation of local velocities in the vicinity of each particle. Laser pulses were separated by 50 to 100 μ s, with each individual pulse having an energy of approximately 1.5J. Directional ambiguity was addressed in a select number of tests by setting the first inter-pulse interval longer than the second. This procedure resulted in unequally spaced 3 spot patterns which can be used to derive flow direction. Most tests, however, utilised constant inter-pulse intervals of 80 μ s.

During image processing, the film negatives were mounted on an X-Y traverser and interrogated using a CCD camera and microscope lens arrangement. Each 35mm negative was subdivided into 80 frames (512 x 512 pixels) which were individually digitised. Computer software was then employed to automatically identify particle pairs or triples, and determine local velocity. The general set-up of the PIV system is shown in Fig.2.

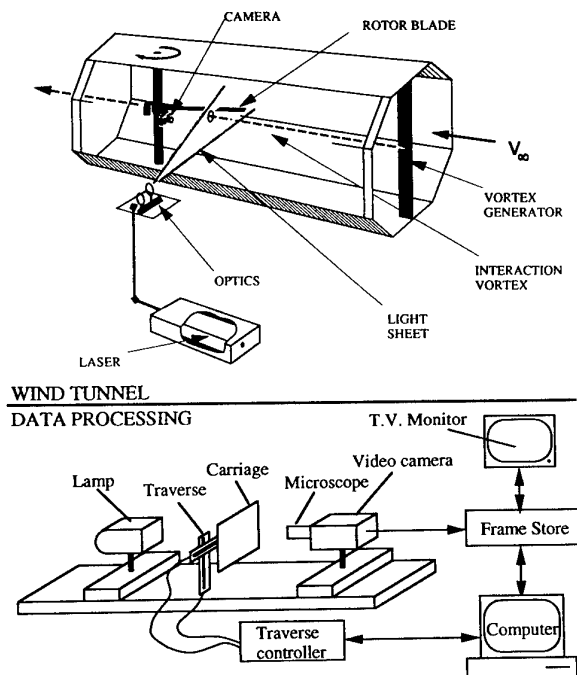


Fig. 2. PIV measurement system

ANIMATION OF PIV IMAGES

For animation purposes, it was necessary to obtain a reasonable sequencing of images throughout the interaction process. To achieve this, around twelve PIV images were recorded at each of a series of azimuth positions for a particular setting of the vortex generator. It was found that the position of the interaction vortex changed by as much as two core radii horizontally and vertically between images recorded for identical geometric configurations. This presented significant problems for conventional averaging methods since the number of images required for each case would have had to have been very high to obtain any meaningful average. When the tests were conducted, the processing time for the particle tracking system was around one hour per negative and so fixed-point averaging was not considered to be a viable option in this case. Interestingly, the capability of the present PIV system is such that it would be possible to adopt this approach if the tests were carried out today. An alternative scheme was, therefore, employed which entailed examining each of the collected images to determine the relative position of the blade and the vortex core. Once this had been done, it was possible to determine a best fit to the vortex trajectory as it passed the blade. Images for sequencing were then selected on the basis of the proximity of the vortex exhibited in the image to this best fit trajectory. A typical vortex track generated by this method is shown in Fig. 3. for a near-miss interaction. It is notable that the vortex track produced by this method is slightly irregular. From this it is obvious that the strength of the PIV images obtained in the study lies in their clear resolution of the spatial domain. Nevertheless, the resulting images will convey the main features of the temporal development of the

flow as the interaction progresses. This is essential if the images are to provide the basis for a subsequent flow animation.

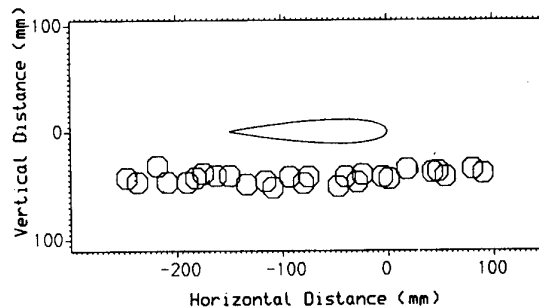


Fig. 3. Typical best-fit vortex trajectory

Unlike correlation methods, particle tracking produces irregular velocity vector plots. Whilst this type of output provides valuable information on the general flow structure, it does not provide the necessary consistency between consecutive frames required for animation. Consequently, the first stage in the animation process was to transform the basic vector plots onto a regular grid. The pitfalls of interpolation of PIV data are well documented (Ref. 17) but, given that the resulting animation was to be used as a qualitative guide to analysis, absolute accuracy was not an overriding concern. For this reason, a simple four-point weighted averaging scheme was used to obtain the required velocity vectors on the regular grid.

At this stage, a series of regular PIV vector plots corresponding to a range of azimuth positions were produced. Since the camera used in the experiments had a fixed position, a grid point in one frame was spatially coincident with the corresponding points in all the other frames. For the example presented in this paper, nine images were used as the basis for an animation covering twenty two degrees of azimuth.

The next stage in the process involved interpolation between these images to produce a high enough frame density for smooth animation. Interpolation was conducted on a point by point basis for both the horizontal and vertical velocity components. This involved determining the velocity components at a given point on the grid in each PIV frame together with the temporal separation of consecutive frames. By curve fitting, or simple interpolation, it was then possible to determine the variation of velocity with time at that particular grid point. Various strategies were employed to establish this velocity variation as a function of time. These included linear interpolation, least squares polynomial fitting and the use of B-splines. In the latter two cases, considerable manual intervention was required to inspect the curve fit and to modify the fitting procedure where necessary. It was found, however, that in the case presented here the general characteristics of the resulting intermediate frames were relatively insensitive to the method of fitting and so direct linear interpolation was used. In cases where the temporal resolution of the PIV frames was lower, the B-spline method proved to be more appropriate.

Once interpolation had been carried out for all the grid points, it was possible to produce a basic animation of the velocity vector field. This form of animation is useful as it highlights the distortion of the main vortex fragments as the interaction progresses. The main weakness, however, of velocity vector plots is that it is often necessary to remove a particular velocity component to allow the main flow features to become distinguishable. This makes it very difficult to gauge the temporal distortion the fluid field under the combined influence of the aerofoil and the interacting vortex. To do this, it is necessary to use the information contained in the vector plots to numerically reconstruct the fluid behaviour. In the present study, this was achieved by the animation of particles introduced into the flow on the same initial grid as that used in the vector diagrams. The initial particle positions are shown in Fig. 4. It should be noted that the particle image frame represents a flow area of 355mm by 355mm and that all vector plots are scaled in the same way.

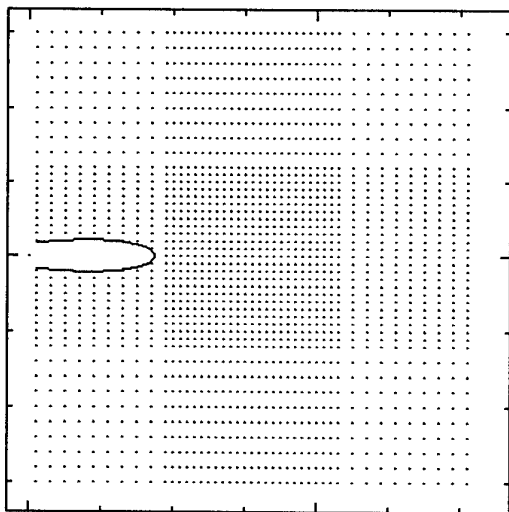


Fig. 4. Initial particle field

The movement of particles within a temporally varying velocity field can be estimated by a suitable multi-step method or via some form of predictor-corrector algorithm. Previous studies of numerical vortex models (Ref. 18) have indicated that a third order Adams-Bashforth multi-step integration scheme provides suitable accuracy for a velocity field of this type. This method can only be applied after the flow has progressed beyond the first two time steps and so it is necessary to adopt a different initial approach. Since the time step used in the present calculation was very small, corresponding to less than 0.5 degrees of azimuth movement, the initial particle displacements could be estimated by a simple displacement based solely on the initial velocity field, i.e.

$$\bar{r}(t_1) = \bar{r}(t_0) + \bar{V}(t_0, \bar{r}(t_0)) \cdot \Delta t \quad (1)$$

Once this displacement had been computed, a four point weighted average calculation was used to establish the velocities at the new particle locations. The second

displacement of the particles was calculated using the second-order Adams-Bashforth equation

$$\bar{r}(t_2) = \bar{r}(t_1) + \left[\frac{\Delta t}{2} \right] \left[3\bar{V}(t_1, \bar{r}(t_1)) - \bar{V}(t_0, \bar{r}(t_0)) \right] \quad (2)$$

Once again, as was the case after every particle displacement, the new particle velocities were calculated using the weighted four point averaging scheme applied to the appropriate velocity vector map. All subsequent particle displacements were determined using a third-order Adams-Bashforth scheme.

$$\bar{r}(t_N) = \bar{r}(t_{N-1}) + \left[\frac{\Delta t}{12} \right] \begin{bmatrix} 23\bar{V}(t_{N-1}, \bar{r}(t_{N-1})) \\ -16\bar{V}(t_{N-2}, \bar{r}(t_{N-1})) \\ +5\bar{V}(t_{N-3}, \bar{r}(t_{N-3})) \end{bmatrix} \quad (3)$$

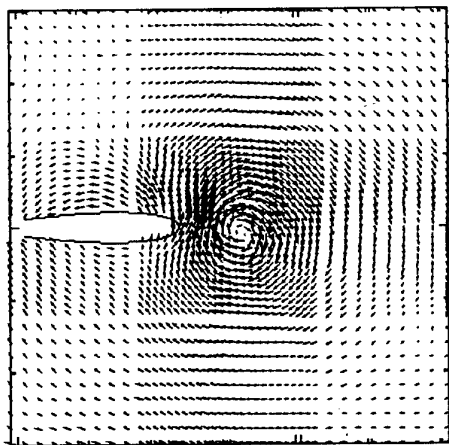
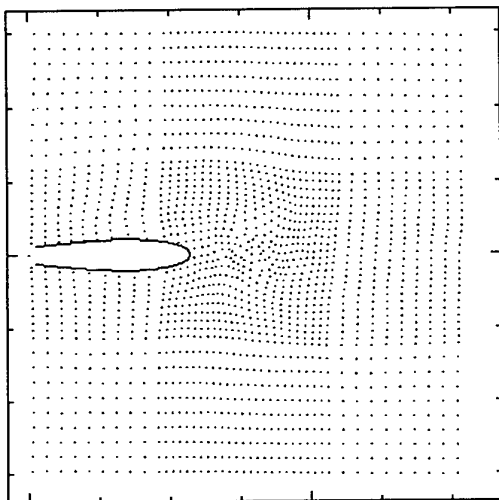
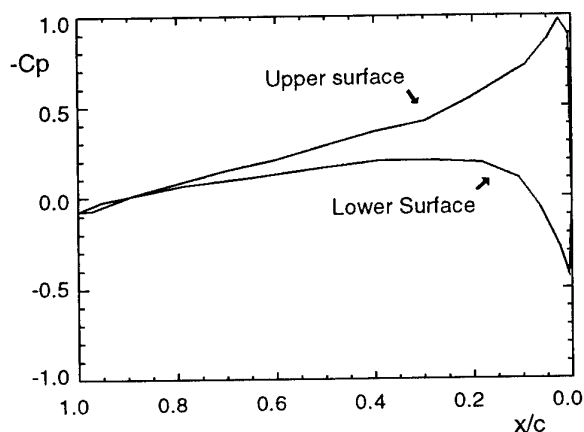
RESULTS AND DISCUSSION

Ideally the results of the animation process are best viewed in video form. It is, however, still informative to examine individual frames which may highlight key flow features. In this section, selected particle and vector plot animation frames are presented together with the original PIV vector plots and pressure data. The particular BVI case considered here is that of a head-on parallel interaction at 78% of the rotor radius. Many of the key physical results from this case have been presented in Ref. 16 and, consequently, only the additional information which can be obtained from animation will be highlighted here.

In Figs. 5a and 5b, frames are presented from the vector plot and particle animations, for the 171 degrees of azimuth case. At this stage, the blade is in close proximity to the interaction vortex and is, consequently experiencing considerable upwash. The vector plot exhibits an arched appearance on the upper surface of the blade where relatively high velocities exist. Although enhanced velocities are also experienced on the lower surface, these are considerably less than their upper surface counterparts. The distortion of the particle field also illustrates these effects. In particular, the acceleration of the fluid upwards past the leading edge of the blade is characterised by a convex distortion of the particle field on the left hand side of the vortex. Similarly, the increased velocity on the upper surface of the blade appears as curvature in the particle grid.

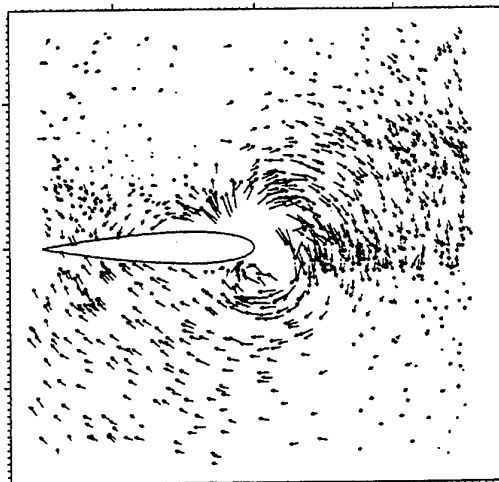
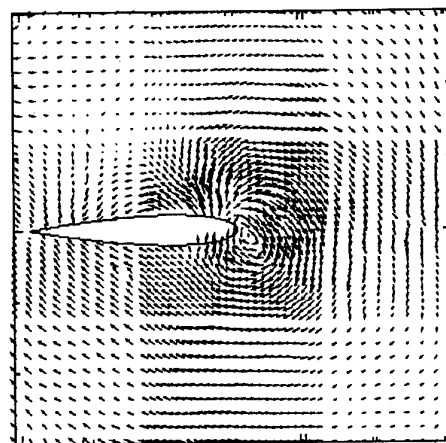
As may be expected from the above, the corresponding chordwise pressure distribution presented in Fig. 5c. has the general appearance of a blade at positive incidence.

By 174 degrees of azimuth, the blade has begun to penetrate the vortex core and, in doing so, begins to experience weaker upwash than before. This is illustrated in the original PIV vector plot, Fig. 6a, in the interpolated vector plot, Fig. 6b and in the particle field, Fig 6c. At this stage, the distortion of the vortex is considerable and, in fact, this distortion is a precursor to separation of the core into upper and lower surface fragments.

Fig. 5a. Interpolated vector field ($\Psi=171^\circ$)Fig. 5b. Particle field ($\Psi=171^\circ$)Fig. 5c. Chordal pressure distribution
($\Psi=171^\circ$)

The interpolated vector field mirrors the original PIV results well. Some problems are however, apparent near the leading edge of the blade where very high velocities are directed towards the surface and appear as vectors which apparently penetrate the surface. Closer

examination, however, reveals that the tails of the vectors, at which the velocities are actually evaluated, all lie outside the blade contour. Whilst this effect is not uncommon in vector plots, where high velocity gradients exist close to a surface, it is indicative of a potential weakness of the particle animation method. It is difficult to obtain detailed velocity measurements in very close proximity to the surface of a solid body in this type of flow field. Thus, the information used to displace particles in the numerical flow field lacks the detail necessary to stop a particle from being convected through a solid surface. It would be possible to impose a boundary condition at the solid surface to prevent this but the benefits are minimal, as the gross features of the flow are adequately represented elsewhere. For this reason, particles which convect through the blade surface are, in the present method, simply absorbed.

Fig. 6a. Original PIV vector plot ($\Psi=174^\circ$)Fig. 6b. Interpolated vector plot ($\Psi=174^\circ$)

At this azimuth angle, the extent to which the gross particle field has been deformed is considerable. Of particular note is the region above the leading edge of the blade where the particle density has become sparse. This is caused by divergence of the flow at the edge of the vortex as some particles try to follow the vortex rotation whilst others accelerate over the upper surface of the wing.

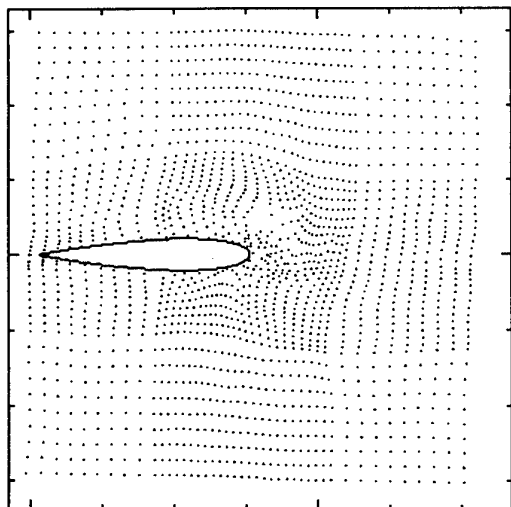


Fig. 6c. Particle field ($\Psi=174^\circ$)

It is interesting to note here that the distortion of the particle field depends on the history of the velocity field. For this reason, distortions in the particle field will tend to lag the dominant features of the vector plots. This effect is clearly illustrated when considering the region of flow divergence identified above. In the vector plots, divergence occurs slightly aft of the leading edge, whereas the evacuated region in the particle field, which has been generated as the blade moves towards and into the vortex, is ahead of the blade.

Another interesting feature of these results is the impression of fluid rotation which they give. The vector plots, which do not include the motion of the blade, appear, for example in Fig. 5, to show a vortex rotating rapidly ahead of the blade. It is, of course, possible to clarify this in the vector plots by adding a velocity legend or a reference vector for the blade speed but, even then, the deformation of the vortex during the interaction prohibits a clear inference of this effect. In fact, the edge of the undisturbed vortex core would only progress through half a revolution in the time taken for the full interaction to occur.

The relative rotation of the vortex with respect to the aerofoil motion is more clearly illustrated in Fig. 7, where the distortion of the central section of the particle grid is shown as the interaction progresses. In fact, the figure shows that the rotation of the near field is slowed substantially during the interaction. It would also appear that it only regains momentum well after the vortex has left the trailing edge of the blade.

In Fig. 7, by 174 degrees of azimuth, the central grid has rotated from its original position and is beginning to deform as the blade penetrates the vortex. The deformation of the grid continues as the interaction progresses to 180 degrees of azimuth. At this stage, as shown in Fig. 8a, the vortex has apparently divided into upper and lower surface fragments which convect across the chord at different speeds. These fragments influence the local pressure distribution in the manner described by Horner (Ref. 16), to the extent that their manifestation is easily identified in Fig. 8b. It is also interesting to

note that, with the rearward progression of the vortex, the lower surface of the blade has become the suction side.

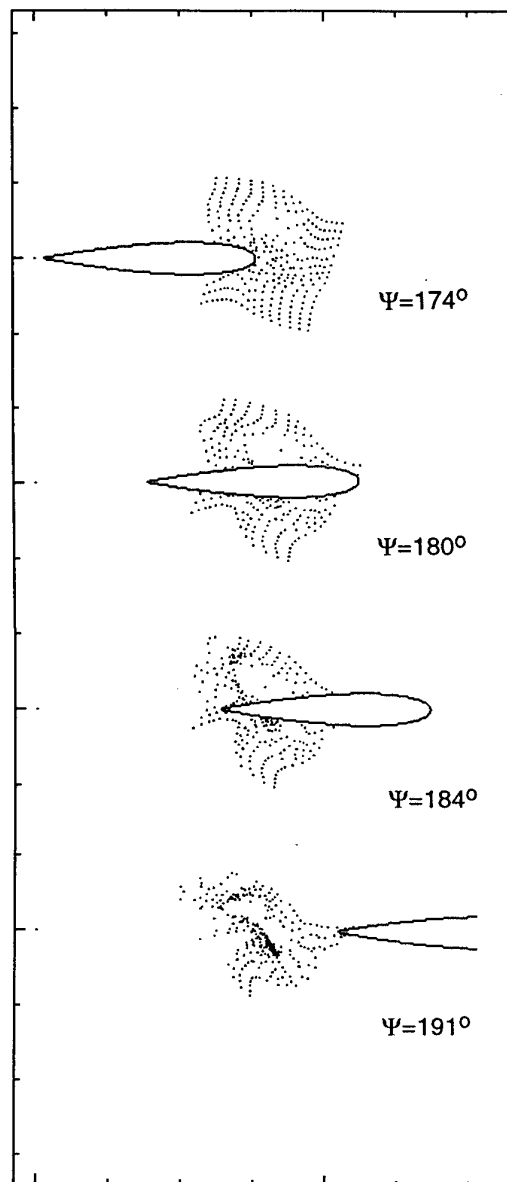


Fig. 7. Deformation of near field during interaction

By 184 degrees of azimuth, the particles above the blade in Fig. 7 have become clustered around the core of the upper vortex fragment shown in the original vector plot in Fig. 9. Below the blade, particles are also clustered near the apparent core of the lower vortex fragment and the deformation of the grid is increased by the upward curvature of the flow towards the trailing edge.

As the vortex passes the trailing edge, it interacts with the wake of the blade and vorticity which is shed during its passage. The resulting flow pattern is complex and is well illustrated by the interpolated vector flow field at 189 degrees of azimuth in Fig. 10. It should be noted that the area of rotation at the far left of Fig. 10, is the vortex trailed from the tip of the rotating blade and has, thus, not been produced by the local interaction considered here. Apart from this, it is possible to

discern both the upper and lower surface fragments and an additional shed vortex.

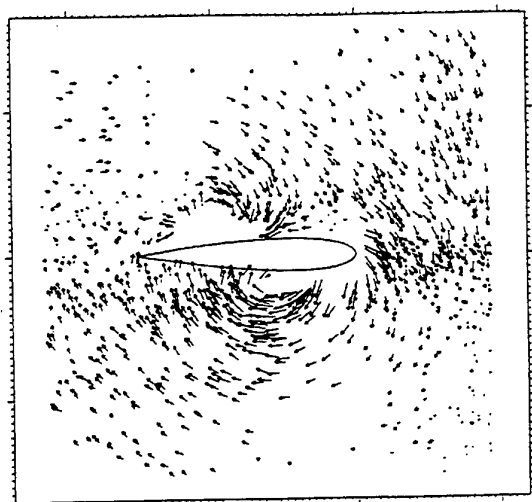


Fig. 8a. Original PIV vector field ($\Psi=180^\circ$)

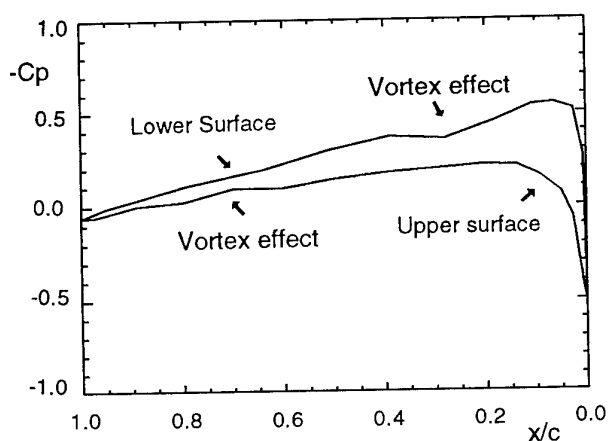


Fig. 8b. Surface pressure distribution ($\Psi=180^\circ$)

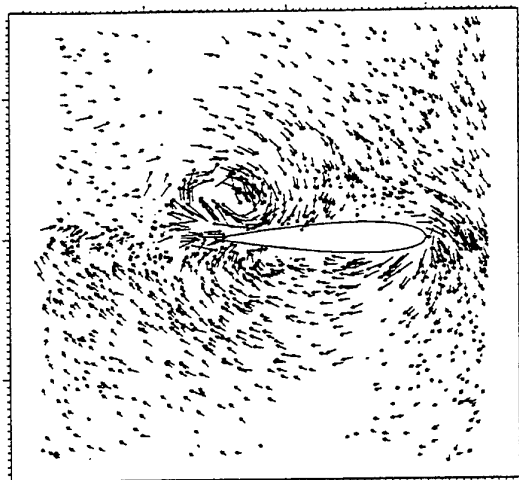


Fig. 9. Original PIV vector field ($\Psi=184^\circ$)

The distortion of the central particle grid, caused by the passage of the vortex from the blade, is illustrated in the final image of Fig. 7. corresponding to an azimuth angle of 191 degrees. As may be expected, the level of distortion in this image is substantially greater than before. Despite this, the link between the upper and lower vortex fragments, is illustrated well by the clustering of the particles. The extent to which the interaction has affected the entire flow field is illustrated in Fig. 11. In addition to the features already discussed, the upward convection of the aerofoil wake due to the influence of the vortex is clearly visible in this figure.

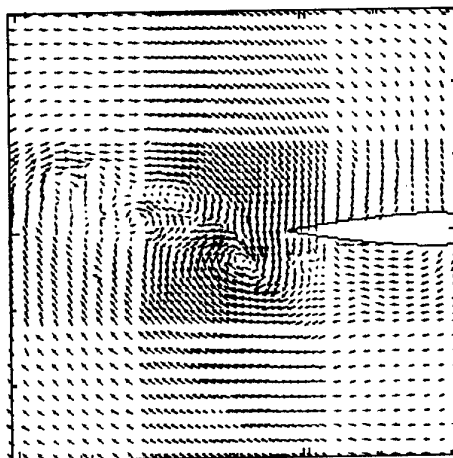


Fig. 10. Interpolated vector field ($\Psi=189^\circ$)

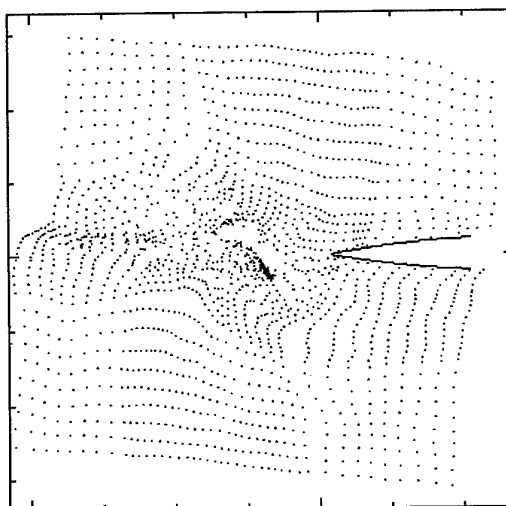


Fig. 11. Particle field ($\Psi=191^\circ$)

Although the particle fields presented here appear to correlate well with the original PIV images, care must be taken when interpreting them as they are based on a discrete series of vector plots of cross-flow velocity. In fact, since the flow is not planar, new particle positions are actually those which would be expected at a distance downstream of the measurement plane, corresponding to the travel of the freestream in the animation time step. over the full interaction presented here, a particle initially in the measurement plane would be expected to travel 0.3m downstream. If the flow is two-dimensional, then this presents no difficulty. In this

case, however, the interaction, although nominally parallel, is known to produce deformation of the convecting line vortex (Ref. 18). The error introduced into the animation results by this effect is uncertain since the extent of the vortex deformation is, itself, unknown. Nevertheless, it is unlikely that any curvature in the vortex trajectory significant enough to induce large-scale errors. This sensitivity of the animation to this effect will, however, be investigated in future studies by using the bank of available results to increase the temporal resolution of the PIV images on which the animation is based.

CONCLUSIONS

The results from a wind tunnel based PIV study of blade vortex interaction have been used to create velocity vector and particle animations of the flow field. Frames from these animations, which illustrate many of the key features of the interaction process, have been presented together with the original PIV results and unsteady pressure data. The animation provides a useful supplement to conventional techniques, particularly in the initial stages of analysis of spatial and time varying flow fields.

ACKNOWLEDGEMENTS

The authors would like to acknowledge the support of the British Ministry of Defence and the Defence Research Agency for the initial wind tunnel study which provided the basis for the present work. The authors also wish to acknowledge the contributions of Dr. M.B. Horner and Dr. J.N. Stewart to the original study.

REFERENCES

1. Merzkirch, W., "Techniques of Flow Visualisation", AGARDograph No. 302, May 1987
2. Hurst, D.H., Galbraith, R.A.McD., Grant, I. and Coton, F.N., "A Facility for Simultaneous PIV and High Resolution Unsteady Pressure Measurement", CEAS Conference on Wind Tunnels and Wind Tunnel Test Techniques, Cambridge, April 1997
3. Coton, F.N., Galbraith, R.A.McD., Jiang, D. and Gilmour, R., "An experimental study of the effect of the pitch rate on the dynamic stall of a finite wing", Conference on Unsteady Aerodynamics, The Royal Aeronautical Society, London, 1996
4. Galbraith, R.A.McD., Coton, F.N., Jiang, D. and Gilmour, R., "The comparison between the dynamic stall of a finite wing with straight and swept tips", 20th Congress of the International Council of the Aeronautical Sciences, Sorrento, 1996
5. Kokkalis, A. and Galbraith, R.A.McD., "Results from the Glasgow University blade-vortex interaction facility", Proceedings of 13th European Rotorcraft and Powered Lift Aircraft Forum, Arles, France, 1987.
6. Horner, M.B., Saliveros, E., Kokkalis, A. and Galbraith, R.A.McD., "Results from a set of low speed blade-vortex interaction experiments", Journal of Experiments in Fluids, 14, pp. 341-352, May 1993.
7. Grant, I. (Editor), "Selected papers on PIV", SPIE Milestone Volume MS99, 1994, Published by the Society of Photo-Optical Instrumentation Engineers, Bellingham, Washington, USA.
8. Grant, I., "Particle image velocimetry; a review". Proceedings Part C, The Institution of Mechanical Engineers, February 1997.
9. Grant, I. and Liu, A., "Method for the efficient incoherent analysis of particle image velocimetry images", Applied Optics, 28, 10, May 1989.
10. Grant, I. and Pan, X., "An investigation of the performance of multi layer neural networks applied to the analysis of PIV images", Experiments in Fluids, 19, 159-166, 1995.
11. Grant, I. and Liu, A., "Directional ambiguity resolution in particle image velocimetry by pulse tagging", Experiments in Fluids, 10, 71-76, 1990.
12. Padakannaya, R., "Experimental study of rotor unsteady airloads due to blade vortex interaction", NASA CR-1909, 1971.
13. Caradonna, F.X., Strawn, R.C. and Bridgeman, J.O., "An experimental and computational study of rotor-vortex interactions", Proceedings of 14th European Rotorcraft and Powered Lift Aircraft Forum, Milan, Italy, 1988.
14. Kitaplioglu, C. and Caradonna, F.X., "A study of blade-vortex interaction aeroacoustics utilizing an independently generated vortex", in "Aerodynamics and Aeroacoustics of Rotorcraft", AGARD CP 552, Aug. 1995, paper 20
15. Horner, M.B., Saliveros, E. and Galbraith, R.A. McD., "An examination of vortex convection effects during blade-vortex interaction", The Aeronautical Journal, Vol. 96, No. 960, December 1992.
16. Horner, M.B., Stewart, N., Galbraith, R.A.McD., Grant, I., and Coton, F.N., "An examination of vortex deformation during blade-vortex interaction utilising particle image velocimetry", AIAA Journal, May 1996.
17. Agui, J.C. and Jimenez, J., "On the performance of particle tracking", J. of Fluid Mechanics, 185, 1987, pp 447-468
18. Coton, F.N., De La Iglesia Moreno, F., Galbraith, R.A.McD., Horner, M.B., "A three-dimensional model of low-speed blade-vortex interaction", 20th European Rotorcraft Forum, Amsterdam, Oct. 1994

Recent Advances in Particle Image Velocimetry

by

L. Lourenco, A. Krothapalli
FAMU/FSU College of Engineering
Fluid Mechanics Research Laboratory, Florida State University
2525 Pottsdamer Street
Building 114, Tallahassee, FL 32306, USA
and C.A. Smith
NASA Ames Research Center
Mail Stop 258-7
Moffett Field, CA 94035-1000, USA

Abstract

This paper presents new trends in Particle Image Velocimetry and practical aspects relevant to the application of the technique to large scale wind tunnel testing. The various problems and their solutions to the operation of PIV in large scale wind tunnels are discussed. Application of the technique in mapping complex flows are also presented.

1. Introduction

The Particle Image Velocimetry technique was first developed in the late seventies and early eighties to provide the two, in-plane, velocity components in a two-dimensional region of a seeded flow. Since its introduction the PIV technique has gained tremendous acceptance and has been successfully used to map a wide variety of flows ranging from very low velocity laminar flows in liquids to supersonic flows. Most of the reported measurements to date were carried out in relatively small scale and in well controlled laboratory settings. The fact that the practice of PIV requires relatively modest means and that experiments can be conducted with reduced turnaround time and economy, as well as its inherent high data capacity, PIV is regarded as having great potential to become a major measurement tool in large research and production type wind-tunnels. As such the introduction of PIV as a standard wind tunnel measurement tool would result in superior diagnostic capabilities and economy. Therefore the challenge is to make this transition from small to large scale facilities feasible. With this goal in mind, an experiment was carried out in the 7x10 foot wind tunnel at the NASA Ames Research Center, in the Summer of 1996. The experiment was aimed at evaluating the capabilities of current PIV systems and

technological barriers needed to be overcome to make its usage economical, easy and with a high degree of accuracy. Specifically, we set out to demonstrate that the PIV method can be applied to large scale environments, and capable to map a complex flow field. Based on this experience, a program was set forth to design, develop and implement an integrated PIV system into large scale wind tunnels at NASA Ames Research Center. In the following various solutions to problems encountered in the 7'x10' test are proposed and tested in laboratory experiments.

2. Summary of the NASA Ames 7x10 foot Wind-tunnel test

The test carried out at NASA Ames consisted of mapping the cross-stream velocity field of a vortex generated by a flap edge. The test was performed in the 7x10 foot, subsonic, wind-tunnel.

As shown in figure 1, the test-section of the close circuit wind-tunnel is 7feet high by 10 feet wide, and a length of 15 feet. The wing model tested was a NACA 63₂-215 Mod B profile airfoil with 2.5 ft chord and a span of 5 ft. It featured both a ¾ leading edge LB-546 slat with a chord of 4.5 inches at a 10 degree angle of attack, and an half span Fowler flap with a 9 inch chord, fixed at an angle of attack of 39 degrees. The flap edge generates a highly turbulent vortical structure which is the measurement subject. The free stream flow velocity was maintained at about 65 m/sec. The PIV set-up is illustrated in figure 2. The flow was seeded by small micron size (0.5-5 µm) smoke particles, produced by a pair of Rosco 4500 generators, and illuminated by a dual cavity, Spectra-Physics PIV-400 Nd-Yag laser, delivering 400 mJ/pulse at wavelength of 532nm. The laser light was directed from the

laser, just outside the test section, by a system of mirrors mounted on an optical rail attached to the tunnel floor. The light beam was shaped into a 0.5 mm thick sheet by a system of cylindrical lenses. Furthermore the laser sheet was positioned at 18 inches from the flap trailing edge.

The flow images were acquired as double exposures by a Kodak 4.2 Megapixels digital camera with a resolution of 2000x2000, square 9 micron pixels. The camera was fitted with an especially designed, f#4, 75mm focal length, Tessar form lens, and a rotating mirror to resolve the velocity direction ambiguity. An area of the cross stream of about $0.4 \times 0.4 \text{ m}^2$ was recorded by the camera which was positioned inside the tunnel test section, in the protective pod at a distance of 1.7 meters from the illuminated plane and with its axis normal to the plane. The image acquisition and processing system resided on an IBM 390 RISC Station capable of storing up to 32 image pairs at a rate of 1.5 Hz. The recording camera was mounted on a protective pod (Figure 3) attached by a rigid mount to the floor of the tunnel.

A typical double exposure image is shown in Figure 4. In this image the region of lighter seeding corresponding to the vortex core. These flow images are processed by an algorithm from which the velocity is obtained by correlating the images of corresponding particles.

To obtain valid and accurate measures of the velocity, good quality doubly exposed images are essential. Good quality images are those in which the majority of the particles illuminated by the first laser pulse are also illuminated by the second illumination pulse. In flows with a very significant out-of-plane velocity component, such as in the present case, this is not easily achieved. To ensure that the highest number of corresponding image pairs is acquired we purposely misaligned the combining optics of the dual laser cavity to produce the second illumination pulse downstream of the first one. The single frame cross correlation algorithm was used to convert the image data into velocity field. Each velocity vector was the result of an interrogation of 64×64 pixels which in turn corresponded to a physical size of about 3 ~ 4 mm. The velocity field and its corresponding vorticity field are shown in Figure 5. The data shows that the flap-edge vortex was captured with fidelity. Although this test was for the most part successful, there

were some important lessons learned to make PIV an user friendly instrument in large scale wind tunnels. These are detailed in the next section.

3. The relevant issues in PIV Wind Tunnel testing

Notwithstanding the importance of correctly managing the flow seeding, the most important factors were the laser illumination, simplification of the image acquisition set-up, improved accuracy and resolution of the processing scheme and capability to obtain time resolved data.

3.1 Laser Illumination

Typically, the light detected by the recording media in PIV measurements is that which has been scattered 90° to the incoming laser light. Extremely energetic light sources are required because of the low efficiency of this scattering process, and the small dimension of the scattering particles. The specific amount of laser energy required in a particular situation is a function of tracer type and size, concentration, recording lens aperture and magnification, and on the sensitivity of the solid state array at the particular laser light frequency. The timing between laser pulses is the other important requirement. In order to capture two closely spaced images produced by high speed tracers, i.e. spacing of the order of $100\text{-}300 \mu\text{m}$, the time interval between laser pulses is typically of the order of $1 \mu\text{sec}$.

Solid state frequency-doubled Nd-Yag lasers are the only available laser sources capable of satisfying these requirements. These laser systems can provide repetition rates from 10-100 Hz and pulse energies up to 0.5J/pulse in the single pulse mode of operation. The operation of these lasers in a double pulse mode, necessary for PIV use, has been a major difficulty. Typically manufacturers only have been capable of providing dual pulse operation with pulse separations in the range from 1-150 μsec , at the expense of energy output. This limited range is obviously insufficient to cover all ranges in velocity, in particular in very high-speed flows. A method of solution to this problem is the dual laser configuration. This configuration originally used by Kompenhans and Reichmuth and Lourenco is currently marketed by laser manufacturers and presents

both advantages and inconveniences. The advantage of this system is its flexibility of use, as it provides dual laser pulses with the same energy over an infinite range of time separations. The difficulties in the usage of such a system are due to the stringent alignment requirements to keep the two beams collinear, and the difficulty of obtaining perfectly similar beams from the two lasers. These factors contribute for decreased correlation between the image pairs as particles illuminated by the first light pulse are not illuminated by the second pulse and vice versa. Therefore appropriate laser illumination is obtained only when the light beam has sufficient energy to produce detectable images by the recording sensor, i.e. the CCD array. One has also to ensure that the illumination sheet produced by each of the lasers of the dual cavity be properly aligned. The definition of "proper" alignment being dependent on the flow characteristics. For a two-dimensional, or quasi-two dimensional, flow, it means that both sheets must lay in the same plane, whereas in a three-dimensional condition, as it was the case of the flap edge experiment, the optimal configuration may involve a slight lateral shift. As illustrated in figure 6 the optimal lateral shift results in a maximum number of pairings. Since this condition is not unique, a solution to ensure optimal laser alignment has been proposed and is currently being implemented.

The proposed arrangement is sketched in figure 7. It consists of two cameras that intercept the laser beams image at two locations of the beam path. Optimal beam alignment is achieved by manipulation of the mirrors 1 and 2 and when the cross correlation of the images is maximum. A parallel displacement between the two beams is accomplished by means of a beam displacer in the path of beam 1 before the combining element 3.

3.2 Camera Set-up

Two aspects need to be considered. First, elimination of the optical and mechanical complexity imposed by the rotating mirror, i.e. introduce alternative means to resolve the direction of the velocity vector. Second, eliminate the need to place the camera at fixed 90 degrees view to the image plane, thus allowing for its placement outside the tunnel test section.

The elimination of the rotating mirror apparatus is now possible by the introduction of video cameras capable of recording two images in quick succession from which the velocity field is derived using a cross-correlation algorithm. At Fluid Mechanics Research Laboratory the Kodak ES1.0 camera is fully integrated in the PIV systems. This camera was implemented by Kodak in collaboration with the FMRL. At the heart of camera is the CCD interline transfer sensor, KAI-1001 with a resolution of 1008(H) x 1018(V) pixels. Each square pixel measures 9 μm on the side with 60 percent fill ratio with microlens, and a center to center spacing of 9 μm . The camera is also equipped with a fast electronic shutter and outputs eight bit digital images, via a progressive scan readout system, at a rate of 30 frames per second. A unique feature of the camera is its ability to be operated in the "triggered dual exposure mode". Operation in this mode is possible due to the CCD sensor architecture, which incorporates both a light sensitive photodiode array and a masked register array. During the exposure cycle, light is converted to charge in the photodiode area of the array; after exposure, the charge on the photodiode is transferred to the masked area of the array. The maximum time for complete transfer of the charge is 5 μsec ; using a programming feature of the camera's control electronics, this time setting can be made as small as 1 μsec ; however image quality may not be preserved, as the times less than 5 μsec may be too short to ensure that all charge is transferred, especially in the case of very high intensity images. The image acquisition sequence in the "triggered dual exposure mode" is as follows: the image acquisition is initiated by an external trigger signal; the first image is illuminated by the first laser of the dual laser system, which is triggered in advance, to account for the usual delay between flash lamp trigger and Pockells cell trigger, i.e. by 160-180 μsec . The first image is then transferred to the read-out section of the sensor, within 1-5 μsec , and a second laser pulse illuminates the again the photodiode section of the sensor, which has been depleted of the charge. To achieve total separation between the two images, the second trigger pulse to the Pockells cell of the laser is delayed with respect to the first pulse by an amount that exceeds 5 μsec .

The above described arrangement makes it possible to acquire up to 15 image pairs per second. The fact that the image pairs are recorded in separate frames, and that the image pair separation is variable from 1 microsecond up to several hundreds of microseconds, makes this instrument appropriate for general and simple use in flows with velocity reversals as well as very wide dynamic velocity range from very low speed (mm's/sec) up to very high speed (100's m/sec) flows.

The camera is integrated with either a PC Pentium or Dec-Alpha computers with image data acquisition is done using an Imaging Technologies ICPCI board, which resides on a single slot of the PCI bus. The computer's operating system in use are the Windows 95 or NT environment. The image acquisition program has the flexibility to store image sequences directly to RAM at a rate up to 120 MByte/sec. Because of this high rate up to four cameras may be used simultaneously by a single computer. This feature is essential for some of the work described in the following paragraphs, namely the mapping of the three velocity components, and the resolving of time velocity fluctuations.

The conventional mode for PIV recording uses the camera normal to the laser sheet. However, it is not always possible to use this mode, especially when it dictates that the camera be placed inside the Wind tunnel facility. To overcome this problem it is desirable to place the camera at an angle. In this off-axis mode, the condition for sharp focus across the image plane is obtained under the so-called Scheimpflug condition. As shown in figure 8 the condition is satisfied when the object plane, the image plane and the lens plane intersect at a common point. The condition for sharp focus is obtained at the expense of a varied magnification across the image plane, combined with a perspective view. Automatic algorithms for the perspective correction have been developed and calibrated against known displacements. Also shown in figure 8 is a example of one of such calibration experiments. In this experiment a pure rotation is imposed on a flat target that generates a speckle pattern. Using the image recordings before and after the rotation a displacement field is obtained. The field is then post processed to account for the perspective and the original rotation is recovered.

The above experiment shows that it is possible to recover with the least amount of error a purely two dimensional motion from off-axis recordings. The problem is more involved when a third component exists. In this case it is necessary to have two simultaneous recordings of the same scene to resolve the displacement field, as shown in figure 9. The arrangement in figure 9 is the one currently adopted for three-dimensional measurements in our laboratory. Automatic features for camera focusing and triangulation algorithm for the accurate determination of the vector field are being developed and tested at present. An additional benefit for using the cameras in the off-axis mode is that alignment towards the forward scatter mode of the seeding particles results in recording that detect smaller particles in higher numbers, resulting in increased signal to noise ratio and accuracy.

3.3 High resolution algorithms.

In order to obtain details of boundary layer structures and strain rates such as vorticity, it is essential that the velocity field is captured with high degree of accuracy and spatial density. In particular, the velocity gradients near solid surfaces are of importance to characterize near wall flow structure.

An image matching approach is used for the digital processing of the image pairs to produce the displacement field. In this approach one sets up a cost function, C , to be maximized (or minimized), which models the match between two corresponding regions of the images. Typically, if I_1 and the I_2 are the image intensity distributions of the first and the second image, we write,

$$C(\vec{s}) = C\{I_1(\vec{x}), I_2(\vec{x})\}$$

where it is assumed that the second image is an exact translated copy of the first image, we may write,

$$I_2(\vec{x}) = I_1(\vec{x} - \Delta \vec{s})$$

or

$$I_2(\vec{x}) = I_1(\vec{x}) * \delta(\vec{x} + \Delta \vec{s})$$

where $\Delta \vec{s}$ is the average image translation and the function I_2 usually represents a small block (interrogation window) in a larger image, I_1 .

The match is obtained for the value \vec{s} that

maximizes (or minimizes) C . The cost function we choose to maximize is the cross-correlation, G , defined as:

$$G(\vec{x}) = I_1(\vec{x}) * I_2(\vec{x}) = \int_{-\infty}^{\infty} I_1(\vec{x}) I_2(\vec{x} - \vec{u}) d\vec{u}$$

The cross-correlation is effectively computed using Fourier transforms. The peak position is found with sub-pixel resolution by means of a Gaussian interpolator as described by Lourenco and Krothapalli (1995).

An extension of this method aimed at obtaining velocity data with high spatial resolution has been developed and successfully implemented. This development is aimed at resolving some of the drawbacks that afflict the conventional cross-correlation approach when applied to the study of flow with large velocity and/or seeding density gradients. Because the typical correlation size are of the order of 16-32 square pixels or so, the measurement represents an average over the same interrogation region, which can be weighted towards the areas of higher seeding density and reduced velocity within the interrogation region itself. With the new processing approach the particle images themselves comprise the interrogation region, which have sizes ranging from 3 to 4 pixel square. Such a scheme will allow not only accurate representation of the gradient fields as well as measurements in the proximity of a solid surface.

The displacement between corresponding image pairs is found in the usual manner by means of a cross-correlation, and to each location half way the distance between image pairs a velocity (displacement) vector is assigned. Therefore, unlike the traditional way the velocity is evaluated in an unstructured grid. The velocity at regular grid points is computed using a least squares fitting algorithm that uses the velocity vectors in the neighborhood of a grid point to fit a second order polynomial such as:

$$\vec{u} = \vec{a} \cdot x^2 + \vec{b} \cdot x + \vec{c} \cdot y^2 + \vec{d} \cdot y + \vec{e} \cdot x \cdot y + \vec{f}$$

A marked advantage of this approach is that the accuracy of interpolated velocity remains of second order, as well as that of its derivatives found by differentiating the previous equation.

$$\frac{\partial \vec{u}}{\partial x} = 2 \vec{a} \cdot x + \vec{b} + \vec{e} \cdot y$$

$$\frac{\partial \vec{u}}{\partial y} = 2 \vec{c} \cdot y + \vec{d} + \vec{e} \cdot x$$

A comparison of the results calculated for the shear layer of a jet using the conventional and the high resolution processing was carried out. Figure 10 is the superposition of the original flow images obtained in quick succession with the mesh where the velocity and its derivatives are calculated. The corresponding velocity and vorticity fields, computed with the high resolution and conventional schemes are displayed in figures 11 and 12 respectively. Visual inspection of the results illustrates vividly the previous argument. The new scheme which is very efficient, incorporates a vector validation procedure, which makes it independent of an operator. The time it takes to compute a vector field depends on the computer hardware and it ranges from 350 mesh points/sec on a PC 133 MHz Pentium to 1,400 mesh points /sec on a 200 MHz dual Pro.

3.4 Time resolved data

An inconvenience of conventional PIV is that the time representation of the flow is usually limited to the frame rate of the recording camera. This drawback, however, can be resolved if two cameras record the same location in space but separated by a small time interval. In this fashion the cross-correlation of the velocity, or that matter, any derivative field may be obtained. From the cross correlation function the corresponding spectrum can be computed. The advantage here being that the spectra is now obtained for all points in space. This idea was put to test using a well documented jet flow, as we set out to determine the shear layer roll-up frequency. Groups of 15 velocity fields delayed with respect to other 15 fields by times that ranged from 0 to 1.2 msec were used to compute the cross-correlation of the vorticity field. Figure 13 is a composite that shows the evolution of the correlation with time.

4. Conclusions

The objective of our research program is to develop and implement a fully integrated PIV system for use in large scale, e.g. 80x120 foot wind tunnel at the NASA Ames Research Center. A first attempt towards this goal was an experiment conducted in the 7x10 foot,

production, wind tunnel, which identified critical areas for development of a user friendly PIV system. A requirement for this system is that it must be used by non PIV expert personnel.

Optimal solutions for the identified shortcomings of standard PIV systems, namely the camera set-up, illumination management and processing schemes were developed and thoroughly tested in a laboratory environment.

As a result, a second generation high resolution PIV system has been developed. This system features the following capabilities:

- Multi-camera imaging capability which supports three velocity component as well as time resolved measurements,
- High density coupled with very high spatial resolution and accuracy of the velocity and its derivatives,
- Self-check for measurement errors,
- Very efficient computation algorithms portable to any computer platform.

Acknowledgments

This research was supported by the NASA Ames Research Center and the Boeing Company. Our thanks to Mr. Steve Walker and Mr. Bahadir Alkislar for their assistance. We would like to thank our monitors Dr. James Ross and Dr. Rahul Sen.

References

Stearns, S. D. and Hush, D. R., 1990 Digital Signal Analysis, Prentice-Hall, 75

Lourenco, L. M., 1996 VKI Lecture Series 1996-03

Lourenco, L., Gogenini, S. and LaSalle, R., "On-Line PIV: An integrated Approach", to appear in Applied Optics.

Adrian, R. J. "Image Shifting technique to resolve directional ambiguity in double pulsed velocimetry". Applied Optics, vol. 25, (1986)

Lourenco, L., Krothapalli, A., Riethmuller, M. L., Buchlin, J. M., "A Non-Invasive Experimental Technique for the Measurement of Unsteady Velocity and Vorticity Fields". AGARD-CP-413, pp.23-1 - 23-9, 1986

Crisler, W., Krothapalli, A., and Lourenco, L., "PIV Investigation of High Speed Flow Over a Pitching Airfoil". AIAA 32nd Aerospace Sciences Meeting, Reno, 1994.

Lourenco, L. and Krothapalli A., (1995). On the accuracy of velocity and vorticity measurements with PIV. Exp. in Fluids 18, 421-428.

Gauthier, V., Riethmuller, M. L., 1988: Application of PIDV to complex flows: Measurements of the third component. In: VKI-LS 1986-06 Particle Image Velocimetry, von Karman Institute for Fluid Dynamics, Rd-St-Genese, Belgium.

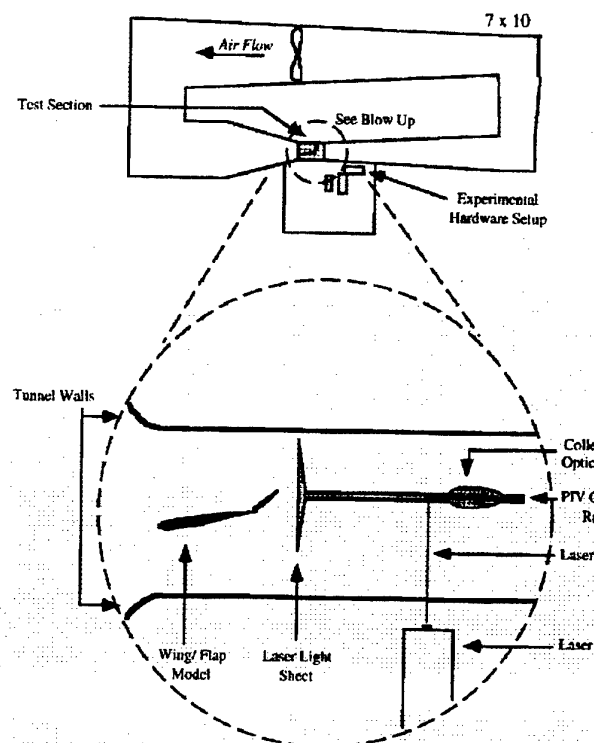


Figure 1: 7x10 foot Wind-tunnel schematic

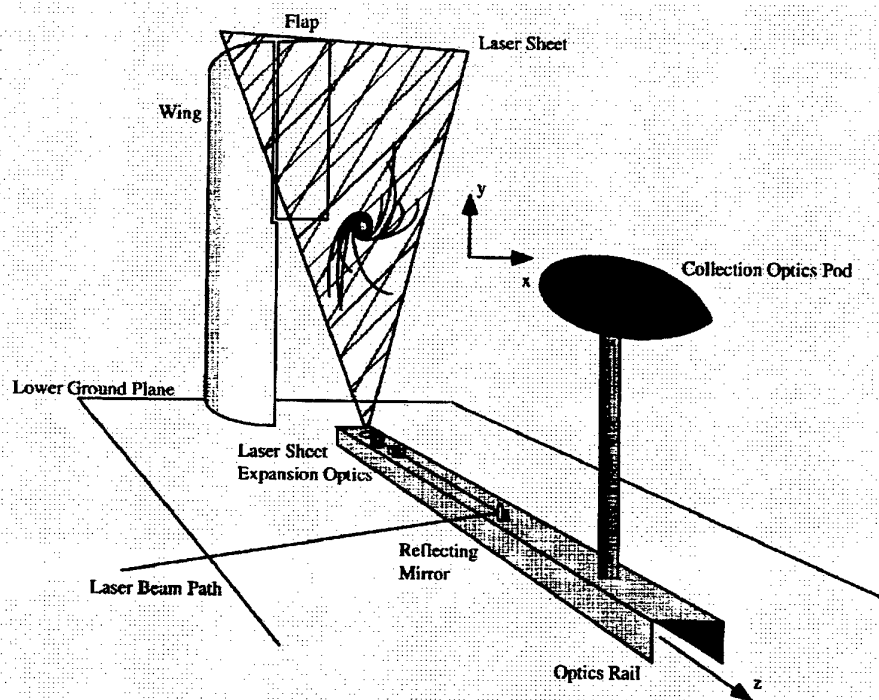


Figure 2: Experimental Set-up

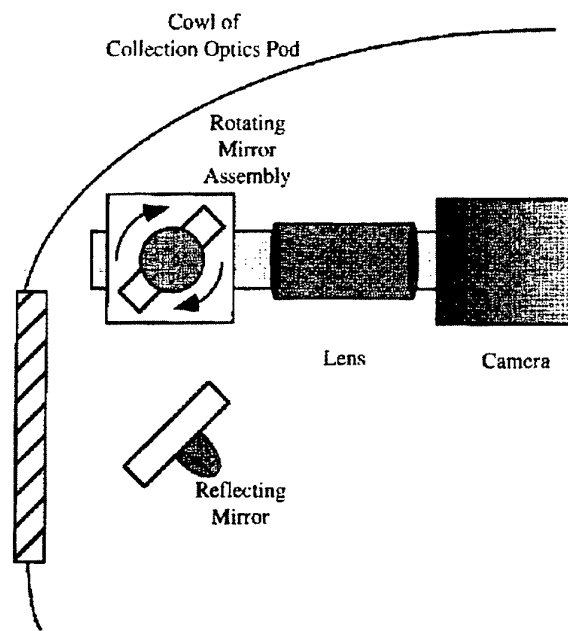


Figure 3: Camera and protective pod assembly

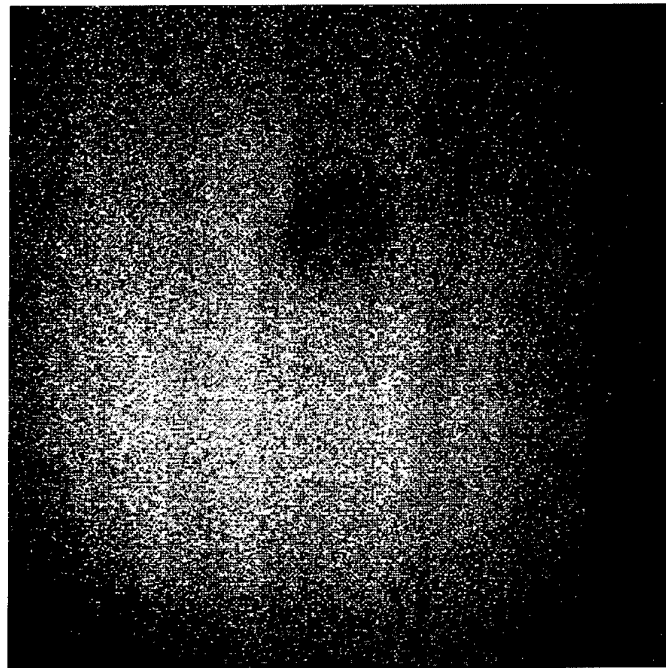


Figure 4: Dual exposure image of trailing edge vortex

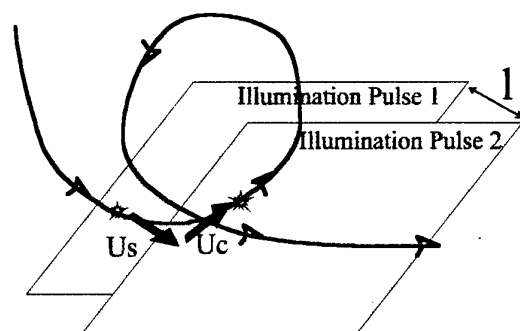


Figure 6: The effect of displacing the laser sheet

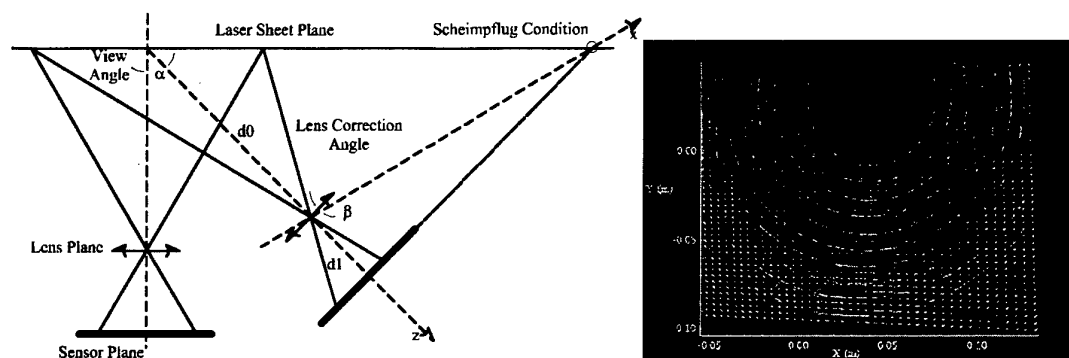


Figure 8: The Scheimpflug condition and corrected displacement field

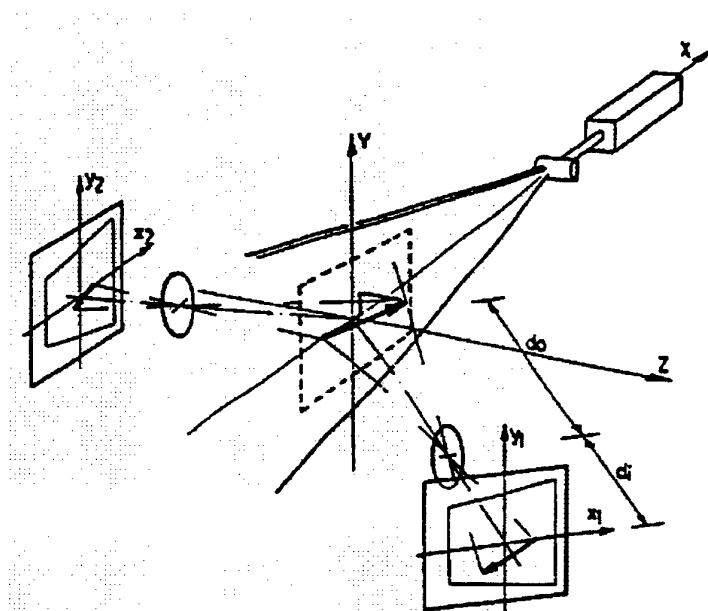


Figure 9: Recording Set-up for three-dimensional fields

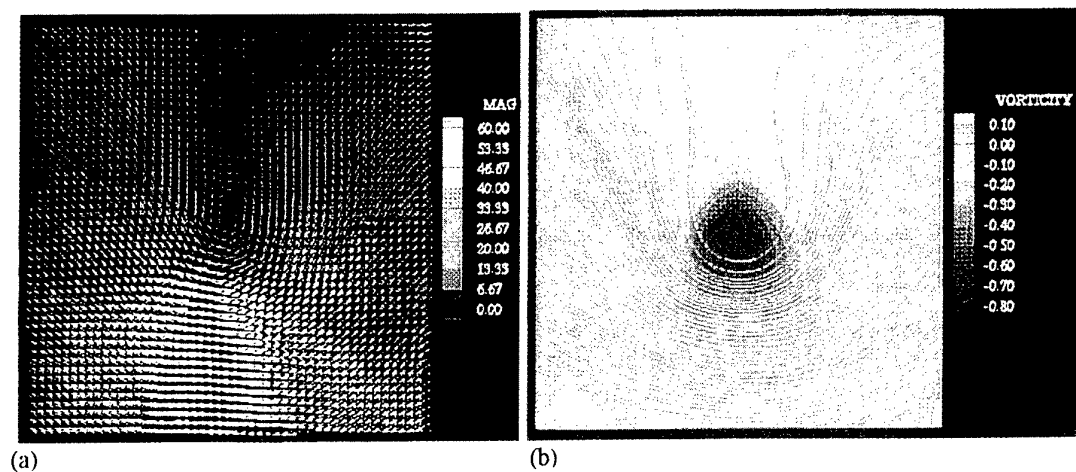


Figure 5(a): Cross-stream velocity vector and magnitude field

Figure 5(b): Color coded vorticity field and streamline pattern

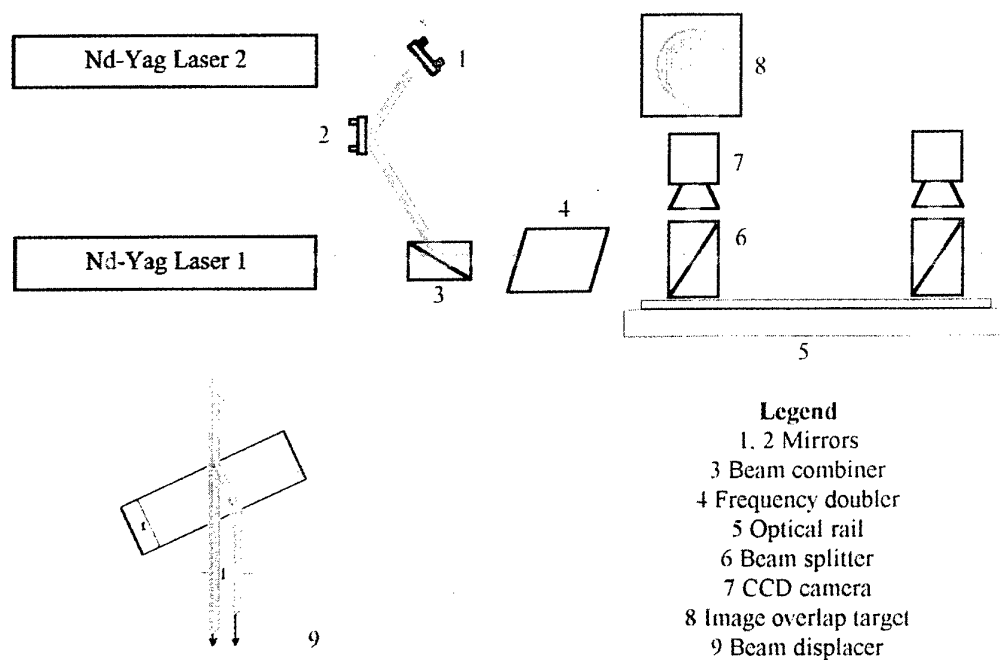


Figure 7: Beam alignment monitoring and setting device

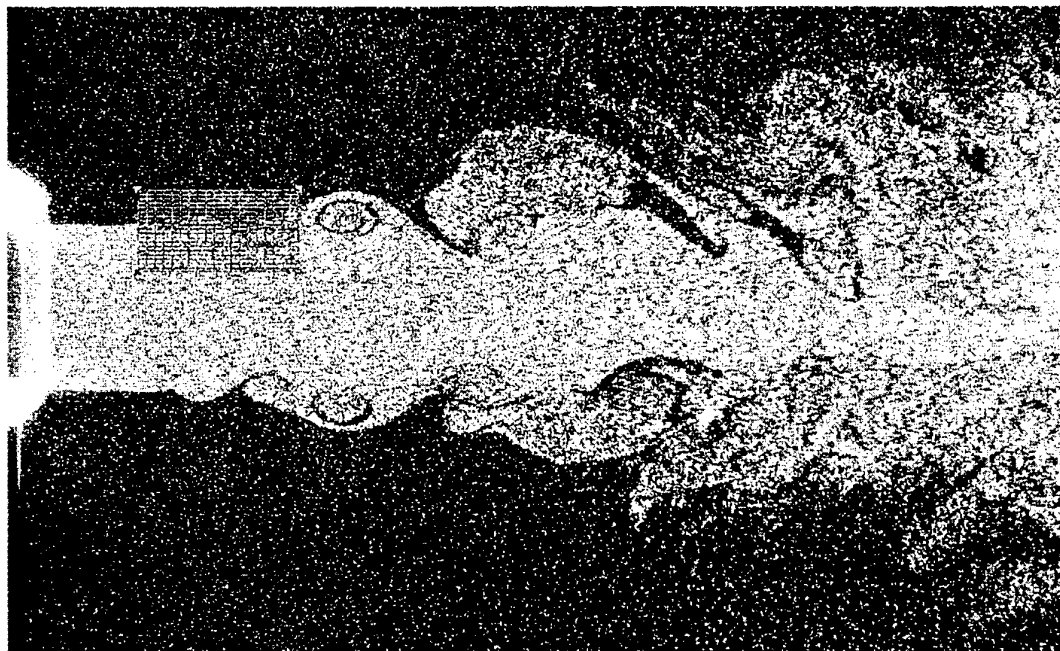


Figure 10: Raw image data for jet flow with computation mesh

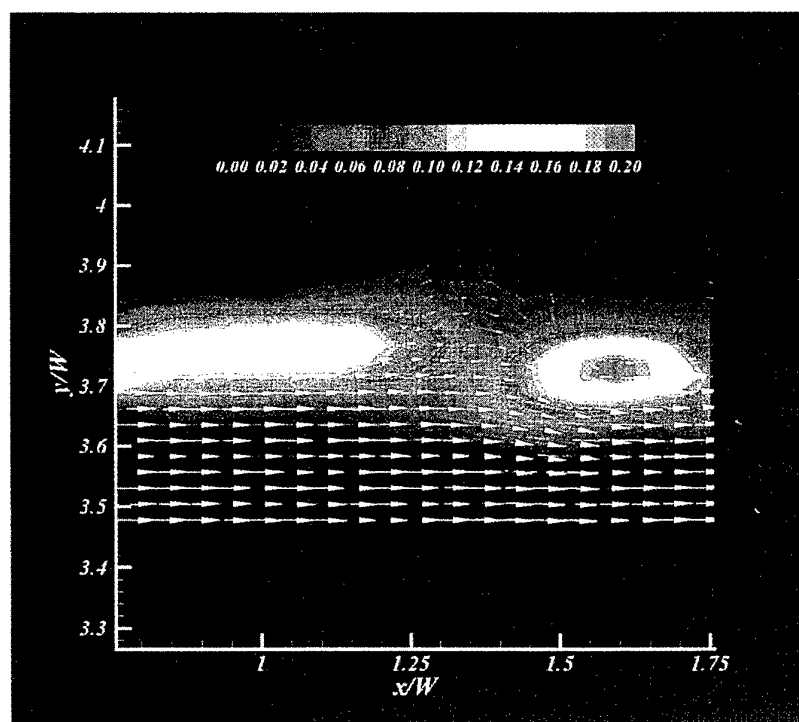


Figure 11: High resolution velocity and vorticity data

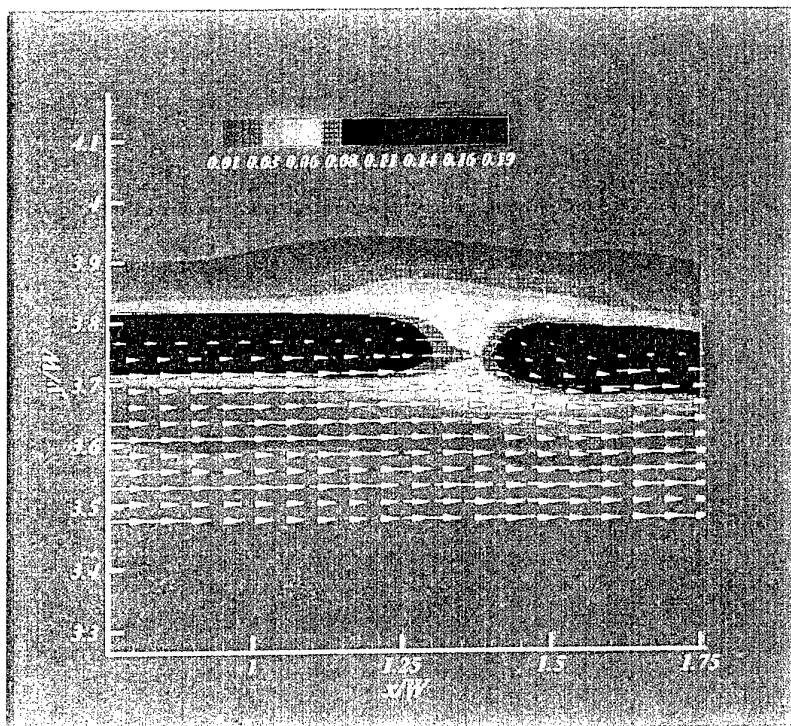


Figure 12: Velocity and vorticity data computed from conventional scheme
Interrogation size is 16^2 pixels

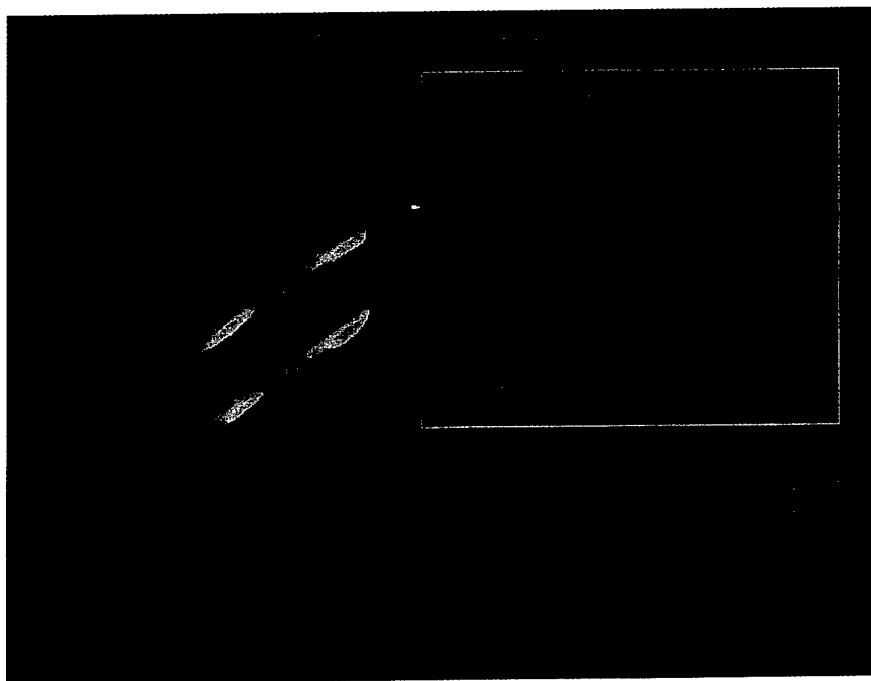


Figure 13: Cross-correlation of vorticity signal.
Isocontour is for all points in y at $x/w=1.4$
XY plot is the signal for $x/w=1.4$ and $y/w=0.5$

Recent Developments in Doppler Global Velocimetry

Thomas J. Beutner, Ph.D.

Henry D. Baust

Wright Laboratory, WL/FIMO

Building 24C, 2145 Fifth Street, Ste 1

Wright Patterson AFB, Ohio 45433-7005, USA

Abstract

Doppler Global Velocimetry is a non-intrusive wind tunnel diagnostic technique which has the potential to make simultaneous three-component velocity measurements over entire planes in the flow field. Measurements of velocity are based on determining the Doppler shift of single frequency laser light scattered off particles in the flow field. This technique has been used in the Subsonic Aerodynamic Research Laboratory wind tunnel at Wright Laboratory to make qualitative measurements of the flow associated with a vortex-tail interaction. This flow field is typical of the flows seen on twin-tail fighter aircraft. This paper presents results obtained with the DGV instrument and reports the current progress and recommendations towards developing an improved diagnostic system.

Background

Doppler Global Velocimetry¹⁻⁴ (DGV) and the closely related techniques of Filtered Rayleigh Scattering⁵⁻⁷, Planar Doppler Velocimetry⁸⁻¹¹, and Filtered Planar Velocimetry¹²⁻¹³ are a relatively new class of diagnostic techniques which offer the promise of making non-intrusive, simultaneous velocity measurements over an entire plane in the flow field. DGV measures the Doppler shift of light scattered by seed particles in the flow. The Doppler shift (Δv) of light scattered from a moving particle is dependent on the incident light wavelength (λ), the velocity of the scattering particle (V), and the observation (\hat{o}) and incident light (\hat{i}) directions. This relationship is given as:

$$\Delta v = \frac{V \cdot (\hat{o} - \hat{i})}{\lambda} \quad (1)$$

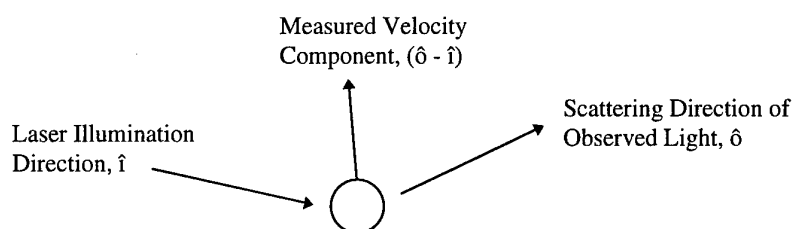


Figure 1. Vector relationships of incident and scattered light and the measured velocity component.

Thus, the measured velocity component lies along the bisector of the incident light and observation direction vectors. If the frequency shifts are accurately measured, the velocity of a particle in the flow field may be determined. The crucial aspect of this technique is the ability to make measurements of the rather small frequency shifts associated with the scattered light. For this measurement, an absorption line of molecular iodine is used. By using a laser light sheet and cameras to image an entire plane of the flow, the velocity measurements may be extended over that plane as well. In addition, since the measured velocity shift is made in the direction determined by the vector difference of the \hat{o} and \hat{i} vectors, different velocity components may be measured by using cameras which observe the light sheet from different directions. Thus, it is possible to make three-component velocity measurements over an entire plane of the flow field.

The iodine cell has steep absorption profiles at the frequencies of both an argon-ion laser (514.5 nm) and a doubled Nd:YAG laser (532 nm). Velocimetry systems based on this technique have been demonstrated using both of these laser systems. Both laser systems have unique advantages associated with them. Argon-ion laser systems are widely available, having been used in fringe-type laser velocimetry systems. The argon-ion laser is a continuous wave laser, which reduces the system integration requirements

for synchronization with cameras, and which can reduce laser speckle problems in the data images. The argon-ion laser also has a narrow linewidth (approximately 10 MHz) when operated with an etalon. Tuning of the argon-ion laser frequency is accomplished by tilting the etalon, resulting in discrete mode hops in the laser frequency. A frequency doubled Nd:YAG laser can be operated in single frequency mode by using a seeding laser which offers finer control of the laser frequency. This fine control is useful not only for adjusting the laser to the desired point on the iodine absorption line, but also for experimental determinations of the absorption line shape. The Nd:YAG laser also allows unsteady flows to be investigated with short duration (10 nanosecond long) pulses, eliminating the implicit time-averaging of the argon-ion laser. However, the short pulse duration of Nd:YAG lasers also creates high power loadings on optical elements, which can lead to damage on some wind tunnel windows. The Nd:YAG laser also has a wider bandwidth of approximately 50 to 100 MHz, and a 10 MHz pulse-to-pulse variation in frequency as a result of the frequency lock-in system used to match the cavity length to the frequency. An additional difficulty of implementing Nd:YAG lasers in a DGV system is the reported presence of a frequency variation across the laser beam. This chirp has been identified by at least two researchers^{6,10} and is suspected as an error source in measurements with a third Nd:YAG system⁹. This chirp could create both a nominal frequency variation, as well as a line width variation across a light sheet formed with a Nd:YAG laser.

Experimental Setup

The availability of an existing argon-ion laser system, as well as the advantages of that system for use in the desired wind tunnel governed the laser choice for this preliminary investigation. The experimental setup used in this work is shown in Figure 2. The laser light sheet was formed by scanning the laser beam over a plane oriented normal to the model surface. For each velocity component measured, two cameras were used, both of which viewed the same field in the flow. The signal camera viewed the field through the iodine cell, while the reference camera viewed the field directly. The reference camera allowed intensity variations not due to Doppler shifts (i.e. light sheet power variations, smoke variations, etc.) to be accounted for in the image processing. While this system results in the signal and reference cameras viewing the flow field from slightly different angles, it has an advantage over split image systems in that higher signal levels can be obtained by eliminating the beam splitter. This advantage can be important for cases where large fields are to be imaged or in cases where laser power or smoke density is limited. Smoke was introduced at the inlet of the wind tunnel using a 100 port smoke generation array and theatrical smoke generation fluid. In addition, condensation occurs naturally in the vortex core regions.

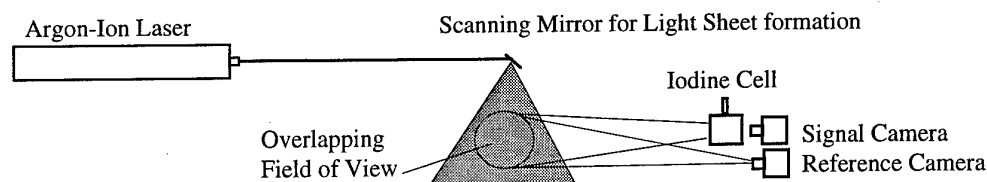


Figure 2. Schematic of Optical configuration.

The cameras used were monochrome RS-170 video standard cameras. The analog output from these cameras was fed to 8-bit analog-to-digital frame grabbers. The cameras were operated in an interlaced mode which produced alternate odd and even fields every 1/60th of a second. Each field produced a 512 (H) by 256 (V) field. Since the scanning light sheet and smoke density both change considerably during this interval, the odd and even fields were separated and processed as separate images. A video sync generator was used to synchronize all six camera fields and frames.

During normal operation, slow drifts in frequency will be observed in the argon-ion laser. In addition, the laser will occasionally hop between two stable modes, separated in this case by approximately 76 MHz. Therefore, it is necessary to monitor the nominal frequency of the laser, and occasionally to manually tune the laser back to the center of the iodine absorption curve. This monitoring was achieved by splitting off a small portion of the laser beam and passing it through a separate iodine cell. Two photodiodes monitored the intensity of the sampled beam before and after it passed through the iodine cell, and this information was recorded with each camera image and was used to determine the nominal laser frequency at the time the cameras acquired a frame.

A 7.6 cm diameter, 5.1 cm long iodine cell was used and was housed in a 12.1 cm long insulated box with secondary windows to reduce cooling on the iodine cell windows. Copper cladding and strip heaters were used to control the temperature of the body at 65 degrees C, and the cold finger at 45 degrees C. Experimental scans of the absorption line, obtained by mode-hopping the laser through the absorption line, were used in conjunction with a theoretical iodine absorption profile⁵ to develop the nominal absorption line curves. Temperatures were monitored on both the barrel and cold finger of the iodine cell and were used to adjust the absorption line curve based on the theoretical model. For this iodine cell design, the barrel temperature is taken as the vapor temperature, and the cold finger temperature is used to determine the vapor pressure based on an empirical equation¹⁴. Figure 3 shows three nominal absorption profiles: one corresponding to the test conditions, one showing the effect of a 5 degree C variation in the body temperature, and one showing the effect of a 5 degree C variation in the cold finger temperature.

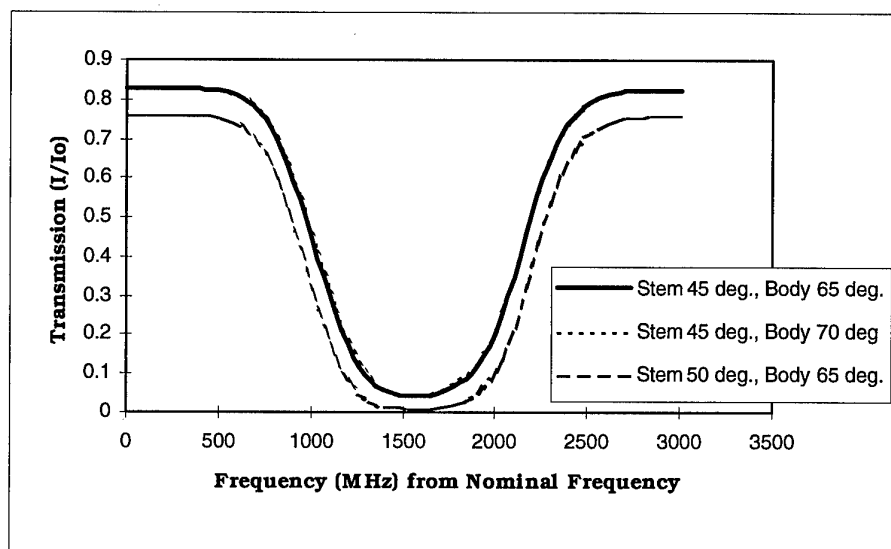


Figure 3. Iodine Absorption Profile near 514.5 nm.

As can be seen in Figure 3, the absorption profile is rather insensitive to the vapor temperature, so that temperature variations over the body of the cell are unimportant, provided that the temperature of the body is sufficiently high to avoid crystallization of iodine on the cell windows. The absorption profile is very sensitive to temperature variations in the cold finger, however, and careful control and monitoring of the cold finger temperature is crucial to stabilize the absorption profile.

By tuning the laser frequency to the center of one side of the iodine absorption profile, small shifts in the frequency of the laser light show up as large intensity variations when viewed through the iodine cell. The second camera serves as a reference camera for the measurement, and allows intensity variations due to effects other than frequency shifts to be accounted for. For a nominal camera location on top of the wind tunnel, a shift of approximately 3 MHz is expected for a 1 m/s velocity component in the direction of sensitivity.

Data Processing

Multiple steps are required to process the DGV data. As the technique is based on intensity measurements, care must be applied throughout the processing to preserve the accuracy of the intensity measurements on a pixel-by-pixel basis.

Minor manufacturing variations in the production of CCD arrays may cause pixel-to-pixel differences in gain and offset values. Pixel calibrations were performed on each camera to flatten the sensitivity of the array. These calibrations were based on diffuse illumination of the array at two distinct intensities, and resulted in a relative gain curve for each pixel in the array. Background shots were subtracted from data shots to remove stray light illumination and dark current values on a pixel by pixel basis.

Flat field corrections were also performed in place to account for optical path differences between the two cameras. For these calibrations, smoke was used to fill the light sheet field and the laser was tuned outside the absorption curve in order to obtain a flat field which was most representative of the illumination obtained in data shots. Flat field corrections of this sort could also be performed using a white card in the plane of the light sheet, however the broad-band absorption characteristics of the iodine cell are different from the absorption in response to a narrow bandwidth signal at the peak of the absorption curve. Therefore, use of a white card for this correction will result in an offset in the flat field correction. A series of 60 images were recorded and the processed images were averaged for these flat field corrections in order to minimize the effect of any variations in smoke density throughout the field of view.

The data from the six cameras must also be mapped into overlaying images. This was accomplished using a dot card image in the plane of the laser light sheet to perform a bilinear interpolation of the raw images into overlaying images. This procedure also eliminated perspective distortions and any slight magnification differences from the data images.

By ratioing the corrected images from the signal and reference cameras, a measure of the transmission of light through the iodine cell is obtained. This information, combined with a lookup table of the iodine transmission profile and a reference system monitoring the nominal laser frequency, gives a measure of the frequency shift of the scattered light collected across the field of view. Use of Equation 1 allows this information to be transformed into a velocity map of the flow field.

Low pass filtering is essential to reduce high frequency noise in the images. The modulation transfer function is a measure of the sharpness of an image. The MTF of the camera-lens system results from a combination of electronic leakage and the f number of the lens. By choosing a low pass filter which removes frequency variations higher than the MTF in the raw image, the high frequency noise associated with pixel-to-pixel variations can be removed without degrading the signal. In this case, a 5 by 5 low pass filter was applied to each of the images before perspective distortions were removed.

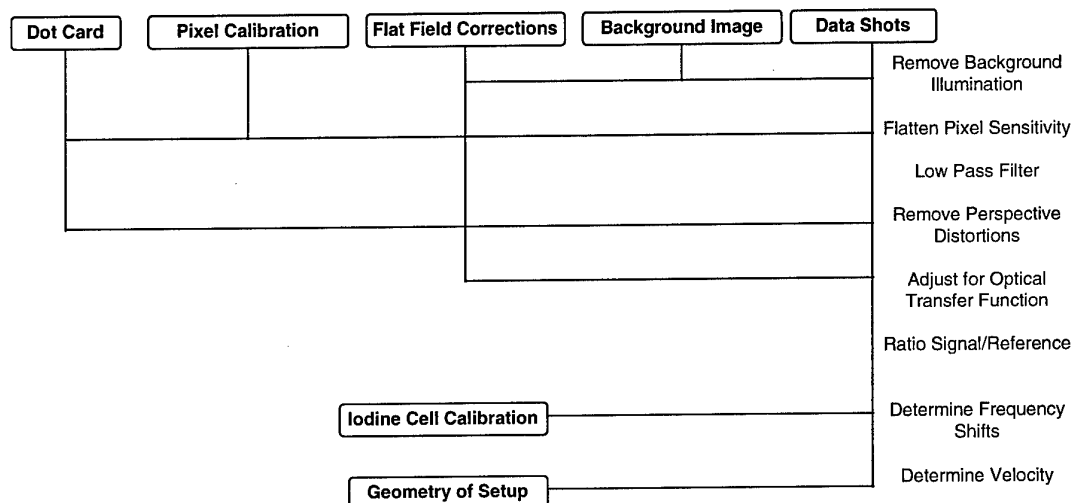


Figure 4. Data processing flow chart.

Wind Tunnel

Wind tunnel testing was conducted in the Subsonic Aerodynamics Research Laboratory (SARL) wind tunnel at Wright Laboratory. The SARL wind tunnel is an open circuit, low speed tunnel and has a 3.05m x 2.13m test section, see Figure 5. Over 50 per cent of the test section walls are made of optical quality plexiglas windows. This test section configuration is ideal for the implementation of DGV and similar optical techniques, since it allows optical access from a wide range of viewing angles.

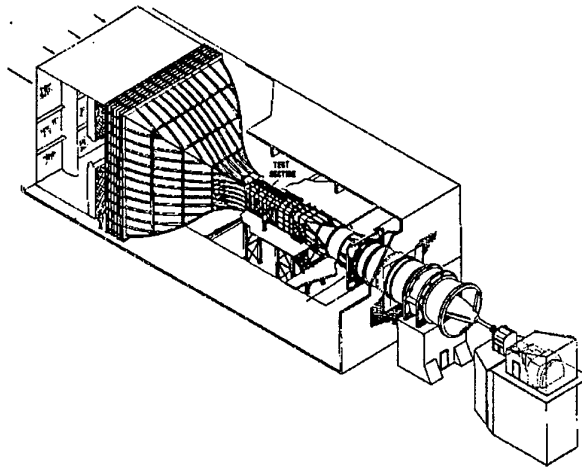


Figure 5. Subsonic Aerodynamic Research Laboratory (SARL) wind tunnel.

These tests measured the interaction of a leading edge vortex generated by a sharp leading edge delta wing with twin vertical tails. Leading edge sweep on the model was 70 degrees. The tail shape was chosen to be characteristic of an F-15 tail planform. Tails were located along a radial line originating at the apex of the delta wing. This tail position was chosen to lie along the vortex core trajectory. Tests were conducted both on the clean wing and on the wing with tails, shown in Figure 6. The model had sharp leading edges on both the wing and tail surfaces in order to fix separation points. The model was tested at 23 degrees angle of attack at a Mach number of 0.2 and a Reynolds number of 1.94×10^6 (based on root chord). At this condition, no vortex bursting was present over the model surface on the clean delta wing. However the presence of the tails caused the vortices to burst near the mid-chord location. Furthermore, the bursting is unsteady and a considerable oscillation can be observed in the burst location.

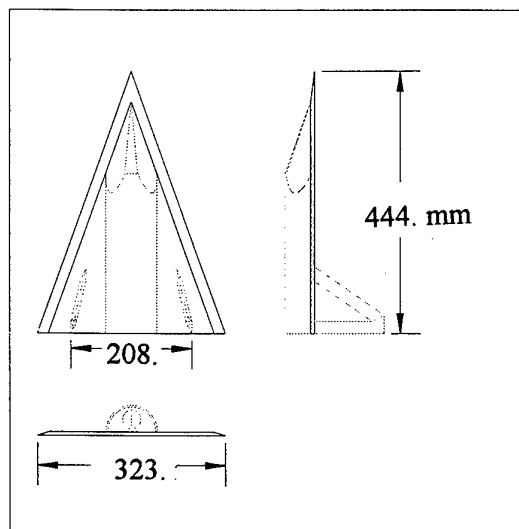


Figure 6. Delta wing model with tails.

Limitations of the Technique

Since this technique is based on making intensity measurements in order to determine frequency shifts, there are a variety of error sources which may lead to biases or random uncertainties in the data. Any effect which varies the intensity of the recorded light could result in an error in the measured velocity. Some

effects, such as smoke variations or laser power variation, may be accounted for by using the reference image. Some optical effects have the potential of varying the intensity recorded between the reference and signal cameras. These effects can include camera variations, polarization sensitivities, angular dependence of the scattering intensity, background light variations, etc. Some of the effects can be minimized by in-situ calibration procedures or careful setup of the optical system, but residual errors remain difficult to quantify. Secondary scattering off particles, wind tunnel windows, and the model surface will contribute to the noise level in the recorded images. Additionally, any effect which alters the frequency of the laser or the absorption characteristics of the iodine cell will result in uncertainties in the velocity measurement. The argon ion laser will mode hop between stable modes when used with an etalon, and must be monitored during data acquisition. Iodine cells must be operated at stable temperatures, and the absorption length of the cell will vary for off-axis light rays.

Many of these effects have been considered in laboratory studies, and attempts to address the ultimate capability of the technique have indicated a 2 to 5 m/s accuracy may be achievable, however, this has not been consistently demonstrated in practice. An added complication of working in a large facility is the effect of environmental variables, vibrations, temperature changes, etc. on the system. At the present state of development, the Doppler Global Velocimetry instrument described here is qualitative in nature.

As the intent of these tests was a feasibility demonstration, a rigorous error analysis has not been undertaken. The dominant source of error in these tests was expected to be the least significant bit errors from the 8-bit video cameras used for data acquisition. When combined with the frame grabber boards, these cameras gave an effective 6.5 bit resolution, suitable only for qualitative studies. In addition, residual errors associated with polarization sensitivities, secondary scattering of light from both particles and the model surface, and calibrations in the data processing are difficult to assess. While this technique is advancing rapidly towards a quantitative capability, it is useful as a velocity discriminating flow visualization technique in its current state of development.

Results

Typical results obtained by conventional flow visualization are shown in Figures 6 and 7. These show a laser light sheet flow visualization study on a delta wing with and without vertical tails. The light sheet is located at 97% of the root chord and is oriented perpendicular to the model, which is at 23 degrees angle of attack. Typical of such qualitative flow visualization, these images are useful in locating the position of the vortex core. In the SARL wind tunnel, condensation can be achieved in the vortex core if the relative humidity of the atmosphere is sufficiently high. In addition, smoke introduced at the inlet of the wind tunnel can be used to visualize the vortex flow patterns outside the vortex core.

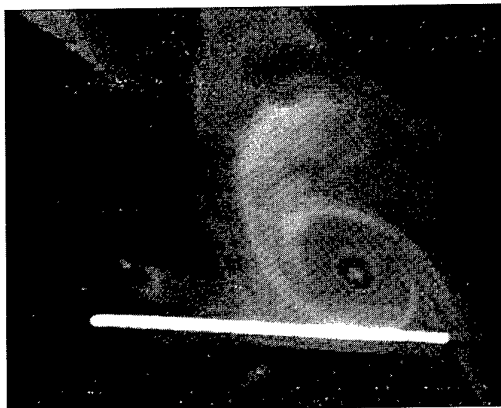


Figure 6. Delta wing flow visualization.

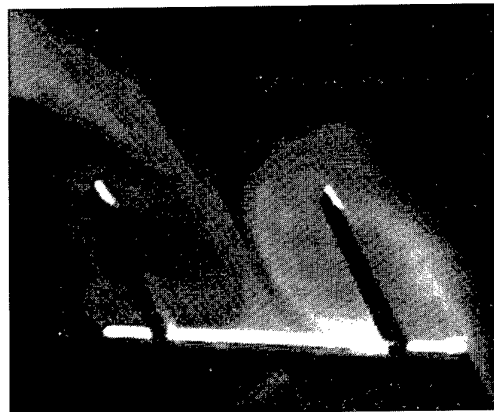


Figure 7. Delta wing with tails flow visualization.

Figures 8 and 9 show the same data as Figures 6 and 7, but in this case the images have been postprocessed to remove perspective distortions. In addition, saturation regions have been removed from the images. This allows a much better measurement of the vortex locations, and is also a necessary step in the processing of the data for the DGV technique.



Figure 8. Delta wing flow visualization with perspective distortions removed.

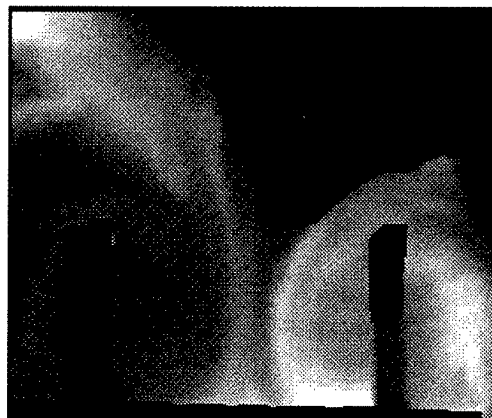


Figure 9. Delta wing with tails flow visualization with perspective distortions removed.

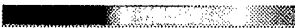
-40 m/s  +15 m/s



Figure 10. Delta wing flow at 97% chord.



Figure 11. Delta wing with tails flow at 97% chord.

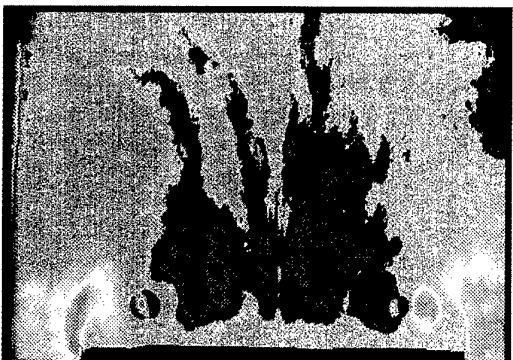


Figure 12. Delta wing flow at 75% chord.

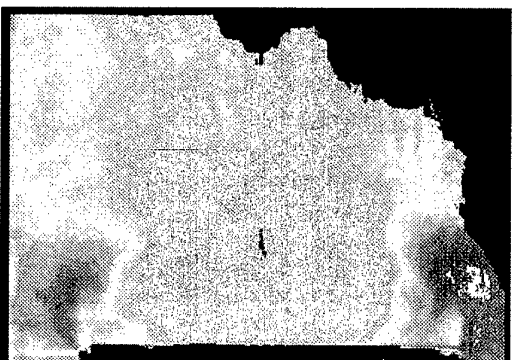


Figure 13. Delta wing with tails flow at 75% chord.

The value of the DGV instrument for flow visualization is clearly seen in the next two figures. Figures 10 and 11 show typical DGV results on the same configuration as above. These figures show considerably more details of the vortical flow on the delta wing at 98% root chord. The measurements are

sensitive to a velocity component in the direction $(-.211 \hat{i}, -.005 \hat{j}, .978 \hat{k})$, where \hat{i} , \hat{j} , and \hat{k} are unit vectors in the downstream, spanwise and upward directions, respectively. Results are shown both with and without tails in place, and represent an average of 60 camera frames. A clear difference is seen between the two flow fields, showing the strong influence of the tails on the overall flow field. These figures also reveal structure in the vortex flow around the tails which cannot be discerned in the conventional flow visualization measurements above. Since 60 frames are averaged, and since an individual frame represents an exposure which is quite long with respect to some of the unsteady aerodynamic effects contained in this flow, these frames may be considered to be time-averaged, and therefore indicate an artificially diffuse vorticity field for the unsteady case.

The sensitivity of this overall flowfield to the presence of the tails can be seen in the next two figures. Figures 12 and 13 show DGV results on the delta wing at 75% of the root chord. This location corresponds to the leading edge of the tail root. While this plane is ahead of the tails, the effect of the tails is felt upstream, as they cause vortex bursting well upstream of their location. This effect can be seen in Figures 12 and 13, as a strong vortex core is observed in Figure 12, whereas a more diffuse vortex is seen in Figure 13.

Although signal fill on each of the individual cameras was acceptable, inconsistencies in smoke seeding resulted in areas of saturation and signal dropout on each of the component cameras. As a result, the determination of orthogonal velocity components was limited to small regions having acceptable signal levels on all six cameras simultaneously. These problems could be addressed by improvements in the smoke seeder system, as well as the use of scientific grade cameras having a better dynamic range.

Comparisons to a computational fluid dynamics (CFD) solution¹⁵ of the clean delta wing showed that while the qualitative results obtained with the DGV instrument matched the solution quite well, the DGV instrument had remaining gain and bias errors for these measurements. Some of these errors were traced to cross-talk between frame grabber boards used with the cameras. Other possible problems include the potential for Mie scattering intensity variations over the small angle spread of the two cameras, and associated polarization sensitivities in the system. This issue can be addressed by using an optical configuration similar to that used by McKenzie⁹, but with an associated drop in signal levels to the cameras.

Continued investigation of this technique in the SARL wind tunnel is proceeding. Several modifications and improvements to the system described above have been made. A scientific grade camera has been incorporated in the system in place of the 8-bit cameras used for the results shown above. This camera provides 14-bit intensity data and 1024 by 1024 pixel arrays. A Nd:YAG laser has been incorporated in the system. This laser allows for finer frequency tuning and increased power levels. The short duration pulse also allows camera shutter speeds to be increased. This is particularly useful for reducing background illumination from sunlight entering the tunnel through the inlet, diffuser and building windows. A split image system is currently being used which allows simultaneous imaging of both the signal and reference images on a single camera. This system has the advantage that only one high quality camera is required for each velocity component, and that angular variations in Mie scattering are less problematic. However, cross-talk between the signal and reference sides of the split image system is severe for the middle third of the array. A polarizer has been incorporated in front of the beam splitter cube to reduce polarization sensitivities in the receiving optics and to suppress some secondary scattering off the windows and model surface. Preliminary investigations with these modifications in place indicate that the improved dynamic range of the cameras and higher power of the Nd:YAG allow this imaging system to be used while maintaining acceptable signal levels in both the reference and signal images.

Conclusions

Doppler Global Velocimetry has been demonstrated as a technology capable of making non-intrusive, velocity discriminated measurements simultaneously over an entire plane in a wind tunnel flow field. Continued advancements to the accuracy and robustness of the technique are resulting in more varied applications in complex flow fields. The technique is capable of providing coherent views of unsteady flow fields while simultaneously improving wind tunnel productivity. These tests have demonstrated the feasibility of making DGV measurements in a large scale facility, and also point to several remaining challenges associated with applying a DGV system in a large facility. Continued refinements to the system design are expected to advance this technique to a quantitative velocity measurement technique which will

simultaneously provide detailed flowfield measurements in wind tunnels while reducing the run time required for those measurements.

Acknowledgments

The authors gratefully acknowledge the assistance of James F. Meyers, Joseph Lee, and Mark Fletcher of NASA Langley Research Center, and Angello Cavone and Richard Schwartz of NYMA in the acquisition and processing of the data shown in this report.

References

- ¹ Komine, H., Brosnan, S.J., Litton, A.B., and Stappaerts, E.A., "Real-Time, Doppler Global Velocimetry." 29th Aerospace Sciences Meeting, AIAA 91-0337, Reno, NV, January, 1991.
- ² Meyers, J.F., "Development of Doppler Global Velocimetry for Wind Tunnel Testing." 18th Aerospace Ground Testing Conference, AIAA 94-2582, Colorado Springs, CO, June, 1994.
- ³ Meyers, J.F., "Evolution of Doppler Global Velocimetry Data Processing." Eighth International Symposium on Applications of Laser Techniques to Fluid Mechanics, Lisbon, Portugal, July, 1996.
- ⁴ Beutner, T.J., Baust, H.D., Meyers, J.F., "Doppler Global Velocimetry Measurements of a Vortex-Tail Interaction." Proceedings of the Seventh International Symposium on Flow Visualization, Seattle, WA, Sept. 1995.
- ⁵ Forkey, J.N., "Development and Demonstration of Filtered Rayleigh Scattering—A Laser Based Flow Diagnostic for Planar Measurement of Velocity, Temperature and Pressure," Technical Report No. 2067, (also Ph.D. dissertation No. 2067-T) Princeton University, Department of Mechanical and Aerospace Engineering, Princeton, NJ, April 1996.
- ⁶ Forkey, J.N., Finkelstein, N.D., Lempert, W.R., and Miles, R.B., "Demonstration and Characterization of Filtered Rayleigh Scattering for Planar Velocity Measurements." AIAA Journal, March 1996, Vol. 34, No. 3, pp. 442-448.
- ⁷ Miles, R.B., Forkey, J.N., and Lempert, W.R., "Filtered Rayleigh Scattering Measurements in Supersonic/Hypersonic Facilities," Paper 92-3894, AIAA 17th Aerospace Ground Testing Conference, July 6-8, 1992, Nashville, TN.
- ⁸ McKenzie, R.L., "Measurement Capabilities of Planar Doppler Velocimetry Using Pulsed Lasers," 33rd Aerospace Sciences Meeting, AIAA 95-0297, Reno, NV, January, 1995.
- ⁹ McKenzie, R.L., "Planar Doppler Velocimetry Performance in Low-Speed Flows," 35th Aerospace Sciences Meeting, AIAA 97-0498, Reno, NV, January, 1997.
- ¹⁰ Clancy, P.S., and Samimy, M., "Multiple-Component Velocimetry in High Speed Flows Using Planar Doppler Velocimetry," 35th Aerospace Sciences Meeting, AIAA 97-0497, Reno, NV, January, 1997.
- ¹¹ Smith, M.W. and Northam, G.B. "Application of Absorption Filter-Planar Doppler Velocimetry to Sonic and Supersonic Jets," AIAA Paper 95-0299, 33rd Aerospace Sciences Meeting, Reno, NV, January, 1995.
- ¹² Elliott, G.S., Samimy, M., and Arnette, S.A., "Molecular Filter-Based Diagnostics in High Speed Flows," 31st Aerospace Sciences Meeting, AIAA 93-0512, Reno, NV, January, 1993.
- ¹³ Arnette, S.A., Samimy, M., Elliott, G.S. "Two-Component Filtered Planar Velocimetry in the Compressible Turbulent Boundary Layer," 34th Aerospace Sciences Meeting, AIAA 96-0305, Reno, NV, January, 1996.
- ¹⁴ Tellinghuisen, J., "Transition strengths in the visible-infrared absorption spectrum of I₂," Journal of Chemical Physics, Vol. 76, No. 10, May 15, 1982, pp. 4736-43.
- ¹⁵ Rizzetta, D.P., "Numerical Simulation of the Interaction between a Leading-Edge Vortex and a Vertical Tail," AIAA Paper 96-2012, 27th AIAA Fluid Dynamics Conference, June 17-20, New Orleans, LA.

Planar Doppler Velocimetry for Large-Scale Wind Tunnel Applications

Robert L. McKenzie

* NASA Ames Research Center, MS 260-1, Moffett Field, CA 94035-1000, USA

Abstract

Planar Doppler Velocimetry (PDV) concepts using a pulsed laser are described and the obtainable minimum resolved velocities in large-scale wind tunnels are evaluated. Velocity-field measurements are shown to be possible at ranges of tens of meters and with single-pulse resolutions as low as 2 m/s. Velocity measurements in the flow of a low-speed, turbulent jet are reported that demonstrate the ability of PDV to acquire both average velocity fields and their fluctuation amplitudes, using procedures that are compatible with large-scale facility operations. The advantages of PDV over current Laser Doppler Anemometry and Particle Image Velocimetry techniques appear to be significant for applications to large facilities.

1. INTRODUCTION

Planar Doppler Velocimetry (PDV) has been shown by several laboratories¹⁻⁷ to offer an attractive means for measuring spatially resolved, three-dimensional velocity vectors everywhere in the plane of a laser light sheet in a flow. When compared to other well-known optical methods for measuring flow velocities, PDV is particularly advantageous for use in large wind tunnels, even at low speeds, because of its inherently strong radio-metric signals, the simplicity of its optical alignment requirements, its relaxed requirements on the nature of the aerosols that must be seeded into the flow, and the absence of any need to optically resolve or track individual particles.^{1,2} Early demonstrations of PDV (also called "Doppler Global Velocimetry" by some authors) were made in low-speed flows,³⁻⁴ but with only limited quantitative comparisons to other measurements. More recent demonstrations were made in supersonic flows⁵⁻⁷ where the Doppler shift is large and less sensitive to measurement noise. The use of both pulsed and

continuous-wave (*cw*) lasers have been demonstrated, but PDV using pulsed lasers is particularly attractive because it provides repetitive, instantaneous, images of the velocity field, from which both average velocities and their instantaneous and statistical fluctuations may be determined.

This paper updates and summarizes the studies reported in Refs. 1 and 2, in which the factors that affect the measurement capabilities of PDV using pulsed lasers are characterized and its low-speed performance is demonstrated. The applications of particular interest are to large, low-speed, wind tunnel facilities of the type used for the developmental testing of commercial aircraft. There, velocities can be less than 100 m/s while distances from the test region to external instrument locations can exceed several meters.

Reference 1 reported a detailed theoretical evaluation of PDV that was designed to determine the fundamental measurement capabilities of the technique. The results showed that signal levels from a practical instrument should be large enough to allow the useful application of PDV in large-scale facilities and that minimum velocity resolutions less than 2 m/s are feasible for a wide range of test conditions and facility sizes. Reference 2 reported an experimental study that incorporated a high-fidelity, single-velocity-component, PDV system and a suite of PDV image-processing software designed for pulsed laser applications. The main objectives were to validate the PDV measurement noise model used to characterize the measurement uncertainties and to experimentally demonstrate the minimum resolved velocity that could be achieved using a PDV system designed for high accuracy. In this paper, the preceding PDV performance evaluations are updated to include all of the experimentally revealed and evaluated contributors that affect the minimum resolved velocities. The predictions of minimum resolved velocities are supported by PDV

* Author's address after Jan. 1, 1998: Physical Sciences Research Associates, 825 Cathedral Drive, Sunnyvale, CA 94087. E-mail address: mckenzie@netgate.net

measurements of the known surface speeds of a rotating wheel. In addition, the application of PDV to a low-speed, turbulent jet flow is reviewed that demonstrates an experimental procedure allowing the average velocities fields and their turbulent fluctuations to be determined in a way that is compatible with large wind tunnel operations.

2. FUNDAMENTALS OF PLANAR DOPPLER VELOCIMETRY

2.1 The PDV Concept

Figure 1 illustrates the PDV concept along with some optical refinements that were used for these studies. Light is scattered by aerosols in the flow from a light sheet created by a pulsed, narrowband laser. The scattered light image is recorded by a charge-coupled-device (CCD) camera system with optics that split the image into two paths; one that passes through an iodine vapor cell and the other that bypasses the cell. The iodine vapor provides a sharp-edged spectral filter with optical transmissions at certain frequencies that are sensitive to small changes in the frequency of light scattered from the moving particles. The frequency changes are caused by the Doppler effect owing to the motion of the scattering particles. The images from each optical path enter the camera lens with a slight displacement so that they are separated into two views of the same scattering region.

A laser that is particularly suitable for this application is the frequency-doubled, injection-seeded, Nd-YAG system. It is a high energy, pulsed laser that operates at a wavelength of 532 nm where the iodine absorption spectra is rich with spectral features. It can also be made to operate with a bandwidth of less than 150 MHz, which is sufficiently narrow compared to the 400 MHz spectral half-width of most of the iodine spectral features, so that frequency changes as small as 1 MHz can be resolved.

Normally, the laser is tuned to a frequency where the transmission of the iodine vapor filter is approximately 50 percent. Doppler shifting of the scattered light frequency then causes the light energy that is transmitted by the filter to either increase or decrease from its unshifted value, depending on the direction of the particle motion.

Subsequent image processing determines the locations of pixels in each view of the split-image that record light from the same object region, and then maps and divides the filtered view by the unfiltered view, pixel by pixel.² The result is a normalized image with gray scales that ideally depend only on the magnitude of the Doppler frequency shift. The image of Doppler-frequency-shifts from each laser pulse can then be related to the instantaneous magnitude of one component of the flow velocity vector for all points in the light sheet. The direction of the component depends on the observation angle. Three identical camera systems with different observation angles provide three separate vector components, all for the same laser pulse.

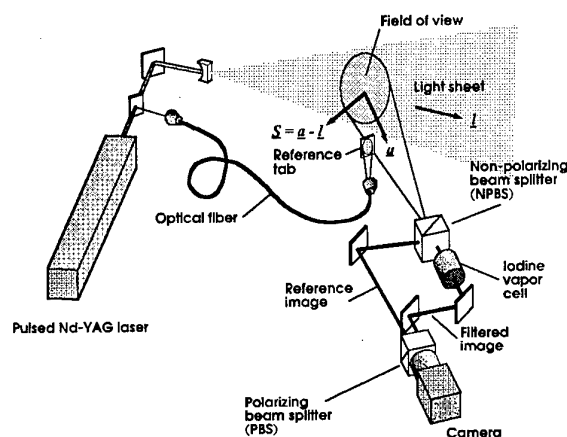


Fig. 1. Planar Doppler Velocimetry configuration for the measurement of one velocity component.

The equation governing the Doppler shift in frequency owing to light scattered by a moving particle can be written in generalized vector notation as

$$\Delta\nu = \left[\frac{\nu_0}{c} (\underline{a} \cdot \underline{l}) \right] \cdot \underline{V} \quad (1)$$

where $\Delta\nu$ is the difference between the frequency of the Doppler shifted light and the incident laser light, ν_0 is the frequency of the incident laser light, and c is the speed of light. The geometry of the measurement is described by the underlined variables, which are vectors as shown in Fig. 1. The unit vector \underline{l} defines the direction of the incident light, the unit vector \underline{a} defines the direction of light scattered toward the observer, and \underline{V} is the velocity vector of

the scattering particle. The difference vector, $\underline{S} = \underline{a} - \underline{l}$, determines the direction and relative magnitude of the velocity component that is associated with the measured Doppler shift. An analysis of Eq. (1) shows that for observation azimuth angles between 45 and 135 degrees, measured relative to the direction of \underline{l} , and a laser wavelength of 532 nm, the term in brackets varies from 1.5 to 3 MHz per m/s, thereby indicating the magnitude of Doppler frequency shift that must be resolved for a given velocity resolution.

2.2 Optical System Refinements

Several optical refinements appear in Fig. 1 when compared to the PDV optical systems first reported.^{3,4} One is the use of a single camera with a split-image optical system in place of the simpler, but more costly, two-camera systems originally reported. This feature makes more acceptable the use of expensive, scientific-grade, camera systems to achieve the maximum, single-pulse, accuracy possible from a PDV instrument.

The iodine cell used here, with a vapor path length of 15.2 cm, is several times longer than most other cells designed for PDV. The increased length reduces the fractional influence of localized thermal gradients from convection-cooled window faces on the spectral transmission uniformity across the field of view. A penalty of this feature is the slightly reduced field of view that results from a more distant entrance aperture.

A reference tab is shown in the camera view ahead of the light sheet. It provides a stationary target to monitor the laser frequency fluctuations from pulse to pulse. This requirement is necessary because the fundamental PDV measurement is the instantaneous difference in frequency between the light scattered by the moving particles and the incident laser light. The laser frequency fluctuates from pulse to pulse because the high-energy, Nd-YAG, laser system uses a low-energy, narrowband, injection laser to induce its oscillation to a narrow band width. Frequency locking between the two lasers is maintained by modulating the cavity length of the host laser to match the axial-mode frequency of the injection laser. Consequently, the output frequency of the host laser is also modulated with peak am-

plitudes of approximately ± 10 MHz that are randomly sampled by the laser pulses. Without monitoring of the laser frequency from pulse to pulse, the modulation would appear as a false PDV velocity fluctuation of ± 3 to 7 m/s that would dominate all other noise sources. Moreover, during the time-period of a typical PDV measurement, the mean laser frequency may drift by a significant amount, thereby adding a possible, time-dependent, systematic velocity error. However, frequency differences can be resolved that are much smaller than 10 MHz by using the unshifted transmission of light from the reference tab to determine the instantaneous laser frequency for each pulse. The difference is measured most accurately if all targets are viewed through the same iodine filter cell. For this work, the reference tab was illuminated by diverting a small fraction of light from the laser beam, transporting it through an optical fiber, and projecting it onto the tab.

The optical arrangement shown in Fig. 1 includes the usual placement of a non-polarizing beam splitter (NPBS) ahead of the iodine cell to separate the incident light into filtered and unfiltered views. For this study, it was combined with a polarizing beam splitter (PBS) in front of the camera lens to minimize errors in the normalized image that are related to variations in the polarization of the scattered light. Ideally, the NPBS must divide the image into two views with a consistent ratio of transmission to reflection, regardless of the polarization of the scattered light. Although the incident laser light usually maintains some definite, fixed, polarization characteristic, the scattered light from aerosol scattering is generally slightly depolarized while the secondary scattering from windows and walls is almost entirely depolarized. This depolarization energy fluctuates with variations in the local aerosol density and will appear as uncompensated signal fluctuations in the normalized image unless the NPBS transmission for s- and p-polarizations are exactly equal, or only one polarization component reaches the camera lens. For an NPBS that is used at its design wavelength, the transmissions for s- and p-polarizations are typically specified to be matched within 3% but the difference can be much

larger at other nearby wavelengths or when quality control is poor. Thus, to limit the observed light to just one polarization after image splitting, a PBS was placed in front of the camera lens. Fortunately, when a linearly polarized laser is used, most of the scattered light from the aerosol is also linearly polarized. Hence, by rotating the PBS to maximize its transmission for a particular optical system orientation, there is no significant signal loss from aerosol scattering but any depolarized light from windows and walls is attenuated up to 50%.

3. RESPONSE FUNCTION

The response function is the fundamental feature that controls the quantitative accuracy of a PDV measurement. It relates the normalized signal for each pixel to a relative frequency. (i.e., a frequency in absolute units but relative to an arbitrary offset frequency, ν' .) An example is shown in Fig. 2. Once the response function is known, the normalized signals from all pixels in the PDV image can be converted to relative frequencies. The differences in frequencies between the incident laser, determined from the stationary reference tab image, and those obtained from the aerosol scattering image establish the Doppler frequency shifts, $\Delta\nu$, which can then be directly related to one component of the absolute velocities everywhere in the image using Eq. (1).

The shape of the response function depends on several spectral features of the iodine filter cell, including: the radiative strength of the selected iodine spectral absorption feature, the presence of underlying spectral features, the optical path length through the filter cell, and the temperature and pressure of the iodine vapor in the filter cell. The spectral transition group cataloged⁸ as line number 1109 was shown to be one of the stronger absorption features within the tuning range of the 532 nm laser and its blue side was shown to have minimum interference from neighboring transitions.¹ Filter cell conditions can be easily achieved so that its spectral transmission varies with frequency from near zero to approximately 0.8, where a non-resonant background absorption becomes dominant.

The filter cell used for these measurements con-

tained iodine vapor at its vapor pressure of approximately 1 torr. The cell was made of fused silica and consisted of a cylindrical body that enclosed

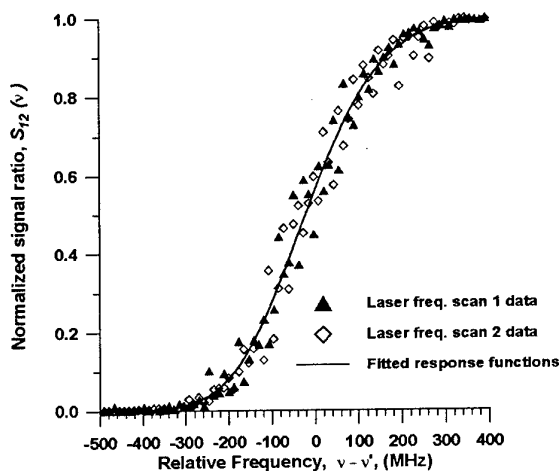


Fig. 2. The response function for the blue side of the iodine vapor line 1109 at a cell stem temperature of 45 °C and a body temperature of 100 °C. The repeatability of the fitted response function is shown for two, independent, laser frequency scans. The fits for each scan are indistinguishable.

the optical path and a small side stem. The 7.6-cm-diameter body cylinder had optically flat windows at each end with an internal separation of 15.2 cm. The 7-cm-long by 1-cm-diameter stem was attached perpendicular to the body cylindrical wall and centered on its longitudinal axis. The entire assembly was encased in an insulated housing with only the window faces exposed. The body was heated to temperatures higher than the stem so that iodine condensation always occurred in the cooler stem. Consequently, the iodine vapor pressure was controlled by the stem temperature while the vapor temperature was coupled to the body temperature. The body and stem temperatures were maintained by two, independently controlled, heater tapes; one that heated the body cylinder to approximately 100 °C and the other that heated a copper heat-sink surrounding the stem to approximately 45 °C. These conditions have been shown to maximize the spectral sensitivity of the response function for the cell length used here.¹ However, accurate knowledge of the iodine vapor pressure and temperature was never necessary because the actual response func-

tion was always determined experimentally.

The response function can be determined using the PDV system in place by scanning the laser frequency while recording a sequence of images that include a view of the reference tab. As an example, the normalized reference tab signals from two independent spectral scans are shown in Fig. 2. The scatter in the data is caused by the pulse-to-pulse random sampling of the ± 10 MHz laser frequency modulation used to maintain narrowband locking. To obtain a smooth response function that is both physically realistic and representative of the experimental data, an synthetic iodine spectrum is computed for vapor conditions that approximate the cell conditions. It is used as a basis function and fitted to the scan data with a nonlinear, least-squares method. The fit is optimized by adjusting three parameters that control the amplitude of the basis function, its frequency span, and its frequency offset. The basis function for Fig. 2 was computed assuming a stem temperature of 45 °C and a body temperature of 100 °C, which were the set-point values of the temperature controllers. The adjusted fits for the two scans are overlapping and not distinguishable in Fig. 2. The basis function is most sensitive to the assumed stem temperature.¹ However, similar fits starting with basis functions computed for stem temperatures of 40 to 50 °C were also nearly indistinguishable from those shown. Thus, the repeatability of the response function obtained using this data analysis scheme is generally very consistent, providing the thermal condition of the cell is kept stable. Since the actual response function is particularly sensitive to small changes in the cell stem temperature, its measurement is repeated whenever a change in cell environment is suspected.

4. IMAGE PROCESSING

4.1 Background and Flatfield Corrections

The CCD image can contain a substantial electronic background signal in addition to contributions from stray laser and room light. An average background image may be recorded with low noise by accumulating a large number of open-shutter exposures, either with the laser beam blocked or without aerosols in the flow. However, this aver-

aged background does not contain possible contributions of secondary scattering from nearby windows and walls that are illuminated by aerosol scattering. The experiment must be configured to minimize those contributions.

The flatfield image provides a measure of the non-uniform optical response distribution at the image plane and it enables the necessary correction of the PDV images. The optical response distribution includes the variations in pixel sensitivities and the aggregate transmission variations in the optical system along all optical paths from each point in the object plane to the pixel that is illuminated by it. The acquisition of a correct flatfield image is a particularly critical step toward achieving accurate PDV measurements because the optical response distribution is always different for each split-image view. The ratio of the two images is undistorted only after a suitable flatfield correction is made to the entire image. On the other hand, the flatfield image does not require a uniformly illuminated target because both split-image views see the same illumination distribution, but it must reproduce the optical losses for the total light energy reaching each pixel over all optical paths through the collection optics. This requires the flatfield to have its target located at the object plane where the optical system is focused, which is the plane of the laser light sheet. Moreover, to best reproduce the frequency-dependence of the transmission losses through the iodine cell and its surrounding optics, the flatfield should be acquired using laser illumination with the laser operating at a frequency that falls near the spectral range of the response function.

One convenient laser frequency for flatfield acquisition is where the iodine cell transmission has a spectral plateau so that the transmission is locally insensitive to frequency. Then a flatfield may be obtained using aerosol scattering from the laser light sheet with the seeded air flowing. However, the laser frequency must be sufficiently displaced from the onset of any frequency-dependent cell absorption, or the flow speed reduced, so that the transmission remains unaffected by Doppler shifts induced by the flow. This approach takes advantage of the situation in low-speed flows where the Dop-

pler shifts are generally small compared to the spectral plateau widths available in the iodine spectrum. An alternative and easier approach is to operate the laser broadband so that its spectral bandwidth encompasses several iodine spectral features. The filter is then insensitive to all Doppler shifts. However, while this latter approach appears to be valid, it has not yet been demonstrated successfully.

Both the PDV image and the flatfield can also be affected significantly by the strong angular dependence of aerosol scattering in polarized light, particularly for scattering at azimuth angles greater than 45° from the incident light direction. The large angular variations in scattered intensities can create large signal gradients across the aperture of the camera lens so that slight differences in alignment of the two split-image views will create a different signal distribution in each view. However, these polarization effects will be identical in both the PDV image and in the flatfield image if they are both acquired at the same aerosol scattering conditions. *Thus, the most accurate flatfields are always acquired using aerosol scattering from the flow.* This approach should be favorable for large-scale wind tunnel applications because it can be performed just before acquisition of the PDV data and without requiring entry into the test section or a change in facility operating conditions.

4.2 Split-Image Mapping

Pixel mapping to allow image normalization was accomplished for this study by first obtaining an image of a mapping card that contains an orthogonal array of equally spaced dots and a central registration cross. To provide accurate mapping, the card must be located in the same object plane as the light sheet and its image must be obtained using the same aperture (f -number) used for the PDV measurements. For this study using a single camera system, the card was aligned normal to the camera axis so that all regions of the card remained within the focal depth of the image. However, when more than one camera system is in use, the mapping card must be aligned in the plane of the laser light sheet so that pixels in all camera systems can be registered to the same locations in the light sheet. Having the

card aligned with the light sheet also provides a convenient means to determine each camera's azimuth and elevation angles relative to the incident light direction, as required by Eq. (1), by measuring the apparent change in dot spacings and the relative angles between their rows and columns.

The mapping errors were evaluated by comparing interpolated pixel mapping coordinates from images for two different card orientations. The bilinear interpolation schemes used for this work were found to achieve root-mean-square (rms) average differences over the entire image of less than 0.3 pixel units, with maximum differences up to 1.5 pixels near the image boundaries.

4.3 Sampling Errors and the Necessity of Pixel Binning

In addition to mapping uncertainties, signal sampling errors by the finite-sized pixel areas also degrade the accuracy of the normalized images. Each pixel acts as an integrator of the underlying charge-distribution induced in its semi-conductor substrate. This integrated sampling loses some of the spatial detail in the incident signal distribution and can lead to large signal ratio errors when the signal gradients are large over a pixel dimension. Reference 2 shows that the sampling can introduce signal ratio errors as large as a factor of two in extreme cases for a single pixel-pair. An obvious means of reducing sampling errors is to integrate the signal distribution over larger areas by collecting blocks of pixels into bins and summing their signals. No signal is lost but the spatial resolution is reduced. Bin sizes with three pixels on a side (so-called "3x3 binning") was shown to be a minimum size for reducing the sampling errors to acceptable levels.² Although binning sacrifices spatial resolution, it minimizes excessive spatial noise that would otherwise degrade the useful spatial resolution of the velocity field. Thus, very little recoverable information is actually lost. Moreover, in cases where signal gradients in the image are small compared to a pixel dimension, 3x3 binning has no significant effect on the spatial resolution.

5. PDV MEASUREMENT UNCERTAINTIES

The uncertainties in measured velocities are re-

lated to the statistical uncertainties that affect the individual pixel signals in each split-image view and their normalization ratios.¹ Recalling the notation from Ref. 1, the combined effects of statistically-independent fluctuations from all stochastic processes, whether from noise in the PDV signals or due to the turbulent fluctuations in the flow, can be characterized by the sum of their individual mean-square variances. An equivalent parameter is the square-root of the total variance, traditionally called the root-mean-square (rms) standard deviation. The noise-to-signal ratio (*NSR*) is then the ratio of the rms-standard-deviation of signals from each pixel to its average signal for a multitude of pulsed images. Reference 1 develops a formulation to estimate the noise/signal ratio of the normalized image, which contains the signal ratios, $S_{12}=S_1/S_2$, where S_1 and S_2 denote the signals in individual pixel pairs from the filtered and unfiltered views of the split image, respectively. The noise-to-signal ratio for S_{12} is denoted as NSR_{12} . Since S_{12} is the independent variable for the response function, the variance of S_{12} combines with the response function sensitivity (i.e., $\partial v/\partial S_{12}$ in Fig. 2.) to determine the variance in the frequency differences and their corresponding velocity variances. The related rms-standard-deviations in velocity are defined here as the so-called "minimum resolved velocities."

5.1 Sources of PDV Measurement Noise

Sources of noise in PDV signals can be separated into two types; those that are statistically-independent for each view in the PDV split image, and those that maintain some correlation between the filtered and unfiltered views. The statistically-independent noise originates from radiometric sources that are associated with the detection of light and with the electronic nature of CCD detectors, such as photon-statistical noise, readout noise, and dark charge noise. The primary source of correlated noise is the high-contrast, granular, speckle pattern that appears in any observation of scattered light from a target illuminated by a coherent laser. For PDV using *cw* lasers and video cameras, the speckle noise is usually time-averaged nearly to zero over the usual 30-ms video cycle period and is consequently diminished in the PDV images. How-

ever, for PDV using pulsed lasers, the instantaneous speckle noise amplitudes in an unnormalized image dominate all other noise sources. Fortunately, only the signal ratios from two, simultaneously recorded, views are necessary for the PDV signal analysis and both views contain nearly the same speckle pattern from each laser pulse. If the observation angles of both views were exactly identical and the mapping was precise, the speckle pattern would be completely correlated and would disappear in the signal ratios from pulsed lasers, just as all other spatial features disappear that are common to both views. However, the speckle pattern is highly sensitive to observation angle while identical observation angles are rarely achieved, so that only partial correlation can be expected in practice. An important difference between the behaviors of radiometric noise and speckle noise is that the NSR_{12} for radiometric noise depends on the local average signal levels, while for speckle noise it is independent of signal level and controlled mainly by the *f*-number of the collection optics.²

5.2 Noise Reduction by Binning and the Unexplained Speckle Background

The reduction of the signal-ratio variance by binning depends on the nature of the noise. If a bin contains N_B pixels, the variance in the signal ratio is normally reduced as if the related NSR_{12} were multiplied by a factor of $1/N_B$. However, preliminary experiments² have shown that when speckle was the dominant noise source, one component of NSR_{12} varied with *f*-number and decreased with N_B as expected; but an additional, residual background was also present that could be defined by a constant $NSR_{12} \approx 0.04$, independent of *f*-number. Moreover, it was not reduced by binning. Although the origin of the background is not completely understood at this time, several observations and conjectures can be made. For the background to be insensitive to binning, it must be the consequence of an uncompensated, temporal variation in the sequence of split-image signals. In addition, since the background noise occurs in the signal ratios even when the laser is broadband, it is not believed to be from temporal fluctuations either in laser pulse energy or in its pulse frequency. Finally, since the background

noise only appears when speckle is dominant, it is suspected to be related to the highly sensitive polarization effects that are always present when speckle is a dominant feature. Such effects would be time-dependent because of temporal variations in the behavior of polarized scattering by the aerosol field from pulse to pulse and would be observable because the flatfield correction compensates only for the average behavior of the aerosol scattering. However, more definitive experiments will be necessary to confirm these speculations.

6. ROTATING WHEEL EXPERIMENTS

A rotating wheel is an ideal target to evaluate the PDV minimum resolved velocities because it provides a surface that is moving with a linear distribution of known velocities. The results provide a preliminary indication of the minimum resolved velocities that are possible in fluid flows, at least to the extent that the uncertainties in PDV measurements associated with scattering from an opaque surface correspond to those for aerosol scattering in a fluid flow.

Examples of average velocity field images and their corresponding uncertainty amplitude images from a rotating wheel are reported in Ref. 2. The rim speed was 57.9 m/s, with a corresponding rim-to-rim Doppler shift of ± 111 MHz. The radial distribution of average velocities along a line from the center of rotation to the advancing rim is plotted in Fig. 3. It follows a linear distribution with the expected average slope but contains an organized modulation of approximately ± 5 m/s that appears only on the advancing side of the wheel. Since the modulation is a systematic error in the average velocity, it is not caused by noise in the measurement. It appears to be the result of spatially distributed frequency variations in the expanded laser beam that have discrete steps of approximately 10 MHz. A similar behavior with larger modulations was observed by Forkey et al.⁹ for the same type of laser. However, the organized modulations appearing in Fig. 3 will be spatially compressed in the thin light sheets used for PDV in fluid flows and their organized behavior suggests that correction methods analogous to the flatfield corrections might be possible.

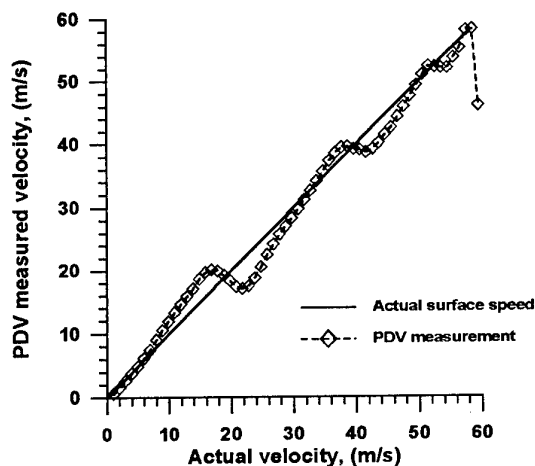


Fig. 3. Comparison of PDV average velocities on a rotating wheel with actual surface velocities, along a radial line from the wheel center to the advancing rim. The modulations are believed to be caused by spatially-separated variations in the frequency of the expanded laser beam.

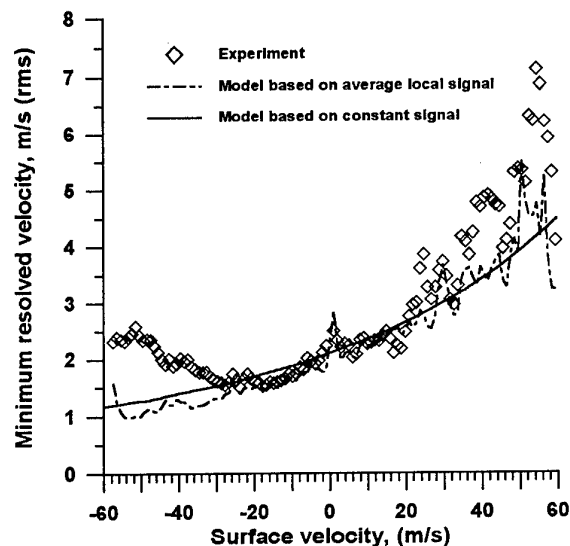


Fig. 4. Comparison of experimental minimum resolved velocities along a radial line on the rotating wheel with estimates using constant and local average signals.

The measured distribution of minimum resolved velocity on a line from rim to rim through the center of the rotating wheel is shown in Fig. 4, along with two estimates that include the effects of speckle and binning.² For one estimate, the local average signals are used. Those results match the experimental data near the wheel center but under-estimate it with a

growing difference as the rims are approached. This radially-symmetric departure behaves as if it were the consequence of poor wheel-speed regulation that is oscillatory about the set-point. Additional noise in the velocity measurements on the advancing side of the wheel may be caused by intensity amplitude fluctuations in the apparent laser side-band frequency components, thereby accounting for the larger differences on the advancing side. The other noise estimate is based on a constant average signal, chosen to match the noise at the wheel center. It demonstrates that the radial distribution of velocity uncertainty is controlled mainly by the variation of the response function sensitivity with S_{12} . In any case, Fig. 4 demonstrates that velocities can be measured using PDV with uncertainties generally less than 5 m/s and with minimum uncertainties below 2 m/s.

7. LOW-SPEED, JET FLOW EXPERIMENTS

Velocity fields and their fluctuations have also been measured in the unsteady, low-speed, flow from a free-jet with axial velocities near 60 m/s. The primary objectives were to demonstrate the ability of PDV velocity field measurements to yield the expected results in a fluctuating air flow that is seeded with an aerosol of a type used in large facilities, and to do so using procedures that are compatible with large-scale wind tunnel operations.

The jet was a bench-top apparatus that incorporated a 27-cm-diameter rotary blower. Air from the room was entrained into the center of the impeller and exhausted radially into a tangential plenum. The unsteady flow from the plenum exited into the room air through a 5-cm-diameter, cylindrical, nozzle as a free jet. To provide aerosol seeding, a train of drops from a commercial "fog fluid," that is used for the generation of theatrical smoke (believed to be a mixture of propylene glycol and water) was heated on the recessed tip of a soldering iron. The resulting vapor was drawn by a venturi tube into the impeller inlet flow. The seeding system provided small concentrations of a liquid aerosol in the jet that were not easily visible in room light but could be readily seen in the laser light sheet.

The laser beam was formed into a parallel sheet, approximately 1-mm-thick, that encompassed all of

the seeded jet flow. Two optical configurations were used that measured velocity components with different directions. In one, the light sheet crossed the jet centerline axis at 90° and the scattering was observed at an azimuth angle of 41° from the jet centerline axis, which resulted in PDV measurements in a plane normal to the jet axis but with velocity components that pointed downstream 20° from the jet centerline. The axial component was estimated by projecting the measured component onto the axial direction. The second configuration used a light sheet that crossed the jet centerline axis at 45° but measured velocity components aligned with the jet axis. The light sheets in both arrangements crossed the jet centerline at the same axial location and shared a common vertical line. The axial velocities obtained from both configurations on the common line were found to be the same, which confirmed the lack of any significant transverse components and justified the use of projections of the non-axial velocity components to infer axial velocities in the plane normal to the jet axis.

PDV velocity fields in the jet flow were obtained using a procedure that is favorable for large-scale wind tunnel operations because, once the map card image is obtained for a given camera alignment, no entry into the test region is required and all subsequent data may be acquired remotely. The background and response function data were obtained prior to operating the jet, and the flatfield image was taken using aerosol scattering from the seeded flow with the laser detuned, as discussed in Sec. 3.

Figure 5(a) shows the average axial velocity field derived from a 100-frame sequence of PDV images, using the optical geometry that measured velocity components 20° to the jet axis. The image has been numerically rotated to simulate a view looking directly upstream. The velocity fluctuations are characterized by the velocity fluctuation field, $\langle U' \rangle / U$, shown in Fig. 5(b), where $\langle U' \rangle$ denotes the rms-standard-deviation of axial velocity and U is its local average value. The measured velocity fluctuations have been corrected to remove the estimated contributions from measurement noise, which was statistically subtracted with the aid of a noise model that computed the noise variance using the average PDV signals from the flow.² The rela-

tive fluctuation amplitudes in the flow become large in the shear layer while individual single-pulse images display an ensemble of intermittent radial flow excursions by large eddies. Although this intermittent behavior in free jets is expected, data of this type illustrate the unique capabilities of a PDV system using a pulsed laser to reveal the average, time-dependent, and statistical nature of an unsteady flow.

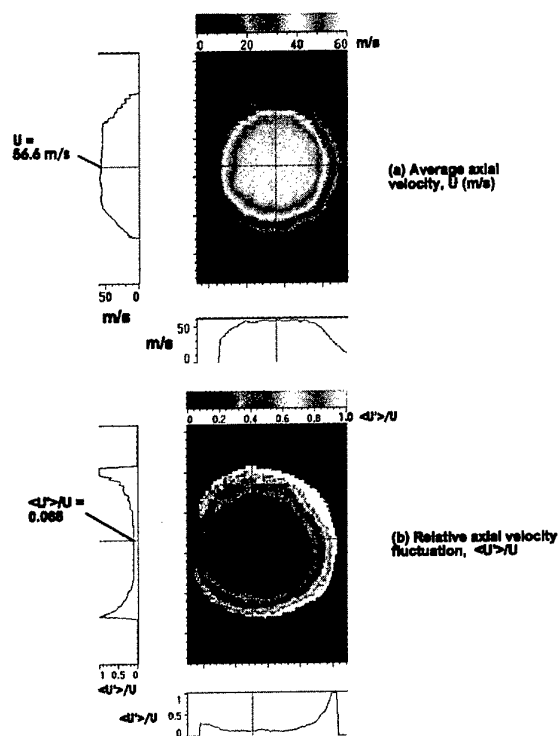


Fig. 5. The average axial velocity field and its relative fluctuation field, measured in a plane normal to the centerline axis of a low-speed, turbulent jet. The view in each image is upstream along the jet centerline. U denotes the local, time-averaged, velocity and $\langle U' \rangle$ is the standard deviation of velocity fluctuation amplitudes that have been corrected to remove the estimated measurement noise contributions.

An indication of the quantitative accuracy of the average PDV measurements in the turbulent jet is shown in Fig. 6, where the average axial velocities implied from impact pressure probe measurements compare reasonably well with PDV measurements along the same radial line across the jet. Disturbances to the average PDV velocities from side-

band frequency variations in the laser beam would not be as obvious here as they are in the rotating wheel measurements because they are spatially compressed in the light sheet and fall mostly outside the shear layer where velocities are near, or below, the minimum resolution.

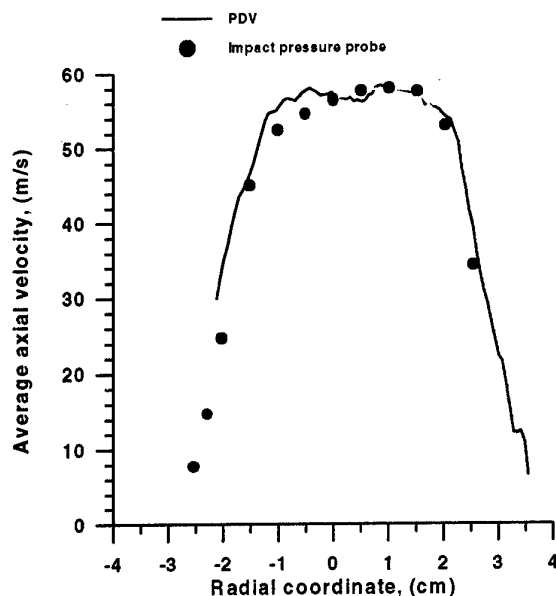


Fig. 6. Comparison of PDV average axial velocities along a radial line through the jet center with velocities implied from impact pressure probe measurements.

8. PDV CAPABILITIES FOR LARGE-SCALE WIND TUNNEL APPLICATIONS

The measurement capabilities of PDV can be characterized using estimates of the limiting observation ranges and aerosol optical densities that are associated with signal levels covering the full dynamic range of modern CCD detector arrays, and combined with an evaluation the minimum resolved velocities that are achievable at those signal levels.

8.1 Observation Ranges and Aerosol Density Requirements

To determine the limiting observation ranges and aerosol optical densities, an aerosol-scattering model has been developed¹ that relates the scattering efficiency of a typical seed material and the parameters of the collection optics to the CCD detec-

tor signal levels. The formulation is based on Mie scattering theory and an empirical model of aerosols with a distributed range of particle sizes that simulate the smoke or seed materials usually introduced into large wind tunnels flows. The results are shown in Fig. 7, where the range, R , is the distance from the sample volume to the collection optics and is proportional to the size of the facility. The optical path length, C_{path} , is the sum of the distance that the laser light must travel through the seeded flow to the sample volume, plus the distance that the scattered light must travel back to the detector. The primary parameters are the unfiltered CCD signal level, S_2 , the observation range, R , and the optical density of the aerosol. The optical density depends on the aerosol particle density and on the aggregate scattering efficiency by its distribution of particle sizes. To define the optical density in terms that are readily measurable, it can be related to its effect on the easily-measured laser beam transmission along the optical path. The transmission is characterized by the laser pulse energy ratio, E/E_o , where E_o is the pulse energy entering the path and E is the attenuated pulse energy at the path exit. The remaining independent parameters were chosen to represent typical experimental conditions for a large wind tunnel application. Their values are listed in the title of Fig. 7. The choice of laser sheet height, Δy , may be related to the facility size (range) and to the CCD array size by requiring that the light sheet fill at least 1/2 of the field of view of the CCD image to accommodate the split-image optics. This criteria leads to a maximum sheet height of $\Delta y = 0.1R$ for a typical 10-mm CCD array height when combined with a normal photographic lens focal length of 50 mm.¹ Consequently, the height of the light sheet will also increase with range to match the increase in scale of the flow being studied.

Two representative flow-seeding cases are shown in Fig. 7. Case 1 represents the situation in smaller facilities where the seed material is allowed to fill the entire flow channel. Then the total laser transmission path is at least $C_{path} = 2R$. Case 2 represents the alternative situation for very large facilities where seeding is best done only in the flow region being investigated, which avoids unnecessary

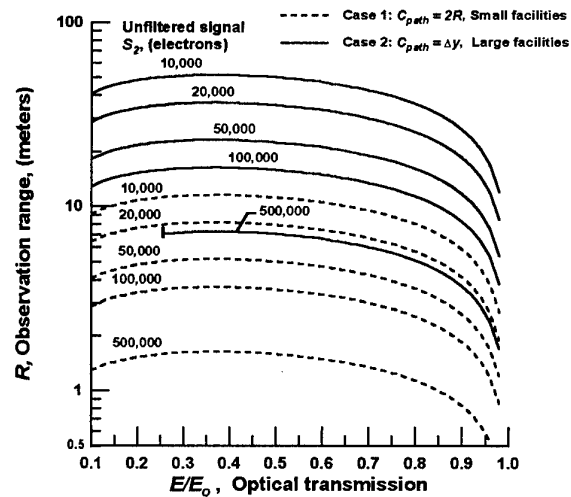


Fig. 7. Estimated observation ranges for selected unfiltered scattering signals, S_2 , and a constant ratio of laser sheet height to range, $\Delta y/R = 0.1$. Estimates are for a laser pulse energy = 300 mJ, pixel area = $25 \times 25 \mu\text{m}^2$, CCD detector quantum efficiency = 0.3, and f/1.4 collection optics.

attenuation of the laser and scattered light by the aerosol. In that case, the minimum dimension of the seeded region must be at least equal to the sheet height, so that $C_{path} = \Delta y$. However, in both cases the sheet height fills half of the field of view, so that $\Delta y/R = 0.1$ is maintained. In addition, the optical density has been limited to the maximum that is possible from customary smoke-generation equipment. However, that limit affects only the minimum optical transmission obtainable in Case 2 and only at the maximum signal that can be recorded (500,000 electrons). Hence, most types of commonly-used smoke generators are expected to be adequate for PDV applications at all useful ranges.

Fig. 7 indicates that for facility sizes less than 1.5 meters (Case 1), signals should be readily obtainable that will reach the saturation signal of the CCD array ($S_2 = 500,000$ electrons). In addition, it shows that when localized seeding is used (Case 2), accurate PDV measurements (i.e., for $S_2 \geq 10,000$ electrons) should be possible at ranges up to 50 meters when $\Delta y/R = 0.1$. Figure 7 also shows that the range becomes insensitive to optical transmission below $E/E_o \approx 0.8$, so that the use of greater

aerosol optical densities will not increase the signal levels or the useful range significantly.

8.2 Minimum Resolved Velocity Capabilities

The minimum resolved velocity is estimated by combining a realistic model of the noise sources in the PDV signals with the spectral response function of the iodine vapor filter. The results of the previous estimates¹ are upgraded here to match the radiometric noise parameters to those determined experimentally as described in Ref. 2, and to add the effects of speckle noise. The assumed detector parameters simulate state-of-the-art, commercially available, scientific-grade, CCD arrays selected because of their suitability for PDV measurements. Specifically, they pertain to a 576 by 384 pixel array with a readout rate of 430 kHz, cooled to -50 °C, and with 16-bit digital resolution. The combined readout noise, dark charge noise, and digital uncertainty is then only ± 2 counts out of 50,000. However, signal-dependent photon-statistical noise and uncorrelated speckle noise will add to that value.

The estimated minimum resolved velocities are shown in Fig. 8 for a data analysis that incorporates 3x3 binning. The response function is the same as shown in Fig. 2. The range of mean velocities for each case shown is limited by the dynamic range of the response function, which was confined to signal ratios between .05 and .95. The laser frequency was chosen to give an unshifted filter transmission of 0.2, which encompasses a wider range of positive mean velocities. Similar curves, predicted for the laser tuned to frequencies with an unshifted filter transmission closer to 0.5, will have the nearly same dynamic range of mean velocities and minimum resolved velocities, but will be shifted to lower mean velocities. This feature allows the dynamic range of the velocity measurements to be adjusted to match the experiment. Other schemes have been proposed that extend the dynamic range by adding an inert gas to the cell vapor mixture to reduce the response function sensitivity.⁵ Two unfiltered signal levels are represented in Fig. 8; one at the minimum useful value (10,000 electrons) and one that is mid-range (250,000 electrons) for a CCD detector with a well depth of 500,000 electrons. Two noise models are also represented; one in which the speckle

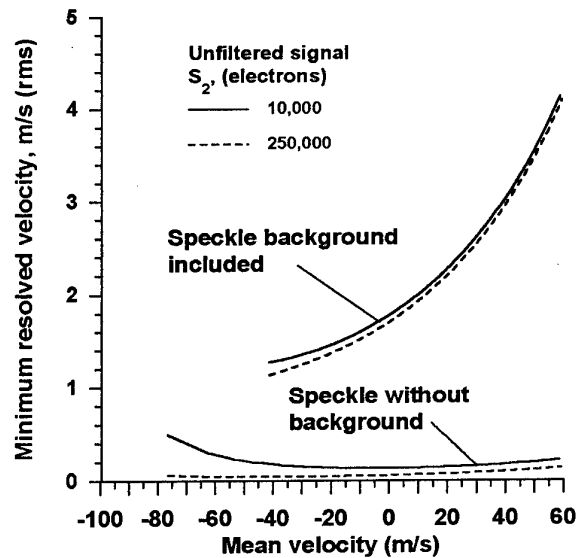


Fig. 8. Estimated minimum resolved velocities using a PDV noise model for selected unfiltered scattering signals, S_2 , with and without the constant speckle background represented by $NSR_{12}=0.4$. Both cases assume 3x3 binning.

background is included and one without it. Because the speckle background is represented by a constant $NSR_{12} = 0.04$ that dominates all other noise sources, the minimum resolved velocities predicted with it included depend mainly on the average signal ratio and follow the shape of the response function. They are relatively insensitive to the magnitude of the unfiltered signal level because the signal-dependent noise is not the primary contributor. However, without the speckle background, the minimum resolved velocities are nearly an order of magnitude lower and show a primary dependence on the unfiltered signal level. These results motivate the search for a means of reducing the speckle background. In any case, the lowest resolved velocities in Fig. 8 agree with the rotating wheel results and show that the resolution of single-pulse velocities below 2 m/s should be possible. When pulse averaging for N_{pulse} pulses is incorporated, minimum resolved velocities will be reduced by a factor of $(1/N_{pulse})^{1/2}$. Thus, the averaging of velocity fields from 100 laser pulses should provide averaged velocity resolutions as low as 0.2 m/s.

Figures 7 and 8 are related by their common values of the unfiltered signal level, S_2 . They com-

bine to show that single-pulse PDV measurements with minimum resolved velocities below 2 m/s should be possible in aerodynamic test facilities with sizes to tens of meters.

9. SUMMARY

The main objective of this study has been to evaluate the application of Planar Doppler Velocimetry (PDV) using a pulsed laser to low-speed flows that are typical of large-scale wind tunnel facilities. The predictions of minimum resolved velocities are improved by including experimentally characterized noise sources and are verified by PDV measurements of the known surface speed of a rotating wheel. In addition, PDV measurements in the flow of a low-speed, unsteady, jet flow demonstrate a procedure that measures both average flow velocities and their fluctuations in a way that is compatible with large wind tunnel operations. Finally, an aerosol scattering model is combined with a model of the noise sources in a PDV measurement to estimate the limiting facility sizes and minimum resolved velocities that are possible with a high-fidelity PDV system using a pulsed laser. In general, this study indicates that PDV velocity field measurements, using commercially available, Nd-YAG laser and CCD imaging systems, should be possible at ranges of tens of meters, and with single-pulse, minimum resolved velocities below 2 m/s.

The advantages of PDV over current Laser Doppler Anemometry and Particle Image Velocimetry techniques appear to be significant for applications to large aerodynamic facilities. In particular, the main attributes of PDV that are not matched by the other methods are: (a) PDV with a pulsed laser can provide all three components of velocity, everywhere in the field of a single light sheet, from individual laser pulses, while using relatively simple image processing and data analysis procedures, (b) PDV does not require the alignment of multiple laser beams or light sheets, thereby relaxing the sensitivity of the optical system to facility movement or vibration and reducing the complexity of its installation and operation, and (c) PDV does not require the optical resolution or tracking of individual particles or aerosol gradients, thereby relaxing the control requirements for seed material densities and

sizes, extending the useful observation range, and possibly even allowing the use of intrinsic smoke or dust that may be present in the flow of some facilities or flight environments. Although the other methods can usually provide lower minimum resolved velocities, they appear to become advantageous only when lower velocity resolutions are a key requirement in the aerodynamic experiment.

References

1. McKenzie, R.L., "Measurement Capabilities of Planar Doppler Velocimetry Using Pulsed Lasers," *Applied Optics*, Vol. 35, No. 6, 20 Feb., 1996, pp.948-964. Also AIAA Paper 95-0297.
2. McKenzie, R.L., "Planar Doppler Velocimetry Performance in Low-Speed Flows," Paper 97-0498, AIAA 35th Aerospace Sciences Meeting, Jan. 6-10, 1997, Reno, NV.
3. Komine, H., Brosnan, S.J., Litton, A.B., and Stappaerts, E.A., "Real-Time, Doppler Global Velocimetry," Paper 91-0337, AIAA 29th Aerospace Sciences Meeting, Jan. 7-10, 1991, Reno, NV.
4. Meyers, J.F., "Doppler Global Velocimetry. The Next Generation?," Paper 92-3897, AIAA 17th Aerospace Ground Testing Conference., July 6-8, 1992, Nashville, TN.
5. Elliott, G.S., Samimy, M., and Arnette, S.A., "Details of a Molecular Filter-Based Velocimetry Technique," Paper 94-0490, AIAA 32nd Aerospace Sciences Meeting, Jan. 10-13, 1994, Reno, NV.
6. Smith, M.W., Northam, G.B., and Drummond, J.P., "Application of Absorption Filter Planar Doppler Velocimetry to Sonic and Supersonic Jets," *AIAA Journal*, Vol. 34, No. 3, March 1996, pp. 434-441.
7. Clancy, P.S and Samimy, M., "Multiple-Component Velocimetry in High Speed Flows Using Planar Doppler Velocimetry," Paper 97-0497, AIAA 35th Aerospace Sciences Meeting, Jan. 6-10, 1997, Reno, NV.
8. Gerstenkorn, S. and Luc, P., "Identification des Transitions du Systeme (B-X) de la Molecule d' Iode et Facteurs de Franck-Condon 14000-15600 cm^{-1} ," Publication of C.N.R.S., Laboratoire AIME-COTTON, C.N.R.S., II - 91405, Orsay, France, 1986.
9. Forkey, J.N., Finkelstein, N.D., Lempert, W.R., and Miles, R.B., "Demonstration and Characterization of Filtered Rayleigh Scattering for Planar Velocity Measurements," *AIAA Journal*, Vol. 34, No. 3, March 1996, pp. 442-448.

Intérêt de l'Utilisation d'une Source Laser Accordable en Vélométrie Doppler Globale

B. Leporcq, J.-F. Le Roy, B. Pinchemel *, S. Hostyn
Office National d'Etudes et de Recherches Aéronautiques
Institut de Mécanique des Fluides de Lille
5 Boulevard Paul Painlevé 59045 Lille Cedex France

* Laboratoire de Dynamique Moléculaire et Photonique, URA CNRS 779 Université des Sciences et Technologies de Lille,
Centre d'Etudes et de Recherches Lasers et Applications, UFR de Physique Bât P5 59655 Villeneuve d'Ascq Cedex - France

1. SOMMAIRE :

La Vélométrie Doppler Globale est une méthode non intrusive basée sur la mesure du décalage Doppler de la lumière diffusée par un écoulement ensemencé en particules illuminées par un plan laser à la fréquence ν . Observé à travers une cellule d'iode tout décalage Doppler est traduit immédiatement en une variation de l'absorption de la lumière. Cette technique permet de donner le champ des vitesses de l'écoulement ensemencé, à une cadence d'acquisition qui ne dépend que du dispositif d'enregistrement.

Les études réalisées à ce jour utilisent un laser à argon ionisé monomode dont la raie verte est fortuitement accordée sur deux raies d'absorption non résolues de l'iode dont l'intensité dépend fortement de la température. Pour s'en affranchir, un laser à colorant continu accordable en fréquence a été utilisé, permettant un choix extrêmement aisé d'une raie d'absorption d'une molécule dont la population est peu dépendante de la température et le profil plus ou moins raide en fonction de la gamme de vitesse à mesurer.

Les premiers tests ont été réalisés sur un disque tournant, les vitesses déterminées par DGV sont en bon accord avec celle mesurées par tachymétrie, puis des mesures ont été réalisées en soufflerie. Le point est fait sur les améliorations apportées pour augmenter la précision.

2. INTRODUCTION

Les moyens de mesures des vitesses en aérodynamique étaient, pendant de nombreuses années, limités aux sondes à fil chaud ou anémométriques introduites dans l'écoulement et dont l'embout coïncide avec le volume de mesure. Ces dispositifs classiques présentent l'avantage d'une grande simplicité d'utilisation. Les inconvénients inhérents à de telles sondes proviennent principalement du champ de perturbation créé par la sonde qui modifie la grandeur locale au point de mesure considéré.

Les techniques optiques non intrusives de vélocimétrie laser interférentielle et de vélocimétrie bipoint [1, 2] ne permettent d'accéder à la mesure de la vitesse qu'en un point de l'écoulement, et sont inadaptées aux écoulements perturbés dans lesquels les informations spatiales varient plus rapidement que le temps d'acquisition des données.

Dans le domaine d'investigation des écoulements tourbillonnaires, l'apport de la Vélométrie Doppler Globale, en anglais DGV (Doppler Global Velocimetry) est capital. En effet, cette méthode non intrusive permet non seulement de visualiser un écoulement mais aussi d'obtenir les caractéristiques du champ de vitesse en de nombreux points de celui-ci en un temps très court, ce qui n'impose plus à l'écoulement d'être stationnaire. L'application de

cette méthode de mesure s'ouvre donc à des essais en souffleries et à des essais en vol de maquettes de laboratoire au cours desquels on s'intéresse particulièrement à l'évolution temporelle du sillage.

3. PRINCIPE DE LA VÉLOCIMÉTRIE DOPPLER GLOBALE

La tomoscopie laser est une technique très utilisée depuis plusieurs décennies pour visualiser les écoulements et mettre en évidence la structure des tourbillons. Pour cela un moyen de visualisation tel qu'une caméra observe un plan laser rendu visible par un ensemencement de l'écoulement avec des particules [3].

Les premiers travaux concernant la DGV ont débuté aux U.S.A. en 1991. La DGV est une nouvelle technique non intrusive qui permet de déterminer le champ de vitesse à partir de la lumière diffusée par les particules traceur de l'écoulement. La mesure est effectuée simultanément pour tous les points du plan. Le principe de la DGV, décrit dans les travaux de J. F. Meyers et coll [4, 5], est basé sur la mesure du décalage Doppler de la lumière diffusée par des particules ensemencant l'écoulement et éclairées par une nappe laser à la fréquence ν accordée sur une raie d'absorption de l'iode. Les particules suivant un écoulement de vitesse moyenne V , et traversant un faisceau laser à la fréquence ν sont d'abord considérées comme récepteurs en mouvement, puis comme sources en mouvement. La relation donnant le décalage en fréquence reçu par le détecteur est :

$$\Delta\nu = \frac{v(\vec{o} - \vec{i})}{c} \cdot \vec{v} \quad (1)$$

où \vec{i} représente le vecteur unitaire dans la direction de propagation du laser, \vec{o} le vecteur unitaire dans la direction d'observation et c la célérité de la lumière. Vue à travers une cellule remplie de vapeur d'iode jouant le rôle de discriminateur de fréquence, la variation de fréquence de la lumière diffusée est immédiatement traduite par une variation d'absorption. La variation locale d'intensité correspond à la mesure locale de la vitesse. Cette variation d'intensité lumineuse ainsi produite est normalisée par rapport à une image de référence. La fonction de la caméra de référence est d'obtenir la carte d'intensité issue du champ de particules illuminées sans l'influence du filtre. Le traitement de l'information est effectué à la vitesse d'acquisition du moyen de prise de vue utilisé.

Le montage de la figure 1 peut se décomposer en trois parties : la source lumineuse, la cellule à iode, et la partie détection et acquisition des informations qui s'articulent autour d'un écoulement ensemencé en particules.

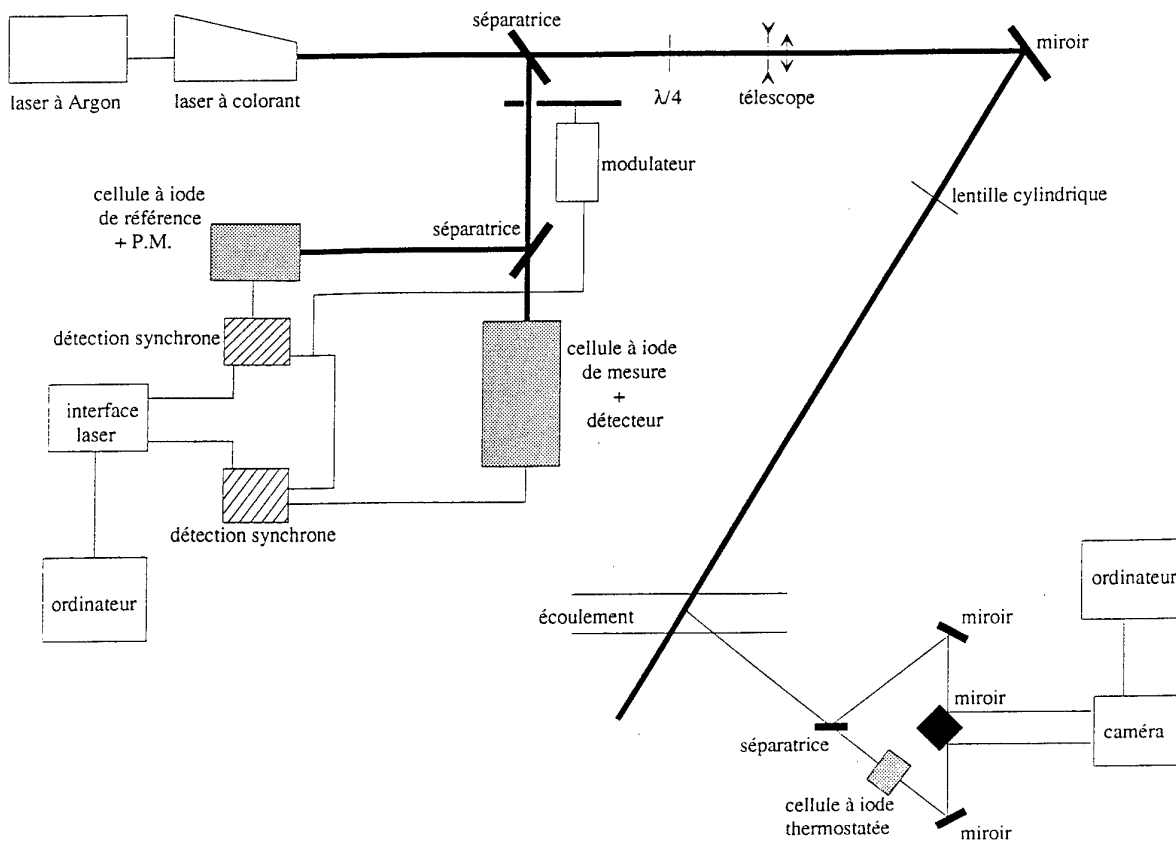


Figure 1 : Montage expérimental de la DGV

La partie du rayonnement la plus intense (95%) forme un plan de lumière. La lumière diffusée par les particules traceur de l'écoulement est visualisée dans notre installation par une caméra unique suivant un chemin optique de référence et un chemin traversant la cellule d'iode. La deuxième partie du faisceau (5%) est envoyée sur une cellule à iode de référence pour étudier la fluorescence et l'absorption de l'iode. L'enregistrement de la fluorescence par un photomultiplicateur, associé à un filtre passe-haut, permet d'identifier les raies de l'iode. Le photomultiplicateur et l'amplificateur à détection synchrone sont reliés à l'interface du laser. Un boîtier de commande permet de fixer la fréquence d'émission du laser très précisément à mieux de 1MHz dans le profil de la raie.

Le rapport des niveaux d'éclairage obtenus pour les couples de pixels de référence et de mesure permet de remonter à la vitesse locale. Ce traitement permet d'éliminer les variations d'intensité causées par d'autres phénomènes que ceux liés à la vitesse (variation en densité de particules, diffusion de lumière, réflexions parasites, taille de particules et puissance laser par exemple).

En déplaçant le détecteur, donc en modifiant la direction ($\vec{O} \cdot \vec{i}$) ou en changeant la direction de propagation de la nappe laser (\vec{i}) il est possible de mesurer d'autres composantes de la vitesse. Il est facile de concevoir une technique de DGV à trois composantes en utilisant plusieurs détecteurs ou de multiples faisceaux avec différentes directions de propagation.

4. EMISSION LASER

4.1 Laser à fréquence fixe

Les premières expériences [4, 5] ont utilisé un laser à argon rendu monomode longitudinal à 514,5nm. Un laser fonctionnant sur un seul mode longitudinal et un seul mode transverse est la meilleure source de lumière monochromatique connue. La largeur spectrale d'un laser monomode (3 MHz) est très inférieure à celle de la double raie d'absorption P13 -R15 (43-0) de l'iode, et même souvent inférieure à la largeur naturelle (1,5 GHz) due à la durée de vie finie de l'état excité. Une des méthodes utilisées pour obtenir un rayonnement laser monomode [6], est celle de l'étalon intracavité. De fortes pertes sont générées pour tous les modes sauf un en introduisant une petite cavité Fabry-Pérot, d'espacement fixe, dans la cavité laser. La cavité est une lame de verre à faces rigoureusement parallèles, à faible facteur de réflexion. Typiquement, au moins 75% de la puissance, qui était répartie dans l'ensemble des modes qui oscillaient simultanément avant l'introduction de la lame, peut se retrouver dans le mode unique obtenu. En inclinant plus ou moins la lame par rapport à l'axe du laser on peut changer la fréquence de résonance privilégiée, à l'intérieur de la largeur de la raie. Dans cette étroite limite, la fréquence du laser est accordable, soit par inclinaison de la lame étalon, soit en faisant varier la température de celle-ci. Pour un laser à argon ionisé, une largeur de raie de quelques MHz est obtenue grâce à l'utilisation d'un interféromètre Fabry-Pérot intracavité et de deux miroirs équipés de cales piézoélectriques installés sur un résonateur en Invar.

4.2 Laser accordable en fréquence

L'émission laser issue d'un laser à colorant est généralement monomode (500KHz) et accordable. Le milieu actif est un colorant organique, dont la particularité est de présenter une émission qui fluoresce sur une très large bande. Le colorant est excité par l'absorption de lumière fournie par une source de lumière extérieure et émet des radiations de longueur d'onde plus élevée que celle de la lumière de pompage. Ces lasers doivent être pompés par une autre source laser émettant dans le voisinage du maximum de la bande d'absorption du colorant. Le choix du colorant est conditionné par le domaine spectral d'émission désiré, domaine dans lequel la longueur d'onde peut être accordée à toute valeur au moyen d'un filtre de Lyot et de deux étalons de Fabry Péro... Tous les colorants n'ont pas le même rendement : les rhodamines 110 et 6G sont de loin les colorants qui présentent le meilleur rendement : pour une puissance de pompage de 8W (laser Ar+), la Rhodamine 6G peut émettre une puissance maximale d'environ 1,5 W en fonctionnement monomode dans la région 570-620nm.

Afin d'exploiter de manière optimale les propriétés d'accordabilité de cette cavité laser et de réduire encore la largeur de la raie monomode, la source laser est munie d'un dispositif de stabilisation en fréquence et de mesure précise de la longueur d'onde. L'ensemble des éléments constituant le laser à colorant commercialisé par COHERENT est piloté par un système informatique AUTOSCAN. Ce système permet le pilotage en fréquence du laser, la gestion des séquences de balayage en fréquence et la création de fichiers comportant la fréquence optique et plusieurs données acquises sur des entrées périphériques sous forme d'une tension analogique [0 - 10 V].

La DGV nécessite une nappe laser continue présentant des paramètres géométriques réglables (hauteur, divergence et épaisseur). Il est possible d'utiliser un ensemble compact associant des lentilles sphériques et cylindriques qui permet, sans changer les composants, d'obtenir une nappe laser à bords parallèles et de largeur réglable [7].

Pour des besoins en soufflerie où la nappe laser doit être de grande dimension, il faut :

- soit se contenter d'une nappe à bords divergents qui nécessite de repérer l'angle d'illumination de chaque point du plan ;
- soit utiliser un système comprenant un miroir multifacettes placé à la focale d'un miroir sphérique ou d'une lentille de Fresnel de très grande dimension. Dans ce cas le balayage du faisceau ne permet pas de réaliser des mesures pour des écoulements fortement instationnaires.

Les lasers à argon classiquement utilisés en DGV travaillent à une puissance maximale de l'ordre de 5W. Le laser à colorant peut fournir une puissance laser monomode accordable de 2W.

5. LE DISCRIMINATEUR DE FRÉQUENCE

5.1 La cellule d'iode

La cellule d'iode est constituée d'un cylindre en verre fermé par deux fenêtres en verre à faces parallèles dans laquelle ont été placés

quelques cristaux d'iode avant d'être scellée sous vide. Pour éviter la condensation de l'iode sur les parois de la cellule, la quantité d'iode introduite est totalement vaporisée à la température de thermostatisation. La pression de vapeur saturante de l'iode solide est donnée en fonction de la température par la loi de Dewar [8] :

$$\log(P(\text{mmHg})) = 10,0392 - (3137/T) \quad (2)$$

La température de remplissage de la cellule à iode est de 313K. La cellule est installée dans une enceinte thermostatée à 323K à ± 1 K.

5.2 Choix des raies et prise en compte de la structure hyperfine

La molécule d'iode présente deux états électroniques principaux : l'état X, état de plus basse énergie ou état fondamental et l'état B, un état excité. Il existe de nombreuses transitions entre l'état X et l'état B conduisant à un spectre d'absorption comportant un grand nombre de raies. Le spectre d'absorption de la molécule d'iode est parfaitement identifié, il sert de référence pour calibrer les spectres d'autres molécules [9]. Les raies d'absorption ou d'émission des molécules ne sont jamais tout à fait monochromatiques : elles présentent, à des pressions très faibles et à très basse température, une largeur dite naturelle et lorsque la pression et la température augmentent, les raies subissent différents types d'élargissement. A basse pression, inférieure à quelques centaines de Pa, les raies subissent principalement un élargissement Doppler. La vitesse due à l'agitation thermique des espèces absorbantes induit un décalage fréquentiel autour de la fréquence centrale ν_0 , par effet Doppler. L'élargissement obtenu est inhomogène puisque chaque molécule émet à une fréquence différente, proportionnelle à sa vitesse propre. La largeur Doppler de la raie à mi-hauteur est :

$$\Delta \nu_D = \sqrt{\frac{8 k T \ln 2}{m c^2}} \nu_0 \quad (3)$$

avec :

m, masse moléculaire de l'espèce absorbante ou émettrice,
c, la célérité de la lumière,
k, constante de Boltzman,
T, la température absolue.

Les différents niveaux rotationnels présentent une structure hyperfine due au couplage entre le moment cinétique de rotation et le moment cinétique nucléaire. Pour la molécule d'iode chaque niveau rotationnel de nombre quantique pair se subdivise en 15 composantes hyperfines et chaque niveau de nombre quantique impair en 21 composantes. La structure hyperfine conduit à un élargissement inhomogène de la raie, ayant des conséquences similaires à l'élargissement par effet Doppler, c'est-à-dire un étalement de la fréquence centrale de la transition. La figure 2 présente l'enregistrement de la transmission des raies d'absorption de l'iode R70 (23-0) et P 73 (23-0) en fonction de la fréquence.

Le spectre d'absorption montre des raies dissymétriques dues à la présence d'une structure hyperfine non résolue et une forme différente suivant le caractère pair ou impair de la raie. Le profil de transmission de la raie paire est plus "tassé" que celui de la raie impaire qui couvre de façon évidente un plus vaste domaine spectral.

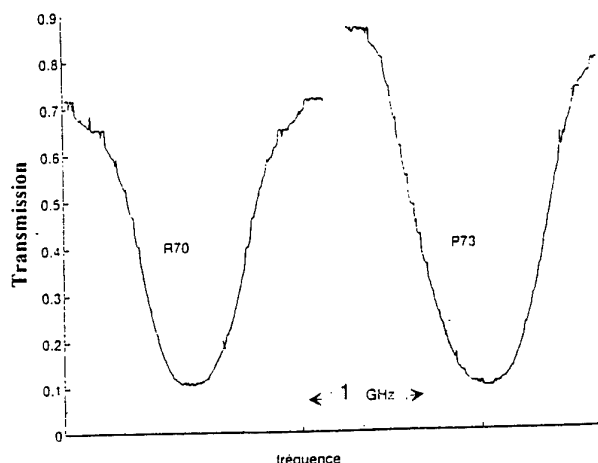


Figure 2 : Spectres de transmission des raies R70 et P73

Pour réaliser le discriminateur de fréquence, le choix se porte sur une raie d'absorption de l'iode parfaitement résolue dans la gamme d'émission du laser présentant une forte absorption. La raie doit présenter un profil d'aile le plus linéaire possible. La longueur du profil doit être choisie en fonction du domaine de vitesse étudié de manière à contenir le décalage induit par effet Doppler. Pour les gammes de vitesses élevées, comprises entre 150 m/s et 450 m/s, et pour des variations de vitesses de l'ordre de plus ou moins 150 m/s, l'amplitude du décalage Doppler, pour des angles d'observation classiques, est d'environ 0,3 GHz. Pour des vitesses plus élevées trois solutions sont possibles.

La première consiste à accorder le laser sur une fréquence située en dehors de la raie de l'iode afin que la fréquence de la lumière diffusée après décalage Doppler soit ramenée dans une aile du profil d'absorption.

La seconde technique consiste à rechercher dans le spectre d'absorption une zone d'absorption mal résolue dans laquelle plusieurs raies superposées conduisent à un élargissement plus important qu'une raie isolée.

La troisième méthode consiste à passer d'un profil Doppler de la raie à un profil collisionnel en jouant sur la pression partielle de gaz neutre dans la cellule [10, 11]. Dans ce dernier cas un gain important en domaine de fréquence peut être obtenu aux dépens de la sensibilité. Pour le domaine des faibles vitesses, entre -50 m/s et + 50 m/s, le choix se portera sur des raies présentant un profil le plus raide possible. Dans le cas de l'iode moléculaire, le nombre de composantes hyperfines (15 ou 21) facilite ce choix. Une alternative consisterait à choisir une autre molécule présentant une structure hyperfine plus étroite, c'est à dire un profil de raie d'absorption plus raide permettant d'accéder à une gamme de vitesse inférieure à plus ou moins 50 m/s sans nuire à la sensibilité. C'est le cas en particulier du Brome.

5.3 Mesure de l'absorption de l'iode

L'étalonnage en fréquence d'une raie d'absorption de l'iode est réalisé directement dans la zone étudiée au cours d'un balayage en fréquence. La figure 3 donne l'évolution de l'absorption pour la raie P75 (23-0). Une partie de la lumière diffusée par les particules traceur maintenues à vitesse nulle dans la zone de l'écoulement

traverse la cellule d'iode thermostatée placée devant la partie mesure de la caméra.

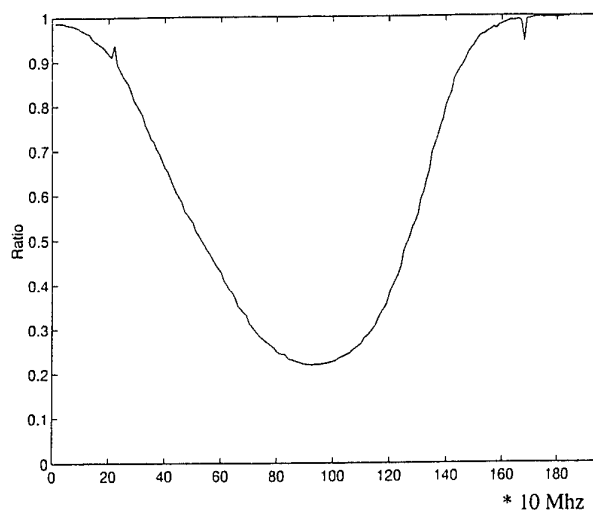


Figure 3 : Evolution de l'absorption en fonction de la fréquence pour la raie P75 (23-0)

La raie P75 (23-0) présente une évolution du profil dissymétrique. L'aile droite de la raie d'absorption présente un profil quasiment linéaire dans sa partie médiane avec une pente beaucoup plus raide (+7,35 MHz/ % absorption) que pour sa partie gauche (-12,52 MHz/ % absorption). Le spectre d'étalonnage est obtenu en effectuant une acquisition d'une image par pas de 10MHz lors du balayage en fréquence de la raie à la cadence d'acquisition de la caméra. Afin de ne pas bruyter les images, celles-ci sont stockées directement dans la mémoire RAM de l'ordinateur. La caméra utilisée est une caméra COHU 4912-5000. Pour chaque partie de la raie d'absorption un polynôme d'ordre 5 permet de recalculer le décalage Doppler en fonction de la variation d'absorption pour le dépouillement des images de DGV.

Le choix de la raie d'absorption se porte sur une raie très intense permettant l'obtention d'une pente du profil d'absorption importante. Un certain nombre de paramètres spectroscopiques (facteurs de Franck Condon, taux d'absorption, ...) sont à prendre en considération pour se placer dans les conditions expérimentales optimum. Celle-ci sont aisément remplies grâce à la souplesse du laser accordable en fréquence.

5.4 Dépendance en température de la raie d'absorption

La variation de pression de vapeur saturante de l'iode varie fortement avec la température (2). Dans le cas de la DGV, il apparaît immédiatement que la stabilisation en température de la cellule à iode est importante puisque dans une gamme de température de 273K à 340K, un défaut de thermostatisation de 1K conduit à une fluctuation de pression comprise entre 5 et 10%. Il est donc nécessaire de stabiliser la température de la cellule à une valeur inférieure à $\pm 0,1K$ afin de limiter à $\pm 1\%$ l'erreur absolue sur la pression. Comme il a déjà été précisé, ce problème peut être en partie résolu en fabriquant une cellule à iode scellée sous vide dans laquelle des cristaux d'iode ont été placés en masse suffisante pour atteindre la concentration nécessaire à l'absorption requise,

puis de chauffer cette cellule à une température supérieure à la température de vaporisation T . Dans ces conditions, même en chauffant la cellule à une température supérieure à T , la concentration en iode ne variera pas.

Seule la population rovibrationnelle évoluera. En effet, la fraction de Boltzmann (f_i) des niveaux rovibrationnels fondamentaux $v''=0$, J'' varie en fonction de la température. L'évolution de la fraction rotationnelle Δf_r en % / K est inférieure à $\pm 0,02$ %/K pour $J''=75$ alors qu'elle atteint 0,3%/K pour $J''=15$ dans la gamme de température comprise entre 300K et 325K. Une stabilisation en température de ± 1 K est donc relativement facile à obtenir. Le choix des raies d'absorption de l'iode s'orientera vers des raies présentant un niveau rotationnel J'' correspondant au maximum de la fraction de Boltzmann f_i dans la gamme de température choisie [11]. Ensuite il reste à accorder la fréquence du laser sur une raie d'absorption. Le choix correspond à la raie $v''=0$; $J''=75$ (23-0) à la fréquence de 519813,4126GHz. Dans ces conditions, une variation en température de 3K se traduira par une variation en concentration de l'iode dans l'état J'' de 0,05%.

La figure 4 présente la variation de l'absorption maximale dans la cellule en fonction de la température pour la raie P75 (23-0). La transmission a été obtenue en jouant non pas sur l'épaisseur de la cellule d'iode mais sur la concentration en iode, tout en gardant une pression inférieure à 1500 Pa pour éviter un élargissement collisionnel des raies de l'iode.

5.5 Cellule de brome

Selon la gamme de vitesse rencontrée, il est possible d'appliquer la technique de discrimination fréquentielle sur une autre molécule que l'iode afin d'obtenir une évolution d'absorption différente. Dans le cas des vitesses faibles, l'utilisation du brome se justifie par la présence de structures hyperfines à 6 ou 9 composantes au lieu de 15 ou 21 pour l'iode, d'où un spectre d'absorption moins large. Les faibles vitesses seront alors déterminées avec une plus grande précision. De plus le brome présente l'avantage d'être une molécule relativement bien caractérisée par les spectroscopistes. La pression de vapeur saturante varie en fonction de la température suivant la loi :

$$P_{br2}(\text{Pa}) = \exp(-41,885 + 0,42776 T - 0,0013747 T^2) \quad (4)$$

Pour la DGV, la stabilisation en température de la cellule à brome est encore plus délicate que dans le cas de l'iode puisqu'une variation de température de 1K conduit à une fluctuation de pression comprise entre 4 et 6%. Il est donc nécessaire de stabiliser la température de la cellule à mieux de $\pm 0,2$ K pour avoir une erreur absolue sur la pression de vapeur saturante inférieure à $\pm 1\%$. De même que pour la cellule d'iode, en utilisant une cellule de brome scellée sous vide, en augmentant la température la concentration en brome ne variera pas. Il suffit alors de se placer au minimum de variation de la fraction de Boltzmann correspondant à $J''=50$ pour éviter une évolution de la population rovibrationnelle trop importante. Pour une variation en température de ± 5 K l'évolution de la fraction rotationnelle est inférieure à $\pm 0,1\%$ pour des J'' compris entre 50 et 70. Le mode opératoire sera alors le même que pour la cellule d'iode, c'est-à-dire qu'il suffira de chauffer la cellule de brome à une température supérieure à la température utilisée pour le remplissage et d'accorder la fréquence du laser sur une raie d'absorption J'' proche de 60.

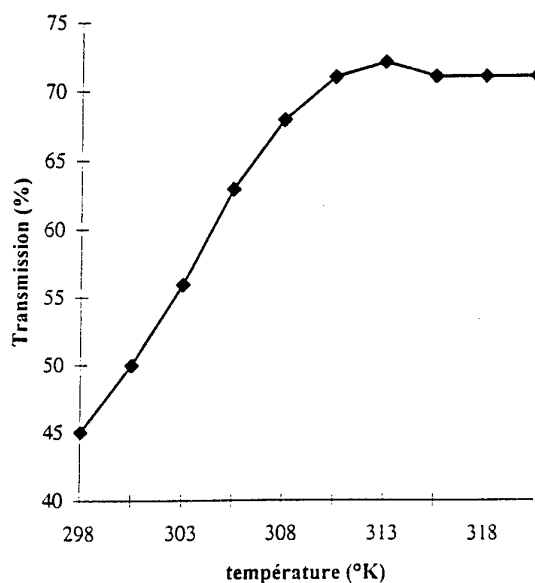


Figure 4 : Evolution du maximum d'absorption en fonction de la température de la cellule d'iode pour la raie P75 (23-0)

6. AMÉLIORATIONS DES MESURES

6.1 Optimisation des mesures de DGV

La qualité des mesures de DGV nécessite l'optimisation de plusieurs points. Certains ont déjà été présentés, il s'agit en particulier :

- de la possibilité de choisir une raie d'absorption de l'iode en fonction du domaine de vitesse à étudier ;
- du choix d'une raie d'absorption peu sensible à des fluctuations de température ce qui simplifie la thermostatisation de la cellule d'iode ;
- de l'étalonnage sur site de l'absorption en fonction de la fréquence d'émission du laser avec des pas en fréquence très faible pour modéliser le mieux possible l'évolution de la loi d'absorption en fonction du décalage en fréquence.

D'autres points importants doivent être pris en compte pour améliorer la précision de mesures de DGV, il s'agit en particulier de l'ensemencement en particules, de la prise de vue, et du traitement des images.

6.2 Ensemencement en particules

L'ensemencement en particules traceur de l'écoulement est un problème délicat commun à plusieurs techniques aussi bien qualitatives (tomographie) que quantitatives (vélocimétries interférentielle et bipoint, PIV et DGV). Le problème principal concerne le suivi le plus fidèle possible des particules dans les zones à fort gradient de vitesse. Pour cela les particules submicroniques suivent mieux l'écoulement que les particules de taille supérieure, mais cela au détriment de la diffusion de la lumière qui est fonction du paramètre de taille. Il a été choisi de tracer l'écoulement avec des particules d'encens. Ces particules sont submicroniques, et polluent très peu les hublots de visualisation.

6.3 Etalonnage des caméras

La DGV met en œuvre des caméras CCD. Chaque pixel de la caméra ne donne pas une réponse équivalente aux autres pixels pour un même niveau d'éclairement. De même le courant d'obscurité varie pour chaque pixel. Le niveau de gris de chaque pixel est donc corrigé en fonction d'une loi d'étalonnage prenant en compte la réponse pour différents niveaux de gris et du courant d'obscurité. Différentes lois de corrections ont été utilisées, la loi faisant appel à un polynôme du deuxième degré donne de bons résultats. Cet étalonnage est réalisé à partir de prises de vue pour différents diaphragmes d'un écran monochrome éclairé uniformément. Cette correction est de loin la plus importante.

6.4 Méthode optique de mesure d'angles

Comme le montre la figure 5, la composante de vitesse mesurée est la projection de la vitesse sur le vecteur $\vec{o} - \vec{i}$.

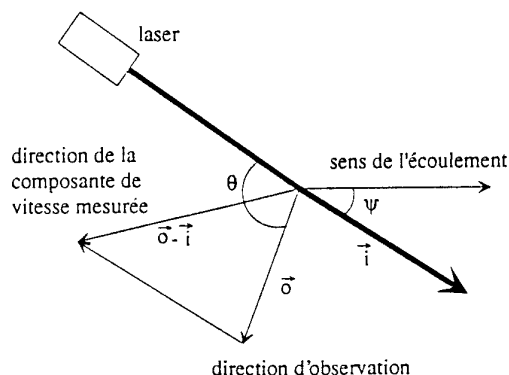


Figure 5 : Position des angles d'observation et d'illumination en DGV

Le décalage Doppler présente une forte dépendance angulaire qui s'exprime alors par :

$$\Delta v = v \left| \frac{v}{c} \right| [\cos(\theta + \psi) - \cos(\psi)] \quad (5)$$

avec θ l'angle entre le rayon laser et l'axe optique de la caméra, ψ l'angle entre le rayon laser et le vecteur vitesse. La projection du vecteur vitesse sur $\vec{o} - \vec{i}$ est proportionnelle à $\cos(\theta - \psi)$, et la projection de v sur $-\vec{i}$ est proportionnelle à $\cos \psi$. Il est nécessaire de mesurer au moins deux angles : l'angle entre la direction incidente de la lumière et la direction d'observation et l'angle entre la direction incidente de la lumière et l'axe principal de l'écoulement. Or, il s'avère qu'une imprécision de mesure de $\pm 1^\circ$ sur chaque angle induit une erreur totale de 1.5% sur la détermination de la vitesse. Une méthode précise de mesure de ces angles est donc indispensable. Cette méthode fait appel à des mesures par autocollimation du faisceau. Une erreur maximale de lecture sur chacune des positions est de $3'$, l'erreur totale sur la détermination de la vitesse est de 0.03%.

6.5 Traitement de l'image

La caméra CCD détecte une image de 752 pixels par 582 pixels sur une profondeur de 8 bits. Chaque image enregistrée est constituée

de deux demi-images (figure 6) : celle de droite correspondant au signal référence et celle de gauche correspondant au signal ayant traversé la cellule d'iode noté A.L.F. Pour éliminer les fluctuations de la lumière émise par le laser ainsi que les inhomogénéités du plan laser, l'image A.L.F. est normalisée par rapport à l'image de référence. Les deux images doivent alors être superposables.

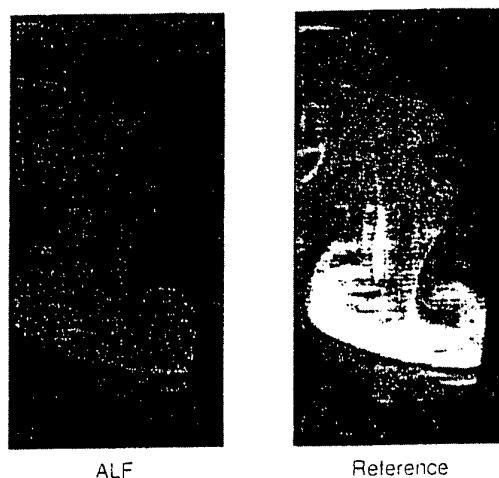


Figure 6 : Enregistrement d'une image de DGV

6.6 Recalage des images

L'enregistrement des deux images d'une mire montre que l'image A.L.F. est déformée par rapport à l'image de référence. En effet, celle-ci a subi des déformations dues principalement à la différence de chemin optique entre la lame séparatrice et le miroir, à la position du miroir qui n'est pas parfaitement perpendiculaire au plan laser, et à la présence des deux hublots de la cellule d'iode. L'image enregistrée est divisée en deux images de 376 pixels par 582 pixels chacune. Pour être superposables les deux images doivent avoir exactement la même taille et la même position. Celles-ci sont caractérisées par les coordonnées d'une vingtaine de points sélectionnés au pixel près sur chaque image.

Soient (x, y) et (x', y') les coordonnées respectives des points sélectionnés sur les images A.L.F. et référence. Donner à la mire "A.L.F." la même position et la même taille que la mire "Référence" revient à transformer les coordonnées (x, y) en (x', y') . Il s'agit de trouver la composition d'une rotation d'angle θ , d'une translation de coordonnées (h, k) et de deux homothéties (S_x, S_y) respectivement suivant x et y tels que :

$$\begin{aligned} x' &= S_x x \cos \theta - S_y y \sin \theta + h \\ y' &= S_y y \cos \theta + S_x x \sin \theta + k \end{aligned}$$

Cependant, étant donné que les points sont sélectionnés à plus ou moins un pixel près la transformation n'est pas exacte. Ainsi, la transformation recherchée est celle minimisant l'erreur :

$$E = \sum \{ [x'_i - (S_x x_i \cos \theta - S_y y_i \sin \theta) - h]^2 + [y'_i - (S_y y_i \cos \theta + S_x x_i \sin \theta) - k]^2 \}$$

L'étude de l'algorithme de minimisation est détaillée dans le

paragraphe suivant. Pour une sélection de 20 points, l'erreur E est inférieure à 0,4 pixel par point.

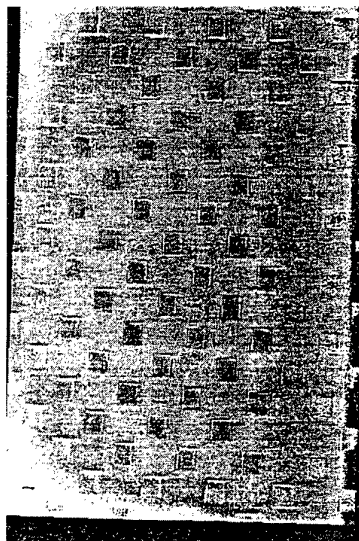


Figure 7 : Exemple de recalage d'une mire

6.7 Algorithme de minimisation

L'opération de minimisation de E est réalisée sous le logiciel MATLAB. L'algorithme de minimisation, ou méthode de descente, utilisé ici se base sur les techniques d'interpolation quadratique et cubique. Celui-ci fait appel à des processus itératifs du type :

$$x_{k+1} = x_k + \alpha^* p$$

où p détermine la direction de déplacement à partir du point x_k et α^* est un facteur dont la grandeur donne la longueur du pas dans la direction p.

Soit d la fonction à minimiser telle que :

$$d = \|F(A, x) - f(x)\|$$

Le problème ici consiste à déterminer le point le plus bas de l'ensemble K tel que :

$$K = \{(A, d) \mid \|F(A, x) - f(x)\| \leq d\}$$

Le principe de base de la méthode de la descente est le suivant : une première estimation (A_k, d_k) du point le plus bas (A^*, d^*) de K est donnée. Une direction descendante déterminée est suivie pour obtenir une estimation (A_{k+1}, d_{k+1}) pour laquelle $d_{k+1} < d_k$. Si K est un ensemble convexe, il existe un seul point pour lequel on ne peut aller plus bas, c'est le point le plus bas de K. Il est donc possible de trouver un système particulier engendrant une suite d'estimations toujours décroissantes et qui converge vers (A^*, d^*) . La méthode de descente comporte deux étapes : la détermination de la direction de descente p, et la détermination du déplacement limite le long de cette direction. Ici, une méthode polynomiale impliquant une interpolation est utilisée pour déterminer la direction p. L'interpolation quadratique prend en compte une fonction d'ordre 2 et l'interpolation cubique. Le minimum de ces fonctions est déterminé pour la valeur du déplacement limite le long de la direction de descente α^* . La détermination des coefficients des

deux équations est réalisée en combinant trois (cubique) ou quatre (quadratique) gradients. La direction de descente est déterminée en construisant une famille de normales à K dirigées vers l'extérieur.

6.8 Dégauchissement des images

L'image d'un plan laser vue par une caméra dont l'axe optique diffère de la normale conduit à une déformation de celle-ci. Un dégauchissement de l'image doit donc être effectué à la fois verticalement et horizontalement. La figure 8 présente les résultats d'une image vue sous un angle de 12° redressée verticalement puis horizontalement.

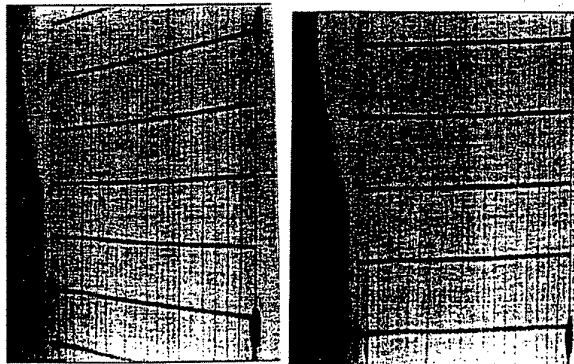


Figure 8 : Image de mire vue sous un angle de 12° puis dégauchie

7. APPLICATION À LA MESURE DE VITESSE PAR DGV

7.1 Détermination de la vitesse d'un disque en rotation

Les premiers travaux ont été effectués sur un disque tournant de 8cm de diamètre dont la vitesse de rotation, comprise entre 5000 et 30000 tours/minute, est mesurée par un tachymètre [12 à 14]. Le montage expérimental est sensiblement le même que précédemment, un faisceau de lumière parallèle à la fréquence ν du laser éclaire le disque de façon uniforme. La lumière diffusée par l'ensemble du disque est observée. La fréquence laser est fixée la plus proche possible de la fréquence du milieu de l'aile de la raie d'absorption choisie. Sur le diamètre vertical du disque est relevée l'intensité absorbée (figure 9). C'est en effet sur cette ligne que sont observées les variations des vitesses les plus grandes.

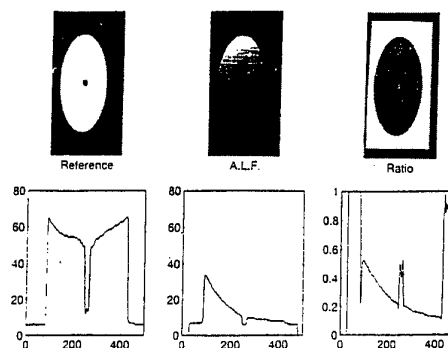


Figure 9 : Evolution de l'absorption le long d'un diamètre vertical d'un disque tournant

A chacune de ces intensités, est attribué, à partir de la courbe d'étalonnage de la raie en transmission en fonction de la fréquence, un décalage Doppler auquel correspond une vitesse. Les vitesses mesurées par DGV et tachymétrie sont en bon accord (figure 10).

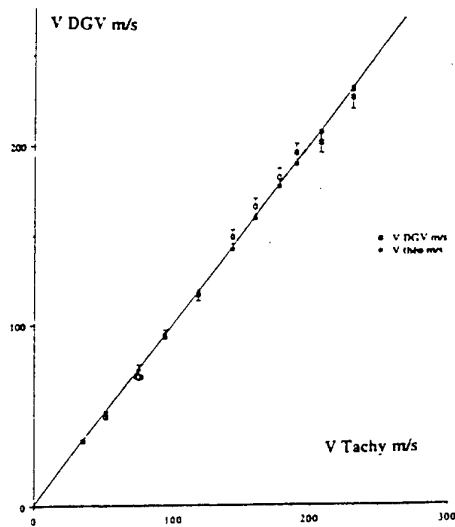


Figure 10 : Comparaison de la vitesse déterminée par DGV et par tachymètre.

7.2 Validation des mesures de DGV sur un écoulement

Afin de valider les mesures de DGV sur un écoulement, des essais ont été réalisés en soufflerie dans une veine vide. L'écoulement estensemencé par de la fumée d'encens. L'étalonnage de l'absorption en fonction de la fréquence a été réalisé sur un verre dépoli placé dans le plan laser ou sur la fumée d'encens maintenue à vitesse nulle. La figure 11 présente le balayage en fréquence de la raie P75(23-0) de l'iode pour deux écoulements ensemencés, l'un à vitesse nulle, l'autre à la vitesse de 57 m/s mesuré par Pitot.

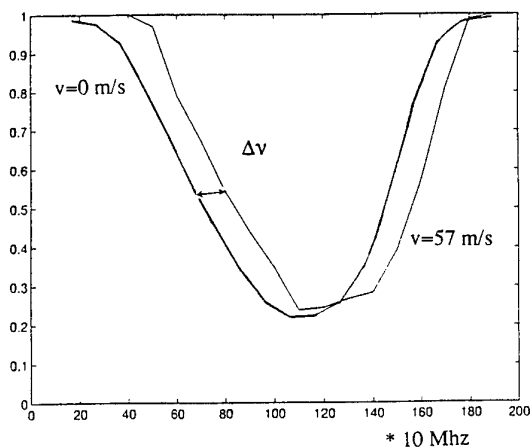


Figure 11 : Etalonnage de l'absorption à deux vitesses différentes en fonction de la fréquence [raie P75 (23-0)] .

Le balayage est réalisé à la cadence de 250 Mhz par seconde et l'enregistrement des images à la vitesse de 25 images par seconde.

Il apparaît immédiatement que les deux courbes présentent un décalage constant sauf dans la région du maximum d'absorption ce qui prouve que l'étalonnage de la raie peut être effectué à vitesse constante.

Sur la figure 12 sont comparées les mesures de DGV réalisées sur trois écoulements à vitesses différentes aux mesures effectuées par Pitot. Les résultats présentent une bonne concordance. Les mesures présentées, ont été réalisées à partir d'une image moyenne provenant de 150 images. Le traitement des images uniques a conduit à des résultats comparables. Pour les mesures déterminées par DGV deux calculs ont été effectués. Le premier modèle correspond à une approximation linéaire de l'évolution de l'aile droite de la raie d'absorption (noté DGV linéaire). Le deuxième modèle fait appel à une évolution polynomiale d'ordre 4 de l'absorption en fonction de la fréquence. Cette méthode est la plus précise lorsque les décalages Doppler deviennent importants.

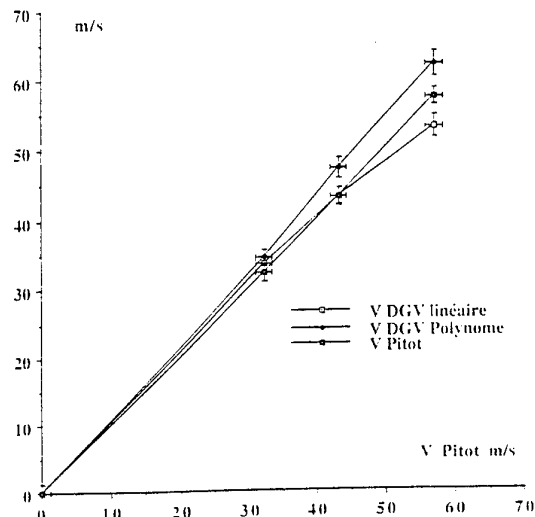


Figure 12 : Comparaison des mesures de vitesse par DGV et Pitot effectuées en soufflerie.

7.3 Détermination du champ de vitesse d'un écoulement par DGV

Un exemple complet du traitement d'une image est présenté, il s'agit d'un écoulement ensemencé en particules d'encens. La taille de la fenêtre visualisée est de 150 mm de haut par 90 mm de large. L'épaisseur du plan laser est de 1 mm, ce qui correspond à un volume par pixel de 0.114 mm³.

La figure 13 correspond à une image dont les premiers traitements ont été une correction du niveau de gris et de courant d'obscurité pour chaque pixel de la caméra. Sur les deux demi-images, une réflexion parasite du plan laser sur le hublot de la soufflerie est visible. Un défaut ponctuel apparaît en bas de chaque demi-image. L'ensemencement est assez inhomogène, il est situé dans la partie basse de la zone visualisée, et présente une structure bilobée, avec la partie basse plus riche en particules que la partie haute.

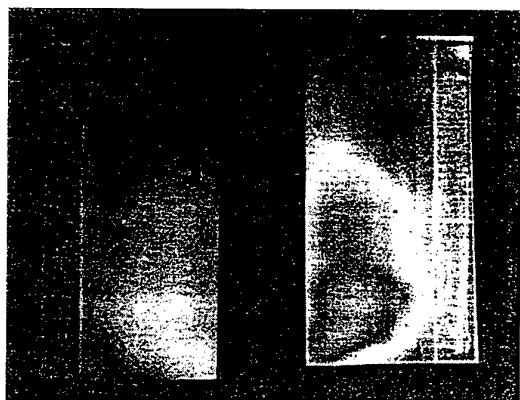


Figure 13 : Image de DGV après correction en niveau de gris et courant d'obscurité de la caméra

Pour éliminer le bruit de chaque pixel un traitement faisant appel à un filtre passe bas a été effectué. Le résultat est reporté en figure 14.

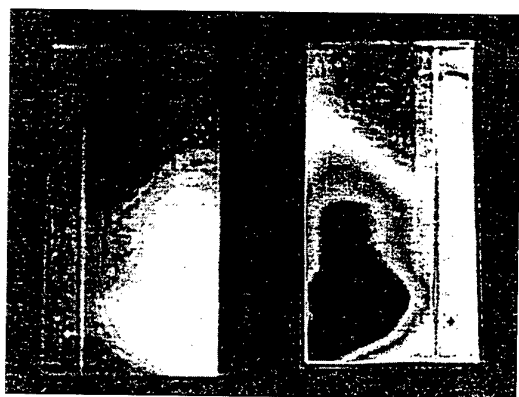


Figure 14 : Image de DGV traitement par un filtre passe-bas



Figure 15 : Image de DGV après recalage

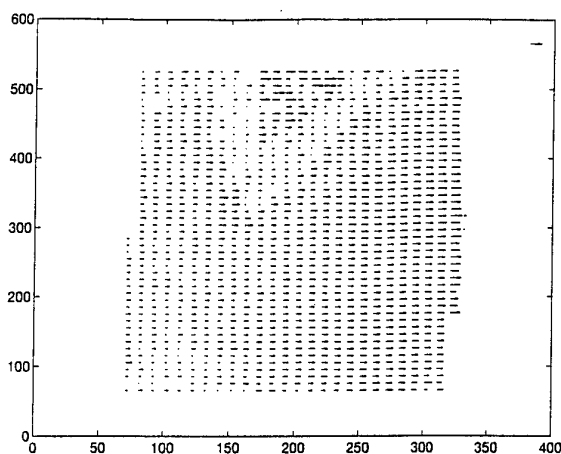


Figure 16 : Carte des vitesses

La demi-image référence est ensuite recalée sur la demi-image vue à travers la cellule d'iode après avoir soustrait une image correspondant au bruit de fond, le résultat est présenté en figure 15. Une image assez homogène est obtenue, les zones ensemencées conduisent à un niveau de gris, relativement constant. La zone non ensemencée reste très bruitée.

A partir de l'image recalée un premier traitement permet de passer au décalage Doppler en comparant les variations de transmission à la courbe d'étalonnage de la raie en transmission en fonction de la fréquence. Puis un deuxième calcul est effectué prenant en compte les angles d'observation et d'illumination pour chaque point du plan observé. La carte des vitesses obtenue est présentée en figure 16.

8. CONCLUSION ET PERSPECTIVES

La DGV est une technique qui présente un grand intérêt en mécanique des fluides et tout particulièrement pour déterminer le champ des vitesses aérodynamiques d'un écoulement, ce dernier pouvant être interne ou externe.

Cette méthode, décrite pour la première fois en 1991, met en oeuvre un laser à argon ionisé rendu monomode par l'utilisation d'une cavité Pérot-Fabry et excitant fortuitement les raies d'absorption P13 et R15 (43-0) de l'iode moléculaire.

La nouveauté essentielle apportée par ce travail repose sur l'utilisation d'un laser à colorant monomode accordable en fréquence. Nous avons ainsi fait apparaître les points déterminants pouvant bénéficier de sa souplesse par comparaison à la DGV réalisée à fréquence fixe :

- un accord en longueur d'onde associé à une connaissance précise de sa fréquence d'émission obtenue à partir des mesures de fluorescence dans une cellule d'iode de référence ;
- le balayage en fréquence de la raie d'absorption choisie pour réaliser l'étalonnage de la transmission ;
- le choix d'une raie d'absorption d'une molécule utilisée comme discriminateur de fréquence présentant une faible dépendance en température de sa fraction rovibrationnelle, une forte absorption, et une forme optimisée de sa

transmission en fonction de la gamme de vitesse à étudier.

Les premières mesures de vitesses par DGV appliquées à un disque tournant présentent une bonne concordance avec les vitesses obtenues à partir de la connaissance de la vitesse de rotation du disque.

Les mesures réalisées sur un écoulement en soufflerie sont également en bon accord avec les mesures obtenues par Pitot.

Outre l'apport du laser à colorant l'amélioration de la qualité des mesures passe par un bon recalage des images, par un étalonnage de chaque pixel en niveau de gris, par une thermostatisation de la cellule d'iode, par un ensemencement le plus homogène possible. Tous ces points traités avec le plus grand soin, améliorent de façon sensible les résultats.

BIBLIOGRAPHIE

- [1] J.F. Meyers, P.S. Wilkinson, "A Comparison of Turbulence Intensity Measurements using a Laser Velocimetry and Hot Wire in Low Speed Jet Flow", International Symposium of Laser Doppler Anemometry to Fluid Mechanics pp. 17.4-1 to 17.4-14, 1982.
- [2] A. Boutier, "Vélocimétrie laser", Les techniques de l'Ingénieur, R2161, p. 35-43.
- [3] C. Vêret, "Flow visualization by light sheet", Flow visualization III, W.J. Yang, third intern. symp., Ann Arbor, Sept. 1983.
- [4] J. W. Usry, J. F. Meyers, L. Scott Miller, "Doppler Global Velocimeter Measurements of the Vortical Flow Above a Thin Delta Wing", AIAA 92-0005, January 1992.
- [5] J. W. Lee, J. F. Meyers, A. A. Cavone, K. E. Suzuki, "Doppler Global Velocimeter Measurements of the Vortical Flow Above an F/A-18, AIAA 93-0414, January 1993.
- [6] A. Orszag et G. Herpner, "Introduction aux laser et leurs applications", Masson 1980.
- [7] G. Diemunsch, J.P. Prenel, "A compact light sheet generator for flow generations", Optics and Laser Technology, Vol.19, n°3 June 1987.
- [8] P. Pascal, "Nouveau traité de chimie minérale", Propriétés physiques de l'iode. p 456 à 468.
- [9] Gerstenkorn, P.Luc, "Atlas du spectre de la molécule d'iode de 14800 à 20000 cm⁻¹", Editions du CNRS5, Edition Masson et cie.
- [10] F. Lemoine, B. Leporcq, "Investigation on an optical pressure measurement using laser induced fluorescence", ZFW. 19 (1995) 109-118.
- [11] F. Lemoine, "Application de la fluorescence induite de l'iode par laser à la mesure de pression. Extension aux principes de la mesure de vitesse", Thèse de Doctorat de

l'Université de Paris VI, 1993.

- [12] B. Leporcq, J-F. Le Roy, B. Pinchemel, C. Dufour, "An Improvement in Doppler global velocimetry, the use of a CW dye laser", 8th International Symposium of Laser Techniques to Fluid Mechanics, Lisbon 8 - 11 July 1996.
- [13] B. Leporcq, J-F. Le Roy, B. Pinchemel, C. Dufour, "Interest of a CW dye laser in Doppler global velocimetry", 1996 ASME Fluids Engineering Division, Summer Meeting, San Diego July 7 - 11, 1996.
- [14] B. Leporcq, J-F. Le Roy, M. Eléaume, B. Pinchemel, C. Dufour, "Utilisation d'un laser à colorant monomode accordable en vélocimétrie Doppler globale", 5ème Congrès Francophone de Vélocimétrie Laser, Rouen 24 - 27 Septembre 1996.

Surface Integral Method to Quantify the Droplet Non-sphericity Effect on Rainbow Thermometry

J.P.A.J. van Beeck and M.L. Riethmuller

von Karman Institute for Fluid Dynamics,

Chaussée de Waterloo 72, B-1640 Rhode-Saint-Genèse, Belgium

Tel: +32 2 35.99.611, Fax: +32 2 35.99.600, E-mail: vanbeeck@vki.ac.be

1 SUMMARY

A theoretical model is presented to compute the monochromatic rainbow interference pattern formed by ellipsoidal homogeneous, transparent particles. The model is applied to predict the effect of droplet non-sphericity on the errors in the particle temperature and size measurements, performed by rainbow thermometry. These results have been employed to achieve a quantitative validation of the experimental non-sphericity detection method, based on the comparison of different types of size measurements of the same droplet, derived from different interference structures that are visible in the rainbow pattern. As such, confidence can be established in the temperature measurement as far as the selected spherical droplets are concerned.

2 INTRODUCTION

2.1 Rainbow Thermometry

Rainbow thermometry is a unique laser-based, non-intrusive technique which measures the temperature of an individual transparent, spherical particle. In 1988, the technique was introduced in the domain of fluid dynamics by Roth, Anders and Frohn (Refs. 1, 2) and later further developed by Van Beeck and Riethmuller (Ref. 3) towards the measurement of particle size and velocity and to the detection of non-sphericity. Sankar et al. (Refs. 4, 5, 6) studied the applicability of the technique for fuel combustion sprays. However, the potential of the technique lies in the entire field of research on transparent sprays, droplets and spraying systems as far as thermal energy is involved.

The principle of rainbow thermometry is the determination of the refractive index of the particle, thus its temperature, from the angular position of the primary monochromatic rainbow that is generated by a single particle illuminated by a laser beam. Fig. 1 represents the standard optical configuration to detect a rainbow interference pattern in a spray. The system consists of a spatial filter to select a probe volume containing one particle at a time. The sensor is a linear CCD camera placed at focal distance of the lens system so that the position of the rainbow on the CCD array is independent of the position of the single particle in the probe volume.

Fig. 2 shows the far-field intensity in the monochromatic rainbow as a function of the scattering angle θ , for a wavelength of 632.8 nm . The ratio of the refractive index of the particle and that of the surrounding medium equals 1.33534. The figure has been created with the help of the Lorenz-Mie theory which provides a rigorous solution for the scattering of a plane electro-magnetic wave front by a homogeneous sphere (Refs. 7, 8). As the CCD camera is placed in the focal plane of the lens system, each pixel number of the CCD array can be related to a certain relative scattering angle. The absolute scattering angle is obtained by means of a dynamic calibration procedure carried out with a particle of known refractive index (Refs. 9, 10).

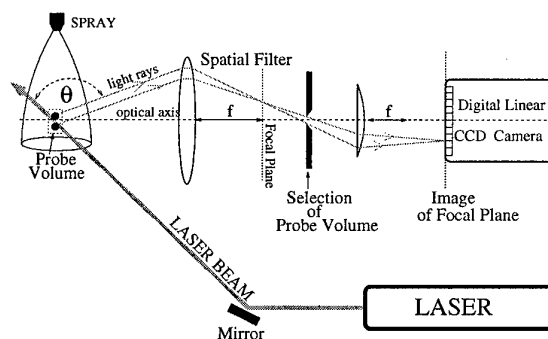


Fig. 1: The standard optical configuration used in rainbow thermometry. θ is the angle between a scattered light ray and the laser beam.

The rainbow exhibits two main interference structures as is also clear from the power spectrum shown in Fig. 3¹. Angular frequency F_1 arises from the low-frequency Airy fringes. These fringes result from laser light having experienced one internal reflection by the particle surface. The high-frequency ripple structure is represented by peaks at frequencies F_2 and F_3 . This interference structure is formed by optical interference between internal and external reflection. Both interference structures can be employed to obtain the particle size without having prior knowledge of the temperature. Subsequently, the temperature is deduced from the angular position of the main rainbow maximum. For this, the size is needed because the angular position of the main rainbow maximum depends also on the dimension of the particle. As such, a surprisingly

¹The reason for showing the derivative is to remove the pedestal in the power spectrum near the origin.

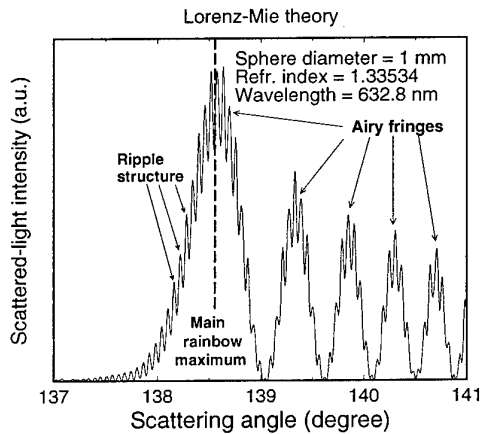


Fig. 2: The intensity of the monochromatic rainbow as a function of the scattering angle. Because the CCD camera is placed in the focal plane of the lens system (see Fig. 1), each pixel of the CCD camera is related to a certain scattering angle θ . The angular position of the main rainbow maximum depends on the particle temperature and size.

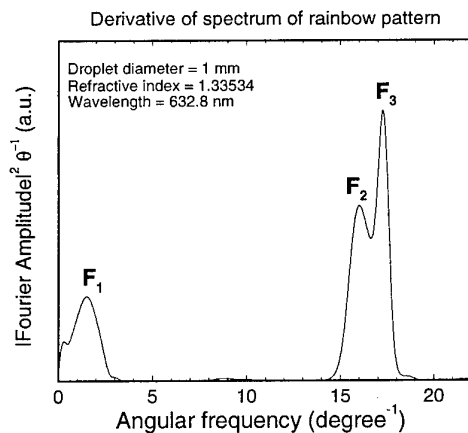


Fig. 3: The power spectrum of the monochromatic rainbow as depicted in Fig. 2. The positions of the peaks at angular frequencies F_1 and F_3 are employed for measuring the particle size.

simple laser-based, non-intrusive technique, consisting of one laser beam and one linear CCD camera, has been established for measuring simultaneously the size and temperature of a spherical particle.

Later developments have led to the measurement of the particle velocity from the rainbow pattern. But the main purpose of the technique remains the determination of the temperature as this physical quantity cannot be measured by means of conventional laser-based, non-intrusive techniques such as laser-Doppler (Ref. 11) or phase-Doppler anemometry (Ref. 12).

2.2 Detection of Particle Non-Sphericity

Unfortunately, the shape of the scatterer has a large influence on the accuracy of rainbow thermometry. Al-

ready in 1980, Marston (Ref. 13) recognized that the different rainbow interference structures, i.e. the Airy fringes and the ripple structure, allow a perfect detection of the non-sphericity of the scatterer. The large influence of particle non-sphericity on the measurement accuracy of the temperature measurement was later observed by Van Beeck and Riethmuller (Ref. 9). The authors decided to process only spherical particles selected by a diameter comparison method (Ref. 14). This method compares the particle diameter D_{Airy} , obtained from the Airy fringe spacing, to the diameter D_{ripple} which is derived from the ripple structure superimposed on the Airy fringes. When the difference between the diameters is larger than the uncertainty in the size measurement, the particle is supposed to be non-spherical, thus the rainbow signal is rejected to avoid erroneous temperature measurements. Qualitative experimental validation of this non-sphericity detection method has been reported (Ref. 3). In the present paper, the theoretical proof will be given.

3 THE SURFACE INTEGRAL METHOD: PRINCIPLE

Here, the principle of the surface integral method for light scattering by a non-spherical particle will be outlined. The method will be applied later in this paper to an ellipsoidal particle to validate the non-sphericity detection method. Consequently, one aims to predict the behaviour of the Airy fringes and the ripple structure in the primary rainbow region.

The theoretical model is based on a combination of wave and geometrical optics for the description of light propagation (Ref. 10).

3.1 Wave Optics: Kirchhoff Integral

Let \mathbf{r} be the radial position vector for the surface of the non-spherical scatterer and let \mathbf{r}_p be the vector for observation point P, where the light detector is placed. Wave optics is applied to express the electric field \mathbf{E}_p in the observation point as a function of the scattered electric field \mathbf{E}_s at the surface \mathcal{S} , entirely enclosing the scatterer (Fig. 4). This leads to the vector Kirchhoff integral relation (Ref. 15):

$$\mathbf{E}_p = \oint_{\mathcal{S}} (\mathbf{n} \cdot \mathbf{E}_s) \nabla G + (\mathbf{n} \times \mathbf{E}_s) \times \nabla G + iG(\mathbf{n} \times (\mathbf{k}_s \times \mathbf{E}_s)) da. \quad (1)$$

da is a surface element on \mathcal{S} having a unit vector normal \mathbf{n} . \mathbf{k}_s represents the wave vector assigned to \mathbf{E}_s . \mathbf{k}_p is the wave vector for the electric field \mathbf{E}_p at a distance from the particle where the scattered waves propagate as spherically diverging waves as sketched in Fig. 4.

For G in Eq. 1, one has to substitute the free field Green's function (Refs. 15, 10):

$$G = \frac{1}{4\pi r_p} e^{ik_p r_p} e^{-i(\mathbf{k}_p \cdot \mathbf{r})}. \quad (2)$$

Subsequently, Eq. 1 becomes a simple diffraction-like integral which is the basis of most of the work on diffraction (Refs. 16, 17).

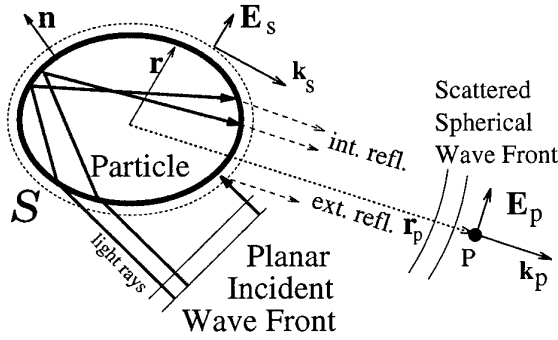


Fig. 4: The scattering problem solved by the surface integral method to quantify the non-sphericity effect on rainbow thermometry.

3.2 Geometrical Optics

The field E_s on surface S , as it appears in Eq. 1, can be associated to geometrical rays that are traced with the help of the laws of geometrical optics. In the primary rainbow region, external and one internal reflections are the dominant geometrical contributions. Consequently, the total electric field E_s on surface S will be the sum of the electric field E_s^{ext} , assigned to the externally traced ray, and the electric field E_s^{int} , assigned to the once-internally reflected ray:

$$E_s = E_s^{\text{ext}} + E_s^{\text{int}}. \quad (3)$$

The direction of each electric field vector is determined by the polarization vectors p_s^{ext} and p_s^{int} on the surface S . These vectors are obtained by computing the change of the incident polarization vector as it interacts with the particle interface according to the laws of reflection and refraction and the coefficients of Fresnel (Refs. 18, 10).

It is essential for the prediction of the different interference structures that the phase σ , assigned to each electric field on the droplet surface, is computed correctly. First, the Fresnel reflection coefficients may change the phase by 180° upon interaction of a light ray with the surface of the scatterer. Secondly, the length of the optical path followed induces a phase shift with respect to the phase in the incident wave front. Finally, one has to realize that the phase advances 90° whenever two adjacent rays cross each other, i.e. focus. The latter phase change has been discussed by Van de Hulst (Ref. 19) and Hovenac (Ref. 20). l^{int} is the number of focal points encountered by internally reflected rays upon emerging from the particle. Similarly, l^{ext} represents the number of focal points for external reflection; hence, $l^{\text{ext}} = 0$.

The shape of the particle also influences the scattered light intensity distribution. This is accounted for by the gain factor \mathcal{G} which is defined as the ratio of the scattered energy flux at a certain position on surface S and the incident energy flux (Ref. 10). \mathcal{G}^{ext} and \mathcal{G}^{int} are the gain factors for external and internal reflection, respectively.

Ray tracing, the computation of the state of the scattered polarization vectors, the phase changes and the gain factors are the necessary tools needed to find the

expressions for the electric fields E_s^{ext} and E_s^{int} near the droplet surface:

$$E_s^{\text{ext}} = E_b p_s^{\text{ext}} \sqrt{\mathcal{G}^{\text{ext}}} e^{-i(\omega t - \sigma^{\text{ext}} - l^{\text{ext}} \pi/2)}, \quad (4)$$

$$E_s^{\text{int}} = E_b p_s^{\text{int}} \sqrt{\mathcal{G}^{\text{int}}} e^{-i(\omega t - \sigma^{\text{int}} - l^{\text{int}} \pi/2)}. \quad (5)$$

Here, E_b is the amplitude of the electric field in the incoming wave front, t is the time and ω the circular frequency of light. The symbols \mathcal{G} , σ and l have been discussed before and the superscripts **ext** and **int** pertain to external reflection and internal reflection, respectively. Substitution of Eqs. 2 to 5 in the vector Kirchhoff integral relation, Eq. 1, completes the surface integral method, giving a hybrid solution to the problem of rainbow scattering by non-spherical particles. Numerical results of the Kirchhoff integral will be presented in the following section.

4 THE SURFACE INTEGRAL METHOD: NUMERICAL RESULTS

The Kirchhoff integral will be solved for the primary rainbow formed by external and one internal reflection of a planar wave front by a non-absorbing, homogeneous, ellipsoidal particle. The solution will be compared to the purely geometrical computations of Moebius (Ref. 21). It is interesting to look to the latter computations first.

4.1 Moebius' geometrical computations

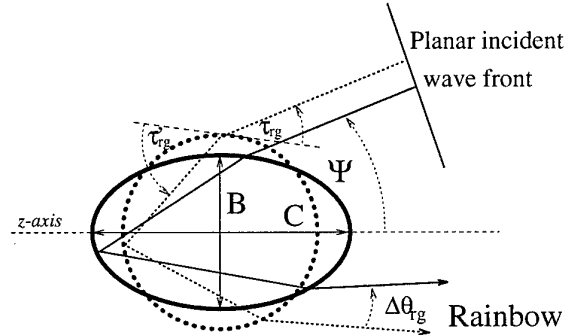


Fig. 5: The scattering problem considered by Moebius (Ref. 21) in 1910 AD. His aim was to compute the deviation of the geometric rainbow angle θ_{rg} as a function of the angle Ψ and the axis ratio B/C .

The problem of rainbow scattering by non-spherical particles has already been considered by Moebius (Ref. 21) in the beginning of this century. His computations were purely geometrical, that is to say, no optical interference was included. Consequently, he could not predict the effect of non-sphericity on the different interference structures. However, he was able to give an idea of the approximate angular position of the rainbow interference pattern.

Fig. 5 shows the 2D scattering problem considered by

Moebius. An ellipse is illuminated by a planar wave front having a wave vector making an angle Ψ with the z -axis. The geometric rainbow angle θ_{rg} is related to the ray that has undergone the smallest deviation with respect to the incident beam direction upon emerging from the particle after one internal reflection. By means of geometrical optics, θ_{rg} is related to a certain incidence angle τ_{rg} . For a sphere, this relationship is given by the following expressions:

$$\theta_{rg} = 4\tau'_{rg} - 2\tau_{rg}, \quad (6)$$

$$\sin \tau_{rg} = \sqrt{\frac{m^2 - 1}{3}}, \quad (7)$$

$$m \cos \tau'_{rg} = \cos \tau_{rg}, \quad (8)$$

where m is the ratio of the refractive index of the particle and that of the surrounding medium.

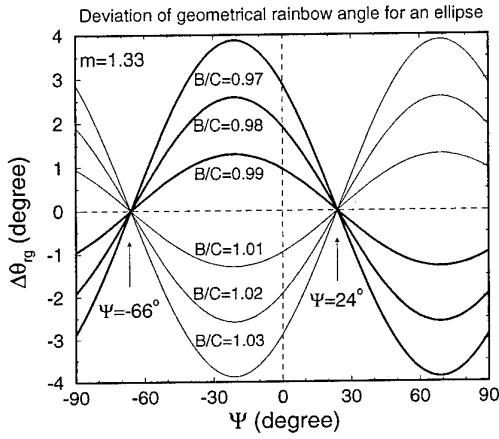


Fig. 6: $\Delta\theta_{rg}$ as a function of the axis ratio B/C and the angle Ψ according to expression 9.

The solution found by Moebius for an ellipse is limited to an axis ratio B/C close to unity. Moreover, the 2D-approach implies that the solution only holds for rays that lie in one plane. For these conditions, the difference between the geometric rainbow angle for a sphere and that of an ellipse reads

$$\Delta\theta_{rg} = 16 \left(\frac{B-C}{B+C} \right) \frac{\cos \tau_{rg}}{m} \sin^2(\arccos(\frac{\cos \tau_{rg}}{m})) \cos(\theta_{rg} - 2\Psi). \quad (9)$$

Moebius' results are presented in Fig. 6, created with the help of Eqs. 6 to 9. This figure tells that a non-sphericity of 3% (i.e. $B/C = 0.97$) may lead to a shift of about 4° , although for $\Psi = -66^\circ$ and for $\Psi = 24^\circ$ there is no deviation in θ_{rg} at all.

4.2 Surface Integral Method for Prolates

At this point, Moebius' scattering problem of Fig. 6 is going to be solved with the help of the surface integral method, introduced in Sec. 3. Therefore, the Kirchhoff integral of Eq. 1 is utilized. This 3D vectorial integral relation transforms into a sum of two independent Kirchhoff integrals after substitution of the electric field vector \mathbf{E}_s by $\mathbf{E}_s^{\text{int}} + \mathbf{E}_s^{\text{ext}}$ (Eq. 3):

$$\mathbf{E}_p = \mathbf{K}^{\text{int}} + \mathbf{K}^{\text{ext}}. \quad (10)$$

\mathbf{K}^{int} is the Kirchhoff integral for the internally-reflected light and \mathbf{K}^{ext} represents the contribution of external reflection. In order to avoid the computation of the three orthogonal components of the field vector \mathbf{E}_p , one asks for the field amplitude with polarization vector \mathbf{p}_p and wave vector \mathbf{k}_p in the observation point. As a consequence, one has to solve numerically the scalar integrals $(\mathbf{p}_p \cdot \mathbf{K}^{\text{int}})$ and $(\mathbf{p}_p \cdot \mathbf{K}^{\text{ext}})$. Here, the direction of the polarization vector \mathbf{p}_p will be chosen to be similar to that of the incident polarization, that is to say perpendicular to the scattering plane taken through the scattered and the incident wave vectors. For this sense of polarization, the primary rainbow is the most intense as far as spherical particles are concerned; for ellipsoids this might not be true. However, a direction of the polarization vector perpendicular to the scattering plane will not change its direction due to optical interaction with the homogeneous particle surface provided that the paths of the geometrically-traced rays lie in one plane. This condition reduces the validity of the 3D surface integral method to two dimensions which nevertheless is sufficient to solve Moebius' 2D scattering problem. An advantage of the reduction of the scattering problem to two dimensions is that the time of numerical computation decreases considerably because one does not have to integrate over the entire particle surface any longer. The integration of both Kirchhoff integrals will be carried out over a path on the particle surface \mathcal{S} that is formed by the intersection of that surface and the scattering plane. In fact, this path connects the various stationary points that appear in the phase functions of the Kirchhoff integrals and that dominate the integrals. The direction perpendicular to this path of integration is approximated by the method of stationary phase (Refs. 22, 10).

Once the Kirchhoff integrals for the field amplitudes have been computed, the far-field scattered light intensity, detected at the observation point P , can be calculated explicitly by

$$I = (\mathbf{p}_p \cdot \mathbf{E}_p)^* (\mathbf{p}_p \cdot \mathbf{E}_p), \quad (11)$$

where $*$ denotes the complex conjugate.

Fig. 7 shows two theoretical rainbow interference patterns made by a prolate and one produced by a sphere. The surface integral method was used for these computations. A prolate is an ellipsoid with one long and two short axes of equal length, like a rugby ball. The short axis diameter measures $1000 \mu\text{m}$ and the long axis diameter is $1030 \mu\text{m}$. The incident wave vector lies in the plane made by the long and one short axes, making the scattering problem identical to the one sketched in Fig. 5. The thin curve in Fig. 7 corresponds to collimated illumination perpendicular to the long axis (i.e. $B/C = 1.03$, $\Psi = 0^\circ$); the bold curve is the result of illumination parallel to the long axis ($B/C = 0.97$ and $\Psi = 0^\circ$). Moebius predicts for these parameters a symmetric shift of $\pm 2.96^\circ$ of the geometric rainbow angle with respect to the sphere solution (Eq. 9). The surface integral method computes slightly asymmetric shifts of the rainbow patterns of -2.70° and $+3.01^\circ$ with respect to the sphere solution for an equivalent diameter of $1015 \mu\text{m}$ (dotted curve in Fig. 7).

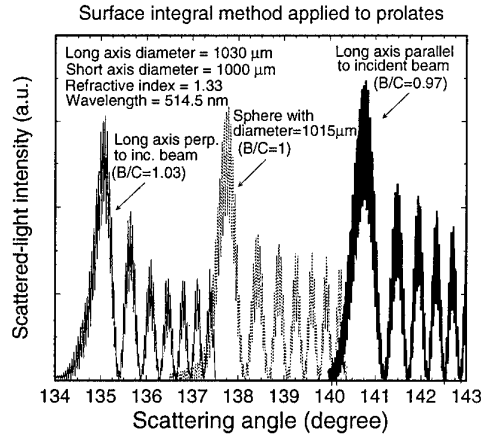


Fig. 7: Angular Rainbow patterns created by prolate-shaped transparent particle with one long axis of $1030 \mu\text{m}$ and two short axes having a length of $1000 \mu\text{m}$.

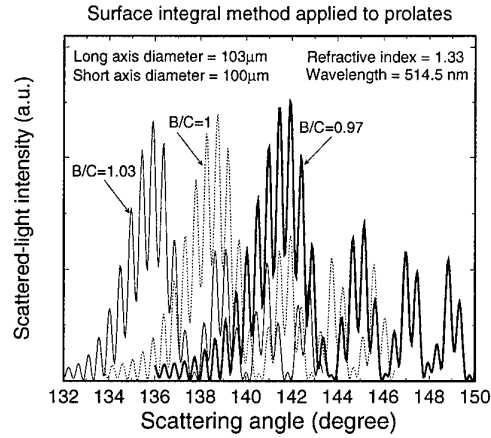


Fig. 9: Angular Rainbow patterns created by a prolate-shaped transparent particle with one long axis of $103 \mu\text{m}$ and two short axes having a length of $100 \mu\text{m}$.

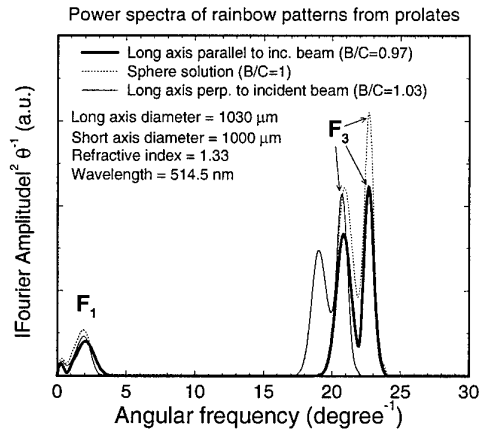


Fig. 8: Derivative of spectra of the rainbow patterns in Fig. 7.

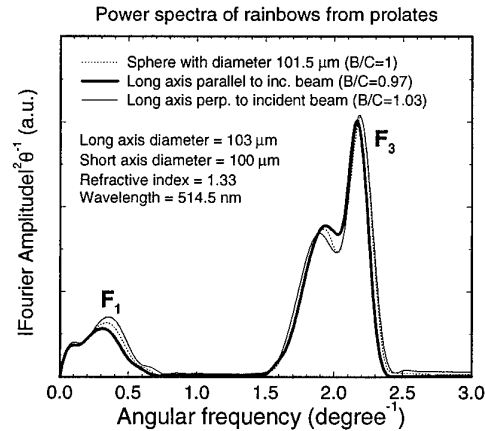


Fig. 10: Derivative of spectra of the rainbow patterns in Fig. 9.

Fig. 8 shows the derivative of the power spectra of the angular rainbow patterns depicted in Fig. 7. The figure shows the influence of particle non-sphericity on the angular frequency of the Airy fringes, denoted by F_1 , and the ripple structure, represented by the two peaks at F_2 and F_3 . Most remarkable is the influence on the ripple structure. The solution for the long axis parallel to the incident wave vector ($B/C=0.97$) gives the same results as the sphere solution, i.e. the positions of the peaks at frequencies F_2 and F_3 do not change. However, for the prolate with the long axis perpendicular to the incident beam ($B/C = 1.03$), these peaks appear to have shifted about $\Delta F_2 = \Delta F_3 = -10\%$ with respect to the sphere solution. The impact of particle non-sphericity on the angular frequency of the Airy fringes is the reverse of that on the angular frequency of the ripple structure. This is to say, for $B/C = 1.03$, the Airy frequency remains almost unchanged (a tiny shift of about $\Delta F_1 = +2\%$) whereas for $B/C = 0.97$ the relative shift of the peak at F_1 is $\Delta F_1 = +9\%$. The importance of these figures for rainbow thermometry will be discussed in Sec. 5.

Figs. 9 and 10 are equivalent to the two preceding figures except for the dimensions of the prolate. The dotted curve now represents a rainbow pattern arising from a sphere of $101.5 \mu\text{m}$ instead of $1015 \mu\text{m}$. The other curves are produced by a prolate with one long axis of $103 \mu\text{m}$ and two short axes of $100 \mu\text{m}$. The angular difference between the main rainbow maxima of the prolate and the sphere solution is -2.78° and $+3.09^\circ$ for perpendicular and parallel illumination with respect to the long axis of the prolate, respectively. Comparison between Fig. 9 and Fig. 7 reveals that the angular shift of the rainbow pattern due to non-sphericity is almost independent of the dimension of the scatterer. This feature was already predicted by Moebius but does not hold for the angular frequencies as seen in the power spectra of Fig. 10. In contrast to Fig. 8, the ripple frequency F_3 is almost independent of the orientation of the prolate whereas the Airy frequency F_1 shifts $\Delta F_1 = -7\%$ for $B/C = 0.97$ and $\Delta F_1 = +6\%$ for $B/C = 1.03$. The impact of these numerical results on the rainbow technique will be discussed in the following section.

5 THEORETICAL VALIDATION OF NON-SPHERICITY DETECTION METHOD

The figures presented in the previous section provide a theoretical validation of the non-sphericity detection method.

As described in Subsec. 2.2, the non-sphericity detection method aims to detect the particle non-sphericity in order to prevent erroneous temperature measurement from the rainbow technique. The method compares the Airy diameter D_{Airy} to the ripple diameter D_{ripple} . When the difference between both diameters is larger than the uncertainty in the size measurement, then the particle is supposed to be non-spherical, thus the corresponding rainbow signal is rejected. For the determination of D_{Airy} and D_{ripple} from a single rainbow pattern one uses theoretical models that are only valid for spherical particles. As such, employing the Airy theory for the rainbow (Ref. 23), D_{Airy} is calculated from the angular spacing between the main rainbow maximum and the first supernumerary bow (Ref. 10). Therefore, D_{Airy} is related to \mathbf{F}_1 in the power spectrum; a relative change in \mathbf{F}_1 brings on a relative change in the Airy diameter following

$$\Delta D_{\text{Airy}} = \frac{3}{2} \Delta \mathbf{F}_1. \quad (12)$$

Employing ray optics, D_{ripple} can be deduced from the peak at angular frequency \mathbf{F}_3 in the power spectrum. For $D > 100 \mu\text{m}$, the relative change in D_{ripple} equals $\Delta \mathbf{F}_3$:

$$\Delta D_{\text{ripple}} = \Delta \mathbf{F}_3. \quad (13)$$

The relative difference between D_{Airy} and D_{ripple} is derived from above two equations:

$$\frac{D_{\text{Airy}} - D_{\text{ripple}}}{D} = \frac{3}{2} \Delta \mathbf{F}_1 - \Delta \mathbf{F}_3. \quad (14)$$

D is the diameter of the equivalent sphere which is known for the computations. It is important to realize that the relative difference in the diameters D_{Airy} and D_{ripple} is zero for spherical particles. When applying formula 14 to the numerical results for $\Delta \mathbf{F}_1$ and $\Delta \mathbf{F}_3$, as obtained in the previous section, one observes that $|(D_{\text{Airy}} - D_{\text{ripple}})/D|$ ranges from 9% to 13.5%. This validates the non-sphericity detection method; a non-sphericity in the particle shape, leading to erroneous temperature measurements, will be detected by a difference in the two independent diameter measurements of the same particle. It is important to notify that the results presented in the present paper apply to a non-sphericity of 3% which results in an angular shift of about 3° when the incident illumination is along one of the axes of the ellipsoid. But an angular shift of 3° can also have been produced by a temperature change of about 100°C in the case of water droplets in air. From this, one can conclude that the accuracy in the size measurement of water droplets has to be about 1% in order to achieve an accuracy in the temperature measurement of better than 10°C .

These numerical results, obtained with the help of the surface integral method, furnish a first indication that

the particle non-sphericity can be detected from a single rainbow pattern. However, in the future one will have to perform more computations in a large range of diameters and for different directions Ψ of the incident illumination. These computations should reveal whether there are regimes in D and Ψ for which less accurate size measurements are required. Furthermore, it is suggested to compare these computations to proper experimental data. Therefore, one has to record the rainbow pattern and the shape of the particle at the same time. This can be done by carrying out fundamental experiments on acoustically or optically levitated particles for which the shape can easily be assessed and/or controlled.

6 CONCLUSIONS

The presented surface integral method is an accurate tool to predict the non-sphericity effect on rainbow thermometry. First, the method was compared to Moebius' 2D scattering problem of an ellipse illuminated by a planar wave front. The solution of Moebius predicts an angular shift of the geometric rainbow pattern that compares well with the results given by the surface integral method. Unlike Moebius' solution, the surface integral method is able to predict the influence of particle non-sphericity on the frequency characteristics of the rainbow pattern. This was necessary to proof theoretically the non-sphericity detection method, proposed by Van Beeck and Riethmuller in 1994 (Ref. 14). This method should prevent erroneous particle temperature measurement from the fact that the rainbow interference pattern shifts due to particle non-sphericity and not because of a change in temperature. Theoretical computations show that non-sphericity can be successfully detected by comparing the characteristics of two different interference structures, visible in the rainbow pattern. Therefore, one derives from each interference structure a particle diameter using theories valid for spherical particles only. It appears that both diameters differ from each other in case of non-sphericity. Consequently, this can serve as a criterion to reject rainbow signals coming from non-spherical particles. By processing the remaining rainbows, confidence can be established in the temperature measurement from rainbow thermometry. Preliminary computations have indicated that for ellipsoidal water droplets, illuminated along one of the axes, an accuracy of about 1% in the size measurement is needed in order to achieve a temperature measurement that is more precise than 10°C .

7 REFERENCES

1. N. Roth, K. Anders, and A. Frohn. Simultaneous measurement of temperature and size of droplets in the micrometer range. In *7th International Congress on Optical Methods in Flow and Particle Diagnostics ICALEO 88, L.I.A.*, volume 67, pages 294-304, Sunnyvale, U.S.A., 1988.
2. N. Roth, K. Anders, and A. Frohn. Simultaneous measurement of temperature and size of droplets in the micrometer range. *Journal of Laser Applications*, 2(1):37-42, 1990.

3. J.P.A.J. van Beeck and M.L. Riethmuller. Rainbow phenomena applied to the measurement of droplet size and velocity and to the detection of nonsphericity. *Appl. Opt.*, 35(13):2259-2266, 1996.
4. S.V. Sankar, K.H. Ibrahim, D.H. Buermann, M.J. Fidrich, and W.D. Bachalo. An integrated phase Doppler/rainbow refractometer system for simultaneous measurement of droplet size, velocity, and refractive index. In *The Third International Congress on Optical Particle Sizing*, pages 275-284, Yokohama, Japan, August 1993.
5. S.V. Sankar, D.H. Buermann, and W.D. Bachalo. An advanced rainbow signal processor for improved accuracy in droplet temperature measurements. In *8th International Symposium on Applications of Laser Techniques to Fluid Mechanics*, volume 1, pages 9.3.1-9.3.9. Lisbon, Portugal, July 1996.
6. S.V. Sankar, D.H. Buermann, and W.D. Bachalo. Application of rainbow thermometry to the study of fuel droplet heat-up and evaporation characteristics. In *International Gas Turbine and Aeroengine Congress & Exhibition*, pages 96-GT-21, Birmingham, UK, June 1996.
7. G. Mie. Beitrage zur Optik trüber Medien speziell kolloidaler Metallösungen. *Ann. Phys.*, 25:377-445, 1908.
8. L.V. Lorenz. Upon the light reflected and refracted by a transparent sphere. *Vidensk. Selsk. Shrifter*, 6:1-62, 1890. in Danish.
9. J.P.A.J. van Beeck and M.L. Riethmuller. Nonintrusive measurements of temperature and size of single falling raindrops. *Appl. Opt.*, 34(10):1633-1639, 1995.
10. J.P.A.J. van Beeck. *Rainbow Phenomena: Development of a Laser-based, Nonintrusive Technique for Measurement of Droplet Temperature, Size and Velocity*. PhD thesis, Technische Universiteit Eindhoven, The Netherlands, 1997. ISBN 90-386-0557-9, NUGI 812.
11. Y. Yeh and H.Z. Cummins. Localized flow measurements with an He-Ne laser spectrometer. *Appl. Phys. Letters*, 4:176-178, 1964.
12. W.D. Bachalo and M.J. Houser. Phase-Doppler spray analyzer for simultaneous measurements of drop size and velocity distributions. *Optical Engineering*, 23:403-429, 1984.
13. P.L. Marston. Rainbow phenomena and the detection of nonsphericity in drops. *Appl. Opt.*, 19(5):680-685, 1980.
14. J.P.A.J. van Beeck and M.L. Riethmuller. Détermination non-intrusive de la dimension et de la température des gouttes dans une pulvérisation. In *Recueil des actes du 4^e Congrès Franco-phone de Vélocimétrie Laser*, pages 2.2.1-2.2.8, Poitiers, France, September 1994. Laboratoire de Chimie Physique de la Combustion, Université de Poitiers-CNRS.
15. J.D. Jackson. *Classical Electrodynamics*. John Wiley & Sons, Inc., New York, 2th edition, 1975. Chap. 9, pp. 432-435.
16. R.P. Feynman. *QED: The Strange Theory of Light and Matter*. Princeton U.P., Princeton, NJ, 1985. Chap. 2.
17. James A. Lock and James H. Andrews. Optical caustics in natural phenomena. *Am. J. Phys.*, 60(5):397-407, 1992.
18. Eugene Hecht. *Optics*. Addison Wesley Publishing Company, 2th edition, 1987. Chap. 4, pp. 92-113.
19. H.C. van de Hulst. *Light Scattering by Small Particles*. Dover Publications, Inc., N.Y., 1981. Chap. 12, pp. 206-207, originally published in 1957 by John Wiley & Sons, Inc., N.Y.
20. Edward A. Hovenac. Calculation of far-field scattering from nonspherical particles using a geometrical optics approach. *Appl. Opt.*, 30(33):4739-4746, 1991.
21. W. Moebius. Zur Theorie des Regenbogens und ihrer experimentellen Prüfung. *Ann. Phys. (Leipzig)*, 33:1493-1558, 1910.
22. David C. Wilcox. *Perturbation Methods in the Computer Age*. DCW Industries, Inc. La Cañada, California, 1995. Chap. 2, pp. 34-48.
23. G.B. Airy. On the intensity of light in the neighbourhood of a caustic. *Trans. Camb. Phil. Soc.*, 6:379-402, 1838.

AIRPLANE FLOW-FIELD MEASUREMENTS AND THE FLYING STRUT

J. P. Crowder
Boeing Technical Fellow
Aerodynamics Laboratory
Boeing Commercial Airplane Group
P. O. Box 3707
Seattle, WA 98124
USA

SUMMARY

The prospect for useful measurements of airplane flow-field properties are reviewed. Early experience in flow-field measurements at Boeing is described, as are the requirements for quantitative flow-field surveys in industrial wind tunnels. Recent examples of quantitative flow-field measurements of lift and drag distributions in subsonic and transonic wind tunnels are presented. A new invention, called the Flying Strut, is introduced as a practical system for flow-field surveys in large wind tunnels and in flight.

1.0 INTRODUCTION

The flow field surrounding an airplane contains a wealth of information that has, historically, been difficult to extract. This information takes many forms: from flow visualization with smoke; to distributions of total pressure depicting wake shapes; or quantitative integrations of lift and drag. In all of these applications, there is a common need to position an object, such as a pressure probe or a smoke dispenser, inside the flow field and move it throughout a range of measurement positions. The apparatus that accomplishes this task is the flow-field traverser.

Experience at Boeing in developing flow-field measurement techniques has emphasized the need for appropriate flow-field traversing equipment which is crucial for the success of flow-field measurements. We have deployed several different traversing machines in various low speed and transonic wind tunnels. Most of these applications use traversing equipment designed to mount rigidly in the flow and operate with high-torque servo motors.

A new invention, called the Flying Strut, offers an alternate approach to the design of traversing equipment for wind tunnel or flight testing. This device employs a pair of linked struts with low-drag airfoil sections that are controlled in angle-of-attack to trim out the aerodynamic normal force. Each strut element develops only enough lift to support its weight. In addition, all the actuating force for the traversing motion is produced by slight changes in angle of attack to control the aerodynamic normal force developed by the strut elements.

This paper is a summary of our recent experience with wind tunnel flow-field surveys using conventional traversing equipment. Flying Strut applications in wind tunnels and in flight are described.

2.0 THE FLOW FIELD

The flow field is the region surrounding an airplane where the airflow perturbations are significant. The flow field can be

divided into two distinctly different regions: the inviscid and the viscous. The inviscid flow field extends away from the model surface long distances in all directions and the perturbations die out gradually with distance. In this region the magnitude of the total pressure is exactly constant, although the direction of the total pressure vector varies widely.

The viscous region, also called the wake, is concentrated in a small area downstream of the airplane. Close to the airplane, the shape of the wake resembles a projected rear view of the airplane. The wake evolves as it is swept downstream and takes on distinctive and predictable shapes. These shapes provide valuable qualitative indications of various flow conditions, such as regions of high drag or high concentrations of vorticity.

3.0 FLOW FIELD MEASUREMENTS

Several measurement techniques for extracting information from an airplane flow field have been developed and employed at Boeing. Some of these are discussed further below.

3.1 Smoke Flow Visualization

Smoke flow visualization is often considered for flow-field studies, but seldom produces useful results. It depends on having a flow field with certain distinctive flow features like vortex roll-up to make visual effects that can be recognized. In the absence of these features, smoke flow visualization often produces indistinct clouds without an obvious structure.

If smoke is introduced into the flow field upstream of the model and positioned properly, it becomes entrained into the flow field and produces distinctive visual features. This requires a traversing system to position the smoke-dispensing site. The optimal dispensing location is seldom known beforehand, so the traverser must be able to survey over a region to determine the desired location. Since it is upstream of the model, it is extremely important that the traverser not disturb the flow.

This type of experiment has not been practical in large industrial wind tunnels until the invention of the Flying Strut traverser. Smoke flow-visualization experiments have previously been conducted in small, special purpose wind tunnels or in situations where the smoke can be dispensed at a previously identified location on the model.

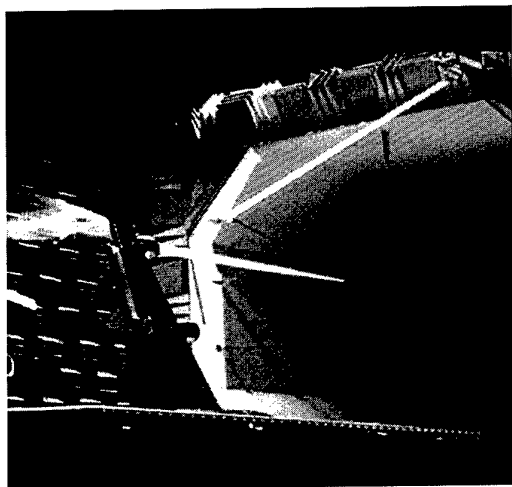


Figure 1. Smoke in Boeing acoustic wind tunnel.

Figure 1 shows smoke flow visualization marking the flow at the tip of a wing flap. The flap tip has a strong vortex that produces a smoke image with a distinctive spiral shape. This picture was taken in the 8x10-foot Boeing Acoustic Wind Tunnel at a test Mach number of 0.25. The smoke is dispensed from a Flying Strut traverser mounted to the ceiling of the test section upstream of the model.

3.2 Qualitative Wake Imaging

Qualitative wake imaging was invented at Boeing [1] using the Wake Imaging System (WIS). This device was designed to make experiments fast and easy by deliberately reducing the resolution of the pressure data in exchange for greatly increased spatial resolution. In addition, a unique optical-position readout system was implemented to eliminate the need for computer data-acquisition and display equipment.

A multi-colored light emitting diode (LED) is attached to the probe next to a total pressure pickup. A camera is installed in the darkened wind tunnel which records a long time exposure photograph of the model flow-field area. As the traverser sweeps the probe through the wake, the LED displays different colors appropriate to the instantaneous pressure level. Colored streaks are "painted" on the camera film. If the streaks are closely spaced they merge into color regions that directly depict the wake intensity, shape, and location.

Figure 2 shows an image of the wake produced from the system. A unique feature of this system is that the position of the probe is measured optically, so that probe deflections do not introduce error. The traverser in this case is mounted outside the test section with a strut extending through a small hole in the ceiling. The traverser employs polar-coordinate motion with rapid, back-and-forth sweeps along an arc and small incremental moves in the radial direction every time the arc sweep changes direction.

This simple device produced many dramatic images of airplane wakes that had never been seen before, and did so in run times of less than 10 minutes per data point. The results were available in near-real-time as color Polaroid photographs.

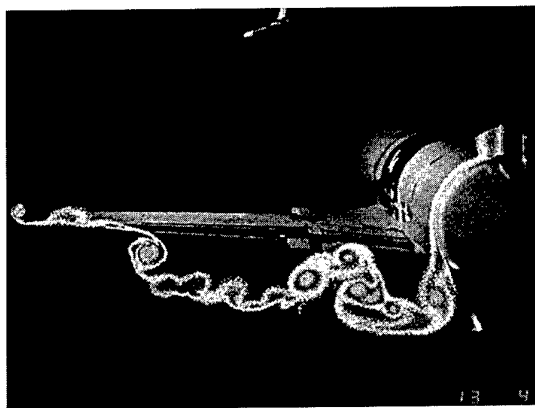


Figure 2. Wake Imaging System (WIS).

Soon after the initial development of the WIS, personal computers with good color graphics became available, making the WIS less desirable. A follow-on apparatus, called the EWIS ("E" for electronic), was developed which produced similar images in high-resolution digital graphics form [2]. Figure 3 shows a typical EWIS data image produced on a PC color graphics system. This is a more convenient storage medium, but lacks some of the real-life graphical quality.

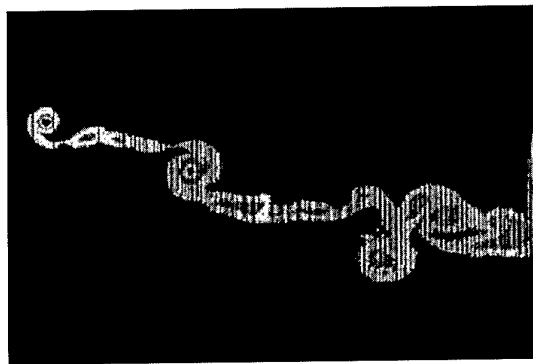


Figure 3. Electronic Wake Imaging System (EWIS).

An important result of our WIS and EWIS experience was to illustrate the complexity of wake regions and their long term stability and repeatability. They also showed that many graphical features visible in the image could be correlated with aerodynamic phenomena. This gave confidence that such wake features could be accurately measured with a physical probe.

3.3 Quantitative Flow-Field Surveys

There has been a growing need for quantitative flow-field measurements that could be correlated with other wind-tunnel data and computational fluid dynamics solutions. Consequently, we began a program based on the pioneering work of Maskell [3]. This system is now running in several production wind tunnels [4,5] and is called the QWIS ("Q" for quantitative).

Maskell demonstrated that complete lift and drag forces can be derived from a flow-field survey limited to the wake region in a single downstream plane. These results include not only the

total values, but the spatial distributions of lift and drag. Furthermore, the drag can be decomposed into profile drag and induced drag components. The induced drag had never before been directly measured and existed only as a computational result. This was (and still is) a revolutionary development. The poor reaction of the aeronautical testing community at the time was probably due to the fact that the process was impractically slow for routine use. A single data point required as much as 150 hours of wind tunnel time.

3.4 Traverser Design

A major aspect of the program undertaken at Boeing to support quantitative wake surveys was the development of wind-tunnel traversing systems. In order to reduce testing times for flow-field surveys, traversing machinery with rapid survey rates, fast responding sensors and reduced intrusiveness was required. In addition, an advanced real-time motion control and data-acquisition system was developed. This capability is essential for optimizing the survey area, implementing adaptive traverse limits, and for on-line data display.

A common approach in the design of survey equipment is to employ an array (called a rake) of pressure probes so that, in principle, the range of motion is reduced (10 probes: 1/10 the motion). We have deliberately rejected that approach for some of the following reasons:

- Rakes produce more blockage.
- The survey geometry imposed by rakes is not optimal in that it is difficult to accommodate any other geometry but a rectangular grid.
- Recording data at a high rate is more difficult and requires an intricate data-acquisition and data-reduction scheme.

Instead, our systems employ a single probe with a more capable traverser that surveys only the necessary region in the flow.

The type of motion is another fundamental consideration in the initial design. The most obvious types of motion are Cartesian (linear motion in two perpendicular directions) and polar (rotary motion along an arc combined with linear motion along the arc radius). We have, at various times, employed both of these. Based on these early experiences, we eventually selected a basic system architecture called double-rotary. This consists of two linked struts rotating at their ends. We can point to nature as the inspiration for this selection, for animals do not use linear motion.

Figure 4 shows a typical double-rotary traverser. This unit is called the Mark 16 traverser and is shown installed in the NASA Langley Research Center 14-by-22-foot low-speed wind tunnel. It has a reach of 90 inches and can accomplish accurate quantitative surveys at traverse rates up to 25 inches per second. In this installation, the apparatus must conduct surveys surrounding the model support sting without contacting it. The controller is programmed to avoid a preset region defined by the user with a limiting boundary around any solid object.

3.5 Quantitative Flow Field Survey Results

Typical data from a series of tests in the NASA Langley Research Center 14-by-22-foot low-speed wind tunnel are

presented in Figures 5 and 6. These data were derived from flow-field measurements using a 5-hole probe with a diameter of 0.25 inch to obtain static pressure and total pressure vectors distributed over the survey plane. The survey plane is about 1 inch behind the wing tip trailing edge. The raw pressure measurements are converted to velocity components and vorticity. The lift and drag results are computed using the momentum-integral analysis of Maskell and Betz, as refined by Brune and Kusunose [4, 5]. Approximately 50,000 individual measurement points are taken in the survey plane.

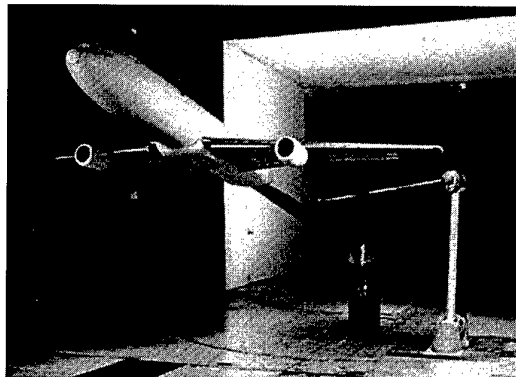


Figure 4. Mark 16 traverser in 14x22 low speed wind tunnel.

A computer controller, using in-house written Visual C++ software on a Pentium Pro PC, is implemented for performing the wake surveys. When a survey is completed, the pressure data are sent to another networked computer for further analysis so that little time is lost between surveys. The system provides control of probe speed, automated traverse limits, and optimization of the survey region. Consequently, significant reductions in wake-survey data-acquisition time have been realized. Typical full-wake surveys require approximately 20-30 minutes to complete, depending on the size of the wake-survey region and probe speed. The final data (displayed as total pressure isobars, velocity vectors, vorticity contours or loading distributions) are available approximately ten minutes after the completion of the run.

Figure 5 shows the spanwise distribution of lift for a four-engine transport airplane in both a landing and cruise configuration. It is interesting to note the local regions of increased lift loading, apparently associated with flow around the engine nacelles and pylons.

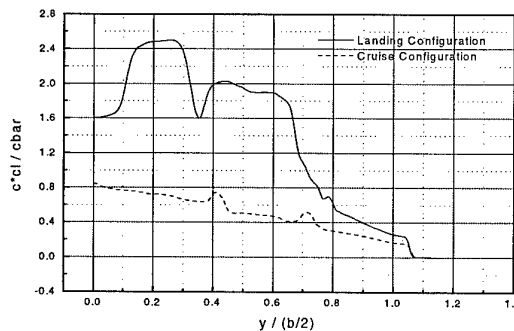


Figure 5. Lift spanload from flow field surveys.

Figure 6 shows a vorticity contour plot for the same airplane in a high-lift configuration. The vorticity plots resemble the general shape of total pressure distributions and are useful in identifying distinctive flow field features. In this example, the direction of lift on the horizontal tail is indicated by the circulation of the tip vortices indicating lift downward.

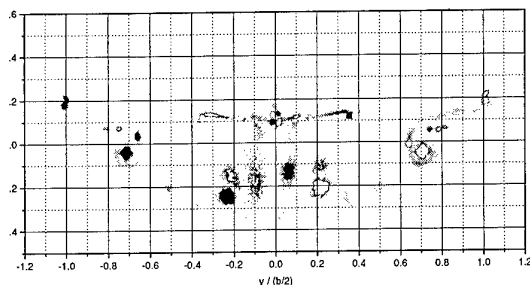


Figure 6. Vorticity contours for high-lift configuration.

Comparing the total integrated lift and drag values with balance data provides a good indication of the overall accuracy of the quantitative wake-survey data. When comparing balance data with the integrated flow field values, it is essential to understand the various corrections associated with the balance data (e.g. upflow, buoyancy, etc.) and which corrections need to be applied to the integrated wake data. When the appropriate flow corrections are applied, the maximum difference between the lift coefficient derived from the flow field and that from the balance was not more than 1% for this low-speed test.

The most recent QWIS application was performed in the Boeing Transonic Wind Tunnel (BTWT). The test conditions in this wind tunnel are considerably more difficult to accommodate than those present in a low-speed wind tunnel. There is a much greater dynamic pressure loading on the traverser and a greater sensitivity of the test section flow to disturbances from downstream.

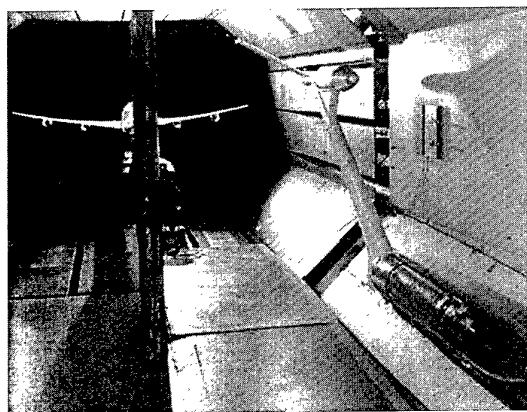


Figure 7. Mark 15 traverser in BTWT.

Figure 7 shows the Mark 15 traverser installed in the 8-by-12 foot Boeing Transonic Wind Tunnel (BTWT.) This machine employs a double-rotary motion system. The struts are made with a 60 degree forward-sweep angle to distribute the volume

of the machinery over a long streamwise distance and to place the bulk of the system behind the test section in the wind-tunnel diffuser.

The entire apparatus is mounted on a linear drive under the wind tunnel floor to allow movement of the traverser to different survey planes and to park it in a position far downstream of the test section when not in use. This allows the system to be brought into a ready state from standby in less than two minutes. It also allows coordinated motion in arbitrary survey planes such as parallel to a swept-wing trailing edge.

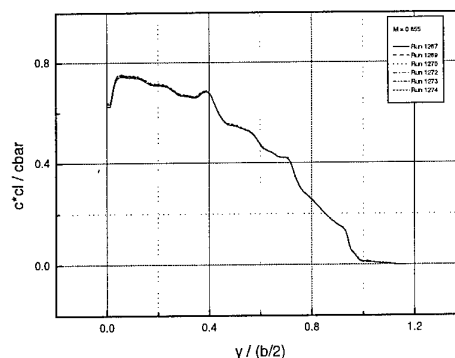


Figure 8. Lift spanload repeatability.

A recent series of tests with the Mark 15 in BTWT examined the repeatability of the wake-survey data at transonic conditions. Figure 8 shows the spanwise lift distribution obtained from six repeat runs. As is apparent from the figure, excellent repeatability in lift is obtained with a maximum variation of less than 1% in the local lift coefficient. Similar to the low speed experience, we have found that the lift data from the flow field surveys agree with the balance to within an error of 1.5%. Comparisons of the drag data, however, are not as good. Differences of drag between the balance and the flow field integrations have ranged from 2% to 15%.

Further investigation into the large drag differences is underway. A more detailed discussion of the capabilities and error analysis of the wake-survey system will be presented in an upcoming publication [6].

3.6 OPTICAL VELOCIMETERS

Considerable work has been done to develop various types of optical velocimeters. Three of the most prominent systems are the Laser Doppler Velocimeter (LDV), Doppler Global Velocimeter (DGV) and the Particle Image Velocimeter (PIV). One common characteristic of these devices is that they have no physical presence in the flow, and are therefore said to be non-intrusive.

The approach taken in our work has been to use a measurement system that could be termed "low-intrusive". Our experience with subsonic and transonic wind-tunnel-model flow fields suggests that a system based on a physical probe can indeed be made with a low enough intrusiveness to avoid any significant disturbance and loss of accuracy to the flow-field measurements.

Even though the optical systems have no presence in the flow, they can have a disruptive presence in and around the wind tunnel test section because of complicated optical access requirements and expensive equipment. In that sense they may have a very significant intrusiveness in terms of time, effort and cost.

However, the fundamental limitation of optical velocimeters is that they only measure velocity components. They cannot provide a measure of total pressure values. The profile drag and wave drag components of the airplane aerodynamics depend mostly on total pressure losses. Consequently, we have concluded that optical velocimeters are of little interest in our particular wind tunnel testing programs.

4.0 FLYING STRUT

The Flying Strut is an invention aimed at simplifying flow-field surveys. This device is smaller and lighter than a conventional rigid traverser with the potential for a greatly reduced intrusiveness to the flow and much lower cost. A Flying Strut traverser can be at least an order of magnitude lighter and less intrusive than an equivalent mechanically driven traverser. This is an essential requirement if flow-field surveys are to be employed for flight testing.

The basis of the Flying Strut is a system of linked struts with an airfoil cross section. The angle-of-attack of each strut element is controlled by a simple linkage coupled to the strut position, similar to a servo tab on an airplane control surface. The effect is to make each strut element develop just enough lift load to support its weight.

Figure 9 shows a large Flying Strut system used as a smoke dispenser in the NASA Langley Research Center 14-by-22-foot low speed wind tunnel. With the wind off, as in the figure, the strut elements hang limp and can be moved around by hand. When the air flows around the strut elements, they become rigidly fixed in position, depending on the control settings and the onset flow, and maintain a stable position. The system shown here has an extension of 12 feet and weighs approximately 30 pounds. It has operated at a Mach number as high as 0.3.

A natural question is whether or not this system will supercede the rigid, mechanically driven traversers of the type used in the Mark 15 and 16 machines. We have been cautious in approaching that application and it will depend on further studies concerning the response of Flying Struts to wake disturbances.

The stability of the Flying Strut depends on the uniformity of the wind tunnel flow. The struts follow any unsteadiness in the airstream. This tends to make the system exhibit unsteady motion in airplane wakes where the surveys are required. This behavior may also provoke unstable motion such as flutter. Until the dynamic properties of the Flying Strut are better understood, we have found it prudent to apply the system mostly in regions of undisturbed flow.

Another important factor is the relative difficulty of implementing one or the other type of apparatus. We have

found that in small to medium size wind tunnels, the mechanically driven traverser is generally more convenient. For test sections larger than 15 feet or so, the size and mass of the heavy machinery becomes troublesome. In this size range, the Flying Strut has the greatest advantage due to its substantially reduced weight.

Applications for in-flight surveys are considerably more difficult with a mechanically driven traverser because of the high stiffness and mass requirements. This is where the ultimate advantage of the Flying Strut is expected to prove invaluable.



Figure 9. Large scale Flying Strut system.

4.1 Flying Strut Control Mechanism

A Flying Strut system utilizes several different trimming mechanisms to control its position. The simplest of these mechanisms is called the skewed-hinge. A diagram of a skewed-hinge hub is shown in Figure 10a.

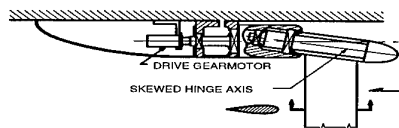


Figure 10a. Skewed hinge trimming mechanism.

The strut elements are supported by free bearings on the skewed shaft which is skewed away from the flow direction by a small angle, typically about ten degrees. As the control motor rotates the skewed shaft, the strut element develops a slight change in angle of attack that automatically causes the strut to produce the lift necessary to follow the motion of the skewed shaft.

Since the aerodynamic lift of the strut element acts to overcome all the weight of the apparatus, it relieves the actuating motor of that requirement. Therefore, the motor can be very small with low torque since it only has to rotate the skewed-hinge shaft, not the entire strut weight.

Another type of Flying Strut trimming mechanism uses a gear drive as depicted in Figure 10b. The strut element is free to rotate about two axes at right angles. The feathering axis allows rotation of the strut angle of attack while the flapping axis allows the tip of the strut to rotate in the survey plane. The bevel gear couples the feathering and flapping motion in a way that produces a stable trimming action. As in the skewed hinge mechanism, the actuating motor only needs to produce enough torque to rotate the bevel gear to change the strut angle-of-attack, thus generating enough aerodynamic lift to move the strut.

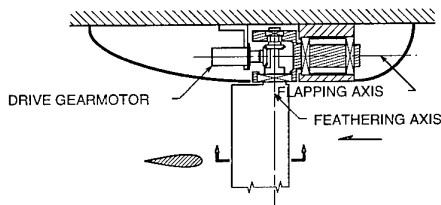


Figure 10b. Gear drive trimming mechanism.

4.2 Flow Field Dispensing

Most early applications of Flying Strut systems have been in locations upstream of the model in the smooth airflow. Smoke dispensing is the most obvious application from that location. Figure 11 shows flow visualization using smoke dispensed from the Flying Strut in the NASA Langley 14-by-22-foot wind tunnel. In this example the Flying Strut was operated at a Mach number of 0.3.



Figure 11. Dispensing smoke in 14x22 wind tunnel.

Other possible applications in the undisturbed flow upstream of a model include the dispensing of seed material for a laser doppler velocimeter (LDV.) This would allow local seeding which could be servo-controlled to follow the traversing motion of the LDV and eliminates the requirement to fill the entire wind tunnel volume with seed material.

4.3 Transonic Flying Strut

Early Flying Strut systems were developed by trial and error, without benefit of any stability analysis. This was generally successful at low speeds. In an attempt at developing the Flying Strut for transonic wind-tunnel calibration surveys, a similar trial-and-error approach proved unsuccessful. Several small versions were evaluated in the BTWT, but they all exhibited a periodic oscillation that rendered the system unusable. These attempts were abandoned until recently.

As part of a program to upgrade BTWT, we have a requirement and renewed interest in developing the Flying Strut for empty test-section calibration surveys. A research program has been underway with the Central Aero-Hydrodynamic Institute in Russia (TsAGI), under the direction of G. Amiryantz, for the last several years. The goal of this work is to develop an understanding of the instabilities encountered during earlier tests and to develop a practical survey system for calibration of the BTWT test section.

This has required an extensive design-and-analysis study focusing on dynamic behavior, including flutter susceptibility. Last year this program resulted in a successful demonstration of a transonic Flying Strut in the TsAGI T-128 wind tunnel at a Mach number of 0.95 and a pressure of two atmospheres. Figure 12 shows a photograph of this device installed in the test section. The strut elements are swept forward at a 45 degree angle to reduce the local blockage at the survey plane.

Based on this experience, we are now proceeding with the design of a Flying Strut for calibration of the BTWT empty test section. This will allow measurement of the complete flow properties over more than 90% of the test section.

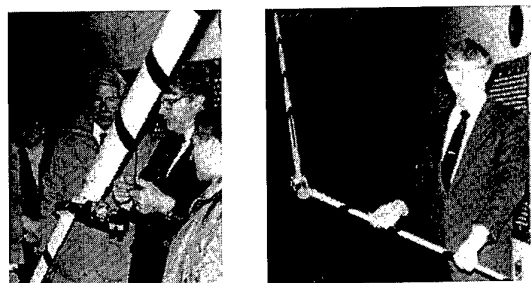


Figure 12. Transonic Flying Strut.

4.4 In-Flight Demonstrations

Originally the Flying Strut was proposed as a practical method for conducting flow field surveys in flight. Its very light weight, low disturbance and extensive reach are all vital properties of an in-flight survey system.

Figure 13 shows a successful version of the Flying Strut operating on a twin-engine airplane. The 2-axis Flying Strut had a total reach of 9 feet and weighs approximately 15 pounds. This demonstration operated at an airspeed up to 190 knots.

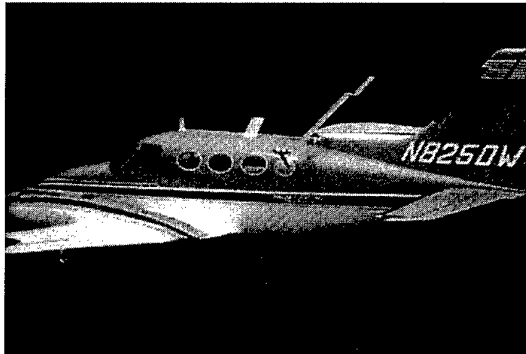


Figure 13. Flying Strut in-flight.

The proposed application, in this case, was to survey the inboard wing and propeller slipstream. The program did not proceed due to lack of interest and funding.

4.5 In-Flight Camera Mount

In an unusual application, a single-axis Flying Strut was attached to the tail cone of a twin turboprop airplane for use as a controllable camera mount. The airplane had been tufted on the fuselage bottom and the camera mount replaced the need for a chase plane to observe the tuft behavior.

Figure 14 shows the view of the airplane, as seen by the camera behind the vertical tail. In this application the system was very steady, even in the wake of the tail surface.



Figure 14. Flying Strut in-flight camera mount.

5.0 CONCLUSIONS

Information contained in airplane flow fields can now be accessed in a variety of ways in large industrial wind tunnels. Qualitative wake surveys of total pressure isobars have shown valuable diagnostic utility. With slightly more effort, however, the full quantitative properties of flow fields can be measured to yield spatial distributions of lift and drag, including induced

drag and wave drag components. This is a breakthrough in measurement technology.

We have seen this experiment develop from a curiosity, requiring 300 minutes per data point, to a valuable engineering application requiring less than 20 minutes. Further optimization of traverser motion control and data acquisition strategies promises further reductions in the required test time. In addition, the Flying Strut has demonstrated in low speed wind tunnels that it can be a very practical system for supporting and moving a variety of probes or dispenser systems.

Transonic application to empty test-section calibration surveys has been demonstrated in a prototype and will soon be available for routine usage. Substitution of the Flying Strut instead of a conventional rigid traverser in small to medium size wind tunnels is problematical. However in large wind tunnel (more than 15 feet) the system should offer a substantial advantage over conventional mechanically-driven traverser systems.

The ultimate application of the Flying Strut will be to permit the entire range of flow field measurements on board airplanes in flight. The in-flight realm is, after all, the only way to make all model support, wall effects and Reynolds number scaling problems disappear.

How much effort is it worth to access this realm?

6.0 REFERENCES

- 1 Crowder, J. P., "Quick and easy flow field surveys, *Astronautics and Aeronautics*, Vol. 18, 10, pp. 38-39, October, 1980.
- 2 Crowder, J. P. and Beck, H. M., *Electronic Wake Imaging System*, in *Flow Visualization 3: Proceedings of the Third International Symposium on Flow Visualization*, Ann Arbor, ed. W.-J. Yang, pp. 715-719, Hemisphere, Washington, D.C., 1985.
- 3 Maskell, E. C., Progress towards a method for the measurement of the components of the drag of a wing of finite span, RAE Technical Report 72232, 1972.
- 4 Brune, G., "Quantitative low-speed wake surveys," *AIAA Journal of Aircraft*, vol 31, no 2, pp 259-255, March-April 1994.
- 5 Kusunose, K., "Development of a universal wake survey data analysis code," AIAA paper 97-2294, June, 1997.
- 6 Crowder, J.P., Krutckoff, T.K. and Watzlavick, R.L., *Airplane Flow-Field Measurements*, World Aviation Congress Exposition, Oct. 1997

MOLECULAR DIAGNOSTICS FOR RAREFIED FLOWS

J.P. Taran
 LAERTE Director
 ONERA, Fort de Palaiseau
 91120, Palaiseau
 France

ABSTRACT

The paper reviews the various optical techniques which can be applied for point, line of sight or imaging measurements. In the category of point measurements, light scattering methods like Raman, Rayleigh or Electron Beam Fluorescence (EBF) are treated first, but briefly since they are of little use, especially when enthalpy is very high and flow naturally bright. The emphasis is placed instead on nonlinear laser spectroscopy like Coherent anti-Stokes Raman Scattering (CARS), which has recently achieved great success at getting temperatures and density in high enthalpy shocks. Then the diode laser absorption spectroscopy is described. A high data rate instrument now gives on a routine basis the static temperature and the velocity of the stream in the hot shot facility F4 of ONERA, at stagnation enthalpies in excess of 15 MJ/kg. EBF imaging in that same facility has permitted measurements of velocity to be performed across the external boundary layer into the flow core thanks to a high energy pulsed electron gun. Finally, the technique of Collective Light Scattering is briefly described and its capabilities demonstrated.

1 - INTRODUCTION

The interest in reentry of space vehicles, in high speed transportation and in single stage to orbit concepts continues to stimulate the research on hypersonic aerodynamics. This research is conducted in dedicated facilities that simulate flight at high altitude and high velocity, and that are employed for model studies and for computer code validation.

High Mach number, high enthalpy facilities are still being designed and constructed throughout the world for this purpose.

They pose an exceptional challenge to data acquisition.

Well established techniques have long been used for the measurement of such key parameters as:

- force and moment exerted by the flow on the model (using strain gauges);
- wall pressure, using classical pressure transducers, and pressure-sensitive paints for near isothermal flows;
- wall friction, using gauges, and oil film or liquid crystal visualisation;
- heat fluxes, by means of infra-red imaging, temperature-sensitive paints, liquid crystals and thin film thermocouples;
- main stream velocity and temperature by Pitot tubes, thermocouples, etc.

All these techniques are intrusive, generally limited to measurements at the stream interface with a model or a nozzle wall. For a long time, only some line of sight optical techniques like emission spectroscopy or schlieren were capable of providing information from the gas phase without interfering with the flow, but with very limited spatial resolution and measurement accuracy. Recently, new methods have become available for the acquisition of key flow parameters like velocity, temperature and density in the boundary layers near the model. They now are an essential complement to the conventional probes in modern facilities. Validation of computer codes has greatly benefited from their generalisation. In addition, these high enthalpy facilities pose special difficulties, as non-equilibrium conditions (real gas effects)

prevail both in the free stream and in the shock and boundary layers. Then the flow can no longer be described with the usual parameters temperature, density and velocity only. Several temperatures, like those of the rotational, translational and vibrational degrees of freedom need to be simultaneously determined, together with dissociation and ionisation. The duration of the runs is often exceedingly short. That complicates the task, as the flow rarely reaches a steady state. The data then need to be taken on a very short time scale and carefully dated. In particular, in any turbulent flow, the fluctuating, highly non-stationary character of flow variables increases the difficulty of taking the measurements. The frequency range of the fluctuations is large, typically up to several MHz. A wide extent of spatial scales is also generally observed, this extent being proportional to the Reynolds number.

The search for non-intrusive, non-seeding methods is a crucial aspect of experimental research for rarefied, high speed flows. Diagnostics based on molecular properties are specially attractive. An excellent review of the techniques for hypersonics that were available a few years ago can be found in Reference 1. But since most mechanical, macroscopic fluid properties do not rely on the detailed atomic ones, one may also look for measurements based on large scale optical phenomena that reveal information about the macroscopic properties. Obtaining information on the density and pressure field fluctuations is particularly important. The technique of Collective Light Scattering (CLS) is very well suited for that task.²

All of these optical methods now greatly expand our capabilities in measuring the properties of the stream non-intrusively. For the clarity of presentation, we classify in the following these methods into four groups, namely point, line of sight, imaging and collective measurements.

In the first part of this paper, the point

measurements are reviewed. Point methods generally yield good measurement accuracy. We briefly outline the laser-based, incoherent methods like Rayleigh, Raman and Laser-Induced Fluorescence (LIF). We also summarise the principle of Electron-Beam-induced Fluorescence (EBF) which, in a variant where X-rays are detected, has great potential for accurate density measurements. The bulk of this section, however, is devoted to the technique of Coherent anti-Stokes Raman Scattering (CARS) which has recently demonstrated its great potential in the analysis of high-enthalpy streams.

In the second part, we focus on Diode Laser Absorption Spectroscopy (DLAS), which is a line of sight technique. DLAS has a potential for great accuracy in acquiring stream translational temperature and velocity, and is now used routinely in a high-enthalpy hot-shot tunnel.

Section three covers imaging. Imaging is rarely quantitative. However, it can locate discontinuities accurately. It is therefore useful at measuring shock front position. Some recent achievements in imaging of the velocity field using EBF are here presented. This turns out to be difficult in high enthalpy streams because of the stray light, but usage of the pseudo-spark switching device, which produces a strong electron beam, overcomes the problem. The velocity field could be recorded across a boundary layer into the flow core.

Finally, the fourth part describes the coherent elastic scattering off density inhomogeneities. This technique provides density, mean and turbulent velocity, and acoustic wave characteristics.

2 - POINT MEASUREMENTS

Point measurements are primarily performed by using laser scattering off the molecules or particles seeded into the flow. They can be implemented using either incoherent scattering of a laser beam or coherent, nonlinear optical arrangements; the molecules can also be excited by electron beams of

several keV, which can induce fluorescence in the visible, UV and X-ray regions.

2.1. Incoherent scattering

Incoherent scattering is observed by illuminating the gas with a focused laser beam (Fig. 1). The light scattered at right angles by the gas molecules is collected by a lens, spectrally analysed using a spectrograph, and detected by means of phototubes or detector arrays. Three sorts of scattering processes in molecules are usually recognised and schematically depicted in the energy level diagrams in Figure 2. Commercial pulsed lasers can be employed, giving time resolution of 10 ns typically, which is suitable for short duration facilities. The energy per pulse needed is in the range 10-100 mJ; cw lasers also can be used for steady state studies; the spatial resolution is typically 0.1 to 1 mm³.

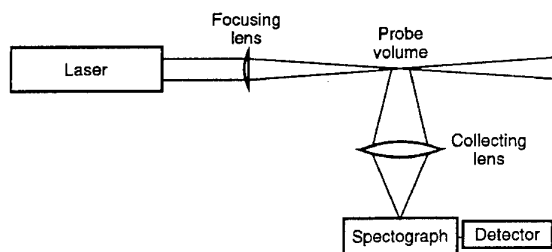


Fig. 1. Schematic diagram for observing scattering of a laser beam by molecules in a gas.

- **Rayleigh scattering** (process (a)) is produced by molecules. The photons are scattered in all directions and have the same energy as the laser photons. It is a weak process, that requires total absence of stray light at or near the laser wavelength. Also, the laser beam should not impact any solid surface near the volume under probe to avoid strong interference. Particles suspended in the flow also cause Mie scattering (see below) that constitutes another form of interference.

This problem actually limits the sensitivity of the method to densities of the order 10^{-1} to 10^{-2} normal at best. Its potential use is thus restricted to classical subsonic and low supersonic tunnels. Proximity of a wall also is a major source of interference because the laser light scattered off the surface is many orders of magnitude stronger than that from the molecules. Rayleigh scattering is thus proscribed in boundary layer studies.

- **Raman scattering** (b) is similar to Rayleigh scattering, except that the scattered photons have an energy different from that of the laser photons. The energy difference is equal to the energy of the vibrational quantum. This property is extremely interesting, because it affords:

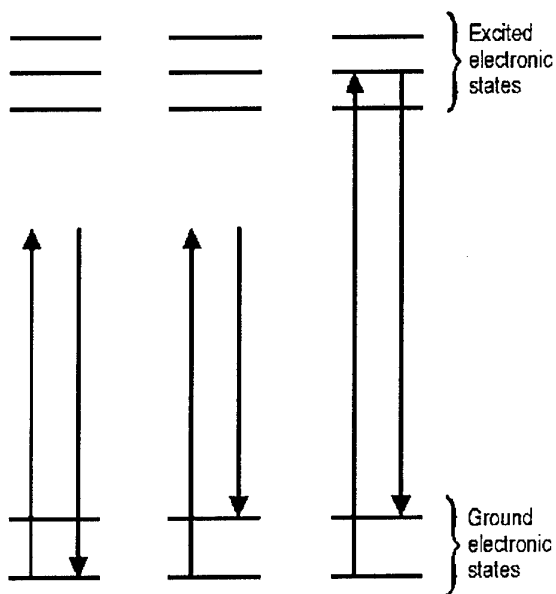


Fig. 2. Energy level diagram for Rayleigh (a), Raman (b) and fluorescence (c) scattering.

- chemical selectivity, since the vibrational quanta differ from molecule to molecule; spectroscopy of the scattered light thus reveals the presence of the various chemicals and permits concentration measurements;

- temperature measurement capability, because the energy of the vibrational quantum slightly depends on the rotational

state of the molecule; each rotational state thus gives a specific line, which is separable from its neighbours under high spectroscopic resolution. The states being populated according to the Boltzmann law, spectral analysis yields the rotational temperature; the latter is generally equal to the static temperature of the gas. Measurement accuracy is of the order of 50-100 K if signal to noise ratio is good. Even better performance seems attainable under special conditions using a variant called rotational Raman scattering.

Raman scattering is even weaker than Rayleigh scattering, by a factor of 100-1000 typically. Its use, in spite of its other attractive characteristics, is thus restricted to aerodynamic flows above or close to normal density, and to weakly luminous flames.³ Its effective detection sensitivity with state of the art lasers and detection optics is in the range 10^{15} - 10^{16} particles cm^{-3} for a spatial resolution set at 1 mm^3 . Thus it has little future in hypersonics with today's lasers and detectors unless densities as high as 10^{-1} normal at least are achieved in the free stream, and stray light and flow luminosity are kept very low. Some applications of Raman scattering to aerodynamic flows had been developed as early as 1973.³

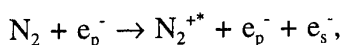
- **Fluorescence scattering**, often called Laser-Induced Fluorescence (LIF), combines the species selectivity of Raman scattering with far stronger signal intensities. It is closely related to Raman, but with the exciting laser tuned into resonance with the one-photon absorption lines of the molecule to detect. This trick enhances by many orders of magnitude the scattering cross-section, therefore the signal strength, and makes it possible to detect ppm-level traces in flames like the OH radical or the NO pollutant. Detection sensitivities lie in the range 10^{10} - 10^{12} cm^{-3} . LIF has at first been used for point measurements, particularly in flames and in supersonic, low pressure streams (for mixing studies using traces of iodine gas as a seeder); however, it has for the past 5-10 years primarily been employed at flame and flowfield imaging (see Section 4) thanks to

the introduction of intensified 2D CCD detector arrays.

Several applications to hypersonics are compiled in Reference 1, Session 3. Recent work has focused on concentration measurements of copper⁵ and oxygen atoms.^{6,7} By scanning the absorption lines with their tunable lasers, these authors could also detect the Doppler shift resulting from the flow motion and to deduce the flow velocity and turbulence. Velocity measurement accuracies are of the order 10-15%.

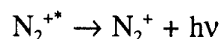
- **Mie scattering** designates the signal scattered by particles with sizes comparable to or larger than the wavelength of the illuminating laser (0.4-0.6 μm typically). It is a close parent of Rayleigh scattering. It is the phenomenon employed in Laser Doppler Velocimetry (LDV). While LDV works remarkably well in subsonic and low supersonic flows, it has been met with mixed success in hypersonics, because the flow density is too low to "carry" the particles especially through shocks. An interesting assessment is found in Reference 1, Session 5.

- **Electron beam fluorescence (EBF)** bears some resemblance to LIF, except that the laser beam is replaced by a high energy electron beam in the diagram of figure 1. Electron guns like those employed in electron microscopy are used, but even more powerful sources like pseudo-sparks are sometimes utilised. The high energy electrons induce broadband excitations onto the molecules under probe and eventually ionise them. For N_2 at 10^{-4} normal density, the main process is:

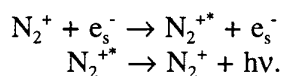


where e_p^- is a primary electron (from the electron beam) and e_s^- a secondary electron of a few eV energy emitted during the formation of the N_2^+ ion; this ion which is excited by the collision on one of its vibronic states, denoted by the * symbol, promptly

loses its electronic energy via emission of a photon:



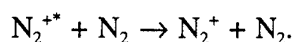
in the near UV. The luminescence is interesting because its intensity is proportional to the N_2 number density and its spectral content reveals the original population distribution on the quantum states of the N_2 , allowing temperature measurements to be performed. The secondary electrons remain confined in the immediate vicinity of the ions by the space charge, and keep having low energy collisions with them; these collisions re-excite them and maintain a luminescence by the processes:



This causes the luminescence to persist several μs or tens of μs after the high energy electron beam has been turned off. This phenomenon can be exploited for free stream velocity measurements, by flow tagging followed by time of flight detection.⁸ EBF is also used to measure rotational and vibrational temperatures, by dispersing the spectrum of the emitted fluorescence.

Typical applications of EBF can be found in Reference 1, Sessions 3 and 5. Both point measurements and imaging (see below) have been used. The spatial resolution is of the order of 1 mm^3 ; it is usually a little worse than in the laser scattering techniques. Recently, encouraging results were reported using a pseudo-spark mounted in a model.⁹

However, EBF suffers a difficulty associated with the quenching:



Quenching reduces the fluorescence yield and interferes with the concentration measurements at densities above a few 10^{-4} normal. Detection of the X-ray emission,

which results from a Brehmstrahlung process and suffers no quenching, offers an interesting alternative.¹⁰

2.2. Coherent scattering

- **Coherent Anti-Stokes Raman Scattering (CARS)** is a nonlinear optical method that affords the species selectivity of Raman scattering combined with excellent signal generation efficiency and stray light rejection.¹¹ Unlike the incoherent laser scattering methods, it requires the use of two pulsed lasers, one of which is fixed in frequency (angular frequency ω_1) and the other tunable (frequency ω_2 , with $\omega_2 < \omega_1$). The beams from the two lasers are colinearly focused at the point of interest (Fig. 3).

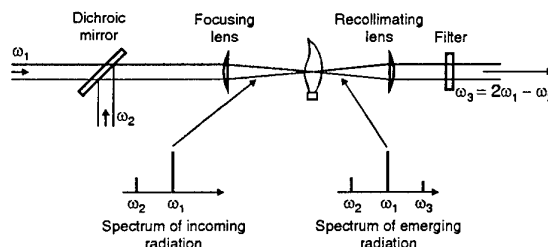


Fig. 3. Schematic of the experimental arrangement for generating coherent signal off the molecular vibration, with spectrum of the radiation emerging from the gas. The two strong laser lines are practically unchanged; the anti-Stokes sideband is exactly superimposed on them, with very small divergence.

If their frequency difference is precisely equal to the vibration frequency of a molecular species present at the focus, the vibrations of the molecules are driven coherently, generating a coherent phase grating in the gas that scatters the incoming "pump" laser beams into new colinear and coherent signal beams at frequencies $\omega_1 + (\omega_1 - \omega_2)$, called the anti-Stokes sideband, and $\omega_2 - (\omega_1 - \omega_2)$, the Stokes sideband (not shown in the figure). The first one being easier to detect is preferred experimentally. The energy in this signal is proportional to

the square of the molecular concentration. Thus, with proper calibration, one can both detect the species of interest and measure its concentration by this method. By tuning ω_2 to the right frequency, all the species present can be detected. Further, as their vibration frequencies slightly depend on the rotational state from which the scattering takes place, a fine spectral analysis of their response (Fig. 4) yields the populations on the quantum states, like in spontaneous Raman. If those are populated according to the Boltzmann law, i.e., if rotational equilibrium exists, then the rotational temperature can be measured. Similarly, a vibrational temperature can be obtained.

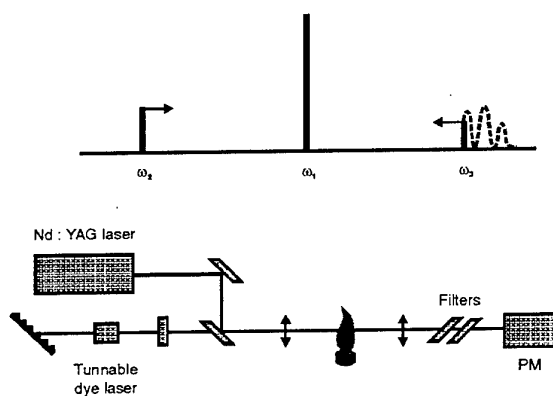


Fig. 4. Principle of the spectral analysis in scanning CARS.

CARS is a remarkable tool because it affords spatial resolution (typically 1-10 mm long, with a beam diameter of 50 μm), excellent signal strength, perfect stray light rejection. Spectral analysis can be performed by scanning, which gives good sensitivity, but a variant called multiplex CARS (Fig. 5) which uses a broadband dye laser can be employed for single shot measurements. This is done at a cost in sensitivity, but the high temporal resolution is precious in unstable media like turbulent flames and transient flows. Recently, the two-line or dual-line CARS, which combines the sensitivity of scanning CARS with the single shot capability, and the transient CARS, which is a variant capable of measuring the velocity and the static

temperature in a single shot, were introduced and tested.^{12,13}

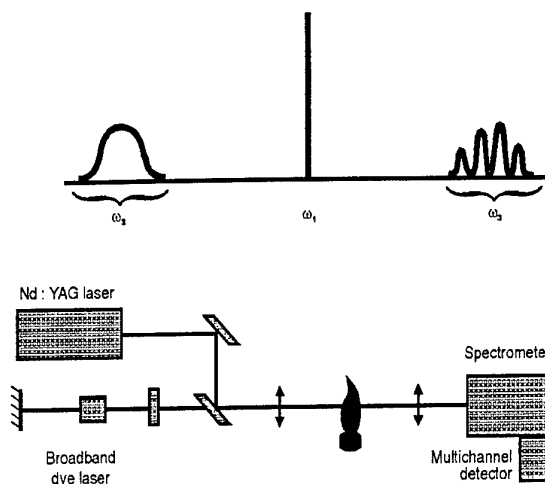


Fig. 5. Single shot recording of spectra using multiplex CARS.

While CARS has been primarily used in combustion research, work at lower pressures in plasmas, gas laser media and aerodynamic flows has been performed. To our knowledge, the only research in practical hypersonic wind tunnels has been performed at ONERA. Density, temperatures and velocities have been obtained, including free streams and shock layers. In particular, boundary layers were explored (Fig. 6) using dual-line CARS.

In this work, which is conducted in the Mach 10 R5Ch facility, the flow has a free stream velocity of 1500 m/s, a static temperature of 56 K and a static pressure of 6 Pa. Each data point is the average of 20 consecutive laser shots at 10 Hz repetition rate. Given the signal levels and calibrations performed, the measurements in the free stream, shock and boundary layer have a relative uncertainty of $\pm 10\%$. The agreement between experiment and computations is excellent for $0 < X/L < 1$. Beyond, the edge effects from the sides of

the plate cause deviations particularly at the higher elevations above the plate.

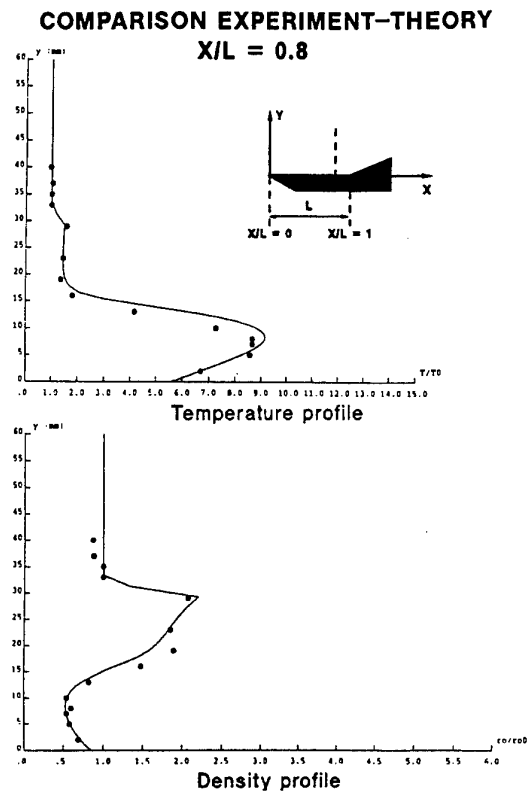


Fig. 6. Temperature and density profiles over a flat plate with elevation at R5 using dual-line CARS; the results are compared with computations from the HOMARD code.

A shock layer against a cylinder with axis perpendicular to the flow was also studied at the R5Ch facility (Fig. 7); noteworthy is the agreement found between experiment and theory, as the validation bears on both temperature and density. An oblique shock impacting the shock layer has also been carefully documented. Formerly, these cases were only accessible to schlieren and interferometry, and measurement precision was somewhat inferior.

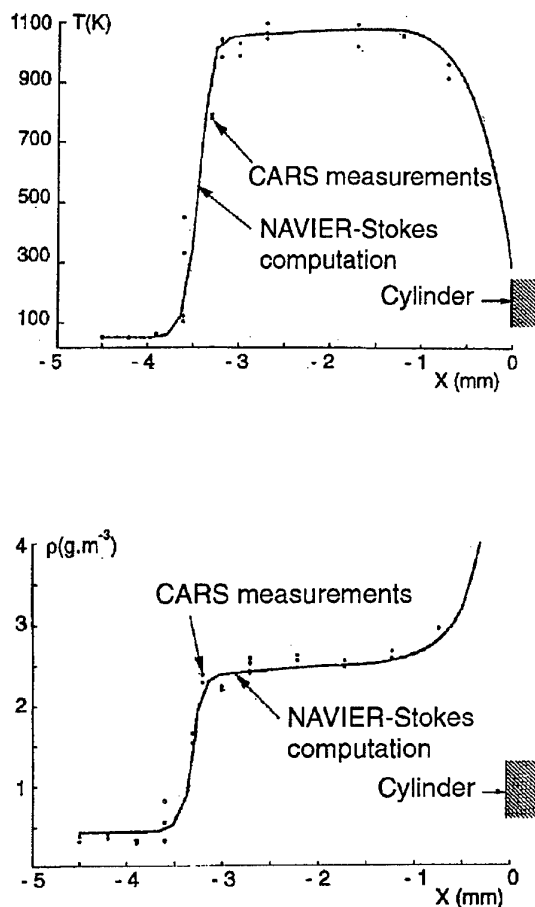
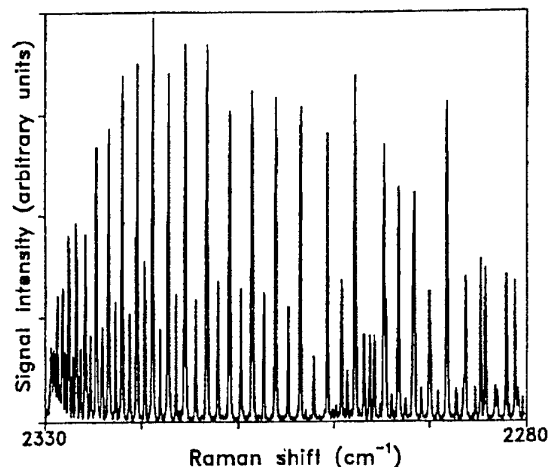


Fig. 7. Temperature and density profiles along flow centerline in shock layer in front of a 16 mm-dia cylinder at R5.

Similar studies were also done in a high enthalpy flow. Non-equilibrium conditions were seen in shock layers in the L2K tunnel of the DLR using scanning CARS; this work, presented in a companion paper in the same session of this conference,¹⁴ yields a clear direct demonstration of the presence of non-equilibrium between rotational and vibrational degrees of freedom; notably it shows partial vibrational freezing of the free

stream, a fast rotational heating and a slow vibrational heating as the gas penetrates into the shock and an anomalous abundance ratio between the ortho and para forms of the nitrogen (Fig. 8).



nitrogen CARS spectrum

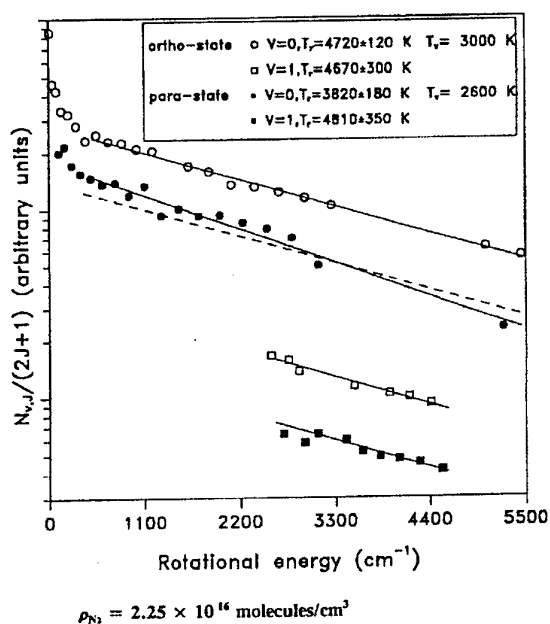


Fig. 8. scanning CARS spectrum of N_2 in the shock layer against a flat disk at the LBK facility of the DLR showing the non-equilibrium in both the rotation and the vibration.

Multiplex CARS was also used in the expanding plume of the decomposition products of lead azide, exposing a non-equilibrium gas and demonstrating a priori the feasibility of this technique for short duration flows at static pressures a few 10^{-3} normal (Fig. 9,10).

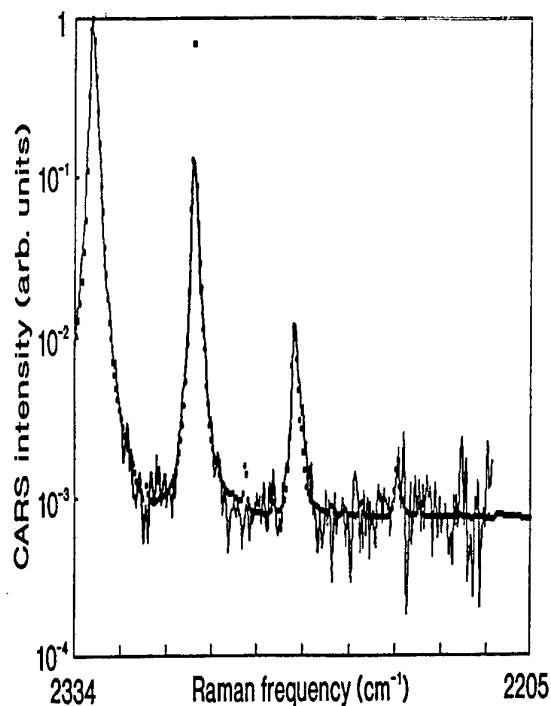


Fig. 9. Multiplex CARS spectrum of the plume of decomposition products of a lead azide pellet 33 mm above the pellet and 9 μ s after ignition.

Lately, CARS has also been shown to provide velocity from single shot, spatially-resolved recordings of transient signals from the flow heterodyned against, e.g., a static cell signal. The technique operates at pressures as low as 5 Pa and Mach number 10 at R5Ch; it has been demonstrated in the free stream¹⁵ and in boundary layers near models (Fig. 11 and 12). The measurement volume can be brought as close as 100 μ m to a surface without any interference whatsoever.

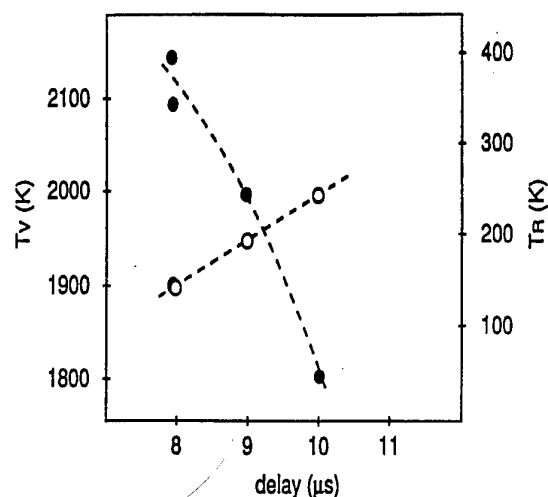


Fig. 10. Rotational and vibrational temperature evolution vs time obtained from spectra such as that of Fig. 9.

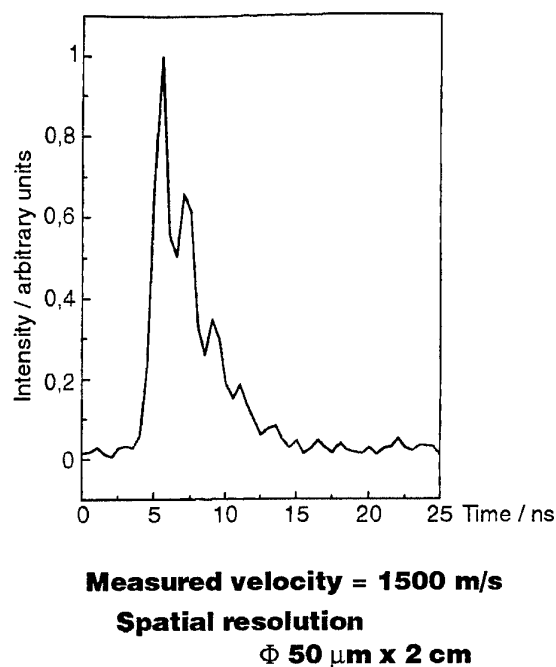


Fig. 12. Typical transient CARS self heterodyning trace at R5, from which temperature and velocity are derived.

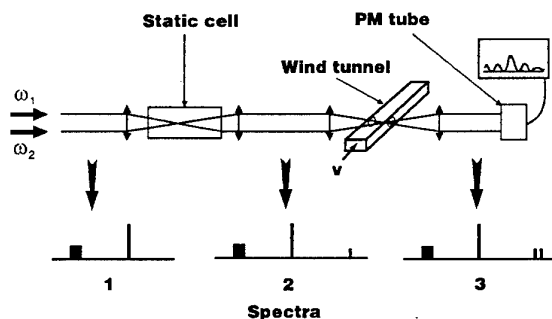


Fig. 11. Principle of non-intrusive, single shot velocity measurement by transient CARS.

Resonance-enhanced CARS and Degenerate Four Wave Mixing (DFWM) are to CARS the equivalent of LIF to spontaneous Raman scattering. They offer enhanced detection sensitivity and have been used mostly in combustion diagnostics.^{16,17} They have a potential in hypersonics as well, but no application has been given so far, to our knowledge. Recent work done at ONERA¹⁸ and elsewhere in combustion clearly demonstrates the feasibility of NO detection.

3 - LINE OF SIGHT METHODS

These methods essentially rest on absorption and emission spectroscopy.

- In **emission**, one collects the light coming from the free stream or from some boundary layer. This light is passed and dispersed through a spectrograph for analysis. Spectral lines are generally detected which reveal the presence of chemicals like metal vapours (in the visible and UV) or of vibrationally excited molecules (in the infra-red). Presence of these lines indicates presence of the compound. The method suffers from major drawbacks, like the impossibility to determine the position of the radiating species along the line of sight of the collection optics; this is fatal if zones of different temperature and composition are contributing. In addition, it is also impossible to determine concentrations in a quantitative manner, even if only a homogeneous zone contributes. The latter difficulty stems from the fact that the radiating quantum states are

populated via complex collisional mechanisms with electrons or hot species in the non-equilibrium flow and depopulated by both radiative and collisional (quenching) processes with other species. Emission is thus used primarily for establishing the presence of trace species or contaminants.

- **Absorption**, like emission spectroscopy, does not indicate the position of the absorbing species. It is, however, capable of measuring populations on the ground rovibrational states, which are the most populated. Therefore, concentrations can be measured, at least if the absorbing medium is homogeneous or presents some spatial symmetry. Technically, the best measurements are performed with laser sources having a spectral resolution capable of resolving the molecular or atomic lines. Today, the most useful measurements in hypersonics have been performed with tunable diode lasers in the infra-red. Semiconductor diode lasers constitute very narrow linewidth infrared sources in the absorption domain of molecules like NO or H₂O. The wavelength can be easily and finely tuned (less than 10^{-3} cm^{-1}) by adjusting the temperature and the current through the diode, which makes these sources attractive for absorption spectroscopy. The DLAS measurements are based on isolated absorption lines of NO or H₂O which are often naturally present in the wind tunnels. The lines are scanned at up to 10 kHz using a spectrally tuned diode laser beam (around $5 \mu\text{m}$) crossing the flow. The velocity of the flow is deduced from the Doppler shift of the lines, when the beam is not perpendicular to the flow axis; the measurement can here be fairly accurate. Rotational or vibrational temperatures can also be derived from the intensity ratio of two different absorption lines. The high spectral resolution of the tuning brings negligible contribution to the absorption lineshape; which can thus be exploited to obtain static temperature and pressure of the medium crossed. Once the temperatures are known, the density of the absorbing species can be deduced from the integrated area under a line.

Figure 13 shows the experimental arrangement in the F4 wind tunnel. The emitting and receiving optics remain outside the vacuum chamber. The lead salt semiconductor diode is kept in a cryostat cooled at 10 K by a helium compressor. Stabilised generators are used to monitor the diode temperature and current for laser emission. Different optical components are used to collimate and filter this emission into a single-mode laser beam. Part of this beam is used for wavelength and intensity calibration with the help of a Perot-Fabry and a low pressure cell filled with a known quantity of NO. The beam enters the vacuum chamber through CaF₂ windows and crosses the flow at an angle of 60° relative to the axis in order to enable Doppler shift for velocity measurement. HgCdTe photodetectors, with 2 MHz bandwidth, are used to measure the beam intensity. The electric signals are digitised at 1 MHz to get adequately resolved spectra.

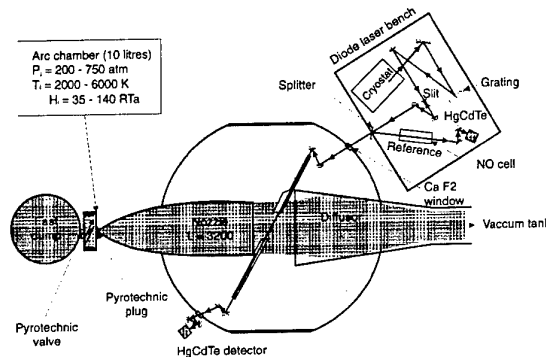


Fig. 13. Schematic of the DLAS spectrometer at F4.

Two hundred pairs of spectra are taken at 1 kHz for each wind tunnel run. Each flow absorption spectrum must at first be calibrated in wavelength and intensity using its corresponding etalon spectrum. The corrected absorption spectrum is then matched to simulated spectra through an iterative non linear least-squares fitting procedure: one then derives the velocity of

the flow, the temperatures and concentrations of the absorbing species.

Figure 14 shows a typical evolution of absorption spectra during a run in about 50 ms intervals. As the flow establishes, the Doppler-shifted line appears alone; subsequently, the line with zero Doppler shift grows as the test tank gradually fills with the spent gases. The derived velocity and static temperature are displayed in figure 15 versus time.

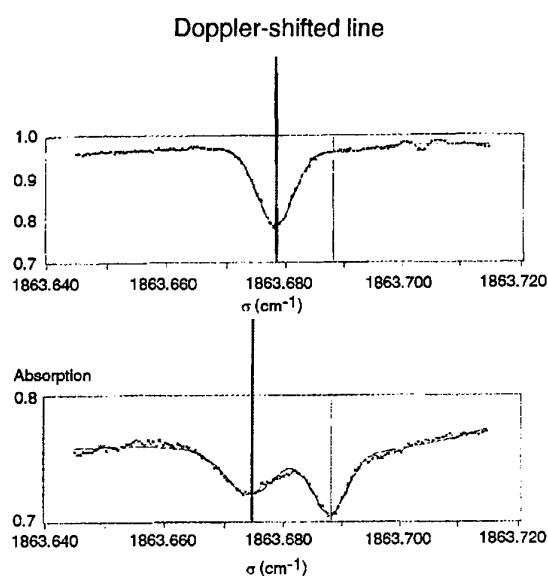


Fig. 14. NO spectrum recorded during one of the F4 runs at reduced enthalpy 100.

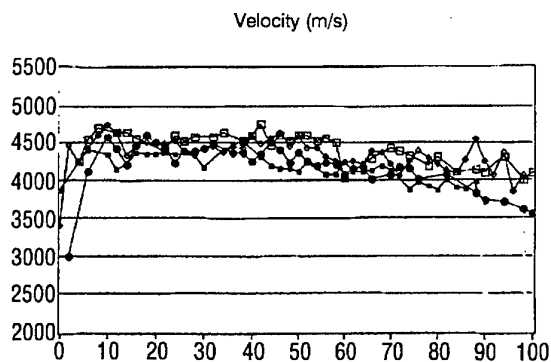


Fig. 15. Resulting velocity from the sequence of spectra recorded in the same run.

4 - IMAGING

Imaging has long rested on the use of schlieren and interferometry; the latter being more sensitive is often preferred for probing the low density flows. Recently, tomography using either lasers or an electron beam for excitation, has been introduced. Unlike the preceding two methods, which give integrated information along the line of sight, tomography provides 3D resolution.

LIF has first been employed successfully in combustion, and then in high enthalpy hypersonics for the detection of NO in the free stream. Significant work has been performed at the Stanford High Temperature Gas Dynamics Laboratory and at the DLR.^{1,19} By exciting two separate absorption lines, the DLR were also able to determine the rotational temperature. An interesting use of LIF is in the RELIEF method for velocity imaging developed at Princeton University.²⁰ In spite of its great advantages and simplicity, LIF suffers from stray light interference, particularly from the spontaneous emission from the electronic states whose fluorescence is detected, and from the considerably enhanced complexity of the absorption spectra when attempting to probe shock layers in the high enthalpy facilities.

EBF has so far been used primarily in low or medium enthalpy facilities for imaging. Illumination is achieved by rastering the cw beam emitted by the electron gun, giving a triangular field. Reference⁷ gives studies by this method of the shock-shock interaction configuration between a flat plate and a cylinder. In spite of the quality of such images, work at high enthalpy facilities is impaired by the weakness of the scattering and the strength of the stray light. Higher current electron beams are then required. Recently, a new electron beam source capable of delivering a thin pulsed sheet of 45 cm length has been introduced. This source allows 1 μs-long single exposures to be taken with intensified CCD cameras and shows great promise for future work in high

enthalpy facilities. However, the main constraint remains that flows should not exceed densities of 10^{-3} normal to avoid excessive electron beam blow-up.

EBF can also be used for velocity measurements. If a pulsed beam of small diameter is employed, the plasma it creates in a thin column of excited gas can be photographed after some delay, showing its displacement. One can then visualise the velocity field along one line, over a length of about 20 cm. The pseudo-spark source is an ideal electron gun for such work. Success was obtained recently at F4 using this approach.²¹ The Figure 16 shows the plasma column convected by the flow after 5 μ s (top). The top of the column, which lies in the boundary layer, is bent, showing the velocity profile. The lower quarter is in the jet core. There one measure velocities of the order of 4000-4500 m/s, typically within 5-10% at most of the DLAS results. This mutual vindication of the two techniques has caused a shift away from the cheaper, but more delicate to use, solid probes. Some small problems still need attention. A thin ground electrode aligned along the flow is used to collect the charges; thus this method is not fully non intrusive. Further, the penetration depth is only 20 cm for the moment. But we believe the pseudo-spark holds considerable promise for high enthalpy facilities.

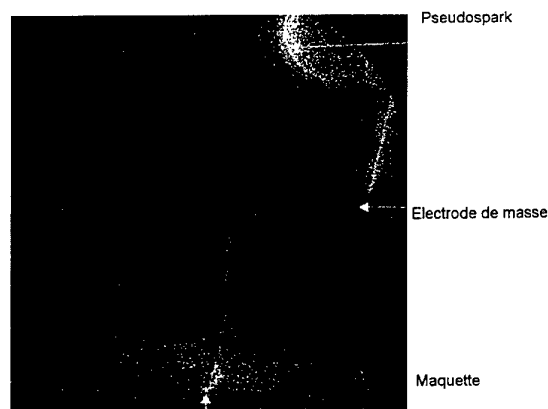


Fig. 16. EBF image taken at F4 using a 60 kV pseudo-spark gun (top, on the edge of the circular field); exposure time 0.3 μ s. The circular field of view has a diameter of 40 cm. The model is an 8 cm-dia sphere.

5 - COLLECTIVE LIGHT SCATTERING (CLS)

On the microscopic scale, CLS rests on spontaneous Rayleigh scattering off the atoms and molecules in the gas, more precisely on their fluctuations as a result of thermal and acoustic fluctuations, and it aims at detecting these fluctuations. However, it banks on coherent detection for improved sensitivity. Experimentally, a cw laser beam, the pump beam, is applied to the gas at the point of interest (Fig. 17). Observation of the light scattered from this point is performed at an angle θ to the laser beam. Part of the laser beam is deflected using an acousto-optic modulator. The deflected beam is also

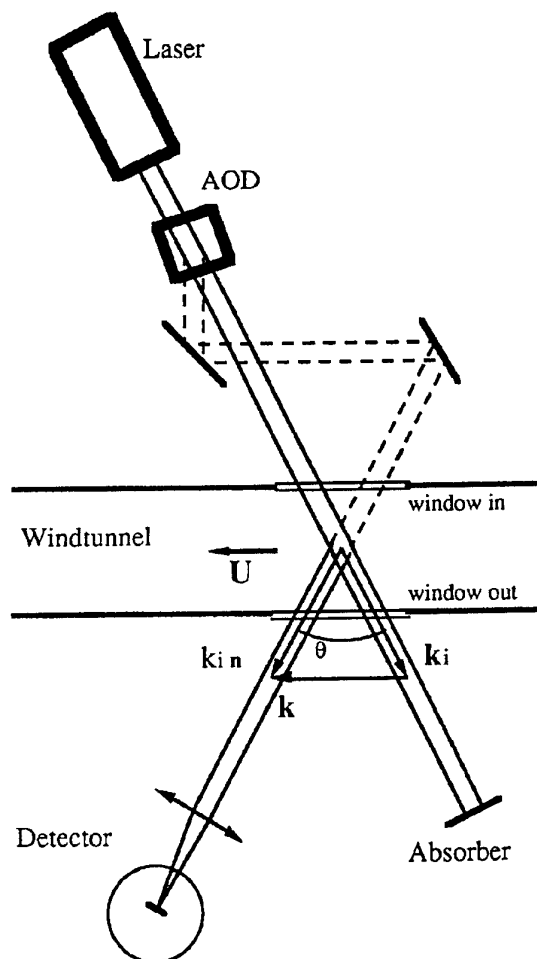


Fig. 17. Schematic diagram for CLS. Probe beam is diffracted off using acousto-optic deflector AOD. The scattered Rayleigh light with optical wave vector k_{in} is heterodyned by the probe beam at the detector. k_i is the pump beam wave vector and k that of the acoustic disturbance (from reference 22, with permission).

applied at the same point and aimed into the same direction for heterodyning the scattered light onto the detector. A more detailed presentation of the physics is given elsewhere.²²

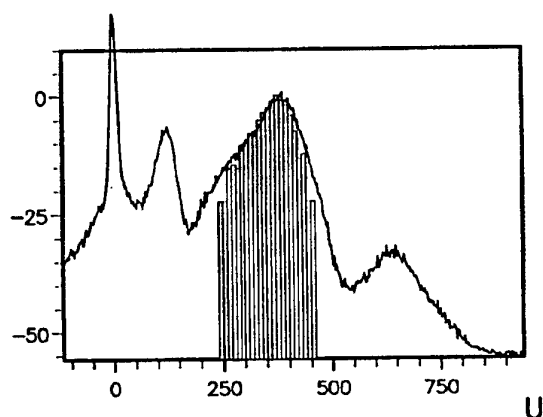


Fig. 18. Frequency spectrum of the CLS signal in a supersonic flow. Velocity U is in m/s. spectral density is in log scale. The main peak at 370 m/s corresponds to the flow speed. Vertical bars give the conventional laser Doppler velocimetry results. Sharp peak is reference at zero frequency; the two bumps on either side of the main velocity histogram are contributed by acoustic waves travelling in opposite directions in the convected gas (from reference 22, with permission).

CLS can be used for measuring density, mean and fluctuating velocities, etc. An example of velocity measurement is presented in the Figure 18. This technique can be used at pressures down to about 10^3 Pa, with a priori no restrictions at higher pressures other than working in media that are transparent for the $10.6 \mu\text{m}$ laser radiation.

6. CONCLUSION

Spectacular progress has been made in the development of new, non-intrusive optical methods for probing hypersonic flows in the ground testing facilities.

- Diode laser absorption spectroscopy is remarkably well suited for free stream measurement of velocity and static temperature, along with trace species concentration measurements; it requires, however, the flow to be quite homogeneous;

- CARS for point measurement of rotational and vibrational temperatures, and of N_2 density; in the near future, point measurements of velocity and translational should be demonstrated;

- EBF and LIF can be employed for qualitative imaging and visualisation; visualisation of shocks, and, particularly, the convection of a plasma column burned into the flow, can be used very elegantly in the most difficult streams to extract velocity profiles.

- The CLS reveals the dynamical properties of these flows, which tend to be extremely non-stationary, and gives measurements of sound speed, density fluctuations spectrum, etc.

If one now turns to the future, measurements of O atom density in the high enthalpy streams will soon become available using non-linear laser spectroscopy like CARS or DFWM. Work in progress at ONERA has shown very encouraging results.²³

In the low enthalpy wind tunnels, the same methods can be employed; however, if the density is higher, diode laser absorption will lose ground in the velocity measurements and seeding with NO or other trace gases may become necessary. EBF will also lose all of its applications, while techniques like Rayleigh and Raman scattering will gain.

BIBLIOGRAPHY

- 1 Boutier A., "New trends in instrumentation for hypersonics research", Proceedings of the NATO Advanced Research Workshop on Instrumentation for Hypersonic Research, ONERA Le Fauga-Mauzac Center, France, 27 April-1 May 1992, , Ed., Kluwer, Dordrecht, Boston, London.
- 2 Grésillon, D. and Honoré, C., "Collective Light Scattering: an Introduction", in "Optical Diagnostics for Flow Processes", Lars Lading et al., Ed., Plenum, New York, 1994, pp 229-243.

- 3 Marshall Lapp and C.M. Penney, "Laser Raman Gas Diagnostics", Proceedings of the Project Squid Laser Raman Workshop on the Measurement of Gas Properties, Schenectady, NY, May 10-11, 1973, Ed., 1974, Plenum, New York, London.
- 4 Bobin L. "Experimental investigation of a jet in a cross flow by spontaneous Raman scattering", ICIASF, ISL, Saint-Louis, France, 20-23 Sept. 1993, EEE publication 93CH3199-7.
- 5 Marinelli W.J., Kessler W.J., Allen M.G., Davis S.J., Arepalli S. and Scott C.D., "Copper atom based measurements of velocity and turbulence in arc jet flows", AIAA 29th Aerospace Sciences Meeting, January 7-10, 1991, Reno, AIAA Paper 91-0358.
- 6 Bamford D.J., O'Keefe A., Babikian D.S., Stewart D. and Strawa A.W., "Characterization of arc-jet flows using laser-induced fluorescence", AIAA 32nd Aerospace Sciences Meeting, January 10-13, 1994, Reno, AIAA Paper 94-0690.
- 7 Meyer S., Sharma S., Bershader D., Whiting E., Exberger R. and Gilmore J., "Absorption line shape measurement of atomic oxygen at 130 nm using a Raman-shifted excimer laser", AIAA 29th Aerospace Sciences Meeting, January 9-12, 1995, Reno, AIAA Paper 95-0290.
- 8 Mohamed A.K., Pot T. and Chanetz B., "Diagnostics by Electron Beam Fluorescence in Hypersonics", 16th International Congress on Aerospace Simulation Facilities, Dayton, OH, July 18-21, 1995, section 14.1
- 9 Lutfy F.M. and Muntz E.P., "Initial experimental study of pulsed electron beam fluorescence", AIAA J. **34**, 1996, pp 478-482.
- 10 Voronel' E.S., Kuznetsov L.I., Parfenov M.V. and Yarygin V.N., "Electron-X-ray method for measuring the local density in pulsed erosion jets", Quantum Electronics **24**, 1010 (1994).
- 11 Druet S.A.J. and Taran J.P., "CARS spectroscopy", Prog. Quant. Elec. **7**, 1981, pp 1-72.
- 12 Péalat M. and Lefebvre M., "Temperature measurement by dual-line CARS in low-pressure flows" Appl. Phys. **B53**, 1991, pp. 23-29;
Lefebvre M., Scherrer B., Bouchardy P. and Pot T., "Transient Grating Induced by Single-Shot Time-Domain Coherent anti-Stokes Raman Scattering: Application to Velocity Measurements in Hypersonic flows", JOSA B, **13**, 1996, pp 514-20
- 13 Lefebvre M., Péalat M. and Strempel J., "Single shot time-domain CARS: application to temperature and velocity measurement in supersonic flows" Opt. Letters **17**, 1992, pp 1806-1808.
- 14 Grisch F., Bouchardy P., Koch U., Gülhan A. and Esser B. "Rotational and Vibrational Temperature and density measurements by Coherent anti-Stokes Scattering in a Non-equilibrium Shock Layer flow"
- 15 Lefebvre M., Chanetz B., Pot T., Bouchardy P. and Varghese Ph., "Mesures par Diffusion Raman anti-Stokes Cohérente dans la Soufflerie R5Ch", Recherche Aéronautique, **4**, 1994, pp 295-8
- 16 Attal-Trétout B., Berlemont P. and Taran J.P., "Three-colour CARS spectroscopy of the OH radical at triple resonance", Mol. Phys. **70**, 1990, pp 1-51

- 17 Bervas H., Attal-Trétout B., Le Boiteux S. and Taran J.P., "OH detection and spectroscopy by DFWM in flames; comparison with CARS", J. Phys. B: At. Mol. Opt. Phys. **25**, 1992, pp 949-69
- 18 Grisch F., Attal-Trétout B., Bouchardy P., Katta V., Roquemore M., "Vortex-flame interaction study using four-wave mixing techniques", Journal Nonlinear Optical Physics & Materials, to be published.
- 19 Koch U., Gülhan A. Esser B. Grisch F. and Bouchardy P. "Rotational and Vibrational Temperature and density measurements by Planar Laser-Induced NO-Fluorescence in a Non-equilibrium Shock Layer flow", same session
- 20 Miles, R. and Lempert, W. Quantitative Flow Visualisation in Unseeded flows", Ann. Rev. Fluid Mech., **29**, 1997, pp 285-326.
- 21 Larigaldie S., Ory M., Bize D., Soutadé J., Mohamed A. and Taran, J.-P., "Velocity Measurements in High Enthalpy Hypersonic Flows with Modified Pseudo Spark Electron Gun, to be published.
- 22 Bonnet, J.P., Grésillon, D., Cabrit, B. and Frolov V., "Collective Light Scattering as Non-particle Laser Velocimetry", Measurement Science and Technology, **6**, 1995, pp 620-36.
- 23 Picard Y., Grisch F., Attal-Trétout B. and Le Boiteux S., "Atomic Oxygen Detection Using Two-Photon Degenerate Four Wave Mixing", Z. Phys. **D39**, 1997, pp 49-58.

Rotational and Vibrational Temperatures and Density measurements by Coherent Anti-Stokes Raman Scattering in a Nonequilibrium Shock Layer Flow

F. Grisch, P. Bouchardy

Office National d'Etudes et de Recherches Aéronautiques
Fort de Palaiseau, 91120 Palaiseau, France

U. Koch, A. Gülhan

Deutsche Forschungsanstalt für Luft und Raumfahrt
Postfach 906058
D-5000 Köln, Germany

SUMMARY

Coherent anti-Stokes Raman scattering studies are carried out in a nonequilibrium shock layer air flow induced by a two-dimensional body. Rovibrational spectra of molecular nitrogen are recorded by scanning CARS in the free stream and within the shock layer at moderately high enthalpy (7.3 MJ/kg). Difficulties peculiar to the application of the optical technique to a high enthalpy flow are discussed and flow parameters are given. The rotational temperature, vibrational temperature and number density are measured and compared to theoretical values predicted by a Navier-Stokes solver. A Good agreement is found.

1. INTRODUCTION

The various physical and chemical phenomena that take place in the hypervelocity flowfields during the reentry phase of aerospace flight are extremely important to the design of the next generation of reusable spacecraft. Improving our understanding of these complex phenomena is being achieved through the combined developments of computational fluid dynamics (CFD) and experiments in hypersonic facilities.

Within this frame, arc-heater wind tunnels are useful to simulate hypersonic flow conditions for measurements on realistic models, that will be extrapolated to flight conditions. These tools are also of great interest for code validation purposes. However, the aerothermodynamic states of the flows produced in them are not yet well understood. This is due to the complexity of the physical and chemical phenomena occurring in these facilities. The flow undergoes vibrational excitation, dissociation and ionization. Because of the relatively low density environment produced in the facility, it is generally in nonequilibrium in both chemical composition and internal modes. Even if the real flight conditions cannot be reproduced, a significant prediction of the thermal and chemical states of the flow upstream of the model along with its non uniformity calculations will allow to compare experiments and numerical results around the model.

Experimentally, laser diagnostics based on molecular scattering have received considerable attention for application in hypersonic test facilities thanks to their non-intrusive nature and their capabilities for excellent temporal and spatial resolutions. These methods can provide information directly related to the parameters of the molecular state of the gas including temperature, density and velocity. Among these techniques, Raman scattering, electron beam fluorescence and laser-induced by fluorescence (LIF) seems promising in low density and high-temperature hypersonic flows [1-5]. In particular, Coherent anti-Stokes Raman scattering (CARS) belongs to the powerful techniques. Both local number densities and temperatures can be determined from the CARS signal. The density is related to the intensities of the spectral features while temperatures can be inferred from the distribution of molecular rotational and vibrational state populations contributing to the CARS spectrum. Determining these properties simultaneously would be then extremely useful in high enthalpy flows.

The objective of the present work is aimed at studying the behaviour of a nonequilibrium hypersonic air flow interacting with a shock wave surrounding a model. Scanning CARS [6], well adapted to the study of low pressure continuous flows, is used to probe N_2 in a nonequilibrium hypersonic flow produced in the arc-heater wind tunnel. This arc-jet facility is commonly used for the investigation of heat protection material in the spacecraft reentry conditions with relevant chemistry. From the data, rotational temperatures, vibrational temperatures and N_2 number densities have been deduced in the free stream and behind a shock wave surrounding a blunt body placed in the flow. The results are used as data base to validate the Navier-Stokes solver developed for prediction of laminar viscous flows in chemical and thermal nonequilibrium. The calculated temperatures and density are in fair agreement with the measurements. The experiment completes previous efforts already done using planar laser Induced fluorescence on NO [7].

2. THEORETICAL CONSIDERATIONS

2.1 Coherent anti-Stokes Raman scattering

The theory of CARS has been described in detail elsewhere [8]. CARS is a nonlinear optical technique which may be used to measure the rotational and vibrational population distributions of any molecule having a Raman active transition. From such distributions, one then deduces the number density of the species under study and its rotational and vibrational temperatures if the distributions are Boltzmann-like. In principle, CARS is observed when three waves of frequencies ω_0 , ω_1 and ω_2 pass through a gas mixture. If the frequency difference $(\omega_1 - \omega_2)$ is close to the Raman-active vibrational frequency ω_p , an intense beam with frequency $\omega_3 = \omega_0 + (\omega_1 - \omega_2)$ will be generated in the forward direction of the incident waves. The two coherent incident waves ω_1 and ω_2 force the molecules to oscillate in phase at the frequency $(\omega_1 - \omega_2)$. Then the ω_0 radiation is scattered off by molecules whose polarizability is modulated by the oscillation. The new coherent wave is created through the third-order non linear susceptibility $\chi^{(3)}$. Usually, the same wave is used to pump and probe the molecular oscillation ($\omega_0 = \omega_1$) and the anti-Stokes frequency is then given by $\omega_3 = \omega_1 + (\omega_1 - \omega_2)$.

As is customary in CARS, information about the state of the molecular system is derived from lineshapes and line intensities. Spectra are recorded as a function of the frequency difference $(\omega_1 - \omega_2)$. In the case of monochromatic laser sources, the intensity is proportional to the square of the nonlinear susceptibility $\chi^{(3)}$, the resonances of the latter having an amplitude proportional to quantum state population differences [8]. When non-monochromatic lasers are used, the signal is given by a convolution integral. When the pump laser at ω_1 is monochromatic, the CARS intensity $I_{vj}(\omega_1 - \omega_2)$ for an isolated line at ω_{vj} is given by the simpler form [9]:

$$I_{vj}(\omega_1 - \omega_2) = K \left\{ \Delta N_{vj} \left(\frac{d\sigma}{d\Omega} \right)_{vj} \right\}^2 S(\omega_1 - \omega_2) \times \left\{ \int_{\Delta t} P_1^2 \sum_k P_2^k \left| \int \frac{g(v_z) dv_z}{(\omega_1 - \omega_2^k) - \omega_{vj} \left(1 - \frac{v_z}{c} \right) - i\Gamma_c} + \chi_{nr} \right|^2 \right\} \quad (1)$$

where the summation integrates the contribution of each mode ω_2^k of the ω_2 laser and the integral describes the Raman profile. P_1 and P_2 are the pump and the Stokes laser powers. ΔN_{vj} is the population difference between the initial and the final states of the Raman line. The Doppler shift is given by the term $\omega_{vj} v_z / c$ and $g(v_z)$ is the Maxwell-Boltzmann distribution function. v_z is the projection of the velocity along the difference of wave vectors $(\mathbf{K}_1 - \mathbf{K}_2)$ of the pump and

Stokes waves. Γ_c is the collisional broadening (HWHM). K is a constant which takes into account the optical transmission and the detector efficiency. χ_{nr} is a slowly varying non-resonant term which is a background contribution due to electrons and remote resonances from the other species present. For all spectra reported here, χ_{nr} was found to be negligible and was systematically neglected. $S(\omega_1 - \omega_2)$ represents the effects of saturation due to the Raman pumping and the Stark effect [10]. It describes the deviation of the CARS signal strength vs pump powers from the classical $P_1^2 P_2$ dependence. Without saturation effects, $S(\omega_1 - \omega_2) = 1$. With saturation, this value depends on many parameters and a resolution of the time evolution of the density matrix equation for each velocity group is necessary [11].

The spontaneous cross section for the Q-branch of the stretching mode is

$$\frac{d\sigma}{d\Omega} = \left[\alpha^2 + \frac{4}{45} \gamma^2 \frac{J(J+1)}{(2J-1)(2J+3)} \right] (v+1) \quad (2)$$

J and v are the rotational and vibrational quantum numbers, respectively, of the initial level. α and γ are the mean molecular polarizability and anisotropy, respectively.

For a nonequilibrium flow, the population fractions in Eq. (1) can be written as

$$N_{vj} = g_j \frac{N(2J+1) \exp(-G(v) / kT_{vib}) \exp(-F_v(J) / kT_{rot})}{Q_{vib} Q_{rot}} \quad (3)$$

where the vibrational temperature T_{vib} is allowed to be different from the rotational temperature T_{rot} . $G(v)$ and $F_v(J)$ are the vibrational and rotational term values [12]. The nuclear spin multiplicity g_j differs from unity for molecules with ortho and para species like nitrogen. These species are assumed not to interconvert during the expansion, so that the rotational partition function Q_{rot} is calculated by summing over only even (or odd) J values for a given spin species. Q_{vib} is the vibrational partition function.

Because of the low density nature of the expanding flow, Scanning CARS has been chosen to record the rovibrational populations of molecular species to ensure the best instrumental sensitivity. It uses a monochromatic laser for the pump beam and a tunable narrow-band laser for the Stokes beam. The total intensity $I_{vj}(\omega_1 - \omega_2)$ is recorded as a function of the frequency difference $(\omega_1 - \omega_2)$ by scanning step by step the Stokes frequency while the pump frequency is fixed. In the same time, a second CARS signal $R(\omega_1 - \omega_2)$ is generated in a reference channel identical to the main detection channel. The latter is used to monitor signal

fluctuations resulting from laser power instabilities and from changes in dye efficiency vs wavelength. Thanks to the reference and to various calibration procedures, the error in the absolute population measurements is estimated to be less than 10 % for all levels probed.

2.2 Data handling

According to Eqs. (1) to (3), the area under each Q rotational line, with the quantity $\{I_{vj}(\omega_1 - \omega_2)/R(\omega_1 - \omega_2)\}^{1/2}$ is calculated by integrating the line profile and divided by the reference signal. This result is proportional to ΔN_{vj} , the population density difference between the lower and the upper vibrational states. The rotational temperature T_{rot} of a vibrational band v is then measured from the plot of $\Delta N_{vj}/(2J+1)g_J$ vs rotational energy $F_v(J)$. A correction for Doppler broadening is next calculated. This correction is applied to all the ΔN 's in order to take into account the fact that the detection sensitivity depends on the linewidth which is roughly proportional to $T_{rot}^{1/2}$ and also depends slightly on v and J , the linewidth being proportional to the Raman shifts. Knowing the rotational temperature of each vibrational band, the vibrational temperature T_{vib} is then obtained from the ratio of the populations of two different vibrational states. Detailed expressions of the data processing to obtain the vibrational populations may be found in a previous paper [6]. The number density of the species is deduced from the ratio $\{I_{vj}(\omega_1 - \omega_2)/R(\omega_1 - \omega_2)\}^{1/2}$ using a scaling factor obtained from a calibration experiment in which the temperature and the pressure are known.

2.2 The CELHYO Solver

The Navier-Stokes solver CELHYO [13], modelling the hypersonic laminar viscous flow in chemical and thermal nonequilibrium has been used to simulate the two-dimensional high enthalpy flow.

The CELHYO code treats ideal mixtures of perfect gases made of n_h heavy species, n_m of them being molecular species. The mixture is assumed to be composed of the five neutral species N_2 , O_2 , NO , N and O . All the species are described with the same mean velocity \mathbf{v} . Three degrees of freedom are considered: 1) translation and rotation, described by one temperature T_{trans} ; 2) vibration; 3) dissociation. Energy is supposed to follow a Boltzmann-distribution. We assume that n_v molecular species, $1 \leq n_v \leq n_m$, have their own temperature T_{vj} , $j \in \{1, \dots, n_v\}$ such as N_2 and O_2 for air.

The second order diffusive convective system governing the mixture under consideration writes:

$$\partial_t \mathbf{u} + \text{div}(\mathbf{f}(\mathbf{u})) - D(\mathbf{u})\text{gradu} = \Omega \quad (4)$$

where \mathbf{f} denotes the inviscid fluxes. Dissipative phenomena are here modeled by the diffusive tensor D .

The source term Ω represents the presence of nonequilibrium phenomena. The variable \mathbf{u} is

$$\mathbf{u}^T = (\rho_\alpha)_{1 \leq \alpha \leq n_h}, \rho v_1, \rho v_2, \rho E, (\rho \beta e_{v,\beta})_{1 \leq \beta \leq n_v} = \Omega \quad (5)$$

where E denotes the total energy of the mixture and $\mathbf{v} = (v_1, v_2)$ is the mean velocity. $e_{v,\beta}$ refers to the vibrational energy of the molecular species β assumed to be in thermal nonequilibrium. The mixture pressure p is defined by

$$p = \kappa_{tr} \left(\rho E - \frac{1}{2} \rho v^2 - \sum_{\beta} \rho_{\beta} e_{v,\beta} - \sum_{\alpha} \rho_{\alpha} (h_{\alpha}^0 + e_{\alpha}(T)) \right) \quad (6)$$

where $\kappa_{tr} = \gamma_{tr} - 1$. e_{α} and h_{α}^0 respectively refer to the translation and the heat of formation of species α .

Detailed expressions of source terms and of the diffusive tensor may be found in a previous paper [13]. The chemical reaction model taken for air is Gardiner's [14]. It consists of 15 dissociation reactions and two exchange reactions. The vibrational relaxation of diatomic species (N_2 and O_2 for air) occurs through V-T transfers which are modeled following the Landau-Teller rule [15], and using the data given in [16] for the collisions with molecules (N_2 , O_2 , NO) and in [17] for the collisions with atoms (N , O). V-V processes can also be taken into account with the formulation for the source term and the data given in [17].

The CELHYO code solves the Navier-Stokes balance equations on curvilinear structured meshes using a fully implicit, finite-volume method. The viscous part is discretized according to a central differencing procedure, while a quasi-second-order accurate upwind scheme yields an approximation for the inviscid operator. Upstreaming is achieved using an approach for upwind bias referred to as the Hybrid Upwind Splitting [18]. The method is designed to combine the natural strengths of the Oscher solver and the Van Leer splitting in order to get accuracy in the resolution of boundary layers and robustness in the capture of non-linear waves respectively. It is emphasized that no switch to be tuned up is involved here. Second-order accuracy is achieved using a MUSCL approach written in primitive variables. Special attention is paid when the method is applied to mass fractions in order to preserve the local numbers of elements.

The implicit operator is made up of a linearization of both the inviscid and viscous fluxes plus all the source term jacobian matrices. For a detailed presentation of this time-marching algorithm, the reader is referred to [13].

A no-slip velocity condition together with a constant temperature T_w for the translational and vibrational modes are prescribed for the wall boundary. The wall is

assumed to be noncatalytic and the normal gradient of pressure at the wall is zero.

3. EXPERIMENTAL SETUP

3.1 The Arc-heater Wind tunnel

The facility is the arc-heater wind tunnel L2K of the DLR-Cologne [19]. It is used primarily for testing under high enthalpy the thermal protection materials developed for spacecrafts. L2K is designed to run continuously during several hours. It offers a wide choice of operating conditions typical of those encountered at the stagnation point during a shuttle reentry. The main parts of the arc-heated wind tunnel are the arc heater and the power supply, the test chamber with expansion nozzle, free jet and diffuser, the heat exchanger and the supply equipment. The electrical power-supply system is based on a thyristor-controlled rectifier consisting of four units of 354 kW (600 A, 590 V) which can be switched alternatively to a parallel or series connection. The current is controlled during the test while the effective voltage depends on the resistance of the arc heater. An arc heater of the hollow-electrode concept (Huels-type) has been applied for the experiments. Using the arc heater one should try to enlarge the voltage as much as possible, especially in the case of high mass flow rates. There is a reason for using high voltages with respect to flow quantity. Contamination of the gas by burning off of electrodes cannot be completely avoided. This effect increases with current strength and is dependent on the total pressure. A value of contamination less than 10 ppm is reached for total pressure of 10 bar in the facility. The arc heater is supplied with atmospheric air delivered by 1000 m³ storage tank which may be pressurized to 6.10⁶ Pa. Mass flow rates up to 300 g/s can be controlled during the test time. The high-enthalpy gas flows through a small settling chamber, then through a conical nozzle toward a vacuum chamber. The total nozzle length, the throat diameter, the exit diameter and the nozzle-half angle are 0.40 m, 0.029 m, 0.20 m and 12 degrees, respectively. The testing chamber has a cylindrical shape with a diameter of 2.6 m and a length of 2 m transversal to the flow direction. The test chamber is connected to the pumping system by a diffuser consisting of several cylindrical segments. The heat exchanger is installed downstream of the diffuser to cool down the heated gas to a temperature equivalent for the intake of the pumping system.

For the experiments reported here, an arc current of 600 A is set with a mass flow rate of 0.049 kg.s⁻¹ and a stagnation pressure of 1.3 10⁵ Pa. The reservoir conditions are determined by from data on the settling chamber pressure in front of the nozzle and the total mass flow rate. Both values are easily measured and are used to calculate total temperature and total enthalpy based on equilibrium flow solution from the reservoir to the throat. The total enthalpy delivered to the gases is

then 7.3 MJ.kg⁻¹ and the temperature is assumed to be equal to 3910 K.

A water-cooled copper model is used for the experiment. It consists of a circular disk with its axis along the center of the nozzle. The diameter of the disk is 50 mm. The model is mounted on a holder which can be moved in the range of 1000 mm transversal to the flow direction and 1500 mm in the flow direction.

3.2 The optical setup

The core of the CARS system is an injection-seeded Q-switched Nd:YAG laser chain delivering 800 mJ of 1064 nm radiation in 17 ns long pulses at a repetition rate of 10 Hz. The laser chain is composed of two laser heads (Quantel SF611) and a cw diode-pumped seeder (Quantel YS700). the Nd:YAG rods are 7 mm in diameter and 9 mm in diameter for the oscillator and the amplifier, respectively. The 1064 nm output beam is frequency doubled by a KD*P crystal giving 380 mJ at 532.1 nm with 14 ns pulses length and a spectral linewidth (FWHM) less than 0.003 cm⁻¹. The 1064 nm beam left by the first crystal is again doubled by a KDP crystal. Some 40 mJ at 532.1 nm are produced and used to pump a narrow-band dye laser oscillator. Part of the 380 mJ main beam is used to pump the dye amplifier and the remainder is used as the ω_1 pump beam. The resonator of the dye laser comprises a 2100 grooves mm⁻¹ holographic grating at grazing incidence, a flat rotating back mirror and an intracavity prism beam expander yielding a linewidth (FWHM) of about 0.08 cm⁻¹. The wavelength is selected by tilting the back mirror which allows a coarse sweep from 500 to 800 nm in steps of 0.5 nm or a fine sweep of 6 nm around the coarse drive setting in fine steps of 0.01 nm. After the amplification, the ω_2 beam passes through a telescope to control the divergence and through appropriate optics for positioning the beam. The Stokes laser is tuned close to 607 nm and delivers 4 mJ in 11 ns pulses. At the output of the emitter bench, the ω_1 beam has already been split in two parallel beams separated of 15mm and one of them is overlapped with the ω_2 beam (planar BOXCARS arrangement [8]). All beams are horizontally polarized.

A schematic diagram of the CARS experimental configuration is presented in Fig 1. The beams are focused first in the testing chamber with their axis perpendicular to the flow axis where the ω_3 signal is created. Then, that CARS signal is split-off and the laser beams pass in a 1 atm pressure slow flow of argon where they are refocused. A weak CARS signal is then created to monitor the fluctuations of direction and of pulse energy of the ω_1 and ω_2 beams. The reference and the sample CARS signals are filtered out from the pump beams using dichroic filters backed by double monochromators. Then, they are transported to the photomultipliers using optical fibers. The single-pulse digitized sample and reference signals from gated electronics are recorded by the computer which also

drive the scanning of the dye laser frequency. The software calculates the signal to reference ratio and averages N laser shots at each laser position.

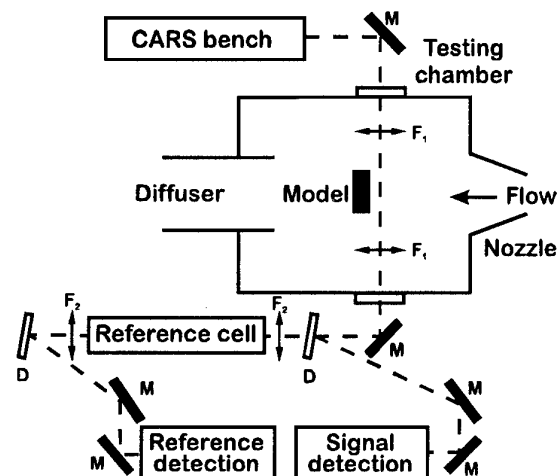


Fig. 1 - Schematic diagram of the CARS arrangement; F_1 , F_2 : achromats; M : 400-700 nm broadband mirror; D : Dichroic mirror.

The focal lengths of the focusing optics inside the testing chamber are chosen according to the following conflicting constraints: 1) short focal lengths are preferable in order to shorten the probe volume; 2) long focal lengths are preferable in order to reduce the saturation effects which are likely to appear because powerful lasers are required to create the CARS signals in low pressure media; 3) the set of the focal lengths must be adapted to the dimensions of the facility. Knowing that 2×30 mJ of pump laser and 4 mJ of Stokes laser are the required energies to create measurable signals for the expected N_2 densities the sample is selected in order to maintain [10]

$$0.1 \Omega_S < \Delta\omega, \Delta\omega_d \quad (4)$$

and

$$0.1 \Omega_R \tau < 1 \quad (5)$$

where Ω_S is the Stark frequency shift at pulse maximum, Ω_R the Rabi frequency, $\Delta\omega$ the free spectral range between the Stokes laser modes, $\Delta\omega_d$ the Doppler linewidth (FWHM) and τ the pulse duration. Following the development of Péalat et al [10] and supposing $\Delta\omega \approx 0.01 \text{ cm}^{-1}$, $\Delta\omega_d \approx 0.016 \text{ cm}^{-1}$ and $\tau = 14 \text{ ns}$, focal lengths longer than 700 mm verify the above constraints and cause negligible saturation effects.

The measurements are carried out at a position of 555 mm downstream from the nozzle exit and on the centerline region of the nozzle flow. The sample focal lengths are 750 mm. As a result, the achromats are installed inside the testing chamber. The sample probe

volume (defined as the distance along which the entire anti-Stokes are created) is 25 mm long and 100 μm in diameter. The focal lengths of the focusing optics in the reference channel are 500 mm in respect with the dimensions of the cell.

4. RESULTS

4.1 CARS measurements

Figure 2 presents a sample nitrogen CARS spectrum recorded in the free stream during a run. The experimental spectrum is recorded at 600 spectral positions with a frequency step of 0.01 cm^{-1} and a spectral resolution of 0.08 cm^{-1} . About 10 photoelectrons per pulse are detected at the peak. Consequently, each data point is the average of 30 laser shots and the time needed to record a spectrum is about 40 mn. As indicated in Fig. 2, the spectral bands detected by CARS were identified as the Q-branches of vibrational transitions 0-1 and 1-2. For each vibrational transition, clearly resolved are the para rotational lines (J odd) from $J \geq 9$ and the stronger ortho lines (J even) with $J \geq 2$. Rotational distributions between the ortho-states and the para-states of the 0-1 vibrational band display an intensity alternation in the ratio 1.5:1 whereas this ratio is equal to 2:1 for the 1-2 vibrational band. This result is inconsistent with the theory which predicts a natural abundance ratio of 2:1 for all the vibrational bands of nitrogen. The ortho and para populations ratio could be altered because of the rapid cooling of the gases during the expansion. However, no data are available at the present time to confirm this trend. It requires more experimental investigations.

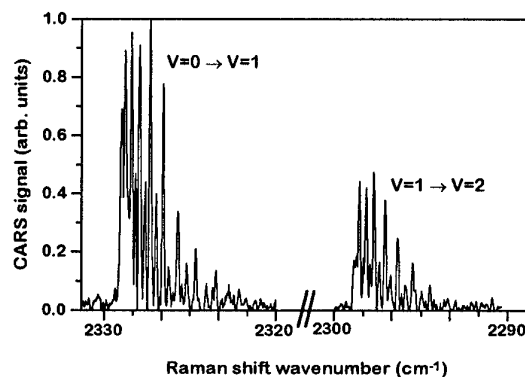


Fig. 2 - Nitrogen CARS spectrum of the 0-1 and 1-2 vibrational transitions recorded in the free stream

Despite this limitation, rotational temperatures in each vibrational transition have been deduced by plotting the ortho-lines intensities above $J=6$ as a function of energy of the rotational states. The log scale plot as shown in Fig. 3 indicates that within experimental errors, the rotational energy levels are in equilibrium. The rotational temperature may be then calculated from the slope of the linear best fit to the data which is inversely proportional to the rotational temperature. The scatter

of the data points about the straight line, $\pm 3\%$, merely reflects errors such as measurement uncertainty together with temporal fluctuations in flowing gas mass flow rate, arc current, etc. The rotational temperatures, 330 K and 334 K for the 0-1 and 1-2 vibrational transitions respectively, are found nearly identical and demonstrates that the rotational distributions do not depend upon v . The vibrational temperature, calculated from the ratio between $v=1$ and $v=0$ populations is $2510 \text{ K} \pm 130 \text{ K}$ where the accuracy reflects the 5% uncertainty on the ratio of the $v=0$ and $v=1$ populations. The experimental nitrogen density in the free stream is determined using the peak intensity of different rotational lines compared with that of the static temperature scan at known pressure (130 Pa). For this comparison, it is necessary to compute the theoretical ratio of peak intensities using Eqs. (1) and (3). Note that the difference of population between the ortho-states and the para-states are also systematically taken into account. The resulting nitrogen number density ρ_{N_2} in the free stream is then found equal to $2.25 \cdot 10^{15}$ molecules/cm³ with a standard deviation of 5 %.

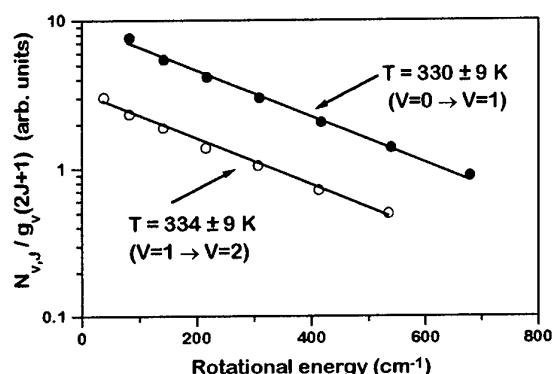


Fig. 3 - Boltzmann plots of the ortho-rotational populations of the 0-1 (●) and 1-2 (○) vibrational transitions recorded in the free stream.

To increase data accuracy, average repetitive CARS measurements are performed during six runs at the same location in the free stream. As a result, a mean rotational temperature of $332 \pm 6 \text{ K}$, a mean vibrational temperature of $2510 \pm 80 \text{ K}$ and a mean nitrogen number density of $2.2 \cdot 10^{15}$ molecules/cm³ with a standard deviation of 5 % have been deduced indicating the reproducibility of the experiments and of the test conditions of the runs.

CARS measurements are then performed at several positions in the shock layer induced by the disk model. For the experiments, the CARS spectra were recorded by moving the position of the model relative to a fixed optical axis. The shock wave is located around 13 mm from the surface of the model. Measurements have been performed at positions between 1 mm and 15 mm. Far downstream from the shock wave (i.d. between 1 mm

and 11 mm), the CARS spectrum presents the same profile for all positions. For instance, figure 4 shows a typical nitrogen CARS spectrum recorded at a position of 2 mm from the model. Recording nitrogen spectra now requires 1900 points with 30 laser shots averaged. The peak intensity of the signal is also of the order of 10 photoelectrons per pulse. From Fig. 4, several points may be noted. First, the spectral bands detected are the 0-1, the 1-2 and the bandhead of the 2-3 vibrational transitions. For each vibrational transition, rotational lines up to $J = 50$ are detected. Second, the anomaly on the intensity alternation shown in the free stream conditions is always present. The ratio of populations between the ortho-states and the para-states is always close to 1.5 while the population ratio on the 1-2 vibrational band is closer to 2.

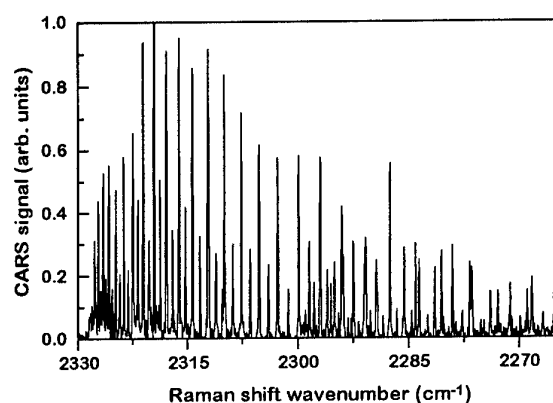


Fig. 4 - Nitrogen CARS spectrum of the 0-1 and 1-2 vibrational transitions recorded downstream the shock-wave.

Considering possible different behaviors for the para-states and the ortho-states of nitrogen, rotational temperature and vibrational temperature have been now deduced for each state of the molecule. For instance, rotational populations for the 0-1 and 1-2 have been plotted on Boltzmann diagrams shown in Fig. 5. The two resulting distributions are in equilibrium and the rotational temperatures associated to the 0-1 and the 1-2 vibrational transitions are found equal to $4280 \pm 90 \text{ K}$ and $4125 \pm 180 \text{ K}$, respectively. In the same manner, rotational temperatures deduced from the para-rotational populations of each vibrational transition are similar. The vibrational temperatures deduced from the ratio of populations between the $v=0$ and $v=1$ for each state of nitrogen are also found similar and to be less than the rotational temperatures ($\sim 2800 \text{ K}$). From these results and despite the abnormal behavior of the intensity alternation in the spectrum, it can be concluded that the two states of the molecules have the same enthalpy level and the same behaviour in the shock layer. The total number density of N_2 is deduced like the free stream experiments.

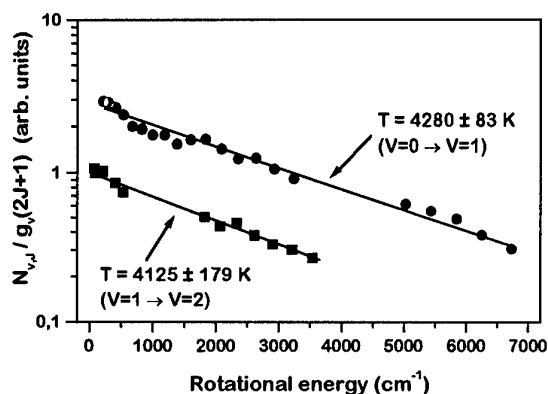


Fig. 5 - Boltzmann plots of the ortho-rotational populations of the 0-1 (●) and 1-2 (○) vibrational transitions recorded at $x=2$ mm from the model.

Close to the shock-wave (i.d. between 12 mm and 13 mm), the behaviour of the rotational populations changes rapidly. As shown in Fig. 6, rotational populations are aligned along a straight line except for the first J-lines which are disturbed. Two reasons can explain this anomaly. The first one can result from the dimensions of the probe volume and of the shape of the shock wave. Although the shock wave is slightly curved, the dimensions of the probe volume, 20 mm long and 100 μ m in diameter, seems to be longer. Cold gases coming from the free stream and hot gases coming from the shock layer can be simultaneously present in the probe volume and so can affect the populations of the rotationals lines. A second reason can derive from a temporal jitter of the position of the shock layer due to small flow disturbances induced by the temporal fluctuations of the test conditions. The rotational temperature corresponding to the hot gases may be however deduced from these distributions by neglecting the influence of the first J-lines.

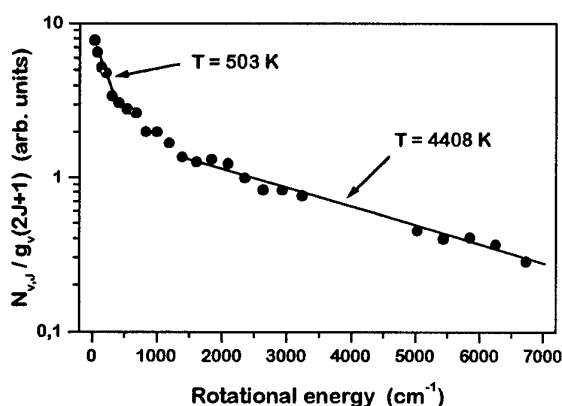


Fig. 6 - Boltzmann plots of the ortho-rotational populations of the 0-1 (●) vibrational transition at $x=12$ mm from the model.

4.2 comparison theory-experiment

The results are presented in the figures 7 to 9. Figure 7 shows the temperature distributions along the axis during the gas expansion calculated with the CELHYO solver. In this calculation, the relaxation of N_2 and O_2 occurs through the V-T transfers with the molecules (O_2 , N_2 , NO) and the atoms (O, N) of the gas mixture with relaxation rates given by [16] for the molecules and by [17] for the atoms. In the expansion, the freezing of the vibrational energy is brought into evidence by the different temperature distributions. The temperatures deduced from the experiments are shown on the same figure. At the point where measurements were performed, the mach number is equal to 7.6. The calculated temperatures, $T=305$ K and $T_{vib}(N_2)=2690$ K, are in rather good agreement with the corresponding experimental values: $T_{rot} = 332 \pm 6$ K (assumed in equilibrium with the translational mode) and $T_{vib}(N_2) = 2510 \pm 80$ K. However, the deviation between the theoretical and the experimental data could be explained by the influence of H_2O on the relaxation processes on N_2 . Indeed, H_2O is known to catalyse the vibrational relaxation of numerous molecules. For example, its effect on the vibrational relaxation of $N_2(v=1)$ is several orders of magnitude more efficient than that of other N_2 molecules. Recent calculations of this flow expansion including the influence of H_2O on the vibrational relaxation processes of N_2 show noticeable differences on the temperature distributions [20]. With a mass fraction of 0.02 for H_2O , the calculation leads to a decrease equal to 500 K on the vibrational temperature and an increase of about 30 K on the translational temperature with respect to the case without water. This trend, similar to the experiment one, shows that the influence of contaminants like H_2O is important and has to be taken into account for the simulation of the flow.

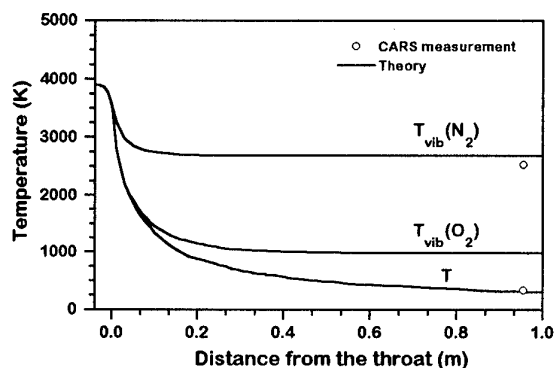


Fig. 7 - Axial temperature distributions along the flow expansion

The experimental total density of the flowfield is deduced from the number density of nitrogen assuming that the mole fractions of the gases are those predicted by the CELHYO solver. The total density in the free stream at the experimental position is then $1.40 \cdot 10^{-4} \pm$

$0.07 \cdot 10^{-4} \text{ kg/m}^3$. This value is in good agreement with the calculated total density which is equal to $1.6 \cdot 10^{-4} \text{ kg/m}^3$.

Figure 8 shows the temperature distributions on the symmetry axis in the shock layer. The continuous and dotted lines display the theoretical translational and nitrogen vibrational temperatures, respectively. The calculation is performed using the free stream conditions previously calculated as input conditions. The wall is supposed non catalytic and its temperature is set at a constant value $T_{\text{wall}} = 1300 \text{ K}$, value measured by a pyrometer during the experiment. The calculation brings into evidence an important increase of translational temperature through the 2 mm shock-wave. Then the translational temperature displays a flat profile in a large portion of the shock layer before decreasing strongly close to the wall. The vibrational temperature varies slowly in the shock layer from 2690 K to about 2900 K. Near the wall, both temperatures become the same indicating a thermal equilibrium for the gases. The experimental data are also shown on the same figure. All the rotational temperatures, measured by the analysis of the different rotational distributions of each state of the molecule, are displayed by the open symbols whereas the black symbols show the vibrational temperatures. Experimental rotational temperature profile agrees fairly well with the theoretical predictions. The shock wave is well captured at the same theoretical position. Nevertheless, the experimental temperatures in the flat region exceed by 10 % the theoretical temperatures. This disagreement may be derived from a precise unknowledge of the experimental temperature of the gases in the reservoir. The measured vibrational temperature profile agrees with the CELHYO predictions except close to the wall where temperatures are higher. This increase could be due to a possible wall catalysis which may lead to the formation of vibrationally excited molecules. More refined measurements closer to the wall would be necessary to confirm this trend.

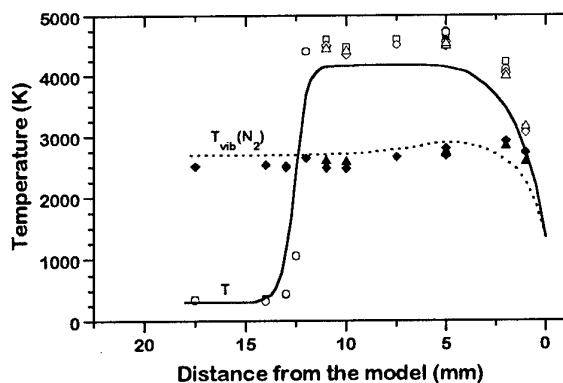


Fig. 8 - Axial temperature distributions downstream of the shock-wave.

Figure 9 presents the comparison between experimental and theoretical density profiles in the shock layer. Whatever the position, differences of only 10 % are noted demonstrating a good agreement between experiment and theory.

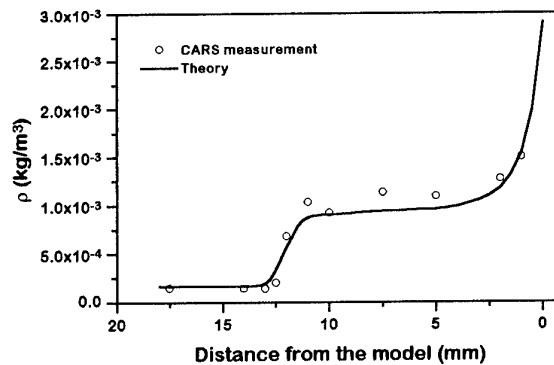


Fig. 9 - Axial density distribution downstream of the shock-wave.

5. CONCLUSIONS

Experimental measurements of rotational and vibrational temperatures and density measurements have been obtained in a continuous high-enthalpy arc heater wind tunnel, both in the free stream and in the shock layer induced by a disk. As expected, vibrational nonequilibrium is demonstrated. These results are due to the good detectivity of the scanning CARS which proves to be a powerful and reliable technique for hypersonic studies. Good agreement has been obtained between the measurements and the theoretical predictions obtained with the CELHYO solver.

References

1. Gillespie W.D., Bershader D., Sharma S.P., Ruffin S.M., 'Raman scattering measurements of vibrational and rotational distributions in expanding nitrogen', 1993, AIAA paper 93-0274.
2. Mohamed A.K., Pot T., Chanetz B., 'Diagnostics by electron beam fluorescence in hypersonics', 16th International congress on instrumentation in aerospace simulation facilities', 18-21 July 1995, Dayton USA.
3. Beck W.H., Koch U., Müller M., 'Spectroscopic diagnostic techniques for the high enthalpy shock tunnel in Göttingen (HEG): preparatory LIF studies on other facilities', Proceedings of the NATO advanced Research Workshop edited by A. Boutier, Series E: Applied Sciences-Vol. 224, 1993.
4. Pham-Van-Diep G.C., Muntz E.P., Boyd I.D., 'Measurement of rotational and vibrational population distributions in a hypersonic flow of chemically reacting iodine vapor', 1993, AIAA paper 93-2996.
5. Arepalli S., Yuen E.H., Scott C.D., 'Application of laser induced fluorescence for flow diagnostics in arc jets', 1990, AIAA paper 90-1763.

6. Massabiaux B., Gousset G., Lefebvre M., Péalat M., 'Determination of $N_2(X)$ vibrational level populations and rotational temperatures using CARS in a D.C. low pressure discharge', *J. Physique*, 48, 1987, pp 1939-1949.
7. Koch U., Gülhan A., Esser B., Grisch F., Bouchardy P., 'Rotational and vibrational temperature and density measurements by planar laser induced NO-fluorescence spectroscopy in a nonequilibrium high enthalpy flow', RTO/AGARD fluid dynamics panel symposium, Advanced aerodynamic measurement technology, 22-25 September 1997, Seattle USA.
8. Druet S., Taran J.P., 'CARS spectroscopy', *Prog. Quant. Electr.*, 7, 1981, pp 1-72.
9. Druet S. Taran J.P., Borde C., 'Line shape and Doppler broadening in resonant CARS and related nonlinear processes through a diagrammatic approach', *Journal de Physique*, 40, 1979, pp 819-840.
10. Péalat M., Lefebvre M., Taran J.P., Kelley P.L., 'Sensitivity of quantitative vibrational coherent anti-Stokes Raman spectroscopy to saturation and Stark shifts', *Physical Review A*, 38, 1988, pp 1948-1965.
11. Lucht R.P., Farrow R.L., 'Saturation effects in coherent anti-Stokes Raman scattering spectroscopy of hydrogen', *J. Opt. Soc. Am. B*, 6, 1989, pp 2313-2325.
12. Herzberg G., 'Molecular spectra and Molecular structure I: Diatomic Molecules', ed. Prentice Hall, New York, 1939.
13. Coquel F., Flament C., Joly V., Marmignon C., 'Viscous Nonequilibrium Flow Calculations', *Computing Hypersonic Flows*, Vol. 3, ed. Bertin J.J., Périaux J., Ballmann J., Birkhäuser, Boston, 1993.
14. Gardiner W.C. Jr., 'Combustion Chemistry', Springer Verlag, 1984.
15. Landau L., Teller E., 'Theory of sound dispersion', *Physikalische Zeitschrift der Sowjetunion*, 10, 1936, pp 34-43.
16. Millikan R.C., White D.R., 'Systematics of vibrational relaxation', *J. Chem. Phys.*, 31, 1959, pp 3209-3213.
17. Thivet F., Perrin M.Y., Candel S., 'A unified Nonequilibrium Model for hypersonic flows', *Physics of fluid A*, 3, 1991, pp 2799.
18. Coquel F., Joly V., Marmignon C., 'Méthodes de décentrement hybrides pour la simulation d'écoulements en déséquilibre thermique et chimique, Progress and Challenges in CFD Methods and Algorithms, 77th AGARD FDP symposium, Seville, October 1995.
19. Gülhan A., Jörres V., Kindler K., 'Experiments on the catalytic efficiency of heat protection materials in the arc-heated facility wind tunnel (LBK) in Cologne', *Proceedings of the NATO advanced Research Workshop* edited by A. Boutier, Series E: Applied Sciences-Vol. 224, 1993.
20. Joly V., Marmignon C., 'Effect of H₂O vapor on the vibrational relaxation in hypersonic wind tunnels', 31st AIAA Thermophysics Conference, New Orleans (USA), 1996, AIAA paper 96-1855.

Rotational and Vibrational Temperature and Density Measurements by Planar Laser Induced NO-Fluorescence Spectroscopy in a Nonequilibrium High Enthalpy Flow

U. Koch, A. Gülhan, B. Esser
Deutsche Forschungsanstalt für Luft- und Raumfahrt
Linder Höhe, D-51147 Köln, Germany
and

F. Grisch, P. Bouchardy
Office National d'Etudes et de Recherches Aérospatiales
ONERA, Fort de Palaiseau, F-91120 Palaiseau, France

LIF experiments were performed in the flow field of the high enthalpy facility L2K. This arc heated facility, which is mainly used for testing thermal protection materials, offers a wide choice of flow conditions to simulate the stagnation conditions during shuttle re-entry. The flow conditions are dominated by nonequilibrium effects. For the operation conditions of L2K translational and rotational temperature are assumed to be in equilibrium, but large differences between rotational, vibrational and electronic temperature occur. Laser induced fluorescence is used to determine rotational and vibrational temperature and the density of NO in the free stream and behind a bow shock upstream of a blunt body. The flow is modelled numerically using a quasi 1D-code. Good agreement is achieved between the experimental and numerical data in the free stream. The data are also compared with the CARS measurements performed at the same flow conditions in the same facility. Differences in the free stream vibrational temperature of N_2 and NO are due to the faster vibrational relaxation of NO-molecules.

Nomenclature

A_{ki}	Einstein coefficient
B	electronic state
B_e	rotational constant
c	velocity of light, $c = 2997924558$ m/s
C	constant
D	electronic state of NO
D_v	rotational constant
E_{rot}	rotational energy
E_{trans}	translational energy
E_{vib}	vibrational energy
F (J)	rotational term value
G (v)	vibrational term value
h	Planck constant $h = 6.62607 \cdot 10^{-34}$ Js
I	intensity
J	rotational quantum number
k	Boltzmann constant, $k = 1.3806 \cdot 10^{-23}$ J/K
L2K	1.4 MW arc heated facility of DLR
LIF	laser induced fluorescence
m	mass flow rate
M	mass number
N	number density
p	pressure

P_l	laser power
q	Frank-Condon-Factor
Q	partition function
R	distance
S_{ll}	Hönl-London-Factor
T	temperature
λ	wavelength
ν	frequency
τ	lifetime

1. INTRODUCTION

Physical and chemical processes, which take place during the re-entry phase of aerospace flight are extremely important for the design of thermal protection materials of reusable spacecrafts. The qualification of thermal protection materials under re-entry conditions is frequently performed in arc heated facilities. The flow field in these facilities is dominated by nonequilibrium phenomena. Therefore the use of nonintrusive diagnostic techniques is strongly required for the characterisation of the high enthalpy flow, in order to perform a detailed description of the thermodynamic state and a theoretical study of the physical properties.

Computational fluid dynamics and experimental techniques are used to improve the understanding of these complex phenomena. In the frame of the DLR-ONERA co-operation for the development of nonintrusive measurement techniques for high enthalpy flow facilities, measurements in the L2K facility were performed using two different optical diagnostic techniques. The CARS and the LIF technique have been applied to characterise the flow conditions using the same flow and model configurations.

In the present paper, the flow field properties of high enthalpy flows have been measured using two dimensional Laser Induced Fluorescence spectroscopy (2D-LIF). This optical technique allows to measure rotational temperatures, vibrational temperatures and number densities of NO with excellent spatial resolution.

The main advantages of LIF technique are its high sensitivity and the selective analysis of the chemical gas composition. However, the large number of parameters, such as laser source, detector system, optical set-up, requires a full and precise optimisation [1-5].

The fundamentals of LIF technique are presented in section 2 together with the procedure for the evaluation of temperatures and densities. Section 3 describes the temperature determination from spectra. The experimental facility, the optical set-up and its calibration follow in section 4. Section 5 includes the experimental results and their comparison with numerical computation and CARS data.

2. FLUORESCENCE IMAGING AND THERMOMETRY

Fluorescence signal

The LIF technique is based on the excitation of a molecule with light of a ArF excimer laser, which matches the possible energy differences of this molecule. After excitation the molecule returns to its ground state by emitting red shifted radiation or by thermal relaxation due to collisions with other molecules. Under conditions, where all the excited molecules return to the lower states by radiation, the emitted intensity is directly proportional to the density of the molecules within the lower energetic state. For an excitation spectrum the intensity of the emitted light is recorded as a function of the wavelength of the excitation light, thus probing different densities of the lower energetic states of the molecules. **Figure 1** shows the physics of LIF process for recording excitation spectra.

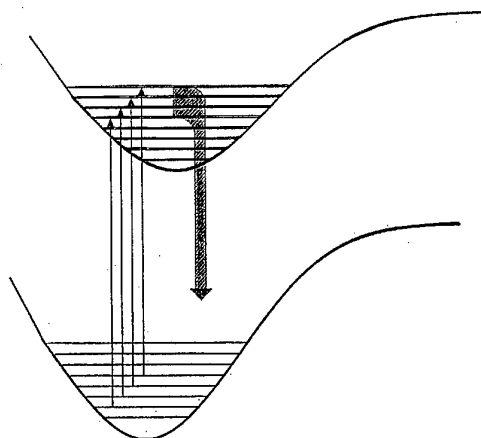


Fig. 1 Diagram of the LIF process.

Assuming that the distribution of the molecules corresponds to Maxwell-Boltzmann thermal equilibrium, the intensity of a spectral line is given by

$$I_{ki} = N_k h c \nu A_{ki} \quad (1)$$

The total intensity is

$$I = C P_f N'' q S_{ij} \frac{1}{\tau} \frac{1}{2J'+1} \quad (2)$$

with

$$N'' = \frac{1}{Q_{(vib)}} \exp\left(\frac{-E_{(vib)}}{kT_{(vib)}}\right) \cdot \frac{1}{Q_{(rot)}} (2J''+1) \exp\left(\frac{-E_{(rot)}}{k \cdot T_{(rot)}}\right) \quad (3)$$

The subscripts ' and '' denote the upper and lower states, respectively. Different rotational and vibrational temperatures of the molecules can be considered by separating the corresponding terms in Eq. (3).

The energy level diagram of NO and possible transitions in the tuning range of the ArF excimer laser are shown in **Fig. 2**.

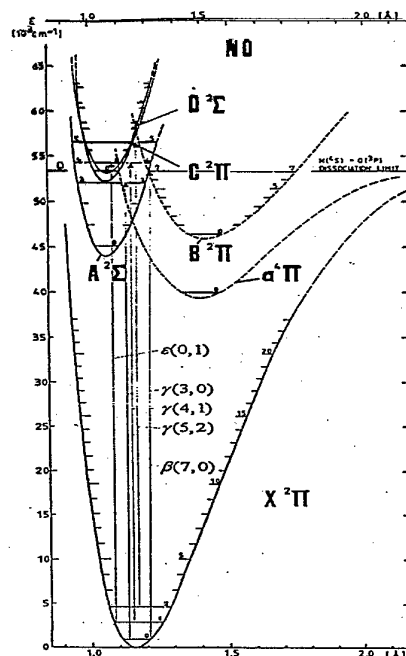


Fig 2 NO energy level diagram.

The parameters in Eq. (2) are taken from the literature [6-9]. The values for the NO-transitions with high intensity within the considered temperature range are given in **Table 1**. The Hönl-London-Factors were calculated according to the formulas given by Bennett [10].

Band	J-range	Lifetime [ns]	Frank-Condon-factor
β (7-0)	23.5-35.5	330	0.027819
β (8-0)	42.5-51.5	330	0.038444
β (9-1)	22.5-35.5	330	0.063933
γ (3-0)	29.5-62.5	217	0.147
γ (4,1)	6.5-50.5	196	0.24039
γ (5-2)	1.5-24.5	177	0.21521
ϵ (0,1)	11.5-43.5	20	0.1008

Table 1 Considered NO-Bands in the ArF laser tuning range.

The constant C includes the fluorescence volume, the excitation efficiency of the excited molecules, the quantum yield and constants of the LIF apparatus. It has to be determined by measuring the fluorescence intensity at known NO densities at defined

temperatures. For given temperatures the number density is directly proportional to the laser intensity.

From a measured spectrum the rotational temperature of each vibrational state is determined by Boltzmann plots. Based on the determined rotational temperature, the population of each vibrational band is calculated by comparing the line intensities of transitions coupled to different vibrational ground states. So the vibrational temperature is obtained from the ratio of the populations of two different vibrational states.

From the temperatures the number densities of the probed species are deduced by comparing the line intensities with intensities from calibration measurements at known temperature and density conditions.

The ratio of two fluorescence signals from the same volume and the same vibrational level is given by:

$$r_{ab} = \frac{N_a}{N_b} = \frac{B_a(2J'_a + 1)}{B_b(2J'_b + 1)} \cdot \exp\left(\frac{F(J'_a) - F(J'_b)}{kT}\right) \quad (4)$$

and the temperature is defined as:

$$T = \frac{F(J'_b) - F(J'_a)}{k \ln(r_{ab} / C_{ab})} \quad (5)$$

where the subscripts a and b identify different lower laser coupled states [11].

The collection efficiency dependence is omitted, because the same optical set-up is used and for each transition in the considered wavelength range are similar.

The effects of rotational energy transfer, vibrational energy transfer and the fluorescence yield are discarded by collecting and the fluorescence yield cancel in the ratio, because the quenching cross sections, fluorescence lifetimes and fluorescence branching ratio are insensitive to rotational quantum number, at least for the A-state of NO [12,13,14].

The overlap integrals may be eliminated if shot to shot fluctuations in the laser spectral profile are insignificant and the broadening and the shift of the absorption line are independent of the rotational level, as is valid for NO.

Supposing, that the laser intensities are sufficiently low to avoid saturation effects, the signals can be accurately corrected for temporal and spatial fluctuations in laser intensity by monitoring the pulse

energy during the experiment, assuming a constant laser sheet profile.

Quenching

No measured values for quenching cross section of NO are known for O-atoms. However a small cross section for quenching of NO by O-atoms is predicted by Paul et al. [15]. Quenching was considered for by using Eq. (6)

$$q = \frac{A_a}{A_a + Q_a} \quad (6)$$

where A_a and Q_a denote the total radiative and non-radiative decay rates of the level a , respectively. The dominant quenchers in the flow field of L2K are NO and N_2 . Electronic energy transfer is important for excited NO (D) with molecular nitrogen. The efficiency of this cascade transition relative to the sum of all collisionally decay processes was found to be 0.8 ± 0.2 for D(0) and 0.4 ± 0.1 for D(1) [21]. A nonthermal distribution in NO ($A, v = 0$) results. However the fluorescence from these levels is also monitored with the detection optics.

Quenching constants of the A-state are listed in Table 2.

v	0	1	2	3	4	5
k_{NO}	2.30(8)	2.03(4)	1.75(12)		2.7	2.5
k_{N_2}	$8(3) \times 10^{-4}$	$1.53(4) \times 10^{-2}$	$7.7(7) \times 10^{-3}$			
k_{O_2}	1.41(8)	1.4(2)				
k_{Ar}	4.2×10^{-4}					
k_{He}					0.0017	0.56

where k is given in $10^{-10} \text{ cm}^3 \text{ molecule}^{-1} \text{ s}^{-1}$

Table 2 Quenching constants for NO.

For the B-state the quenching constants $k_{NO} = 126 \cdot 10^{-10} \text{ cm}^3 \text{ s}^{-1}$ and $k_{N_2} = 6 \cdot 10^{-13} \text{ cm}^3 \text{ s}^{-1}$ were used [5].

Measurement uncertainties

In LIF experiments the main source of measurement uncertainty arises from photon statistics. However in the experiment the error can be reduced by averaging.

The relative uncertainty of temperature is found to be

$$\Delta T / T \propto T / \Delta E \cdot \Delta I / I \quad (7)$$

Obviously the relative error of temperature measurement depends on the relative uncertainty of the intensity ratio, the energy difference of the ground state levels, i.e. smaller energy differences yield larger errors, and the absolute temperature, i.e. higher temperatures yield larger relative error. The error in temperature affects the accuracy of the density determination by the Boltzmann fraction. This error can be minimised if it is possible to choose a ground state level for which the Boltzmann fraction does not vary significantly within the measured temperature range. In contrast to the determination of temperature, the uncertainty of number density does strongly depend on the accuracy of the statistical weights and partition functions.

3. SPECTRUM CALCULATION

Spectra were calculated according to the procedure described in [16]. The transition frequencies for the tuning range of the ArF-laser were taken from M. Scheer et al. [17]. The uncertainty of these transitions is claimed to be better than 0.3 cm^{-1} and good agreement with measured transitions could be found. The procedure allows to prescribe different values for rotational and vibrational temperature.

For comparison with an experiment the linewidth, which is determined by the spectral linewidth of the exciting laser (0.3 pm), could be adapted and intensities for the full spectra could be calculated.

For equilibrium states the calculated spectra show that up to temperatures of 350 K only the well resolved XB 0-7 lines of NO are present. XD (1-0) lines appear at temperatures above 350 K and dominate in the whole temperature range, while the XB 0-7 lines become less intensive. At 1000 K the AX 0-3 transition appears.

4. TEST FACILITY AND OPTICAL SET-UP

Test facility

The LIF experiments were performed in the flow field of the arc heated high enthalpy facility L2K. A sketch of the experimental set-up is shown in Fig. 3.

The experiments were performed using a conical nozzle with 29 mm throat diameter, 200 mm exit diameter and 12° half angle. Measurements were taken at a location of 555 mm downstream the nozzle exit. A water cooled flat faced cylindrical model with a diameter of 50 mm, was placed downstream this position, with its axis parallel to the flow. The test chamber is equipped with 6 windows to allow optical access.

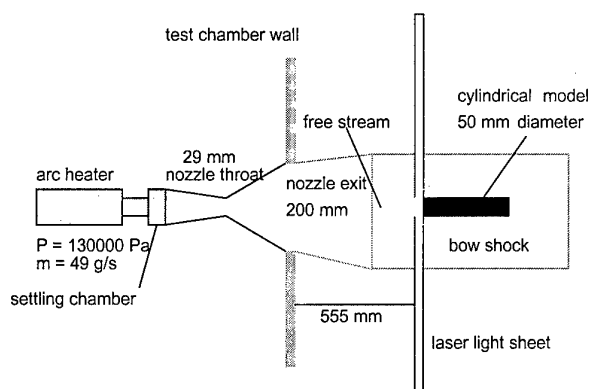


Fig. 3 Sketch of the arc heated facility L2K.

The facility is operated with cleaned and dried air from 200 m³ storage tanks. The air mass flow rate was set to 49 g/s at a stagnation pressure of $1.3 \cdot 10^5$ Pa.

Optical set-up

The main components of the optical set-up are a tuneable excimer laser (Lambda Physics LPX150) and the detection system. Figure 4 shows a sketch of the optical set-up at L2K.

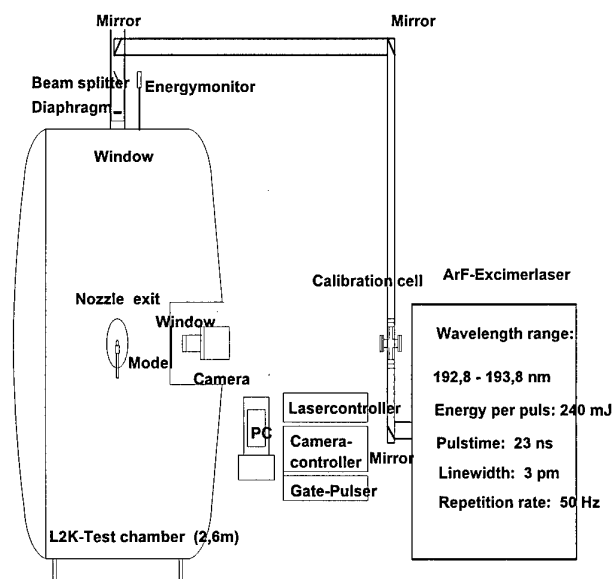


Fig. 4 Optical set-up at L2K.

The laser is completely computer controlled and is operated with ArF to generate light pulses with a duration of 23 ns and a power of up to 240 mJ in the wavelength range from 192.8 up to 193.8 nm with a linewidth of 3 pm. Figure 5 shows the intensity output of the ArF laser as a function of wavelength.

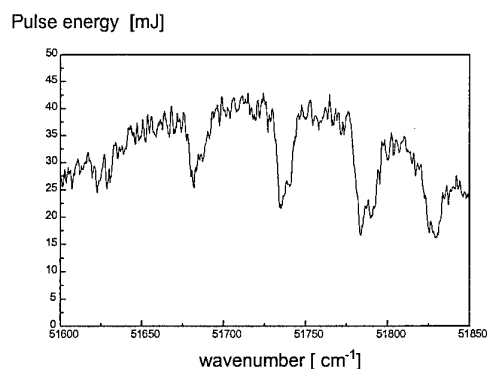


Fig. 5 The intensity output of the ArF laser as a function of wavelength.

The light path between the excimer laser and the test chamber is established by three mirrors and for safety reasons the light path is protected by aluminium pipes. During the experiment the pipes were flushed with N₂ to reduce the absorption of molecular oxygen in the light path. The light was directed on the flow axis in front of the model where it had an approximately rectangular intensity profile with dimensions of 30 mm and 3 mm. No focusing optics were used to avoid saturation effects. In front of the test chamber window a beam splitter was installed. The reflected light was used to monitor the power of each laser pulse with a photodiode, which was referenced to a calibrated power meter (Lambda Physik). A rectangular diaphragm blocked the excessive light from the original dimensions (10 x 30 mm²) of the laser beam.

The fluorescence was imaged with f/4.5 UV Nikkor lenses onto a cooled intensified camera (Princeton Instruments) with a 384 x 578 pixel array mounted perpendicular to the laser sheet. An interference filter with a maximum transmission at 220 nm (± 10 nm), placed in front of the lens, blocked the scattered laser light as well as the visible emission from the test gas and the model.

Experiments were performed by scanning the full tuning range of the laser with wavelength increments of 0.5 pm at a repetition rate of 1 Hz. Synchronisation of the laser pulse and camera illumination was performed with a photodiode and controlled with an oscilloscope. Illumination time of the CCD-camera was 200 ns. In order to avoid detection of parasitic emission from the model, the laser pulses were synchronised to the illumination interval.

Images and spectra were acquired and processed with a personal computer using the software from the manufacturer of the camera (CSMA, Princeton Instruments). Excitation spectra were recorded simultaneously at 10 different axial profiles during a

run. The intensity of 38 pixels radial to the flow direction is accumulated on-chip, thus conserving the information along the flow direction.

The simultaneously probed area was 30 mm x 80 mm in height, with a spatial resolution of $0.3 \times 0.3 \text{ mm}^2$ per pixel. **Figure 6** shows the details of the detection geometry.

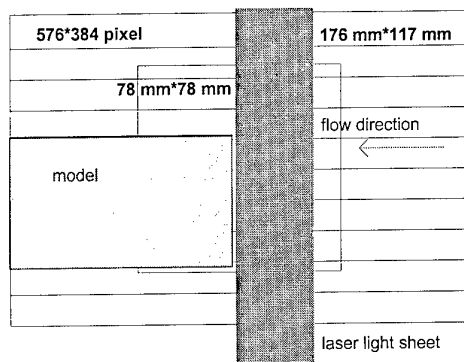


Fig. 6 Details of the detection geometry.

Calibration

Calibration experiments are needed to verify that the fluorescence signal is linear dependent on laser power and for the density determination. For this purpose the test chamber was filled with a 4/1 mixture of N_2 and NO at a pressure of 500 Pa and a temperature of 295 K. Only NO XB 7-0 lines appear at this temperature. The line intensities of the recorded spectrum served as reference for the density determination. No non-linear effects due to absorption of the laser light were observed.

The fluctuation of the intensity distribution along the laser light sheet was checked for the full tuning range of the excimer laser. Less than 8% variation of the spatial laser intensity profile was measured. The laser power was varied by a factor of 10 to prove the linearity of the signal with laser power.

For practical reasons the intensities XB 0-7 lines were referenced to the Rayleigh signal which was recorded without the optical filter using the same experimental set-up, but the test chamber filled with air at a pressure of 101.2 kPa.

A heatable test cell filled with a mixture of NO and N_2 (500 Pa) was placed in the position of the measurement volume to check the agreement between measured and calculated spectra. The temperature was varied in the range between 300 K and 800 K. The line positions and calculated intensities agreed very well for XB, XD, and XA 1-4

transition in the tuning range of the excimer laser. However, the transitions due to XA 0-3 excitation appeared with unpredicted high intensity. As this effect was linear with temperature and laser power, the effect was assigned to the spectral response of the detection system.

5. RESULTS

Calculated flow parameters

Flow calculations were performed a computer code, which is based on a quasi one-dimensional flow through a nozzle of specified geometry [18]. Nozzle geometry, mass flow rate and stagnation pressure are used as input values for the computation. The flow is assumed to start from an upstream reservoir in which the gases are assumed to be in thermochemical equilibrium at reservoir temperature and pressure. Calculations were performed using chemical nonequilibrium nozzle flow. The species taken into account are N_2 , O_2 , O , N , NO , NO^+ and electrons. Vibrational temperatures were assumed to be either in equilibrium or frozen at reservoir level.

The result of the calculation are presented in **Table 3**.

Measured quantities	
mass flow rate	49 g s ⁻¹
stagnation pressure	130 kPa
distance between model and nozzle exit	555 mm
diameter of the nozzle throat	29 mm
diameter of the nozzle exit	200 mm
Calculated quantities	
stagnation temperature	3910 K
frozen temperature in the free stream	247 K
equilibrium temperature in the free stream	340 K
total density in the free stream	$1.44 \cdot 10^{-4} \text{ kg/m}^3$
NO mole fraction in the free stream	0.04365
Pitot pressure	1188 Pa
stagnation enthalpy	7.3 MJ/kg
static pressure	16 Pa
frozen Mach number	7.57

Table 3 Test conditions in L2K.

Data analysis

The raw data were corrected for camera background, laser power and with the intensity distribution along the laser sheet as described by McMillin et al. [19]. The wavelength scale was calibrated internally using

the recorded spectra and the known wavelengths of the XB 0-7 transitions.

Free stream conditions

A typical free stream excitation spectrum is shown in **Fig. 7**. Compared to calculated spectra and spectra from a test cell, the R22 transitions recorded in the free stream appear with reduced intensities.

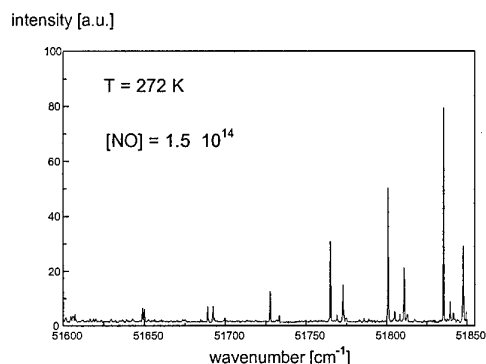


Fig. 7 Free stream NO-spectrum.

However, the analysis of the remaining line intensities leads to a temperature of $272 \text{ K} \pm 20$. As no signal due to vibrational excited NO molecules was detected, the upper limit of the free stream vibrational temperature NO is 450 K. The vibrational temperature of NO is much lower than the one of N_2 , which was determined by CARS measurements [20]. This effect can be explained with the faster vibrationally relaxation of NO.

Since the same optical set-up was used for the calibration experiments and the measurements for each transition and the wavelength ranges concerned, the collection efficiency has no influence. Using the above described calibration procedure for the free stream and applying the quenching corrections, a NO number density of $15 \cdot 10^{14} \pm 0,5 \text{ cm}^{-3}$ was calculated. This number is in good agreement with the quasi-1D-computations and the calculated total number density of $15 \cdot 10^{15}$ the free stream CARS experiments [20].

The spectra were corrected for quenching using the known cross sections and the calculated mole fractions.

Visualisation of shock

Figure 8 shows the shock regions with excitation frequency of $51\,625 \text{ cm}^{-1}$. The shock shape is well visible with a shock stand off distance of 13-14 mm at the model axis.



Fig. 8 2D-LIF-intensity in the shock region.

The intensity increase in the region of the bow shock is partly due to a density increase and to a temperature increase. Due to quenching the intensity decreases in regions closer to the model. Dissociation of NO has not to be taken into account due to reduced intensity in the intensity profile.

Conditions behind the shock

Behind the bow shock the determination of the temperature becomes complicated due to the spectral overlap of the rotational lines. Only the XD 1-0 R22 27.5 line in the full spectrum is well extracted. However combinations of lines coupled to the same vibrational level can be used to analyse the rotational and vibrational temperature. The constants for the analysed lines are given in **Table 4**.

Transition	Ground state [cm ⁻¹]	Transition wavenumber [cm ⁻¹]	Hönl-London factor	Frank-Condon factor
XA 0-3 R22 43.5	3225.5	51679.8	9.60	0.147
XB 0-7 P22 28.5	1557.4	51649.0	27.6	0.027819
XD 1-0 P22 37.5	2556.7	51645.2	8.41	0.1008
XA 1-4 P11 37.5	2383.2	51645.0	8.24	0.24039
XD 1-0 R22 27.5	1446.7	51696.2	5.47	0.1008

Table 4 Constants of the transitions, which were used for the analysis of rotational and vibrational temperature.

The lines which were used to analyse the spatial temperature distribution are marked in the spectrum (**Fig. 9**), which was recorded in the bow shock region 11 mm in front of the model.

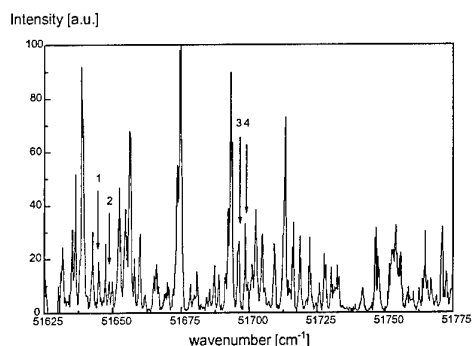


Fig. 9 NO excitation spectrum 11 mm in front of the model, 1: XA 1-4, XD 1-0; 2: XB 0-7; 3: XD 1-0; 4: XA 0-3.

The rotational temperature from a Boltzmann plot, which is shown in **Fig. 10**, results in a temperature of 3150 K with an estimated error of ± 650 K for the XA 0-3 transitions and 2670 K ± 650 K for the XD 1-0 transitions.

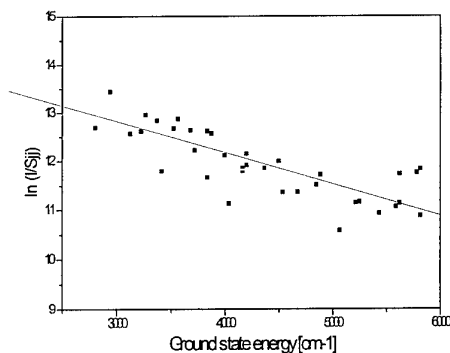


Fig. 10 Boltzmann plots of XD 1-0 and XA 0-3 transition.

The relatively large scattering of the data can be explained with the uncertainty of the intensity assignment of overlapped lines and the appearance of low intensity transitions which were not considered in the calculations of the relative line intensities.

The laser intensity profiles of the line combination as a function of distance to the model surface is shown in **Fig. 11**. Only the region up to a distance of 6 mm to the model is presented, because the laser intensity drops dramatically closer to the model.

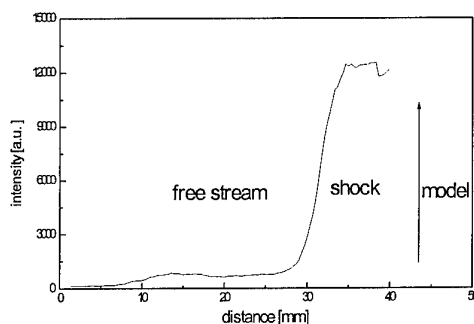


Fig. 11 Intensity profiles of the XB 0-7 line in front of the model.

Moving from the free stream to the model surface, a dramatic increase of the intensity of XB 0-7 transitions is noticed in the region of the shock. The intensity increases by a factor of 17-19 and stays at the same level nearer to the model surface. A plateau is also recognised for the XA 0-3 transitions. The sharp intensity variation can be explained by combined density and temperature increases behind the shock. Theoretical estimation predicts a density increase by a factor of about 6 and a temperature increase by a factor of more than 10. The intensity of the XD 1-0, XA 1-4 transitions increases drastically in the shock region but shows a smoother gradient closer to the model.

Using the values from Table 3 the temperature dependence of the intensities ratios was calculated and applied to the measured intensity ratios. The result is plotted in **Fig. 12**, where the development of the vibrational and rotational temperature profile from the free stream to the model surface is shown.

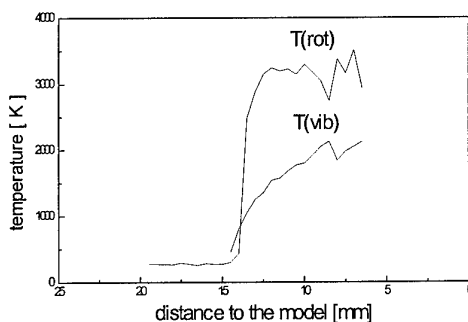


Fig. 12 Temperature profile in front of the model.

The rotational temperature increases in the shock region from 272 K to 3150 K. The vibrational temperature shows a sharp increase in the region of the shock

and increases from values of lower than 450 K in the free stream to about 1200 K at the bow shock and reaches a value of 2130 K at a distance of 6 mm to the model surface.

CARS experiments at the same flow conditions of L2K [20] have shown, that the flow in the free stream is in nonequilibrium with a vibrational temperature of 2800 K and a rotational temperature of 328 K. The maximum vibrational temperature determined by NO-LIF in the free stream was estimated to be 450 K. The rotational temperature yielded a value of 272 ± 20 K. The discrepancy for the vibrational temperatures of NO and N_2 may be explained with the faster vibrational relaxation of NO. The rotational temperature of NO should be higher when the vibrational relaxation for NO is more pronounced.

The measured rotational temperature of 272 K lies between calculated two temperatures using thermal equilibrium or frozen vibrational levels at reservoir conditions. This result indicates thermal nonequilibrium of the flow field.

Rotational relaxation compared to vibrational relaxation is a fast process, that means in the region of the shock the NO rotational temperature and the rotational temperature of N_2 should have the same value. As described, the temperature determination in the shock region using the LIF techniques is complicated because the overlap of the lines introduces an error in the intensity determination of single lines.

Quenching rates of the NO-fluorescence at high temperatures are known not very well. This may be the reason for the different rotational temperatures measured by LIF and CARS.

6. CONCLUSIONS

In arc heated high enthalpy facilities with long test duration, like L2K, relaxation processes in nonequilibrium flows can be studied using the 2D-LIF technique. This method allows to determine temperature and density fields for a wide range of temperatures and densities.

Vibrational relaxation could be monitored up to a distance of 6 mm to the model surface with a maximum vibrational temperature, which was lower than the rotational temperature.

Further experiments will be performed to increase the accuracy of the LIF-technique at high temperatures and densities. Correction of the measured intensity with the actual intensity profile for each laser shot, spectral filtering, gating techniques and reducing the

linewidth of the laser output are planned to improve the accuracy.

7. REFERENCES

- 1) Beck, W. H., Koch, U., and Müller, M., „Spectroscopic diagnostic techniques for the high enthalpy shock tunnel in Göttingen (HEG): preparatory LIF studies on other facilities“, Proceedings of the NATO advanced Research Workshop, edited by A. Boutier, Series E: Applied Sciences, Vol. 224, 1993.
- 2) Seitzman, J. M., and Hanson, R. K., „Comparison of Excitation Techniques for Quantitative Fluorescence Imaging of Reacting Flows“, AIAA J., vol. 31, no. 3, pp. 513-519, 1993.
- 3) Hanson, R. K., Chang, A. Y., Seitzman, J. M., Lee, M. P., Paul, P. H., and Battles, B. E., „Laser-Induced Fluorescence Diagnostics for Supersonic Flows“, AIAA 90-0625, 1990.
- 4) Palmer, J. L., McMillin, B. K., and Hanson, R. K., „Planar Laser-Induced Fluorescence Imaging of Velocity and Temperature in Shock Tunnel Free Jet Flow“, AIAA 92-0762, 1992.
- 5) Okabe, H., „Photochemistry of Small Molecules“, Wiley, New York, 1978.
- 6) Huber, K. P., and Herzberg, G., „Molecular Spectra and Molecular Structure“, Vol. 4, Constants of Diatomic Molecules, Princeton NJ, USA, Von Nostrand (1979).
- 7) Hinz, A., Wells, J., and Maki, A. G., „Heterodyne Frequency Measurement on the Nitric Oxide Fundamental Band“, J. Mol. Spec 119, 1986, pp. 120-125.
- 8) Amiot, C., and Verges, J., „Spin Rotation Doubling in the NO Electronic States by Emission Fourier Transform Spectroscopy“, Chem. Phys. Lett. 66 (3), 1979, pp. 570-573.
- 9) Amiot, C., and Verges, J., „Fourier Transform Spectroscopy of the $D^2\Sigma^+ - A^2\Sigma^+$ and $E^2\Sigma^+ - A^2\Sigma^+$ Systems of Nitric Oxide“, Phys. Scripta 26, 1982, pp. 422-438.
- 10) Bennett, R. J. M., „Hönl-London Factors for Doublet Transitions in Diatomic Molecules“, Mon. Not. R. Astr. Soc 147, 1970, pp. 35-46.
- 11) Houwing, A. F. P., and Boyce, R. R., „Comparison of Planar Fluorescence Measurements

and Computational Modelling of Shock-Layer Flow", AIAA J., vol. 34, no. 3, 1996, pp. 470-477.

12) Drake, M. C., and Ratcliffe, J. W., „High Temperature Quenching Cross Sections for Nitric Oxide Laser-Induced Fluorescence Measurements", Journal of Chemical Physics, Vol. 98, No. 5, 1993, pp. 3850-3865.

13) Zacharias, H., Halpern, J. P., and Welge, K. H., „Two-Photon Excitation of NO ($A^2\Sigma^+; v' = 0, 1, 2$) and Radiation Lifetime and Quenching Measurements", Chemical Physics Letters, Vol. 43, No. 1, 1976, pp. 41-44.

14) Paul, P. H., Gray, J. A., Durant Jr., J. L., and Thoman Jr., J. W., „Collisional Quenching Corrections for Laser-Induced Fluorescence Measurements of NO $A^2\Sigma^+$ ", AIAA J., vol. 32, no. 8, 1994, pp. 1670-1675.

15) Paul, P. H., Durant, J. L., and Thoman, J. W., „Collisional Quenching Corrections for Laser-Induced Fluorescence Measurements of NO $A^2\Sigma^+$ ", AIAA Journal, Vol. 32, No. 8, 1994, pp. 1670-1675.

16) Gundlach, G., „Untersuchung der Rotationsenergie-Wechselwirkung von NO an technischen Oberflächen in verdünnter Hyperschallströmung mit laserinduzierter Fluoreszenz", DLR-Forschungsbericht 95-38, 1995.

17) Scheer, M., Wollenhaupt, M., Rosenbauer, M., and Beck, W.H., „Temperature and Density Measurements on Hypersonic Wind Tunnels Using Laser Induced Fluorescence of NO, Including a Study of NO Spectroscopy Using a Novel Heated Cell", DLR-IB 223-96 A32, 1996.

18) Gülhan, A., and Esser, B., „Numerical computation of gas properties at characterization test conditions", DLR IB-39113-92C32, 1992.

19) McMillin, B. K., Palmer, J. L., and Hanson, R. K., „Temporally resolved, two line fluorescence imaging of NO temperature in a traverse jet in a supersonic cross flow", Applied Optics, Vol. 32, No. 36, 1993, pp. 7532-7545.

20) Grisch, F., Bouchardy, P., Koch, U., and Gülhan, A., „Rotational and Vibrational Temperature and Density Measurements by Coherent Anti-Stokes Raman Scattering in a Nonequilibrium Shock Layer Flow", RTO/ AGARD Fluid Dynamics Panel Symposium, Advanced Aerodynamic Measurement Technology, 22-25 September 1997, Seattle, USA.

21) Imajo, T., Shibuya, K., and Tanaka, I., „Energy transfer and electronic quenching of the low-lying Rydberg states of NO in NO/N₂ mixtures", J. Phys. Chem. 90, 1986, pp. 6006-11.

Time Resolved Measurements of the Energy Separation Process in a Transonic Turbine Vane Wake Flow

W.E. Carscallen ¹S.I. Hogg ²J.P. Gostelow ³D.R. Buttsworth ⁴

¹
Institute for Aerospace Research
Aerodynamics Laboratory
National Research Council Canada
Ottawa, Ontario, Canada
K1G 0R6

^{2, 3}
Dept. of Engineering
University of Leicester
University Road
Leicester, UK.
LE1 7RH

⁴
Dept. of Engineering Science
University of Oxford
Parks Road
Oxford, UK.
OX1 3PJ

1. Summary

This paper describes the application of a new, fast response, stagnation temperature probe and the associated measurement technique to an unsteady transonic turbine vane wake flow in which energy separation occurs due to vortex shedding.

2. Introduction

In 1943 Eckert and Weise (Ref. 1) discovered a phenomenon in which the stagnation temperature measured at the base of a thermally insulated cylinder, immersed in an air stream, was lower in value than that of the incoming air. This phenomenon, now known and defined by Kurosaka et al, (Ref. 2, 3) as the Eckert-Weise effect was attributed to the shedding of a von Karman vortex street from the cylinder and refers 'to the defect in time averaged surface temperature or stagnation temperature in the flow'. The research of Kurosaka et al was carried out at low Mach numbers and they used an inviscid Navier Stokes code to investigate how the vortex shedding caused the cooling phenomenon. Their CFD investigation revealed unexpected features of the flow in the form of hot spots which existed simultaneously with the anticipated cold spots.

In 1989, Carscallen and Oosthuizen (Ref. 4) independently published time averaged

stagnation temperature and pressure data taken downstream of transonic turbine vanes mounted in the National Research Council of Canada's Large Scale Transonic Planar Cascade (LSTPC). The turbine vanes had a relatively thick trailing edge as they had been designed to allow for trailing edge cooling, this feature was not implemented for the experiments. The temporally averaged data from these experiments showed that in addition to the depressed temperatures in the centre of the wake there was also an increase in stagnation temperature at the edges of the vane wake, this separation of stagnation temperature, ΔT_o across the wake and the loss coefficient, C_{po} were both functions of Mach number, Ma. The maximum ΔT_o and C_{po} occurred at a Ma of approximately 0.95 and both ΔT_o and C_{po} decreased as the flow became sonic. As with the results of Kurosaka et al the contour plots of ΔT_o and C_{po} were replicas of each other, thus implying the redistribution of stagnation temperature and pressure were related to the production of entropy.

In order to experimentally validate the work of Kurosaka et al. Carscallen et al, 1994, 1996 (Ref. 5, 6) undertook a research investigation to demonstrate the existence and extent of von Karman vortex shedding in the wake of a transonic turbine vane. Their results, based on high speed schlieren

visualization and time resolved pressure measurements showed that strong vortex shedding occurred over the Ma range studied ($0.7 \leq Ma \leq 1.17$). At subsonic Mach numbers the vortices were shed as a classic von Karman vortex street while as the transonic regime was approached and crossed the coherent structures within the wake became unstable, less von Karman like, and occurred less frequently. This change in the vortex street was correlated to the migration of the origin of the vortices from the vane trailing edge to the junction of the two trailing edge shear layers and trailing edge shock waves. Even though these data revealed some of the physics of the vortex shedding phenomena they were inconclusive and thus incomplete. In 1996 an additional experimental program was undertaken to study the time dependent behaviour of the unsteady wake. This program relied on a new, fast-response, stagnation temperature probe based on transient thin film heat flux gauge technology, Buttsworth & Jones, 1996 (Ref. 7) mated with a fast response stagnation pressure probe. This paper presents the results from this experimental investigation.

3. Experimental Apparatus and Instrumentation

The transonic turbine vane wake flows were measured in the LSTPC facility described by Carscallen and Oosthuizen, 1989. The cascade was operated continuously as an in-flow type facility, in which air was drawn from the laboratory and through the cascade at up to 3.83 kg/s, by a 2.0 megawatt exhaustor plant. The planar cascade contained six vanes which were nominally 3.5 time engine size. The turning angle was 76° and the chord of the vanes was 175.3mm, their trailing edge thickness was 6.35 mm. The relatively thick trailing edge made the vanes susceptible to vortex shedding at frequencies around 10 kHz

which is similar to that of the passing frequency of compressor blades in a modern gas turbine engine.

Simultaneous time resolved stagnation temperature and stagnation pressure measurements were made of vane wake flow using the device shown in Figure 1. Three probes can be seen protruding from the head of the device.

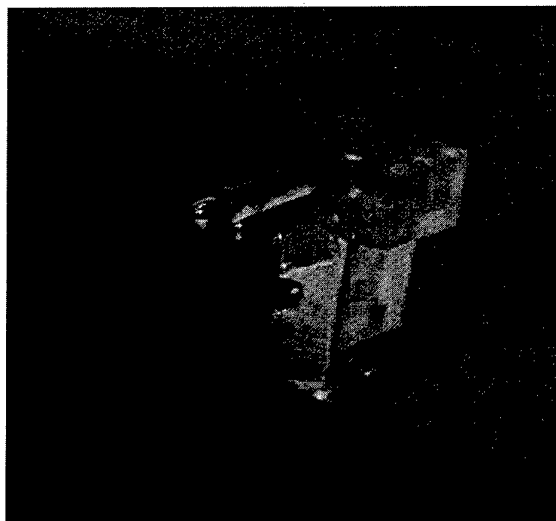


Figure 1 - Probe Head

The first of these (on the right) is a tube-mounted fast response miniature pressure transducer. The front face of the pressure transducer is flush with the end of the support tube, allowing the pressure of the flow stagnating on its face to be measured directly. The outer diameter of the tube was 2.5 mm. The two remaining probes (centre & left) were required to measure stagnation temperature using the new fast-response technique of Buttsworth & Jones, 1996. Both probes were made from 3 mm diameter fused quartz, and have thin film platinum resistance thermometers painted onto their hemispherical ends. The three probes are mounted in the plexiglass head such that the measuring points at their tips are in a line. This line runs parallel to the trailing edge of

the test vane and is at the same downstream location as the wedge probes utilized by Carscallen (Ref. 4). All probe measurements were made in the nominally two-dimensional flow from the centre of the vane. The large vortical structures shed from the trailing edge, which are the focus of attention in the present study, are also expected to be essentially two-dimensional in this region. By orientating the probes in this way, all three tips see identical points in any given vortical flow event despite their displaced locations (3.5 mm between centres).

The new stagnation temperature measurement technique employed in this experimental campaign was described in detail by Buttsworth & Jones, 1996 and so only a brief overview is given here. The heat transfer between the quartz tip of each probe and the flow was governed by the stagnation heat transfer coefficient, the surface temperature of the quartz and the temperature of the flow stagnating at the tip, i.e. the local stagnation temperature of the flow. The thin film gauges were run in constant current mode so the temperature of the quartz could be determined directly from the voltage drop across the gauge. A surface heat transfer signal was also generated from the gauge voltage using Oldfield et al's, 1982, (Ref. 8) heat transfer analogue unit. The quartz probes were operated at different temperatures by heating one of them with a small internal electrical heater prior to use. The heat transfer coefficient and the stagnation temperature of the flow were the unknowns in the heat transfer process for each probe. As the quartz probes were essentially geometrically identical it was assumed that the heat transfer coefficient was the same for both. This allowed the stagnation temperature of the flow to be calculated by simultaneous solution of the heat transfer

equation for each probe. Corrections were applied for surface curvature effects and lateral conduction around the probe tip, as described by Buttsworth & Jones, 1996. Their error analysis of the technique showed that a measurement accuracy of $\pm 3\text{K}$ can be expected. As there is no stagnation enthalpy change across the probe bow shocks, the technique is applicable for a wide range of Mach numbers. In the present tests, the bandwidth of the stagnation temperature measurement was limited to 87 kHz by the conditioning electronics used to process the thin film signals. Despite this, the technique is still considerably faster than previous methods e.g. Ng & Epstein, 1983, (Ref. 9).

This method of measuring fluctuating stagnation temperatures was initially developed for use in short duration transient facilities. The tests described in this paper were the first application of this new measurement technique in a continuously running facility. In most applications, operating times are limited to less than a second before the temperature difference between the probes drops to a level where measurement errors become unacceptable. This is less of an issue in transient testing, where probe heating could take place prior to firing the tunnel and the operating time of the probe often exceeds the run time of the facility. Unfortunately, neither of the above are true when testing in continuously operating facilities and as a result the measurement technique had to be adapted accordingly. A shielded cavity was created in the porous tailboard of the cascade, Figure 2. The probe was mounted on a support mechanism which allowed the head to be withdrawn from the flow into the cavity whilst the tunnel was operating. The shielding of the cavity was such that conditions within the cavity were essentially stagnant, resulting in a temperature close to

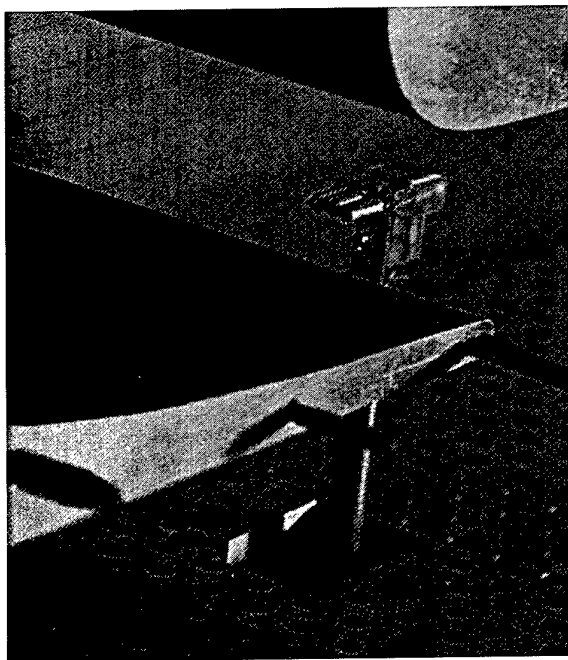


Figure 2 - View of Probe and Cavity in the Porous Tailboard

the stagnation temperature of the free stream cascade flow. As described earlier, this value is the ambient temperature of the laboratory air surrounding the LSTPC. Once the head was shielded from the flow, probe heating could take place. The design of the probe mounting allowed the head to be moved rapidly from the cavity into position downstream of the test vane when the desired differential temperature between the two quartz probes had been obtained. As the operating time of the probe was short, this movement had to be very rapid. In all of the tests described in this paper, the probe was released from the tailboard cavity and brought to rest in a prescribed position within the vane wake in less than 0.1s. Cross-wake traverse data were obtained by adjusting the probe mounting so that the head stopped at different cross-wake positions.

Typical heat flux signals from the quartz probes are shown in Figure 3. All of the

signals from the probes were digitized at 250 kHz for 0.5 s after release from the tailboard. To avoid any aliasing effects the signals were passed through a 100 kHz low-pass filter prior to logging. The traces in Figure 3 shows the initial transients as the head moves from the tailboard, across the freestream flow and into the cross-wake position. The transients are dissipated in the first 0.1 s. The lower trace is for the heated probe.

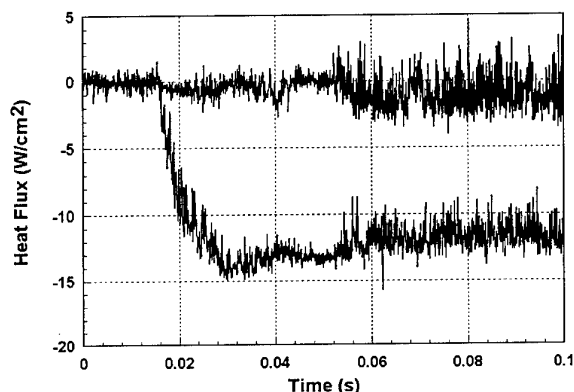


Figure 3 - Probe Transient Heat Flux Signals

In order to provide a timing signal which could be used as a phase reference between probe signals from different cross-wake traverse positions in relation to the vortex shedding process, a second, fast response pressure transducer was mounted in the trailing edge of the test vane to measure base pressure. To avoid uncertainty in this phase reference signal the transducer was mounted so that it was more susceptible to vortex shedding from the vane's trailing edge suction surface. This signal was logged simultaneously with the probe signals in the tests. This is clearly seen in Figure 4. Both the probe stagnation pressure transducer and the base pressure transducer were calibrated to an accuracy of better than $\pm 0.025\%$ of the indicated value prior to the tests.

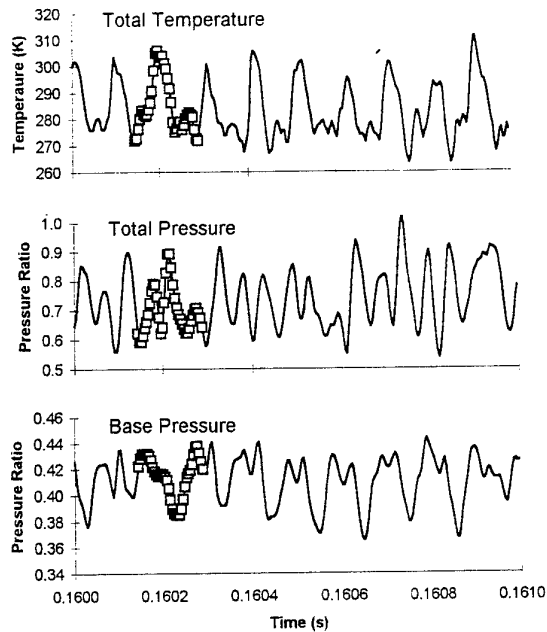


Figure 4 - Sample of Traces for Stagnation Temperature and Pressure and, Base Pressure

After application of calibration procedures to the raw data which resulted in the production of temperature and pressure signals in physical units, the first 37,500 readings (0.15 seconds of data) were discarded to ensure that all data had reached steady state conditions. The 212,500 remaining data were then analyzed in blocks of 200 readings. This permitted the phase reference to be applied and the 128 readings immediately following the reference to be stored. In the rare case of a poor or ambiguous phase reference this allowed one vortex shedding cycle to be discarded. It was therefore possible to obtain a satisfactorily phase-referenced record of 128 readings in all cases. For each data record this procedure was repeated 64 times, allowing 64 traces to be collected. A simple phase lock averaging procedure, Gostelow 1977, (Ref. 13) was then applied resulting in phase-averaged traces of stagnation

pressure and stagnation temperature. The phase-averaged traces from all cross-wake traverse locations were combined using the common phase reference and contouring procedures were applied to the resulting traces. Note, the centre of the wake, which corresponded to the vane trailing edge metal angle was chosen as a datum and the notation adopted was such that the suction side values shown on the Y-axis of contour plots were positive.

4. RESULTS & DISCUSSION

Records of stagnation temperature, stagnation pressure and base pressure were obtained, at each of eleven cross-wake traverse locations. The traverses were in a plane normal to the wake at a distance of 36.6mm, or 6.1 trailing edge diameters, downstream from the vane trailing edge.

Contour plots are presented for 100 readings, or 0.4 ms, of phase-averaged data in Figures 5 and 6. These data have been presented in reversed time sequence to relate more closely to Lagrangian views of the vortical wake obtained from schlieren visualization and computational simulations. To obtain a realistic view of the vortex shedding process it was necessary to apply a vortex propagation velocity to the readings as recommended by Zaman and Hussain, 1981 (Ref. 14). For the vane row under investigation at a free-stream Mach number of 0.95 this had been shown to be 178 m/s, (Ref 6).

The pressure and temperature contours of Figures 5 and 6 clearly represent a periodic structure with stagnation pressure dropping to less than 70% of the free stream value in the vortex cores. It is not, however, immediately obvious that this corresponds to a conventional von Karman vortex street. Clarification and interpretation are required and are attempted subsequently.

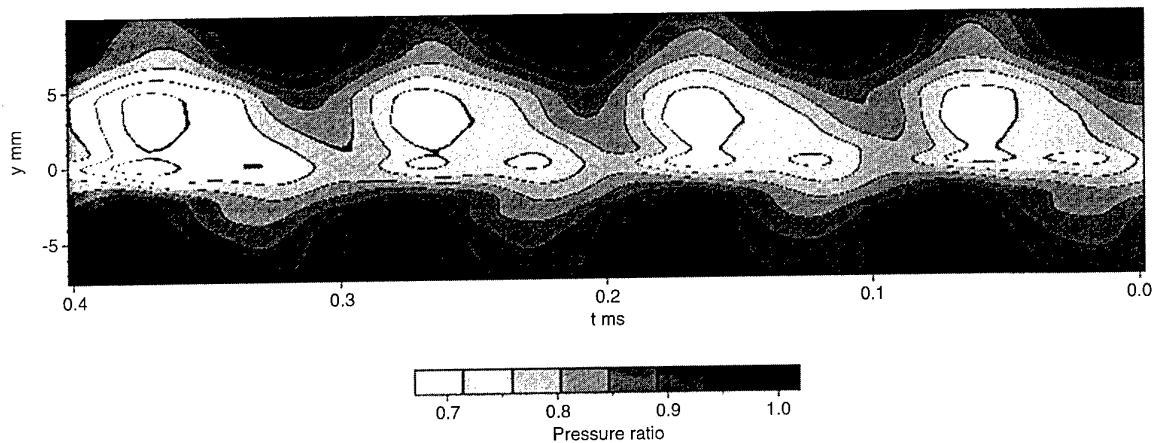


Figure 5 - Contour Plots of Phase-averaged Stagnation Pressure Variation with Time

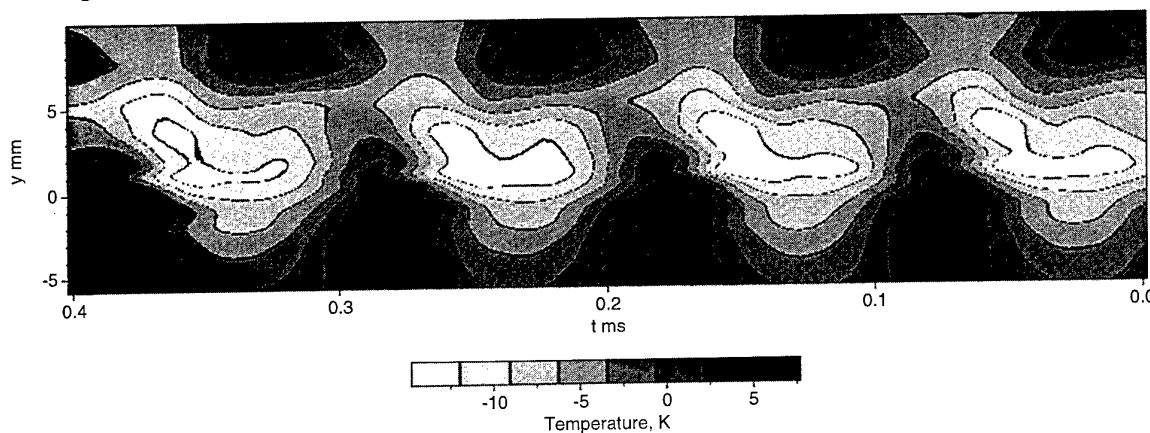


Figure 6 - Contour Plots of Phase-averaged Stagnation Temperature Variation with Time

The temperature contours indicate strong stagnation temperature redistribution and Figure 7 presents minimum, maximum and average values of the stagnation temperature traces at each Y location. Stagnation temperatures may be 16K lower than free stream values in the vortex cores and indicate hot spots of over 8K greater than the average free-stream values at the outer edge of the pressure side of the vortex wake. On the suction side this difference is just over 6K. It should be recalled that these data are subject to low-pass filtering at 100kHz giving a maximum resolution of approximately ten readings per cycle (vortex

shedding frequency approximately 10kHz) and eliminating short duration fluctuations from consideration. The phase averaging procedure will also have caused the elimination or reduction of short duration structures, thus the real instantaneous variations will tend to be greater than the values indicated in the contour plots.

When the stagnation temperature readings at the wake centre region are averaged over time a temperature deficiency of over 10K is obtained. In Figure 8 this temperature deficiency is compared with earlier results measured by a wedge probe capable of

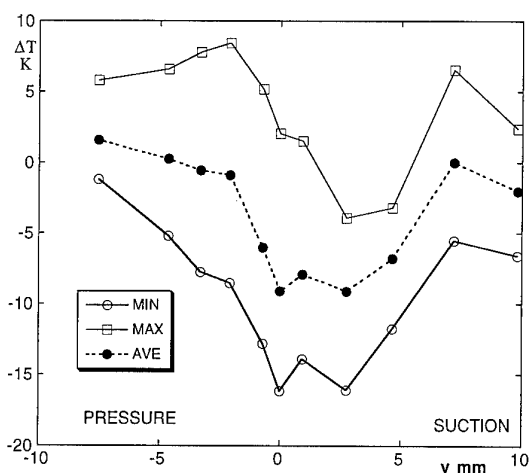


Figure 7 - Variation of Min., Max. and Ave. Values of Phase-averaged Stagnation Temperature Across the Wake

measuring both stagnation pressure and temperature. The present results are seen to agree very well with these earlier results. This confirms that the previous, supposedly anomalous results (Ref. 4) were actually the result of energy separation in the vortex wake as described by Kurosaka et al. 1987.

The low temperatures found in the vortex cores were not a surprise, although previously no direct measurements had been made of these behind turbine vanes due to the limited bandwidth of available instrumentation. It was a surprise to find such pronounced hot spots on the edge of the wake. These had only previously been observed for shed vortices in the computational work of Kurosaka et al. but not experimentally and certainly not in vortex shedding at high shedding frequencies of the order of 10kHz. These hot and cold spots when time averaged manifested themselves as areas of depressed stagnation temperatures in the centre of the wake and increased stagnation temperatures at the edge of the vane wake as was found in the experiments of Carscallen and Oosthuizen (Ref. 4).

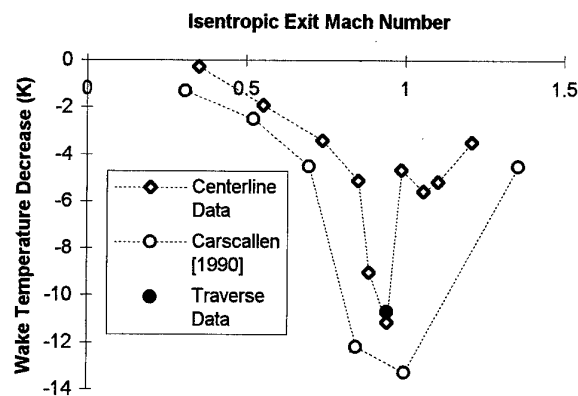


Figure 8 - Comparison Between Phase-averaged Temperature Measurements and Previous Results Measured with Wedge Probe

The present time resolved stagnation temperature measurements therefore support observations of energy separation through the Eckert-Weise effect as defined by Kurosaka et al. and observed by others (Ref. 4, 10) and extends these to flows behind turbine vanes at shedding frequencies of the order of 10 kHz. They also validate the use of the combined stagnation pressure and temperature probe under conditions fully representative of transonic turbomachinery under normal operating conditions. It is clear, for example, that the probe has the potential to be used to give time-resolved stagnation temperature measurements in the rotor wakes of transonic fan blading and hence time-resolved efficiency measurements.

An equivalent data reduction approach is to use the pressure and temperature measurements to provide contours of total entropy increase. The usual relationship for the entropy increase, $(S_2 - S_1)$ of a perfect gas (C_p , R) between conditions 1 and 2 is used in terms of stagnation temperature, (T_{02}/T_{01}) and pressure, (P_{02}/P_{01}) ratios:

$$S_2 - S_1 = C_p \ln(T_{02}/T_{01}) - R \ln(P_{02}/P_{01})$$

The phase-averaged stagnation pressure and temperature data may therefore be combined in the form of contours of entropy increase. This has been done in Figure 9. The result is contours of an unfamiliar serpentine form which certainly require elucidation. What may be deduced from the contours is that although a single, distinct and conventional vortical structure is shed from the pressure side each shedding period, no such simple conclusion may be reached with regard to the suction side.

The literature offers little other direct experimental evidence to assist in the interpretation of this behavioral difference between the vortical structures emanating from the two surfaces. Clues are nevertheless given in information such as the smoke traces of Roberts and Denton, 1996 (Ref. 11). For a body having similar trailing edge aerodynamic characteristics to these vanes the vortices from the pressure surface rolled up tightly into coherent cylindrical structures; those from the suction surface were far more diffuse. The salient difference was that the suction surface trailing edge boundary layer was turbulent and much thicker than the boundary layer on the pressure surface.

More direct guidance was obtained from the computational work of Arnone and Pacciani, 1997, (Ref. 12). These are the only known computations of vortex shedding behind turbine vanes in which entropy contours are presented. A large scale plot of these contours is presented in Figure 10; these data are from the same set of results as Figure 9B of Reference 12. This turbine nozzle cascade is less highly loaded than the NRC cascade and is operating at a lower isentropic exit Mach number of 0.4 but otherwise conditions are quite similar. A Lagrangian view of the downstream flow field is presented for the calculation results as

compared with the Eulerian view from a fixed downstream plane for the present experimental results but the computations may be used with care to aid interpretation of the experimental results.

The experimental measurements were made in a cross-wake plane 6.1 trailing edge diameters downstream of the vane trailing edge and a broken line has been drawn on the computational results (Figure 10) to indicate this same relative position. It is instructive to observe the vortical structures just upstream and downstream of that line. The vortical structures do seem to bear a close resemblance to the experimentally-observed structures centred about the 0.2 ms time mark; indeed they provide an explanation of these observed structures. It is clear from the computational results that the vortical structures emanating from the relatively thick suction surface boundary layer do not remain as tightly-rolled cylindrical vortices but become stretched toward the centre line of the wake. The entropy increase contours associated with the suction surface shedding have the appearance of bands which are oriented normal to the flow direction.

The computational work is able to show this in much finer detail than the experimental work because the latter is limited to a bandwidth of 100kHz. Nevertheless it is thought that in all important respects the experimental vortical structures, although not exact, are compatible with the computational work and therefore lend credence to the computational results of Arnone and Pacciani. Investigation of the raw stagnation temperature traces was undertaken to see if fine scale structure could be discerned. Little such structure was observed and it was concluded that a significant improvement in the measurement bandwidth would have been needed to observe fine-scale structure.

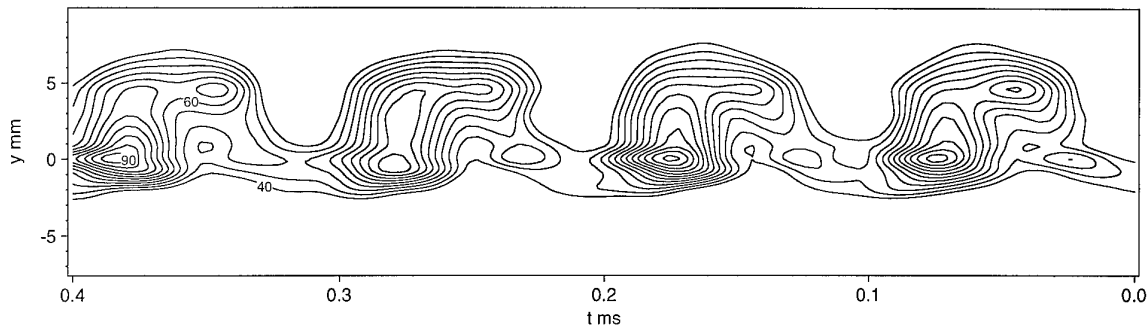


Figure 9 - Contour Plots of Phased-averaged Entropy Variation with Time

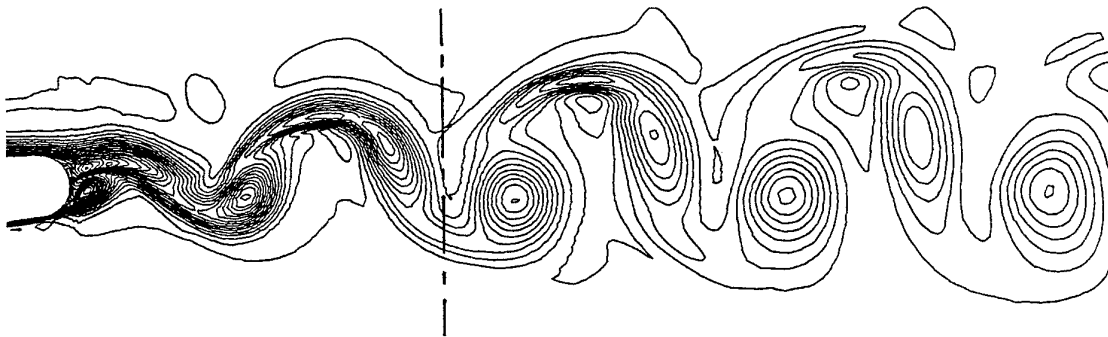


Figure 10 - Lagrangian Contours of Entropy Increase from CFD Work of Ref. 12

Such an improvement in the probe and the electronics is feasible. Some experimental observations of much higher frequencies have been performed on these vortical structures. These are the sub-microsecond spark schlieren photographs which were taken. An example of these is given in Figure 11. This photograph is compatible with the picture obtained from the computational work. In particular ribs of fine scale structure are frequently observed in the schlieren photographs.

5. CONCLUSIONS

This paper has described the application of a new, fast response, stagnation temperature probe and a modified measurement technique to an unsteady transonic turbine vane wake flow in which energy separation occurred due to vortex

shedding. Although the probe was developed for use in a transient facility it has been evolved for the study of unsteady turbine vane wakes in a continuously operating transonic planar cascade. The topology of the wake vortical structures caused due to vortex behind blunt trailing-edged turbine vanes has become clearer but is yet to be fully understood. Time averaged data obtained with the new fast response stagnation temperature probe have been shown to agree very well with stagnation temperature data taken with a conventional wedge probe.

6. ACKNOWLEDGMENTS

The authors wish to acknowledge the expert support of Mr. P. Hunt of NRC and Professor Andrea Arnone who kindly provided more detailed computational results.



Figure 11 - Schlieren Visualization of Vortex Wake at $Ma=0.95$

7. REFERENCES

1. Eckert, E.R.G. and Weise, W., "Messung der Temperaturverteilung auf der Oberfläche schnell angeströmter unbeheizter Körper", *Forsch. Geb. Ing. Wesen*, 1943, Vol. 13, pp 246-254.
2. Kurosaka, M., Gertz, J.B., Graham, J.E., Goodman, J.R., Sundaram, P., Riner, W.C., Kuroda, H., and Hankey, W.L., "Energy Separation in a Vortex Street", 1987, *J. Fluid Mech.*, vol. 178, pp. 1-29.
3. Kurosaka, M., Graham, J.E., Shang, J.S., "Negative Heat Transfer in Separated Flows", *Int. J. Heat and Mass Transfer*, vol. 32, pp. 1192-1195, 1989.
4. Carscallen, W.E., Oosthuizen, P.O., "The Effect of Secondary Flow on the Redistribution of the Total Temperature Field Downstream of a Stationary Turbine Cascade", 1989, AGARD-CP-469.
5. Carscallen, W.E., Gostelow, J.P., "Observations of Vortex Shedding in the Wake from Transonic Turbine Nozzles", Fifth International Symposium on Transport Phenomena and Dynamics of Rotating Machinery (ISROMAC-5), Kaanapali, Hawaii, U.S.A., May 8-10, 1994.
6. Carscallen, W.E., Fleige, H.U., and Gostelow, J.P., "Transonic Turbine Wake Flows", ASME International Gas Turbine Conference, Birmingham, U.K., 96-GT-419, 1996.
7. Buttsworth, D.R. & Jones, T.V., "A Fast-Response Total Temperature Probe for Unsteady Compressible Flows", ASME International Gas Turbine Conference, Birmingham, U.K., 96-GT-350, 1996.
8. Oldfield, M.L.G., Burd, H.J. & Doe, N.G., "Design of Wide-Bandwidth Analogue Circuits for Heat Transfer Instrumentation in Transient Tunnels", 16th Symposium of International Centre for Heat and Mass Transfer, Hemisphere Publishing, pp. 233-257, 1982.
9. Ng, W.F. & Epstein, A.H. "High Frequency Temperature and Pressure Probe for Unsteady Compressible Flows", *Rev. Sci. Instrum.*, Vol. 54, No 12, pp. 1678-1683., 1983.
10. Eckert, E.R.G., "Energy Separation in Fluid Streams", *Int. Comm. Heat Mass Transfer*, Vol. 13, pp. 127-143, 1986.

11. Roberts, Q.D., and Denton, J.D., "Loss production in the wake of a simulated subsonic turbine blade", ASME Paper 96-GT-421, 1996.
12. Arnone, A. and Pacciani, R., "Numerical prediction of trailing edge wake shedding", ASME Paper 97-GT-89, 1997.
13. Gostelow, J.P., "A new approach to the experimental study of turbomachinery flow phenomena", Transactions of the ASME, Journal of Engineering for Power, January 1977.
14. Zaman, K.B.M.Q. and Hussain, A.K.M.F., "Taylor hypothesis and large scale coherent structures", Journal of Fluid Mechanics, 112, pp. 379 - 396, 1981.

APPLICATION OF OPTICAL AND INTERFERENCE METHODS IN EXPERIMENTAL AERODYNAMICS

V.P.Koulech, S.D.Fonov, V.A.Yakovlev

Central Aerohydrodynamic Institute (TsAGI)
140160, Zhukovskiy, Moscow region, Russia

Summary

The review of optical methods, which were developed and used during the last years in TsAGI for investigations of aircraft aerodynamics and aeroelasticity, is presented. Non-traditional methods of flow investigations are considered in more details: a raster-type shadowgraph method of flow visualization, laser interferometry with a narrow reference beam, shift interferometry and laser holographic interferometry, a laser-knife method. The combination of visualization by a laser-knife method with local measurements of velocity distribution with the help of a laser Doppler velocimeter (LDV) is offered, which allows to optimize a grid of nodes of velocity measurement. To study the shape, motion and deformation of the aerodynamic models and aircraft structure elements in aerodynamic wind tunnels a number of optical, laser and videogrammetric systems ensuring high sensitivity and processing of results in real time is developed.

Introduction

Study of interaction between a flow and a surface of a model assumes, on the one hand, investigations of structure and parameters of a gas flow passing around the model, and processes of its effect on the surface, and on the other hand, investigation of motion and deformation of the model surface under action of aerodynamic and inertial forces.

In the experimental solution of both problems optical methods and means, the main advantages of which are high spatial and time resolution, possibility of non-contact measurements and informational capacity, have found the broad application.

One of the most widespread means to study flows is the visualization of gas flow fields around models in aerodynamic wind tunnels. The conventional methods of visualization - shadowgraph and interference- are widely applied. The majority of aerodynamic wind tunnels of TsAGI of small and medium size are equipped with standard shadowgraph systems. These devices ensure visual view up to 400 mm. However, frequently in experiments there is a necessity to visualize flows of the greater size, investigate flow regions located outside optical windows in the walls of a wind tunnel test section, to research flows in wind tunnel and at facilities not equipped with standard shadowgraph devices.

For the solution of such problems, mobile means of visualization were developed at TsAGI in 1970-1980. They are a raster-type shadowgraph system of flows visualization in large aerodynamic wind tunnels (V.P.Koulech - 1984), a shift interferometer with capability of sensitivity control (V.A.Yakovlev - 1979), a laser-knife (light sheet) system for visualization of

spatial gas flows (A.A.Orlov - 1976). Laser interferometers with a narrow reference beam (A.A.Orlov and V.P.Koulech - 1974) and holographic interferometers (V.A.Yakovlev) ensure a capability of quantitative decoding of a flow structure, but they are more stable against external disturbances, than classical two-beam interferometers.

For detailed investigation of a flow structure at the beginning of the seventies at TsAGI under Prof. G.L.Grodzovsky's guidance laser Doppler velocity meters (LDV) were developed and introduced into subsonic and supersonic wind tunnels. The technique of combination of flow visualization by a laser-knife method with measurements by means of LDV, allowing optimally distribute the nodes of a measurement grid was proposed (V.P.Koulech - 1979). A large cycle of investigations of various configurations of fighters was performed in conformity with this technique (V.A.Pesetsky - 1986).

To solve the problems of aeroelasticity and strength investigations of the shape, motion and deformation of the model or structure elements surfaces were implemented by methods of a conventional photogrammetry (V.A.Yakovlev, V.N.Shmyreva). Frequently these methods did not provide required accuracy and had low efficiency stipulated by duration of processes of development of photographic films and high labor consumption of image decoding. To increase the sensitivity while measuring parameters of motion and deformation in such researches a method of laser differential interferometry with photographic registration was developed at the beginning of the eighties under Prof. A.K.Martynov's guidance. It has found application for the study of motion and deformation of the model of a helicopter main rotor blade in a wind tunnel, for visualization of the oscillations forms of structure elements, for measurements of standing waves on the surface of liquid (S.D.Fonov, V.P.Koulech).

At the beginning of the nineties with appearance of efficient CCD video cameras and computer facilities, the videogrammetry received its development (S.D.Fonov, V.P.Koulech). The systems to control geometrical parameters of models for their conformity to the computational form, for measurement of a model deformation under action of aerodynamic loads in a wind tunnel, for measurements of motion and deformation parameters of a helicopter full-scale main rotor blade in actual time were developed. The methods of videogrammetry which were developed at TsAGI have found their use also in the system for line control of geometrical parameters of wheels at a steel works (V.P.Koulech, V.D.Vermel - 1996).

1. Methods of Gas Flow Visualization

Shadowgraph methods of visualization are based on the effect of refraction of a light beam, which passed path 1 in medium with a density gradient $\text{grad}\rho$, to angle,

$$\epsilon = K \cdot l \cdot \text{grad}\rho$$

Where K - the factor low dependent on gas parameter; for air $K = 2.26 \cdot 10^{-4} \text{ m}^3/\text{kg}$

1.1 Shadowgraph Methods

The most inexpensive and simple for realization is a direct shadowgraph method. Through the flow under study the collimated light beam is passed. The light beams refracted in inhomogeneous medium having a density gradient, deviate from initial direction and displace to a distance $\Delta x = L \cdot K \cdot l \cdot \text{grad}\rho$ in a plane of registration, making a shadow contour of optical non-uniformity. The sensitivity of the direct shadowgraph method is proportional to distance L from section under study up to the plane of registration. This distance is limited from above by increasing influence of diffraction phenomena and external disturbances, and from below - by wind tunnel test section design. Therefore, the direct shadowgraph method provides qualitative pictures while studying gas flows with mean density gradients. The simplicity of realization allows applying it in complex conditions at facilities, which are not equipped with standard devices for visualization.

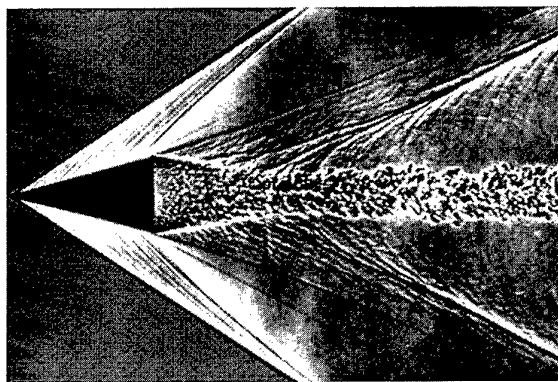
To investigate transonic and supersonic gas flows with normal and high density the reduced sensitivity is necessary. To control sensitivity in these cases a modified shadowgraph method is used.

The modification consists in location of a receiving objective lens between section under study and a plane of registration. The sensitivity of the modified shadowgraph method is proportional to distance L from section under study up to plane optically conjugated to plane of registration. This distance can be varied in unlimited range.

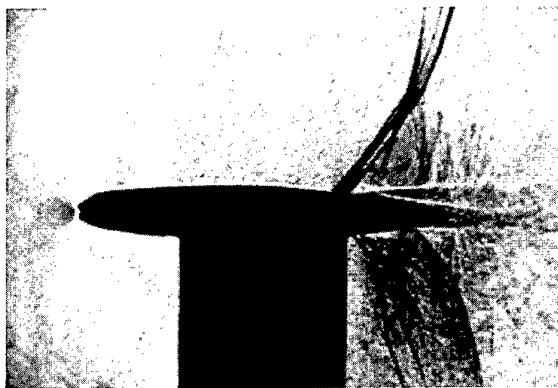
Fig.1,a shows the examples of visual research of a shell flight on a ballistic range, and Fig.1,b - flow patterns of a wing profile a cryogenic wind tunnel. The size of the visualization area is about 150 mm. The quality of the picture in the second case is worsened by hoarfrost, settling down on optical windows.

Fig.1,c and d show the examples of visual research by a modified shadowgraph method of interaction between shock waves in the flow at a Mach number of 6 in the pulse Ludwig wind tunnel. The diameter of the visualization area is about 120 mm.

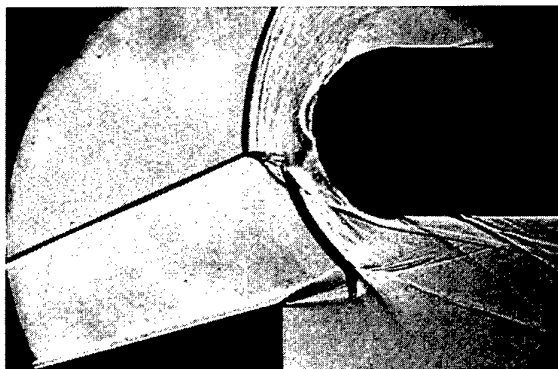
The images (c) and (d) demonstrate efficiency of sensitivity control with a modified method of visualization: the flow mode is the same, but image (c) is obtained with set-up $L \approx 150 \text{ mm}$, and (d) - $L \approx 40 \text{ mm}$. In the first case the images of shock waves are too great and overlap a small-sized flow structure. In the second variant the image of shock waves are made



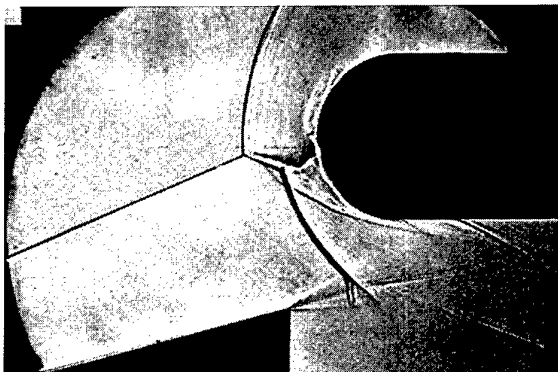
a



b



c



d

Fig.1

rather thin and the small-sized details are clearly distinct. It is necessary to note, that in this case the direct shadowgraph method cannot be applied at all,

because the minimum distance of the recording system possible location is about 400 mm - at such conditions a flow pattern is distorted unrecognizably.

A Schlieren shadowgraph method is applied for visual study of flows with a narrow range of density gradients. Its sensitivity is increased by introduction of a cutting off knife in the image plane of a light source receiving objective lens. Thus, the sensitivity is proportional to a distance, which is close to the objective lens focal length F . The majority of wind tunnels are equipped by Schlieren systems of visualization. The size of a visualization area is determined by dimensions of optical elements of Schlieren systems and, as a rule, does not exceed 400 mm. The systems of visualization with a large area are very expensive and, therefore, rare.

1.2 Raster-type Method

A raster-type method of visualization is a version of multiple-sources Schlieren method offered in 1949 by R.A.Burton. The raster-type shadowgraph system for transonic and supersonic gas flows visualization in large wind tunnels with a field up to one meter was developed in TsAGI.

The sensitivity of the raster-type method is rather low as a receiving objective lens with a focal length about $F=300$ mm is used. However it has such advantages as

- visualization of large fields without use of expensive large-dimensional optical elements;
- capability of visualization through small-sized optical windows or even through perforated walls of the wind tunnel test section;
- low cost and simplicity of realization.

Fig.2 shows the basic optical scheme of the system, and Fig.3 presents an exterior of the raster screen (a) and the receiving apparatus with a possibility to conduct video and photo registration. (b).

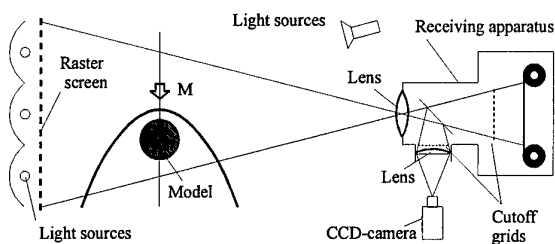
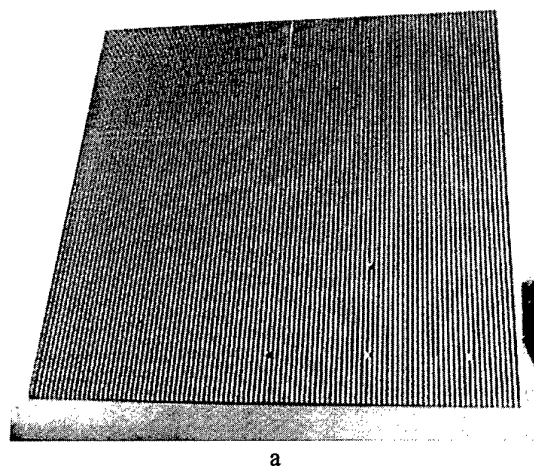
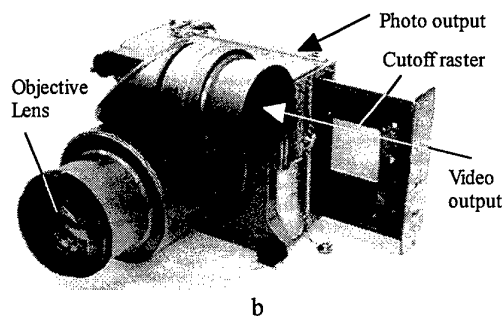


Fig.2

The system is installed inside a test section or pressure chamber. On the one side of the flow region under study, a lighting raster screen is located. It contains a set of regularly arranged light-emitting elements. In this case, the set is a number of straight strips of a 5mm width located along the whole screen with an interval of 10 mm. The raster screen can be light-transparent or light-reflecting and is illuminated by a continuous and pulse light source. On the opposite side of the flow the optical apparatus including a receiving objective lens, cutting off raster, video camera and device for photo registration are installed.



a



b

Fig.3

The cutting off raster is located in a plane optically conjugated to a raster screen plane and it is a negative image of the raster screen. The plane of the registration device is optically conjugated to the flow section under study. In an undisturbed flow all light rays from each light-emitting element of the lighting raster screen pass through the same place of the cutoff raster, undergoing identical effect from its part, and create uniformly illuminated field in the plane of observation. If there is an optical non-uniformity, the light beams, which passed the areas with a gradient of density, deviate from the initial direction and pass through other parts of the cutting off raster. This results in creation of a contrast shadow image of the flow non-uniformity in the image plane. The system provides continuous video-screen monitoring of the flow pattern and instantaneous photographic registration of selected flow regimes.

The sizes of a visualized area are limited by the sizes of the lighting raster, which are determined by a wind tunnel design. The raster-type system is in use within several years in wind tunnels TPD-1000 and T-109. The characteristic size of the visualized area is 600-700 mm with the size of the raster screen $1\text{m} \times 1\text{m}$.

Fig.4 presents the examples of visualization of external flows around aircraft models and elements (a, b), investigations of supersonic jets of jet engines (c), jet elements for control (d). Fig.4,e shows a picture obtained by the raster-type method through the perforated walls of the T-109 wind tunnel test section and demonstrates how the jet goes out from the rocket nozzle.

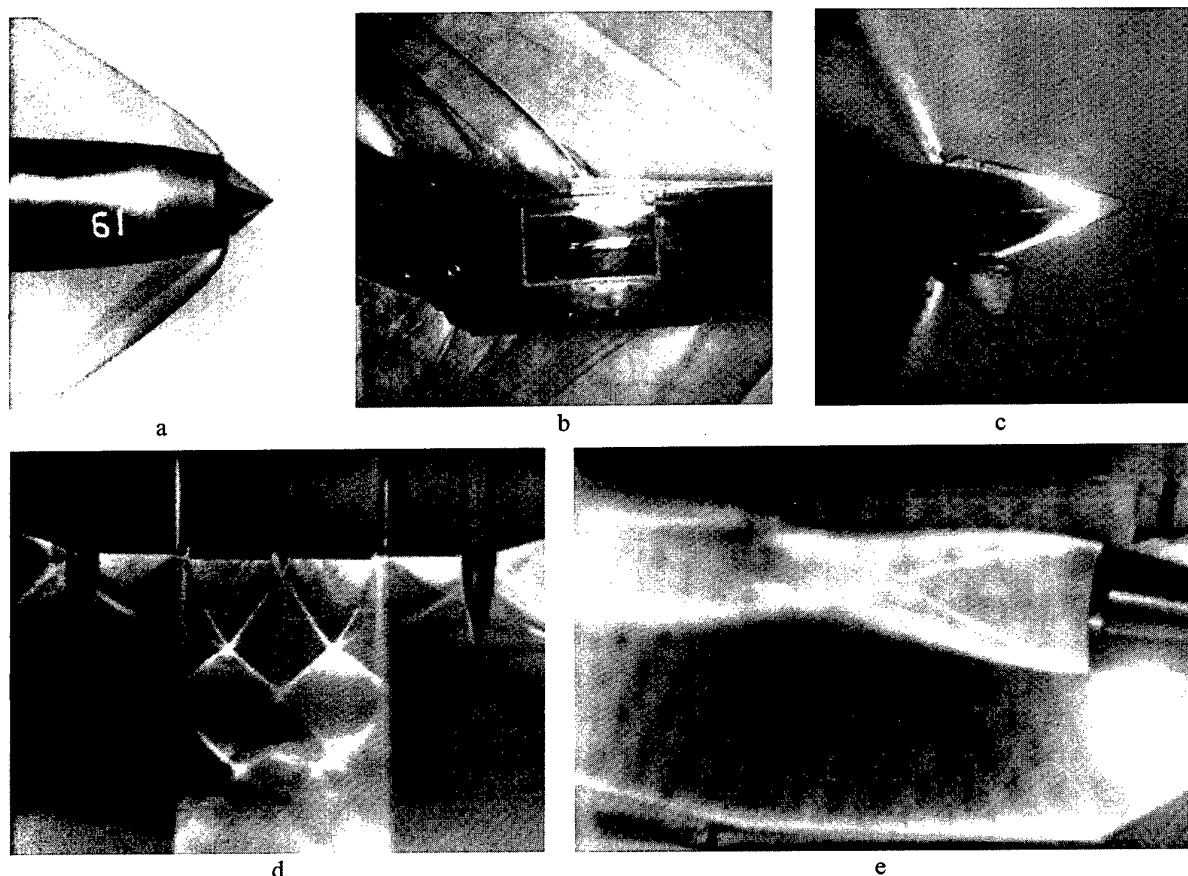


Fig.4

2. Interference and Holographic Methods

To investigate flows with small gradients of density-subsonic flows and hypersonic rarefied gas flows, the more sensitive well-known interference and holographic methods are applied. The interference methods are based on registration of distribution of a light wave phase delay φ passed path l in medium with density ρ , as a kind of an interference picture.

$$\varphi = K \cdot \rho / \lambda,$$

where λ is the wavelength of light in vacuum. The phase φ is expressed here in the numbers of wavelengths. The interference picture is formed at coherent superposition of the light wave, passed through the environment under study, with the reference, undistorted wave.

Interferometry is not only a good method of visualization, but also allows in a number of cases to receive the quantitative information on distribution of gas density in a flow. The quantitative decoding of interference pictures consists of measuring the distribution of interference fringe numbers and determination, according the indicated formula, of distribution of gas density averaged along a light beam crossing the flow. To find out local density values additional information about flow structure or symmetry is necessary.

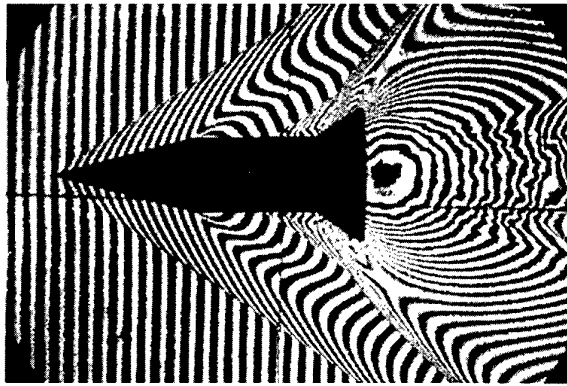
2.1 Classical Interferometry

Some wind tunnels are equipped with fixed interferometers with the classical two-beam Mach-Zehnder scheme. The examples of such interferometer using for research of the flow around a shell on a ballistic range (a) and the model of boundary layer formation with an injection of gas through a porous surface of the model into the subsonic flow (b) are shown in Fig.5.

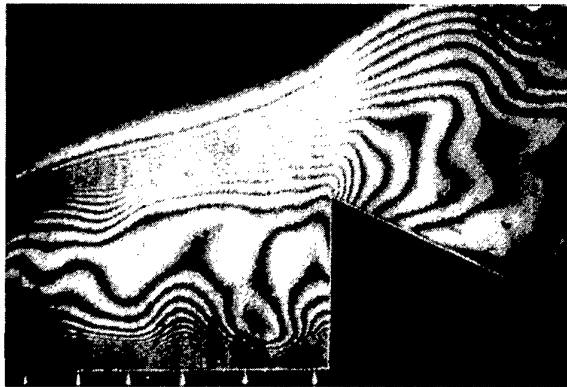
1.2 Interferometer with a Narrow Reference Beam

The interferometers based on the classical scheme are very sensitive to external influence: to mechanical vibrations, temperature oscillations and convective flows outside a wind tunnel test section. Therefore, it is more convenient to use a laser interferometer with a narrow reference beam to study flows in wind tunnels, if there are external disturbing factors. The scheme for the variant with a concave spherical reflecting mirror and a field about 300 mm is shown in Fig.6. Other variant is realized based on a standard Schlieren shadowgraph system with a visualization area of 230mm.

The advantage of laser interferometer with a narrow reference beam is that a broad measuring beam and narrow reference light beam pass approximately identical paths through the same optical elements of the interferometer and the experimental facility,



a



b

Fig.5

undergoing similarly effects of the same external influence factors. At interference of these light beams, the influence of the factors is mutually compensated.

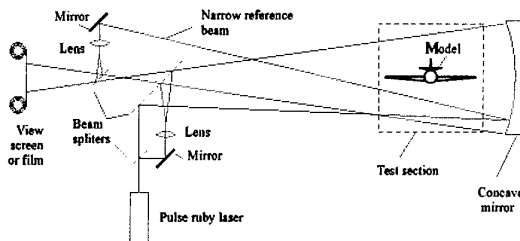


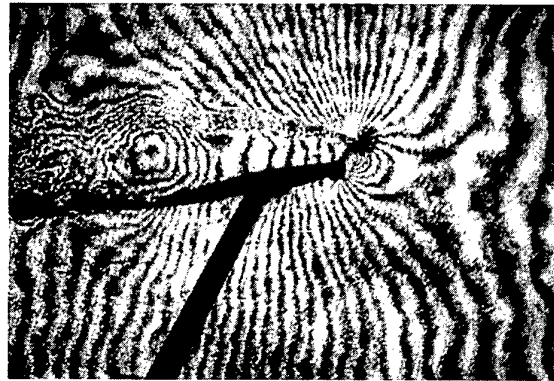
Fig.6

Fig.7 presents interference pictures, obtained with the interferometer with a spherical reflecting mirror in researches of transonic flow around a wing profile with deviating leading edge (a) and with the interferometer based on the optical Schlieren shadowgraph system - in researches of flow of supercritical wing profile (b).

1.3 Shift (Differential) Interferometry

Interference researches of flows with low and large density gradients may be conducted by means of shift (differential) interferometer. Shift interferometer means that two interfering light waves are formed by splitting of one object wave into two parts, and superposed on a photodetector with small relative transversal displacement Δr . Such interferometers are sensitive to a gas density gradient in the direction of the displacement.

Changing the displacement value Δr it is possible to vary sensitivity of the interferometer.



a



b

Fig.7

Some TsAGI's wind tunnels are equipped with fixed shift interferometers developed and manufactured in the State Optical Institute. The simplified scheme of the shift interferometer is shown in Fig.8.

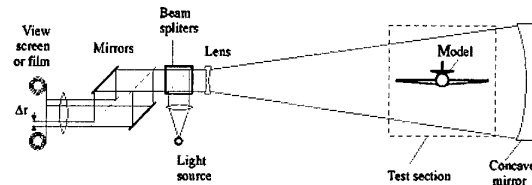


Fig.8

Flow field pictures obtained with shift interferometer having working field 400 mm are presented in Fig.9.

1.4 Holographic Interferometry

Holographic interferometry is characterized by low sensitivity to the quality of the optical components and external influence that is valid then wind tunnel design or testing environment does not permit using of the standard optical methods. Sensitivity of the holographic interferometers is the same as the double beam interferometry systems. In addition, holographic interferometry possesses significant advantage – single exposed during experiment hologram permits to rebuild and to analyze wave front after experiment. It provides possibility to obtain double beam interferogram, shift interferogram, direct shadowgraph and Schlieren pictures.

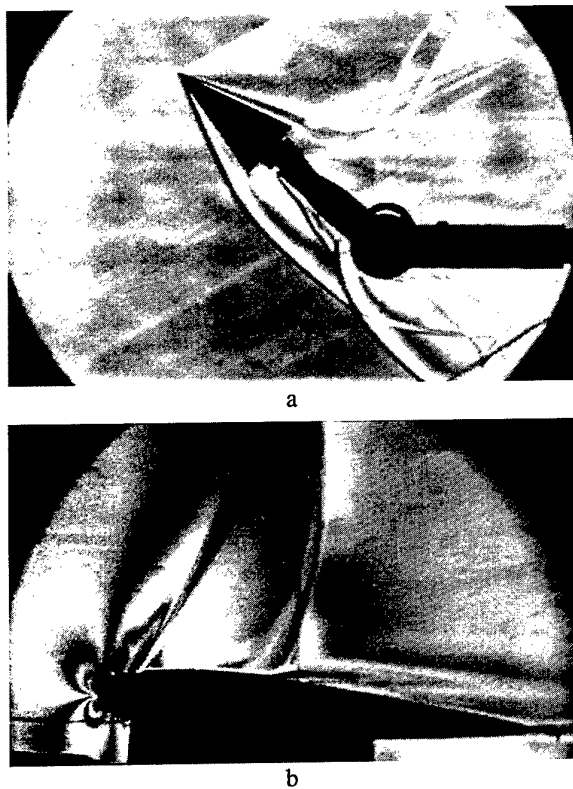


Fig.9

Double beam interferogram of the subsonic flow field around the wing profile is presented in Fig.10,a. This interferogram was obtained by double expose method. Interferogram in Fig.10,b was obtained by single expose method and demonstrates supersonic flow field around fighter model.

Using a single exposed hologram permits to use heterodyne interferometry for automatic decoding of the interference pictures. The scheme of the optical system of hologram recording in a wind tunnel is presented in Fig.11,a and scheme of the original heterodyne decoding system is shown in Fig.11,b. These optical systems are geometrically identical but in the second case the light frequency of the one from reconstructing waves is shifted on value Ω in radio frequency range. The signal having frequency Ω and a phase equaled phase of recorded light wave will arise on the output of a quadratic photoelectric detector placed in the interference field. Scanning of the total interference field and phase measuring permit to digitize the phase distribution in the object wave.

An Electro-Optical Frequency Modulator provides required frequency shifting. This modulator is based on double transverse Pockels Electro-optical effect and was developed at TsAGI. A range of the light frequency shift is from zero to 5 MHz. A voltage of the excitation signal is 90 V.

External view of the modulator is presented in Fig.12.

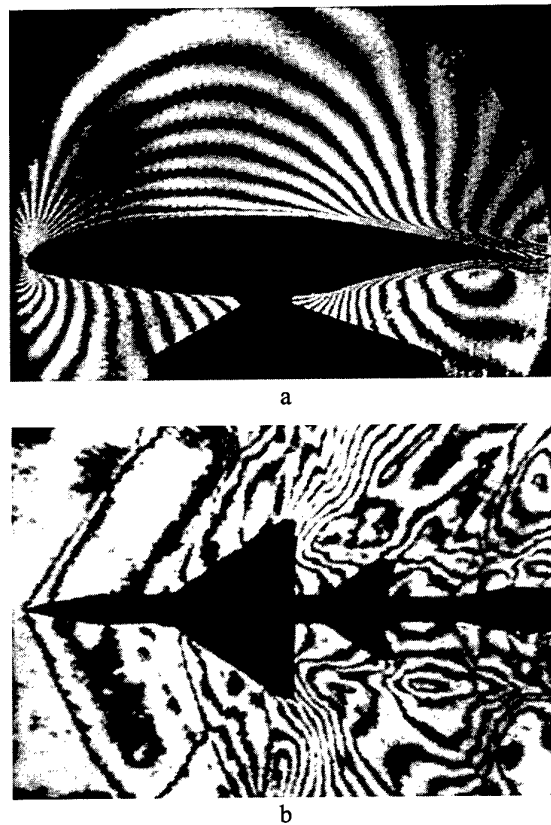


Fig.10

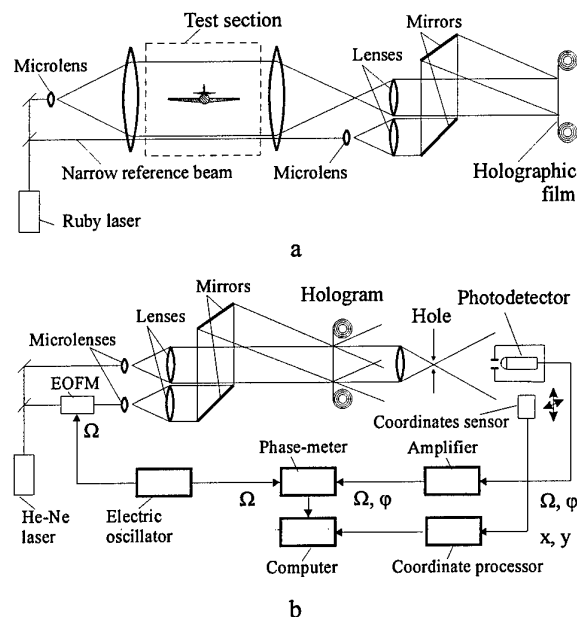


Fig.11

3. Combination of LDV and Laser-knife Methods

3.1 Laser-knife Method

The investigations of the complex 3-dimensional flow fields require non-standard optical methods. It resulted to development of new means of the flow field visualization such as Laser-knife technique.

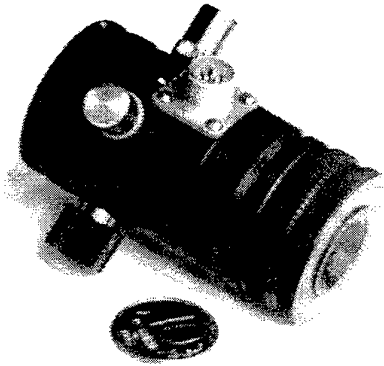


Fig.12

In this method, the flow field under study is cut by intensive laser beam expanded in a light sheet and appropriate image detector acquires light scattered by aerosol presented in the flow. Detected image represents the distribution of the aerosol concentration in the light sheet plane. Taking into account additional information about flow field phenomena this image can give information about flow particulars: vortexes, chock waves, separation zones, etc. The laser-knife method is used in TsAGI's facilities beginning from low subsonic velocities – the T-103 wind tunnel,- up to supersonic velocities – the SVS-2 and the T-33 wind tunnels. Some results of flow visualization in the T-103 wind tunnel are presented in Fig.13. These pictures show the complex vortex flow over the delta-wing model at high angle of attack.

3.2 Laser Doppler Velocimeter

Laser Doppler Velocimeter is an effective means of velocity field investigation. LDV is applied at TsAGI in the subsonic wind tunnel T-103 having flow dimensions of 2m×4m and in a set of supersonic wind tunnels having smaller tests section dimensions.

The scanning of the flow field around the model with large number of sampling point is sometimes non-effective and is accompanied by the large number of non-useful information. To optimize position of the sampling point for LDV measurements the combination of laser-knife and LDV was suggested. Laser-knife method visualized positions of the interesting flow field elements and after that the optimized grid of the sampling points for LDV was chosen.

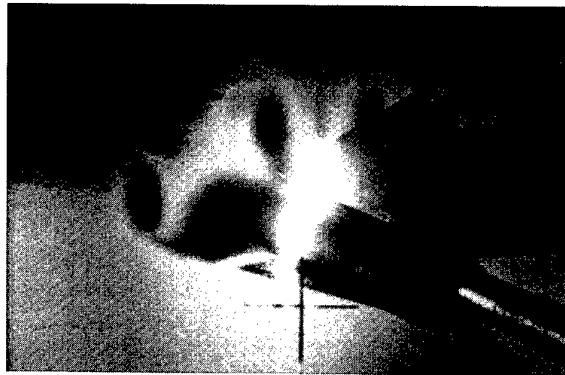
Some results of such combined investigations of the fighter model conducted in T-103 WT are presented in Fig.14. Solid lines are plotted to show positions of the vortexes and separation zones revealed by Laser-knife method.

4. Shape, Motion and Deformation Measurements

The problems of aeroelasticity require simultaneous measurements of the airframe deformation in large number of points. These problems can be easily solved by a standard non-contact photogrammetry method.



a



b

Fig.13

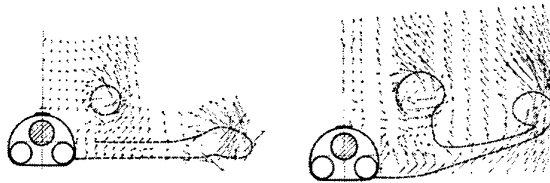


Fig.14

The contrast markers are applied on the model surface in the measurement points. The images of the model surface are registered in all spatial position in the absence of the flow and in the flow where aerodynamic forces deform or displace the model. The more labor consuming part in photogrammetry is marker recognition and its coordinate measurements on the images. This procedure is accomplished under operator control with the special systems, like stereocomparators.

The more effective application field for photogrammetry is investigation of large-scale objects having soft surface or water submerged objects. To illustrate the first application the image of the deformed envelope of the pneumatic hangar over 6m wide is presented in Fig.15. These tests were conducted in the T-101 wind tunnel.

To investigate deformations of fast rotating objects the photogrammetric system with pulse illumination and laser synch was developed. The measurements are conducted by object registering in the appropriate time events.

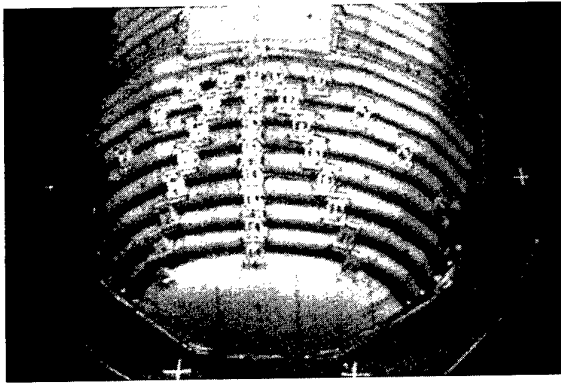
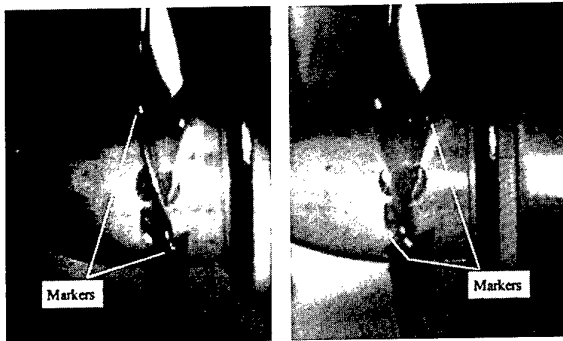


Fig. 15

The system simultaneously registers the two frames with different focus planes that are necessary to provide measurements of the objects having large dimensions along view sight (Fig. 16).



a) Focus plane on the blade tip b) Focus plane on the blade root
Fig. 16

The accuracy of the linear coordinate measurements does not exceed 0.3 - 0.5mm and angular - 6 angular minutes. Expose time is about 10μsec. The system was used for investigations of bending and twist deformation of the propeller blade of IL-114 airplane engine. Experiments were conducted in the T-104 wind tunnel.

5. Differential Interferometry Method

Differential interferometry method is perspective direction of non-contact measurements of surface deformation. Measurement volume may be created by intersection of the two collimated coherent laser beams near the surface under study (Fig. 17,a). Resulting interference field consists of layers of maximum and minimum intensity regularly distributed in space. Interference fringes which are formed along the curves of intersection this layers with test surface carry information about the surface shape. The distance Λ between interference layers is a measure of the surface points location:

$$\Lambda = \frac{\lambda}{2 \cdot \sin(\vartheta / 2)},$$

where ϑ is the angle between laser beams.

It is practically impossible to form wide collimated beams while investigation of the large size objects and

two divergent laser beams can be used to create measurement volume (Fig. 17,b).

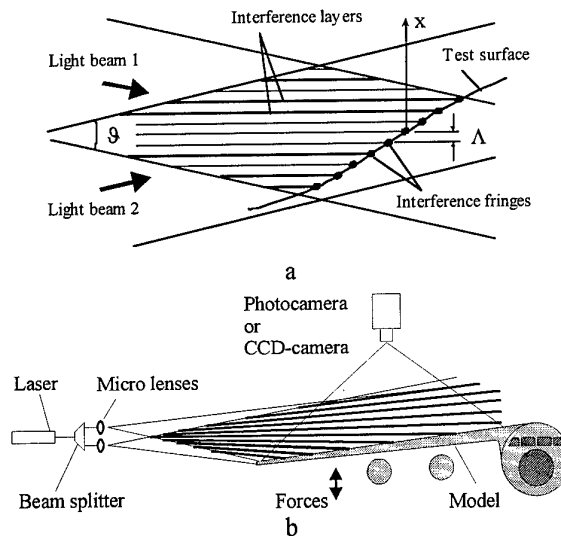


Fig. 17

In this case, intensity spatial modulation in the measurement volume will have some spatial distribution, which can be determined by additional calibration. Normal coordinates of two points on the surface belonging to adjacent interference fringes are differ by Λ - a local period of the spatial modulation in the measurement volume. Thus, enumerating of the interference fringes on the surface image give information about its shape. The samples presented in Fig. 18 illustrate such interference pictures obtained while investigation of the deformation of a passenger aircraft model (a), deformation of a wing model (b), standing waves on the surface of liquid placed in oscillating volume.

To investigate deformation two images are registered: the first in the absence of deformation and the second under deformation. The changing of the fringe number ΔN in chosen point corresponds to displacement of this point in $\Lambda \times \Delta N$ distance.

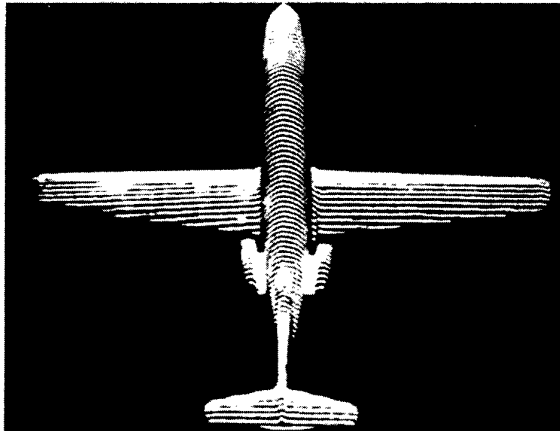
5.1 Laser Measurement System "Relief"

On the base of differential method the laser measurement system "Relief" was developed. This system was used for measurements of spatial motion and bending-twisting deformations of the helicopter blade model in the T-105 wind tunnel. Fig. 19 shows the measurement system scheme (a), experimental setup in the T-105 WT (b) and fragment of the interference fringe pattern on the blade model surface (c).

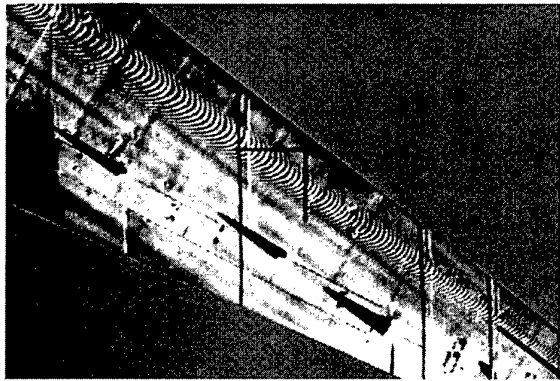
In this system the step Λ of interference field modulation varies from 0.05 to 0.5mm. The absolute error of linear displacement measurement was 0.01mm near the rotor hub and about 0.1mm near the blade tip. Measurement range was about 100mm.

The total number of the interference fringes on the image was about 200...400. Special laser heterodyne

system was developed to analyze such interference pictures characterizing by quasi-periodic structure.



a



b



c

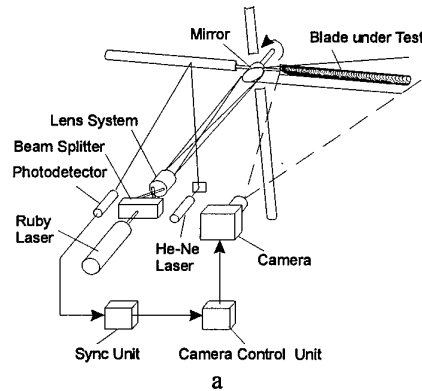
Fig.18

5.2 Visualizing of the Natural Modes of Oscillation

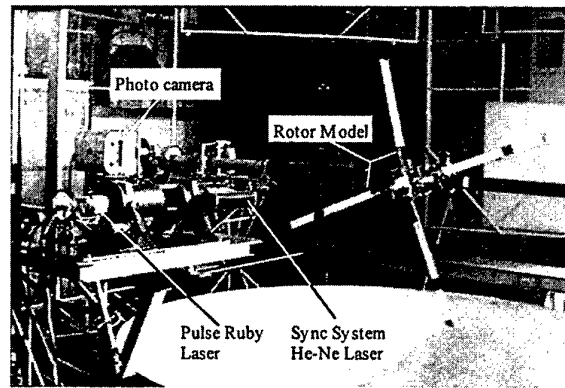
The method of differential interferometry was very effective tool for visualization of natural oscillating modes. The same interference light field illuminates oscillating surface and surface image is registered with expose time divisible by oscillating period or significantly larger then this period. As a result, the interference field is modulated by the Bessel function of a zero order

$$M = J_0\left(\frac{2\pi A}{\Lambda}\right),$$

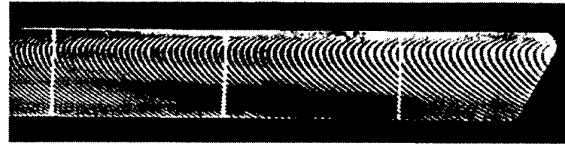
which argument is proportional to local vibration amplitude A.



a



b



c

Fig.19

To visualize oscillating modes an optical spatial filtering of the registered interference picture must be applied in accordance with scheme presented in Fig.20. Fig.21 illustrate visualizing of the natural oscillation modes of the delta wing model (a, b, c) and fragment of the fuselage skin (d, e). These images allows to obtain also the numeric data for oscillation amplitude. Fig.22 shows the amplitude distributions in two section 1 and 2 of the fuselage skin fragment in case presented in Fig.21,e.

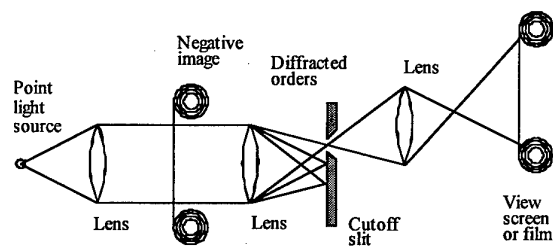


Fig.20

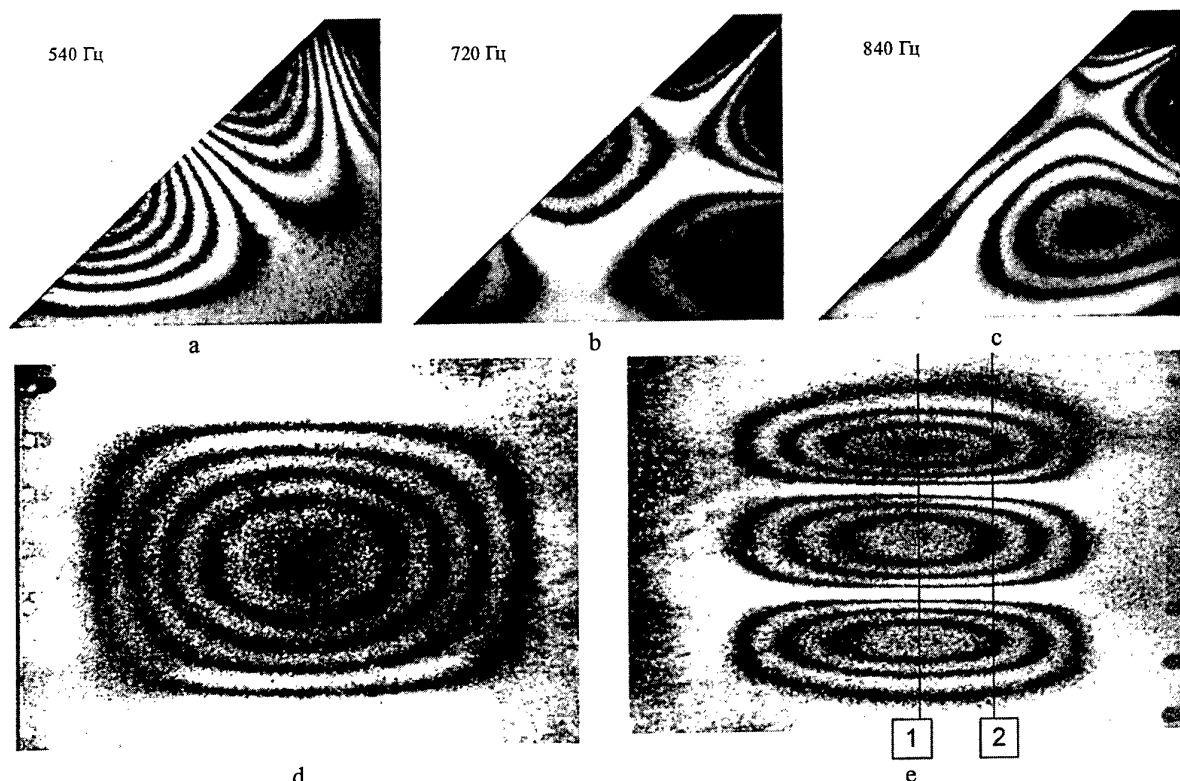


Fig.21

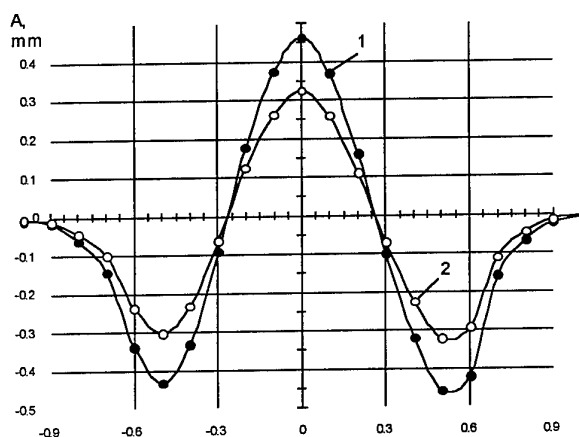


Fig.22

6. Videogrammetry Methods

Non-contact optical method of videogrammetry is very powerful tool for measurements of geometrical parameters and deformations of the objects having complex shape. This method is an improvement of the standard photogrammetry method where photographic registration is replaced by modern TV registration and digital image processing.

The essence of this method is in the rebuilding of the three-dimensional coordinates of some point on the object by two-dimensional coordinates of the point image. There are three basic means to solve the rebuilding uncertainty:

- to use two or more registration cameras observing object from different directions – the total analogy of the standard stereo photogrammetry;
- to use additional information about limitations on the object degree of freedom or about geometry of initial marker position on the object surface;
- to use the structured illumination beam. For example, it may be the laser sheet with known spatial position or the parallel light beam with known direction.

6.1 Measurements of Object Geometry

Videogrammetry method with light sheet illumination is usually applied in laboratory environments for non-contact measurements of object geometry. The scheme of such setup is presented in Fig. 23.

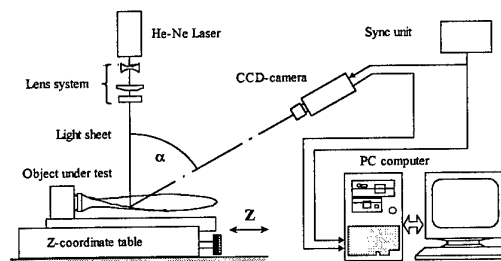


Fig.23

Results of accuracy investigation showed that mean squared deviation in 35 points on the object area having dimensions $120 \times 120 \text{ mm}^2$ were about 0.03-0.04mm. The plots in Fig.24 illustrate results of the blade cross

section measurements by the videogrammetric system (VGMS) in comparison with the results obtained by the standard 3D coordinate measurement system «Alpha».

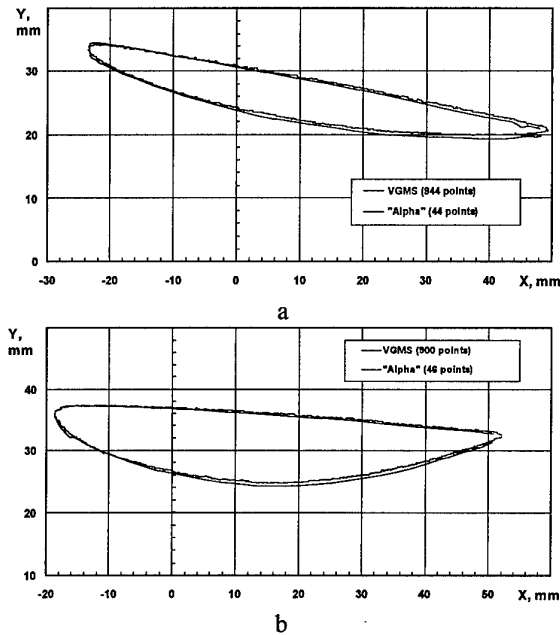


Fig.24

6.2 Railway Wheels Survey System

Videogrammetry method with cutting light sheet was successfully applied for testing of the railway wheels on the production line of one steel works. Measurement system has three videogrammetric channels. Two of them built upon the identical light sheet scheme are used for testing the backsides of the wheels and the third based on the shadowgraph scheme is used for testing of the wheel rolling surface. Measurement accuracy in the first two channels does not exceed 0.1mm and in the third channel – 0.05mm. The results of measurements of a radial wheel section are shown in Fig.25.

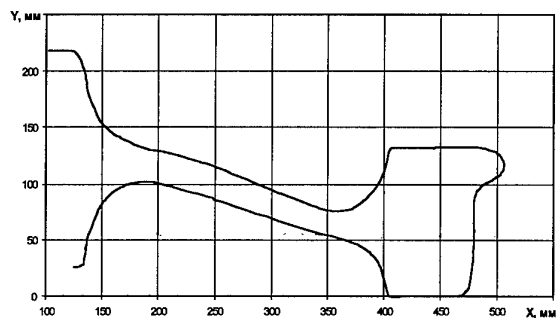


Fig.25

This system provides measurements of 6...12 radial sections per wheel revolution and has productivity about 80 wheels per hour.

6.3 Model Deformation Measurements in Wind Tunnel

Usually some additional information about model position is known during tests in a wind tunnel. This

situation exists, for example, during measurements of the model deformations in wind tunnel where it is possible to assume that displacements of each point take place in one plane. One model of the passenger aircraft was tested in the T-128 wind tunnel and wing deformations were under investigation. The markers were painted with white paint on the black model surface: two markers on the model fuselage and two marker pairs on the wing at the relative distances 0.68 and 0.99.

The plots in Fig.26 illustrate the measurement results: a) vertical displacements, b) total model attack angle, c) bending and d) twisting deformation of the wing relative fuselage all as function of the lift force.

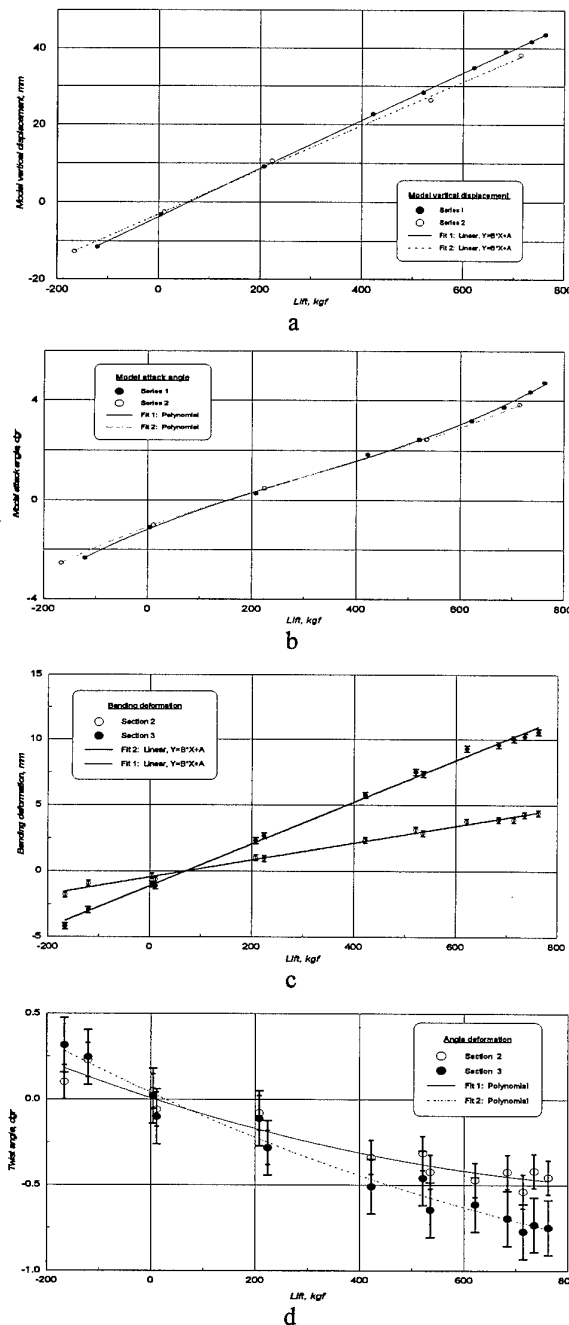
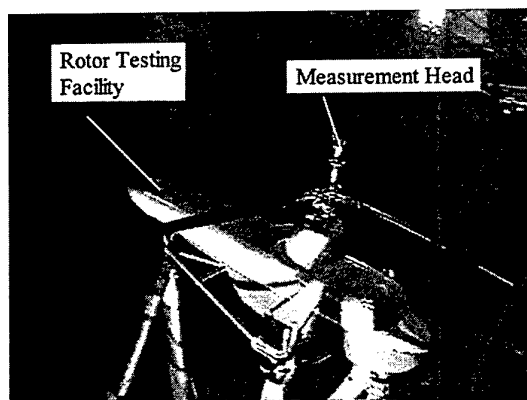


Fig.26

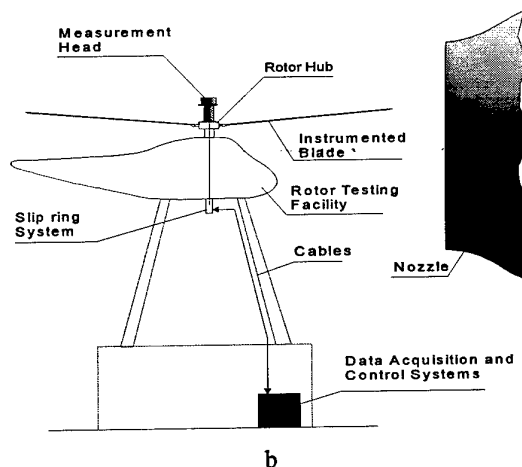
6.4 Blade Deformation Measurement System

Similar approach was used in the blade deformation measurement system (BDMS) developed for testing of the large-scale helicopter rotor system in the T-101 wind tunnel or in the hovering ring environments. The arrangement view and scheme of the measurement system is presented in Fig.27.

The system includes measurement head, image acquisition and processing unit and synch unit. A set of markers in pairs is glued on the blade surface in the required sections. There are two CCD cameras and a flash lamp with power source in the measurement head. The measurement head is placed on the rotor hub and view axis of the CCD cameras are directed on the blade with the markers. Synch unit provides control of both the CCD cameras and the flash lamp and measurement of the azimuth angle corresponding to the flash events. System provides acquisition rate up to 100 half frames per second. The error of the marker coordinate measurements reaches maximum value at the tip of the blade and for blade having radius 6.5 m is 0.6mm. The error of the blade torsion measurement for blade tip section having chord about 140mm is about $0.2^\circ - 0.25^\circ$. The plots in Fig.28 demonstrate some measurements results: a) blade flap motion and b) section installation angle as function of the azimuth angle.

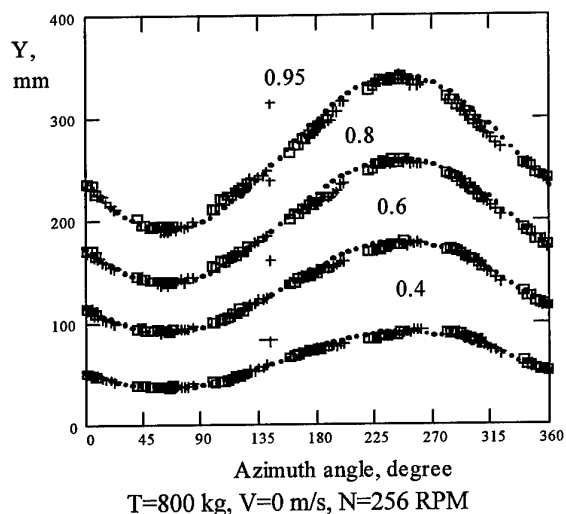


a

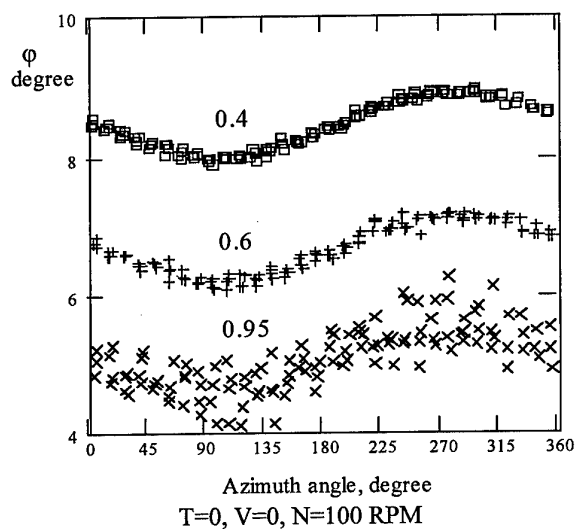


b

Fig.27



a



b

Fig.28

Conclusion

The TsAGI has accumulated the large experience in the development and application of the optical and interference measurements system. These systems are widely used in TsAGI's facilities for investigation of flow fields and model deformations under action of aerodynamic and inertia forces. The modern achievements in optics, laser technique, video technique and image processing systems are used in these systems. Accumulated experience proved validity of the optical measurements, which for many cases are irreplaceable.

Enregistrement et Traitement des Interférogrammes par Caractérisation Spectrale de la Chaîne Optique.

Desse J.M.

Office National d'Etudes et de Recherches Aérospatiales,
Institut de Mécanique des Fluides de Lille,
5, Boulevard Paul Painlevé, F-59045, Lille-Cedex, France.

1. RÉSUMÉ

L'enregistrement et le traitement des interférogrammes est grandement amélioré par la possibilité de pouvoir recréer sur un micro-ordinateur muni d'une carte de traitement d'image l'échelle des teintes expérimentales d'un interféromètre équipé d'une source blanche connue et d'un prisme de Wollaston donné. En tenant compte des caractéristiques spectrales de la source lumineuse et des trois filtres de la caméra vidéo RVB, on est capable d'exprimer analytiquement l'intensité lumineuse des franges d'interférence lorsque la différence de marche varie et de reconstituer sur le moniteur les couleurs qui vont être visualisées expérimentalement. La connaissance de l'échelle des teintes de l'interféromètre permet d'une part de piloter d'une manière optimale la position du prisme à l'enregistrement des clichés, et d'autre part de traiter les interférogrammes d'une manière automatique et avec une très grande précision.

2. INTRODUCTION

Depuis plusieurs années l'Institut de Mécanique des Fluides de Lille s'est attaché à mettre en oeuvre des techniques de visualisation basées sur l'interférométrie différentielle en lumière blanche utilisant un prisme de Wollaston <1>. Le développement et l'extension de ces méthodes ont permis d'analyser des phénomènes aérodynamiques instationnaires en obtenant avec une certaine précision des informations quantitatives sur la masse volumique ou la température <2> et <3>. Cependant cette méthode optique est limitée par deux opérations: l'enregistrement qui passe par un étalonnage des couleurs observées lorsque la différence de marche varie dans l'interféromètre et le traitement qui était effectué manuellement, par reconnaissance des teintes sur le cliché. Pour améliorer les performances de la méthode il nous a semblé utile de mettre en place un dépouillement automatisé des interférogrammes enregistrés en lumière blanche, problème peu abordé jusqu'à présent dans la littérature.

Par contre, en lumière monochromatique, plusieurs auteurs ont proposé des solutions concernant le dépouillement automatisé des interférogrammes. Bien souvent, deux types de méthodes sont utilisées. La reconnaissance et le relevé du déplacement des franges d'interférences permet à Hunter et Collins <4> d'analyser d'une manière semi-automatique les interférogrammes. Mastin et Ghiglia <5> ont cherché à déterminer le contour des franges d'interférences tandis que McKen et Tarasuk <6>, ou encore Yu <7>, se sont intéressés à la position exacte des franges. Par ailleurs, Krishnaswamy <8> a proposé récemment un algorithme assez performant pour l'identification et la reconnaissance des franges. L'analyse de l'interférogramme peut être faite également par transformée de Fourier. Takeda et al <9> ont montré l'intérêt de la méthode de transformée de Fourier pour analyser le

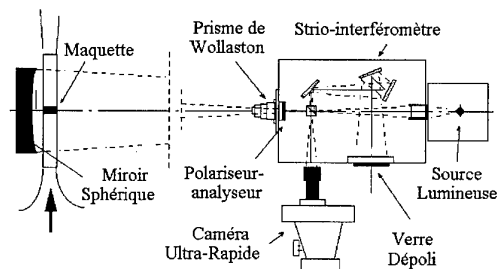
système de franges. D'autres auteurs ont également utilisé cette technique (Bone et al. <10>, Roddier et Roddier <11>) ou des techniques analogues basées sur l'approximation par les premiers termes de la série de Fourier (Mertz <12>).

Toutes ces techniques de dépouillement nécessitent en fait un traitement a posteriori de l'interférogramme, mais aucune d'entre elles n'est basée sur la caractérisation spectrale de la chaîne optique. Le but de cet article est de montrer que si on tient compte des caractéristiques spectrales de la source lumineuse (cohérente ou non) et des trois filtres de la caméra vidéo Rouge, Vert et Bleu, on peut exprimer analytiquement l'intensité lumineuse des franges d'interférence en fonction de la différence de marche. A l'aide d'une carte de traitement d'image on est alors capable de reconstituer sur un moniteur l'échelle des teintes expérimentales de l'interféromètre équipé d'une source blanche connue et d'un prisme de Wollaston donné.

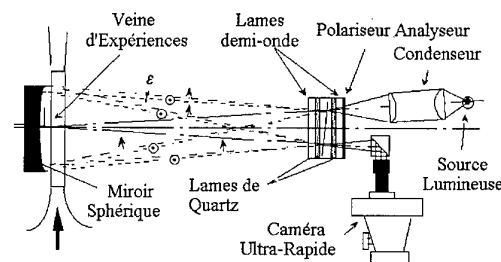
3. ENREGISTREMENT ET TRAITEMENT MANUEL DES INTERFÉROGRAMMES.

3.1 Rappel du montage optique

Le montage optique le plus souvent utilisé à l'IMFL est celui qui est présenté sur la figure 1.



Montage d'Interférométrie Différentielle



Trajet des Faisceaux Lumineux

Fig.1 Interférométrie différentielle ultra-rapide

Le principe de fonctionnement de l'interférométrie différentielle en lumière blanche utilisant un biprisme de Wollaston est détaillé dans Gontier <13>. On pourra trouver dans Desse <1> et Desse et Pegneaux <2> et <3> un bref rappel de la technique optique ainsi que les améliorations qui lui ont été apportées depuis une dizaine d'années.

La technique d'interférométrie différentielle en lumière blanche peut paraître concurrente des techniques interférentielles utilisant une source monochromatique, mais en fait, celle-ci est tout à fait complémentaire surtout lorsque les variations d'indice à mesurer deviennent très petites. De plus, le coût de mise en oeuvre est faible, comparé aux techniques utilisant les lasers. On peut voir sur la figure 1 que les principaux éléments optiques du montage se limitent à un miroir sphérique et un strio-interféromètre qui a été reconstruit et modifié récemment à l'IMFL. L'encombrement de cet ensemble très réduit permet un réglage facile et rapide. Actuellement, les limitations sont liées essentiellement à l'étalonnage et au dépouillement manuel.

3.2 Dépouillement manuel des interférogrammes.

Le dépouillement manuel des interférogrammes ne peut être fait que si on a réalisé au préalable l'étalonnage liant la position ξ du prisme aux couleurs observées dans l'interféromètre. La déviation lumineuse θ_x ou θ_y est obtenue à l'aide du raisonnement explicité ci-dessous. Si $n_e - n_o$ est la biréfringence du prisme et α l'angle de collage des prismes, l'angle de biréfringence du prisme s'écrit :

$$\epsilon = \epsilon(\lambda) = 2(n_e - n_o) \tan \alpha \quad (1)$$

car la biréfringence du prisme est une fonction de la longueur d'onde.

Si R est le rayon de courbure du miroir sphérique placé derrière la veine d'expériences, L' la distance virtuelle du milieu de la veine d'expériences au miroir sphérique, la distance dx ou dy entre les deux faisceaux qui interfèrent au niveau de la veine est égale à :

$$dx = \epsilon \cdot (R - L') \quad (2)$$

Soit ξ la position transversal du prisme, il est facile de montrer qu'en absence d'écoulement, le déplacement relatif $\xi - \xi_0$ du prisme provoque une différence de marche Δ entre les faisceaux aller et retour dans le prisme de :

$$\Delta = 2 \epsilon (\xi - \xi_0) \quad (3)$$

Si le prisme est déplacé d'une distance ζ du centre de courbure du miroir sphérique vers la veine d'expériences, des franges d'interférences apparaissent perpendiculaires à la direction x et la différence de marche Δ dépend de la coordonnée x :

$$\Delta = 2 \epsilon \left((\xi - \xi_0) + \frac{\zeta}{(R - L')} x \right) \quad (4)$$

On peut observer le résultat de cette différence de marche sur l'interféromètre par une variation de la teinte de fond uniforme lorsque $\zeta = 0$ et par des franges d'interférences lorsque $\zeta \neq 0$. Les teintes qui apparaissent sont voisines de celles trouvées dans l'échelle des teintes de Newton.

En fonctionnement, un rayon lumineux traversant le corps à analyser est dévié d'un angle θ_x ou θ_y . Cet angle est :

$$\theta_x = dE / dx \text{ ou } \theta_y = dE / dy \quad (5)$$

Comme le système optique est à double traversée de la veine

d'expériences, la différence de marche δ produite par le corps observé s'écrit :

$$\delta = 2 dE \quad (6)$$

A l'aide des relations (2) et (5) on a :

$$\delta = 2 \epsilon (R - L') \theta_x \quad (7)$$

Les différences de marche δ et Δ sont égales si la teinte observée en fonctionnement est celle qui est observée par un déplacement du biprisme au repos. Dans ces conditions, les relations (3) et (7) donnent :

$$2 \epsilon (R - L') \theta_x = 2 \epsilon (\xi - \xi_0) \quad (8)$$

et la déviation lumineuse s'exprime par :

$$\theta_x = (\xi - \xi_0) / (R - L') \quad (9)$$

On voit que la déviation lumineuse est obtenue simplement par la mesure de deux longueurs : le déplacement du biprisme $\xi - \xi_0$ et le rayon de courbure du miroir sphérique R . Pour obtenir la courbe d'étalonnage du montage optique, il suffit de déplacer progressivement le prisme et de relever la teinte sur l'interféromètre.

Pour dépouiller l'interférogramme on part d'une position où la teinte de fond est uniforme et où la masse volumique est connue et, en se déplaçant normalement aux franges d'interférences, on relève la position des teintes observées. La courbe d'étalonnage obtenue par la relation (9) permet d'obtenir en chaque point la déviation lumineuse. L'épaisseur optique E est obtenue par intégration de la déviation lumineuse :

$$E - E_0 = \int \theta_x dx \quad (10)$$

Si la masse volumique ρ_0 est connue en un point du champ, la relation de Gladstone-Dale permet d'obtenir l'indice de réfraction en ce point :

$$n_0 - 1 = K \cdot \rho_0 / \rho_s \quad (11)$$

où K est la constante de Gladstone-Dale (296.10^{-6}) et ρ_s la masse volumique calculée dans les conditions standard (1 atmosphère et 273 K).

Si e est la largeur de la veine d'expériences, l'épaisseur optique E_0 est donnée par :

$$E_0 = (n_0 - 1) \cdot e = K \cdot e \cdot \rho_0 / \rho_s \quad (12)$$

Comme l'épaisseur optique est proportionnelle à la masse volumique du gaz, on a :

$$(E - E_0) / E_0 = (\rho - \rho_0) / \rho_0 \quad (13)$$

d'où :

$$\rho / \rho_0 = (E - E_0) / E_0 + 1 \quad (14)$$

Dans la relation (14), E_0 est donné par (12) et $E - E_0$ par (10).

4. MODÉLISATION DES FRANGES D'INTERFÉRENCES.

4.1 Construction du modèle.

Dans le cas de l'enregistrement et du traitement automatisé des interférogrammes, l'approche du problème est tout à fait différente car elle est fondée sur la caractérisation spectrale de toute la chaîne interférométrique, le but étant de recréer sur un micro-ordinateur muni d'une carte de traitement d'image l'échelle des teintes expérimentales de l'interféromètre. Pour cela nous allons montrer qu'il suffit de faire l'analyse spectrale de la source lumineuse et de prendre en compte les fonctions de transfert de l'optique liée à l'interféromètre et des trois filtres rouge (R), vert (V) et bleu (B) de la caméra utilisée pour la numérisation de l'interférogramme. Plusieurs configurations peuvent se présenter à l'enregistrement ou à la restitution des interférogrammes. A l'enregistrement, l'interférogramme peut être soit directement numérisé, soit enregistré sur un film photographique et numérisé en temps

différé. A la restitution, la procédure de numérisation du cliché impose d'éclairer l'interférogramme avec la source lumineuse qui a servi à l'enregistrement, mais dans certains cas les sources lumineuses peuvent être différentes. Par exemple, si une étincelle sert de source lumineuse et si à la restitution, la numérisation est effectuée à l'aide d'une source lumineuse continue.

4.2 Numérisation directe de l'interférogramme.

Pour construire les couleurs des franges d'interférences il faut connaître le spectre de la source utilisée dans l'interféromètre, la fonction d'atténuation des optiques internes au strio-interféromètre et également les fonctions de transfert des trois filtres R V B de la caméra vidéo. La figure 2 donne un exemple.

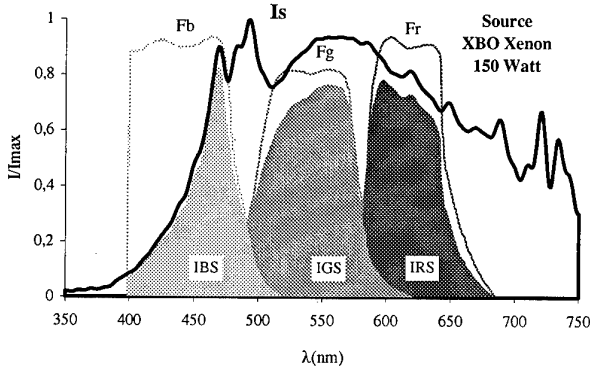


Fig.2 Numérisation directe : Source Xénon et filtres de la caméra vidéo Sony 325P

Le spectre d'une source Xénon XBO de 150 Watts a été enregistré à la sortie de l'interféromètre lorsque le biprisme de Wollaston est placé rigoureusement au centre de courbure du miroir sphérique et sans écoulement. Ainsi, aucune différence de marche n'est créée et seul l'effet des optiques internes à l'interféromètre est pris en compte. L'analyse spectrale de la source lumineuse est réalisée à l'aide d'un monochromateur couplé à un photomultiplicateur. Les trois courbes en cloche représentent les fonctions de transfert des trois filtres internes de la caméra vidéo qui est utilisée soit pour filmer les franges expérimentales, soit pour la numérisation de l'interférogramme à la restitution. La caméra vidéo est une SONY 325P possédant des sorties R V B séparées dont les fonctions de transfert des trois filtres $F_r(\lambda)$, $F_v(\lambda)$ et $F_b(\lambda)$ ont été fournies par les constructeur. Sur la figure 2, on a superposé aux trois courbes en cloche l'intensité spectrale $I_s(\lambda)$ de la source et on a calculé et tracé les intensités spectrales $I_{RS}(\lambda)$, $I_{VS}(\lambda)$ et $I_{BS}(\lambda)$ au travers des trois filtres à l'aide des relations suivantes:

$$\begin{aligned} I_{RS}(\lambda) &= I_s(\lambda) \cdot F_r(\lambda) \\ I_{VS}(\lambda) &= I_s(\lambda) \cdot F_v(\lambda) \\ I_{BS}(\lambda) &= I_s(\lambda) \cdot F_b(\lambda) \end{aligned} \quad (15)$$

Ceci revient à éclairer la veine d'expériences avec trois sources lumineuses de spectre connu et décalé dans l'échelle des longueurs d'ondes. En lumière monochromatique de longueur d'onde λ_0 , l'intensité lumineuse des franges d'interférences s'écrit:

$$I(\delta) = 4 I_0 \cos^2(\pi \delta / \lambda_0) \quad (16)$$

si les vibrations qui interfèrent ont la même amplitude. Dans ce cas précis, la différence de marche δ est indépendante de la longueur d'onde λ_0 et, à l'aide de la relation (4), on a:

$$I(x, \xi, \zeta) = 4 I_0 \cos^2(2 \pi \epsilon(\lambda_0) \frac{(\xi - \xi_0) + \frac{\zeta}{(R-L')} x}{\lambda_0}) \quad (17)$$

Nous pouvons étendre la relation (16) aux interférences en lumière blanche. L'intensité lumineuse I_0 qui était constante est remplacée par $I_s(\lambda)$ et l'angle de biréfringence devient une fonction de la longueur d'onde. L'intensité résultante est donc calculée par l'intégrale suivante:

$$I(x, \xi, \zeta) =$$

$$4 \int_{\lambda=0.4}^{\lambda=0.8} I_s(\lambda) \cos^2(2 \pi \epsilon(\lambda) x \frac{(\xi - \xi_0) + \frac{\zeta}{(R-L')} x}{\lambda}) d\lambda \quad (18)$$

Comme ϵ varie avec la longueur d'onde, on prend pour chaque triplet (x, ξ, ζ) une différence de marche δ en utilisant une valeur de ϵ calculée pour une longueur d'onde moyenne $\lambda_0(\lambda_0 = 560 \text{ nm})$:

$$\delta = 2 \epsilon(\lambda_0) \left((\xi - \xi_0) + \frac{\zeta}{(R-L')} x \right)$$

$$I(\delta) = 4 \int_{\lambda=0.4}^{\lambda=0.8} I_s(\lambda) \cos^2\left(\frac{\pi \delta}{\lambda} \frac{\epsilon(\lambda)}{\epsilon(\lambda_0)}\right) d\lambda \quad (19)$$

Pour calculer l'intensité des franges d'interférences sur les voies rouge, verte et bleue, on applique la relation (19) avec les trois sources construites à partir de la relation (15), ce qui donne:

$$\begin{aligned} I_R(\delta) &= 4 \cdot \int I_{RS}(\lambda) \cdot \cos^2(2 \cdot \pi \cdot \delta \cdot \epsilon(\lambda) / \lambda \cdot \epsilon(\lambda_0)) \cdot d\lambda \\ I_V(\delta) &= 4 \cdot \int I_{VS}(\lambda) \cdot \cos^2(2 \cdot \pi \cdot \delta \cdot \epsilon(\lambda) / \lambda \cdot \epsilon(\lambda_0)) \cdot d\lambda \\ I_B(\delta) &= 4 \cdot \int I_{BS}(\lambda) \cdot \cos^2(2 \cdot \pi \cdot \delta \cdot \epsilon(\lambda) / \lambda \cdot \epsilon(\lambda_0)) \cdot d\lambda \end{aligned} \quad (20)$$

Le résultat est envoyé sur les entrées R V B de la carte de traitement d'image. La carte utilisée est une MATROX MVP 512x512 pixels qui permet de visualiser chaque voie indépendamment en niveau de gris, ou l'image en couleur par superposition des trois plans R V B. Dans ce cas l'intensité totale est donnée par:

$$I_T(\delta) = I_R(\delta) + I_V(\delta) + I_B(\delta) \quad (21)$$

Pour pouvoir comparer dans la même échelle les intensités des franges calculées aux intensités des franges expérimentales, le prisme de Wollaston est positionné aux valeurs ξ et ζ utilisés dans le modèle. Les seuils des minima R_{min} , V_{min} et B_{min} et des maxima R_{max} , V_{max} et B_{max} des franges expérimentales sont donnés par l'intensité de la frange blanche et par l'intensité de la frange la plus sombre du premier ordre. Les intensités envoyées aux entrées R, V et B s'écrivent donc:

$$\begin{aligned} I_{mr}(\delta) &= R_{min} + (R_{max} - R_{min}) \cdot I_R(\delta) / \|I_R(\delta)\| \\ I_{mv}(\delta) &= V_{min} + (V_{max} - V_{min}) \cdot I_V(\delta) / \|I_V(\delta)\| \\ I_{mb}(\delta) &= B_{min} + (B_{max} - B_{min}) \cdot I_B(\delta) / \|I_B(\delta)\| \end{aligned} \quad (22)$$

avec $\|I(\delta)\| = \max(I(\delta))$
La figure 3 présente la comparaison entre les franges expérimentales et les franges construites à partir du modèle.

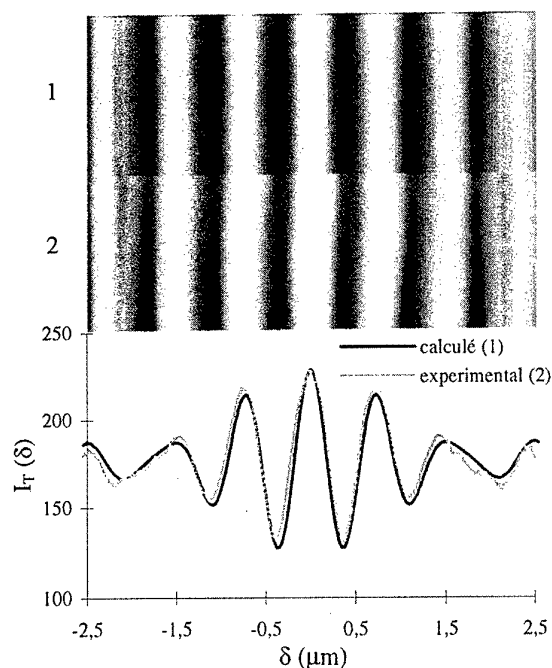


Fig.3 Comparaison entre les couleurs des franges et les intensités lumineuses (numérisation directe)

On peut voir que les caractéristiques de luminance (intensité lumineuse d'excitation visuelle) et de chrominance (couleur d'un point de vue qualitatif) sont étonnamment bien reproduites. Ceci montre que si on a tenu compte de toutes les caractéristiques spectrales de la chaîne optique, on est capable de reproduire numériquement les teintes d'un interféromètre lorsque la différence de marche varie.

4.3 Enregistrement de l'interférogramme sur un film photographique.

Bien souvent, les interférogrammes sont enregistrés sur un film photographique et, dans ce cas, la réponse spectrale du film doit être prise en compte. Pour cela, nous avons adopté la procédure suivante: en absence d'écoulement, on place le biprisme de Wollaston au centre de courbure du miroir sphérique et on enregistre un interférogramme en teinte de fond blanche uniforme (polariseur et analyseur parallèle) dans des conditions identiques à celles des essais. Après développement de l'interférogramme, on éclaire celui-ci avec la même source lumineuse et on effectue l'analyse spectrale de la teinte blanche et uniforme enregistrée sur le film. L'allure spectrale de la source lumineuse est donc atténuée par la réponse spectrale du film. Pour éviter les problèmes liés au développement du film, l'interférogramme en teinte de fond uniforme et l'interférogramme de mesure sont développés au même instant et dans les mêmes bains.

Cette fois les fonctions de transfert RVB de la caméra vidéo interviennent à la restitution pendant la numérisation de l'interférogramme de mesure et on applique le processus de comparaison des franges décrit au 4.2. La figure 4 montre le spectre et les trois sources lumineuses obtenus par les filtres de la caméra.

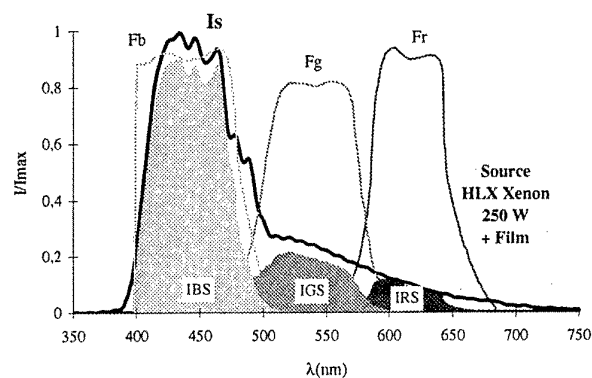


Fig.4 Spectre d'un interférogramme enregistré en teinte de fond uniforme

Un interférogramme enregistré en franges resserrées permet d'une part d'obtenir les valeurs des minima et des maxima et d'autre part d'effectuer la comparaison entre les franges calculées et les franges expérimentales (figure 5).

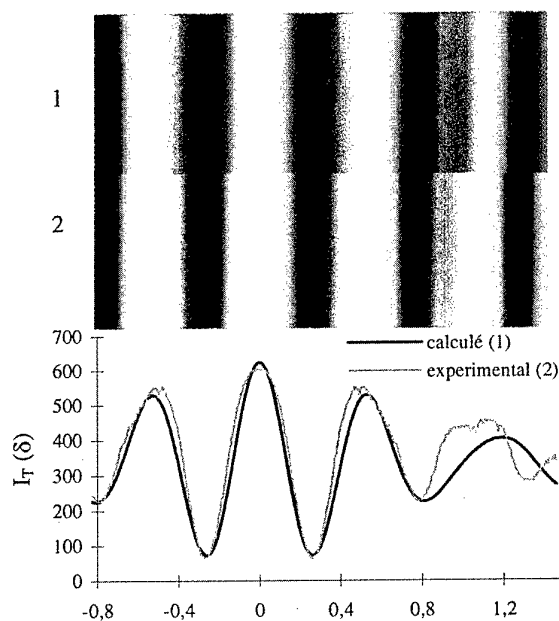


Fig.5 Comparaison entre les couleurs des franges et les intensités lumineuses (enregistrement sur film)

On peut remarquer quelques légères différences de chromaticité entre les ordres d'interférences élevés. Néanmoins, la position des franges et des ordres d'interférences est la même, ce qui permet d'appliquer l'échelle de la différence de marche théorique aux teintes expérimentales. Il n'est donc plus nécessaire d'effectuer à l'enregistrement des clichés un étalonnage de la chaîne interférométrique.

5. ENREGISTREMENT ET TRAITEMENT ASSISTÉS DES INTERFÉROGRAMMES.

La bonne correspondance entre les franges théoriques et expérimentales permet d'assister l'opérateur pour régler à l'enregistrement l'interféromètre en teinte de fond uniforme.

En effet, le réglage est facilité car il s'appuie sur un pilotage "deux axes" du système biréfringent. Pendant les essais la caméra enregistre les interférences en franges resserrées et envoie le signal d'intensité lumineuse des franges à un micro-ordinateur qui les compare aux franges théoriques. Cette comparaison permet de calculer les coordonnées spatiales du biprisme par rapport au centre C du rayon de courbure du miroir sphérique pour le positionner automatiquement en ce point C. Une palette constituée par les teintes de fond expérimentales est enregistrée automatiquement par un déplacement progressif et automatiquement de 30 millimicrons, ce qui permet de choisir la couleur de la teinte de fond pour l'enregistrement de l'interférogramme. La figure 6 montre un synoptique de la chaîne de mesure à l'enregistrement et à la restitution.

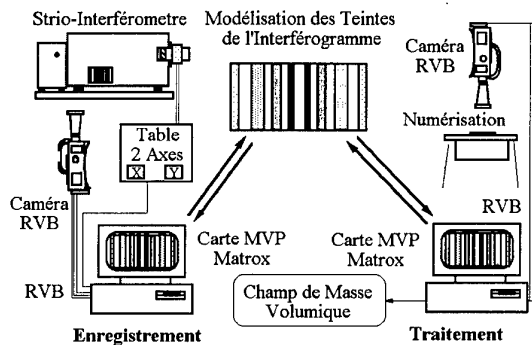


Fig.6 Chaîne de mesure à l'enregistrement et au traitement des interférogrammes

Pour le traitement des interférogrammes, le logiciel permet de choisir une fenêtre de dépouillement, le sens du dépouillement (normalement à la position des franges d'interférences) et le pas entre deux lignes de dépouillement. Avec le logiciel, on analyse les pixels de chaque ligne de dépouillement en effectuant pour chaque pixel une recherche de la teinte du pixel dans la palette des couleurs expérimentales. Lorsque la couleur est trouvée dans la palette, le pixel analysé est affiché sur le moniteur avec cette couleur. Lorsqu'on dépouille un point de l'obstacle, la couleur est affichée en rouge. Lorsqu'on ne trouve pas de correspondance, le pixel est affiché en noir. A l'aide de la correspondance entre les palettes numériques et expérimentales, on sait qu'à une couleur correspond à une différence de marche. Celle-ci est également affichée sur le moniteur. Pour chaque abscisse dépouillée on obtient une courbe liant la différence de marche à l'ordonnée. L'épaisseur optique est obtenue par intégration et la masse volumique par la relation de Gladstone-Dale. La figure 7 montre une illustration du dépouillement pour un écoulement instationnaire bidimensionnel en aval d'un culot circulaire. La hauteur du culot est $D=15\text{mm}$, la largeur de la veine d'expériences 42mm et le nombre de Mach au décollement est fixé à 0.4 . Les interférogrammes sont enregistrés à une cadence de $20\,000$ images/s et le temps de pose de chaque cliché est de $1.5\,\mu\text{s}$. Le dédoublement entre les deux faisceaux qui interfèrent est vertical et la teinte de fond est uniforme. L'interférogramme de l'écoulement moyen présenté en haut de la figure 7 permet de visualiser la longueur du domaine de recirculation (environ $1.5D$). Les interférogrammes ultra-rapides ont été enregistrés suivant la technique décrite par Desse <1> et le dépouillement de plusieurs interférogrammes successifs permet d'obtenir la reconstruction du champ de

masse volumique et l'évolution du champ dans le temps. La masse volumique est rapportée à la masse volumique à l'extérieur du sillage (ρ_e).

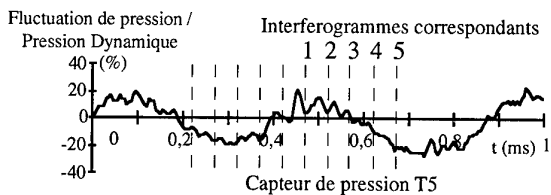
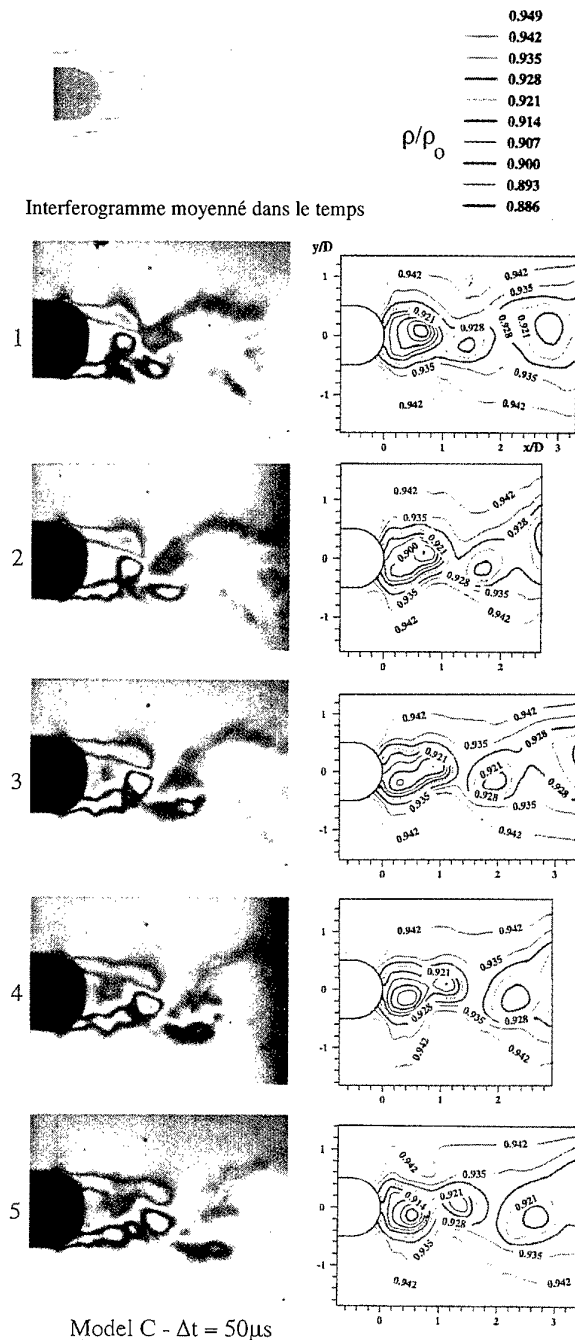


Fig.7 Interférogrammes ultra-rapides synchronisés avec la pression instationnaire

Les champs de densité présentés en vis-à-vis des interférogrammes montrent que les tourbillons sont représentés par des anneaux concentriques où la masse volumique décroît en son centre. Ces tourbillons passent d'une phase de formation où la masse volumique diminue au centre à une phase de dissipation où la masse volumique et la taille du tourbillon augmente. Par exemple, le premier tourbillon émis dans l'allée inférieure est dans une phase de formation sur les photos 3 à 5 car la courbe iso-densité ρ/ρ_e passe de 0.907 à 0.886 au centre du tourbillon et le premier tourbillon de l'allée supérieure est dans une phase de dissipation sur les photos 1 à 5 car ρ/ρ_e passe de 0.886 à 0.921.

Un signal de pression instationnaire fourni par un capteur situé à l'azimut 80° (0° sur l'axe) a été enregistré simultanément avec les interférogrammes ultra-rapides dans le but de synchroniser les mesures de pression instationnaire au bord de fuite de la maquette et les champs de masse volumique. Ce signal de pression et les interférogrammes correspondants sont présentés dans le bas de la figure 7.

6. CONCLUSION

Si les caractéristiques spectrales de la source lumineuse et des trois filtres de la caméra vidéo RVB sont correctement déterminées, on est capable d'exprimer analytiquement l'intensité lumineuse des franges d'interférence lorsque la différence de marche varie et de reconstituer sur le moniteur les couleurs qui sont visualisées expérimentalement par l'interférogramme. La connaissance de l'échelle des teintes de l'interféromètre permet d'une part de piloter d'une manière optimale la position du prisme à l'enregistrement des clichés, et d'autre part de traiter les interférogrammes d'une manière automatique. Le dépouillement est très précis car on obtient une fonction continue de la variation d'indice en tout point du champ d'observation. Cette technique de dépouillement a été testée avec succès pour l'analyser l'écoulement instationnaire en aval d'un culot circulaire.

7. RÉFÉRENCES:

- Desse, J.M. "Instantaneous density measurement in two dimensional gas flow by high speed differential interferometry", *Exp Fluids* 9, 1990, pp 85-91.
- Desse J.C.; Pegneaux J.C. "Whole-field measurement of gas density from simultaneously recorded interferograms", *Exp Fluids* 12, 1991, pp 1-9.
- Desse J.C.; Pegneaux J.C. "Direct measurement of the field density using high speed differential interferometry", *Exp Fluids* 15, 1993, pp 452-458.
- Hunter, J.C.; Collins, M.W. "The semi-automatic analysis of compressible flow interferograms", *Meas. Sci. Tech.*, 1, 1990, pp 238-246.
- Mastin, G.A.; Ghiglia, D.C. "Digital extraction of interference fringe contours", *Ap. Optics*, 24, n 12, 1985, p 1727.
- McKeen, W.J.; Tarasuk, J.D. "Accurate method for locating fringes on an interferogram", *Rev. Sci. Instrum.*, 52(8), 1981, p 1223.
- Yu, Q. "Spin filtering processes and automatic extraction of fringe centerlines in digital interferometric patterns. *Ap. Optics*, 27, n 18, 1988, p 3782.
- Krishnaswamy, S. "Algorithm for computer tracing of interference fringe", *Ap. Optics*, 30, n 13, 1991, p 1624.
- Takeda, M.; Ina, H.; Kobayashi, S. "Fourier-transform method of fringe-pattern analysis for computer-based topography and interferometry", *J. Opt. Soc. Am.*, 72, n 1, 1982, p 156.
- Bone, D.J.; Bachor, H.A.; Sanderman, R. J. "Fringe-pattern analysis using 2D Fourier transform", *Ap. Optics* 25, n 10, 1986, p 1653.
- Roddier, C.; Roddier, F. "Interferogram analysis using Fourier transform techniques", *Ap. Optics*, 26, n 9, 1987, p 1668.
- Mertz, J. "Real-time fringe-pattern analysis", *Ap. Optics*, 22, n 10, 1983, pp 1535-1539.
- Gontier, G. "Contribution à l'étude d'interférométrie différentielle à biprisme de Wollaston", *Pub. Sci. et Tech. du Ministère de l'air*, 1957, n 338.

ADVANCES IN AERODYNAMIC HOLOGRAPHY

James D. Trolinger, James Millerd, David Weber, and Michael Brown
MetroLaser
18006 Skypark Circle #108
Irvine, CA, 92714
USA

SUMMARY

Researchers continue to find new ways to employ holography to measure aerodynamic parameters in almost all flow regimes. Since holography provides a method to store optical wavefronts in such a fashion as to allow their reconstruction and analysis at a later time, it is a natural intermediate step for many conventional optical diagnostic procedures that employ interferometry, schlieren, deflectometry, particle image velocimetry, and three-dimensional visualization.^{1,2} For example, optical wavefronts representing one condition of a flow can be interfered directly with those representing a second condition, simply by storing the wavefronts holographically, providing at the same time a simple mechanism to subtract out all non varying conditions (such as optical defects). The result is a powerful method for the study of turbulent flow.

These procedures have now been in use for many years and are reaching maturity, but the field is by no means stagnant. More recently, holographic techniques have been extended to include multiple wavelength recording holography at a wavelength tuned to include a resonance of a constituent in the flow, real-time holography (four wave mixing), and recording in photorefractive materials, SLM's, and CCD's. Also, new ways of using holograms to record, reconstruct and produce unique wavefronts for measurement have evolved. For example, holograms can be placed directly on a model surface to aid in measurement (optically smart surfaces).

In resonance interferometry, sensitivity is enhanced by tuning the light to the resonance line of a substance, exploiting the large refractive index change caused by anomalous dispersion at resonance. Holography enhances this unique form of interferometry by allowing useful interference between two beams (of different wavelength) that pass through exactly the same paths at the same time. This further allows interferograms to be recorded in photorefractive materials in such a way that a cine-

holographic interferometry movie of the selected substance in the field of interest can be recorded.

Four wave mixing (sometimes called real-time holography) provides a unique way to measure temperature in high pressure flows, where other optical methods usually fail.

This paper will describe the principles behind holographic flow diagnostics with emphasis on the more recently developed methods, and will consider the future potential of holographic diagnostics in aerodynamics.

LIST OF SYMBOLS

(O)	Object waves
(R)	Reference waves
I	Light intensity
A	Constant bias
B	Modulation amplitude
ϕ	Equivalence ratios
θ	Arbitrary phase term
I_i	Intensity of i^{th} value
$\Delta\lambda$	Difference between the two wavelengths
λ	Average wavelength
λ_s	Synthetic wavelength,
(D ₂)	Strong potassium doublet absorption features
N_{max}	Maximum number density
μ_m	Micrometers
C_s	Sonic velocity
R	Gas constant
T	Temperature
γ	Heat capacity ratio
M	Molecular mass of the gas mixture
f_B	Frequency
n	Thermal or electrostrictive signals, respectively
Λ	Parameter set by design
OPD	Optical path difference

1. HOLOGRAPHIC INTERFEROMETRY

Because holograms store optical wavefronts in such a fashion that they can be reconstructed for later analysis, they provide a tremendous enhancement to

interferometry, enabling many types of measurements that cannot be otherwise achieved. Consequently holographic interferometry has led to many new types of measurements.^{3,4,5} Most types of interferometry⁶ quantify and compare wavefronts by combining a spherical or collimated reference wavefront with the data wavefront to produce interference fringes (the interferogram) that can be interpreted in terms of the phase of the wavefront. The data wavefront is produced by passing light through a field of interest or reflecting it from a surface to pick up phase information that depicts changes in refractive index or some movement of the surface. Measures must be taken to ensure that all optical components and windows are of extremely high quality and free of contaminants to prevent the introduction of phase changes that are not interpretable. Imperfections in the path of either the reference or object waves introduce phase modulations that show up as unwanted fringes or fringe modulations in the interferogram that at best are an annoyance and at worst can confuse or obscure legitimate data. In addition, if the phase variations in the object field or surface under inspection are large or complex, the resulting fringe density can be so large as to make any reasonable data interpretation impossible.

The use of holography greatly enhances the reduction of unwanted phase noise as well as allowing for the interpretation of extremely complex wavefronts. In holography a coherent wavefront of arbitrary complexity is recorded onto a photosensitive media by combining it with a simple reference wavefront. The interference pattern formed by the two wavefronts allows both the intensity and phase of the object wavefront to be saved and reconstructed on demand when the hologram is re-illuminated with a reconstruction wave that is sufficiently similar to the original reference wave used during recording. In holographic interferometry, the reconstructed wavefront is combined with a second wavefront of the same subject or test cell after some change has occurred. This second wavefront may be a live scene or another holographic reconstruction. In either case, both wavefronts experience the same optical path and pass through and/or reflect off the same optical components. Thus, only differences in the subject itself produce interference fringes, no matter how complex the individual wavefronts themselves may be. Since both wavefronts pass through the same optical path, this approach also relaxes the

requirement for high quality lenses, windows, and mirrors.

Because holograms can store wavefronts that can be reconstructed at a later time they lead to the following possibilities that will be illustrated in the paper:

- System imperfections are canceled out because both wavefronts that form the interferogram experience the same imperfections.
- Object properties (no matter how complicated) that effect wavefronts that are fixed in time can be holographically recorded and optically subtracted from other, similar wavefronts.
- Wavefronts that existed at different times can be stored holographically, reconstructed later, then added or subtracted (or processed in other ways).
- PSI and HI can be performed on a reconstructed wavefront recorded from an instant in time with a pulsed laser. (PSI and HI normally require time for introducing phase shifts and cw lasers.)
- Wavefronts from two mutually incoherent lasers can be stored holographically then reconstructed and interfered later at a single wavelength, effectively allowing interferometry of two different wavelengths.

Holography offers other enhancements to the field of interferometry. Techniques that improve the sensitivity and accuracy of interferometry, such as phase shifting interferometry^{7,8} (PSI), heterodyne interferometry^{9,10} (HI), and resonance interferometry¹¹ (RI), can be further enhanced and implemented in unusual and powerful forms by incorporating holography. Finally, holography allows for the use of multiple wavelength interferometry, in some cases leading to measurements that have no obvious equivalent in conventional interferometry.

Holography can extend the power and flexibility of interferometry by allowing mutually incoherent wavefronts to be interfered. They can be recorded holographically and reconstructed later with a single third wavelength so that they can be either studied independently or interfered and compared. Two special cases of large and small wavelength separation are considered here. When the phase information added to the wavefronts by the measurement field varies with wavelength, the extra wavelengths provide additional diagnostic data. In some cases a large wavelength separation is required

to make such enhancement significant. Such is the usually case when the dispersive properties of the subject field are under investigation. A specific case where this is not true, however, is near the resonance of a material, where anomalous dispersion can cause a drastic change in phase information with a small change in wavelength. Therefore, multiple wavelength interferometry near resonance is meaningful with small differences in wavelength. Another example where small wavelength differences lead to large differences in phase is the measurement of distance.

2. TOMOGRAPHY

Interferometry has been used for many years in flow diagnostics. As with all path integrated measurements, the resulting data comprises line integrals through the flow field. With a single angle-of-view through the field, the integral can be solved only for simple geometries such as two-dimensional or axis-symmetric. Without a way to solve the integral, interferometry is little more than a qualitative flow visualization method.

In general, a full 180 degree viewing angle with many projections through the field at different angles is necessary for tomography. Such access is rarely available in wind tunnels and ranges. Based on the foregoing study, we conclude that aerodynamic tomographic interferometry with restricted viewing is possible and practical through the use of holographic recording procedures. Our study shows that six view angles are adequate for a wide range of useful aerodynamic conditions. Less than six view angles are adequate only for relatively simple, refractive index distributions. An important difference exists, however, between this type of tomography and that normally associated with the medical field. With limited view tomography, *a priori* information must be used to allow the accurate inversion of the projection data to point data. This kind of information is normally available for a given wind tunnel configuration, model and test type; however, the result is that the algorithm must be adapted to each case. So a general, all purpose turn-key system that readily fits all applications is not practical. The hardware for such a system can be assembled but not the software.

2.1 A Tomographic Hologamera

The six-view-angle hologamera, shown in **Figure 1** was designed and constructed by the University of

Florida, Graduate Engineering Research Center. Light from the pulsed ruby laser enters the hologamera as shown on the right hand side of the figure and is split into object (O) and reference (R) waves by a beamsplitter. Seven mirrors, M, serve one each for the six object waves and one reference wave. The complete object path is shown for one view only to simplify the picture. The hologamera stores all six object waves in a single hologram. The six views appear in the hologram as diffusely lit surfaces distributed along a curved line. Two types of holographic interferometry have been used: double exposure and sandwich (double plate).

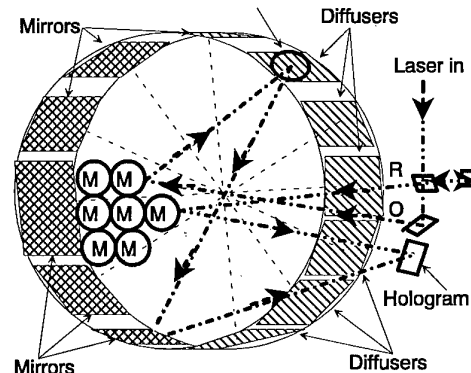


Figure 1. Six view-angle hologamera.

2.2 Reconstruction System.

Figure 2 shows the reconstruction system, developed by MetroLaser, which consists of a 17 milliwatt HeNe laser for reconstruction, a spatial filter to remove spatial intensity noise from the beam, a folding mirror to keep the system compact, an adjustable double plate holder and a Kodak MegaPlus CCD camera. The system is designed so that the CCD camera can be traversed and tilted to access all six of the images in the hologram. The CCD camera interfaces to a controller box via a large Kodak multi-pin connector. The controller box is then attached to the Dipix frame video acquisition board (resident in the host computer) via a 37 pin cable. The video acquisition board has a standard SVGA output that is connected to an SVGA monitor. This monitor will display the real-time images from the camera and is therefore called the *Camera Display* monitor. A second monitor (17") is connected to the computer's video board and displays the windows interface for running the acquisition and data reduction programs. The rotary stage on the double plate holder is computer actuated. The actuator on the stage is connected to "AXIS 1" of

the motor control box via a 15 pin connector. The control box is connected to the host computer via a RS232 cable.

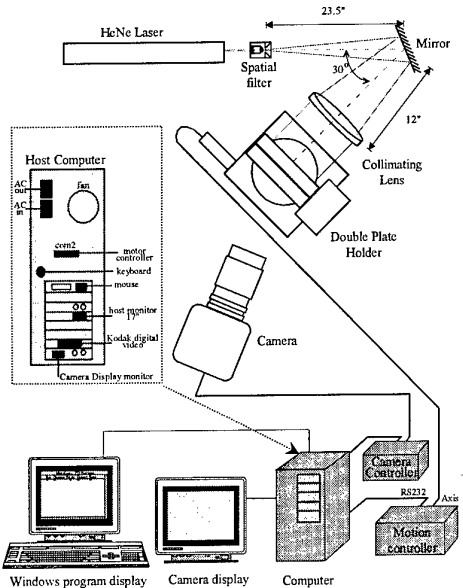


Figure 2. Reconstruction system, optical configuration and electronics.

To record at one wavelength and reconstruct at a second presents practical interferometry problems, caused by aberrations, that cause residual fringes. To correct this we developed a correcting holographic optical element (CHOE) that is produced in the recording system that cancels out such aberrations.¹² The CHOE is held in a specially designed double plate holder, that also makes sandwich holographic interferometry possible. The system is equipped with a phase shift interferometry software analysis program that reduces data to a displacement map.

After an interferogram is produced, the fringe information must be converted to phase information for the wavefront. After analyzing the four basic methods of performing fringe data reduction: fringe tracking,¹³ Fourier transform method¹⁴, heterodyne¹⁵, and phase-shifting interferometry (PSI),^{16,17,18,19,20} we chose PSI because it offered a good trade-off between complexity and accuracy.

PSI solves the interferogram equation for the intensity in the interferogram,

$$I = A + B \cos(\phi + \theta), \quad (1)$$

by shifting the arbitrary phase term, θ , by 3 or more values to produce enough intensity values to solve for the unknowns. Holographic PSI produces the required phase changes by changing the optical path-length difference between the wavefronts derived from the two holograms during hologram reconstruction. Two types of optical layouts are commonly used: the double reference beam setup^{21,22} and the double-plate¹² or sandwich setup. The double reference beam setup modulates the phase of one of the two reference beams and produces required phase variations in the fringe pattern of the interferogram.

In the sandwich configuration, the wavefront to be analyzed is recorded in one hologram and a reference wave for the interferogram is recorded in a second. The two holograms are then put together in a "sandwich" and the two wavefronts are simultaneously reconstructed and mixed to produce the interferogram. Since the two wavefronts come from two different holograms, they are independently adjustable, leading to maximum flexibility. The double-plate setup modulates the phase of the interferogram by changing the optical path-length through the holographic plates. A special sandwich (double-plate) holder was developed to allow precise, independent adjustment and alignment of the two plates and to rotate them accurately to modulate the relative optical path-lengths of the two reconstructed beams.

The Carré algorithm²³ produces four intensity values I_i for Eqn. 1 by shifting three times. The solution is given by,

$$\phi = \tan^{-1} \left\{ \frac{[3(I_2 - I_3) - (I_1 - I_4)][(I_2 - I_3) + (I_1 - I_4)]}{(I_2 + I_3) - (I_1 + I_4)} \right\}. \quad (2)$$

A minimum of three phase-shifted interferograms are required to calculate the optical phase distribution of an interferogram, although a greater number leads to improved accuracy. The data reduction algorithms by three, four, and five-frame algorithms were described by Hariharan, *et. al.* and their error analyses are investigated by Creath. Four and five-frame algorithms are found to be the least sensitive to calibration errors. Preprocessing and post-processing of the interferograms are necessary to eliminate noise.

2.3 Phase Unwrapping Technique

The phase data after the arctangent calculation (Eqn. 2) is analogous to a ramp function that wraps the phase data in the modulo 2π (or intensity in mod

1). If four interferograms are generated, each one with an ω which is $\pi/2$ greater than the previous, then with some mathematical manipulation they can be transformed into a "wrapped phasemap" which has the form,

$$P(x,y) = \left[\left(\frac{OPD(x,y)}{\lambda} + C \right) \bmod 1.0 \right]. \quad (3)$$

A "wrapped phasemap" is a phasemap with a modulo term. To remove this term, one uses a phase map unwrapping program, the basis of which is an algorithm which adds factors of 1.0 wherever it sees a jump from 1 to 0, so that the phasemap is made smooth. A successful unwrapping of a phasemap, produces an unwrapped phasemap which has the formula:

$$P(x,y) = \frac{OPD(x,y)}{\lambda} + C. \quad (4)$$

In principle, phase unwrapping is almost trivial. To achieve phase unwrapping automatically in an image processing system is one of the most difficult tasks of automated processing. The difficulty arises because of optical noise, which contains many discontinuities that are not related to wrapped phase. Therefore, when an automated phase unwrapping system looks for discontinuities it finds many related to speckle, diffraction, and other forms of optical noise.

2.4 Tomography Algorithms

Tomography algorithms provide the three-dimensional refractive index function by solving a set of integral equations represented by the interferograms at different view angles through the refractive index fields. A number of highly developed algorithms are now available.^{24,25,26} The holocamera and reconstruction system produces four phase-shifted interferograms from each of six different views (for a total of 24) through the flow field. From these 24 interferograms, the data reduction algorithm produces six wrapped phase maps. It unwraps each of the maps to produce six phase maps, then applies the tomography algorithm to calculate the three-dimensional distribution of refraction index. If the user gets this far, the tomography algorithms available from many different laboratories have now been proven effective in inverting the projections back to three-dimensional data; however, each algorithm depends to some extent

on the quality and extent of *a priori* knowledge.

To support the system we also developed a program to evaluate and test the completed data reduction and tomography algorithm with synthetic data similar to what is expected in the Aeroballistics range. The computer-generated interferograms are of a conical projectile in motion. The motion of the cone causes a change in the density of the air inside its shock wave, which, in the interferogram, appears as fringes in the region just outside the cone. The tomographically reconstructed profile can be compared to the original starting profile and thus an end-to-end check of the system is possible. Finally, the known and computed data are presented and compared graphically to show how well the algorithm can handle a refractive index distribution of the type initially supplied.

Data from actual holographic interferograms are more difficult to process because of the presence of speckle and other noise. A robust algorithm has been developed that can handle a significant amount of intensity noise. The algorithm has proved highly successful on images taken with direct (non-diffused) light, and has also been successful in processing substantial portions of the interferograms from the Aeroballistics test range. We have demonstrated tomographic reconstruction of a portion of the data from the Aeroballistics Test range.

Figure 3 is a typical interferogram from the aeroballistics range holocamera. The subject is a flared model in supersonic flight. Figure 3B shows the wrapped phase map. The problems introduced by speckle are evident in regions of high fringe density. Even so, large areas of the interferogram are processable as shown in Figure 3C, the unwrapped phase map.

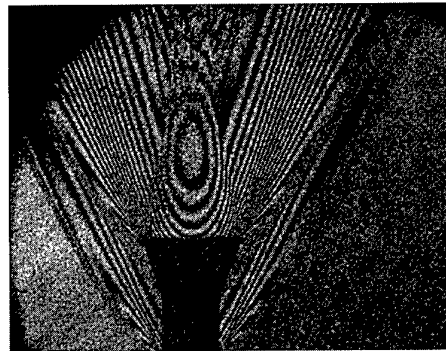


Figure 3A. Reconstructed interferogram of projectile.

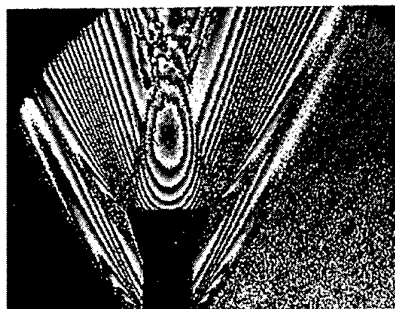


Figure 3B. Wrapped phasemap produced from phase-shifted interferograms.



Figure 3C. Unwrapped phasemap produced from wrapped phasemap shown in A.1.2. Black areas indicate regions that could not be unwrapped.

Figures 3A,B, and C. Interferometry of an Aeroballistics Model.

Figures 4A-C show a complete analysis of one cross-section of the model. Figure 4A includes the unwrapped phase map, Figure 4B provides the refractive index of the cross-section, and 4C the 3-D map for the cross-section.



Figure 4A. Unwrapped phasemap from the projectile used for tomography.

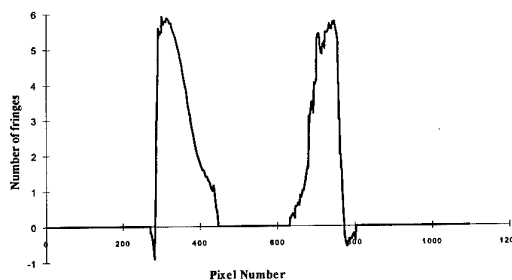


Figure 4B. Horizontal data slice used for tomography. Data was manually adjusted to correct for regions where unwrapping was not possible.

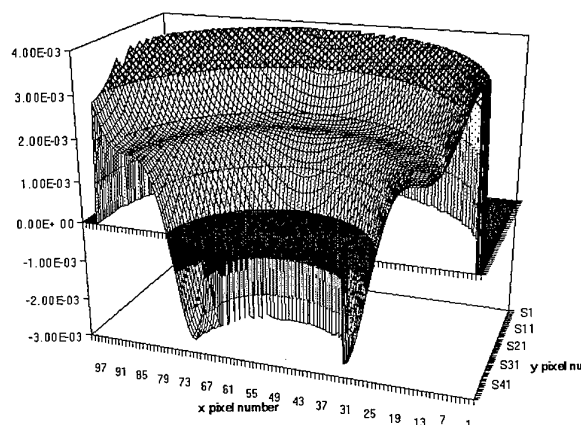


Figure 4C. Tomographically reconstructed 3D refractive index profile around half of the projectile.

Figures 4A, B, and C. Tomographic Analysis of an Aeroballistics Model in Flight.

Although bright interferograms were viewable by eye, speckle noise at the detector plane was significant. Ultimately, this limited the data quality. The unwrapping algorithm was able to successfully unwrap phasemaps in regions where fringe density was low. In high density areas, such as near the shock boundary, the program encountered greater difficulty. The unwrapping algorithm was able to unwrap the image over a large percentage of the interferogram; however, certain areas could not be unwrapped. Difficulties were encountered, particularly near shock boundaries. In some cases the algorithm crossed the shock incorrectly.

We are currently examining ways to deal with the speckle issue so that the entire interferogram can be processed. Two approaches are ongoing. In one

approach we will examine more robust algorithms that employ more sophisticated image processing to recognize and automatically correct for speckle noise. Preliminary steps involving averaging procedures have been partially successful. A second approach is to effectively eliminate speckle effects by converting the recording system for use with direct light as opposed to diffuse light. Preliminary lab tests in which the system was mocked up and experimentally tested show this to be an effective solution to the speckle problem. During the next year one or both of these procedures will be implemented into the operational system.

3. MULTIPLE WAVELENGTH HOLOGRAPHIC INTERFEROMETRY

Multiple wavelength holographic interferometry requires sources at different wavelength, recording material that can record holograms at each wavelength, and a reconstruction procedure that allows accessing the two reconstructed waves in a useful manner. A wide range of possibilities are available to produce two or more wavelengths suitable for multiple wavelength holographic interferometry. Large wavelength separations, up to many hundreds of nanometers, can be achieved with two separate lasers, multiple wavelength lasers, and tunable dye lasers. These sources can also be used for smaller wavelength separation. Other methods for attaining smaller wavelength (frequency) separations ranging from a few kilohertz to a few gigahertz include lasers with special etalons, tunable diode lasers, Bragg cells, and reverse Brillouin scattering cells.

When holograms are recorded at two wavelengths and played back at a single wavelength, two reconstructed waves emerge at different angles that depends on the recording geometry and the wavelength difference. If the two wavefronts are to be used independently, then a large angle is desirable. If they are to be used interferometrically together, then a small angle is required. If the recording subject and reference beams are the same for both wavelengths then the reconstructed waves will be nearly congruent only if the wavelength separation is small. The recording geometry can be chosen such that the two wavefronts emerge at the same angle or with any desired angle between them. This can be achieved by using separate recording and reconstruction reference waves for the two wavelengths and properly choosing the reconstructing wavelength.

Reconstructing at wavelengths that differ from recording wavelengths introduces chromatic aberrations that are especially limiting when different reference wave angles are used. A holographic correcting method has been developed in our studies²⁷ to record wavefronts at two different wavelengths and to achieve the simultaneous, congruent, corrected reconstruction of the two at an arbitrary third wavelength. The reconstruction is achieved with wavefronts generated by another hologram. The method automatically corrects aberrations and aligns the reconstructed wavefronts for interferometry.

The use of a second wavelength via holography introduces a number of interesting interferometric measurements. Multiple wavelength holographic interferometry requires sources at different wavelengths, recording material that can record holograms at each wavelength, and a reconstruction procedure that allows accessing the two reconstructed waves in a useful manner. A wide range of possibilities are available to produce two or more wavelengths suitable for multiple wavelength holographic interferometry. Large wavelength separations of up to many hundreds of nanometers can be achieved using either two separate lasers (e.g., two tunable dye lasers) or a single, multiple wavelength laser (e.g., doubled YAG or Argon). Single laser sources can also be used to produce smaller wavelength separation (e.g., Zeeman or diode laser). Other methods for attaining smaller frequency (wavelength) separations ranging from a few kilohertz to a few gigahertz include lasers with special etalons, tunable diode lasers, Bragg cells, and reverse Brillouin scattering cells.^{28,29,30}

The second wavelength can be used in one of three ways. First, the two wavelengths can be used to create two interferograms that are each analyzed separately. The dispersive properties of a test material are utilized to provide new, independent diagnostic data at the second wavelength. For example, when both temperature and concentration affect the refractive index of a solution, the second wavelength can be used to separate these effects. A large wavelength separation is typically required to make such a measurement useful. A specific case where a large separation is not required; however, is near a resonance line of a material, where anomalous dispersion causes a drastic change in phase information for a small change in wavelength.

Secondly, the two wavelengths can be interfered to produce a third, so-called synthetic (or beat) wavelength that is used as a diagnostic. For instance, HI can be used to measure optical path length with resolutions better than $1/10,000$.^{31,32,33} If the difference between the two wavelengths, $\Delta\lambda$, is much smaller than the average wavelength, λ , then the synthetic wavelength, λ_s , is given by,

$$\lambda_s = \lambda^2 / \Delta\lambda. \quad (5)$$

If either of the two interfering waves is phase shifted, the synthetic wavelength is likewise shifted by the same amount. Since the frequency of the synthetic wave is much lower, phase shifts can be detected and measured electronically in an extremely precise manner. The phase of the synthetic wavelength can thereby be accurately correlated to the relative phase of the two waves, since the change in relative phase of the two waves is followed by the equivalent change in phase of the synthetic wavelength.

The third manner of utilizing the second wavelength is to directly interfere it with the first. This concept is unique to holographic interferometry, since this type of interference does not even have definition in traditional interferometry. Holography, therefore, provides unique and powerful methods for interfering mutually incoherent wavefronts. When holograms are recorded at two wavelengths and played back at a single wavelength, two reconstructed waves emerge at different angles that depend on the recording geometry and the wavelength difference. If the two wavefronts are to be used interferometrically, the angle must be small. If the recording subject and reference beams are the same for both wavelengths, then the reconstructed waves will be nearly congruent only if the wavelength separation is small. The recording geometry can be chosen such that the two wavefronts emerge at the same angle or with any desired angle between them. This can be achieved by using separate recording and reconstruction reference waves for the two wavelengths and properly choosing the reconstructing wavelength. Reconstructing at wavelengths that differ from recording wavelengths, however, introduces chromatic aberrations that are especially limiting when different reference wave angles are used. A holographic correcting method has been developed in our studies to record wavefronts at two different wavelengths and thus achieve the simultaneous, congruent, corrected reconstruction of the two at an arbitrary third wavelength.³⁴ The

reconstruction is achieved with wavefronts generated by another hologram. The method automatically corrects aberrations and aligns the reconstructed wavefronts for interferometry.

An important example of this unique implementation of holographic interferometry is resonant holographic interferometry (RHI). In this application, one of the wavelengths is selected to correspond to a resonance of a particular species of interest in a flow field. Anomalous dispersion of the target species results in extremely large values of refractive index at the resonance wavelength. The phase of a wavefront is, therefore, dramatically altered by the presence of the target species. The concentration of that species can, therefore, be separated from all other constituents in the flow field, which produce very little phase shift in the wavefront.

4. RESONANT HOLOGRAPHIC INTERFEROMETRY (SPECIES IDENTIFICATION AND DISTRIBUTION) AND REAL TIME RECORDING

Resonant holographic interferometry (RHI) uses two wavelengths that are very close together. RHI provides a method for obtaining species specific interferograms by recording two simultaneous holograms in which one of the wavelengths is tuned near a chemical absorption feature and the other tuned off this feature (typically < 0.1 nm separation between lasers).^{35,36} Since phase contributions to the interferogram from background species, thermal and pressure gradients, and optical aberrations are subtracted out in the holographic reconstruction process, the resulting interference fringes correspond uniquely to the density of the species under interrogation. The interferogram permits two-dimensional chemical detection that is useful for combustion and plasma diagnostics, medical imaging, and flow visualization. Real-time RHI has recently been demonstrated using a bacteriorhodopsin (BR) polymer thin film as the recording medium; however, the long lifetimes of BR in the polymer host limited the interferogram acquisition rate to 1 Hz.³⁷

The use of photorefractive semiconductors extends the current RHI technology into the near-infrared (NIR) spectral region, where conventional holographic recording media are unavailable, and enables real-time measurement capability. The NIR region is easily reached with inexpensive, commercially available laser diodes. In addition, laser

diode output can be easily coupled into single-mode fiber optic cables which greatly reduces the size and complexity of the optical delivery system by eliminating multiple beam steering mirrors and periscopes. Holographic images can be recorded, reconstructed and erased in photorefractive semiconductors on time scales less than 10 ns, making it possible to achieve megahertz data rates.³⁸

Photorefractive crystals such as $\text{Bi}_{12}\text{SiO}_{20}$,^{39,40,41} $\text{Bi}_{12}\text{TiO}_{20}$,⁴² and LiNbO_3 ,⁴³ have been used to replace conventional films, allowing *in-situ* exposure, development, and erasure of holographic interferograms; however, these ferroelectric oxides often show a very slow or no response at the NIR wavelengths of commercial laser diodes. Vanadium-doped zinc telluride ($\text{ZnTe}:\text{V}$) has demonstrated fast photorefractive response in the spectral range of 0.6 to 1.3 microns.⁴⁴ The figure of merit corresponding to the electro-optic index change per separated charge, suggests that ZnTe has the highest sensitivity of the known photorefractive semiconductors.⁴⁵

The conceptual design for our real-time RHI system is shown in Figure 5. The laser beams tuned to the on- and off-resonance wavelengths are s-polarized, pass co-linearly through the test object (combustion flow field, plasma reaction chamber, etc.), and are focused down to match the crystal aperture. Two reference beams are also co-linear and s-polarized. By properly selecting the wavelengths and geometry, phase conjugate replicas of both object beams produce interference fringes at the detector plane that correspond to the density of the species under interrogation. The polarization rotational properties of four-wave mixing in semiconductor photorefractive crystals may be utilized to suppress noise from scattering.⁴⁶ The orientation of the photorefractive crystal was chosen so that the diffracted signal of the counter-propagating reconstruction beam has its polarization rotated by 90 degrees. The polarizing beamsplitter (PBS) increases the signal-to-noise ratio by selecting only the diffracted light and rejecting any s-polarized scattered light.

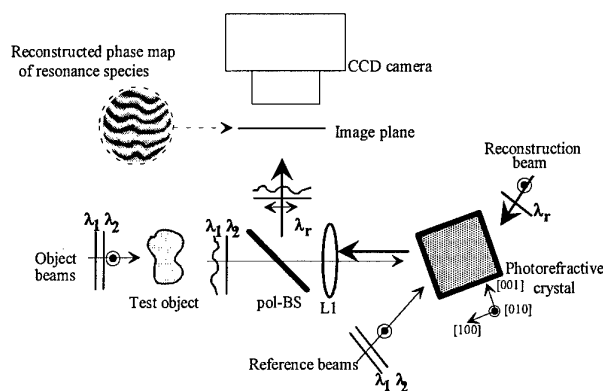


Figure 5. Phase conjugate configuration with polarization switching for real-time resonant holographic interferometry system.

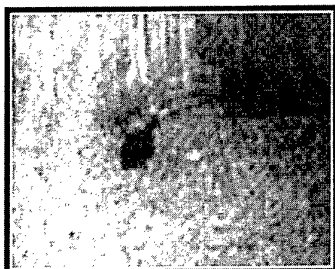
Demonstrations of real-time RHI measurements were performed using one of the strong potassium doublet absorption features (D_2) near 766 nm as our target. In addition to the simplified spectroscopy associated with probing alkali metal atoms, potassium seeding is useful for combustion studies since production of the neutral species (which is detected by RHI) occurs at the flame front. Thus, it provides a method to track the time evolution of the flame front. In addition, potassium may be conveniently seeded into combusting environments in such forms as potassium chloride (KCl).

Dye lasers 1 and 2 were tuned 0.15 nm on either side of the D_2 absorption. Laser energies at the crystal were 1 mJ/pulse. Solutions of KCl in either water, methanol, or glycerol were introduced into various combusting environments including: droplets suspended on fine wires, mono-disperse droplet streams, and sprays.

Results are shown in Figure 6 from experiments using single droplets on the order of 1 mm in diameter. The droplets were suspended from a fine wire, and ignited with a butane lighter. After ignition, the butane lighter was removed, and the droplet was allowed to burn on its own. The evolution of the combustion process was monitored at 10 Hz with the real-time RHI instrument. The figure shows a sequence of successive RHI interferograms of a KCl seeded, burning methanol droplet. The images are separated by 100 ms intervals (10 Hz). Figure 8a shows the droplet just after ignition. The absence of fringes due to thermal gradients highlights the utility of holographic optical background subtraction. In

Figure 8b a partial fringe is just visible in the lower right hand corner next to the droplet. In the subsequent frames, fringes are clearly visible. Such detail is not visible in images simultaneously recorded on conventional video because the flame luminosity totally obscures any detailed chemical and physical dynamics occurring at the thin flame front boundary. These images may reveal many of the finer details of the flame front development, and demonstrate that real-time RHI is a promising diagnostic tool for studying combustng droplets, or other multi-phase, highly luminous, highly scattering events.

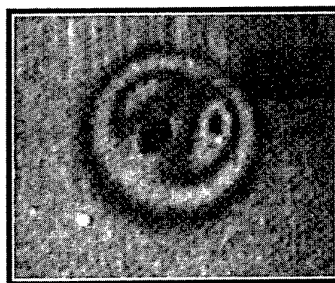
For these demonstrations, the data framing rate was limited to 10 Hz by the laser system. The actual interferograms were recorded, reconstructed, and erased in a single 6 nanoseconds laser pulse. Therefore, the RHI instrument is ultimately capable of MHz data rates. In order to achieve higher data rates, laser pump sources with faster repetition rates and high speed CCD cameras must be used. RHI interferograms of complex combustng sprays were also captured by injecting seeded water and methanol into an oxy/acetylene flame using an atomizer.



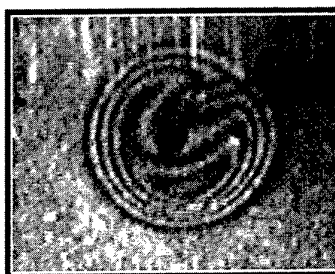
a)



b)



c)



d)

Figure 6. RHI interferograms of burning methanol droplets seeded with KCl. Each image is separated temporally by 100 ms.

Under our test conditions, the interaction length was approximately 0.5 cm and the lasers were tuned ± 0.15 nm symmetrically about the absorption feature (absorption line width = 0.024 nm). A minimum detectable concentration for our experiments was calculated to be 8.6×10^{11} cm⁻³, or 0.2 ppm. Analytical results predicted that the limit of fringe visibility was approximately 11 fringes, corresponding to a maximum measurable concentration of $N_{max} \leq 220$ ppm. The observation of approximately 5 fringes in our experiments (see Figure 8c and d) corresponds to a maximum concentration of 100 ppm. This sensitivity is comparable to that of FM diode laser spectroscopy, a single point, line-of-sight method.

To reduce the information contained in the RHI interferograms, we employed a manual fringe tracking algorithm. This resulted in a resolution of approximately 1/2 of a fringe. **Figure 7** shows gray scale maps corresponding to path-length integrated number density for two RHI interferograms of potassium seeded into a methanol droplet. The density gradient spans an order of magnitude which demonstrates excellent dynamic range. The uncertainty in the measurement is dominated by the

fringe tracking method which has on the order of $1/2$ fringe resolution. Based on our estimates, the value of the maximum integrated number density, shown in the center of the interferogram, is $17 \pm 2 (10^{11} \text{ cm}^{-2})$.

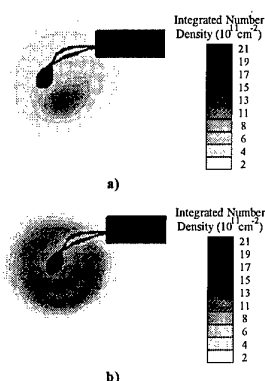


Figure 7. Potassium density maps produced from RHI interferograms, a) shown in Figure 7c and b) shown in Figure 7d. Values represent number density integrated along the line of sight ($L \approx 0.5$ cm). Uncertainty in measurement is dominated by fringe tracking method $\sim 2 \times 10^{11} \text{ cm}^{-2}$.

5. A LONG RANGE HOLOCAMERA

A trailer-mounted, long-range, holocamera was fielded this year for application in outdoor test ranges. The twin-telescope, stereo holocamera employs a 10 joule ruby laser that illuminates a target that can be holographically viewed from two directions recorded on two doubly pulsed holograms. Each hologram is recorded with two separate electro-optically switched reference waves, allowing recordings with time spacings up to 800 microseconds. This enables the interferometric measurement of the target displacement. The system is being used to evaluate ballistic impacts and penetration of structures. The system, illustrated in **Figure 8** is based around a 10 joule, four-pulsed, Q-switched, ruby laser. An object beam, which carries most of the laser output, is directed to the target, which can be located up to 40 meters from the holocamera.

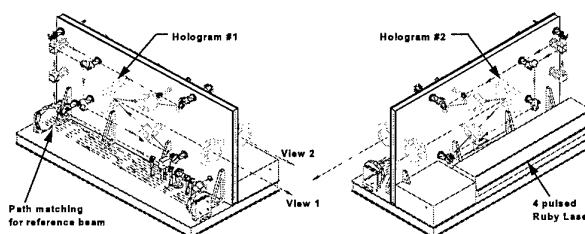


Figure 8. Long Range Holocamera.

Light scattered from the object field is collected and imaged by twin 150 mm telescopes that reimage the light to a pair of hologram recording plates. The twin recording arrangement allows viewing the scene from different angles. Each recording is made with two different reference waves to give flexibility to the reconstruction mode. This is achieved by using a polarization rotator, combined with polarization beamsplitters, to route the reference beam to its correct path.

Matching pathlengths between object and reference wave can be achieved conveniently through a variety of mirror configurations. We easily matched pathlengths up to about 50 meters with the mirror "Herriot" cell employed.

6. FOUR WAVE MIXING FOR TRANSIENT GRATING SPECTROSCOPY (TEMPERATURE MEASUREMENT)

The temperature field of combustion environments is a key diagnostic parameter. It reflects the complex interaction of the local chemistry, fluid dynamics and heat transfer of the combustion gases. For the purposes of testing combustor design and the verification of predictive computer models of combustors, it is imperative that accurate temperature measurements be made. Major challenges to optical diagnostics of practical combustors include high pressure, the presence of particulates (particularly soot), a high background luminosity, optical thickness and limited optical access. To address these challenges and provide quantitative diagnostic information on practical combustors, we explored non-resonant transient grating spectroscopy (TGS) for the measurement of temperature in high-pressure, sooting flames⁴⁷. The non-resonant TGS technique is spatially coherent, does not require a tunable laser system, provides spatially-resolved information and has been demonstrated to work at high pressure.⁴⁸ The process can be described as the writing of a hologram into a gas by mixing two coherent waves,

which alter the gas state in a volume containing interference fringes. A third beam is used to illuminate the hologram which reconstructs a wavefront (the detected signal) that varies in time as the fringes decay. The frequency of the signal is sensitive to the local temperature. We temporally-resolved the TGS signal generated in a high-pressure, sooting flame to extract the local temperature. In short, the TGS technique involves the first-order Bragg scattering of a probe laser off of a grating induced by two crossed pump laser beams. The amplitude and temporal evolution of the spatially coherent signal beam reflects the physical and chemical dynamics of the target medium. The temporal behavior of the signal is a function of the local temperature and transport properties. Historically, TGS techniques have been used to explore many transient phenomena in liquids and solids.^{49,50} Processes as diverse as the transport of excitons in molecular crystals⁵¹ and the kinetics of photoinitiated chemistry in liquids⁵⁰ have been studied using the TGS technique. More recently, investigators have applied the technique to gas-phase studies. Experimental work has been performed in static gases at high pressure,^{48,52} in the infrared⁵³ and in atmospheric flames,⁵⁴ and several groups have modeled^{55, 56, 57,58,59,60,61} the TGS signal.

6.1 Experimental Setup

Figure 9 illustrates a typical TGS system. The frequency-doubled output of a Nd:YAG laser was split into two pump beams of equal energy and passed through a 350 mm focusing lens. To ensure optimal grating formation, the optical paths of the two pump beams were matched to within millimeters. The 488 nm probe beam was directed toward the same lens parallel to the pump beams. During alignment of the detector, 4% of the probe beam was split off and directed at the lens so as to trace out the path of the actual TGS signal beam. At their crossover point, the pump beams formed an optical grating with a period of 10-14 μm . The pump and probe beams lay along the centerline of the burner and their height above the surface was varied from 6 to 16 mm. Two mirrors directed the signal beam through a spatial filter and two 488 nm laser line filters onto a photomultiplier tube. The pump, probe and signal beams passed through uncoated BK-7 windows 0.375" thick. The windows created stray light through diffuse scatter and specular reflection. The line filters rejected the unwanted 532 nm light at the detector and the spatial

filter rejected the unwanted 488 nm light at the detector.

Initial alignment of the pump, probe and signal tracer beams was achieved with the aid of a 100 μm pinhole placed at the crossover point of the beams. All four input beams were held parallel to each other before passing through the focusing lens. To facilitate separation of the actual signal beam from the pump and probe beams on the output side of the high pressure burner (HPB), the probe and signal tracer beams were vertically displaced from the pump beams by about a centimeter. The horizontal displacement between the two pump beams as they passed through the focusing lens was made as small as practically possible (~ 15 mm) with the equipment employed. The horizontal displacement between the probe and false signal beams was then fixed to ensure that they generated a grating spacing identical with that of the pump beams, *i.e.*, phase-matching conditions were met. Small adjustments were then made to the beam-directing mirrors to ensure that the beams maintained their proper horizontal spacing and simultaneously passed through the pinhole.

Once the initial alignment was established, the HPB was filled at ambient temperature with either pressurized air or CO_2 . The electrostrictive response from this static gas sample was used to optimize the TGS signal, and, through signal analysis, was used to accurately determine the actual grating spacing. An example of such a calibration measurement is shown in Figure 10. The index-of-refraction inside the HPB will of course change with changing conditions of density and gas composition; however, it can be shown with the repetitive use of Snell's law that the grating spacing inside the HPB remains constant. (The exact location in space of the overlap may move, but the grating spacing remains fixed.) Hence, the grating spacing is determined entirely by the conditions outside of the test region, *i.e.*, it is a laboratory controlled constant making thermometry feasible in changing environments.

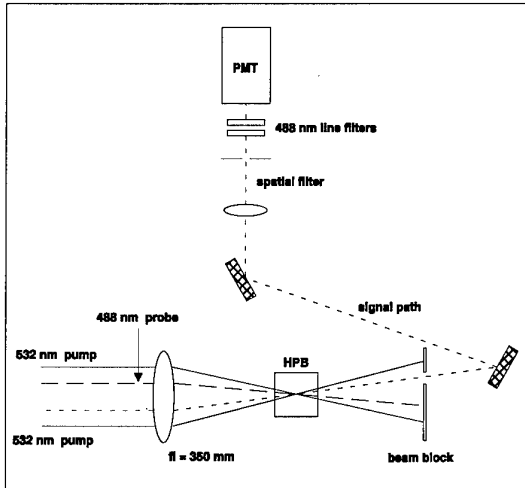


Figure 9. Schematic of the TGS optical setup employed. During alignment, 4% of the probe beam was picked off and used to trace the path of the signal beam.

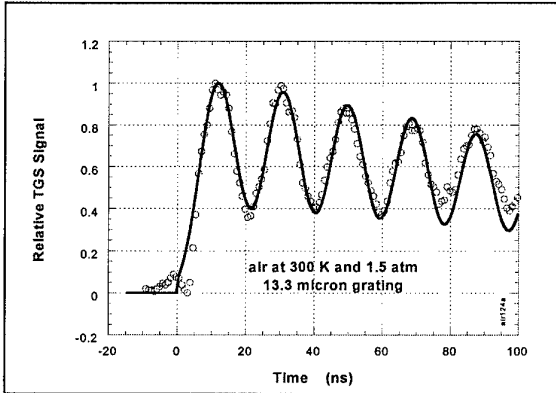


Figure 10. Nonresonant TGS signal in air. The fit to the data was made using a simplified expression based on the full theory by varying the grating spacing.

TGS thermometry is achieved by collecting the signal in a time-resolved fashion. Analysis of the oscillatory frequency of the signal provides a direct measure of the local sound speed which can then be related to temperature through the following equations:

$$C_s = \sqrt{R T \frac{\gamma}{M}}, \text{ and} \quad (6)$$

$$f_B = n \frac{C_s}{\Lambda}, \text{ respectively.} \quad (7)$$

In the above, $n = 1$ or 2 for thermal or electrostrictive signals, respectively, R denotes the gas constant, T the temperature, γ the heat capacity ratio and M the molecular mass of the gas mixture. By inverting Equation 6 and making use of the definition in Equation 7, we can write an expression for the TGS-determined temperature,

$$T = f_B^2 \frac{\Lambda^2}{n^2} \left(\frac{\gamma}{M} \right)^{-1} \frac{1}{R}. \quad (8)$$

The frequency, f_B , is the experimentally measured quantity, Λ is a parameter set by design and R is a constant. The ratio of γ to M is not measured and must be estimated. For a particular fuel and oxidizer this is not difficult and can be done using simple chemistry considerations. Both γ and M are simple sums of the corresponding values for the major gas mixture components weighted by the relative mole fractions and γ exhibits a temperature dependence as well. The γ/M ratio is much more sensitive to fluctuations in the temperature than to fluctuations in the mole fractions of the gas mixture. This fact makes TGS frequency measurements sensitive to local temperature changes and excursions. Empirical expressions for the individual values of γ_i for each combustion gas are found in the literature.⁶² To estimate the mole fractions of the major species in our flame environments we used the output of the CET89 flame code. For equivalence ratios, ϕ , greater than 1, the major species in the flame zone are found to be N_2 , CO and H_2O . Nitrogen accounts for at least 58% of the total number density for $\phi > 1$.

Experiments were carried out in a high pressure burner (HPB) that consisted of a mild steel pressure vessel fitted around a sintered bronze porous plug burner. Three BK-7 windows mounted at 90° to each other in the horizontal plane permitted optical access for the laser beams as well as direct observation of the flat flames generated. The pressure vessel was water cooled and fitted with a needle valve on the exhaust line that was used to regulate the interior pressure. Premixed ethylene/air flames were used for this work. We operated the HPB over a pressure range of 1 to 9 atm using rich fuel/air equivalence ratios varying from 1.6 to 2.0. With these rich gas mixtures, we generated stable sooty flames that appeared yellow to the eye. (At stoichiometric gas conditions this same flame appears light blue.) At equivalence ratios

above 2.0, the flames became unstable and lifted off of the burner surface. TGS measurements were made in the sooting flames using 50 mJ of energy split between the two pump beams (532 nm) and 500 mW of power in the cw probe beam (488 nm).

We extracted temperatures from the TGS signals for comparison with the corrected thermocouple measurements. At equivalence ratios of 1.6 and total pressures of 8 atm, we found a TGS temperature of 1790 ± 175 K and a simultaneous thermocouple temperature of 1710 ± 75 K. The agreement is quite good and we are now investigating ways to minimize the experimental uncertainty. Under very heavy sooting conditions (equivalence ratio of 2) we found that the TGS temperatures were less than the thermocouple temperatures. This suggests that soot fragments produced during vaporization by the pump laser beams may alter the local value of M/γ . This possibility is being investigated further. These experiments successfully demonstrated that TGS measurements can be performed in pressurized sooting flames using the non-resonant format. Soot particles, acting as blackbody absorbers, contribute to the thermal grating signal. Additionally, these demonstration measurements indicate that thermometry is possible with this technique in this environment.

7. CONCLUSIONS

In this paper, a variety of state-of-the-art holographic systems have been reported, including long range holography, tomography, resonance and real-time holography, and four wave mixing. Holographic methods provide powerful aerodynamics tools for obtaining quantitative information from flow fields. The use of more than one wavelength of light during recording and/or the reconstruction process can produce a variety of diverse and powerful measurement techniques that are unique to the holographic approach.

Automated data reduction has reached an operational stage on noise-free interferometry data. Application of tomography has become operational with high quality interferograms. In the reported tomography system 24 distinct, interferograms produced from six views are processed automatically then inverted tomographically to produce a three dimensional density distribution. A computer generated interferogram test method has also been developed to test the algorithms, anticipate how the actual test data

should appear, and assist with data interpretation. A test of the system on computer generated data similar to that expected from ballistic range data shows that the system is capable of providing accurate analysis. When noise is added to the interferometry data, the system operation and results are, of course, not so straightforward.

Resonance holographic interferometry has been established as a method for determining, not only refractive index but also, for a species specific interferometry. When combined with real-time recording the method can provide a quantitative determination of the concentration of a specific species in a field even when that species is not the dominant one.

Four wave mixing has been presented as a powerful tool for determining concentration and temperature of species in cases where many of the other methods fail, such as high pressure and temperatures.

8. ACKNOWLEDGMENTS

The authors wish to thank the many agencies and people who made the work reviewed in this paper possible. With regard to the RHI material, the authors wish to thank Dr. Sudhir Trivedi of the Brimrose Corporation of America for providing the photorefractive crystal, Dr. D. Dunn-Rankin and Mr. R. Dimalanta for technical and laboratory assistance, and Dr. Peter DeBarber and Mr. Neal Brock from MetroLaser for their work and leadership. This work was partially supported by the National Science Foundation, the Air Force Geophysics Lab, the Army Research Office, and the Navy.

The work in tomography and long range holography was supported by contracts with Eglin Air Force Base. The project officers were Gerald Winchenbach and Joseph Gordon. Dr. Ray Snyder produced the preliminary tomography codes used in the program, which were later refined by Joseph Hsu and Michael Gran.

The work in transient grating spectroscopy was supported in part by the U. S. Air Force under contract F33615-96-C-2656.

9. REFERENCES

- ¹ Trolinger, J.D., "Laser Instrumentation for Flow Field Diagnostics," AGARDographs No. 186, and

- 275 published by North Atlantic Treaty Organization, March 1974 and Sept. 1988.
- ² Brooks, R.E., Heflinger, L.O., and Wuerker, R.F., "Interferometry with a Holographically Reconstructed Comparison Beam," *Appl. Phys. Letters*, 7, 1965, p. 248.
 - ³ Horman, M.H., "An Application of Wavefront Reconstruction to Interferometry," *Applied Opt.*, 4, 1965, pp. 333-336.
 - ⁴ Vest, C.M., "Holographic Interferometry", John Wiley & Sons, New York, 1979.
 - ⁵ Trolinger, J.D., "Fundamentals of Interferometry and Holography for Civil and Structural Engineering Measurements", *Optics and Lasers in Engineering* 24, 1996, pp. 89-109.
 - ⁶ Gill, P., "Laser Interferometry for Precision Engineering Metrology", 153 in *Optical Methods in Engineering Metrology*, Edited by D.C. Williams, Chapman and Hall, London, 1993.
 - ⁷ Grievenkamp, J.E. and Bruning, J.H., "Phase Shifting Interferometry", edited by Daniel Malacara, Wiley Interscience Optical Shop Testing, (1992), p. 501.
 - ⁸ Hariharan, P., Oreb, B.F., and Eiju, T., "Digital Phase-Shifting Interferometry: A Simple Error Compensating Phase Calculation" *Applied Optics*, 26, 1987 pp. 2504-2506.
 - ⁹ Sommergren, G.E., "Optical Heterodyne Profilometry", *Applied Optics* 20, 1981, p. 610.
 - ¹⁰ Johnston, R. and Grace, K., "Refractive Index Detector Using Zeeman Interferometry", *Applied Optics*, 29, 1990, p. 4720.
 - ¹¹ Dreiden, G.V., et al, "Plasma Diagnostics by Resonant Interferometry and Holography", *Sov. Journ. of Plasma, Phys.*, 1, 1975, p. 256.
 - ¹² Trolinger, J.D. and Brock, N.J., "Sandwich Double-Reference-Wave, Holographic, Phase Shift Interferometry" *Applied Optics*, 34, 28, Oct. 1995, pp. 6354-6360.
 - ¹³ Becker, F. Becker and Yu, Y., "Digital Fringe Reduction Techniques Applied to the Measurement of 3-D Transonic Flow Fields," *Opt. Eng.*, 24, 3, 1985, p. 429.
 - ¹⁴ Takeda, M., Ina, H., Koyashi, S., "Fourier Transform Method of Fringe Pattern Analysis for Computer-Based Topography and Interferometry", *J. Opt. Soc. Am*, 72, 1982, pp. 156-1160.
 - ¹⁵ Massie, N.A., "High Performance Real Time Heterodyne Interferometry," *Applied Optics*.
 - ¹⁶ Trolinger, J.D., "Application of Generalized Phase Control During Reconstruction to Flow Visualization Holography," *Applied Optics*, 18, 6, 15 March 1979.
 - ¹⁷ Yanta, W.J., Spring, W.C., Gross, D.U. and McArthur, J.C., "Phase Measuring Laser Holographic Interferometer for Use in High Speed Flows" ICIASF 13th Congress on Instrumentation in Aerospace Simulation Facilities, Sept. 1989.
 - ¹⁸ Trolinger, J.D. Trolinger, Craig, J. Tan, H., and Dean, P., "Advanced Holographic Diagnostic Method for 3-D Hypersonic Flow Fields" AIAA-88-4653-CP, Atlanta, GA, 1988.
 - ¹⁹ Dandliker, R. Dandliker, Ineichen, B. and Mottier, F., "High Resolution Hologram Interferometry by Electronic phase Measurement." *Opt. Commun.* 9, 1973, p. 412.
 - ²⁰ Wyant, J.D., "Recent Advances in Interferometric Optical Testing," *Laser Focus*, November 1985.
 - ²¹ Ballard, B., "Double Exposure Holographic Interferometry with Separate Reference Beams." *J. Appl. Phys.*, 39, 1968, pp. 4846.
 - ²² Surget, P.C, "Two Reference Beam Holographic Interferometry for Aerodynamic Flow Studies," *Communication presente la Conference Internationale sur les Applications de l'Holographie et le Traitement Optique des Donnes*, Jerusalem, Aug 1976, pp. 23-26.
 - ²³ Carré "Installation et Utilisation due Comparator Photoelectrique et Interferential due Bureau International des Poids et Mesures", *Metrologia*, 2 1, 1966, pp. 13-23.
 - ²⁴ Cha, S.S. and Sun, J., "Tomography for Reconstructing Continuous Fields from Ill-Posed Multidirectional Interferometric Data" *Appl. Opt.* 29, 1990, pp. 251-258.

- ²⁵ Snyder, R., and Hesselink, L., "Measurement of Mixing Fluid Flows with Optical Tomography", *Optics Letters*, 13, 2, 1988.
- ²⁶ Snyder, R., and Hesselink, L., "High Speed Optical Tomography", *Applied Optics*, 24, 23, 1985.
- ²⁷ Trolinger, J.D., and Brock, N.J. "Sandwich, double reference wave, holographic, phase-shift interferometry", *Applied Optics* 34, 1996, p. 6354.
- ²⁸ Millerd, J.E. and Brock, N.J. "Holographic Profilometry with a Rhodium-Doped Barium Titanate Crystal and a Diode Laser," *Applied Optics*, 36, 11, 1997 pp. 2427-2431.
- ²⁹ Kuo, Y.-S., Choi, K., McIver, J.K., "The effect of pump bandwidth, lens focal length and lens focal point location on stimulated Brillouin Scattering Threshold and Reflectivity" *Optics Commun.*, 80, 3, 4, Jan 1 1991, pp. 233-238.
- ³⁰ Riza, N.A., "Scanning Heterodyne Optical Interferometry" *Rev. of Scientific Instrumentation*, 67, 7, July 1996.
- ³¹ Evans, J.T., "Real Time Metrology using Heterodyne Interferometry", *Proc. SPIE*, 429, 1983, p. 199.
- ³² Sommergren, G.E., "Optical Heterodyne Profilometry", *Applied Optics*, 20, 1981, p. 610.
- ³³ Trolinger, J.D., "Ultra high resolution interferometry", SPIE paper no. 2861-18, presented at Laser Interferometry VIII: Applications Conference, SPIE 1996 International Symposium on Optical Science, Engineering, and Instrumentation, Denver, CO, August 4-9, 1996.
- ³⁴ Trolinger, J.D., and Brock, N.J. "Sandwich, double reference wave, holographic, phase-shift interferometry", *Applied Optics*, 34, 1996, p. 6354.
- ³⁵ Dreiden, G.V., Zaidel, A.N., Ostrovskaya, Ostrivskii, Y.I., Pobedonostseva, N.A., Tanin, L.V., Filippov, V.N. and Shedova, E.N., "Plasma Diagnostics by Resonant Interferometry and Holography," *Sov. J. Plasma Phys.*, 1, 1075, p. 256.
- ³⁶ Rubin, L.F. and Swain, D.M., "Near-resonant holography," *Optics Letters*, 16, 1991, p. 526.
- ³⁷ Millerd, J.E., Brock, N.J., Brown, M.S. and DeBarber, P.A., "Real-time resonant holography using bacteriorhodopsin thin films," *Optics Letters*, 20, 1995, p. 626.
- ³⁸ Valley, G., Dubard, J., Smirl, A., and Glass, A.M. "Picosecond photorefractive response of GaAs:EL2, InP:Fe and CdTe:V," *Optics Letters*, 14, 1989, p. 961.
- ³⁹ Huignard, J.P., and Herriau, J.P., "Real-time double exposure interferometry with Bi₁₂SiO₂₀ crystals in transverse electro-optic configuration," *Applied Optics* 16, 1977, p. 1807.
- ⁴⁰ Kuchel, F.M. and Tiziani, H.J., "Real-time contour holography using BSO crystals," *Opt. Comm.*, 38, 1981, p. 17.
- ⁴¹ Petrov, M.P., Stepanov, S.I. and Khomenko, A.V., "Photorefractive Crystals in Coherent Optical Systems", 1991, Springer-Verlag, New York, Chap. 9 pp. 173-181, Chap. 5, pp. 85-87 and Chap. 2, pp. 20-23.
- ⁴² Frejlich, J., Kamshilin, A.A., Kulikov, V.V., Mokrushina, E.V., "Adaptive Holographic Interferometry Using Photorefractive Crystals," *Optics Commun.*, 70, 1989, pp. 82-86.
- ⁴³ Magnusson, R., Wang, X., Hafiz, A., Black, T. Tello, L., Haji-shelkh, A., Konecni, S., Wilson, D., "Experiments with photorefractive crystals for holographic interferometry," *Optical Engineering*, 33, 1994, pp. 596.
- ⁴⁴ Ziari, M., Steier, W., Ranon, P., Trivedi, S., and Klein, M.B., "Photorefractivity in vanadium-doped ZnTe," *Applied Physics Letters*, 60, 1992, p. 1052.
- ⁴⁵ Millerd, J.E., Partovi, A., Garmire, E., "Near resonant photorefractive effects in bulk semiconductors, Photorefractive Effects and Materials", edited by D. Nolte, Kluwer Academic Publishing, London, 1995, Chapter 6.
- ⁴⁶ Gheen, G. and Cheng, L., "Image processing by four wave mixing in photorefractive GaAs," *Applied Physics Letters*, 51, 1987, p. 1481.
- ⁴⁷ Brown, M.S.,^a and Roberts, W.L.,^b "Thermometry in pressurized, sooting flames using laser-induced gratings", June 1997 SPIE Paper No. 3172 51.

- ⁴⁸ Cummings, E.B., Hornung, H.G., Brown, M.S., and DeBarber, P.A., "Measurement of Gas-Phase Sound Speed and Thermal Diffusivity Over a Broad Pressure Range Using Laser-Induced Thermal Acoustics," *Opt. Lett.* 20, 1995, pp. 1577-1578.
- ⁴⁹ Eichler, H.J., Gunter, P., and Pohl, D.W., "Laser-Induced Dynamic Gratings", Springer-Verlag, Berlin, 1986.
- ⁵⁰ Zhu, X.R., McGraw, D.J. and Harris, J.M., "Holographic Spectroscopy, Diffraction from Laser-Induced Gratings," *Anal. Chem.* 64, 1992, pp. 710A-719A.
- ⁵¹ Salcedo, J.R., Siegman, A.E., Dlott, D.D. and Fayer, M.D., "Dynamics of Energy Transport in Molecular Crystals: The Picosecond Transient-Grating Method," *Phys. Rev. Lett.* 41, 1978, pp. 131-134.
- ⁵² Brown, M.S., DeBarber, P.A., Cummings, E.B. and Hornung, H.G., "Trace Species Concentration and Temperature Measurements at High Pressure Using Laser-Induced Grating Spectroscopy," SPIE paper no. 2546-72 (San Diego, July 1995).
- ⁵³ Dreizler, A., Dreier, T. and Wolfrum, J., "Thermal Grating Effects in Infrared Degenerate Four-Wave Mixing for Trace Gas Detection," *Chem. Phys. Lett.* 233, 1995, pp. 525-532.
- ⁵⁴ Williams, S., Rahn, L.A., Paul, P.H., Forsman, J.W. Zare, and R.N. Zare, "Laser-induced Thermal Grating Effects in Flames," *Opt. Lett.* 19, 1994, pp. 1681-1683.
- ⁵⁵ Boyd, R.W., "Nonlinear Optics", Chap. 8, (Academic Press, Boston, 1992).
- ⁵⁶ Paul, P.H., Farrow, R.L. and Danehy, P.M., "Gas-Phase Thermal-Grating Contributions to Four-Wave Mixing," *J. Opt. Soc. Am. B* 12, 1995, pp. 384-392.
- ⁵⁷ Cummings, E.B., Leyva, I.A. and Hornung, H.G., "Laser-Induced Thermal Acoustics (LITA) Signals From Finite Beams," *Appl. Opt.* 34, 1995, pp. 3290-3302.
- ⁵⁸ Hubschmidt, W., Hemmerling, B. and Stampanoni-Panariello, A., "Rayleigh and Brillouin Modes in Electrostrictive Gratings," *J. Opt. Soc. Am B* 12, 1995, pp. 1850-1854.
- ⁵⁹ Desai, R.C., Levenson, M.D., and Barker, J.A., "Forced Rayleigh Scattering: Thermal and Acoustic Effects in Phase-Conjugate Wave-Front Generation," *Phys. Rev. A* 27, 1983, pp. 1968-1976.
- ⁶⁰ Dean, D.R., "Optically Induced Diffraction Gratings in Liquids and Solids," Technical Report prepared for the Office of Naval Research, NTIS # AD-767-076.
- ⁶¹ Montain, R.D., "Spectral Distribution of Scattered Light in a Simple Fluid," *Rev. Mod. Phys.* 38, 1966, pp. 205-214.
- ⁶² Keenan, J.H., Chao, J., and Kaye, J., "Gas Tables, International Version", (Wiley, New York, 1983).

Holographic and Tomographic Interferometry for the Study of Unsteady Compressible Flows

B.H. Timmerman and P.G. Bakker

Department of Aerospace Engineering

Delft University of Technology

Laboratory for High Speed Aerodynamics

P.O. Box 5058, 2600 GB Delft, The Netherlands

1 SUMMARY

A digital holographic interferometry technique is presented which provides non-intrusive, quantitative measurements of the density distribution in a compressible flow field. Using a pulsed laser, flow fields may be essentially frozen, so that a measurement is obtained for a whole field at a single instant. Thus, also unsteady, turbulent flow fields may be studied. The technique provides a measurement of the density projected along the light path, so that the local density may be determined for two-dimensional and axisymmetric flows. Even for relatively complicated flow fields, quantitative projection data may thus be obtained. By sending several probe beams through a flow field simultaneously at different angles, also the instantaneous three-dimensional density distribution in unsteady fields may be obtained using tomographic reconstruction techniques. To furthermore gain insight into the temporal behaviour of turbulent flows, also quantitative differential recordings can be made. Thus, the technique presented here may be used to examine the (instantaneous) three-dimensional structure of a density field as well as its fluctuations in time. To illustrate the technique, here results are presented for the supersonic flow around a re-entry body, for an under-expanded free jet flow and for an oscillating flow issued by a so-called pipe-collar nozzle.

2 INTRODUCTION

The understanding of compressible flow fields is greatly enhanced by the simultaneous use of experimental and computational methods. Due to the growing capabilities in computing power, memory capacity and the development of smart schemes and fast solvers the computational possibilities have increased tremendously in the near past. To make these advancements beneficial in understanding flow fields the results of numerical modelling have to be compared with experimental data. In that respect code validation which can rely on accurate and reliable quantitative field data of various flow fields is an absolute must. Flow fields of practical interest are in most cases (if not all) three-dimensional and unsteady. Classical flow field measuring techniques, e.g. n -hole probes for mean values of flow field variables or hot-wire for turbulence suffer from the fact that the presence of the probe always influences the flow field giving rise to inaccuracies. This drawback of these flow measurement methods is usually met by probe calibration which suffices as long as space-gradients of the flow variables remain small and time-gradients are absent. Another serious drawback of probe techniques for generating field data is that they are point measurement techniques. To investigate a flow field with a certain accuracy a great number of locations has to be "probed" which can

be a very time-consuming process. As a consequence, probe methods usually suffer from low data-rates and are only suited for studying steady flow phenomena.

Therefore, for the study of turbulent flow fields, non-intrusive techniques are preferable which furthermore cover a whole field at once, instead of being point-measurements. Flow visualisation techniques are important diagnostic tools in experimental high-speed flow research as they provide a whole-field image of a flow at a single instant in time. Further the compressibility effects naturally occurring in high-speed flows allow perfectly non-intrusive measurements, free of flow disturbance and without the need of flow-seeding. Optical techniques based on the deflection of light in non-homogeneous density fields (like shadowgraph and schlieren) can visualise gradients in density, but only qualitative information can be obtained. Interferometry, on the other hand, is based on the distortion of the wave front of a (laser) light beam by spatial density differences and has the potential to yield quantitative information about the absolute flow density.

Digital holographic interferometry is a non-intrusive, quantitative technique which provides the phase delay of a light beam that has passed a flow field with a variable density. The phase delay is directly proportional to the integrated density along the light ray. Using this technique a two-dimensional image of the flow is thus obtained in the form of an integrated density field.

This paper presents the state of the art and capabilities of holographic and tomographic interferometry as developed at the Laboratory for High Speed Aerodynamics of the Delft University of Technology, to study three-dimensional unsteady flow fields in a non-intrusive way. Since light that propagates through a gas flow does not disturb the fluid properties of the gas or its dynamical characteristics, interferometry is a truly non-intrusive method in the fluid-dynamic sense. Furthermore, interferometry provides data for a complete field at one instant in time.

The non-intrusiveness and instantaneous, whole-field capabilities of interferometry make this technique very attractive for studying unsteady (turbulent) compressible flow fields, as it captures an instantaneous image of the flow. By recording two flow images at very short time intervals, a differential image is obtained from which the changes that occur in unsteady flow fields may be studied.

For studying three-dimensional flow situations tomography is introduced. By taking simultaneously multiple images from different directions the three-dimensional density distribution in the original field may be extracted by tomographic reconstruction.

The combination of the differential capabilities and the tomographic system can capture either the instan-

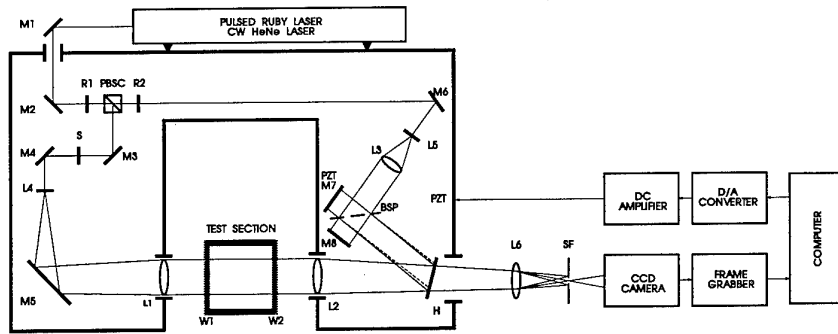


Figure 1: Two-reference-beam, plane-wave holographic interferometer. *BSP*: 50/50 beamsplitter plate; *H*: holographic plate; L_1, \dots, L_3, L_6 : positive lens, L_4, L_5 : negative lens; M_1, \dots, M_4 : 45°-incidence HEL-mirror; M_5, M_7, M_8 : mirror; M_6 : 0°-incidence HEL-mirror; *PBSC*: polarising beamsplitting cube; *PZT*: piezo-electric transducer; R_1, R_2 : $\frac{1}{2}\lambda$ -retardation plate; *S*: mechanical shutter; W_1, W_2 : test-section window; *SF*: spatial filter.

taneous structure of a density field or its evolution over a short time interval.

This paper will elucidate the physical principles and capabilities of holographic/tomographic interferometry to investigate three-dimensional unsteady density fields since they are of importance for transport aircraft aerodynamics. Results are given for the supersonic flow around a hemisphere-cylinder-flare body, compressible free jet flows and the unsteady flow issuing from a pipe-collar nozzle. The latter case shows the possibilities to study some aspects of turbulence in compressible flows.

3 DIGITAL HOLOGRAPHIC INTERFEROMETRY

When a light beam traverses a field with an inhomogeneous refractive index it is retarded locally, so that the phase of the beam leaving the flow field is changed according to the integrated result of the refractive indices it has encountered. For weak refraction, the light may be assumed to follow straight lines, so that the phase delay caused by the field is proportional to a projection of the refractive index field, which according to the Gladstone-Dale relation can be written in terms of the density, as [1]:

$$\Delta\phi(x, y) = \frac{2\pi K}{\lambda} \int [\rho(x, y, z) - \rho_0] dz \quad (1)$$

where λ is the wavelength of the probe beam, ρ is the density distribution, ρ_0 is the (constant) background density field, $\Delta\phi$ is the phase difference between a beam passing through the flow field and one which only passes the background field and K is the Gladstone-Dale constant, which is about $0.225 \cdot 10^{-3} \text{ m}^3/\text{kg}$ for air at a probing wavelength of 694 nm [2]. Here x, y are the projection plane co-ordinates, while z is taken to be the direction of the light path, which is perpendicular to the mean flow direction; the integration is evaluated over the width of the flow field.

To determine the phase delay caused by a flow field, the probe beam (object beam) is combined with a second, coherent light beam. The interference pattern created by these two beams is described by:

$$I(x, y) = I_{bias}(x, y) + I_{mod}(x, y) \cos \Delta\phi(x, y) \quad (2)$$

where I_{bias} is the background intensity, I_{mod} is the modulation intensity (contrast) and $\Delta\phi$ is the phase difference between the interfering beams.

In classical interferometry the two interfering beams propagate along different paths. For the study

of flows generated in a wind tunnel, this means that the object beam will pass the test-section including the windows of the tunnel while the second beam bypasses this. As a consequence the resulting 2-D interferogram is contaminated by information from the optical setup (e.g. windows, mirrors). In a holographic interferometer these contaminations are avoided by using a hologram on which at least one of the interfering beams is stored using a so-called reference beam, so that the same light path can be used for both the disturbed and the undisturbed flow field. In digital holographic interferometry (DHI) the resulting interference patterns are recorded and digitised by a CCD camera and stored in computer memory for further processing.

Using phase-stepping the phase difference can be determined on an interval $0 \leq \Delta\phi < 2\pi$ for each pixel in the projection plane [3]. Next, phase-unwrapping is applied to remove all 2π ambiguities so that the continuous phase map is obtained [4].

In Fig. 1 a plane-wave holographic interferometer with two reference beams, which may be placed over the test section of a wind tunnel, is shown. A ruby pulse laser (Lumonics, HLS1, wavelength 693.4 nm) is used to create a plane wave object beam which passes through the flow field and two collimated reference beams. A flow situation is captured by storing the object beam on a holographic plate using one of the reference beams while the other one is blocked by a mechanical shutter. The laser provides pulses of either 30 ns or 0.5 ms, so that the flow-field data is essentially frozen. Using the two reference beams, two flow situations can thus be recorded producing a double-exposure hologram. After recording, the holographic plate is taken out for developing and bleaching and then put back again in its original position. To minimize errors caused by misplacement of the holographic plate in its holder after photographic processing, only a small angle (approximately 0.5 degrees) is applied between the two reference beams. In the reconstruction stage the plate is illuminated through the reference paths with a continuous wave HeNe laser (wavelength 632.8 nm) that is aligned to the ruby laser. Each reference beam reconstructs the object beam that it recorded, so that by using both reference paths, two object beams are reconstructed that will produce an interference pattern. However, because the angle between the reference beams is only small, undesirable cross-reconstructions overlap the valid reconstructions. Because of the angle between the two reference beams, however, the propagation directions of the cross-reconstructions differ from that of

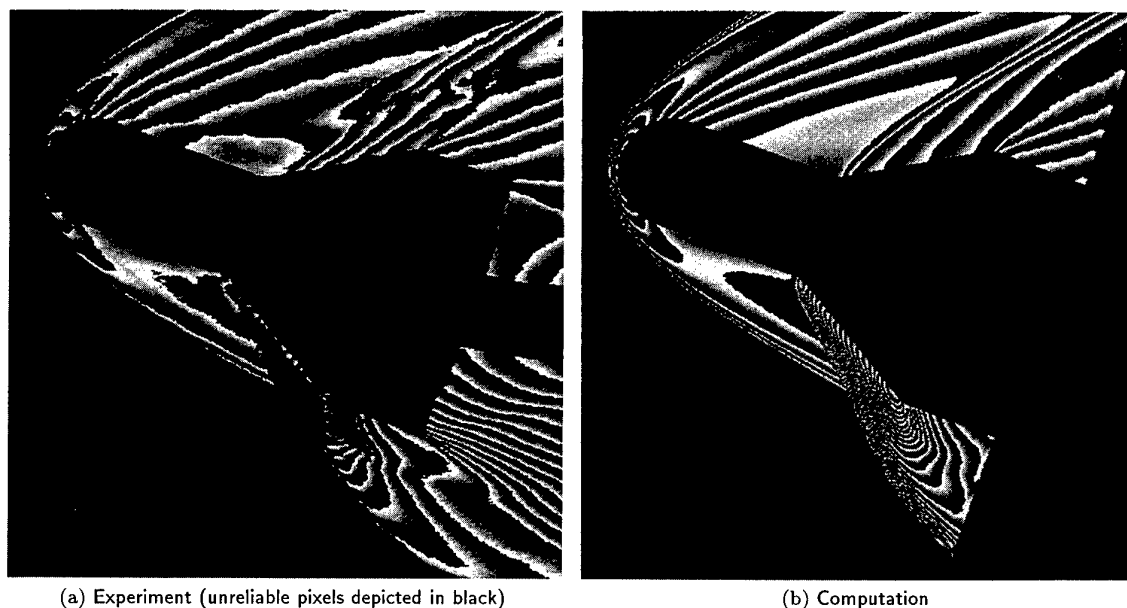


Figure 3: Phase maps modulo 2π for supersonic flow around blunt cylinder-flare model. $M_\infty = 2.95$, $\alpha = 20^\circ$, $\rho_\infty = 0.70 \text{ kg/m}^3$, interval range: λ or 20.5 g/m^3 .

the valid reconstructions of the object beams, making it possible to remove the cross-reconstructions using a spatial filter (diaphragm), which is placed in the Fourier plane of the imaging lens system (Fig. 1) [5].

Thus, speckle-free, plane-wave interferograms are

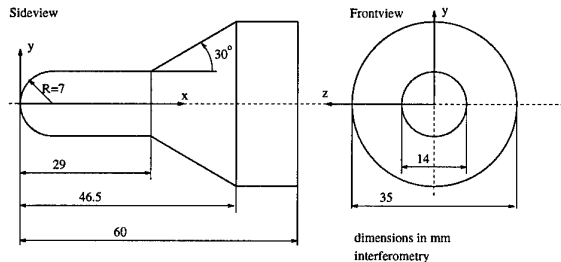


Figure 2: Re-entry model geometry

generated. Tilt fringes which are due to the difference in recording and reconstructing wavelength may be removed by slightly tilting mirror M_8 , or alternatively, in case of a homogeneous background field, by subtracting a linear pattern which is caused solely by the wavelength difference. By translating one of the mirrors in one reference path (in this case M_7 , which is mounted on a piezo-electric transducer), a controllable extra phase-difference is introduced in the interferogram. In the technique used here four of these so-called phase-stepped interferograms are generated, which are digitally stored and processed. From these four interferograms the phase-delay is calculated as a 2-D phase map, which contains information about the flow-field density averaged over the light path using the method of Carré [6]. In the reconstruction stage the CCD-camera is focused at the symmetry plane of the flow, as for axisymmetric flows this has been shown to minimise refraction problems [7]. Thus, for two-dimensional and axisymmetric flow fields the density can be determined at each point in the flow.

Several flow fields were studied this way, e.g. shock-wave boundary-layer interaction [8], Mach 3 flow

around a cone [9] and around an axisymmetric re-entry model at several angles of incidence [10]. This latter flow will be discussed in the next section.

4 RE-ENTRY FLOW

The high supersonic flow around a generic re-entry body (hemispherical-nose-cylinder with conical flare as shown in Fig. 2), at incidence has been investigated both using DHI and numerically. The flow around this model is challenging for this measurement technique, as the flow contains turbulent, 3-D areas and strong curved shocks. The experiments were performed in the test section of $15 \times 15 \text{ cm}^2$ (width \times height) of a blow down wind tunnel. The tunnel is equipped with a symmetrical nozzle, generating a supersonic flow at a Mach number of 2.95 in the test section area. In the interferometric experiments described here the free stream density, ρ_∞ , was 0.7 kg/m^3 and the Reynolds number 2×10^6 , based on the free stream velocity and the length of the model.

In order to study only the effect of the model on the flow and not e.g. wind tunnel wall effects, the flow around the model has to be compared to the undisturbed flow at the same conditions (which will have similar wind tunnel wall effects), rather than to a 'no-flow' situation. To achieve this the wind tunnel is started with the model in the field of view. With mirror M_8 unblocked and M_7 blocked the ruby laser is fired once to record the 'model flow'. Subsequently a recording of the 'undisturbed flow' is made, after having retracted the model out of the field of view, firing the laser for the second time with M_8 blocked and M_7 unblocked.

The experimental DHI results are compared with inviscid flow calculations obtained by a 3-D Euler code based on finite-volume discretization [11, 12]. For this the 3-D numerical results are integrated to obtain a 2-D projection of the integrated density distribution to enable a pixel-wise comparison with the interferometric data. In Fig. 3 the results of both techniques are shown for a free stream flow at $M_\infty = 2.95$ with the model at an angle of attack of $\alpha = 20^\circ$. Both are

shown in the form of a phase map, where the phase increases in cycles from black through grey to white; the integrated density is constant along each line of constant grey-scale value. In some areas, mostly near shock waves, the fringes are too closely packed, for separate fringes to be discerned. This is due to high density gradients. These areas do not satisfy the Nyquist criterion, which requires at least two pixels per fringe to be sampled. Therefore, these areas will not supply any reliable information and therefore have to be circumvented in the phase-unwrapping process to obtain the continuous phase map, and thus the integrated density field. Such areas are indicated in the phase map of Fig. 3a. as black regions (not to be confused with the black lines in the phase pattern).

A comparison of the results shows that the viscous areas are captured very well by interferometry, whereas they are not by the numerical code. Flow separation at the leeward side occurs just downstream of the nose and shows up clearly in the interferometric results as a distortion of the lines of constant integrated density. Downstream of the windward unreliable area, some influences of the shock-shock interaction show up, in the experimental as well as the computational phase maps.

In general, outside the unreliable (black) regions in the experimental phase map and the regions strongly affected by viscous effects, agreement between results is found to be very good as may be seen from Fig. 4, where the unwrapped phase along a vertical line through the cylindrical part of the model (indicated in the small inserted figure) is plotted. The experimental

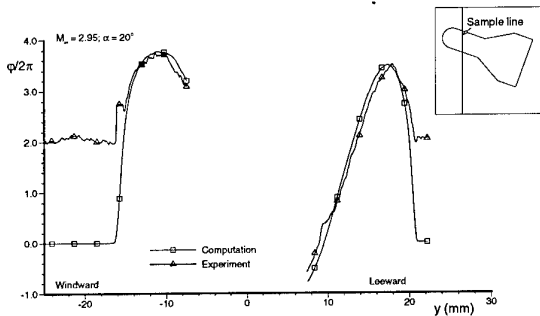


Figure 4: Unwrapped phase along vertical line, $M_\infty = 2.95$, $\alpha = 20^\circ$

phase distribution has been shifted 2π radians with respect to the numerical continuous phases, in order to make a comparison of the interesting flow regions. This shift is necessary, since the phase unwrapping in the experimental results fails at the shock due to the closely packed fringes. For the computations no phase unwrapping is necessary, since the phase angle ϕ is a direct result of the simulation process rather than the phase modulo 2π . The experimental and computational phase distribution agree rather well in the regions which are enclosed by the model and the shock. On the leeward side, the difference is probably caused by the separation shock. Thus, the methods are found to be complementary in some areas (strong discontinuities, viscous effects).

These experiments show that digital holographic interferometry is well-suited for obtaining projection data for complicated density fields in relatively steady high-speed flows. However, from the projection data, the local density distribution may only be derived for two-dimensional or axisymmetric fields. As most flow fields, and especially turbulent ones, are of a truly

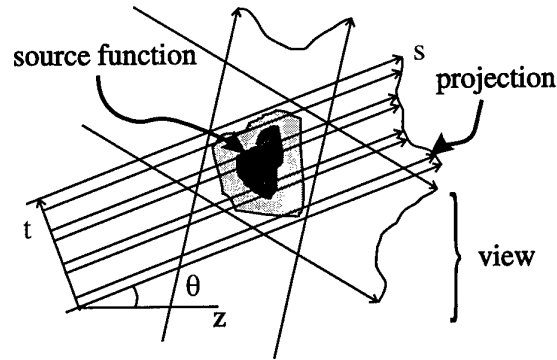


Figure 5: Projection-imaging geometry

three-dimensional nature, to study these flows a technique is needed which can give spatially resolved data.

5 TOMOGRAPHY

The purpose of optical tomography is to obtain 3-D measurements of a scalar quantity from a set of projections like those obtained in compressible flow interferometry. When projections are obtained from several viewing angles the integrals may be inverted to obtain the original scalar density distribution. To solve the problem of finding the original distribution (the 'source'), the three-dimensional field is usually thought of as being subdivided into a set of parallel planes. Each plane then represents a two-dimensional source field. Using tomographic reconstruction a 2-D cross-sectional image ($\tau\omicron\mu\omicron\varsigma$ = slice) of a source function, $f(x, z)$, is obtained from its projections, where here we assume that slices are taken at constant values of y . These projections are described by the Radon transform $R(t, \theta)$ [13, 14]:

$$R(t, \theta) = \int f(x, z) \delta(x - t \cos \theta - s \sin \theta, z - s \cos \theta + t \sin \theta) ds$$

which in the case of interferometry represents the modified phase of a light beam. Here δ is the Dirac delta-function, t is the transverse co-ordinate, θ is the viewing angle and s is the co-ordinate along the ray path (see Fig. 5). By inverting this equation the refractive index distribution and hence the density in the investigated plane can be found. By stacking the reconstructed slices for all parallel planes, the three-dimensional density distribution is obtained.

For continuously sampled data, R can be inverted directly to obtain the source function. However, for data sampled discretely in a limited number of views, the results will be contaminated by reconstruction artefacts.

In general there are two strategies for reconstructing a 3-D image from its projections: analytical inversion (e.g. [13]) and iterative algebraic methods (e.g. ART, SIRT, MART) [15, 16, 17]. The iterative methods are well-suited for including *a priori* knowledge and for cases where the angle of sight is limited.

Unsteady fluid dynamics problems require that all tomographic data must be obtained at a single instant in time, so all views have to be recorded simultaneously. Also, for practical reasons, the number of views has to be minimised, in order to reduce the size and cost of the data acquisition system and the time needed to process the experimental data. Furthermore, the range of available viewing angles is often restricted because of geometric constraints like the presence of wind tunnel walls. Therefore, algebraic

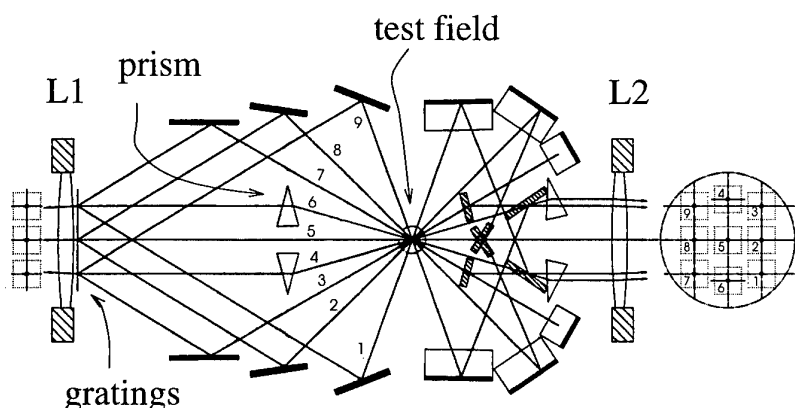


Figure 6: Tomographic part of interferometry set-up, which produces 9 beams that pass a test area (shown here as a circle). On the right the illumination-regions on the holographic plate are shown.

techniques seem to be best qualified for fluid dynamics studies and here only these iterative techniques have been considered.

5.1 Tomographic Interferometry

To be able to study three-dimensional flows a pulsed, phase-shifted, holographic interferometric tomographic set-up has been developed which is based on the two-reference beam interferometer of Fig. 1. For this, the set-up was extended to provide simultaneous multidirectional views (Fig. 6) [18].

After illuminating and developing the holographic plate, each view is imaged separately by the CCD camera, which is focused at the centre plane of the flow for all views. The phase maps that are calculated for each viewing direction using phase-stepping are then used for tomographic reconstruction of the recorded field.

Since each object beam has a different path length between lenses L_1 and L_2 , however, the object distance changes in each view, which causes a variation in the magnification between different projections. This needs to be corrected in the data processing. Furthermore, prior to reconstructing the 3-D field all views have to be aligned properly, so that the correct (projected) pixels are compared. Finally, the corrected projections can then be used to obtain the density field using tomographic reconstruction techniques. Here a Fourier-Bessel method, combined with a conjugate gradient technique is used to obtain the reconstructions. This technique is discussed in two papers by Watt [19, 20]. There are two advantages to this expansion when compared to reconstructions on a square grid. First, since the radial and angular components are represented by separate (but coupled) harmonic expansions, it is easier to match the reconstruction geometry to the sampling of the viewing geometry. Second, this expansion easily accommodates densities above and below the ambient, which is common in compressible flows.

The set-up has been used to measure the density fields of several underexpanded compressible free jet flows [18]. As an example, in Fig. 7 two iso-density surfaces are shown for the underexpanded jet flow from a straight pipe generated at a total pressure of 3 bar. The overall shape of the jet is seen to be round, which is shown clearly in Fig. 7 a. In the areas on either side of the compression regions, the jet is basically round with bulges 'sticking out' and a low-density area

in the centre. These bulges represent regions of locally high density that connect the compression regions (see also Fig. 7 b.). Proceeding downstream, these bulges change shape resulting in a somewhat sinuous shape for the outer envelope.

5.2 Double-Pulse Interferometry for Unsteady Flows

Thus, the three-dimensional instantaneous density field may be determined. As the laser provides very short pulses, also unsteady, turbulent flow fields may be investigated using this technique. Furthermore, the Q-switched ruby laser is capable of generating two 30 ns pulses at a time-interval that is adjustable between 1 and 800 μ s. Thus, differential measurements at time scales relevant for turbulence may be obtained. However, to get quantitative data for the phase differences from differential interferograms the two situations need to be recorded by separate reference beams, so that phase stepping can be used to analyse the interferograms. For this specific purpose, some adjustments were made to the set-up. To use separate reference beams for each pulse, switching between paths has to be accomplished within a microsecond. To meet this fast-switching demand the system is equipped with an electro-optic switch [21]. Both the double exposure and double-pulsed interferograms are processed using phase-stepping techniques.

The complete double-pulsed tomographic system can capture either the instantaneous structure of a density field or its evolution over a short time interval. The system is used to illuminate both the instantaneous structure of a compressible flow and provide insight into the relevant time scales of the flow. Thus coherent density structures may be studied. To investigate these possibilities, the oscillatory jet flow emitted from a so-called pipe-collar nozzle [22] is studied, providing an attractive environment to determine the possibilities of the double-pulsed tomographic interferometry technique.

5.3 Pipe-Collar Flow

The pipe-collar flow is generated by a simple geometry consisting of a pipe with a collar at its exit so that the diameter of the duct is suddenly increased, as is shown in Fig. 8. This set-up forms a so-called "whistler nozzle", which is being used to generate a transient, compressible flow field that has been well

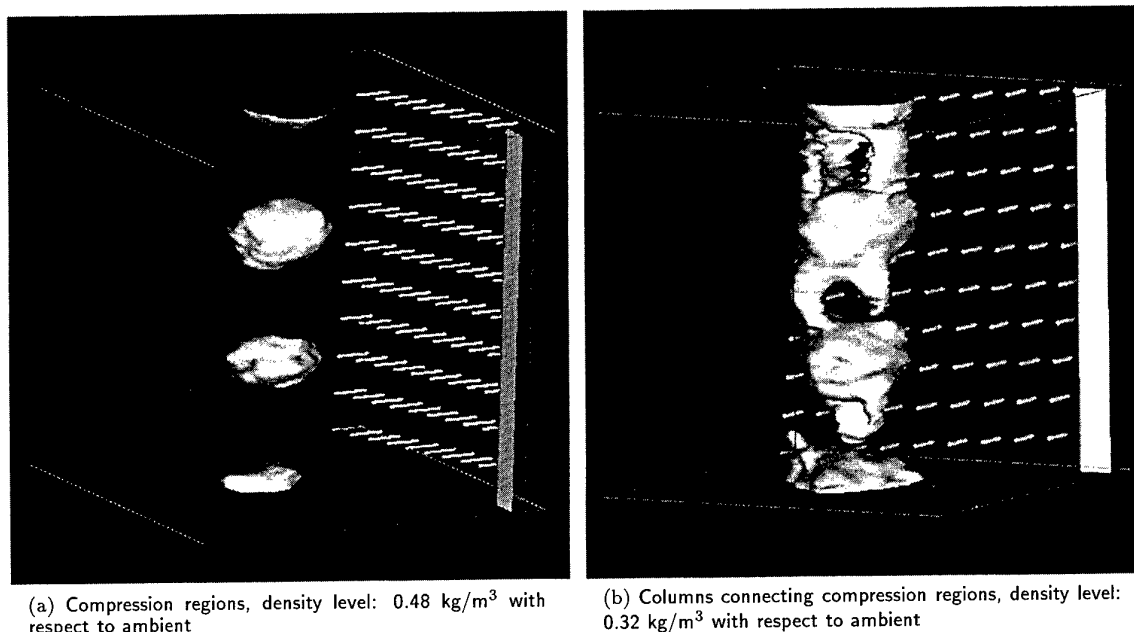


Figure 7: Two iso-density surfaces, emphasizing different flow features of an underexpanded compressible free-jet flow immediately behind the nozzle exit. Flow direction: top-down, settling chamber pressure: 3 bar, inner pipe-diameter $d = 6.5 \text{ mm}$, volume: $20.4 \times 20.4 \times 20.5 \text{ mm}^3$.

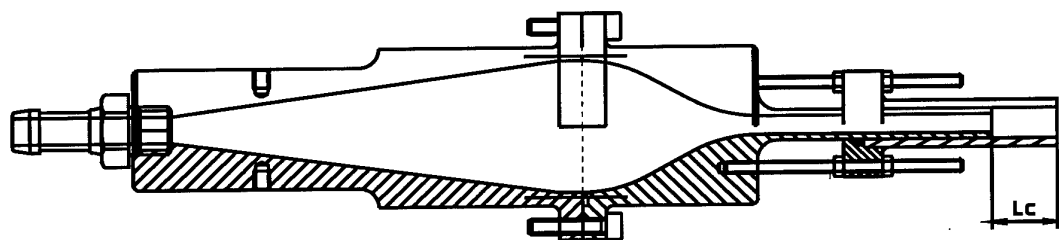


Figure 8: Pipe-collar nozzle configuration. A separate collar can be put over the pipe connected to the settling chamber. The effective length of the collar, L_c , can be adjusted by sliding the collar over the pipe.

documented by Selerowicz et al. [22]. The abrupt step may induce oscillations (and thus large-scale fluctuations) at well-defined frequencies in the jet flow that leaves the nozzle.

The flow generator that is used here is designed to produce a flow with features that are observable in the operating range of the tomographic double-pulsed system (i.e. a frequency range within $10^6 - 1250 \text{ Hz}$).

This configuration generates a flow field that has a more or less axisymmetric mean structure, so as not to deviate too strongly from earlier tomographic tests shown in Fig. 7, but also contains a well-defined, regular unsteady density pattern to investigate the appearance of these patterns in differential measurements.

A high pressure line supplies a small settling chamber (inner diameter 35 mm); the chamber outlet contracts smoothly into a round tube 6.50 mm in diameter and 60 mm long. At the exit of the pipe, a collar with adjustable length is fitted, with a inner diameter of 9.9 mm. Thus, the flow leaving the pipe experiences a step-height of 1.7 mm. The settling chamber pressure is measured and taken as the flow stagnation pressure.

As an example, here a jet flow generated at a settling chamber pressure of 1.9 bar and a collar length of 7.2 mm is studied. This configuration results in an oscillating jet flow, producing a clearly audible screech-

ing sound. Using a Fast Fourier Analyser (Brüel and Kjaer Narrow Band Spectrum Analyser, Type 2031), the dominant frequencies in this flow are measured to be 6550 Hz and 13100 Hz, i.e. the base frequency is 6550 Hz. Thus, the oscillation time is $152.67 \mu\text{s}$. In Fig. 9 a reconstructed iso-density surface is shown, as seen from different angles. The overall shape of the jet is seen to be wavy. The oscillation appears to take place only in one plane which can be seen by comparing Fig. 9 a. and b. which show orthogonal views of the iso-density surface at 0.15 kg/m^3 . In Fig. 10 two iso surfaces are shown representing surfaces of constant density difference. These are obtained from a differential recording at a time interval of $38 \mu\text{s}$, which is about a quarter of the oscillation time. From this image it can be deduced that the high density regions move downstream and rotate 90 degrees about the center [23].

The images produced show clearly that the jet density field has an instantaneous sinuous structure; that is that regions of constant density seem to be oscillating in a single plane rather than in a spiral or other pattern [24, 22]. However, the differential reconstructions indicate that this sinuous pattern is rotating about the jet axis at the acoustic frequency of the jet. The combination of these images provides a perspective of the dynamics of these jets that could not

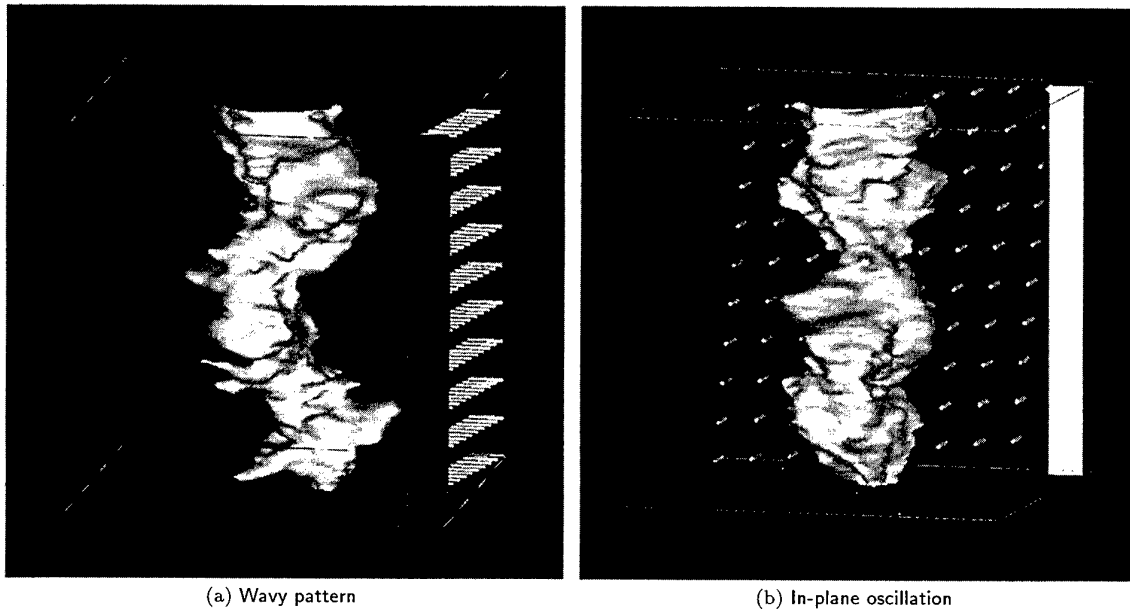


Figure 9: Two orthogonal views of a single iso-density surface at a density of 0.15 kg/m^3 with respect to ambient, showing the flow to be oscillating in one plane. Flow direction: top-down. Volume: $17 \times 17 \times 16.9 \text{ mm}^3$ starting immediately below the collar exit. $L_c = 7.2 \text{ mm}$, $p_s = 1.9 \text{ bar}$, inner diameter pipe $d = 6.5 \text{ mm}$, inner diameter collar $D = 9.9 \text{ mm}$

be achieved in another way. The implications of these aspects of the flow on the local jet dynamics is still a matter of discussion.

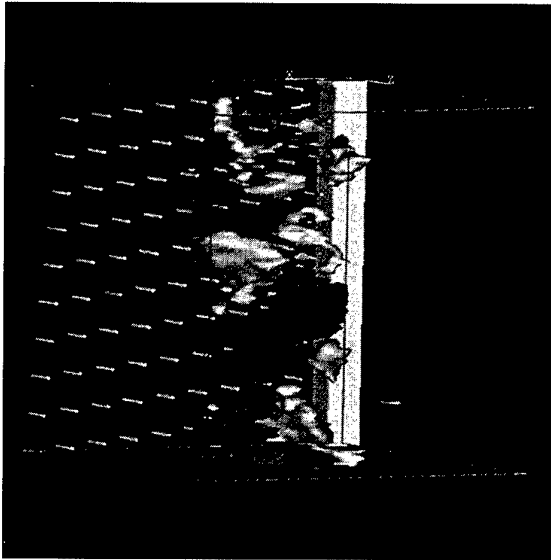


Figure 10: Iso-density-difference surfaces showing structures present in the flow. The bright regions represent a density difference of 0.14 kg/m^3 and the darker regions represent a density difference of -0.14 kg/m^3 . Flow direction: top-down. $p_s = 1.9 \text{ bar}$, $L_c = 7.2 \text{ mm}$, $d = 6.5 \text{ mm}$, $D = 9.9 \text{ mm}$, $\Delta T = 38 \mu\text{s}$, volume $17 \times 17 \times 16.88 \text{ mm}^3$, starting 5.06 mm from the nozzle exit.

6 CONCLUSIONS

The experiment demonstrates the utility of interferometric tomography for probing the instantaneous structure of unsteady high speed flow. A compact geometry with a relatively small number of views using a single hologram is combined with circular harmonic reconstructions to produce very well defined images.

Most importantly, it is shown that the holographic tomographic technique can provide information which cannot be obtained using conventional techniques, illuminating the instantaneous behaviour of unsteady flows.

In summary: a novel measurement technique is presented that enables the quantitative determination of the spatial density distribution in compressible flow fields at one instant in time or its evolution over a short time-interval. In this way the method competes with others developed to get increased accuracy and high data rates.

7 ACKNOWLEDGEMENTS

The contributions of prof. D.W. Watt of the University of New Hampshire, USA, in developing interferometric tomography are gratefully acknowledged. Furthermore, the technical support of Frits Donker-Duyvis and Eric de Keizer of the Laboratory for High Speed Aerodynamics of the TU Delft is greatly appreciated. ECS-8910350, and the NATO Scientific Research Programme. Part of Brenda Timmerman's work was funded by the Dutch Organisation for Scientific Research (NWO) through STW Projectnumber DLR33.3109

REFERENCES

- [1] C.M. Vest. *Holographic Interferometry*. Wiley, 1979.
- [2] W. Merzkirch. *Flow Visualization*. Academic Press Inc., second edition, 1987.
- [3] T.A.W.M. Lanen, C. Nebbeling, and J.L. van Ingen. Phase-stepping holographic interferometry in studying transparent density fields around 2-D objects of arbitrary shape. *Opt. Comm.*, 76(3,4):268-276, May 1990.
- [4] D.J. Bone. Fourier fringe analysis: the two-dimensional phase unwrapping problem. *Applied Optics*, 30(25):3627-3632, September 1991.
- [5] T.A.W.M. Lanen. *Digital Holographic Interferometry in Compressible Flow Research*. PhD thesis, Delft University of Technology, October 1992.
- [6] P. Carré. Installation et utilisation du comparateur photoélectrique et interférentiel du Bureau International des Poids et Mesures. *Metrologia*, 2(1):13-23, 1966.
- [7] G.P. Montgomery and D.L. Reuss. Effects of refraction on axisymmetric flame temperatures measured by holographic interferometry. *Appl. Opt.*, 21:1373-1380, 1982.
- [8] T.A.W.M. Lanen, P.G. Bakker, and P.J. Bryanston-Cross. Digital holographic interferometry in high-speed flow research. *Exp. Fluids*, 13:56-62, 1992.
- [9] T.A.W.M. Lanen, E.M. Houtman, and P.G. Bakker. Quantitative comparison between interferometric measurements and Euler computations for supersonic cone flows. *AIAA Journal*, 33(2):210-216, February 1995.
- [10] B.H. Timmerman and T.A.W.M. Lanen. Digital holographic interferometry compared to a 3-D Euler code in investigating the supersonic flow around an axi-symmetric re-entry model. In *Optical diagnostics in fluid and thermal flow*, volume 2005, pages 516-526. SPIE, July 14-16 1993. San Diego, California.
- [11] E.M. Houtman, W.J. Bannink, and B.H. Timmerman. Experimental and numerical investigation of the high-supersonic flow around an axisymmetric blunt-cylinder-flare model. In *Second European Symposium on Aerothermodynamics for Space Vehicles and Fourth European High-Velocity Database Workshop*, pages 517-522, 21-25 November 1994. Paper S16/6, ESTEC, Noordwijk, The Netherlands, (ESA SP-367, February 1995).
- [12] E.M. Houtman, P.G. Bakker, E. de Vries, and J.C. van den Berg. Modelling of separation using Euler methods. Report LR-776, Dept. of Aerospace Engineering, Delft University of Technology, 1994.
- [13] S.R. Deans. *The Radon transform and some of its applications*. Wiley and Sons, NY, 1983.
- [14] D.W. Watt and C.M. Vest. Turbulent flow visualization by interferometric integral imaging and computed tomography. *Exp. Fluids*, 8:301-311, 1990.
- [15] P. Gilbert. Iterative methods for the three-dimensional reconstruction of an object from projections. *J. theor. Biol.*, 36:105-117, 1972.
- [16] G.T. Herman and A. Lent. Iterative reconstruction algorithm. *Comput. Biol. Med.*, 6:273-294, 1976.
- [17] B.P. Medoff. Image reconstruction from limited data: Theory and application in computerized tomography. In H. Stark, editor, *Image Recovery: Theory and Application*, chapter 9, pages 321-368. Academic Press, NY, 1987.
- [18] B.H. Timmerman and D.W. Watt. Tomographic holographic interferometry for unsteady compressible flows. In *Optical Techniques in Fluid, Thermal, and Combustion Flow*, volume 2546, pages 287-296. SPIE, July 9-14 1995. San Diego, California.
- [19] D.W. Watt. Fourier-Bessel harmonic expansions for tomography of partially opaque objects. *Applied Optics*, 34:7468-7473, 1995.
- [20] D.W. Watt. Fourier-Bessel expansions for tomographic reconstruction from phase and phase-gradient measurements: Theory and experiment. In *Symposium on Experimental and Numerical Flow Visualization and Laser Anemometry, ASME Fluids Engineering Division Summer Meeting, FEDSM-3102*, June 22-26 1997. Vancouver, BC, Canada.
- [21] B.H. Timmerman and D.W. Watt. Tomographic high-speed digital holographic interferometry. *Meas. Sci. Technol.*, 6(9):1270-1277, 1 September 1995.
- [22] W.C. Selerowicz, A.P. Szumowski, and G.E.A. Meier. Self-excited compressible flow in a pipe-collared nozzle. *J. Fluid Mech.*, 228:465-485, 1991.
- [23] B.H. Timmerman and D.W. Watt. Tomographic holographic interferometric study of self-excited compressible jet flows. In *Optical Techniques in Fluid, Thermal, and Combustion Flow III*, volume 3172, page paper number 31. SPIE, 27 July - 1 August 1997. San Diego, California.
- [24] P.E. Dimotakis, R.C. Miake-Lye, and D.A. Papantoniou. Structure and dynamics of round, turbulent jets. *Phys. Fluids*, 26(11):3185-3192, November 1983.

Development of High Speed Interferometry Imaging and Analysis Techniques for Compressible Dynamic Stall

M.S. Chandrasekhara¹

Associate Director and Research Professor

Navy-NASA Joint Institute of Aeronautics, Department of Aeronautics and Astronautics

Naval Postgraduate School, Monterey, CA 93943, U.S.A.

L.W. Carr

Research Scientist and Group Leader, Unsteady Viscous Flows,
Aeroflightdynamics Directorate, Aviation Research, Development and
Engineering Center, U.S. Army ATCOM and,
Fluid Mechanics Laboratory Branch

NASA Ames Research Center, M.S. 260-1, Moffett Field, CA 94035-1000, U.S.A.

and

M.C. Wilder

Senior Research Scientist

MCAT Inc., San Jose, CA, U.S.A.

1. SUMMARY

The development of a high-speed, phase-locked, real-time, point diffraction interferometry system for quantitative imaging unsteady separated flows is described. The system enables recording of up to 224 interferograms of the dynamic stall flow over an oscillating airfoil using a drum camera at rates of up to 40 KHz controlled by custom designed electronic interlocking circuitry. Several thousand interferograms of the flow have been obtained using this system. A comprehensive image analysis package has been developed for automatic processing of this large number of images. The software has been specifically tuned to address the special characteristics of airfoil flow interferograms. Examples of images obtained using the standard and the high-speed interferometry techniques are presented along with a demonstration of the image processing routine's ability to resolve the fine details present in these images.

LIST OF SYMBOLS

C_p	pressure coefficient
c	airfoil chord
f	frequency of oscillation, Hz
k	reduced frequency = $\frac{\pi f c}{U_\infty}$
I	image intensity
M	freestream Mach number
U_∞	freestream velocity
x, y	chordwise and vertical distance
α	angle of attack
α_0	mean angle of attack
α_1	amplitude of oscillation
ϵ	fringe number
ρ	density
ρ_0	density at atmospheric conditions
ρ_r	density at reference conditions

2. INTRODUCTION

Dynamic stall has limited the flight envelope of helicopters for many years. The problem has been studied both in the laboratory and in flight, employing complex surface measurement techniques such as pressure transducers or skin friction gauges. To properly understand the complex physics associated with dynamic stall both surface and off-surface measurements are needed simultaneously. Quantitative visualization of the flow field during compressible conditions can be used in such cases, but in the past this has been possible only through carefully aligned and meticulously reconstructed holographic interferometry.

As part of a long-range effort focused on exploring the physics of compressible dynamic stall, a research wind tunnel was developed at NASA Ames Research Center (ARC) which permits visual access to the full flow field surrounding an oscillating airfoil during compressible dynamic stall (Ref. 1). Initially, a stroboscopic schlieren technique was used for visualization of the stall process (Ref. 2), but the primary research tool has been the real-time, self-aligning technique of Point Diffraction Interferometry (PDI), which has been carefully optimized for use in this project (Ref. 2,3). PDI is a robust, self-aligning interferometry technique. It uses conventional schlieren optical components and is immune to the problems that generally limit the application of other interferometers. Using PDI, both global and surface flow features can be simultaneously documented. It has been shown in Ref. 2 that dynamic stall onset occurs over a very narrow angle of attack range ($O(0.5)$ deg), at instantaneous angles of attack when the airfoil pitch rate is maximum, during which a large leading edge vortex forms and grows rapidly from a fully attached flow. Further, hysteresis results in cycle-to-cycle variation of stall onset which smears the data if acquired by conventional ensemble averaging. Thus, it is required that the flow developments be captured in just one pitch-up cycle which places extraordinary demands on the data acquisition

¹ Mailing Address: M.S. 260-1, NASA Ames Research Center, Moffett Field, CA 94035, U.S.A.

methods. Since the pitch rate could be as large as 4000 deg/sec and the data is needed at a very high resolution to document the details of dynamic stall evolution, extremely rapid real-time imaging rates ($O(20 \text{ KHz})$) become necessary. It is clear that holographic techniques are not applicable here.

The recording of the rapid flow changes also requires freezing the flow events during data acquisition. This implies sampling times of less than a microsecond for the present study. The energy output of even the most powerful laboratory laser is generally less than $200 \mu\text{J}$ for repetitively pulsed conditions. Imaging at such a low light level restricts the choice of recording systems to photographic film since even high speed videos presently do not have a satisfactory response at these low light levels. Trials showed that such systems responded randomly to individual photons of light rather than to light across the whole field of view.

One of the most valuable aspects of PDI is the fact that interferograms can be produced in real-time on a continuous basis through the use of a rapidly-pulsed laser. Pulsing at rates of up to 40 KHz and recording with high-speed film camera produces interferograms at a sufficient resolution (both in space and time) to analyse the rapidly developing unsteady dynamic stall field. In the present experiments, this has been achieved through the use of a high-speed drum camera combined with custom designed electronic circuitry. Interferogram sequences of dynamic stall development during a single oscillation cycle of the airfoil have been recorded at rates of up to 20 KHz. A detailed analysis of the effects of pitch rate, Mach number, Reynolds number, amplitude of oscillation, and other parameters on the dynamic stall process has thus become possible.

The present research has also focused on quantitative determination of the fluid physics of the compressible dynamic stall flow field, including the gradients of pressure in space and time from these interferograms. The development of image analysis techniques specific to PDI interferograms obtained here is a major effort in this quantitative evaluation. Instantaneous pressure distributions can now be obtained semi-automatically making practical the analysis of the thousands of interferograms that are produced in this research.

3. DESCRIPTION OF THE FACILITY AND MEASUREMENT TECHNIQUE

3.1. The Compressible Dynamic Stall Facility

The experimental studies were carried out in the Compressible Dynamic Stall Facility (CDSF) of the ARC Fluid Mechanics Laboratory. The CDSF is an indraft wind tunnel with a 10 in x 14 in test section and is equipped with a drive for producing a sinusoidal variation of the airfoil angle of attack. The tunnel Mach number is controlled by a choked, variable-area, downstream throat in the range of $0.1 \leq M \leq 0.5$. The flow is produced by a 6MW, 240,000 CFM continuously running evacuation compressor. The airfoil mean angle of attack can be set to $0 \leq \alpha \leq 15^\circ$, the amplitude of oscillation to $2^\circ \leq \alpha_1 \leq 10^\circ$, and the oscillation frequency to $0 \leq f \leq 100 \text{ Hz}$. In the CDSF a 3-inch

chord NACA 0012 airfoil is supported by pins between two 6 in diameter optical glass windows. This unique mounting method provides direct optical access to the airfoil surface permitting flow exploration using noninvasive diagnostic techniques, Fig. 1. Tests on a 6-inch chord airfoil mounted between metal ports, with glass inserts for optical access to the first 40% chord of the airfoil are used to establish Reynolds number effects produced at a given freestream Mach number. Blockage effects due to the larger airfoil are small around dynamic stall onset angles of attack. (The correction to pressures is less than 5% at $\alpha = 10 \text{ deg.}$) Encoders on the drive system record the mean and instantaneous angles of attack. The encoder signals are processed in a custom built interface known as the Oscillating Airfoil Position Interface (OAPI) which is also used for conditional sampling and phase locking.

3.2. Description of the PDI Technique

3.2.A. The Interferometry System

As stated earlier, the experimental studies used the real-time technique of point diffraction interferometry. PDI provides detailed, instantaneous and quantitative flow-field-density information, from which both surface and global pressure distributions can be derived. The PDI optical arrangement is similar to that of a schlieren system, but, as shown in Fig. 2, a laser light source is used with a beam expander to fill the entire field of view (determined by the tunnel windows) and a point diffractor (pin-hole) replaces the knife edge. The optics are aligned in the standard Z-type configuration to minimize astigmatism. Imaging optics are set up further downstream along the beam path for recording the flow.

The technique uses one single pass of the laser beam through the test section and depends upon the ability of a pin-hole created *in-situ* in a semi-transparent plate to produce the reference beam. Creation of the pin-hole requires focusing the laser beam on the plate and exposing the plate emulsion to a very high level of laser energy with no-flow in the tunnel. As the photographic emulsion burns away, a clear spot (pin-hole) appears on the plate. With the flow-on, light phase shifted by the flow density changes (signal beam) passes around this spot to produce interference fringes on a continuous basis in real-time. The portion of the beam passing through the pin-hole becomes the reference beam due to the spatial filtering characteristics of the pin-hole. The technique has now evolved considerably and several hundred interferograms can be obtained in a day's work.

3.2.B. Details of the High-Speed Camera, Laser Control and Recording Technique

A Qunatronix Series 100 CW/pumped Nd:YAG laser, capable of operating from DC to 50 KHz was used in the experiments. It could be externally triggered without any detectable delay at all rates. The pulse duration and the energy output varied nonlinearly from 85 ns and $140 \mu\text{J}$ at 500 Hz, 420 ns and $25 \mu\text{J}$ at 40 KHz and 100 ns and $11 \mu\text{J}$ at 50 KHz. At the rates used for the high-speed interferometry experiments being re-

ported, the corresponding numbers were: 140 ns and 65 μJ at 10 KHz and 240 ns and 17 μJ at 20 KHz, at nearly full current settings. The energy density in the laser light pulse at the 10 KHz rate was adequate to give proper exposure on ASA 100 T-MAX film; ASA 400 film was necessary at 20 KHz.

A variable speed Cordin drum camera (DYNAFAX Model 350) was used for image recording. A rotating 8-faceted mirror in the camera reflected the incoming light beam onto film rotating in the same direction in the camera drum. Effective shutter times of 1.35 μsec could be achieved at the 40 KHz framing rate. At 20 KHz, this time was 2.7 μsec . The camera recorded two rows of 16 mm images on a 35 mm film strip, with successive exposures recorded alternately in each row, but displaced by 16 frames. A maximum of 224 frames could be recorded at any framing speed.

The laser was triggered by TTL pulses emitted by custom designed and built (in-house) circuitry installed on the camera. An infrared (IR) emitter/detector was installed in the camera (out of the light path as shown in Fig. 3) to detect reflections from the mirror facets as they passed. The selected film was not sensitive to the 940nm IR wavelength. Each mirror facet detection produced two pulses using fast rise-time (1 nsec) photo diodes to ensure adequate signal level. The pulses were delayed from the time of the IR detection pulse. The time delays were calibrated so that the mirror facet was aligned with the image frame at the time of each laser pulse. Two photo diodes were placed in the camera, one at the frame position in each film track for calibrating the time delays, then removed for operation. The tuning procedure involved adjusting two delay times with the camera running: T_1 , the delay between detecting a mirror facet and emitting the first TTL pulse (the trigger pulse to the laser and for data collection) and T_2 , the time between the two TTL pulses (the time between frames). The delay times T_1 and T_2 were adjusted to maximize the laser light detected by the frame photo detectors. Once tuning was properly completed, the photo detectors were moved from the field of view to permit laser light to reach the film plane. The short effective shutter times (of 1.35 μsec at the maximum camera speed) and the high framing speeds required a careful design of the electronic system that included schemes for proper attenuation of noise.

The lenses in the PDI imaging optics could be adjusted to produce a focused image of the flow area at the film plane of the camera. Aligning the camera along the optical axis of the interferometry system required very accurate adjustment.

3.2.C. Operation

The interframe pulse delay was tuned to the desired rate and the actual rate of the camera was measured using a frequency counter. Several interferogram sequences were then obtained at 11.56 KHz and 19.62 KHz for varying initial phase angles. In order to maintain a consistent pulse energy level, the laser was triggered by an external pulse train at a 40 KHz rate before the images were acquired. This was necessary to protect the laser crystal from the giant pulse that

is normally generated when the laser is pulsed after a short lapse time. In order to prevent these pulses from exposing the film and for safety reasons, a solenoid actuated laser shutter was set up in front of the laser. A hand switch was used to initiate the controlled laser pulsing sequence, which is schematically described in Fig. 4. The corresponding timing sequence is shown in Fig. 5. After the switch was pressed, the circuitry was activated by an event pulse from the OAPI corresponding to the manually preselected angle of attack which in turn triggered the laser safety shutter. The laser pulsing circuit was then inhibited (for 1.1 msec) until the laser shutter fully opened. The laser was enabled at the expiration of the delay and was actually triggered from the next camera pulse, at which time the encoder was latched and recorded in a 512 word first-in-first-out (FIFO) buffer. During this short elapsed time, the laser built up sufficient charge to cause the first pulse to be a "small" giant-pulse, which over-exposed the first frame. This frame served to identify the first image on the film strip; thus, it was possible to accurately match the interferogram images with the phase angle of motion and to correlate the values in the FIFO buffer. A frame counter, started at the first laser-pulse event inhibited the laser after 200 laser pulses. Each film strip can record a maximum of 224 images. Following the completion of the imaging, the shutter was closed and the laser returned to the constant 40 KHz external triggering. The camera alignment was verified by taking test sequences on a Polapan ASA 125 film; the data was obtained on the higher resolution T-MAX 400 film.

3.2.D. Determination of Pressure Coefficients from Fringe Number

The quantitative nature of the interferograms allowed derivation of the pressure distribution over the airfoil when the flow was attached. The interferograms were processed in a manual mode using a specially developed software package. The program read a digitized (256 gray level) interferogram on an IRIS Work Station and over-layed an airfoil using the registration markers on the images. The intersection of the fringes with the airfoil upper and lower surfaces (or the local boundary layer edge, when detectable) were interactively picked by the user. Since each fringe is a line of constant density, the corresponding pressure at the boundary layer edge could be calculated using isentropic flow relations. This pressure was then used as the surface pressure, under the boundary layer assumptions. The density along any fringe could be calculated from the Gladstone - Dale equation, which for the present wind tunnel and laser simplifies to

$$\rho - \rho_r = 0.009421\epsilon$$

where ϵ , the fringe number, is $0, \pm 1, \pm 2, \dots$ for the bright fringes and $\pm \frac{1}{2}, \pm \frac{3}{2}, \pm \frac{5}{2}, \dots$ for the dark fringes. Fringes from the free stream to the stagnation point have positive values. The corresponding C_p values were then computed from the relation

$$C_p = \frac{\left[\left(\frac{\rho}{\rho_r} \right)^\gamma - 1 \right]}{\left[\frac{\gamma}{2} M^2 \right]}$$

In the end, the program provided an output data file containing the various physical variables, in a format suitable for plotting. Typical processing time was about 3 - 5 minutes per image. In cases where the fringe density was high or the fringes were fuzzy, the user could go into the 'off-body' mode and pick fringes along a line parallel to and away from the airfoil surface where the fringes are farther apart. For this purpose, an option to superpose two larger airfoils over the image on the screen was provided. The fringe intersections on the larger airfoils were then suitably projected on to the airfoil surface. At angles of attack near the dynamic stall angle, the fringes near the leading edge region were very dense reflecting the large local density gradients. Further, in this region, optical noise introduced by the shadowgraph effect generally lowered the contrast, making it a location where the off-body mode needed to be invoked.

In the present study the entropy change in the vortical flow was ignored (for lack of a better method). Interferograms with shocks have not been processed for pressures because of this limitation.

3.3. Details of Image Processing

Aside from these manual procedures, a program was also developed for automatic analysis of the interferograms. A number of digital filters and image enhancement procedures are available. The operator is required to register the image (thus masking the airfoil and establishing a coordinate system), choose the filtering and/or enhancement methods, and mark regions of the image for special treatment. Fringe centerlines are automatically traced with processing times approximately one quarter that of fully-manual processing, and operator bias (a potential source of error in the tracing of fringes) is eliminated.

Full automation of image processing requires software capable of addressing the special characteristics of these images, such as variations in lighting and contrast across an image that are inherent to the technique, an occasional broken (or split) fringe, the high fringe density near the suction peak (as many as 50 fringes/mm along the airfoil surface), presence of shocks, etc. Full details of the image processing method, e.g. image filtering, fringe centerline detection, fringe identification, etc., can be found in Ref. 5. The flow chart shown in Fig. 6 illustrates the typical processing procedure. The need for the spin filter, an intensity gradient aligned spatial filter (Ref. 7), depends on the quality of the original image. Filtering and/or contrast enhancement are performed primarily to improve edge detection, the first stage in fringe centerline detection, as described below. For the results presented here, the region around the leading edge of the airfoil was magnified and treated separately from the rest of the image.

Fringe centerlines are located by identifying the local extrema in the image intensity. These extrema are

identified within the background noise through a two-stage procedure which first locates the fringe edges, and then fits a smooth polynomial to the data between successive edges. The location of the extreme value of the approximated data is taken as the location of the fringe centerline. This procedure is a one dimensional operation performed in two passes over the image; rows of pixels are examined in the first pass and columns are examined in the second pass.

A zero-crossing algorithm is used to identify the fringe edges. The zero-crossing threshold level is either the mean intensity along the row or column of pixels under consideration, or the global mean intensity of the image. The global mean is used if the current row or column follows a fringe or crosses only one edge. A noise band around the threshold is specified to eliminate hysteresis crossings due to noise in the image.

The edges are used as a guide to locating the fringe centerlines. Assuming that each successive pair of edge points outline a single fringe, the centerline of the fringe will pass through the point of extreme intensity between these two edge points. In order to unambiguously locate this extreme, a smooth polynomial curve is fit to the data between pairs of edge points using Chebyshev approximation. The image intensity is approximated on the interval $[-1, 1]$ as

$$I(x) \approx \sum_{k=0}^{m-1} c_k T_k(x) - \frac{1}{2} c_0$$

where the Chebyshev polynomials and the coefficients are given by

$$T_k(x) = \cos(k \cos^{-1} x)$$

and

$$c_k = \frac{2}{N} \sum_{j=1}^N I(x_j) T_k(x_j)$$

respectively, and the data ($I(x)$) and the Chebyshev polynomials ($T_k(x)$) are evaluated at the N zeros of $T_N(x)$, namely

$$x_j = \cos\left(\frac{\pi(j - \frac{1}{2})}{N}\right) \quad j = 1, 2, \dots, N.$$

The coefficients are calculated for Chebyshev polynomials of degree N , while the approximating polynomial is truncated to a polynomial of degree $m \ll N$ (typically $N = 20$, $m = 3$). This yields an accurate approximation of degree m to the data [8]. For sufficiently large N , as $m \rightarrow N$ the approximating polynomial reproduces the original data, including the noise. Due to the multiple inflection points in the data, approximating data spanning more than one fringe requires a higher order polynomial (m), which tends to reproduce the noise content. Therefore, the approximation procedure is confined to a single fringe.

This procedure was tested on simulated fringe data (a modulated cosine function with added Gaussian noise) and was found to be accurate to within 2 pixels for

fringes from 5 to 40 pixels in width and to within 5 pixels for fringes up to 240 pixels wide.

The points located this way comprise two sets of pixels, one associated with the dark fringe centerlines and the other with the light fringe centerlines. These data sets form two search lists which are sorted into smaller groups, each tracing a single fringe. Tracing begins arbitrarily with the first point in the search list. A nearest neighbor search is performed with an inner and outer search radius. Any point within the inner search radius of the current point is automatically designated as belonging to the current fringe. Any point found between the inner and outer search radii are assigned to the current fringe if certain criteria are satisfied. These criteria are designed to prevent the tracing procedure from bridging adjacent fringes by examining the image intensity across the gap and by checking for the presence in the gap of data points belonging to the opposite fringe type. Each data point assigned to a fringe is removed from the search list. The search is then repeated relative to each new point added to the fringe in the previous search. The search ends when the end of the fringe is reached or when a gap larger than the outer search radius is encountered. A new fringe is designated and the tracing procedure begins anew with the first point in the search list becoming the first point in the new fringe. The tracing is progressively faster as data points are removed from the search list and placed in fringe lists.

The inner search radius is two pixels, hence, any one-pixel gaps in the data are automatically bridged. The outer radius varies with fringe spacing and is six pixels in the outer flow regions where the fringe spacing is wide, and reduces to three pixels near the leading edge where fringe spacing is often less than five pixels. Due to the small fringe spacing in this region any noise in the data can cause the fringe tracing algorithm to erroneously join fringes together. Therefore, the leading edge is generally treated separately in the form of a magnified image segment.

3.4. Experimental Uncertainties

The uncertainty in C_p depends on the fringe number under consideration and is 1 fringe for the flow in general with about 3 fringes possibly undetectable near the suction peak at $M = 0.3$. Since correction for solid and wake blockage was less than 5% for $C_p = -6.0$ at $M = 0.3$, only uncorrected PDI derived pressures are reported. The losses in the tunnel screens causing a decrease in the stagnation pressure have been included in the computation of the reference density in this otherwise atmospheric flow wind tunnel.

By far the largest uncertainty appears from the very strong density gradients near the airfoil leading edge which introduces strong refractive index gradients. The effect of this is to deflect the light rays towards higher density regions. Hence, a dark region develops on the upper surface near the leading edge (Ref. 6) in some images. No corrections were applied to the C_p values on this account because of the strong dependence of the local density on instantaneous angle of attack, freestream Mach number, and reduced frequency. Also, it was found that by slightly realigning

the PDI optics, much of the distortion could be reduced. With this solution, it was estimated that the true suction peak location could be displaced by less than 0.5% of airfoil chord towards the trailing edge. Support for this can be found by directly comparing the pressures measured using surface taps and those obtained with PDI as shown in Fig. 7 (Ref. 9) for the 6-inch airfoil in steady flow at $M = 0.3$. At $\alpha = 8$ deg, Fig. 7a, the two agree very well. At $\alpha = 13$ deg, Fig. 7b, there is agreement to within the one fringe standard uncertainty of the PDI method. The differences seen at the laminar separation bubble location are due to the insufficient number pressure taps over the airfoil that make it impossible to record the pressures at the resolution of PDI.

With these considerations in mind, the following are the estimated uncertainties in the data:

Mach number:	± 0.005
angle of attack:	0.05 degrees
reduced frequency:	0.005
C_p :	± 0.1 at $M = 0.3$
$C_{p_{min}}$:	-0.5 at $M = 0.3$
	-0.45 at $M = 0.4$

4. RESULTS AND DISCUSSION

Figure 8 presents two interferograms obtained in the studies at $M = 0.3$, $k = 0.05$ and $\alpha = 10$ deg. Fig. 8a shows a standard PDI interferogram, whereas that in Fig. 8b was obtained using the high-speed PDI imaging method at a filming rate of 11.56 KHz. The sharpness of the image in Fig. 8a indicates the quality of the pictures that can be obtained with PDI. The high-speed image in Fig. 8b is still clean even after a linear magnification of about 35. The figure shows a stagnation point on the lower surface and as the flow accelerates, a laminar separation bubble forms downstream of the suction peak. The separation bubble can be inferred where the fringes running parallel to the upper surface abruptly turn normal to the surface. The parallel fringes represent the plateau in the pressure distributions due to the presence of the bubble. In both figures, a slight dark bulge is noticeable near the airfoil leading edge, which is attributed to the steep local density gradient. The global pressure maps are shown in Fig. 9 for the airfoil at an instantaneous angle of attack of 13.99 deg. The comparison also clearly illustrates the differences that can be present in the flow from one oscillation cycle to the next at angles near the dynamic stall onset angle. These differences are especially critical when considering dynamic stall control. Our work has shown that dynamic stall for these test conditions arises from the bursting of a laminar separation bubble, which occurs when the instantaneous pressure gradient exceeds a critical value and so the envelope of activation of a control device for manipulating the adverse pressure gradient will change for each cycle.

Figure 10 shows the effects of pin-hole size on the PDI images at $M = 0.4$. Evaluation of the pin-hole requires recording PDI images on polaroid film. The photographic plate needs to be pre-developed to a level of darkness that results in an optical density of around 1.0. The PDI images were found to be generally insen-

sitive to the shape and size of the PDI spot in the range tested as long as the spot is smaller than the Airy disk diameter of the laser beam. Good interferograms were obtained with pin-holes created by images of both the nearly circular windows and the L-shaped optical glass inserts. The most noticeable effect of a large pin-hole is the many split fringes that form as seen in Fig. 10. These can lead to an incorrect counting of the fringes, causing erroneous pressure distributions to be derived from the automated processes. It should be noted that satisfactory interferograms have been obtained in these studies over a range of pin-hole sizes. Also, somewhat large pin-holes are needed as the flow Mach number increases due to the large density gradient and hence a larger deflection of the laser light near the leading edge. Images can be obtained reliably without much effort if a PDI plate with the right optical density is used for each Mach number. In general, it has been found that a dark plate (optical density of the $O(1)$) is needed to properly capture the finer flow details for the Mach numbers in the range of 0.3-0.45. Lighter plates worked well at lower Mach numbers.

Figures 11 and 12 show the results that have been obtained with the automated image processing program for $M = 0.3$ and $M = 0.45$ respectively. The image in Fig. 11a shows the airfoil at $\alpha = 8.84$ deg for $M = 0.3$ and $k = 0.05$. The corresponding map of the dark fringes is plotted in Fig. 11b. Fig. 12a and 12b show, respectively, an image and its fringe map obtained at $M = 0.45$, $k = 0.05$ and $\alpha = 10^\circ$ on the upstroke. Under these conditions the local velocity exceeded the sonic speed and an oblique shock formed. Moreover, the interaction between the shock and the laminar boundary layer ($Re = 9 \times 10^5$) resulted in the formation of multiple shocks. An enlarged view of the leading edge is shown to emphasize the shocks. The image was magnified by three and was contrast enhanced. No filtering was required. Despite the tight fringe spacing, and distortions due to the shocks considerable success has been achieved in processing the image without manual intervention. Typical processing times were about 5 min. with complicated images requiring longer times.

5. CONCLUSIONS

A novel high-speed, real-time, phase-locked, interferometry system has been developed and applied to study oscillating airfoil compressible dynamic stall flow fields. The technique can generate very sharp images of the flow over an airfoil and can capture the rapid evolution of shocks in this complicated flow. A maximum of 224 interferograms per test condition at rates of up to 40 KHz can be recorded using the system. To date, several thousand images have been obtained at rates of up to 20 KHz. A comprehensive image processing software package has also been developed for processing these large number of interferograms. The software has reduced the time required for this task considerably. It includes features for special treatment of each image using digital filtering, contrast enhancement, local magnification for high fringe density regions, accurate fringe centerline detection, fringe identification, etc. Interferograms containing multiple shocks in the flow have also been satisfactorily analyzed. The effects of vari-

ables such as PDI plate optical density, pin-hole size, etc., have been investigated. The technique is robust, easy to set-up and offers considerable advantages over other interferometric methods. It is a real-time, self-aligning technique and is not affected by extraneous influences such as tunnel vibrations.

Acknowledgements

The project was supported by U.S. Air Force Office of Scientific Research through grants, AFOSR-ISSA-89-0067 and AFOSR-MIPR-92-0004. The continued support received from the Army Research Office through grant ARO MIPR-96-7 to the Naval Postgraduate School that enabled the preparation of this manuscript, the steady support and encouragement of Dr.S.S. Davis, Chief, FML Branch, and the support of Mr.D.D. Squires, Sverdrup Technology, Inc., in the development of the control electronics are all sincerely appreciated.

References

1. Carr, L.W. and Chandrasekhara, M.S., "Design and Development of a Compressible Dynamic Stall Facility", *J. Aircraft*, 29, 3, pp. 314-318, 1992.
2. Chandrasekhara, M.S. and Carr, L.W., "Compressibility Effects on Dynamic Stall of Oscillating Airfoils", in "Aerodynamics and Aeroacoustics of Rotorcraft", AGARD-CP-552, Aug. 1995, Paper 3.
3. Brock, N.J. Chandrasekhara, M.S. and Carr, L.W., "A Real Time Interferometry System for Unsteady Flow Measurements", *ICIASF '91 RECORD*, IEEE Publication 91CH3028-8, pp. 423-430.
4. Chandrasekhara, M. S. Squires, D.D. Wilder, M.C. and Carr, L.W., "A Phase-Locked High-Speed Real-Time Interferometry System for Large Amplitude Unsteady Flows", *Expts. Fluids*, 20, 1995, pp. 61-67.
5. Wilder, M.C. Chandrasekhara, M.S. and Carr, L.W., "Computer-Aided Analysis of Interferometric Images of Unsteady Aerodynamic Flows", *ICIASF'95 RECORD*, IEEE Publication 95-CH3482-7, pp. 44.1-44.11.
6. Cho, Y.C. Carr, L.W. and Chandrasekhara, M.S., "Corrections to Fringe Distortion due to Flow Density Gradients in Optical Interferometry", *AIAA* 93-0631, January 1993.
7. Yu, Q., "Spin Filtering Processes and Automatic Extraction of Fringe Centerlines in Digital Interferometric Patterns", *Applied Optics*, 27, 18, September 1988, pp. 3782-3784.
8. Press, H.P., Teulolsky, S.A., Vetterling, W.T., and Flannery, B.P., "Numerical Recipes in C", Cambridge, U.K., Cambridge University Press, 1992, (ISBN 0-521-43108-5), pp. 190-196.
9. Chandrasekhara, M.S. Wilder, M.C. and Carr, L.W., "Reynolds Number Influence on 2-D Compressible Dynamic Stall", *AIAA* 96-0073, January 1996.

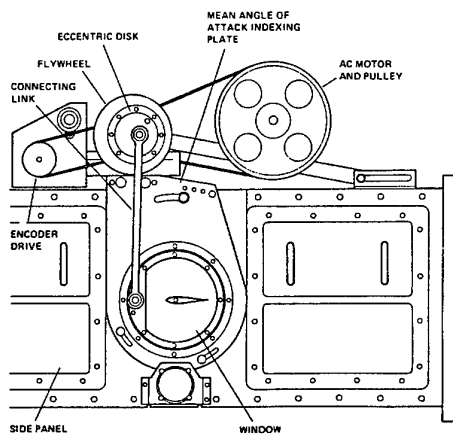


Fig. 1. Schematic of the Compressible Dynamic Stall Facility.

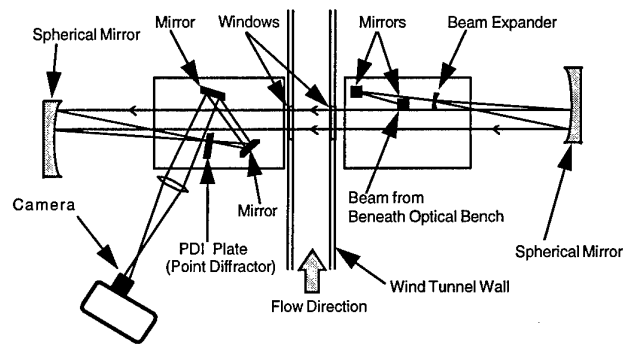


Fig. 2. Schematic of the Point Diffraction Interferometry System.

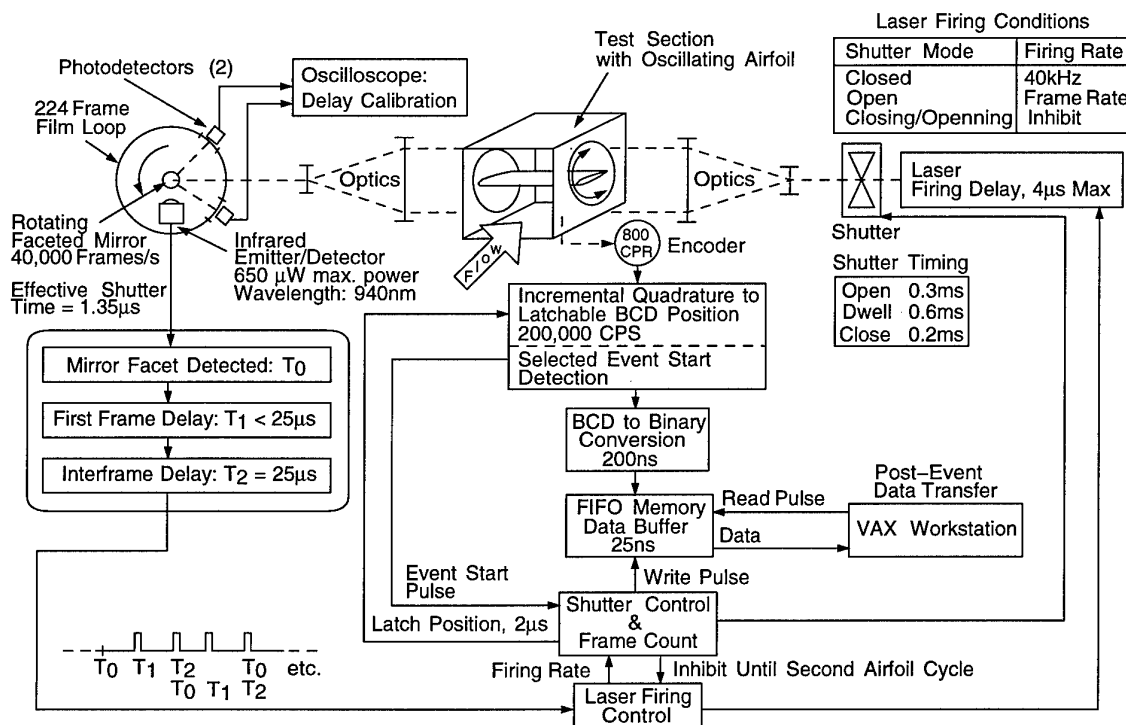


Fig. 3. Block Diagram of Camera/Laser Synchronization for the High-Speed PDI System.

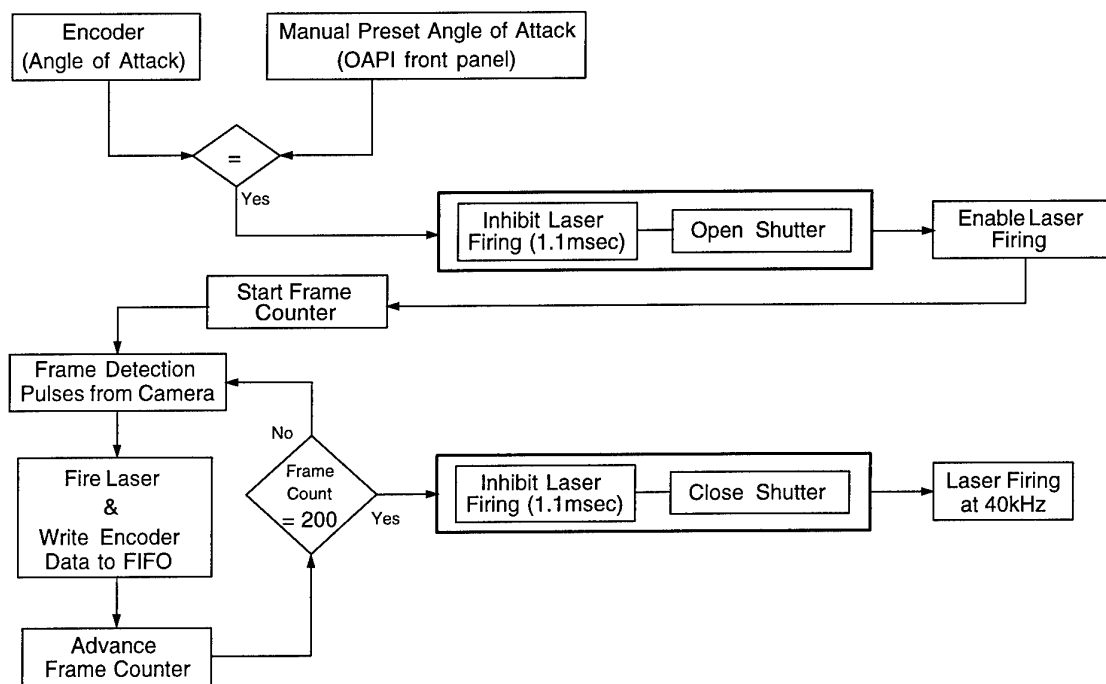


Fig. 4. Flowchart of Events Following Handswitch "FIRE" for the High-Speed Interferometry System.

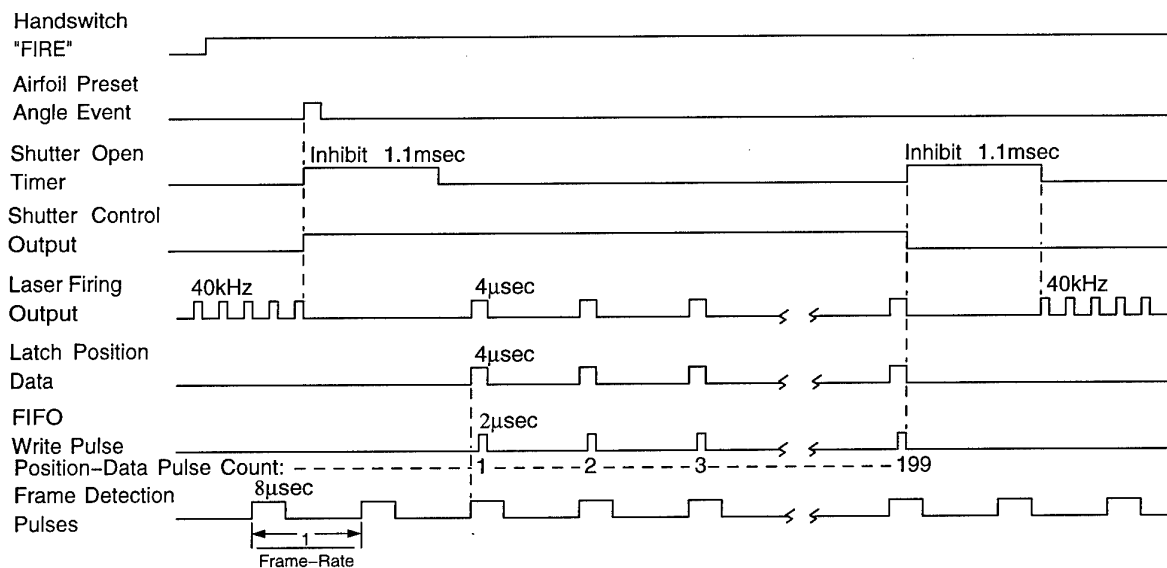


Fig. 5. Timing Sequence for the High-Speed Interferometry System.

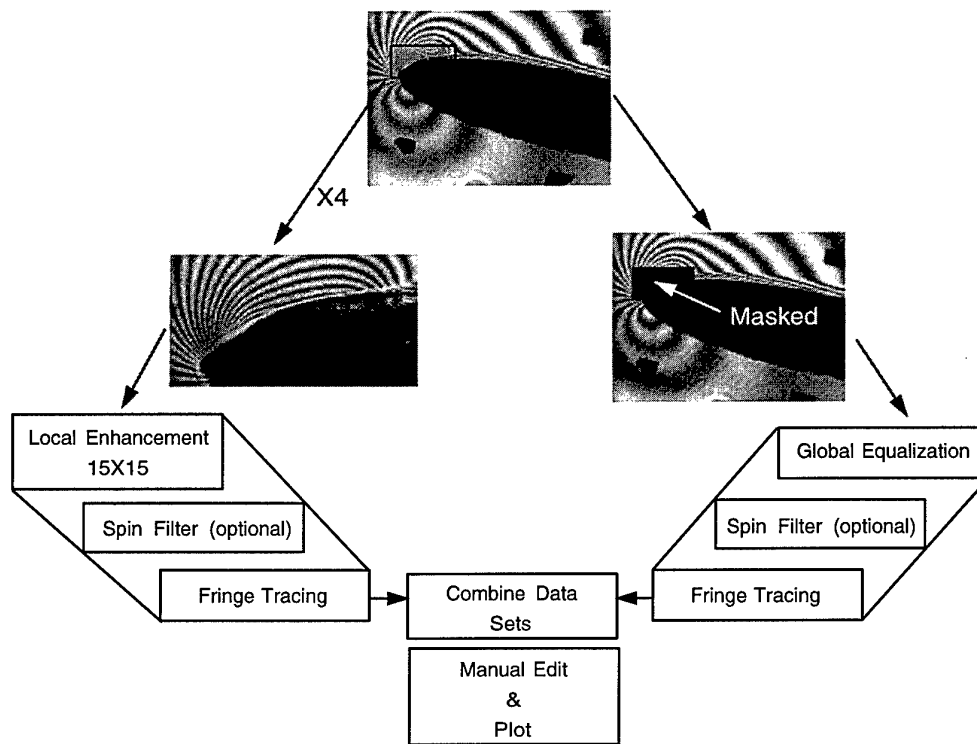
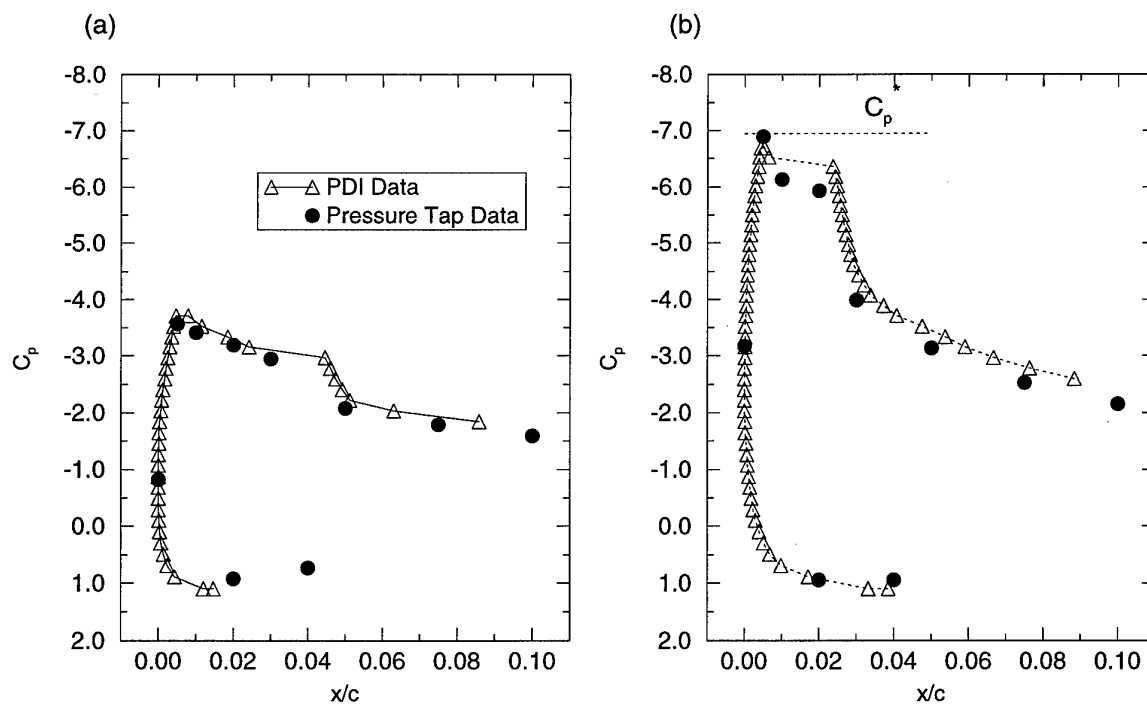


Fig. 6. Flow Chart of Fringe Analysis Procedure.

Fig. 7. Comparison of Pressure Tap Measurements with PDI Determined Pressure Coefficients; $M = 0.3$, $k = 0$. (a) $\alpha = 8.0$ deg, (b) $\alpha = 13.0$ deg.

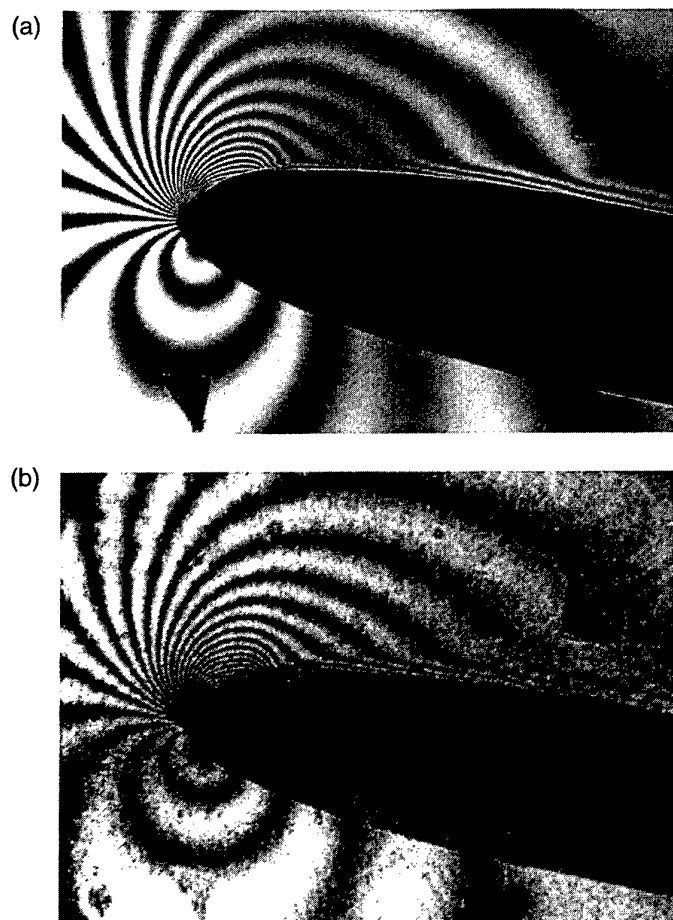


Fig. 8. Representative Interferograms of the Flow Field; $M = 0.3$, $k = 0.05$, $\alpha = 10.07$ deg.
(a) Single Exposure Camera, (b) High-Speed Camera.

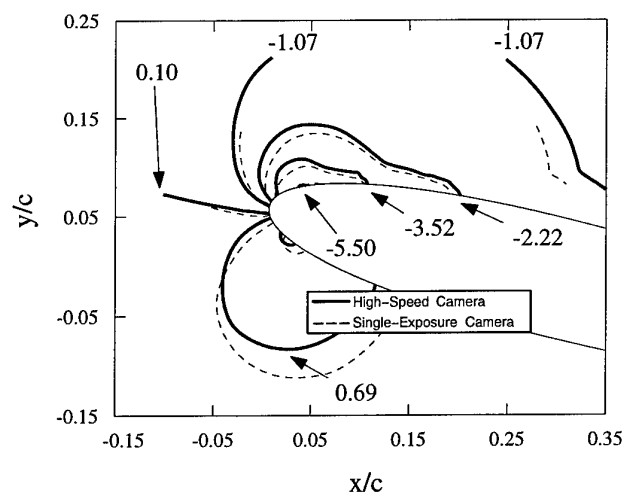


Fig. 9. Comparison of the Global Pressure Distributions at $M = 0.3$, $k = 0.05$,
 $\alpha = 13.99$ deg for Different Oscillation Cycles.

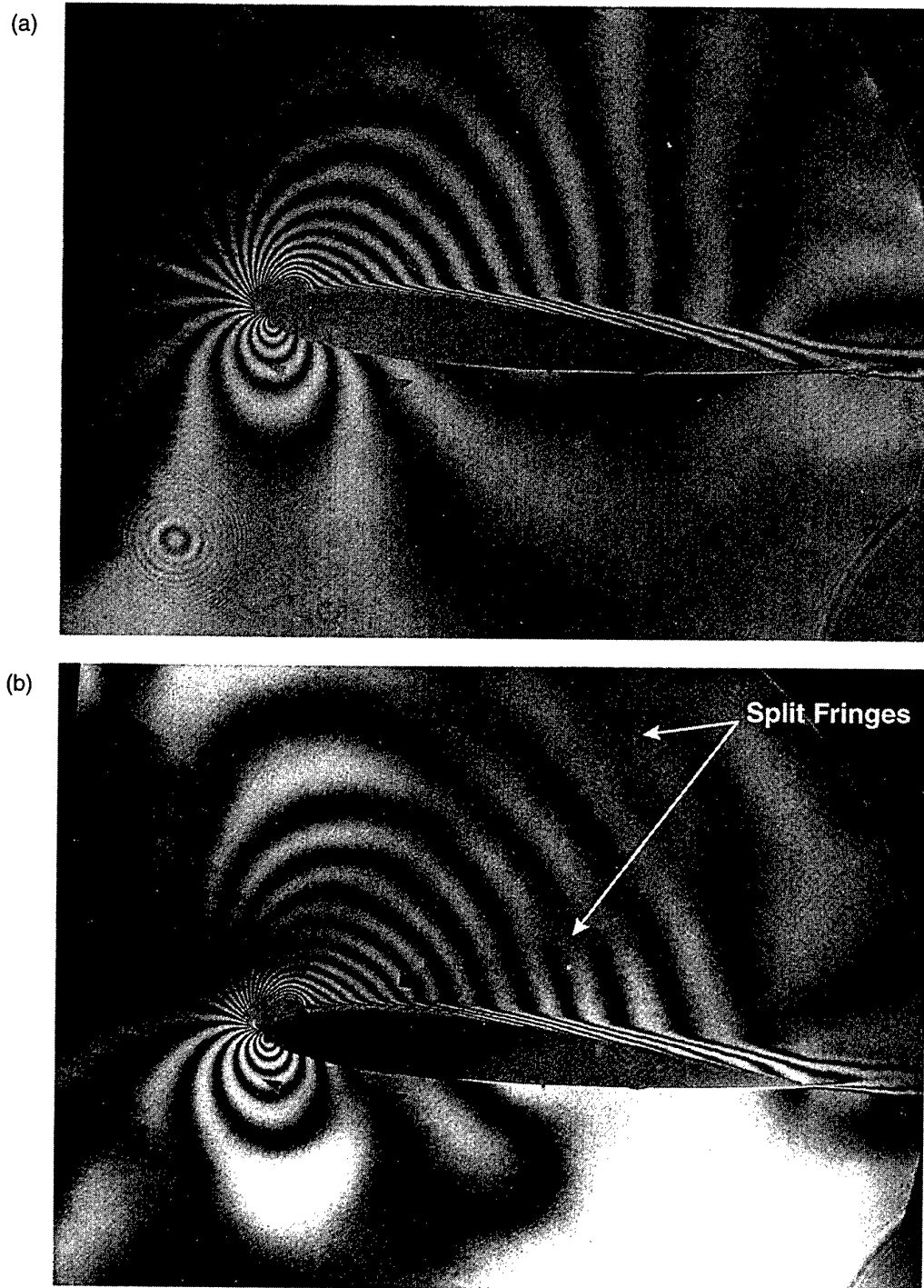


Fig. 10. Effect of Pin-Hole Size on PDI Images; $M = 0.4$, $k = 0$, $a = 8$ deg.
(a) Small Pin-Hole, (b) Large Pin-Hole.

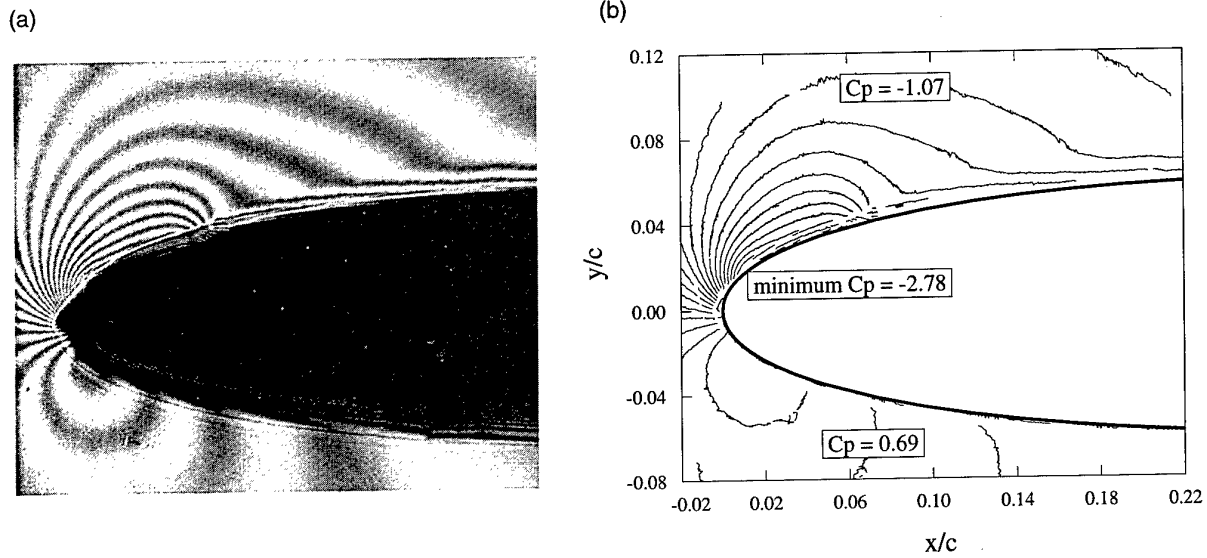


Fig. 11. Automated Image Processing; $M = 0.3$, $k = 0.05$, $\alpha = 8.84$ deg. (a) Leading-Edge Region of PDI Image, (b) Map of Dark Fringes.

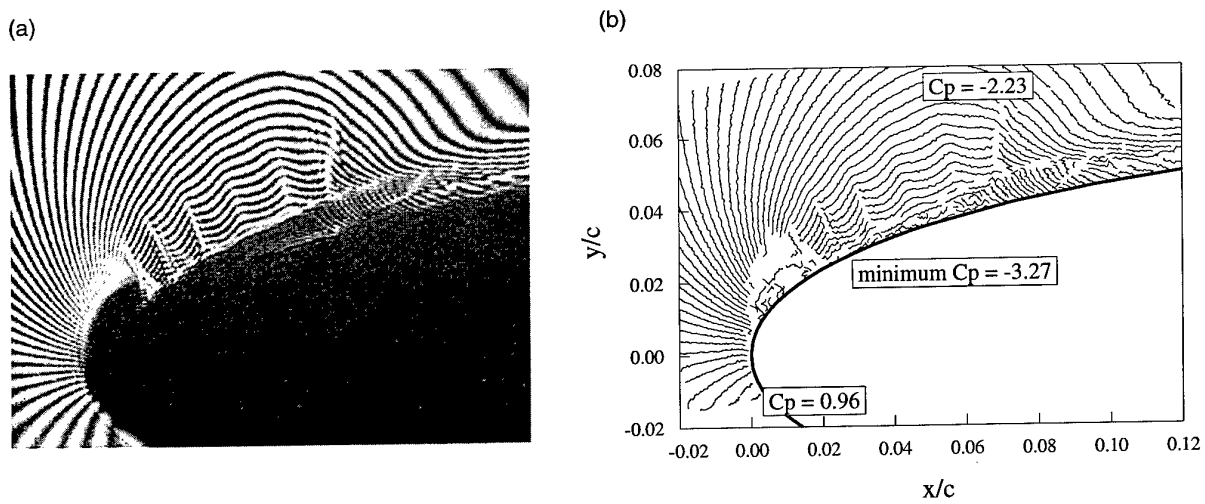


Fig. 12. Automated Image Processing; $M = 0.45$, $k = 0.05$, $\alpha = 10.0$ deg. (a) Digitally Enlarged Region of PDI Image, (b) Map of Dark Fringes.

Wall-shear stress measurement with quantitative IR-thermography

R. Mayer, R.A.W.M. Henkes and J.L. van Ingen

Delft University of Technology,
Faculty of Aerospace Engineering,
Kluyverweg 1,
2629 HS Delft,
The Netherlands

Summary

This paper presents a new non-intrusive and flexible measurement technique for wall-shear stresses, which is based on the theory of hot-films. To overcome the disadvantage of being limited to a single measurement position like the hot-film, the internal electrical heating and internal temperature detection is replaced by external heating using a laser and external temperature measurement using quantitative infrared thermography, respectively.

In this technique the laser is generating a hot spot on the surface of an object. By choosing suitable materials for the solid object with a low thermal conductivity and a high emissivity of thermal radiation a geometrically small but clearly detectable temperature spot can be generated. After the temperature distribution in the solid has become steady, the laser is turned off and the temperature decay of the hot spot is monitored by the camera. From the measured surface-temperature distribution history the heat transfer to the fluid and the wall-shear stress can be derived by using a numerical procedure.

This technique is demonstrated for a Blasius boundary layer in a wind-tunnel experiment, where an accuracy of about 10% has been achieved in the determination of the wall-shear stress.

LIST OF SYMBOLS

a	thermal diffusivity
c	specific heat capacity
c_f	wall-shear stress coefficient, $\frac{\tau_w}{\frac{1}{2}\rho U_e^2}$
h	solid thickness
k	thermal conductivity
L	reference plate length
q_f	wall-heat transfer at the fluid side
q_{ir}	net irradiated laser power
q_s	wall-heat transfer at the solid side
Re_x	local Reynolds number, $Re_x = \frac{U_e x}{\nu}$
T	temperature
u, v	velocity components in x and y -direction
U_e	velocity at the boundary-layer edge
x, y	coordinates along and normal to the plate
δ_T	thermal boundary-layer thickness
δ_U	velocity boundary-layer thickness
ΔT^*	reference temperature difference

ζ	non-dimensional y -coordinate, $y \left(\frac{\tau_w}{\mu a(x-x_0)} \right)^{1/3}$
Θ	non-dimensional temperature, $\frac{T-T_e}{T_w-T_e}$
Θ^*	non-dimensional temperature, $\frac{T-T_e}{\Delta T^*}$
μ	dynamic viscosity
ν	kinematic viscosity
ξ	dimensionless x -coordinate, $\frac{x-x_0}{L}$
ρ	density
τ_w	wall-shear stress, $\mu \left. \frac{\partial u}{\partial y} \right _w$

Subscripts

0	start of the thermal boundary layer
e	boundary-layer edge
f	fluid
s	solid
w	wall

1 Introduction

In 1904 Prandtl has shown that any flow around a solid object can be divided into two regions: a thin region near the surface of the object, e.g. the *boundary layer*, where viscous effects are significant and the outer flow, which can be assumed to be inviscid. Due to the viscosity the tangential flow velocity u increases asymptotically from zero at the wall to the outer-edge velocity U_e . The resulting normal velocity gradient $\partial u / \partial y$ at the wall causes wall-shear stresses. The wall-shear stress and pressure distribution along an object determine its drag and thus the fuel consumption in the case of flows around vehicles.

Because of the importance of the wall-shear stress in drag reduction, a variety of measurement techniques has been developed. The floating-element method directly measures the force on a small plate inserted flush into the surface of the object. The wall-shear stress can also be determined by measuring the velocity gradient $\partial u / \partial y$ at the wall with the help of pressure probes, hot-wire anemometry or laser-Doppler anemometry. Since there is a relation between momentum- and heat exchange, the wall-shear stress can also be determined indirectly by measuring the heat transfer from a heated surface to the fluid (see e.g. Fage and Falkner [1]). This relation is used by hot-films, which comprise electrical heating and temperature measurement in the material of the surface of the film. The rela-

tion between the surface wall-heat transfer q_f to the fluid and the wall-shear stress τ_w is found by calibration (see *e.g.* Mathews and Poll [2]). With certain simplifications also an analytical similarity relation between the wall-shear stress and the wall-heat transfer can be found. Using this relation a new type of hot-film, which is referred to as the integrated silicon flow sensor (Van Oudheusden [3]), has been developed at the Faculty of Electrical Engineering in cooperation with the Faculty of Aerospace Engineering of the Delft University of Technology. The setup of the integrated silicon flow sensor is sketched in figure 1.

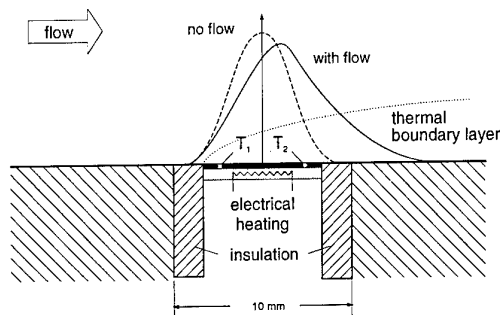


Figure 1: Integrated silicon flow sensor.

The sensor consists of an electrical heating, and four thermocouples measuring the temperature at the four sides of the rectangular sensor. Due to the flow the symmetrical electrical heating system generates an asymmetrical hot spot over the sensor. With the known electrical power of the heater and the temperature differences in two directions both wall-shear stress components along the sensor can be determined.

Next to wall-shear stress sensors, infrared thermography (IR-thermography) has also been introduced for wall-shear stress investigations. With the help of IR-thermography the surface temperature of an object can be measured using an IR-camera. As the wall-shear stress and the heat transfer at the surface are both dependent on the nature of the boundary layer (laminar, turbulent, separation) transition and separation of the flow along a heated object can be detected by a sudden variation of the surface temperature visualized by the IR-camera. Figure 2 shows the temperature variation in the transition region on an airfoil (Boermans [4]).

This technique is purely *qualitative*, because as long as the camera can detect the small variations of the surface temperature due to transition or separation, neither the precise value of the surface temperature nor the precise value of the wall-shear stress needs to be known. Due to the rather simple experimental setup, qualitative IR-thermography has been successfully applied to transition and separation detection for subsonic and transonic (Crowder [5]), as well as for hypersonic flows (Boerrigter and Charbonnier [6]).

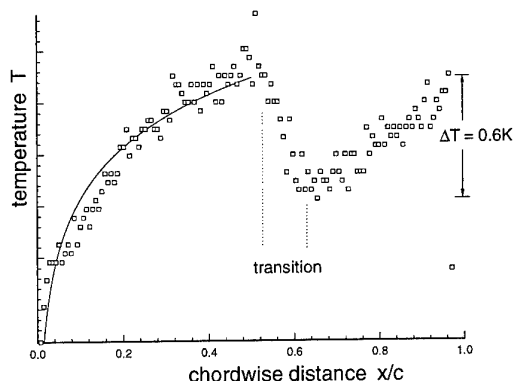


Figure 2: Variation of the surface temperature due to flow transition.

Motivated by the advantages of IR-thermography a new measurement technique has been developed, which is not only able to give a qualitative overview of the wall-shear stress distribution, but which can also give the local wall-shear stress quantitatively. As this measurement technique relies on the accurate measurement of the surface temperature, this technique is referred to as *quantitative* IR-thermography. In comparison to hot-films, the electrical heating is replaced by externally irradiated energy of a laser and the internal surface temperature measurement is replaced by an external measurement performed by an IR-camera. The laser first generates a hot spot until steady state conditions are reached. The surface-temperature measurement at steady state conditions is used to compute the initial temperature distribution in the solid object. After turning off the laser the IR-camera monitors the temperature decay. The measured unsteady surface temperature is used as boundary condition to calculate the heat transfer inside the solid object, which gives, through the total heat balance, the heat transfer from the solid to the flow q_f . In the same way as for the integrated silicon flow sensor, the local wall-shear stress τ_w along the hot spot can then be determined.

Quantitative IR-thermography for the measurement of wall-shear stresses offers two main advantages. Firstly the measurement is non-intrusive, which means that the flow is not disturbed by the presence of a measurement probe. Secondly the measurement point can easily be changed by traversing the laser beam and the IR-camera.

2 Mathematical Formulation

The new technique is in first instance designed to measure the wall-shear stress in low-Mach-number flows, which implies that the properties of the fluid like density, specific heat capacity and viscosity are

constant and that frictional heating can be neglected. To simplify the development of this technique the investigation is also restricted to two-dimensional flows as well as to two-dimensional heat transfer in the fluid and in the solid. Therefore the momentum and the energy transport in the boundary layer can be described by the following set of equations

$$\frac{\partial u}{\partial x} + \frac{\partial v}{\partial y} = 0, \quad (1)$$

$$u \frac{\partial u}{\partial x} + v \frac{\partial u}{\partial y} = -\frac{1}{\rho_f} \frac{dp}{dx} + \nu \frac{\partial^2 u}{\partial y^2}, \quad (2)$$

$$\frac{\partial T}{\partial t} + u \frac{\partial T}{\partial x} + v \frac{\partial T}{\partial y} = a \frac{\partial^2 T}{\partial y^2}. \quad (3)$$

The x -direction corresponds to the flow direction and the y -direction is defined normal to the surface. It is assumed that the velocity boundary layer (described by equation (1) and (2)) is steady and independent of the temperature, but the thermal boundary layer (described by equation (3)) can be unsteady because of the varying surface temperature. The relation between q_f and τ_w , which is used in this investigation, is based on the thermal boundary layer equation. As the surface is only locally heated the equations can be simplified. In contrast to the velocity boundary layer, which starts to grow at $x = 0$, the thermal boundary layer starts at x_0 which is defined as the position where the wall temperature first differs from the ambient temperature. The velocity boundary layer and the thermal boundary layer along the laser-induced hot spot are sketched in figure 3. Details about how a two-dimensional hot spot with a small size in x -direction and a constant temperature in z -direction is generated will be presented in section 3.

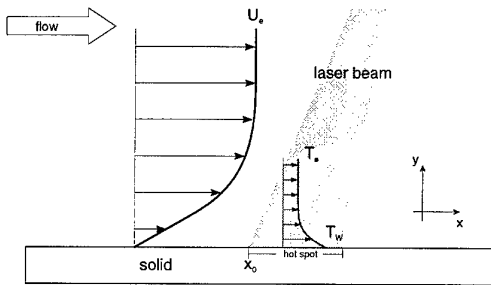


Figure 3: Velocity and thermal boundary layer along a hot spot.

If the hot spot is sufficiently small equation (3) can be further simplified. Using Taylor expansions for the velocity components $u(x, y)$ and $v(x, y)$ in the spot region, the boundary-layer equations give

$$u(x, y) = \frac{\tau_w}{\mu} y + \frac{1}{2\mu} \frac{dp}{dx} y^2$$

$$+ \frac{1}{\mu} \frac{d\tau_w}{dx} (x - x_0) y + \text{3rd order terms},$$

$$v(x, y) = -\frac{1}{\mu} \frac{d\tau_w}{dx} y^2 - \frac{1}{2\mu} \frac{d^2\tau_w}{dx^2} (x - x_0) y^2 - \frac{1}{6\mu} \frac{d^2p}{dx^2} y^3 + \text{4th order terms}.$$

Hence we have to leading order:

$$u(x, y) = \frac{\tau_w}{\mu} y \quad \text{and} \quad v(x, y) = -\frac{1}{\mu} \frac{d\tau_w}{dx} y^2, \quad (4)$$

which only depends on the wall-shear stress, and is independent of the pressure gradient. Substituting approximation (4) in the thermal boundary layer equation (3) gives

$$\frac{\partial T}{\partial t} + \frac{\tau_w}{\mu} y \frac{\partial T}{\partial x} - \frac{1}{\mu} \frac{d\tau_w}{dx} y^2 \frac{\partial T}{\partial y} = a \frac{\partial^2 T}{\partial y^2}. \quad (5)$$

For small local heating it can be further assumed that the x derivatives of the velocity boundary layer (including $d\tau_w/dx$) are much smaller than the x derivatives in the thermal boundary layer. Thus the thermal boundary layer approximately develops in a parallel flow with a linear velocity profile. It can also be shown that the unsteady term in equation (5) can be neglected. As the temporal variation of the surface temperature depends on the heat transfer inside the solid and the heat capacity of the air fluid layer ($\rho_f c_{fl} \delta T$) is much smaller than the heat capacity of the solid ($\rho_s c_s h$, with h being the thickness of the solid layer), the heat transported from the solid to the fluid is almost completely convected downstream in the fluid layer, whereas only a small portion is needed to locally heat up the fluid. The fluid almost immediately adjusts to the temperature changes on the surface of the solid, and the thermal boundary layer can be treated as "quasi" steady. Therefore the thermal boundary layer along the hot spot can be described by

$$\frac{\tau_w}{\mu} y \frac{\partial T}{\partial x} = a \frac{\partial^2 T}{\partial y^2}. \quad (6)$$

Although equation (6) has been derived from the laminar boundary layer equations, it is in principle also valid for turbulent boundary layers as long as it can be assumed that the thermal boundary layer still develops in a parallel flow with a linear velocity profile. To fulfill this assumption measurements in a turbulent boundary layer require much smaller hot spots than measurements in a laminar boundary layer.

To find the similarity solution for equation (6) (see e.g. Lighthill [7]), a sudden jump in the wall temperature from the ambient temperature T_e for $x <$

x_0 to the constant temperature T_w for $x > x_0$ is considered. By introducing the dimensionless variables

$$\xi = (x - x_0)/L, \quad \zeta = y \left(\frac{\tau_w}{\mu a(x - x_0)} \right)^{1/3}$$

$$\Theta = \frac{T - T_e}{T_w - T_e},$$

where L is an arbitrary length scale, equation (6) can be transformed into

$$\Theta'' + \frac{1}{3}\zeta^2\Theta' = 0, \quad (7)$$

where a prime denotes differentiation to ζ . Using the boundary conditions $\Theta(0) = 1$ and $\Theta(\infty) = 0$, the solution of this similarity equations reads

$$\Theta(\zeta) = 1 - C \int_0^\zeta \exp\left(-\frac{1}{9}\zeta^3\right) d\zeta, \quad (8)$$

with $C = 0.5384654921$.

Differentiation of the temperature gives the similarity solution for the wall-heat transfer q_f for a constant wall temperature:

$$\frac{q_f L}{k_f(T_w - T_e)} = C \left(\frac{\tau_w L^2}{\mu a} \right)^{1/3} \xi^{-1/3}. \quad (9)$$

Since equation (6) is a linear differential equation in the temperature, the solution for an arbitrary surface temperature distribution can be written as a superposition of infinitesimal stepwise wall temperature variations $d\Theta^*$ at ξ^* . In this way equation (9) can be generalised to

$$\frac{q_f L}{k_f \Delta T^*} = C \left(\frac{\tau_w L^2}{\mu a} \right)^{1/3} \left[\Theta^*(0) \xi^{-1/3} + \int_0^\xi (\xi - \xi^*)^{-1/3} \frac{d\Theta^*}{d\xi^*} d\xi^* \right]. \quad (10)$$

where Θ^* , which is now a function of nondimensional x , is defined as $T_w - T_e$ divided by an arbitrary reference temperature difference ΔT^* .

As the spot is smooth there is no jump in the wall temperature, which gives $\Theta^*(0) = 0$. Equation (10) relates the wall-heat transfer to the wall-shear stress for an arbitrary wall-temperature distribution.

In contrast to hot-films, where the heat transfer to the flow q_f is given by the electrical power of the heater (assuming perfect insulation), the net irradiated energy q_{ir} and the heat loss into the solid q_s are not known. Therefore q_f needs to be determined by solving the unsteady two-dimensional heat-transfer equation for the solid (Poisson equation), which reads

$$\rho_s c_s \frac{\partial T}{\partial t} = k_s \left(\frac{\partial^2 T}{\partial x^2} + \frac{\partial^2 T}{\partial y^2} \right). \quad (11)$$

It has to be emphasized that the temperature in y -direction can *not* be assumed to be constant, like in most applications of quantitative IR-thermography, which would simplify the determination of q_f significantly. This will be further discussed in section 4.1. The boundary conditions for equation (11) are sketched in figure 4.

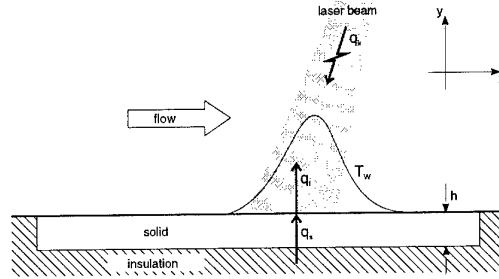


Figure 4: Boundary conditions for the solid.

Except for the side of the solid facing the flow, where q_f is transferred, the three other sides are assumed to be perfectly insulated. As the Poisson equation is unsteady also initial conditions are needed to describe the temperature distribution in the solid at an initial time.

The required wall-heat transfer to the fluid q_f follows from

$$q_f = q_s + q_{ir}, \quad (12)$$

with

$$q_f = \left(-k_f \frac{\partial T}{\partial y} \Big|_w \right)_{\text{fluid}}, \quad q_s = \left(-k_s \frac{\partial T}{\partial y} \Big|_w \right)_{\text{solid}}.$$

Obviously if the laser is switched off ($q_{ir} = 0$), the heat fluxes in the fluid q_f and in the solid q_s at the surface are equal.

Additional to the heat transfer to the flow by heat convection there is also a radiative heat transfer from the surface to the surroundings. However, as the temperature of the spot remains close to ambient temperature the radiative heat transfer, though essential for the measurement by the IR camera, is negligible for the determination of q_f .

3 Experimental Setup

To determine the wall-shear stress with quantitative IR-thermography there are basically three different measurement methods:

1. At time $t = 0$ the laser is turned on and starts to heat up the solid, which has an initial ambient temperature. During the heating period the IR-camera measures the increasing surface temperature.
2. In the steady method the laser first heats up the solid, where after it continuously maintains steady state temperature in the hot spot, which is measured by the IR-camera.

3. The laser heats up the solid until the temperature inside the solid is steady. This state is used as initial condition for the unsteady Poisson equation. Afterwards the laser is turned off and the IR-camera measures the temperature decay.

As described in section 2 the irradiated power q_{ir} is boundary condition for the Poisson equation. This requires not only the measurement of the total laser power but the determination of the power distribution in x -direction at any point of time, which is rather difficult to do. Therefore the third method has been chosen because it is independent of q_{ir} . The performance and the accuracy of the present measurement technique has been tested in a laminar flow along a flat plate without streamwise pressure gradient (Blasius flow). The flat plate has been placed vertically in a closed wind tunnel with a cross section of $40\text{ cm} \times 40\text{ cm}$. The experimental setup and a cross section of the measurement strip are sketched in figure 5 and figure 6.

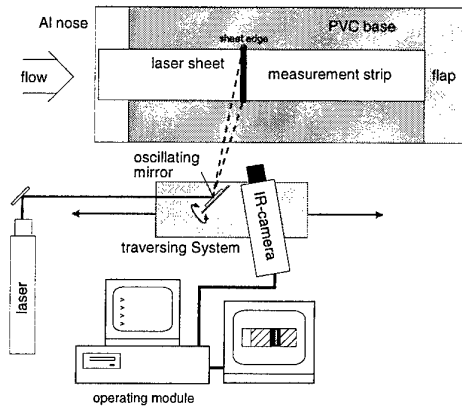


Figure 5: Experimental setup.

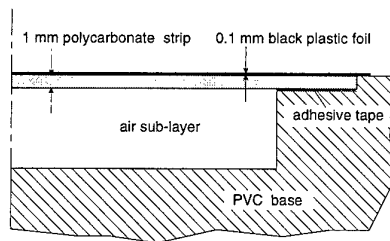


Figure 6: Cross section of the plate.

The plate consists of a 3 cm PVC base. Along the centre line of the base a 1 mm polycarbonate strip is flush inserted, on which the measurements are performed. Like in any application of IR-thermography the emissivity of the surface of the monitored object needs to be as high as possible (Balageas [8]). Therefore the measurement strip has been covered with a 0.1 mm dull black plastic foil. As determined by a fully numerical simulation (see section 4.2) this combination of polycarbonate and plastic foil seems to be a good compromise

to match the requirements for the hot spot with respect to size and decay time. Underneath the measurement strip a 5 mm air sublayer has been milled to provide a nearly perfect insulation as defined in the solution of the Poisson equation. Next to constant thermal properties and thickness the measurement strip also requires a minimum stiffness, because the strip spans the air sublayer. The strip is fixed to the PVC base by double-sided adhesive tape.

The hot spot is heated by a nominally 5 W Argon laser (actual power $< 2\text{ W}$). To obtain a small hot spot in flow direction with a rather constant spanwise temperature, which reduces the heat-transfer problem by one dimension, an oscillating mirror generates a laser sheet. The actual wall-shear stress measurement takes place in the middle of the laser sheet. The mirror and the IR-camera are fixed on a traversing system positioning the measurement point.

As the laser and the IR-camera monitor the measurement strip through the wind-tunnel wall, which usually has a rather low transmittance for infrared radiation, a slit has been cut into the wall. To minimize the disturbances the slit has been covered with a 0.05 mm thin transparent foil reducing the thermal radiation by less than approximately 2%. However due to the small thickness of the foil it is rather fragile. That means the foil is only able to resist small differences between the pressure inside and outside the wind tunnel.

4 Numerical Treatment

As described in section 2 the unsteady Poisson equation needs to be solved to calculate the heat transfer q_f to the flow. Analytical solutions for the Poisson equation exist only for rather simple boundary conditions; therefore the equation is solved numerically. The integration of the similarity equation (10) is also performed numerically.

Next to the required numerics for the experimental method also a full numerical simulation of the heat transfer in the fluid and the solid has been carried out to:

- give more insight in the physics of the hot spot
- optimize the choice for the material of the solid
- determine the accuracy of the similarity equation
- check the data processing for the experimental method

4.1 Full Numerical Simulation of the Fluid and the Solid

Before presenting the results of the simulation for a case, that resembles a typical experimental situa-

tion, a brief description of the numerical procedure of the simulation is given.

First the velocities in the fluid are calculated from the velocity boundary-layer equation (2), which is discretized by a second order finite difference scheme. As the boundary-layer equations are of parabolic nature they can be solved by a straightforward marching procedure, which calculates each new downstream flow station by solving a tridiagonal matrix. The calculation of the velocity has to be performed only once, because the flow field is assumed to be independent of the temperature in the fluid. With the previously calculated velocities the temperature in the fluid is calculated by prescribing the wall-temperature at $t = 0$. The heat flux q_f is calculated from the temperature gradient in the fluid perpendicular to the surface. The heat flux q_s in the solid is given by equation (12). The net heat flux is prescribed as Neumann boundary condition at the side facing the flow and homogeneous Neumann boundary conditions are prescribed at the three other boundaries to calculate the temperature in the solid. The unsteady Poisson equation is discretized by a second-order implicit finite difference scheme in space and in time. The resulting coefficient-matrix is solved by an LU-decomposition. This gives an update of the temperature at the surface, which is used as a boundary condition in the next iteration solving the thermal boundary-layer equation. The iteration process stops when the changes in the wall-temperature distribution have become less than a small convergence criterion.

The following figures show some results of a simulation for a 2 mm wide laser sheet with a power of 1 W per m span heating up the solid at $x = 0.5$ m. The irradiated power distribution along the beam diameter, generating the sheet, is constant. The solid consists of a 1 mm polycarbonate sheet and an 0.1 mm plastic foil. For the velocity boundary layer a constant outer-edge velocity of 10 m/s is prescribed. After steady-state conditions are reached the laser is switched off at $t = t_0$ and the hot-spot temperature starts to decay (see figure 7).

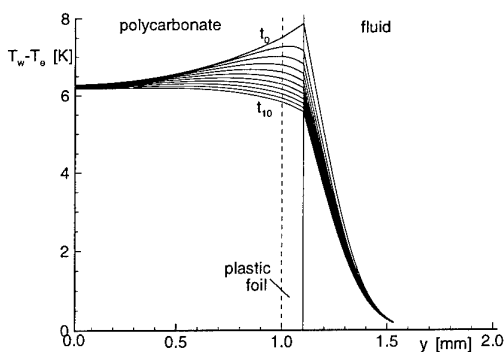


Figure 7: $T_w - T_e$ in the fluid and in the solid in y -direction at $x = 0.5$ m.

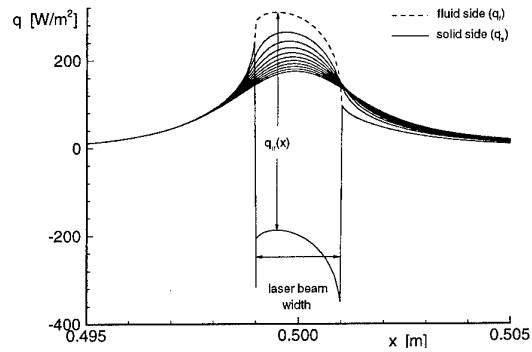


Figure 8: q_f in the fluid and in the solid in x -direction.

When the laser is turned off the wall-heat transfer in the fluid q_f (denoted as a dashed line in fig. 8) is equal to the wall-heat transfer in the solid q_s (denoted as a solid line) for $t > t_0$. For $t = t_0$, just before turning off the laser, there is a difference between both heat fluxes, which is precisely equal to the prescribed irradiated power of the laser.

With the help of the numerical simulation it can also be proven that the heat transfer cannot be assumed to be one-dimensional for a solid with a low thermal conductivity like polycarbonate. This is done by comparing the wall-heat transfer calculated with the 2D Poisson equation and a 1D approximation for a single solid layer, which is found by integrating the 2D Poisson equation in y -direction. Neglecting the y -dependence of $\partial T / \partial t$ and $\partial^2 T / \partial x^2$ the 1D approximation reads

$$\rho_s c_s h \frac{\partial T}{\partial t} = k_s h \left(\frac{\partial^2 T}{\partial x^2} \right) - q_f. \quad (13)$$

Figure 9 shows the result of the comparison for different thicknesses h of polycarbonate.

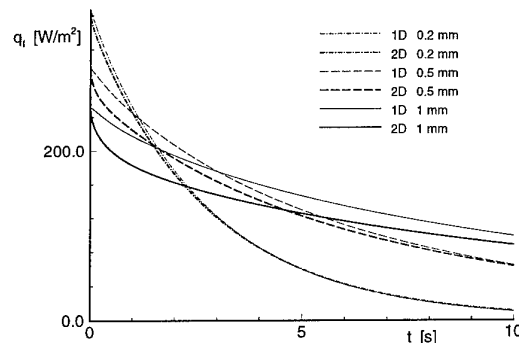


Figure 9: Comparison of q_f obtained with 1D and 2D heat-transfer equation for different solid thicknesses.

As expected the difference between the 1D and the 2D calculation of the wall-heat transfer increases with increasing thickness. In particular shortly after turning off the laser, when only the upper part close to the surface is cooled down the difference is largest.

4.2 Accuracy of the Similarity Relation between Wall-Heat Transfer and Wall-Shear Stress

In this measurement technique the similarity equation (10) is used to calculate the wall-shear stress from the surface temperature measurement. As this equation is valid only for local heating, it is necessary to check the influence of the hot spot size on the accuracy of the wall-shear stress. Therefore the wall-shear stress coefficient calculated with the similarity equation (10), which will be denoted as $c_{f,sim.}$, is compared with the wall-shear stress given by the numerical solution of the velocity boundary-layer equation (2). It has been checked that this solution reproduces the well-known shear-stress law for the Blasius flow

$$c_{f,theor.} = 0.664 Re_x^{-0.5}. \quad (14)$$

Figure 10 shows the relative error $\Delta c_f = (c_{f,sim.} - c_{f,theor.})/c_{f,theor.}$ in [%] as a function of w_{spot} for different free-stream velocities U_e ranging from 5 m/s to 25 m/s. Here w_{spot} is defined as the distance between the two x -positions having a temperature of 50% of the maximum hot spot temperature in x -direction T_{max} .

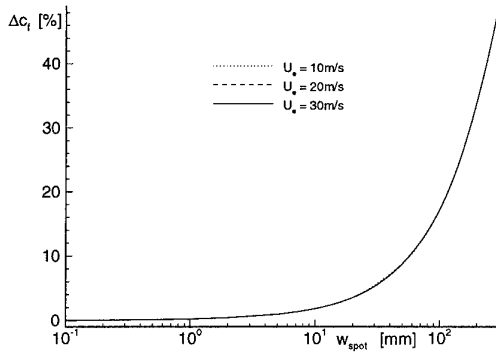


Figure 10: Difference in the wall-shear stress coefficient at $x = 0.5$ m for different w_{spot} obtained with the boundary-layer equation and the similarity equation for different free stream velocities.

The results show that the error Δc_f is below 1% for $w_{spot} \leq 1$ cm. However, w_{spot} must not only match the assumption of local heating it must also match the capabilities of the IR-camera. As the spatial resolution of any camera is limited (Carlo-magno and de Luca [9]), there is a lower limit for the spot size. For the camera used in this investigation (AGEMA 880LWB) the minimum angular size of the observed object is about 4 mrad, which

corresponds to 1 mm in our experimental setup. Therefore a w_{spot} of 5–6 mm has been chosen.

Next to the spot size w_{spot} also T_{max} for each time step and the time scale of the temperature decay t_{spot} , which is defined as the time interval between turning off the laser and the decay of 50% of the initial steady value, are important parameters. Like for w_{spot} also for T_{max} a compromise has to be found. On the one hand a high temperature increases the signal-to-noise ratio of the IR-camera. We will see later that signal noise is crucial in this measurement technique. On the other hand high temperatures lead to changes in the flow properties like density and viscosity, which are assumed to be constant in the boundary-layer equations and in the similarity equation. Furthermore a high temperature affects the behaviour of the flow, such as the transition location.

Not only the spatial resolution but also the time response of the IR-camera is limited. The AGEMA 880LWB needs 40 ms to measure one temperature distribution in the hot spot. Therefore the temperature decay can only be sampled with sufficient accuracy for t_{spot} larger than 1 s.

The three parameters w_{spot} , t_{spot} and T_{max} are influenced by the flow conditions, but they are even more influenced by the thermal properties of the solid, like density, specific heat capacity, thermal conductivity and thickness. To determine the thermal properties of the solid matching all requirements the behaviour of the hot spot for different materials has been simulated fully numerically.

In a preliminary experiment a 0.1 mm stainless steel plate with a 0.05 mm colour coating to increase the emissivity has been used. Therefore this combination of solids has been simulated first. The experiments have shown large variations of w_{spot} for different x -positions, which are caused by deviations in the thickness of the coating ($\approx 20\%$). This is clarified by the results of the numerical simulation shown in figure 11.

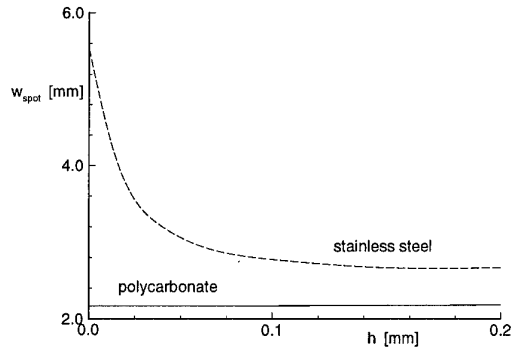


Figure 11: Influence of different coating thicknesses h on 0.1 mm stainless steel or 1 mm polycarbonate on the spot size w_{spot} .

Therefore the coating has been replaced by a 0.1 mm black dull plastic foil, which has nearly the same thermal properties as the colour coating, but has smaller thickness deviations ($< 10\%$). Additionally the stainless steel strip has been replaced by polycarbonate to further reduce the sensitivity to the thickness tolerance of the coating. To achieve a sufficient stiffness of the solid, to insert the strip flush into the test plate, a 1.0 mm polycarbonate strip has been chosen. As can be seen in figure 11 w_{spot} is nearly independent of the thickness of the coating.

The influence of different solid materials on the time scale of the temperature decay t_{spot} has also been investigated. Figure 12 shows the results.

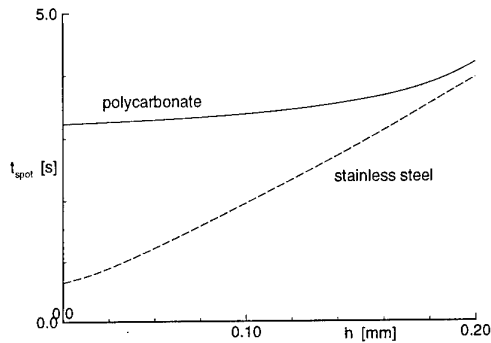


Figure 12: Influence of different coating thicknesses h for 0.1 mm stainless steel or 1 mm polycarbonate on the temperature decay t_{spot} .

Like w_{spot} , also t_{spot} is less sensitive to a varying coating thickness for polycarbonate than for stainless steel. Besides this, t_{spot} is larger for polycarbonate, which enables much more temperature measurements during the temperature decay.

4.3 Numerical Procedures for the Experimental Method

In contrast to the full numerical simulation, in which the heat flux (Neumann boundary conditions) has been prescribed at the interface between fluid and solid, the heat flux is not known in the real experiment. As the IR-camera measures the surface temperature the Neumann boundary conditions are replaced by Dirichlet boundary conditions (prescribed temperature). With these boundary conditions and an initial condition the temperature inside the solid can be calculated. To evaluate this initial condition the surface temperature distribution at steady-state conditions before switching off the laser needs to be measured. For an unsteady calculation of the solid, in which the measured steady-state surface temperature distribution is prescribed at the interface fluid/solid for each time step, the temperature inside the solid converges to a steady state with increasing time. Thus the final numerical procedure to evaluate the heat flux to the flow q_f from the surface temperature measured with the IR-camera

starts with the calculation of the initial temperature inside the solid using the measured steady-state temperature. Over the subsequent time new experimental Dirichlet boundary conditions are prescribed for each new time step and the temperature inside the solid for each time step is calculated. With the given temperature distribution the heat flux to the flow and with it the wall-shear stress can be determined for each time step using the similarity equation (10).

5 Data Processing

Many data processing steps are required to transfer the raw temperature data, measured by the IR-camera, to the temperature distributions for each time step, which are to be used as boundary conditions for the Poisson equation. Since the determination of q_f requires a surface-temperature distribution at steady-state conditions it is essential to heat up the solid sufficiently long ($> 3 \text{ min}$) to achieve steady temperatures in the solid. It has to be emphasized that even when surface temperature seems to be steady the temperature inside the solid might still vary. When the complete steady-state is reached the temperature measurement is started. After a few temperature distributions at steady-state condition have been measured the laser is switched off and the IR-camera measures the temperature decay of the hot spot.

As the laser is turned off after the temperature measurement has already started the exact laser-turn-off-time (LTO) has to be determined. The AGEMA 880LWB is a single sensor camera scanning the field of view (frame) sequentially, which means that each pixel within the frame is measured at a different time. As long as the laser is turned on the temperature difference ΔT between one pixel and the same pixel in the previous frame is approximately zero. The first pixel, which has a larger ΔT than the noise-equivalent-temperature-difference (NETD) has been scanned just after turning off the laser. Since it is known when each pixel is scanned the LTO can be determined.

To simplify the numerical solution of the Poisson equation the numerical time steps between each prescribed temperature boundary condition, after turning off the laser, are equidistant. As the time between the LTO and following temperature measurement is usually not equal to the time between two measurements (40 ms), the temperature boundary conditions need to be interpolated from the measured data. The numerical time step for the interpolation has been taken equal to the measurement time, which is sufficiently small to guarantee accurate numerical solutions.

As already mentioned, this measurement technique is very sensitive to signal noise. This is caused in the first place by the scatter in the temperature measurements, which leads to large errors in the temperature derivatives and thus in the wall-

heat transfer q_f . In the second place the wall-shear stress is proportional to the third power of q_f , which amplifies the error by approximately a factor of 3. Therefore extensive noise-reduction procedures are required. For steady temperature measurements averaging is rather efficient. For the measurement during the temperature decay after turning off the laser two different filter techniques have been applied. In any noise-filtering procedure a compromise has to be found between smoothness and data loss. Due to the large spatial temperature gradients in the hot spot, filtering tends to decrease the maximum temperature T_{max} of the hot spot. By using a least square 5-point cubic data fit in x -direction the high-frequency noise can be reduced without decreasing T_{max} more than 2%. Since the frequency of the noise in the temporal direction is much lower than in spatial direction a fast Fourier transformation with a low-pass filter and a variable cut-off frequency has been applied.

Figure 13 presents the measured T_{max} at each measured time step and the interpolated and filtered T_{max} at each numerical time step.

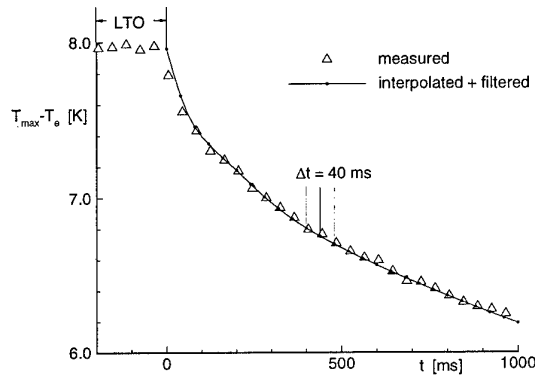


Figure 13: Measured and processed maximum temperature in the hot spot $T_{max} - T_e$.

The corresponding temperature boundary conditions for the Poisson equation are presented in figure 14.

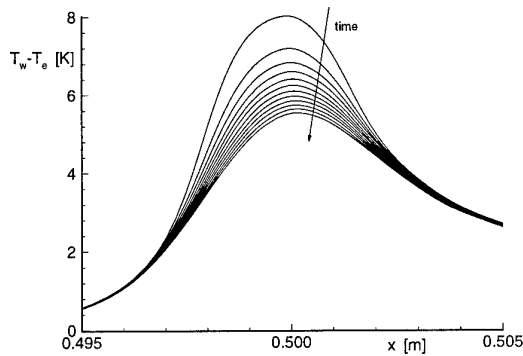


Figure 14: Wall-temperature $T_w - T_e$ after turning off the laser for different time steps ($\Delta t = 40$ ms).

With the filtered temperature data q_f and the wall-

shear stress τ_w can be determined. As the velocity boundary layer and therefore the wall-shear stress is steady, the measured τ_w can be averaged in time to reduce the remaining scatter of the measurement. To achieve a sufficient noise reduction, at least 30 time steps for the temperature distribution in the hot spot are required for one wall-shear stress measurement.

To demonstrate the influence of the noise-filtering procedure figure 15 compares the wall-temperature $T_w - T_e$ and the resulting wall-heat transfer q_f along the hot spot with and without filtering the measured data.

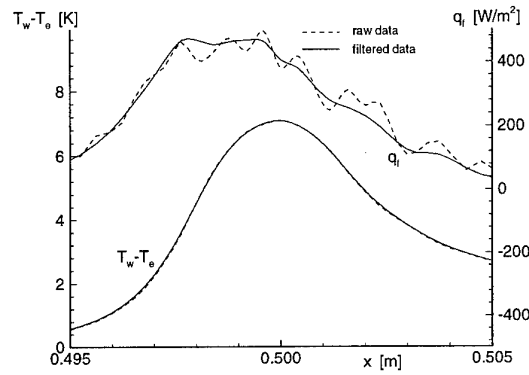


Figure 15: Influence of filtering on the wall-temperature $T_w - T_e$ and the wall-heat transfer q_f along the hot spot.

It has to be pointed out that although the filter seems to have no influence on $T_w - T_e$ the scatter in q_f is significantly reduced. As the scatter in q_f is amplified due to the relation between q_f and τ_w , there are large fluctuations in the relative error $\Delta c_f = (c_{f,exp} - c_{f,theor.}) / c_{f,theor.}$ for each measured time step ($c_{f,exp.}$ denotes the experimental found wall-shear stress), which are shown in figure 16.

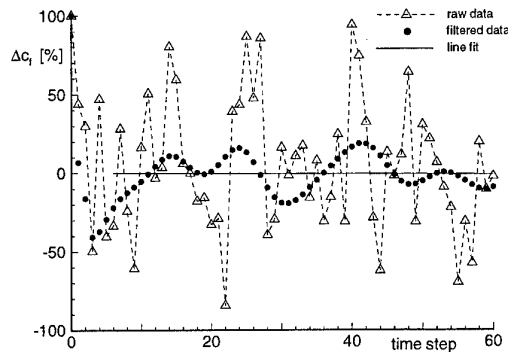


Figure 16: Influence of filtering and averaging on the relative error Δc_f for each measured time step.

The applied filter reduces the large scatter in Δc_f by approximately a factor 5. The straight line in figure 16 represents a least square linear fit to the filtered data. As the line is nearly horizontal it can

be concluded that the wall-shear stress is indeed constant during the measurement.

6 Results

The wall-shear stress coefficient has been measured at three different x -positions and for various free stream velocities ranging from 4 m/s to 23 m/s. The results of these measurements and the theoretical wall-shear stress calculated from the wall-shear stress law (14) are plotted in figure 17.

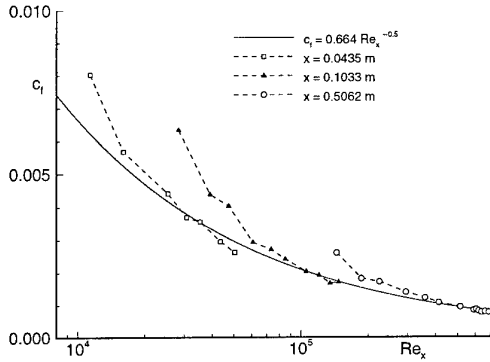


Figure 17: Wall-shear stress measurements c_f for different x -positions and different free stream velocities U_e .

The deviation of c_f between the measured and the theoretical value for a constant x -position decreases with increasing Re_x , which means that the error increases with decreasing free-stream velocity U_e . To clarify this figure 18 shows the relative error Δc_f between the measurement and the theoretical value of the wall-shear stress for different free-stream velocities.

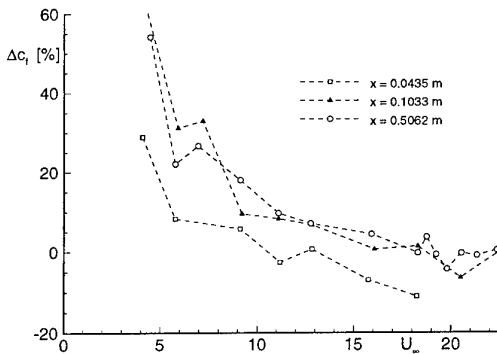


Figure 18: Relative error Δc_f of the measurement for different free-stream velocities U_e .

This deviation may be caused by natural-convection effects along the vertical positioned measurement plate. As the fluid close to the hot spot is heated up, the local density of the fluid decreases, causing

that buoyancy imposes a vertical velocity component to the flow. This additional flow increases the wall-heat transfer and thus the related wall-shear stress. For larger free-stream velocities this additional heat transfer can be neglected. The relative error is about 10% for free-stream velocities larger than 10 m/s.

It is conspicuous that the relative error Δc_f in the measured wall-shear stress for an x -position of 0.0435 m is about 15% lower than for the other x -positions. This is caused by the nose of the plate. For $x < 0.08$ m the measurement strip is fixed to the aluminium nose instead of the PVC base (see figure 5). As the mass of the oscillating mirror is not infinitely small, the temperature in the laser sheet is higher close to the edges of the laser sheet. To fulfill the assumption of no heat transfer in spanwise direction in the middle of the laser sheet the laser sheet is as wide as the measurement strip.

As the heat conductivity of aluminium is about 1000 times higher than the heat conductivity of PVC, a significant amount of energy is transferred from the edges of the laser sheet through the measurement strip and into the aluminium nose, which leads to lower temperature at the edges of the laser sheet than in the middle. This temperature difference leads to a spanwise heat transfer from the middle of the sheet to its edges causing a decrease of the heat transfer to the flow, which corresponds to a decrease in the measured wall-shear stress.

Preliminary measurements in a turbulent boundary layer have been performed. The data of these measurements are presently being processed, but first results indicate, that also in a turbulent boundary layer the wall-shear stress can be measured with the new method with reasonable accuracy.

7 Conclusions

By using quantitative IR-thermography a new flexible and non-intrusive measurement technique for wall-shear stresses has been developed. At this stage an accuracy of about 10% in the measurement of the wall-shear stress has been achieved. The main sources of error are due to the external heating and the restricted capabilities of the available IR-camera.

In contrast to the hot-film technique, in which the wall-heat transfer is given by the electrical power of the heater, in this technique the wall-heat transfer needs to be determined from the measurement of the surface temperature performed by the IR-camera. Since this temperature measurement contains scatter, which is strongly amplified due to the relation between surface temperature, wall-heat transfer and the local wall-shear stress, the overall accuracy of the wall-shear stress measurement depends on the applied noise-reduction methods, which need to be improved. A further improvement of the present measurement technique can possi-

bly be achieved, if the irradiated power distribution along the laser can be measured with a high accuracy, while the IR-camera monitors the hot spot. In that case the wall-shear stress measurement can be performed with a steady hot spot, which would simplify the noise-reduction procedure significantly. Either for an unsteady or a steady temperature measurement the quality of the IR-camera is the most limiting factor. The first limitation is the spatial resolution, which restricts the maximum distance between the camera and the observed object. Therefore more sophisticated optics are required to extend this technique from the laboratory environment with a camera-object distance of less than 30 cm to measuring the wall-shear stress on large-scale objects with distances of a couple of meters. Another significant limitation is the scatter of the temperature measurements, described in the beginning of this section. This scatter is caused by the insufficient signal-to-noise-ratio of the IR-camera, which is generated by the electrical field of the motors moving the mirrors and prism of the scanning system in single-detector cameras. However, the latest IR-cameras with focal plane arrays, having as much IR-sensitive sensors as pixels in the field of view, do not require a scanning system. These cameras have a better signal-to-noise-ratio and just need 3 ms for one complete 2D temperature measurement. These advantages make better data filtering methods possible, which can further improve the accuracy of the wall-shear stress measurement with quantitative IR-thermography.

References

1. A. Fage and V.M. Falkner, *Relation between heat transfer and surface friction for laminar flow*, A.R.C. Reports Memoranda No. 1408, 1931.
2. J. Mathews and D.I.A. Poll, *The theory and application of heated films for the measurement of skin friction*, Cranfield CoA Report No. 8515, 1985.
3. B.W. van Oudheusden, *Integrated Silicon Flow Sensors*, PhD thesis, Faculty of Aerospace Engineering, Delft University of Technology, 1989.
4. L.M.M. Boermans, Private communications, Delft University of Technology, 1993.
5. J.P. Crowder, Infrared cameras for detection of boundary layer transition in transonic and subsonic wind tunnels, *Proceedings of the AIAA 21st Fluid Dynamics, Plasma Dynamics and Lasers Conference*, Seattle, June 18-20 1990, AIAA 90-1450.
6. H.L. Boerrigter and J.M. Charbonnier, On the effect of flowfield non-uniformities on boundary layer transition in hypersonic flow, *Euromech 330, Laminar/Turbulent Transition of Boundary Layer Influenced by Free-Stream Disturbances*, Prague, 10-12 April 1995.
7. M.J. Lighthill, Contribution to the theory of heat transfer through a laminar boundary layer, *Royal Society London* 1950, **202**, 359-377.
8. D.L. Balageas, Fundamentals of infrared techniques, *Lecture of Measurement Techniques*, VKI lecture series 1993-05, 1993.
9. G.M. Carlomagno, Infrared thermography, *Lecture of Measurement Techniques*, VKI lecture series 1993-05, 1993.

SKIN FRICTION MEASUREMENT AND TRANSITION DETECTION TECHNIQUES FOR THE LUDWIG-TUBES AT DLR

E. Schülein, S. Koch, and H. Rosemann
 Institut für Strömungsmechanik
 Deutsche Forschungsanstalt für Luft- und Raumfahrt e. V.
 Bunsenstraße 10
 D-37073 Göttingen
 Germany

SUMMARY

Three different skin friction measurement and transition detection techniques have been developed and adapted to the specific test conditions in the Ludwig-Tube facilities of DLR at Göttingen. The latter are: short run time and thin boundary layers for both, the hypersonic Ludwig-Tube facility (RWG) and the Cryogenic Ludwig-Tube (KRG), and low temperatures for the KRG, which can be operated down to 120 K to achieve high Reynolds numbers.

An oil film technique has been developed and applied to measure skin friction and transition on a flat plate in the RWG at $M = 5$. The results are in good agreement with the Van Driest II and the Young correlation, respectively, and results from velocity profile measurements for the skin friction and hot-wire measurements for the transition location.

Surface mounted hot-films, directly deposited on the model surface, have been used to study shock oscillations on a laminar-type airfoil in the KRG down to cryogenic conditions. Further improvements of the deposition quality will make sensor arrays with about 20 sensors on an airfoil section with 150 mm chord available.

It could be demonstrated that wall mounted thermocouples provide a simple method to determine transition on airfoils in the KRG by detecting the difference in heat flux between laminar and turbulent boundary layers. The results agree well with the interpretation of pressure distribution and wake measurements as well as with the transition location given by the MSES (Drela) code.

1 INTRODUCTION

The DLR operates two different Ludwig-Tube facilities at Göttingen. The supersonic/hypersonic Ludwig-Tube (RWG) covers a Mach number range of $3 \leq M \leq 7$ and a unit Reynolds number range of $5 \times 10^6 \text{ m}^{-1} \leq Re_1 \leq 80 \times 10^6 \text{ m}^{-1}$. The facility consists of an 80-meter long tube used as pressure reservoir which is separated from the nozzles and the test section by a quick-acting gate valve. The tunnel is started by opening this valve. Hypersonic flow is generated by individual nozzle blocks; the test section for the Mach numbers $M = 3$ and 4 has a cross section of $0.5 \times 0.5 \text{ m}^2$, while those for the high Mach numbers have circular cross sections of 0.5 m diameter.

Based on the good experience with this facility, a transonic high Reynolds number facility, the Cryogenic Ludwig-Tube (KRG), has been built with the same operating principle. Major differences in the design are the larger storage tube with a length of 130 m, a subsonic nozzle, the 2-D adaptive test section with a cross section of $0.4 \times 0.35 \text{ m}^2$, an additional valve for Mach number control, and the positioning of the fast-action valve downstream of the test section.

Cryogenic technology is applied to achieve chord-based Reyn-

olds numbers of up to $60 \cdot 10^6$ on 2-D airfoils at run temperatures down to 120 K. More details of the design and the operation of the KRG are given in Ref. 1.

The flow problems being investigated in these facilities, such like shock/boundary layer interaction/control and laminar airfoils require methods to determine boundary layer transition and skin friction to understand the flow field or for CFD validation purposes. The special environment in the cryogenic facility, thin boundary layers, and the short run times (ca. 0.3 s for the RWG and up to 1 s in the KRG) require the development of new and adaptation of standard measurement techniques.

An oil film method for skin friction measurements, developed and tested at $M = 5$ in the RWG, a surface hot-film technique for cryogenic conditions applied in the KRG, and the use of wall-mounted thermocouples for transition detection also in the KRG will be described in this paper.

2 THE GLOBAL INTERFEROMETER SKIN FRICTION METER

2.1 Development of Oil Film Interferometer Techniques

The oil film interferometer technique developed by Tanner and Blows, Ref. 2, overcomes many of the well known limitations of existing methods, since it provides non-intrusive measurements. It is based on the relationship between the thinning of an oil film, placed on the test surface exposed to the flow, and the local surface shear τ_w . The rate of thinning of the oil film is determined using optical interference created when an incident light beam is partially reflected at the oil and test surfaces as shown in Fig. 1.

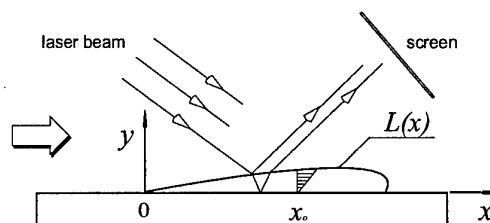


Figure 1: Oil film interferometry. $L(x)$ is the oil film thickness

This method, originally used in low-speed flow, was later modified for 2- and 3D high-speed gradient flows and found in many applications, Ref. 3, 4, 5, 6, 7. The best known version of this method is the Laser Interferometer Skin Friction (LISF) technique, Ref. 8, 3, 9, 10. The thinning of the oil film at a fixed point is determined by a laser beam/photodiode interferometer. However, the LISF technique has some deficiencies: it provides only point-wise data and therefore measuring shear distributions over large surfaces can be very costly; model vibrations, surface waves or particles of dust on the oil film can have a strong influ-

ence on the results or can lead to a total failure of the measurement.

To overcome these deficiencies a variation of the original fringe-imaging technique was developed — the Global Interferometer Skin Friction (GISF) meter — which uses interference pattern to describe the thinning of the oil film, Ref. 4, 5, 11, 7, 6. The oil film thinning rate is determined by measuring the spacing between the fringes in time. The first version of the GISF meter was developed in Ref. 4, 12, 13. Global shear stress distributions in 3D flows can even be obtained with this instrument during a single run of a short duration facility such as the Ludwig-Tube. The size of the test surface is limited only by the need for adequate image quality and resolution. This method requires that a minimum of two (better more) images of the oil film interference pattern in a known time interval are captured during a test run. It requires of course also an optical access to the test section of the wind tunnel. An advantage of this method is that it accounts for wall shear variations not only in different directions on a model surface but, during a test run, also for (specified) changes in the flow conditions.

Another method, developed later and termed Surface Imaging Skin Friction (SISF) meter in Ref. 7, is in principle based on the first GISF meter, Ref. 4, but it has additional advantages. By using a fluorescent tracer in the oil film one can simultaneously determine the surface streamline directions of the flow. The combination of the oil thinning rate and the surface streamline directions allows to calculate the global shear-stress distribution on the test surface.

As deficiency can be seen that the needed equipment is more expensive since two cameras and color filters are needed, but the amount of information, obtained during a single run, surely compensates that.

An alternative and simpler GISF meter was described in Ref. 5, 11 and termed Fringe-Imaging Skin Friction (FISF) technique. This version of the GISF instrument needs only one image of the interference pattern that is recorded after a wind tunnel run. The skin friction coefficient is determined by the rate of thinning of the oil film during the run time. The deficiencies of this method are that it is not designed for the application in 3D flows and that it ignores the changing of flow conditions during start-up and shut-down of the wind tunnel. The uncertainty in the skin friction coefficient is higher than for the GISF meters described above, because the fringe spacing and the development of the interference pattern are given with only one image after the run.

Based on this FISF technique a new instrument was tried to build in Ref. 6 that includes the advantages of existing GISF techniques. This method can be used to provide global shear distributions also in 3D flows over relative large test surfaces with nonuniform wall temperatures. Unfortunately it has retained all drawbacks of its parent as described above.

2.2 Model and Test Conditions

The GISF-meter was adapted for the RWG. The models used in this study were three different flat plates. The flat plates were of equal thickness (10 mm) and width (400 mm), but they had different lengths (plate A = 200 mm, plate B = 300 mm and plate C = 500 mm). Plate C was instrumented with 10 individual ports to accept probes for flow-field surveys along its axis and with 3 additional ports for measurements in the span-wise direction as check of the flow two-dimensionality. Additional static pressure taps were located at different intervals along and across the plate C. The test surfaces were highly reflective. The nominal free-stream conditions in the test section were: Mach number $M =$

5, total temperature $T_0 = 410$ K, total pressure $p_0 = 21.2$ bar and unit Reynolds number $Re_1 = 40 \times 10^6 \text{ m}^{-1}$. The wall temperature of the models was 295 ± 5 K during a run. Run-to-run variations in the local Mach number M_e and velocity U_e , respectively, was less than 0.5%; static temperature T_e varied within 2%.

2.3 Set-up of the Global Interferometer Skin Friction Meter

The present version of the GISF meter is based on descriptions in Ref. 4, 12, 13. Two variants of the instrument were implemented, Fig. 2. In the first the beam from a 2 mW, 633 nm wavelength He-Ne laser is widened by the lenses and sent with a mirror to the test surface with the thin oil film. The thin film interference pattern is recorded via a mirror and a lens by a CCD Camera. In the second variant of the set-up the interference pattern is produced by illuminating the oil film directly without mirrors. Because of the very short test times in the facility, the images were recorded during a run by a SONY VO-9600P video recorder and digitized thereafter by a full frame video capture card Hauppauge Win/Motion 60 and stored on a PC's hard disk at up to 30 frames per second. Typically, 4 to 5 high quality images were captured 40 ms apart at an image resolution of 768×576 pixels. Fig. 3 shows, for example, such a sequence of the fringe-pattern images on a flat plate.

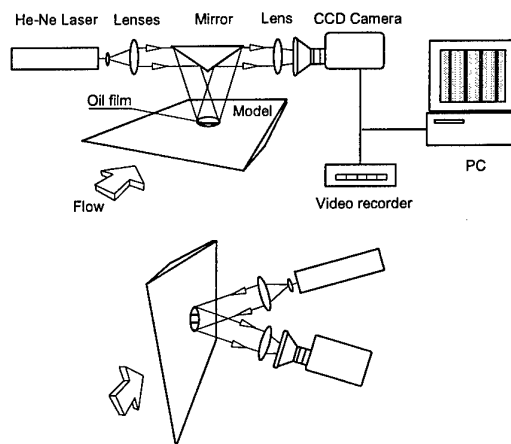


Figure 2: Schematic of the GISF instrument set-up

The oil film thickness is determined directly from the fringe pattern. The intensity distributions along the stream-wise direction are filtered and the peaks detected. The spacing of intensity maximums or minimums (fringe spacing) can be determined. If the incident laser beam is nearly perpendicular to the surface, the fringe spacing corresponds to a change in oil film thickness of $\lambda/2$, with λ being the wavelength of the incident laser light. The skin friction coefficient was calculated by the integral method, described in Ref. 13. The general equation for 2D flows can be expressed for $x = x_0$ as follow:

$$\tau_w = \frac{2\rho\nu}{L^2(x_0)} \frac{d}{dt} \int_0^{x_0} L(x_0) dx$$

where x_0 is the position where the skin friction is to be determined, τ_w is the skin friction, ρ and ν are the oil density and oil kinematic viscosity, respectively, $L(x)$ is the film thickness (see Fig. 1), and t is the time. Further information on this method may be obtained from Ref. 13.

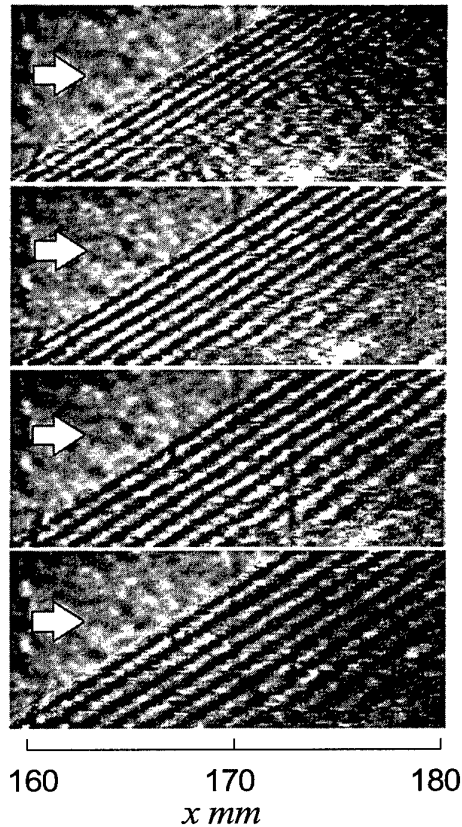


Figure 3: Interferograms of the oil films on a flat plate

The oils used in the present study were Wacker silicon oils AK-10 and AK-0.65 and Shell mineral oil S.5585 with corresponding nominal viscosities of $10 \text{ mm}^2/\text{s}$, $0.65 \text{ mm}^2/\text{s}$, and $5.4 \text{ mm}^2/\text{s}$ at 25°C . The silicon oil AK-10 was used in most of the present experiments. The oil film was applied on the test surface along a line either perpendicular to the free-stream direction or diagonal to it. The latter, suggested in Ref. 5, 11, is for short-time facilities very favorable since a larger area of the test surface can be scanned during a run.

2.4 Velocity Profiles

For comparison with the GISF-meter results velocity profiles were taken in 5 locations along plate C ($x = 266, 296, 316, 336$ and 356 mm) to determine the skin friction coefficients using an alternate method. The pitot surveys in the boundary layer and the free-stream needed here were measured by a miniature probe in conjunction with an ENDEVCO Model 8514-20 or KULITE Model XTC-190M-3.5BAR VG pressure transducer, located directly at the back of the probe. The rated transducer accuracy is quoted by the manufacturer to be of the order of $\pm 0.3\%$ full scale for the ENDEVCO transducer ($\pm 0.003 \times 138000 \text{ Pa}$) and $\pm 0.5\%$ full scale for the KULITE transducer ($\pm 0.005 \times 350000 \text{ Pa}$). The corresponding static pressures were measured at the wall through orifices, 0.3 mm in diameter, which were connected with short-length tubing (150 mm) to a 32-port PSI ('PRESSURE SYSTEMS INC.') pressure transducer module with a measurement range of $\pm 15 \text{ psi}$ ($\pm 103400 \text{ Pa}$) and a rated accuracy of $\pm 0.1\%$ full scale ($\approx \pm 100 \text{ Pa}$) or better.

Skin friction data may be obtained from measured mean velocity profiles after transformation of the velocity profile data to the

corresponding 'incompressible' profile. A least-squares curve fit of the wall-wake law to the velocity profile data may then be performed extracting u_τ (or C_f) and δ as parameters of the curve fit. However, for hypersonic boundary layers it is very important to include in this procedure the viscous sublayer conditions. We have, therefore, used for extracting the skin friction data ($C_{f_{prof}}$) the combined wall-wake law with the Van Driest mixing-length damping function for the viscous sublayer, expressed in Ref. 14 as:

$$U^+ = U_w^+ + \frac{\Pi}{\kappa} w(y/\delta).$$

Here, the 'law of the wall' profile U_w^+ is defined by

$$\frac{dU_w^+}{dy^+} = \frac{2}{\sqrt{1 + 4\ell^{+2} + 1}},$$

$$\ell^+ = \kappa y^+ (1 - e^{-y^+/A^+}), \quad A^+ = 25.53;$$

Π is the wake parameter, used for fitting as a free parameter; $\kappa = 0.41$ and the Coles' wake function is defined by $w(y/\delta) = 1 - \cos(\pi y/\delta)$.

2.5 Skin Friction Distribution on Flat Plates

The results of the skin friction measurements on flat plate models used for validation of the GISF meter in the RWG are shown in Figures 4 and 5. The skin friction values for Plate C (length 500 mm), extracted from the GISF measurements (open symbols) with different oil viscosities used in the tests, show an adequate distribution and good agreement with the data obtained from the velocity profile measurements (black symbols), Fig. 4. Moreover, the skin friction levels at $x > 200 \text{ mm}$ agree with the well-known Van Driest II correlation for the turbulent boundary layer. At $x \leq 100 \text{ mm}$ the skin friction distribution shows a transitional boundary layer and a developing turbulent flow at higher x -values.

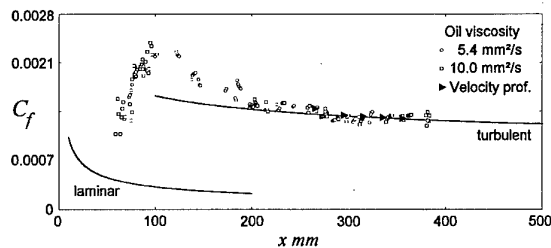


Figure 4: C_f -distributions on Plate C measured by the GISF meter in the RWG

The data measured on the shorter Plates A (length 200 mm) and B (length 300 mm) show qualitatively similar distributions, cf. Fig. 5. The curve for the laminar boundary layer corresponds to the empirical Young correlation, Ref. 15. Very remarkable is the strong influence of the plate length on boundary layer transition. The lengthening of the plate leads in the present tests to early transition with the corresponding value of the transition Reynolds number essentially decreasing, Fig. 6.

The credibility of the present data, measured by the GISF instrument, is also confirmed by a comparison with earlier hot-wire transition measurements on Plate B, Ref. 16. The general result, viz., the dependence on the length of the flat plate, which is somewhat surprising, can be explained by the existing relation

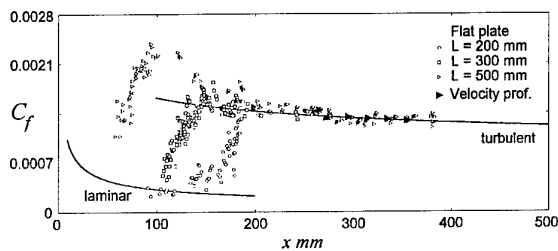


Figure 5: C_f -distributions on the flat plates A, B, and C measured by GSF meter in RWG

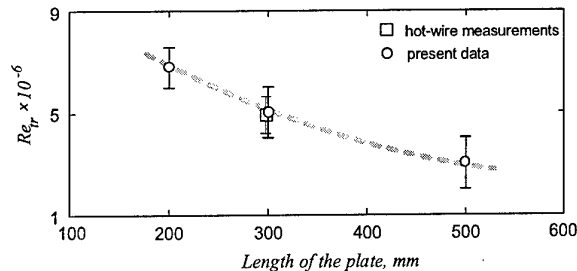


Figure 6: Dependence of boundary layer transition on a flat plate on model dimensions

between the model dimensions and the level of model vibration during a run. The support of the plates was such that the longer plates exhibit stronger vibrations, partly provoked by the start-up process of the impulse-type Ludwig-Tube facility. It is very conceivable, that high model vibrations can lead to early transition of the boundary layer. Scheduled vibration measurements on these flat plates promise to confirm a quantitative dependence of the transition Reynolds number, Re_{tr} .

3 SURFACE HOT-FILMS FOR CRYOGENIC TEMPERATURES

3.1 Design of Hot-Films Manufactured by Direct Deposition

Commercially available surface mounted hot-films, as they are often used in conventional wind tunnels and free-flight tests to measure wall shear stress and determine transition location, are not very well suited for tests in the KRG. Because of the high Reynolds numbers, surface roughness is very critical so that most often the roughness of the hot-film itself is too high. Also the gluing process may cause problems in terms of surface quality and reliability of the sensors at low temperatures. Following an approach of Johnson *et al.* Ref. 17, a 'cryo-hot-film' sensor without these shortcomings can be manufactured by directly coating a system of different layers on the surface of the steel model.

The design of a hot-film sensor which can be operated at cryogenic conditions is shown in Fig. 7. First a "Parylene C" layer, consisting of a soft plastic material, is coated on the model surface in a Chemical Vapor Deposition process (CVD). The Parylene C layer with a thickness of about $7 \mu\text{m}$ is used to provide thermal and electrical insulation. It also compensates differences in thermal expansion between the model and the next layer made of silicon dioxide. The latter, $1 \mu\text{m}$ thick layer consists of a special silicon organic compound. Using different amounts of oxygen during the CVD process, a graded layer is achieved where the lower regions have an organic fraction whereas the upper region consists of pure silicon dioxide. This

way one obtains a softer layer in the lower regions, corresponding to the soft Parylene C, and a stable underground at the top of this layer where the hot-films and leads can be deposited. The nickel hot-films with a final thickness of $0.2 \mu\text{m}$ are sputtered onto this silicon dioxide layer. Finally, the copper leads with a thickness of $0.5 \mu\text{m}$ are sputtered onto the surface overlapping the hot-films which results in a good electrical contact. The layout of the leads and sensors is achieved by using a photolithography technique.

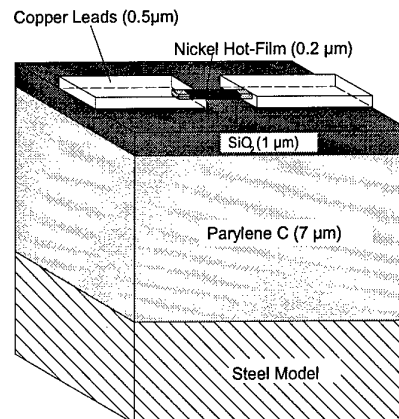


Figure 7: Layer system of a 'cryo-hot-film'

3.2 First Tests with Directly Deposited Hot-Films

A hot-film system as described above was deposited on a cylindrical piece of stainless steel as shown in Fig. 8. After confirming the mechanical stability of the sensors during tests in a cooled box at temperatures down to 100 K, the test sample was installed in the KRG with the surface holding the sensors flush mounted with the sidewall of the test section.

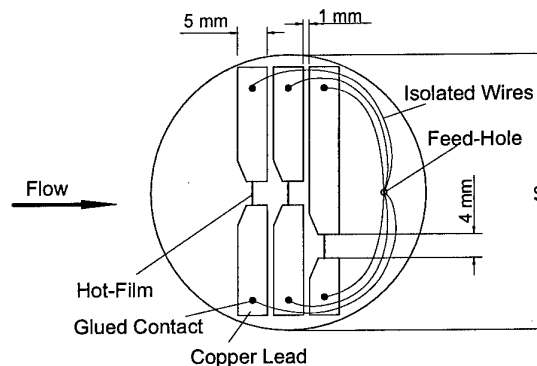


Figure 8: Hot-film array on a steel insert to be mounted in the sidewall of the KRG test section

The hot-films were connected to DISA 55M10 anemometers. The two sensors which were positioned in line with the flow direction were used to measure the convective velocity of turbulent structures in the sidewall boundary layer. This velocity was determined to be 64% of the undisturbed velocity in the center of the test section. This agrees well with measurements of Kreplin (Ref. 18) who obtained a velocity ratio of 62%, although his measurements were performed at much lower Reynolds numbers with hot-films at the sidewall of an oil-channel. Based on centerline velocity and channel width, the Reynolds number was 7700, whereas for the boundary layer at the sidewall of the KRG it was 104×10^6 based on run length and free stream

velocity. Moreover, the power spectrum of the hot-film signal showed the typical shape found in turbulent boundary layers, Fig. 9. Therefore it was concluded, that the hot-film signal really is a presentation of the turbulent flow and not determined by electronic noise.

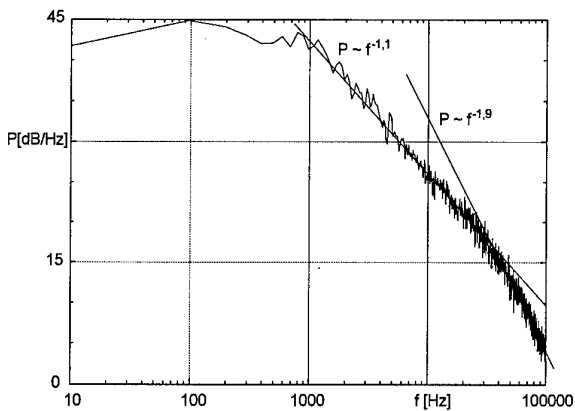


Figure 9: Power spectrum of a hot-film signal obtained at $M = 0.76$ and $Re \approx 50 \times 10^6$

Furthermore, operation in a frequency range of up to 250 kHz was verified during tests at Mach numbers up to $M = 0.8$. This high frequency response is due to a volume to surface ratio of the hot-film which is similar to the one of a hot-wire.

3.3 Hot-Film Measurements on the Airfoil LV2F

For validation measurements the laminar-type airfoil LV2F was chosen; the airfoil model was coated with fifteen hot-film sensors on its upper surface, Fig. 10. The hot-films were located in a staggered pattern to prevent the thermal wake of the sensors positioned upstream to disturb the measurement by a sensor located downstream. The supply lines, brought onto the surface as described above, lead to a flange that was flush mounted with the KRG's sidewall. At this position thin insulated wires were connected to the leads with an adhesive containing over 90% silver. The wires were connected to anemometers outside the test section as shown in Fig. 10. Due to surface contamination, it was not possible to achieve the same good deposition quality on the airfoil model as was obtained for the test specimen described above, resulting in some defect hot-films. Only the sensors four to nine positioned between 25% and 55% of the chord functioned properly.

Transition: Unfortunately, intermittent transitional signals could not be identified with the few hot-films left. We believe that this is mainly due to the transition point movement, triggered by the pressure distribution, which placed, dependent on

Reynolds number, transition either in the shock region or upstream of the first sensing element but never in between. Nevertheless, these sensors functioned up to chord Reynolds numbers of 30×10^6 . The hot-film system did not show any damage after more than 100 test runs with temperatures down to 100 K.

Buffet: Although problems existed in discovering transitional signals due to spatial resolution, it was possible to identify an oscillating lambda-shock at buffet conditions verifying the capability of measuring skin friction as intended. Fig. 11 shows a principle sketch of the situation encountered: A shock is present on the upper surface of the airfoil which separates the laminar boundary layer forming a separation bubble with turbulent re-attachment.

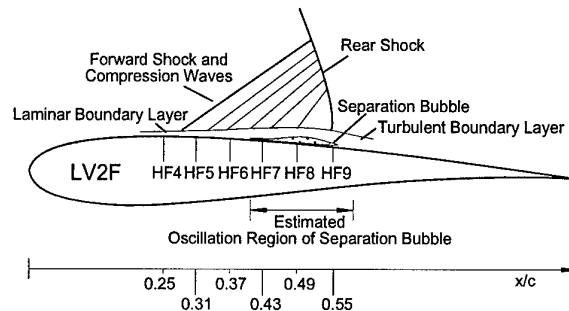


Figure 11: Position of the oscillating lambda-shock on the upper surface of the LV2F-model ($Re = 6.5 \times 10^6$, $M = 0.72$, $\alpha = 3.0^\circ$)

Considering Fig. 12 which shows the alternating part of three hot-film voltages, one observes that the forward shock moves back and forth over the hot-film located at $x/c = 0.43$ (lower plot). When the forward shock is downstream of the sensor a laminar attached flow is shown by the sensor signal. Moving upstream, the signal indicates the separated flow of the separation bubble beneath the lambda-shock with a lower skin friction. The hot-film at $x/c = 0.55$ (upper diagram) shows the rear shock oscillating across this position and one can detect the high-voltage signals of re-attached turbulent flow and again the low signals due to the separation bubble. Finally, the sensor at $x/c = 0.49$ shows all three phenomena: the attached laminar flow (e.g.: $0.821 < t < 0.823$), the re-attached turbulent boundary layer (e.g.: $0.839 < t < 0.841$) and the separation bubble (e.g.: $0.824 < t < 0.827$).

The oscillation frequencies and phase relations were derived from the signals. The frequencies showed good agreement with measurements carried out on a CAST7 airfoil model by Stanewsky and Basler, Ref. 19. For the test case described above, the oscillation frequency was measured to 138 Hz.

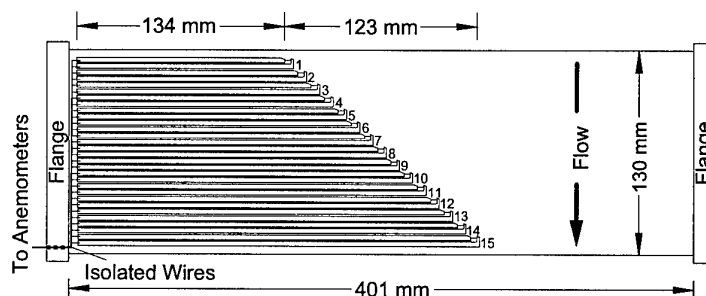


Figure 10: Hot-film arrangement on the upper surface of the laminar-type airfoil LV2F

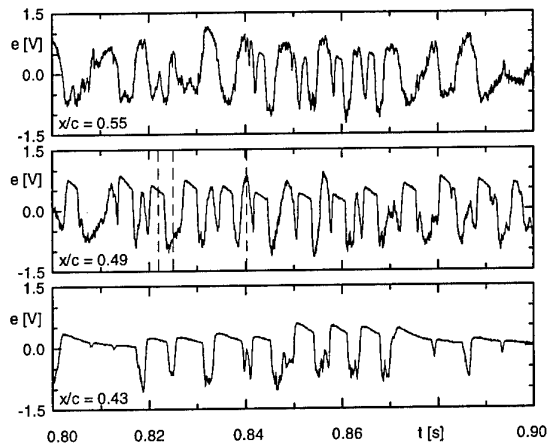


Figure 12: AC-parts of hot-film signals measured at the conditions shown in Fig. 11

Summarizing it can be concluded that the hot-film system as intended by the design is able to measure skin friction at cryogenic conditions. Especially transition measurements at high Reynolds numbers on an airfoil, for instance, are not disturbed since the roughness height of the sensors is within the viscous sublayer of the boundary layer. Although it was not possible to find transitional signals in the present test due to poor spatial resolution, one was able to distinguish between a laminar and a turbulent boundary layer in the case of an unsteady transitional shock boundary layer interaction.

4 TRANSITION DETECTION BY WALL MOUNTED THERMOCOUPLES

4.1 Flow Conditions in the KRG

Another convenient technique for boundary layer transition detection is the infrared imaging technique, exploiting the difference in heat flux between laminar and turbulent boundary layers. However, infrared cameras are currently not available for the very low temperatures in cryogenic facilities. Because of the adaptation mechanism of the flexible wall in the test section of the KRG, the view on the model is also very restricted. It was therefore investigated, whether the heat flux can be measured by more conventional means, such as thermocouples embedded in the model wall, during the short run time of the KRG. Thermocouples have been used before for transition detection in the cryogenic wind tunnel T2 of ONERA at Toulouse, France (Ref. 20, 21), but here the run time is much longer compared to the KRG (between 30 s and 120 s).

As can be shown from one-dimensional unsteady gas dynamics, stagnation pressure and stagnation temperature drop below the pre-test charge values during the start-up of the flow in a Ludwig-Tube, providing a very repeatable temperature difference between the model structure and the flow. As long as viscous effects can be neglected, the amount of pressure and temperature drop is determined only by the test section Mach number and the nozzle contraction ratio.

Fig. 13 shows the ratio of total temperature T_0 to charge temperature T_c for a contraction ratio of 3.6, which applies to the KRG. At $M = 0.3$ the temperature drops by about 3.0% and at $M = 0.7$ by about 5.3%, yielding absolute temperature differences of 8.5 K and 15 K, respectively, between model and flow at the begin of the run at a charge temperature of $T_c = 283$ K.

For critical cases, the model temperature can also be adjusted

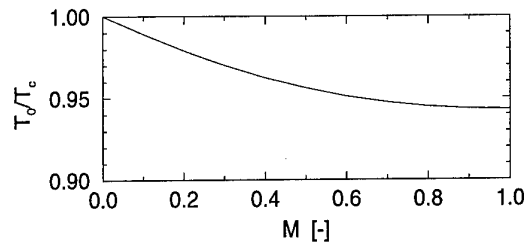


Figure 13: Total temperature drop of the KRG as function of the test section Mach number

before the run to the total flow temperature T_0 , but this is not part of the standard test procedure of the KRG.

With this temperature difference between model and flow, the different heat fluxes in laminar and turbulent boundary layers result in different temporal temperature gradients in the model wall. For the short run time of the KRG, these temperature gradients are measurable only very close to the surface.

4.2 First Tests with a Thin-Skin Model

First test have been carried out with three thermocouples mounted 0.5 mm underneath the surface of a 2-D airfoil model with a wall thickness of 3mm, as sketched in Fig. 14. The model with a chord length of 150 mm was manufactured by DASA¹. It was also equipped with a larger number of thermocouples at the inside of the wall, designed for optimal response in the T2 wind tunnel of ONERA, where the model was investigated as well. These sensors did not show any response within the short test time of the KRG. However, the signals of the three sensors mounted close to the surface could be evaluated, see Fig. 15.

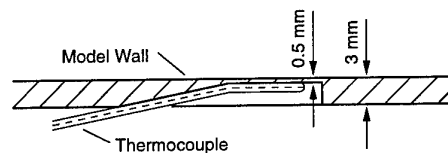


Figure 14: Installation of thermocouples parallel to model surface

The temperature traces for the three sensors located at different chord-wise positions as indicated in the figure are plotted versus test time for three different Reynolds numbers. For comparison, the total temperature trace measured in the flow is shown below. Transition was tripped at 48% chord, just downstream of the third sensor. The tunnel is started at $t \approx 0.25$ s, where the total temperature drop begins. At $t \approx 1.0$ s, the shutdown of the flow is visible.

For the lowest Reynolds number case, all three thermocouples show very small gradients. With increasing Reynolds number, larger temperature gradients are measured, starting with the most downstream sensor at $x/c = 0.475$, whereas for the high Reynolds number case all sensors show larger heat flux.

If the temperature gradients are computed and plotted versus Reynolds number, the forward movement of the transition point from $x/c > 0.475$ at $Re = 4.6 \cdot 10^6$ to $x/c < 0.125$ at $Re = 11.8 \cdot 10^6$ can be determined, as shown in Fig. 16. Also plotted are the corresponding curves for lift and drag coefficient c_L and c_D , and it can be seen very clearly, that the increase in drag

¹Daimler-Benz Aerospace Airbus, Bremen, Germany

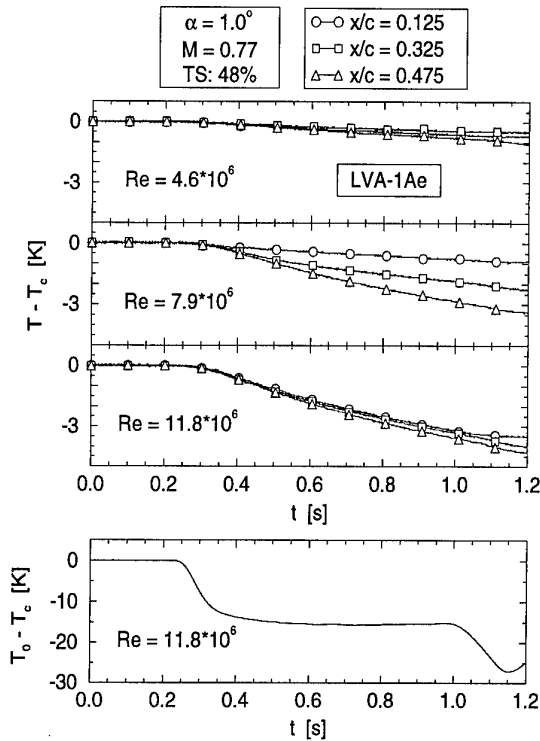


Figure 15: Temperature traces of wall-mounted thermocouples and total temperature probe for different Reynolds numbers

between $Re = 8 \cdot 10^6$ and $Re = 10 \cdot 10^6$ is a result of the forward movement of the transition point in this Reynolds number range.

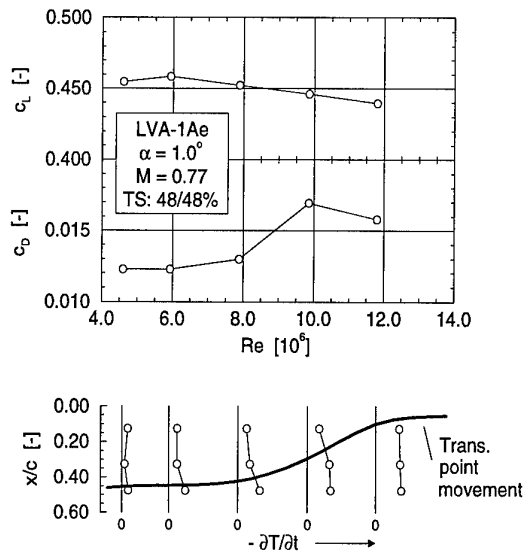


Figure 16: Transition point movement determined by heat flux measurements

4.3 Experiments with a Fully Instrumented Solid Model

Encouraged by these results, another airfoil model with a chord of 180 mm was equipped with a fully instrumented thermocouple section with 13 sensors on the upper and lower side. A slightly different installation was chosen, as shown in Fig. 17.

This method was found to be easier to manufacture for models with very thick walls, as it was the case here with a nearly solid cross section. With this laminar type airfoil, drag measurements showed a development of a so-called laminar 'drag bucket' during first wind tunnel tests. Hereby the results from pressure distribution and wake measurements could be supplemented by the information from the thermocouple measurements.

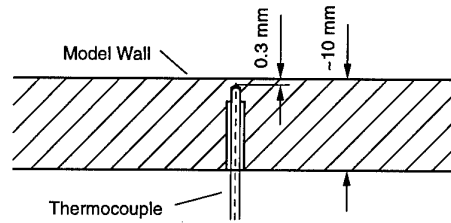


Figure 17: Installation of thermocouples normal to model surface

Figure 18 shows a measured pressure distribution from this laminar-type airfoil at $M = 0.62$ and $Re = 5.0 \times 10^6$. On both sides, at $x/c \approx 0.56$ on the lower and at $x/c \approx 0.52$ on the upper airfoil side, the pressure distribution shows the signature of a laminar separation bubble. Here the laminar boundary layer separates, undergoes transition and re-attaches as a turbulent boundary layer. This transition can be clearly identified also in the thermocouple signals, where the temperature gradient jumps from very small values to about $\partial T / \partial t \approx -1.5 \text{ K/s}$. This particular pressure distribution with separation bubbles was only selected for a good comparison; these bubbles are not necessary, though, to detect the transition with thermocouples.

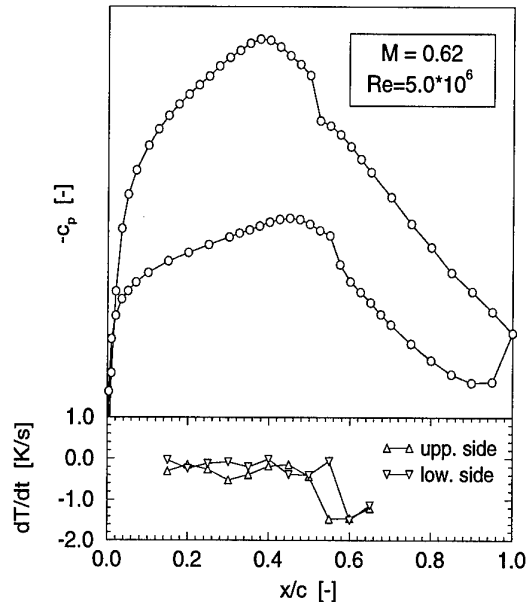


Figure 18: Pressure distribution and temperature gradients on a laminar-type airfoil

Figure 19a presents the measured c_L/c_D polar at $M = 0.3$, $Re = 6.0 \times 10^6$ and free transition together with results from the MSES (Drela, cf. Ref. 22) code, an Euler solver coupled with a boundary layer method. Transition is taken into account by an e^n method and the n-factor was chosen to be $n = 9$, given by Drela as being representative for free-flight conditions. While, as usual, the drag level is somewhat lower in the computational

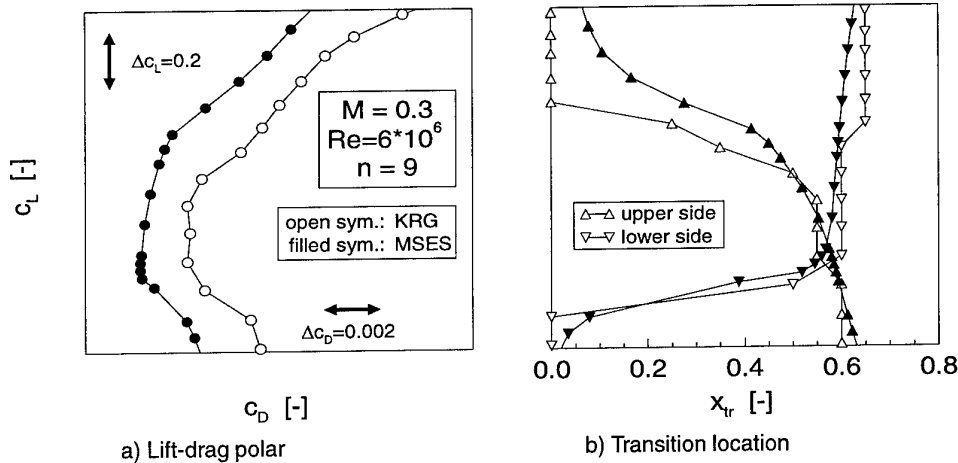


Figure 19: Comparison of experimental and numerical results for drag and transition location

results, the overall shape of the two curves shows good agreement. Both exhibit the laminar 'drag bucket', a region of minimal drag over a certain c_L range. It begins at about the same c_L value for both curves, while it extends to somewhat higher lift in the numerical result compared to the experimental values.

In Fig 19b the corresponding transition locations, deduced from the increase in heat transfer measured with the thermocouples and given by the e^n stability method in the MSES results, are shown. The overall agreement between experimental and numerical results is again very good, if the somewhat limited spatial resolution given by a chord-wise spacing of the sensors of $\Delta x/c = 0.05$ is considered. Since the most upstream sensor is located at $x/c = 0.15$, transition positions further upstream could not be determined and are plotted here at $x_{tr} = 0$.

Beginning at low c_L values, the boundary layer on the upper side stays laminar up to about 60% chord, while, because of the suction peak developing at these negative angles of attack, the lower side shows fully turbulent flow. With increasing lift, the transition moves only very gradually upstream on the upper side, while, for a certain c_L value, a sudden downstream movement on the lower side is observed. Here, where on both sides the boundary stays laminar up to about 50% to 60% chord, the laminar drag bucket begins, cf. Fig 19a.

With further increasing lift the transition point stays at about 60% on the lower side. On the upper side it starts an upstream movement where in the drag polar the upper end of the laminar bucket is reached. In agreement with the difference between experiment and numerical results there, the upstream movement for the numerical curve is delayed to somewhat higher c_L values.

With this model, test measurements were carried out in the Mach number range of $0.3 \leq M \leq 0.72$ at Reynolds numbers up to $Re = 15 \times 10^6$. Transition location could always be deduced from the thermocouple signals, when it was constant across the span at least in the region of the thermocouple section. Some ambiguous results were attributed to the occurrence of turbulent wedges, originating from local disturbances off the thermocouple section and then running into it from the side. In these cases, a 2-D method, like the infrared technique, clearly has some advantages.

5 CONCLUSION AND FUTURE WORK

The applicability of the GISF meter to short-duration facilities like the RWG could be demonstrated with good results. A further validation in the RWG in two- and three-dimensional interacting flows is planned. The flow phenomena to be considered include the interaction of 2D incident shocks and 3D crossing shock-waves with the turbulent boundary layer. The influence of model vibrations on laminar-turbulent transition will also be further investigated.

The first tests with directly deposited surface hot-films at cryogenic conditions have been successful in general, but the reliability of the sensors has to be improved by enhancing and optimizing the various deposition steps. The layer system will also be slightly modified: The thickness of the Parylene C layer will be increased to 15 μm , if possible even to 30 μm . This should result in a better thermal insulation with respect to the metallic model surface and, moreover, it will decrease the electric capacity of the copper leads which was, in the past, hard to compensate by the anemometers used. The number of sensors will also be increased in order to obtain a better chord-wise resolution, while the width of the sensor field in span-wise direction will be decreased. With these improvements, major attention will be paid again in future tests to transition detection on the LV2F airfoil.

Measuring the heat flux by wall-mounted thermocouples provides a simple technique for transition detection at conditions where infrared imaging can not be applied. Because of the point-wise measuring principle, spatial resolution is limited and covering larger areas on the model requires a great number of sensors. If special attention is paid to an installation very close to the surface and a good thermal contact to the model, test times of a few tenths of a second are fully sufficient, allowing an application of this technique in Ludwig-Tube wind tunnels. An evaluation of at cryogenic conditions is planned for next year with a new airfoil model suitable for cryogenic testing and equipped with one chord- and one span-wise thermocouple section.

REFERENCES

1. H. Rosemann. The Cryogenic Ludwig-Tube at Göttingen. In *Special Course on Advances in Cryogenic Wind Tunnel Technology*, AGARD-R-812, DLR, (Cologne, Germany), 20-24 May 1996.
2. L. Tanner and L. Blows. A study of the motion of oil films on surfaces in air flow, with application to the measurement

- of skin friction. *J. Phys. E.: Sci. Instrum.*, 9:194-202, 1976.
3. K.-S. Kim and G. S. Settles. Skin friction measurements by laser interferometry. In H. H. Fernholz, A. J. Smith, and J. P. Dussauge, editors, *A survey of measurements and measurement techniques in rapidly distorted compressible boundary layers*, AGARDograph 315, pages 4-1 to 4-8, November 1988.
 4. V. I. Kornilov, D. K. Mekler, and A. A. Pavlov. On the techniques of skin friction measurement using one beam laser interferometry. In *The methods of aerophysical research*, (Novosibirsk, Russia), 1990.
 5. D. J. Monson, G. G. Mateer, and F. R. Menter. Boundary layer transition and global skin friction measurement with an oil-fringe imaging technique. SAE Paper 932550, SAE Aerotech '93, September 1993.
 6. T. J. Garrison and M. Ackman. Development of a global interferometer skin friction meter. AIAA-96-1968, AIAA, 1996.
 7. J. W. Naughton and J. L. Brown. Surface interferometric skin-friction measurement technique. AIAA-96-2183, AIAA, 1996.
 8. D. J. Monson. A nonintrusive laser interferometer method for measurement of skin friction. *Exp. in Fluids*, 1:15-22, 1983.
 9. T. J. Garrison, G. S. Settles, N. Narayanswami, and D. Knight. Laser interferometer skin-friction measurements of crossing-shock wave/turbulent boundary layer interactions. *AIAA J.*, 32(6):1234-1241, 1994.
 10. J. K. Wideman, J. L. Brown, J. B. Miles, and O. Özcan. Skin-friction measurements in three-dimensional, supersonic shock-wave/boundary-layer interaction. *AIAA J.*, 33(5):805-811, 1995.
 11. G. G. Mateer, D. J. Monson, and F. R. Menter. Skin-friction measurements and calculations on a lifting airfoil. *AIAA J.*, 34(2):231-236, 1996.
 12. V. I. Kornilov, A. A. Pavlov, and S. I. Shpak. On the techniques of skin friction measurement using optical method. In *International conference on the methods of aerophysical research — ICMAR'92*, (Novosibirsk, Russia), 1992.
 13. A. I. Maksimov, A. A. Pavlov, and A. M. Shevchenko. Development of the optical skin friction measurement technique for supersonic gradient flows. In *International conference on the methods of aerophysical research — ICMAR'94*, (Novosibirsk, Russia), 1994.
 14. P. G. Huang, P. Bradshaw, and T. J. Coakley. Skin friction and velocity profile family for compressible turbulent boundary layers. *AIAA J.*, 31(9):1600-1604, 1993.
 15. A. D. Young. In L. Howarth, editor, *Modern Developments in Fluid Mechanics, High Speed Flow*, volume 1, pages 375-475. Clarendon Press, Oxford, 1953.
 16. V. Wendt. Experimental investigation of instability in planar and conical hypersonic laminar boundary layers. DLR Forschungsbericht FB 93-56, DLR, 1993. in german.
 17. C. B. Johnson, D. L. Carraway, P. Hopson, Jr., and S. Q. Tran. Status of a specialized boundary layer transition detection system for use in the U. S. National Transonic Facility. In *Proceedings of the ICIASF Record - International Congress on Instrumentation in Aerospace Simulation Facilities*, pages 141-155, (Williamsburg, VA), 22-25 June 1987.
 18. H.-P. Kreplin and H. Eckelmann. Propagation of perturbations in the viscous sublayer and adjacent wall region. *J. Fluid Mech.*, 95:305-322, 1979.
 19. E. Stanewsky and D. Basler. Experimental investigation of buffet onset and penetration on a supercritical airfoil at transonic speeds. AGARD-Conference Proceeding AGARD-CP 483, 1990.
 20. A. Seraudie, J.-B. Dor, J.-P. Archambaud, and A. Blanchard. Laminar flow testing in the T2 Cryogenic Wind Tunnel. In *Proceedings of the DGLR/AAAF/RAeS 1st European Forum on Laminar Flow Technology*, (Hamburg, Germany), 16-18 March 1992.
 21. G. Redeker, R. Müller, A. Blanchard, and J. Reneaux. Evaluation of transonic laminar airfoil tests under cryogenic conditions including stability analysis and computational results. In *Proceedings of the DGLR/AAAF/RAeS 1st European Forum on Laminar Flow Technology*, pages 141-151, (Hamburg, Germany), 16-18 March 1992.
 22. M. Drela and M. B. Giles. ISES: A two-dimensional viscous aerodynamic design and analysis code. AIAA-86-0424, AIAA, 1987.

Surface Forces Measurements with High Spatial and Temporal Resolution by Means of Liquid Crystal Foils, Piezofuels and Surface Hot-Film Arrays

W. Nitsche, J. Suttan, F. Haselbach, D. Sturzebecher
Technische Universität Berlin, Institut für Luft- und Raumfahrt,
Sekt. F2, Marchstr. 12, 10587 Berlin, Germany

1. SUMMARY

Steady and unsteady surface measurement techniques for subsonic and transonic flows are surveyed emphasizing the capabilities, restrictions and applications of these techniques in experimental aerodynamics. The present paper investigates comparatively the status and capabilities of a number of surface measurement techniques (Liquid Crystals, Hot-Film-Arrays, Piezofuel-Arrays,) which are necessary for the understanding of distributed flow phenomena. Based on exemplary results some of the main features of the measurement techniques are discussed. Emphasis is on recent improvements to obtain higher temporal and spatial resolution. This concerns e.g. the employment of pyroelectrical capabilities for higher signal-to-noise ratios in piezofuel array measurements, or the development of a standard calibration method for multisensor hot-film arrays with small streamwise sensor spacing.

2. NOMENCLATURE

A,B	calibration constants
C	electrical capacity
d_{33}, d_t	material constants of piezofuel
f	frequency
L_{eff}	effective length of a hot-film
l_s^+	non-dimensional sensor length
N_s	Number of sensors operated upstream
p	pressure
Pr	molecular Prandtl number
Q	total heat loss, el. polarization
Q_w	heat flux
R	electrical resistance
Re	Reynolds number
S	spacing of the sensors
T	temperature
U	voltage
u,v,w	velocity components
u_τ	friction velocity
x,y	coordinates
τ_w	wall shear stress
α	angle of attack
δ	boundary layer thickness
ρ	density
λ	thermal conductivity, wavelength
μ	viscosity
ν/u_τ	viscous length scale
ν	kinematic viscosity

3. INTRODUCTION

The analysis of the efficiency and capability of an airfoil design requires a sufficient and reliable experimental data base. Such data base can be provided e.g. by surface measurements investigating local and distributed wall flow phenomena, such as laminar-turbulent transition, shock-boundary layer interference and shock or pressure induced separation. Thus, surface measurement techniques should be capable of both, high spatial and temporal resolution, delivering data for the understanding and control of relevant phenomena in the flow regime investigated. Furthermore, in the scope of hybrid laminar flow or adaptive wings for future transport aircraft, reliable measurement techniques are needed for the monitoring of wall bounded shear flows in order to verify the capabilities of a new wing design and/or to control the flow during service.

In general, surface measurement techniques can be subdivided into steady and unsteady as well as plane and quasi-plane (traversable or array) techniques. According to this, Table 1 presents a survey of some of the currently used measurement techniques in airfoil experiments. The comparative survey presented in this paper is based on a number of experiments in low and high speed flows as well as in wind tunnel and in-flight tests. Emphasis is on the reliability and suitability of surface measurement techniques for experiments in the subsonic and transonic flow environment.

	Steady Surface Measurement Techniques	Unsteady Surface Measurement Techniques
<u>Plane Techniques</u>	<ul style="list-style-type: none"> • Liquid crystals • Infrared Im. • Pressure Sens. Paint 	<ul style="list-style-type: none"> • Liquid crystals ($f < 10\text{Hz}$) • Infrared ($f < 10\text{Hz}$)
<u>Quasi-plane Techniques</u>	<ul style="list-style-type: none"> • Array Techniques • traversed Prest. Tube • Oilfilm-Interferometry 	<ul style="list-style-type: none"> • Array Techniques such as: Piezofuels Hot-Films

Table 1: Some of the currently used surface measurement techniques

4. SURFACE MEASUREMENT TECHNIQUES

4.1 Liquid Crystals

The development of liquid crystal foils has allowed a new method of visualizing wall flows, especially under flight test conditions (Gall & Holmes, 1986, Kasagi et al., 1989). The foils are made out of encapsulated liquid crystals visualizing the local surface temperature ($-30^{\circ}\text{C} < T_s < 115^{\circ}\text{C}$) by changing the color. Therefore, the liquid crystal foil can be used to determine flow phenomena which are associated with significant changes of the local heat flux rate and thus of the surface temperature. Such phenomena can be laminar-turbulent transition, flow separation or shock wave/boundary layer interference. In advantage to infrared cameras the images of liquid crystals can be recorded by consumer CCD-video-cameras. Figure 1 shows a schematic test setup of an on-line video system for the chromatic interpretation of liquid crystal images. The images of liquid crystals can be interpreted directly by the experimenter watching the event or indirectly by photography or video recording. The recorded video images can be evaluated by means of digital image processing.

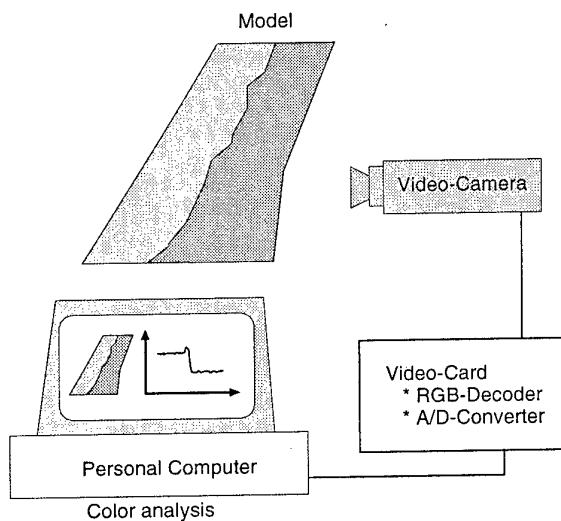


Figure 1: On-line video system for the chromatic interpretation of liquid crystal images

This image processing can be done in the HSL-space, regarding hue, saturation and lightness. A calibration of liquid crystals can be performed by installing thermocouples on the test structure and applying liquid crystals directly above the thermocouples. A result of a liquid crystal calibration is shown in Figure 2. Here, the hue value is plotted as a function of the foil temperature obtained from two different measurement series. As can be seen from the figure, the resulting calibration function is reproducible and has a usable range of about 2.8 K. The measurement accuracy is about $\pm 7\%$ full scale. If the viewing angle is changed, the resulting

color analysis changes considerably (Hoang et al., 1995, Haselbach et al., 1996). Thus for quantitative measurements at least the viewing angles must be kept invariable during calibration and experiment.

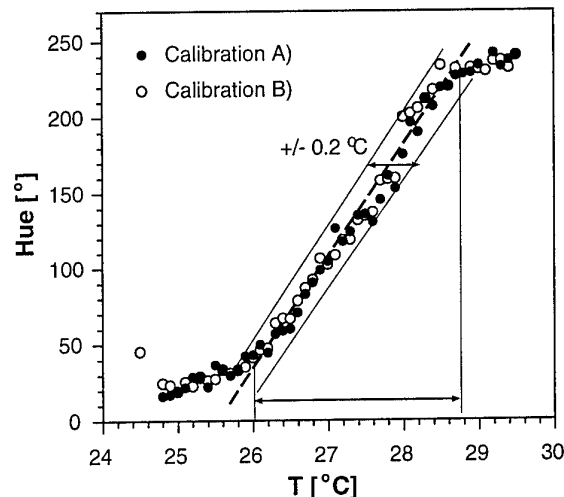


Figure 2: a) Calibration of liquid crystal foil for two different lighting intensities

The spatial resolution of liquid crystals is given by the size of the encapsulated liquid crystal balls, which are of the order of 10 - 50 μm . However, in most cases the restrictive spatial resolution will be given by the video camera system used for the experiments. The temporal resolution capabilities of liquid crystals are dominated by the underlying substrate material, which usually - because of the spatial resolution requirements - is of low thermal conductivity. Thus, only a low temporal resolution ($f_c < 10\text{Hz}$) can be obtained.

4.2 Piezofoil-Arrays

Piezoelectric sensors and sensor arrays have been successfully employed for measurements of unsteady force fluctuations for several years now (Nitsche & Szodruch, 1993, Ewald et al., 1993, Suttan et al., 1995, Swoboda & Nitsche, 1996, Carraway, 1989). A piezofoil consists of a thin PVDF (Polyvinylidenfluorid) film, metallized on both sides. The foil is very thin ($9\mu\text{m} < h < 100\mu\text{m}$) and flexible, so it can be fixed to almost arbitrary surfaces without influencing the flow. By partially etching one side of the metallic coating, it is possible to create sensor arrays which are customized to a given measurement case. A schematic sketch of a piezofoil sensor is shown in Figure 3.a.). Figure 3.b.) shows the layout of a 142-sensor array for flat plate experiments aimed on the evolution of an artificially excited wave train in a transitional boundary layer. The spatial resolution of this array was 10 x 10 mm^2 inside a wedge of 12° downstream from the harmonic point source and 20 x 20 mm^2 in a rectangular shape for control purposes.

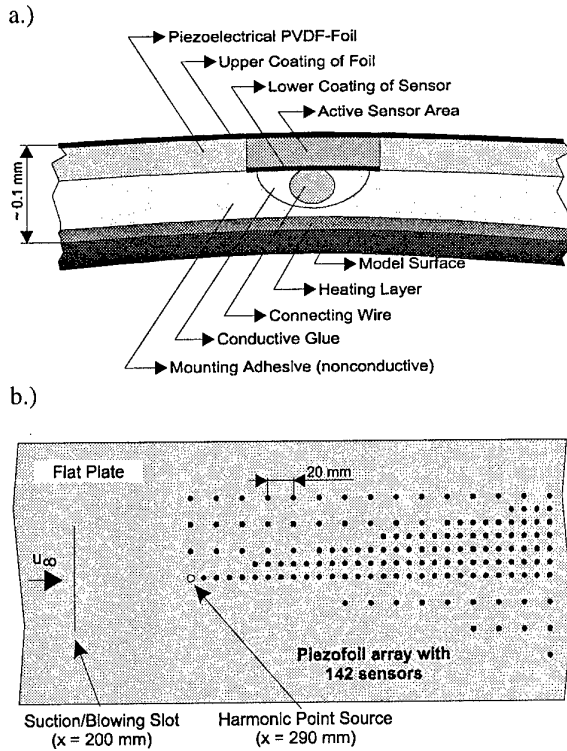


Figure 3: a.) Schematic sketch of a piezofoil sensor, b.) Layout of 142-sensor array for transition experiments

The piezofoil material distinguishes itself by the existence of piezoelectric as well as pyroelectric properties. A single piezofoil sensor can be considered as a plate capacitor with a very low capacity and mass. Assuming a mechanically and electrically unloaded sensor and an adiabatic or isothermal change of state, the change in electrical polarization of a sensor element can be described as

$$\Delta Q = d_{33} \cdot \Delta p \cdot A_{\text{sensor}} \quad (1)$$

with Δp : pressure fluctuation
 A : sensor area. ; d_{33} : piezoelect. constant

When assuming a temperature change while electrical field strength and mechanical tension are constant, the change in electrical polarization results as follows:

$$\Delta Q = d_t \cdot \Delta T \cdot A_{\text{sensor}} \quad (2)$$

with ΔT : temperature fluctuation.
 d_t : pyroel. constant

The sensor signals can be amplified by means of simple charge amplifiers. Thus, its possible frequency range is only limited by the lower limiting frequency of the employed charge amplifiers (typically 1.6 to 160 Hz) and its own resonance frequency (up to 10^9 Hz).

Since the pyroelectric constant d_t is about six orders of magnitude higher than the piezoelectric constant d_{33}

(normal to the sensor surface), a temperature gradient between sensor and fluid can be employed to obtain higher signal amplitudes and thus, signal-to-noise ratios (Sturzebecher et al., 1997). This is especially important for the minimization of sensor size and spacing in array measurement techniques. An example of the improvements regarding absolute signal strength and SNR is given in Figure 4. Figure 4.a.) shows the distribution of RMS-values over a flat plate equipped with a multisensor piezofoil array. Transition position, marked by the sharp increase in RMS-values, can be derived from both test cases, but SNR with heating ($\Delta T = 10$ K) is about 50 times higher than without. A higher SNR not only allows for better determination of time averaged values, but also for detailed signal analysis in the temporal or frequency domain (Fig. 4.b).

In both cases, the artificially induced frequency of 200 Hz, which corresponds to the Tollmien-Schlichting instability frequency of this experiment, is marked by a peak in the frequency spectra. From the time trace without heating, it is visible that the signals from the sensor operating in the piezoelectric way are influenced by external disturbances like noise and vibration of the test setup. With the sensor operated in the pyroelectric way, the TS-waves caused by the suction/blowing slot are more clearly visible. Since pressure fluctuations („piezo“) as well as temperature or shear stress fluctuations („pyro“) are both correlated with near wall velocity fluctuations u' in a boundary layer, the use of the pyroelectric properties is a good means to perform qualitative measurements of surface force fluctuations, especially in transition experiments.

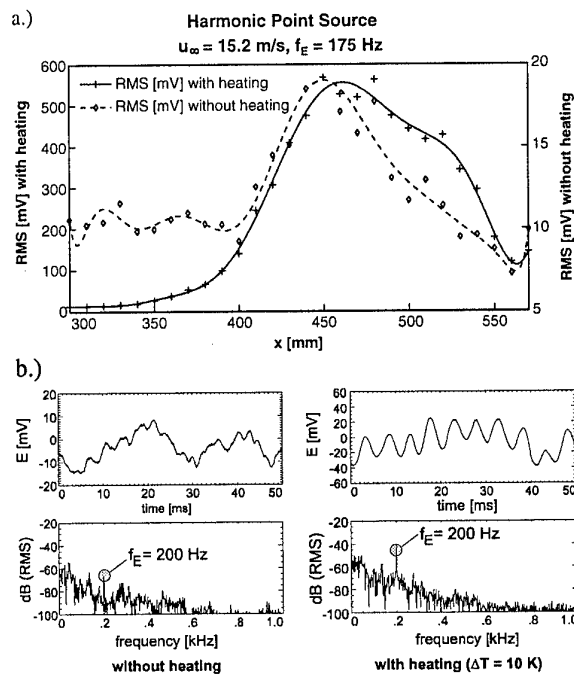


Figure 4: a.) Comparison of RMS-values and b.) Time traces/frequency spectra for transition measurements with and without sensor heating

The number of sensors on a piezofilm array is mainly limited by the capabilities of the employed measurement system. Spatial resolution is only limited by sensor size and the requirement of contacting each sensor to the measurement system with conducting wires. Arrays made from conventional sensors (as described in Figure 3) were built up to now with sensor sizes down to $2 \times 0.9 \text{ mm}^2$ and sensor spacing of 2.5 mm . The minimization in terms of sensor size is limited by the necessity of achieving a good signal-to-noise ratio, in terms of sensor spacing the limiting factor is the distance of the conducting wires from the sensors as well as among themselves to avoid overspeaking. As described above, the SNR can be increased considerably by heating the sensors. This heating is limited by the destabilizing effect which wall heating has on boundary layers (Mack, 1986). Since even a very small temperature gradient ($\Delta T \sim 2 \text{ K}$) between sensor and flow is sufficient to obtain a SNR increase of about 10, this effect can be neglected.

As described above, the frequency range of piezofilm sensors themselves is nearly unlimited. Thus, the limitations in temporal resolution are only set by the capabilities of the measurement system. The lower limiting frequency f_{CA} of the charge amplifiers may be chosen by different settings of R_G and C_G to avoid influences of low frequency disturbances in the measured signal. The upper limiting frequency is given by the maximum sampling frequency f_s of the employed A/D-converters. According to the Shannon theorem, the frequency range is limited by $f_{Sha} = \frac{1}{2} f_s$. To fulfill this boundary condition, a lowpass filter should be employed, but due to the temporal and spatial discretization (sampling rate, sensor size), the sensor signals show decreasing amplitudes with increasing signal frequency, dampening higher frequencies below the immanent noise level of the measurement system. Figure 5 shows a simulation of the frequency response of different piezofilm sensors (circle with $\varnothing 3.5 \text{ mm}$, strip $5 \times 2 \text{ mm}^2$ and strip $10 \times 1 \text{ mm}^2$, equal area) as a function of signal frequency and streamwise sensor length.

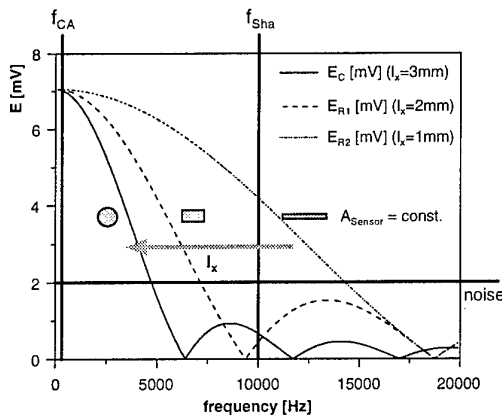


Figure 5: Simulation of frequency response for sensors with different streamwise length

It can be seen that a larger length in streamwise direction leads to an earlier decrease in output amplitude, caused by the integration of signal fluctuations over the sensor's streamwise length.

4.3 Surface Hot-Films

The surface hot-film technique is based on the analogy between local skin friction and heat transfer. The electrical heat loss of a thin electrically heated element is correlated to the local wall shear stress by means of calibration. In experimental aerodynamics the surface hot films rank among the most successful standard measuring techniques (Kreplin & Höhler, 1992, Gartenberg et al., 1995). However, since the calibration of surface hot-films depends on a multitude of flow parameters, surface hot films are widely used for detecting qualitatively unsteady flow phenomena like transition, separation or shock wave oscillation. Especially in laminar flow research, surface hot-film arrays with high temporal and spatial resolution are used. Figure 6 shows the typical layout of a single hot-film sensor and hot-film arrays.

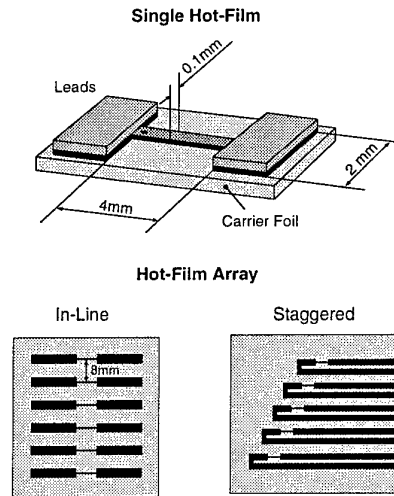


Figure 6: Single hot-film and hot-film arrays

4.3.1 Single Hot-Films

The local heat transfer from a hot-film to a fluid in motion can be related to the local skin friction. For laminar and turbulent boundary layers theoretical analyses have been given by Fage & Falkner (1931) and Ludwig (1949) respectively. From similarity considerations Liepmann and Skinner (1954) derived the following relation between the total heat transfer of a hot-film and the wall shear stress:

$$\frac{Q_w}{\lambda \Delta T} \sim \left(\frac{c_p \rho}{\lambda \mu} L_{eff}^2 \right)^{1/3} \cdot \tau_w^{1/3} \quad (3)$$

This can be written in terms of the heating voltage U and the resistance R of the heated element:

$$\frac{U^2}{l_s R \Delta T} = A + B \cdot \tau_w^{1/3} \quad (4)$$

A and B are constants which are obtained from calibration. This relation is valid for both, laminar and turbulent flow, as long as $L_{eff}^+ < 64 \text{ Pr}$. For practical applications, hot film calibration often is performed according to equation (5). Here, the left-hand side of eq. (4) is represented by the total heat loss of the sensor Q and the constant A is represented by the total heat loss of the sensor in case of free convection Q_0 . Thus, equation (4) can be written as follows:

$$\frac{Q - Q_0}{\Delta T} = B(\rho_w \mu_w \tau_w)^{1/3} \quad (5)$$

The temporal capabilities of surface hot films can be described according to Bellhouse & Schultz (1968) in terms of a theoretical cut-off frequency f_c as follows:

$$f_{c,theo.}^+ = 0.5 \left(\text{Pr} \cdot L_{eff}^+ \right)^{-1/3} \quad (6)$$

According to eq. 3 and the investigations of Gartenberg et al. (1994) the cut-off frequency of the hot-film increases with increasing wall shear stress and high thermal conductivity and diffusivity of the wall material.

4.3.2 Hot-Film Arrays

The calibration of in-line hot-film arrays becomes essential if the skin friction distribution is to be investigated. In this case, the temperature wake induced by a surface hot-film as well as the structural coupling of the sensors becomes increasingly important, see Haselbach & Nitsche (1996). Due to the thermal interference of the sensors, conventional single sensor calibration cannot be applied automatically for such multisensor arrays. As an example for the thermal interference, Figure 7 shows results from temperature measurements in the flow field above a four-sensor in-line hot-film array. Considering the last downstream sensor, it is obvious that the increase in near-wall temperature in front of this sensor will result in a decrease in convective heat loss and hence will lead to a shifted calibration relative to the number of sensors operated upstream.

From Figure 8, showing the calibration of the last downstream sensor for the same test case, it can be seen that the measurement error in terms of wall shear stress τ_w rises with increasing number of sensors operated upstream of the sensor considered and can reach up to $\Delta \tau_w = 47\%$ in case of all upstream sensors being operated.

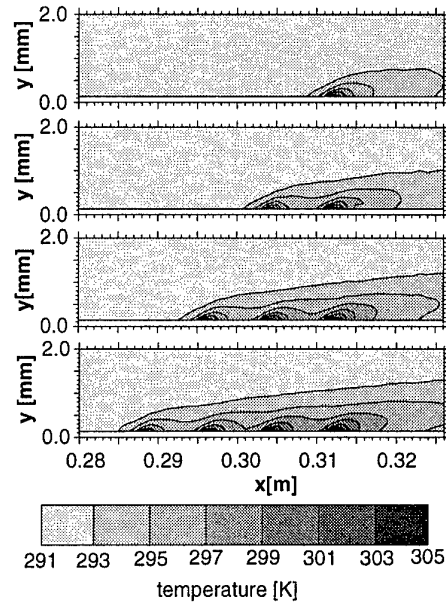


Figure 7: Measured flow temperature distribution above a surface hot-film array ($Re=2 \cdot 10^5$)

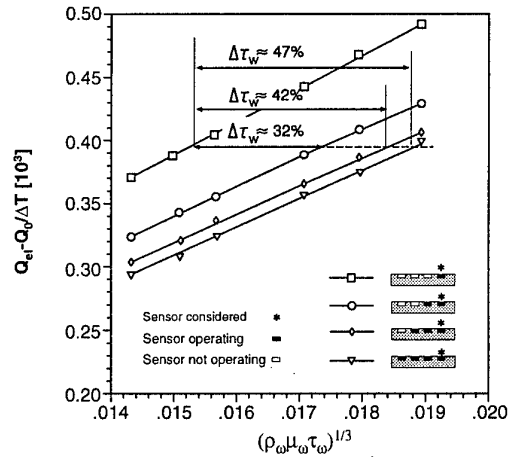


Figure 8: Hot-film array calibration for different number of sensors operated upstream of the sensor considered

5. EXEMPLARY RESULTS

5.1 Liquid Crystals

As an example for the spatial resolution capabilities of liquid crystal foils, Figure 9 shows a turbulent streak in a laminar boundary layer downstream of a disturbance source (harmonic point source). Two turbulent streaks with a distance of 5 mm are clearly visible. This example shows the excellent abilities of the liquid crystal foil technique in determining even small flow disturbances in boundary layers.

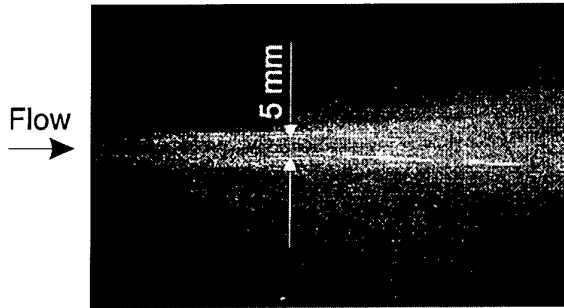


Figure 9: Detail of the turbulent area downstream of a disturbance source (windtunnel test, $Re=3 \cdot 10^5$)

As an example for the applicability of heated liquid crystals for in-flight investigations some results of a laminar wing glove experiment concerning the laminar-turbulent transition are presented in Figure 10. A wing glove was fixed to the right wing of a glider close to the fuselage, with the liquid crystal foil ($0.4 \times 1.2\text{m}$) integrated into the glove. The heating of the liquid crystals was realized by means of an underlying thin layer of uni-directional carbon-fiber.

For the flight tests, the airspeed of the glider was varied from 90 km/h up to 170 km/h, i.e. a maximum Reynolds number $Re=3.7 \cdot 10^6$.

The images were recorded by means of a video camera. The resulting images of the visualization for various air speeds are depicted in Figure 10. Transition is clearly indicated by the white line in the image, moving downstream with increasing speed and accordingly decreasing angle of attack. The corresponding results of the digital image processing are shown on the right hand side of the figure. Here, the resulting color function is plotted as a function of the chordlength for the chordwise centerline of the foil. The strong decrease in the color value in the transition region is clearly visible.

As another example, in this case for high speed flows, Figure 11 shows a result of the visualization of transition due to crossflow on a swept laminar wing ($\phi=45^\circ$) at a Mach number $M_\infty=0.7$ derived from a transonic wind tunnel experiment. Regarding the streaky transition with a average distance of the streaks $s=4.2\text{mm} \approx 6\delta$, the good spatial resolution capabilities of liquid crystals are again clearly visible.

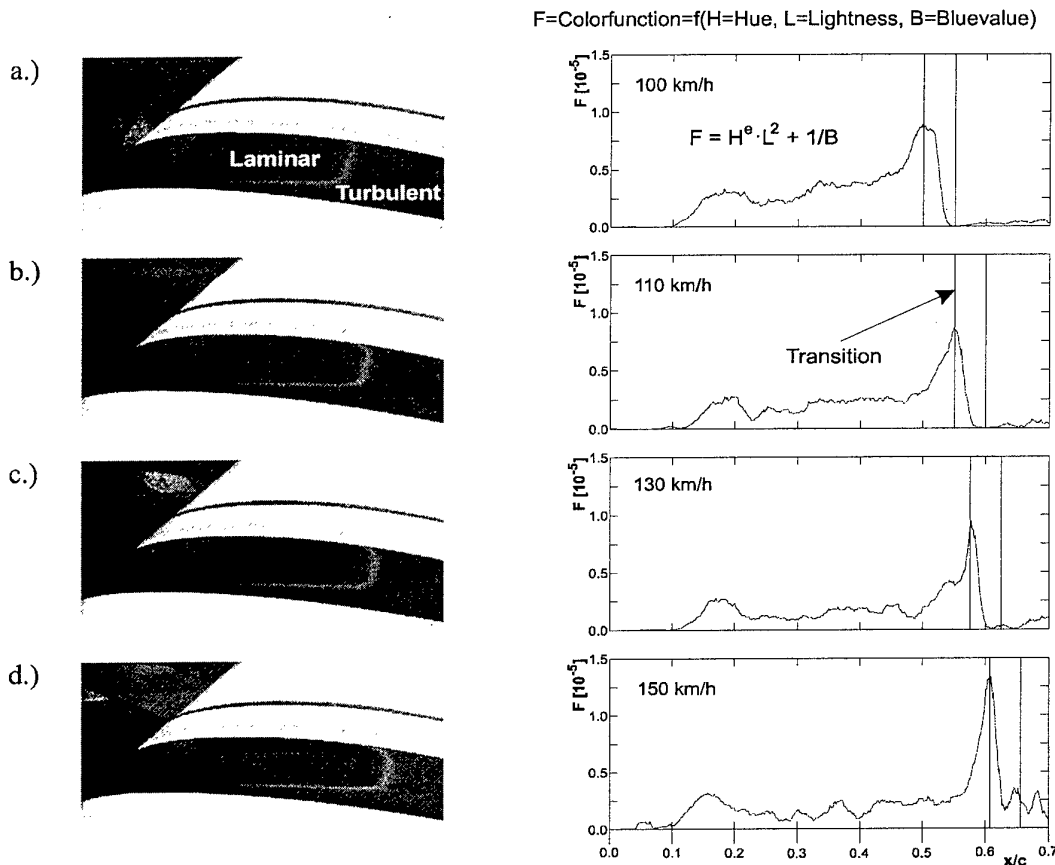


Figure 10: Visualization of the transition on a laminar wing in flight test (left column: video images, right column: resulting color value), a.) 100km/h, b.) 110km/h, c.) 130km/h and d.) 150 km/h

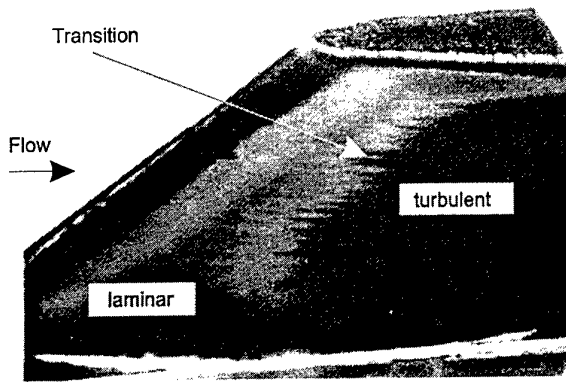


Figure 11: Visualization of the transition due to crossflow on a swept laminar wing ($M=0.7$) by means of liquid crystals for $\alpha=-2^\circ$ (windtunnel test)

5.2 Piezofoil Arrays

For the measurements with multisensor piezofoil arrays, a modular digital multichannel system which allows for simultaneous measurement of up to 192 sensor signals with a sampling frequency of 20 kHz per channel is employed. As a first example, results from experiments concerning the detection of transition location in flight tests are presented in Figure 12. A laminar wing glove equipped with a 48-sensor piezofoil array was mounted on a motorglider. Transition location is marked by the peak in the distribution of RMS-values. Time traces show very small signal fluctuations in the laminar region, a strong increase of low as well as high frequency waves in the transition region and finally, decreasing amplitudes in fully turbulent flow.

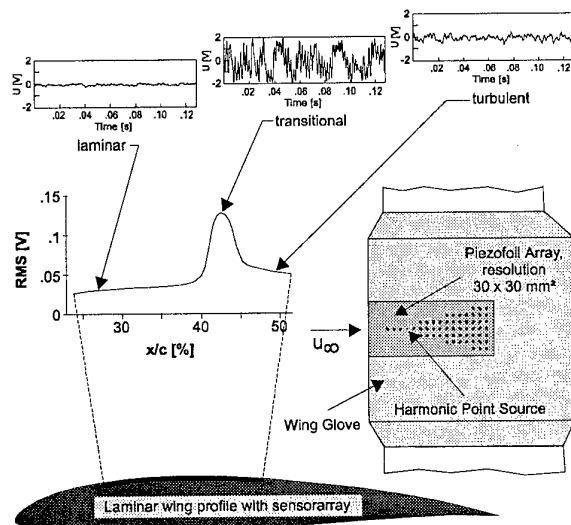


Figure 12: Typical time traces and RMS-value distribution over a laminar wing glove (flight test)

As a further example, Figure 13 shows the evolution of a wave train emanating from a suction/blowing slot during a transition experiment with the 142-sensor array

depicted in Figure 3. Excitation frequency in this case was close to the maximum T-S frequency ($f_{TS} \approx 200$ Hz). At first, the disturbance shows a 2-D excitation up to a x-position of 350 mm. Further downstream, 3-D effects develop and lead to a strong nonlinear increase in wave amplitude.

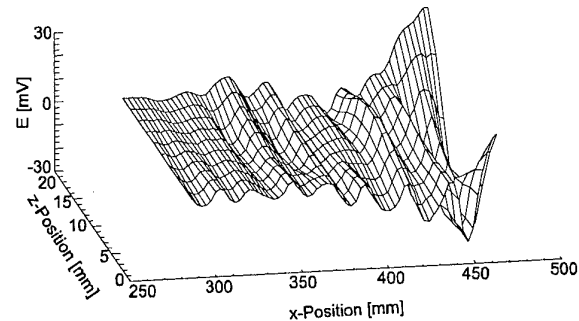


Figure 13: Evolution of a wave train excited by a suction/blowing slot (windtunnel test)

The sensor array which was used for recent flight tests, also concerning the development of instabilities in a transitional boundary layer, consisted of 192 sensors with a streamwise spacing of 6 mm ($\approx \lambda_{TS}/3$) and a spanwise spacing of 11 mm. This high resolution allows for monitoring the downstream travelling and evolution of a wave train ($f_E = 900$ Hz), in this case emanating from a harmonic point source at $x/c=0.27$. The characteristically curved patterns of lines of equal signal amplitude due to this kind of excitation are clearly visible in Figure 14. Here, the development of 3-D instability modes is also obvious from the spanwise distribution of signal amplitude downstream from an x/c -position of 44 % of the chord length.

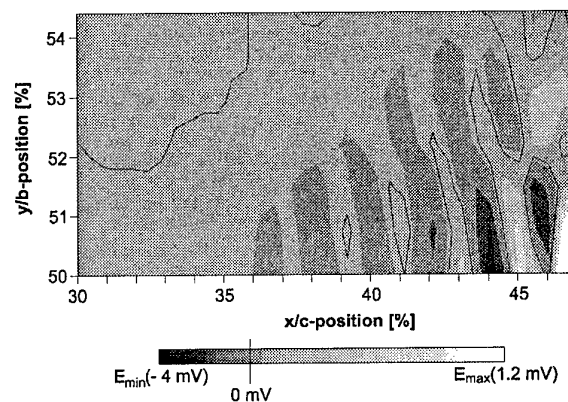


Figure 14: Snapshot of signal amplitudes downstream from a harmonic point source (flight test)

Since the signal amplitude at the point of neutral stability, which is necessary for the determination of n -factors according to the e^N -method, is not known from these experiments, relative n -factors

$$n_{\text{Rel}} = \ln \left(\frac{A_x}{A_{\text{min}}} \right) \quad (7)$$

with A_x : sensor amplitude
 A_{min} : min. Sensor amplitude

were calculated from the sensor signals for different excitation frequencies and are shown in Figure 15. Waves with frequencies close to the natural instability frequency (in this case $f_{TS} \approx 1100$ Hz) show an increase in signal strength immediately downstream from the point source, while lower frequencies are initially dampened and show the increase further downstream, according to the linear stability theory. The measured n_{Rel} -factors of about 5 show the high amplitude ratio which can be achieved with the improved piezofoil measurement technique.

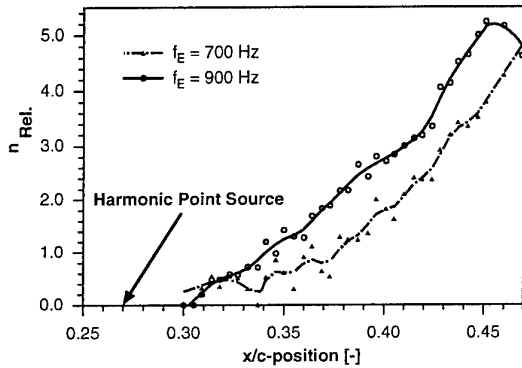


Figure 15: Calculation of n_{Rel} -factors for different excitation frequencies (flight test)

5.3 Surface Hot-Film Arrays

To investigate the measurement errors of in-line hot-film arrays in detail, experimental and numerical investigations concerning the heat balance and calibration of surface hot-film arrays for incompressible and compressible flows, covering a wide range of wall shear stresses ($\tau_w = 0.2 \text{ N/m}^2 - 80 \text{ N/m}^2$) were conducted (Bose et al., 1997, Haselbach & Nitsche, 1996). Here, a shear stress balance (Vakili, 1992) was used as calibration reference. The results obtained from these investigations show that the possible measurement error in terms of $\Delta\tau_w/\tau_w$ increases asymptotically with the number of sensors operated upstream of the sensor considered. On the other hand, the measurement error decreases asymptotically with increased spacing of the sensors, see Figure 16.

The effect of the thermal conductivity of the substrate (wall) material on the thermal interference is depicted in Figure 17. Here, experimental and numerical results are compared in terms of the relative heat loss due to thermal interference. It can be seen from the figure that the effect of thermal interference is decreased by a wall material of high thermal conductivity

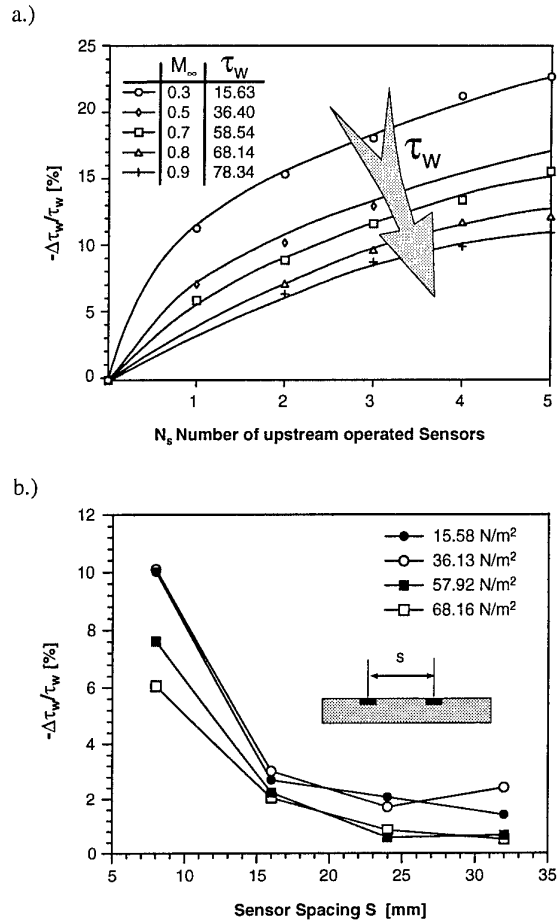


Figure 16: Effect of thermal interference on the calibration of a hot-film sensor out of an in-line hot-film array a.) number of sensors operated upstream, b.) spacing of sensors

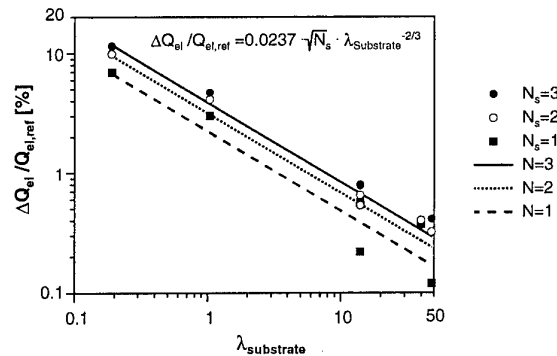


Figure 17: Influence of thermal interference for different wall materials

As a result concerning the calibration of in-line hot-film arrays, it can be shown that the change of the relative heat loss of a hot-film sensor due to an upstream operated sensor is - in case of turbulent flow - a function of the wall shear stress itself. Thus, a standard

calibration procedure can be derived, estimating the influence of the thermal interaction in a wide range of wall shear stress by only a few measurement points. This standard calibration procedure is based on similarity parameters, predominately on the viscous length of the hot-film (Figure 18).

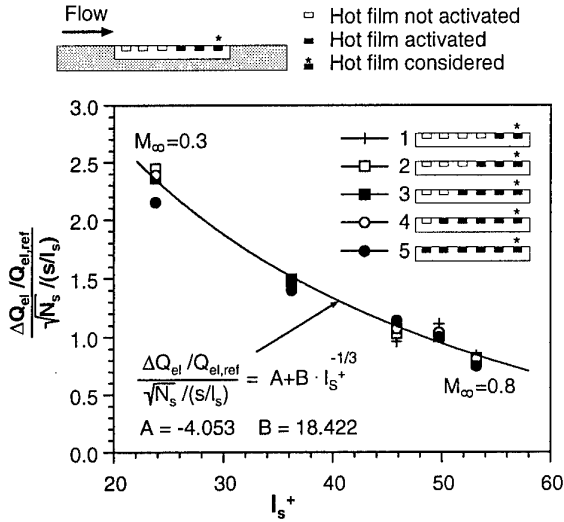


Figure 18: Standard calibration procedure for in-line hot-film arrays (turbulent compressible flow, $dp/dx=0$)

As shown by Haselbach (1997) this standard calibration for in-line hot-film arrays can be written as follows

$$\frac{\Delta Q_{el} / Q_{el,ref}}{\sqrt{N_s} / (s/l_s)} = A + B \cdot l_s^{+ -1/3} \quad (8)$$

and - in turn - can be used to derive a minimum distance for the streamwise spacing of hot-film sensors. Furthermore, taking into account the effect of the thermal conductivity of the wall:

$$\frac{\Delta Q_{el} / Q_{el,ref}}{\sqrt{N_s}} = A \cdot \lambda_{Substrate}^{-2/3}, \quad (9)$$

it is possible to derive design rules for the layout of in-line hot-film arrays which are suitable for different wall shear stress regimes and wall materials.

6. CONCLUSIONS

The paper investigates the capabilities of three currently used surface measurement techniques. The survey is based on experimental and partly numerical results on liquid crystals, piezofoil and surface hot-film arrays. The recent improvements described in this paper are aimed to fulfill the need for qualitative and quantitative surface forces measurement techniques for in-flight

investigations, which are indispensable for the verification and application of new techniques for skin friction drag reduction on modern transport aircraft.

The liquid crystal foil technique proved to be a simple means to obtain insight in the wall flow field for a wide range of flow velocities, from the low subsonic up to the transonic region. Besides the ability to observe large flow areas, it also offers a high spatial resolution for quasistatic flow phenomena like streaky transition due to crossflow instabilities.

The applicability of multisensor piezofoil arrays for the qualitative measurement of surface force fluctuations was considerably improved by using the inherent pyroelectrical capabilities to obtain a higher signal-to-noise ratio along with a decreased sensitivity to external disturbance sources like noise or vibrations. It enables measurements with high spatial as well as temporal resolutions by reducing the necessary sensor size and thus, sensor spacing. Recent experiments showed the ability of the improved piezofoil technique to measure the development of disturbance waves in transitional boundary layers.

Investigations of the behavior of surface hot-film sensors in densely packed hot-film arrays led to the development of a standard calibration method. This enables experimenters to take into account the influences of sensor spacing on the resulting total wall shear stress. Thus, in-line surface hot-film arrays become also applicable for quantitative wall shear stress measurements.

7. REFERENCES

- Bellhouse, B.J., Schultz, D.L., 1968, „The Measurement of Fluctuating Skin Friction in Air with Heated Thin-Film Gauges“, J. Fluid Mech. 32, Vol. 4, pp. 675-680
- Bose, S., Haselbach, F., Nitsche, W., „Comparative Investigations on the Reliability of Direct and Indirect Skin friction Measurement Techniques in Compressible Flow“, 5th FLUCOME, Sept. 1-4, Hayama, Japan, to be published
- Carraway, D.L., 1989, „Use of piezoelectric foils in experimental aerodynamics“, ICIASF'89 Record, pp. 613-626
- Ewald, B., Durst, F., Krause, E., Nitsche, W., 1993, „In-flight measuring techniques for laminar flow wing development“, Zeit. Flugwiss. Weltraumforschung, Heft 17, pp. 294-310
- Fage, A., Falkner, V.M., 1931, „Relation Between Heat Transfer and Surface Friction for Laminar Flow“, R. & M. No. 1408, British A.R.C.

- Gall, P.D., Holmes, B.K., 1986, „Liquid crystals for high altitude in-flight boundary layer flow visualization“, AIAA-paper 86-2592
- Gartenberg, E., Scott, M.A., Martison, S.D., Tran, S.Q., 1994, „Boundary Layer Transition Detection with Hot-Films in Cryogenic Wind Tunnels“, 4th Int. Symposium on Fluid Control, Measurement and Visualization, Toulouse, France
- Haselbach, F., Nitsche, W., 1996, „Calibration of single-surface hot-films and in-line hot-film arrays in laminar or turbulent flows“, in: Meas. Sci. Technol. 7, Vol. 10, Topical Issue: „Thermal Anemometry“, IOP-Publishing Ltd., U.K., pp. 1428-1438
- Haselbach, F., Reyer, M., Nitsche, W., 1996, „In-flight Transition Detection on a Laminar Wing by Means of Heated Liquid Crystal Foils“, Proc. of the 2nd European Forum on Laminar Flow Technology, Bordeaux, pp. 10.42-10.49
- Haselbach, F., 1997, „Thermalhaushalt und Kalibration von Oberflächenheißfilmen und Heißfilmmarrays“, PhD-Thesis, TU-Berlin, Germany, *to be published*
- Henke, R., Capbern, P., Davies, A.J., Hinsinger, R., Santana, J.L., 1996, „The 'A320 HLF Fin-Program': Objectives and Challenges“, Proc. of the 2nd European Forum on Laminar Flow Technology, Bordeaux, pp. 12.3-12.11
- Hoang, Q.H., Toy, N., Savory, E., 1995, „Liquid crystals for surface shear stress measurements“, Proc. of the 7th Intern. Symposium on Flow Visualization, Sept. 11.-14., Seattle, USA, pp. 552-557
- Kasagi, N., Moffat, R.J., Hirata, M., 1989, „Liquid crystals“, Handbook of Flow Visualization, Chapter 8, Ed. W.J. Yang, Hemisphere Publ. corp.
- Liepmann, H.W., Skinner, G.T., 1954, „Shearing Stress Measurements by Use of a Heated Element“, NACA TN 3269
- Ludwig, H., 1949, „Ein Gerät zur Messung der Wandschubspannung turbulenter Reibungsschichten“, Ing.-Arch. 17, pp. 207-218
- Mack, L.M., 1984, „Boundary-layer linear stability theory“, AGARD-R-709, Part 3
- Meier, H.U. Zou, M.D., 1991, „The development of acoustic generators and their application as a boundary layer transition control device“, Experiments in Fluids 11, pp 93-104
- Nitsche, W., Szodruch, J., 1993, „Laminar-flow instrumentation for wind-tunnel and flight experiments“, Journ. of Aircraft, Vol. 30, No. 2, pp. 192-200
- Kreplin, H.P., Höhler, G., 1992, „Application of the surface hot film technique to laminar flow research“, Proc. of the 1st European Forum on Laminar Flow Technology, Paper 92-01-017, DGLR (Ed), Bonn, pp. 123-131
- Sturzebecher, D., Nitsche, W., 1997, „Visualization of the Spatial-Temporal Instability Wave Development in a Laminar Boundary Layer by Means of a Heated PVDF Sensor Array“, Notes on numerical Methods, Vieweg-Verlag, Braunschweig, to be published
- Suttan, J., Baumann, M., Nitsche, W., 1995, „In-flight Measurements on a Laminar Wing-Glove by Means of Surface Sensor Arrays“, In: Laminar-Turbulent Transition, Sendai (Jap.), Springer-Verlag, pp. 121-128
- Swoboda, M., Nitsche, W., 1996, „Shock boundary-layer interaction on transonic airfoils for laminar and turbulent flows“, Journal of Aircraft, Vol. 33, No. 1, pp 100-108

APPLICATION OF OIL FILM INTERFEROMETRY SKIN-FRICTION TO LARGE WIND TUNNELS

David M. Driver

NASA Ames Research Center, M/S 229-1, Moffett Field, California 94035-1000 USA

Summary

The oil film interferometry skin-friction technique is described and applied to flows in some of the NASA Ames large wind tunnel facilities. Various schemes for applying the technique are discussed. Results are shown for tests in several wind tunnels which illustrate the oil film's ability to measure a variety of flow features such as shock waves, separation, and 3D flow.

Nomenclature

c	airfoil chord
C_f	skin friction coefficient
h	oil thickness
M	Mach number
n	index of refraction
q	dynamic pressure
Re	free stream Reynolds number based on airfoil chord
t	time
x	axial coordinate from the oil leading edge
λ	light wavelength
ρ	density
θ_i	incidence angle
θ_r	refraction angle
τ	skin friction
ξ	distance along model surface from oil leading edge
μ	absolute viscosity of oil
ν	kinematic viscosity of oil

Subscripts

f	fringe
o	oil
ref	reference condition
run	duration of run
x	x direction
z	z direction
∞	free stream condition

Introduction

The oil film interferometric technique has been used to measure skin friction for the last 20 years in one form or another^{1,2}. However, it was not until 1993 that the technique gained wide scale acceptance when Monson and Mateer³ modified the technique to use standard room lighting (to visualize the oil interferometric pattern) and a simplified form of the oil-flow equation that only depends on the end state of the oil. This simplified form of the technique allows anyone to make skin-friction measurements with a minimum of equipment (\$500) and set up time (20 minutes). As a result of this improvement to the technique, the number of people working in the field of oil-flow interferometry has exploded^{4,5,6,7,8} and the applications have gone from small scale wind tunnel models to large scale wind tunnel models, vehicles in flight, and automotive aerodynamics.

This paper describes some recent experience using the technique in the production wind tunnels at NASA Ames. Included in the paper are examples of skin-friction measurements on various models in the 12' pressurized wind tunnel, the 40'x80' wind tunnel, and on a helicopter blade in the 80'x120' wind tunnel.

Measurement Technique

The oil film technique works on the principal that oil on a surface, when subjected to shear, will thin at a rate related to the magnitude of the shear. The measurement involves measuring the oil-thickness distribution, logging the history of tunnel run conditions, and knowing the properties of the oil.

Thickness distributions are determined from the interference patterns which are produced in the thin oil film due to interference between reflected light from the model surface and the reflected light from the air-oil interface (see fig. 1). An example of a typical oil film and the associated interference patterns is shown in figure 2, in which 40 or more oil film patches are seen on a wing. The dark streaks seen in each of the oil film patches (referred to as fringes)

are contours of constant oil thickness and can be related to the depth of the oil, h . The spacing between the fringes is proportional to the skin-friction as seen in the equation derived by Monson and Mateer³.

$$C_f = \left(\frac{2n_o \cos(\theta_r) \cdot \Delta x_f}{\lambda} \right) / \left\{ \int_0^{t_{run}} \frac{q_\infty(t)}{\mu(t)} dt \right\}$$

The first grouping on the right hand side of the equation is the reciprocal of the oil's slope and the integral contains the oil's viscosity and the integrated tunnel dynamic pressure. This equation is derived from a 1-D hydraulic oil flow theory and the derivation is shown in Appendix A for the purpose of highlighting the assumptions that go into the equation.

The shear measured by this equation is the component of shear that is perpendicular to the oil's leading edge. The shear parallel to the oil's leading edge does not influence the oil's height distribution in the normal direction.

Procedure

The first step is to prepare the test surface so that it is optically smooth and partially reflective. The easiest approach is to apply thin sheets of MonoKote⁹ (Mylar with black pigment and adhesive backing) to the test surface, the self adhesive back makes it easy to apply and strongly adhered to the surface. The combination of Mylar (index of refraction 1.67) and black pigment embedded in the Mylar provides a partially reflective surface which reflects light with about the same intensity as does the air-oil interface. The interference is a result of the reflected light from the test surface (Mylar) interfering with the light from the air-oil interface (see fig. 1). Test surfaces that are made from polished acrylic or polished stainless steel provide good optical interference without the use of Mylar (polished surfaces need to be 2 micro-inch or better polish).

The second step is to apply small oil patches (line segments, drops, smudges, etc.) to a series of locations on the model surface. Dow Corning provides silicone oil¹⁰ in viscosities of 5, 10, 50, 100, 200, 500, 1000, 5000, 10000, 30000, and 100000 centistokes. The choice of viscosity is based on tunnel run time, dynamic pressure, and desired displacement between adjacent interference patterns (or commonly called fringes). The oil patches should be spaced far enough apart so that one oil flow patch does not significantly run into another patch. The leading edge (upstream side) of the oil flow needs to be uncontaminated by other oil flows.

The third step is to pass air over the model (run the tunnel, fly the airplane, spin up the rotor, drive the car), and record the history of the dynamic pressure and model tempera-

tures during the run. The oil's viscosity is a function of oil temperature.

The fourth step is to record the oil-flow patterns after the tunnel run. The oil flow pattern is "frozen" and does not spread any more in the absence of shear (gravity is negligible on a thin film which is only microns thick). The oil should be illuminated with as nearly a monochromatic light source as possible and photographed with fiducial marks or rulers in place. Measuring of the fringes can be done on a digitized image using various software packages (PhotoShop (by Adobe) or software developed by Zilliac⁷) or it can be done with vernier calipers directly using the print or the test model itself.

Details of Lighting

The oil should be illuminated with as nearly a monochromatic light source as possible -- actually the light source does not have to be monochrome, but the notch filter in front of the camera or observer should be fairly narrow. The light source needs to be spatially coherent over a few microns (which eliminates tungsten bulbs), standard gas filled bulbs usually have these characteristics. Light sources such as fluorescent bulbs, black lights, or other forms of Mercury discharge tubes provide very coherent light with a strong emission at specific wavelengths ($\lambda=546$ nm) easily isolated with notch filters. Xenon flashes from standard studio flashes provide good coherent light sources (but needs to be filtered). Another excellent light source is low pressure sodium bulbs, which emit at a single wavelength, (actually closely spaced doublet), $\lambda=589$ nm and $\lambda=589.6$ nm, making filters unnecessary.

Many light source configurations have been used, ranging from light boxes to elaborate reflective umbrellas which surround the model (see figures 3,4,5 and 6). The basic requirement is that light from the light source needs to specularly reflect from the model's surface directly into camera. The bigger (more expansive) the light source, the bigger is the area of the model which will specularly reflect light from the source to the observer. With small portable light sources, like a light box (fig 3), it is possible to illuminate small regions of the model and subsequently reposition the light box to obtain other regions of the model. The region which reflects light into the camera is shown in figure 3 as a rectangular patch on the model. This works quite well for minimizing the setup time and effort. In other setups, large (1m by 2m) versions of a light box (fig. 4) have been built in which large translucent sheets were back lit with a small viewing hole through the center for the camera -- this is done in an effort to try and illuminate the entire model. Besides this setup being unwieldy, there is a spot on the image (in the middle)

where there camera lens reflection is seen (camera lens doesn't reflect light and produces a dark spot. On other occasions I have set up large white reflective screens which surround the model (something like a tent or umbrella), lights are used to front light the reflective screen, and a small cutout hole in the center of the reflective screen is used to view the model (see fig. 5). This technique works well, but is a little unwieldy. Most recently, I have been using the entire wind tunnel top and side walls as a reflector (with windows painted white), with the camera positioned in one of the overhead windows (small non-painted) viewing hole (see figure 6). An example of an image taken while looking through a window with tunnel walls painted white is shown in figure 7. The black spot in the image is due to the lack of light from the reflection of the camera lens. The hole is usually a smaller percentage of the total area for bigger models, this model is 300mm in span and the hole is 50mm square. Getting permission to paint windows is difficult, but otherwise this works great and offers the possibility of obtaining pictures during the run as opposed to after the run. This improves tunnel run productivity.

Uncertainty

Most of the sources of error are easily controlled. Viscosity is a function of temperature with viscosity varying approximately 1% per degree Fahrenheit. The fringe spacing is easily measured to $\pm 5\%$ accuracy with accuracy being primarily a function of fringe visibility (digital resolution)⁷.

Non-constant run conditions are probably the biggest unknown source of error, with tunnel start-up and shutdown transients producing flow conditions which are different than the test condition. The major assumption used in the development of the oil flow equations is that the C_f is constant for all time; this is less restrictive than requiring that the shear itself (τ) is constant. However, it may not be so good to assume that the C_f is constant with time, especially when shock waves, separation, and transition are changing with changing tunnel conditions (such as Reynolds and Mach number). It is especially important to minimize the duration of the start-up and shutdown periods relative to the time spent on condition since the oils thinning is a function of the entire run. Figure 8 shows the time history of velocity for each of the tunnels in which tests were conducted. The figure shows that some tunnels are able to obtain steady conditions sooner than others.

A conservative estimate of skin-friction uncertainty is to say that the uncertainty is proportional to the ratio of time spent in start-up/shutdown relative to the total run

time. This uncertainty would go away if it were possible to take two pictures separated in time during the tunnel run. However, insitu photographs are usually not feasible.

It is beneficial to hold the model at fixed pitch during the entire run. It is worth noting that the oil-flow technique does not allow for multiple conditions to be tested during the course of a run. For example multiple angle of attacks are not possible (without taking a series of pictures during the run).

Another source of error is due to the assumption that the oil is infinitely thick at the beginning of the run. This source of error is investigated in Appendix B and is determined to be small.

Sample Results

Several results are shown for models in various NASA Ames wind tunnels.

40x80 Tunnel

The first test was performed in the Ames 40x80 wind tunnel on the horizontal stabilizer of a commercial transport type wind tunnel model. In this case hydraulic lifts were wheeled into the test section and used to reach the model which was 6m high. Mylar and 2000 cs oil was applied to the tail upper surface. The tail section was chosen so as to stay away from the wing portion of the model where acoustic tests were in progress. The tunnel was run at Mach 0.275 and atmospheric pressure for a period of 20 minutes. Figure 9 shows the resulting fringe pattern. The C_f distribution is shown in figure 10. A steady decline in C_f is seen with no abrupt increases in C_f which would be indicative of transition from laminar to turbulence. The upper surface is the pressure (windward) side of the horizontal stabilizer (since tail is pitched at a negative angle of attack). Consequently, the surface experiences a favorable pressure gradient and the Reynolds number was low ($Re_c = 1.4$ million), and it seems likely that the flow over this surface was laminar from leading to trailing edge.

12 Foot Pressurized Tunnel

A second test was performed in the Ames 12' pressurized wind tunnel on the wing and flaps of a commercial transport type model in a landing configuration. Mylar and 2000 cs oil was applied to the model in a hurry (20 minutes) so as to minimize the impact on an already busy run schedule. The tunnel was run at 3 atmospheres pressure ($Re = 4$ million/ft) and Mach 0.25. Pictures were taken with a light box and 35mm camera as the model was being disassembled and crated. The resulting oil-flows showed that

the flow was attached almost everywhere with healthy levels of skin-friction ($C_f > 0.001$), except in the vicinity of the winglet (see figure 11) which showed signs of a laminar leading edge vortex followed by reattachment and transition to turbulence downstream of the vortex (see figure 12 for a close-up view). Figure 13 shows the axial component of skin-friction for the winglet. All measurements are lumped onto one plot without regard to the spanwise location. The dashed line is a hand faired curve through the data to aide in viewing.

Rotor in Hover in the NASA Ames 80x120 wind tunnel

A third test was performed on a helicopter rotor blade during hover tests in the 80'x120' wind tunnel (tunnel fans off). Hydraulic lifts were positioned into place and were used to gain access to the model (10 meters high). Mylar and oil were applied to the model. Because of differing aerodynamic forces, oil of 500 cs was used near the root while 10000 cs was used at the tip, with 1000 and 2000 cs oil being used at the intermediate stations. The rotor was spun up to a tip speed of $Mach=0.56$ and held on condition for 15 minutes. Pictures were obtained using a semi-circular (tent) reflective structure over the blade with a hole in the center of the reflector through which a digital camera viewed the blade (setup shown in figure 5). A pair of strobe lights were used to illuminate the reflector while the camera was fitted with a notch filter.

Figure 14 shows the resulting fringe patterns. Oil had been applied in patches with each patch having wetted edges parallel to the blade leading edge and parallel to the chordwise direction. Fringes forming parallel to the leading edge of the rotor blade are spaced proportional to the chordwise component of shear, while fringes forming parallel to the chordwise direction are spaced proportional to the radial component of shear. The centrifugal force affects the oil's motion in the radial direction and thus produces some uncertainty in the radial component of shear. The oil flow in the streamwise direction is unaffected by radial forces so these introduce no additional uncertainties in the chordwise component of shear. Figure 15 shows the skin friction distribution at the 83% span location. It is evident from the rapid increase in C_f at 45% chord that the flow has transitioned from laminar to turbulence.

Discussion

Measurements of skin-friction in the big tunnels is relatively low productivity and is consequently sparsely used to date. This is due to the fact that for each new run condition the tunnel must be shut down, new oil applied, tunnel restarted and run (20 minutes or so) then shut-down and shot photographs. While each measurement cycle can be

performed in as little as 2 hours, this is a relatively high price to pay compared to force and pressure measurements which can be obtained in less than a minute for each condition. The technique is more commonly used in the research environment. However, the payoff is high when one is trying to determine transition strip effectiveness or health of the boundary layer in the vicinity of shocks and the trailing edge. Sometimes C_f measurements are the only convenient way to diagnose anomalies in test data resulting from reverse Reynolds number effects.

The oil film interferometry technique is a definite candidate for replacing sublimation techniques in the determination of transition location. Not only is the information more quantitative in the case of oil flow, but it is also environmentally cleaner.

Tests which are deemed to be Computational Fluid Dynamic (CFD) test cases should without a doubt use the technique to obtain skin friction for the validation of CFD codes. Skin friction data obtained using this technique can already be credited with uncovering one bug in a CFD production code.

Not only is it possible to obtain the chordwise component of skin-friction, it is also possible to determine the shear direction as well. This is described in more detail in Appendix C.

Skin friction measurements are becoming increasingly popular, since improvements made to the technique by Monson and Mateer³. The number of people using oil film interferometry has increased an order of magnitude over the number of people using the original laser based system. No insitu calibrations are needed to obtain highly accurate measurements (better than 10%) and setup is minimal.

Conclusions

This paper shows results from the first application of this technique to the NASA Ames 40'x80' and 80'x120' wind tunnels, and the 12' pressurized tunnel.

While it is possible to obtain skin friction measurements at hundreds of discrete locations on the model in each run, the productivity is relatively low (relative to force and balance measurements). The average time to obtain one set of measurements at one condition is 2 hours. Productivity will need to be increased. One way to do this is to obtain pictures sequentially during the run and take the difference in oil height between adjacent pictures. By so doing one can envision obtaining 4 or so conditions during each run before needing to replenish the oil on the model.

Oil film interferometry has been shown to produce good quantitative measurements of skin friction in and around flows with separation, shock waves, and transition. Methods for obtaining flow direction from the interferometric patterns are also described in the appendix.

Using numerical solutions, the oil film's measurements accuracy has been shown to be relatively insensitive to the initial application of oil. Also, the numerical solutions were used to show that oil flow in the vicinity of shock waves can produce accurate C_f distributions ahead and behind the shock.

References

1. Tanner, L. H. and Blows, L. G.; "A study of the Motion of Oil films on Surfaces in Air Flows, with Application to the Measurement of Skin Friction," Jour. of Physics E: Scientific Instr., Vol. 9, No. 3, Mar. 1976, pp.194-202.
2. Monson, D. J., "A Nonintrusive Laser Interferometer Method for Measurement of Skin Friction," Experiments in Fluids, Vol. 1, No. 1, 1983, pp. 15-22.
3. Monson, D. J., Mateer, G. G., and Menter, F. R.; "Boundary-Layer Transition and Global Skin Friction Measurement with an Oil-Fringe Imaging Technique," SAE Paper 932550, Sept. 1993.
4. Kennelly, R.A. Jr., Westphal, R.V., Mateer, G.G., and Seelen, J.; "Surface Oil Film Interferometry on a Swept Wing Model in Supersonic Flow." I. Proceedings of the 7th International Symposium on Flow Visualization, Sept. 1995. ed J.P.Crowder, pp. 302-307. New York: Begell House
5. Naughton, J.W. and Brown, J.L.; "Surface Interferometric Skin-Friction Measurement Technique," AIAA Paper 96-2183, July 1996.
6. Garrison, T.J. and Ackman, M.; "Development of a Global Interferometer Skin-Friction Meter," AIAA Paper 96-1968, July 1996.
7. Zilliac, G. G.; "Further Developments of the Fringe-Imaging Skin Friction Technique," NASA TM 110425, December 1996.
8. Wadcock, A. J., Yamauchi, G. K., and Driver, D. M.; "Skin friction measurements on a rotor in hover," A.H.S Technical Specialists' Meeting for Rotorcraft Acoustics and Aerodynamics, Williamsburg, VA, October 28-30, 1997.
9. MonoKote, Top Flite Models, Inc. Champaign, IL.
10. "Information About Dow Corning Silicone Fluids," Dow Corning Corp., Midland, MI, 1994.

Acknowledgments

The author would like to thank Robert Kennelly, Jim Brown, Jon Naughton, Greg Zilliac, and George Mateer for the many discussions we have had on the oil film interferometry technique over the years. I would also like to thank the countless wind tunnel technicians and operators who have made this possible. And special thanks go to the various test engineers who have made their models available, in particular Bret Leonhardt, Abdi Khodadoust, Gloria Yamauchi and Alan Wadcock.

Appendix A: Oil-Flow Equation Derivation

This section provides the derivation of the final equation offered by Monson and Mateer³. Starting with the differential form of the oil flow equation

$$A1) \quad \frac{dh}{dt} = \frac{-1}{2\mu_o} \cdot \frac{d}{dx}(\tau \cdot h^2)$$

where h is the thickness of the oil, μ_o is the oil's viscosity, and τ is the shear stress. This equation can be integrated using separation of variables to obtain the usual form of the equation $\tau=(\mu_o x)/(h t)$. An intermediate form of the equation which results from integrating with respect to x is

$$A2) \quad \tau/(\mu_o x) = \frac{-1}{h^2} \cdot \frac{dh}{dt}$$

where x is the distance downstream of the leading edge of the oil and h is the thickness of the oil at location x . If the left hand side is multiplied by q/q we obtain

$$(q \cdot C_f)/(\mu_o x) = \frac{-1}{h^2} \cdot \frac{dh}{dt}$$

then integrating with respect to time, we obtain

$$A3) \quad \int_0^t (q C_f/(\mu_o x)) \cdot dt = -\int_0^t \left(\frac{1}{h^2} \cdot \frac{dh}{dt} \right) dt$$

Assuming C_f is constant during the run we can rearrange and integrate to get

$$A4) \quad (C_f/x) \cdot \int_0^t \left(\frac{q}{\mu_o} \right) dt = \left(\frac{1}{h} \right) \Big|_{h_i}^h$$

The lower limit on $(1/h)$ is assumed to be small as the initial thickness h_i is large and approximated to be infinity to simplify the analysis. This is routinely done by the proponents of the oil flow method. Upon rearranging, the above equation becomes,

$$A5) \quad C_f = \left(\frac{x}{h} \right) \int_0^t \frac{q}{\mu_o} \cdot dt$$

This is the equation presented in Monson and Mateer³. It is worth noting that one of the main assumptions is that the starting thickness of the oil is infinite. While it is not infinite, it is large (on the order of 100 λ), making this a reasonable assumption. However, the possibility exists for taking a pair of pictures spaced in time and computing the C_f using the difference in thickness between the two times, thus making it feasible to get C_f measurements at different run conditions during the same run.

Appendix B Numerical Solution of Thin Film Equation

Starting with the differential form of the thin film equation, $dh/dt = -(1/2\mu) d(\tau h^2)/dx$, it is possible to integrate with respect to time to obtain

$$h^{t+dt} - h^t = -\frac{dt}{2\mu} \cdot \left(\frac{d}{dx} \tau h^2 \right)^{t+\frac{dt}{2}}$$

next we central difference about the mid-point of x_i and x_{i-1} to obtain.

$$h_{i-\frac{1}{2}}^{t+dt} - h_{i-\frac{1}{2}}^t = -\frac{dt}{2\mu} \cdot \left[\frac{(\tau h^2)_i - (\tau h^2)_{i-1}}{dx} \right]^{t+\frac{1}{2} \cdot dt}$$

Following Naughton and Brown⁵ we approximate $(h^2)^{t+dt/2}$ by $h^t h^{t+dt}$ and substitute into the above equation to obtain

$$\begin{aligned} & \frac{(h_i^{t+dt} + h_{i-1}^{t+dt})}{2} - \frac{(h_i^t + h_{i-1}^t)}{2} \\ &= -\frac{dt}{2\mu} \cdot \{ (\tau h^{t+dt} h^t)_i - (\tau h^{t+dt} h^t)_{i-1} \} \end{aligned}$$

Rearranging we obtain

$$h_i^{t+dt} = \left(\frac{h_i^t + h_{i-1}^t - h_{i-1}^{t+dt} \cdot \left(1 - \frac{dt}{\mu dx} \cdot \tau_{i-1} h_{i-1}^t \right)}{1 + \frac{dt}{\mu dx} \cdot \tau_i h_i^t} \right)$$

This equation is marched forward in time starting with an initial distribution of h , which is large. For example 100 times larger than the final thickness of the oil.

One of the worries about the technique is the assumption that the oil is infinitely thick at the beginning of the run, which it is not. Furthermore, the surface downstream of the original spot of oil is often not wetted by oil until some time later in the run. How does this condition effect the final answer for skin-friction? The solution was started with a thick blob of oil at the upstream position in the domain and at time zero shear is imposed on the oil. Figure B1 shows the thickness distribution of the oil film for various times during the run along with the thickness dis-

tribution as from the Monson-Mateer equation A5. The simulation shows that the oil film thickness distribution from the blob of oil follows very nearly the identical solution from equation A5. The difference between these two solutions (normalized by the local oil thickness) is shown in figure B2. The error diminishes with time and is roughly proportional to the ratio of the oil thickness and the initial oil thickness.

A second calculation was performed on a oil film with varying shear. The shear was made to be 5 times higher over the initial 25% of the domain than it is over the remaining 75%. The resulting height distribution is shown in figure B3. After time $T=1.0$ the oil film height distribution is seen to display two distinct regions with different slope. The upstream region has a slope which is predicted by equation A5 and the downstream region has a slope of 5 times the upstream level. This implies that the C_f is a function of the local slope and that the oil is not influenced by what is flowing into it from upstream.

Appendix C Shock Waves and 3D Flow

Flows are usually 3D and the oil flow interferometry is capable of detecting cross flow. By placing a rectangular patch of oil on the surface, the windward sides of the patch will develop leading edges (two sides). These leading edges of the oil can produce two component measurements of the shear, which can be combined to produce the resultant shear component and angle (see figs. C1 and C2). The locus of corner points in the oil flow point in the direction of the shear as indicated by the arrows in the figure. Experience has shown that kinks of any angle (obtuse or acute) will produce a locus of points that point in the direction of the shear. This is because the 2D oil flow equations are very hyperbolic in nature and have characteristic lines that are oriented parallel to the shear lines. Consequently, oil does not move across surface shear lines (streamlines within the oil) and blemishes in the oil (wakes from protuberances) travel in the streamwise direction and do not diffuse in the lateral direction (see fig. C3).

Shock waves produce an abrupt change in the fringe spacing as can be seen in figure C2. Ahead of the shock the oil behaves predictably (by equation A5) with no knowledge that there is a shock downstream. After the shock the oil flows more slowly as a result of lower shear. Numerical simulations have shown that the shear in the downstream region can be approximated using the slope of the oil locally as the input to equation A5 replacing x/h in that equation by dx/dh . Figure C2 also shows how easy it is to determine the shock location using the oil-flow interferometry.

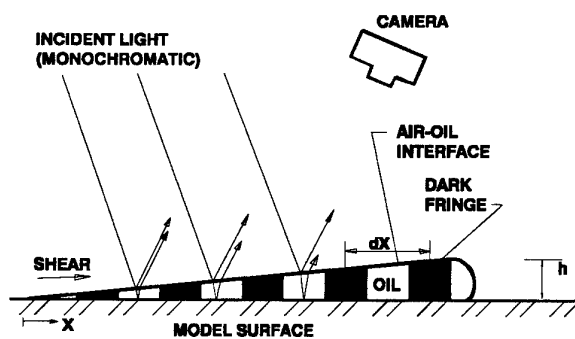


Figure 1. Schematic of oil-film and interference pattern.

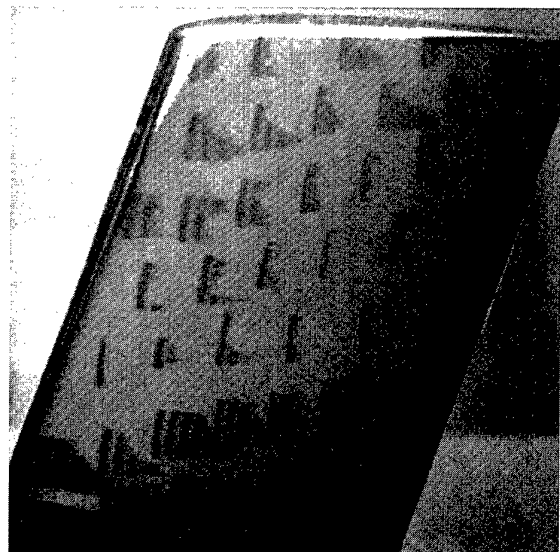


Figure 2. Example of fringes on NACA 0012 wing.

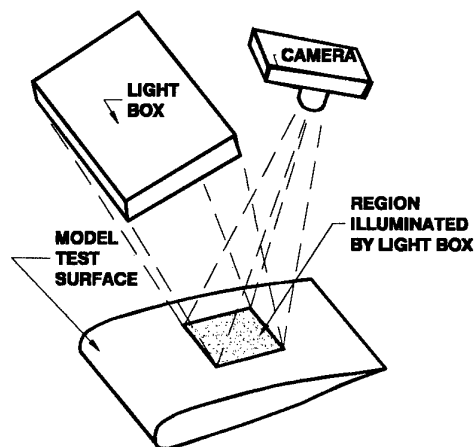


Figure 3. Light box illumination.

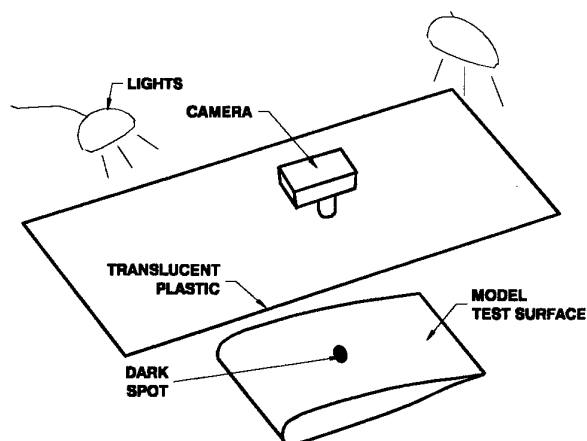


Figure 4. Translucent plastic screen with back lighting.

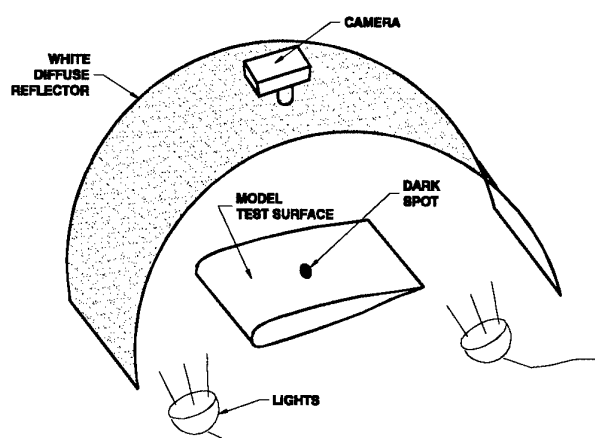


Figure 5. Diffuse reflector with front lighting.

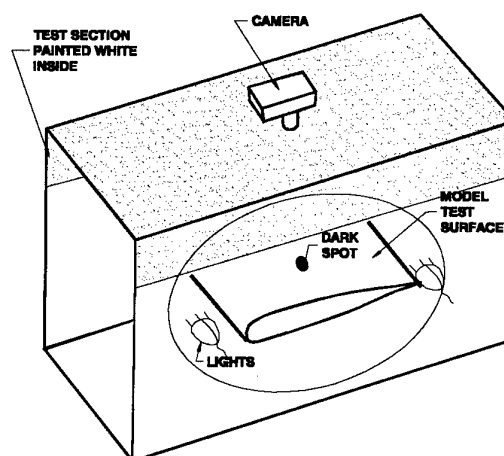


Figure 6. Test section walls painted white – acting as a reflector.

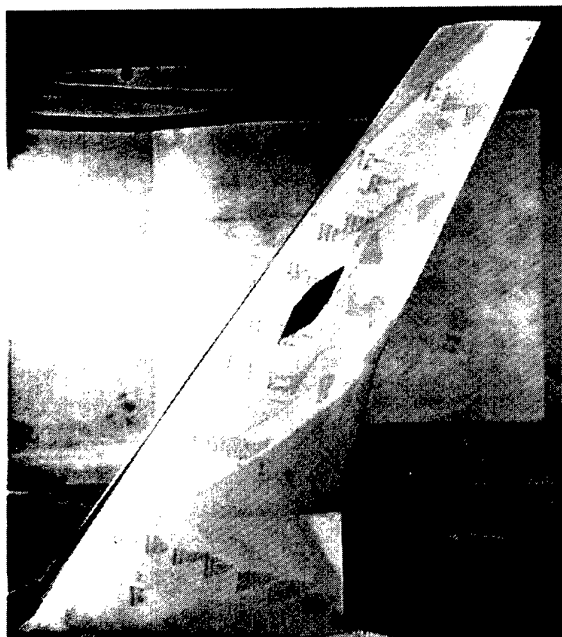


Figure 7. Model illuminated with test section walls.

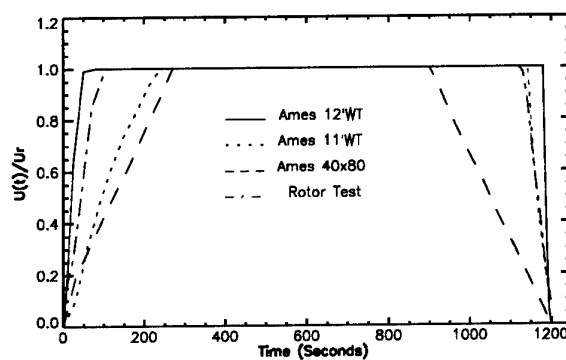


Figure 8. Run history of NASA Ames wind tunnels.

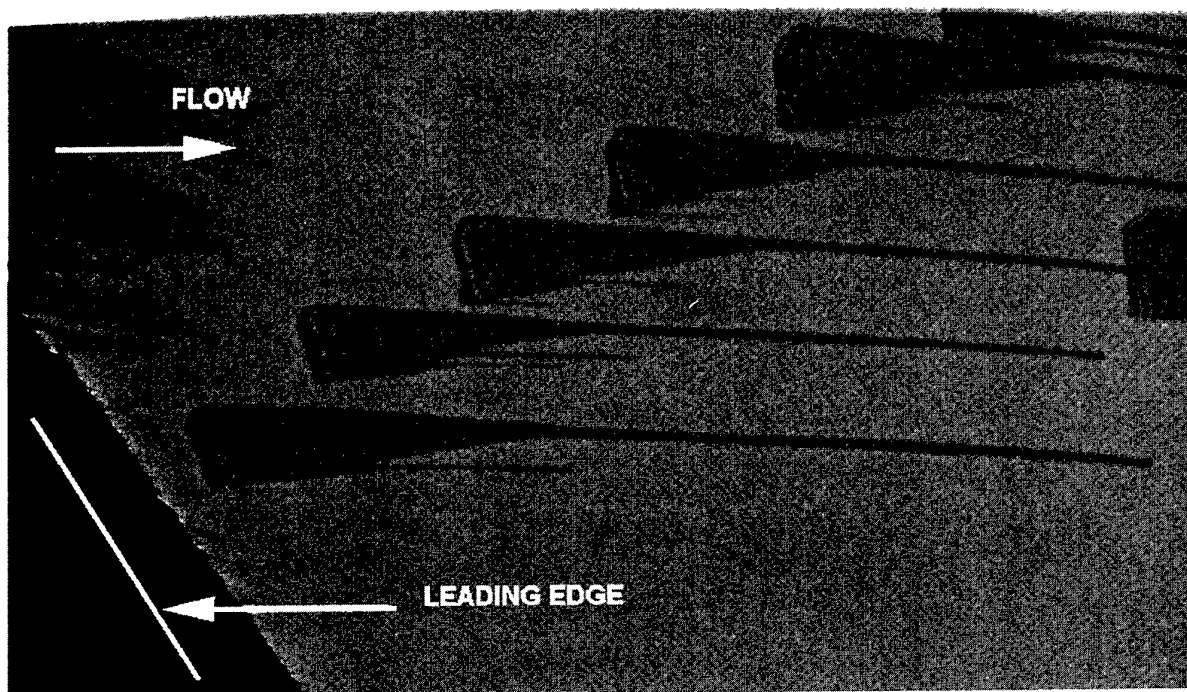


Figure 9. Oil-film patterns on horizontal stabilizer of transport model in the NASA Ames 40x80.

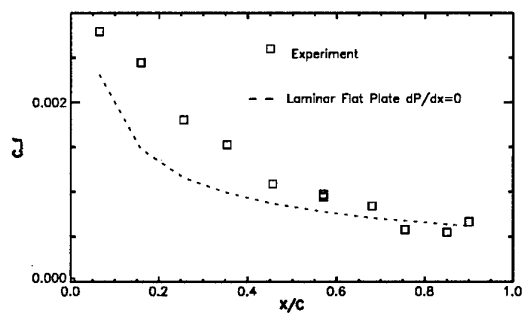


Figure 10. Skin-friction distribution on the horizontal stabilizer of a transport aircraft in the 40x80 wind tunnel.

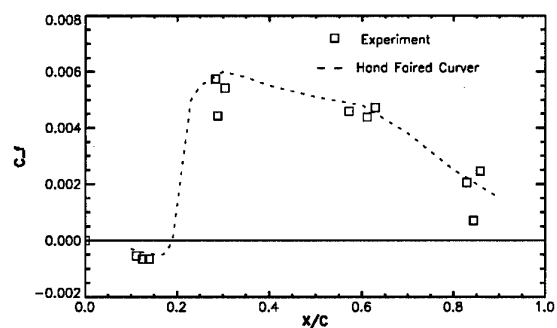


Figure 13. Shear distribution for winglet.

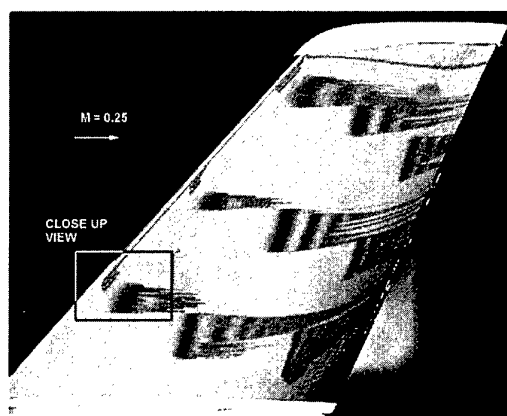


Figure 11. Winglet on transport model in Ames 12' WT.

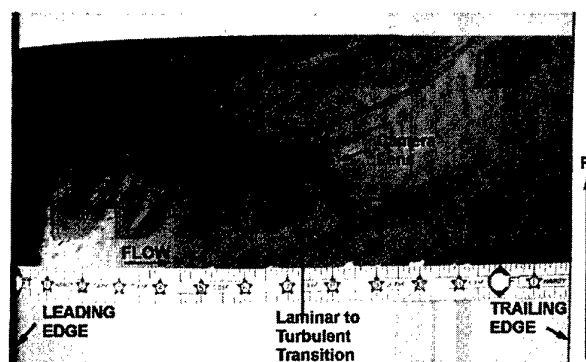


Figure 14. Oil-films on helicopter rotor in hover in Ames 80x120.

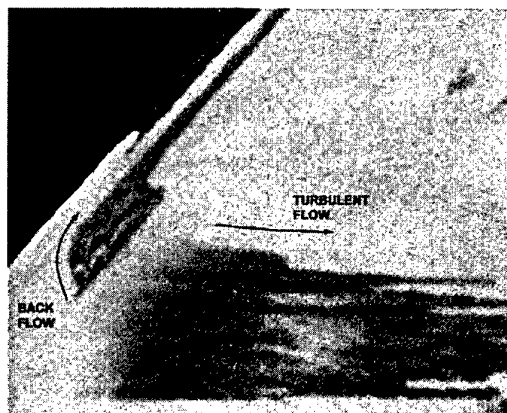


Figure 12. Close up of reversed flow region on winglet.

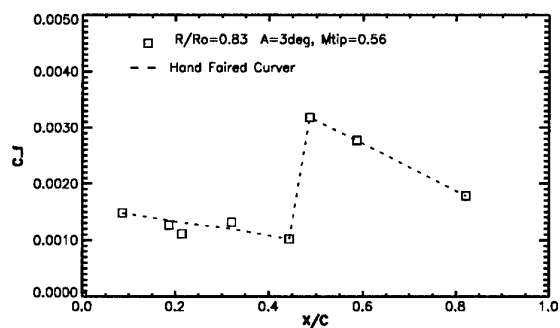


Figure 15. Skin-friction distribution on rotor showing transition from laminar to turbulence.

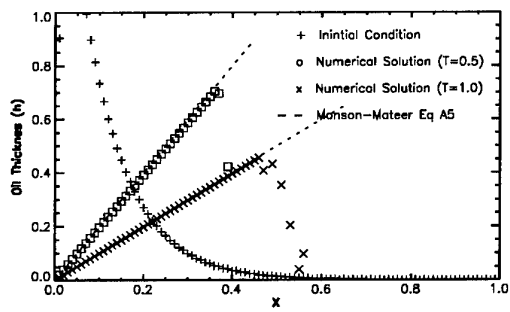


Figure B1. Numerical solution of oil-film height distribution compared to simplified oil-film equation A5. Numerical solution started with finite oil film height.

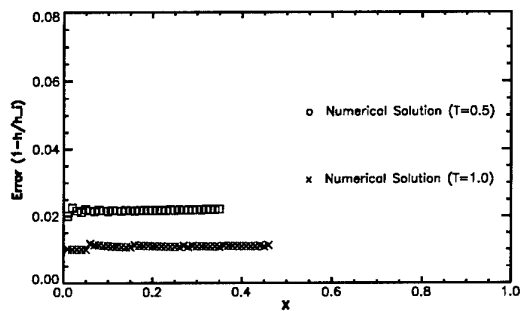


Figure B2. Difference between numerical solution and equation A5.

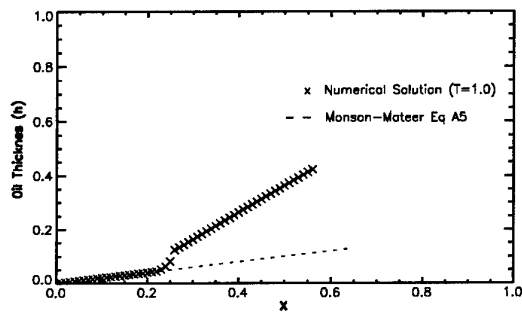


Figure B3. Oil film thickness distribution computed at time $T=1.0$ for variable shear, $0 < x < 0.25$ is 5 times greater than $0.25 < x < 1.0$.

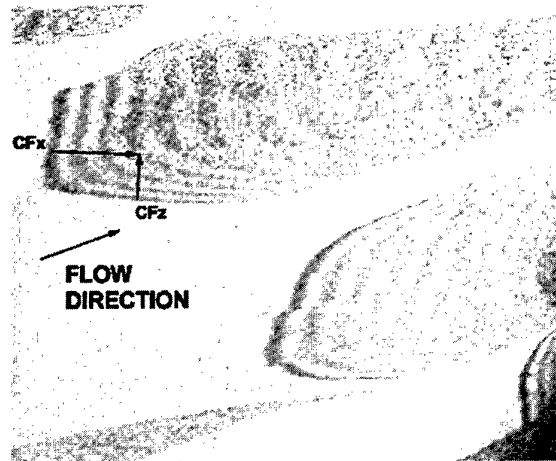


Figure C1. 3D Vector components.

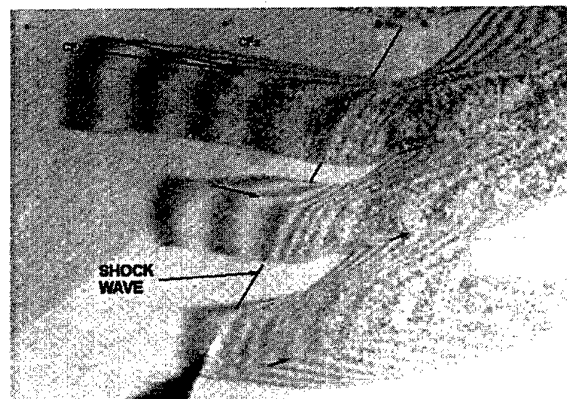


Figure C2. Shock Waves and 3D vector components.

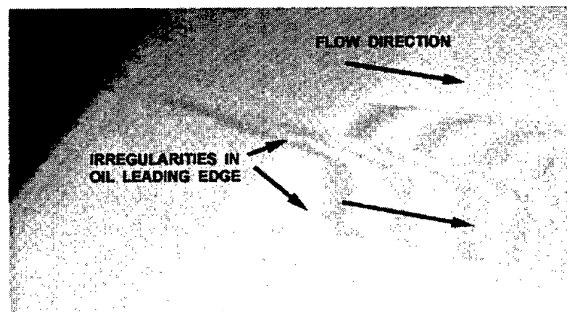


Figure C3. Shear direction determined from irregularities in the oil leading edge.

VISUALIZATION AND MEASUREMENT OF SURFACE SHEAR STRESS VECTOR DISTRIBUTIONS USING LIQUID CRYSTAL COATINGS

Daniel C. Reda and Michael C. Wilder

Fluid Mechanics Laboratory (MS:260-1)
NASA-Ames Research Center
Moffett Field, CA 94035-1000, USA

SUMMARY

When a shear-sensitive liquid crystal coating is illuminated from the normal direction by white light and observed from an oblique above-plane view angle, its color-change response to shear depends on both shear stress vector magnitude and the direction of the applied shear vector relative to the observer's in-plane line of sight. At any point, the maximum color change is always seen or measured when the local shear vector is aligned with, and directed away from, the observer; the magnitude of the color change at this vector/observer aligned orientation scales directly with shear stress magnitude. Conversely, any point exposed to a shear vector with a component directed toward the observer exhibits a non-color-change response, always characterized by a rusty red or brown color, independent of both shear magnitude and direction. Based on this knowledge, full-surface shear stress vector visualization and measurement methodologies were formulated and successfully demonstrated. The present paper reviews the observations and measurements that led to the development of these methodologies and applications of both are discussed.

α	above-plane angle, measured positive upward from zero in plane of test surface
β	relative in-plane view angle between shear vector and observer's in-plane line of sight
λ_D	dominant wavelength
τ	magnitude of surface shear stress vector
τ/τ_r	relative surface shear stress magnitude
ϕ	circumferential angle in plane of test surface, measured positive counter-clockwise from origin on negative X axis
ϕ_r	orientation of surface shear stress vector directed away from observer with an in-plane line of sight at $\phi = \phi_r$

Subscripts

C	camera
J	jet
L	light
P	probe
r	reference value

LIST OF SYMBOLS

C	camera
D	jet exit diameter
GSP	geometric stagnation point
H	hue
HSI	hue, saturation, intensity
L	light; or jet tube length
LCC	liquid crystal coating
M	Mach number at jet exit centerline or in tunnel freestream
P_∞	ambient pressure
P_o	stagnation pressure at jet exit centerline
Re	freestream unit Reynolds number for tunnel flow; or Reynolds number at jet exit centerline based on D
RGB	red, green, blue
X	axial coordinate on test surface; origin at jet exit for tangential jet and at disc center for impinging jet
ΔX	spacing between two X locations
Y	transverse coordinate on test surface; zero at X axis

1. INTRODUCTION

The objective of this continuing research is to develop an image-based instrumentation system for the areal visualization and measurement of the instantaneous shear stress vector distribution acting on any aerodynamic configuration. In fundamental experiments, full-surface measurements of both the magnitudes and the directions of such skin-friction forces would provide modelers with detailed data sets for code-validation purposes, ultimately leading to more advanced design tools. Further, the application of such a visualization and measurement capability to the prototype testing of advanced aerodynamic configurations would greatly increase the productivity of ground-based facilities.

The approach has been to systematically explore the color-change responses of shear-sensitive, temperature-insensitive, liquid crystal coatings (LCC) to applied shear stresses of known magnitudes and known directions relative to the observer.

The liquid crystal phase of matter is a weakly ordered, viscous, fluidlike state that exists between the nonuniform liquid phase and the ordered solid phase of certain organic compounds. Liquid crystals can exhibit optical properties that are characteristic of solid, crystalline materials. If a thin film of liquid crystals is applied to a solid surface and the molecules within the coating are aligned by frictional forces into the required planar state, then this molecular structure selectively scatters incident white light as a three-dimensional spectrum or color space.

It has been known for some time that changes in applied shear stress magnitude cause the liquid crystal molecular structure to change, reorienting the scattered light spectrum in space. A fixed observer thus sees color change in response to the altered shearing force. Such color changes are continuous and reversible, with time response on the order of milliseconds.

Recent research conducted at NASA Ames has shown that LCC color-change response to shear depends on both shear stress magnitude and the direction of the applied shear vector relative to the observer's in-plane line of sight¹. Under normal white light illumination and for oblique above-plane observation, color video images of a LCC subjected to surface shear stress vectors of known direction showed that any point exposed to a shear vector with a component directed away from the observer exhibited a color-change response. This response was characterized by a shift from the no-shear orange color toward the blue end of the visible spectrum, with the extent of the color change being a function of both shear magnitude and shear direction relative to the observer (Fig. 1a on page 26-9). Conversely, any point exposed to a shear vector with a component directed toward the observer exhibited a non-color-change response, always characterized by a rusty-red or brown color, independent of both shear magnitude and direction (Fig. 1b).

In addition, these LCC color-change responses were quantified by subjecting a planar coating to a wall-jet shear flow; scattered-light spectra were measured at a point on the wall-jet centerline using a fiber-optic probe and a spectrophotometer¹ (Fig. 2). At any fixed shear stress magnitude, the maximum color change was always measured when the shear vector was aligned with and directed away from the observer; changes in the relative in-plane view angle to either side of this vector/observer aligned orientation resulted in symmetric Gaussian reductions in measured color change (Fig. 3). For this vector/observer aligned orientation, color change was found to continually increase with increasing relative shear stress magnitude over an eightfold range (Fig. 4). Based on these observations and point-measurement results, full-surface shear stress vector visualization² and measurement³ methodologies were formulated and successfully demonstrated. These two methods are discussed, in sequence, in the following two sections.

2. SHEAR VECTOR VISUALIZATION

To capitalize on these unique shear-direction-indicating capabilities of liquid crystal coatings, two opposing-view, synchronized, color video cameras need to be deployed: one with an oblique, downstream-facing view of the test surface and the other with an oblique, upstream-facing view. Present understanding dictates that the test surface be planarlike, i.e., no regions of extreme curvature, and that it be uniformly illuminated from above. Figure 5 shows a schematic of the experimental arrangement utilized to demonstrate this new technique.

A generic commercial-transport model with a tip-to-tip wing span of 67 in. was positioned on the centerline of the Boeing 8 x 12 ft. transonic wind tunnel. The model had a cylindrical 8-in. diameter centerbody with boundary-layer trips positioned near the nose; the wings were 12-in. root chord and were swept back at a 35-degree angle. No trips were present on the inboard two-thirds span of the test wing.

The test surface was the upper surface of the starboard wing. The inboard portion of this wing was positioned directly below one of the off-centerline window ports and could thus be uniformly illuminated by a white light (L) from above. Two synchronized, opposing-view color video cameras (C) were deployed. The downstream-facing camera was a miniature device positioned within a vent slot in the tunnel ceiling; this placement yielded an optimum 30-deg above-plane view angle of the wing upper surface at zero degrees angle of attack. The upstream-facing camera was positioned outside the test section, within the surrounding plenum chamber, and viewed the test surface through a window at a 43-deg above-plane viewing angle when the model was at 0-deg angle of attack.

In this arrangement, transition to turbulence on the wing upper surface, characterized by an abrupt increase in surface shear stress magnitude in the principal flow direction, was made visible by the LCC color-change response recorded with the downstream-facing camera. Conversely, regions of reverse flow enveloped by upstream-directed shear vectors were made visible by the LCC color-change response recorded with the upstream-facing camera. Regions of the coated test surface exposed to shear vectors directed toward either camera yielded no color-change response, appearing as either dark or reddish-brown zones, depending on the absolute light levels reaching the camera. Any regions of extreme transverse flow, enveloped by shear vectors directed either inboard or outboard and approximately perpendicular to the principal flow direction, would have appeared (if present) as a yellow color-change response simultaneously to both cameras¹.

Figure 6 (page 26-9) illustrates the transition-front visualization capability of the LCC technique. Here, regions of low shear magnitude were delineated by a red or yellow color, whereas regions of high shear magnitude appeared as green or blue. Several important features of the surface shear field were made visible by these LCC color-change responses. Transition at 0-deg angle of attack, for $M = 0.4$ and $Re = 2.5 \times 10^6/\text{ft.}$, was seen to occur along a swept line ranging from ~25% of chord inboard to ~75% of chord outboard with turbulent wedges interspersed. This chordwise transition front moved forward with increasing angle of attack consistent with a dependence on the adverse-pressure-gradient onset location for this airfoil section. The discrete turbulent wedges originating from the wing leading-edge region were a result of isolated roughness elements caused by freestream contaminants impacting the surface.

Figure 7a (page 26-9) shows synchronized LCC color-change responses as recorded by opposing-view cameras for $\alpha = 8$ deg at $M = 0.4$ and $Re = 2.5 \times 10^6/\text{ft.}$ Under these test conditions, a leading-edge separation occurred outboard on the wing upper surface, as indicated by the red zone in the downstream-facing view and the corresponding yellow zone in the upstream-facing view. High-shear (turbulent) attached flow existed everywhere else on the wing upper surface, as indicated by the blue color in the downstream-facing view and no color-change response in the upstream-facing view.

Figure 7b shows synchronized LCC color-change responses as recorded by opposing-view cameras for $\alpha = 5$ deg at $M = 0.8$ and $Re = 3.4 \times 10^6/\text{ft.}$ Under these test conditions, a normal shock wave/laminar boundary-layer interaction occurred slightly downstream of the wing leading edge. Here, the yellow zone along the wing leading edge, recorded by the downstream-facing camera, indicated a low-shear (laminar) region upstream of the interaction. A narrow band of reverse flow formed beneath the interaction region, oriented approximately parallel to the leading edge; this region was indicated by the reddish-brown band in the downstream-facing view and, simultaneously, by the yellow band in the upstream-facing view. This reverse-flow region was breached by numerous turbulent wedges seen emanating from aforementioned roughness elements along the leading edge; passage of these locally attached turbulent wedges through the interaction region are best illustrated by the dark breaks in the yellow band recorded by the upstream-facing camera. High-shear (turbulent) attached flow existed everywhere downstream of the reverse-flow region, as indicated by the extensive blue zone in the downstream-facing view, and corroborated by the absence of color change downstream of the yellow band in the upstream-facing view.

3. SHEAR VECTOR MEASUREMENT

For full-surface shear stress vector measurements, a three-chip red-green-blue (RGB) color video camera, a frame grabber, and a supporting computer are utilized. The coated surface is illuminated from the normal direction ($\alpha_i = 90$ deg), and the camera is positioned at a constant above-plane view angle of $\alpha_c \sim 30$ deg. Figure 8 summarizes the four-step procedure while Fig. 9 serves to illustrate the geometry referred to in the description of the methodology.

In step 1, a single calibration curve of color (hue) vs shear magnitude is obtained for the specific arrangement wherein the calibration shear vector is aligned with, and directed away from, the camera. Conventional point-measurement techniques for shear magnitude can be employed for this purpose⁴. In step 2, full-surface images of the LCC color-change response to an unknown shear field are recorded from multiple in-plane view angles (here, $\phi_{c1}-\phi_{cn}$) encompassing the vector directions to be measured. In step 3, for each physical point on the test surface, a Gaussian curve is fit to the hue vs in-plane view angle data. The in-plane view angle corresponding to the maximum of the curvefit determines the vector orientation (ϕ_v). In step 4, the hue value corresponding to the vector orientation is used along with the calibration curve of step 1 to define the vector magnitude (τ). Steps 3 and 4 are repeated for all surface points to determine the complete shear vector field.

This methodology was first applied to measure the shear stress vector distribution on a planar surface beneath an axisymmetric, turbulent, wall-jet flow³. A schematic of the experimental arrangement is shown in Fig. 9. Reference 3 provides a detailed description of the apparatus and test procedures, along with a discussion of measurement resolution and uncertainty issues. Results are summarized below.

Figure 10 (page 26-9) shows two representations of the wall-jet-induced shear stress vector distribution as measured by the LCC technique. This data set was generated by analyzing seven low-pass-filtered hue images, and it contains approximately 10^5 measured vector values.

Both images shown in Fig. 10 use false color levels to represent the shear stress magnitude distribution. Vector orientations are illustrated by streaklines in Fig. 10a and by vector profiles in Fig. 10b. These streaklines, drawn tangent to the local shear stress vector at every point along their trajectories, were generated from the vector data set using a flow analysis software toolkit widely employed in computational fluid dynamic applications. The vector profiles are drawn every 1.23D (every 40th profile) starting at the axial location of $X/D = 5$. For clarity, only every fourth vector is shown in each profile.

As can be seen, maximum shear stress magnitudes occurred along the jet centerline, decreasing laterally toward the outer edges of the shear field.

Quantitative comparisons with point measurements taken across the jet at a single axial station ($X/D = 9$) are shown in Fig. 11. The point measurements of magnitude were made using the FISO or oil-drop method⁴. Vector directions across this axial station were determined by measuring the tangent angle of the streaklines generated in a separate oil-flow visualization experiment. These comparisons show good overall agreement between the LCC measurements and the point measurements across the entire shear field. Note that the vector directions across the core region of the shear field all fell between ± 10 deg and that the LCC technique measured these directions to within 1-2 deg even though no hue images were recorded between $\phi_c = 0$ and ± 10 deg. This is a clear indication of the robustness of the variation of hue vs ϕ and the Gaussian curvefitting procedure used in the LCC methodology.

This methodology was most recently applied to measure the shear stress vector distribution on a planar surface beneath an inclined, axisymmetric, turbulent impinging jet⁵. Figure 12 shows a schematic of the experimental arrangement. Based on experience gained during this experiment, it is now recommended that the order of the four steps outlined in Fig. 8 be rearranged to the sequence: step 2, step 3, step 1, step 4.

Starting with step 2, a twenty-frame-average RGB image of the complete test surface was recorded from each of fifteen ϕ_c orientations over the arc $0^\circ \leq \phi_c \leq 180^\circ$. Due to the widely varying RGB intensities experienced within each such color image, all ϕ_c images were recorded at two or more exposure settings then mathematically combined to form a single, composite image wherein each pixel was correctly exposed. All such composite images were low-pass filtered using a 5×5 pixel mask and converted from RGB to an HSI color space.

Taking advantage of the symmetry of the flow field, the time-averaged, filtered hue images for $0^\circ \leq \phi_c \leq 180^\circ$ were mirror-imaged across the plane of symmetry (the X axis) to form a complete $0^\circ \leq \phi_c \leq 360^\circ$ image set. These hue images were then subjected to the image processing and data analysis procedure (step 3) to convert them to an unscaled answer set comprised of a vector-aligned hue value (proportional to shear magnitude) and a vector orientation at every grid point location on the test surface.

The calibration points required for the final scaling from vector-aligned hue values to shear magnitudes should be acquired after steps 2 and 3 of Fig. 8 have been completed, i.e., after the magnitudes and locations of the maximum and minimum vector-aligned hue values are known. The

advantage would be the definition of a calibration curve that spans the full range of vector-aligned hue values encountered in the final unscaled answer set.

In the impinging-jet experiment, the oil-drop interferometry technique⁴ was applied at select locations along the X axis (chosen from a single $\phi_c = 0^\circ$ image) to measure shear magnitudes for calibration purposes. These point measurements were obtained before the complete set of LCC images was acquired and analyzed, consistent with the sequence originally outlined by Fig. 8. In the final analysis of the complete image set, vector-aligned hue values slightly above the maximum of the existing calibration curve were encountered at a small number of surface grid points along, and just to either side of, the X axis. Since additional oil-drop interferometry experiments could not be conducted at that time, these slightly out-of-range hue values were equated to the highest shear stress magnitude in the existing calibration data set. A few localized shear magnitude peaks in the final answer set were thus cut off. Further, based on earlier thresholding arguments³, vector-aligned hue values below the lowest non-zero calibration point were dropped from the analysis. Conversion from vector-aligned hue values to shear magnitudes (step 4) was then carried out and the resulting continuous surface shear stress vector distribution is shown in Fig. 13 (page 26-9).

This measured data set contains approximately 2×10^4 non-zero vectors, one at every point on a surface grid whose resolution is 100×100 points per square inch. False color levels are used to represent shear stress magnitudes. Black regions represent the absence of a vector value due either to thresholding at the lowest non-zero calibration point or to the failure to attain an acceptable Gaussian curve fit to the H vs ϕ data set at a particular surface grid point. Vector orientations are illustrated by the vector cross-cut profiles drawn every $|\Delta X|/D = 1$ starting at the Y axis; for clarity, only every fifth vector is shown in each profile.

A local minimum in shear magnitude was seen to occur in the immediate vicinity of the geometric stagnation point (GSP). Shear magnitude increased rapidly in all directions emanating from the stagnation zone as the inclined-jet flow turned to align itself with the plate surface, then accelerated outwards. Peak shear stresses were measured in all radial directions within 2D of the GSP.

Figure 14 shows the shear magnitude distribution on the X axis, along with the oil-drop data used for calibration purposes. A shear minimum occurred just to the negative X side of the GSP. Due to thresholding applied in the LCC method, and/or possibly to the unsteadiness observed in this region, a time-averaged value of zero shear magnitude at the stagnation point was not measured.

Figure 15 shows continuous measurements from the LCC method versus point measurements from the oil-drop

method as acquired on a transverse cross-cut at $X/D = 2$. None of the oil-drop data shown here were used to generate the H vs τ calibration curve. Once again, very good overall agreement was noted between shear vector magnitudes and shear vector orientations measured by these two methodologies. These results provided the first demonstration of the capability of the LCC method to reliably measure continuous shear stress vector distributions on planar surfaces wherein shear vectors of all possible orientations are present.

REFERENCES

1. Reda, D.C. and Muratore, J.J., Jr., "Measurement of Surface Shear Stress Vectors Using Liquid Crystal Coatings," AIAA Journal, Vol. 32, No. 8, 1994, pp. 1576-1582.
2. Reda, D.C., Wilder, M.C., and Crowder, J.P., "Simultaneous, Full-Surface Visualizations of Transition and Separation Using Liquid Crystal Coatings," AIAA Journal, Vol. 35, No. 4, 1997, pp. 615-616.
3. Reda, D.C., Wilder, M.C., Farina, D.J., and Zilliac, G., "New Methodology for the Measurement of Surface Shear Stress Vector Distributions," AIAA Journal, Vol. 35, No. 4, 1997, pp. 608-614.
4. Zilliac, G., "Further Developments of the Fringe-Imaging Skin Friction Technique," NASA TM 110425, Dec. 1996.
5. Reda, D.C., Wilder, M.C., Mehta, R., and Zilliac, G., "Measurement of the Continuous Pressure and Surface Shear Stress Vector Distributions Beneath an Inclined, Impinging Jet Using Coating and Imaging Techniques," AIAA 97-2489, 32nd Thermophysics Conference, Atlanta, GA, June 23-25, 1997.

ACKNOWLEDGEMENTS

The participation of M.C. Wilder in this research was funded by NASA contract NAS2-14109 to MCAT, Inc., San Jose, CA.

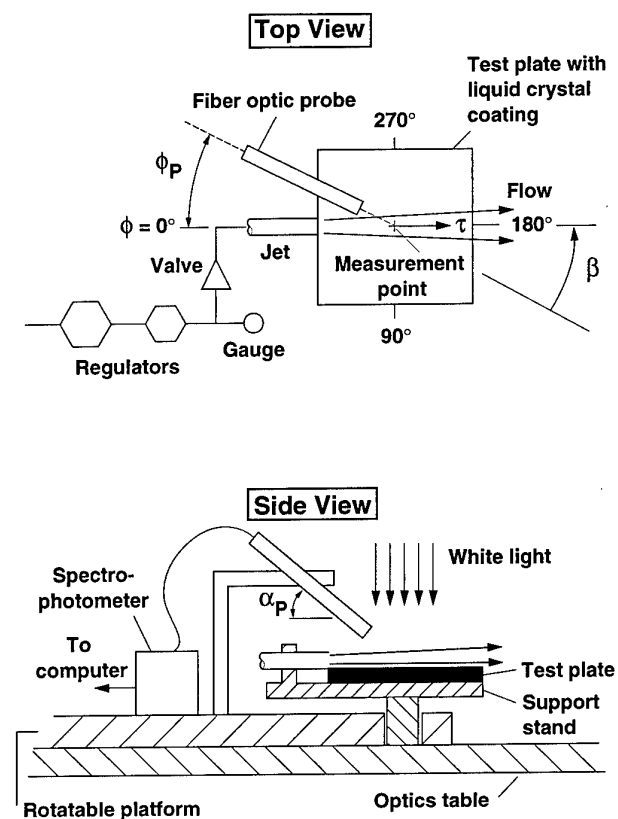


Fig. 2 Schematic of experimental arrangement for spectrophotometer measurements of tangential jet.

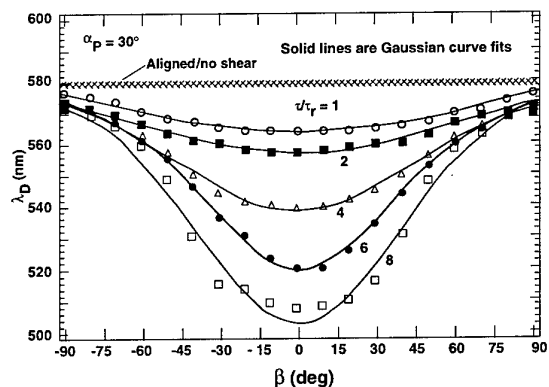


Fig. 3 Dominant wavelength vs. relative in-plane view angle between observer and shear vector, with relative shear magnitude as the parameter.

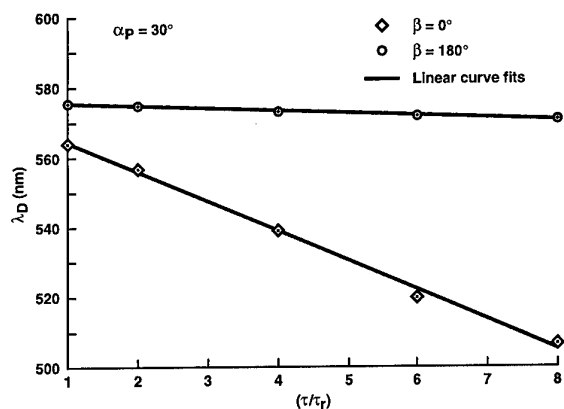


Fig. 4 Dominant wavelength vs. relative shear magnitude for relative in-plane view angles of 0° and 180°.

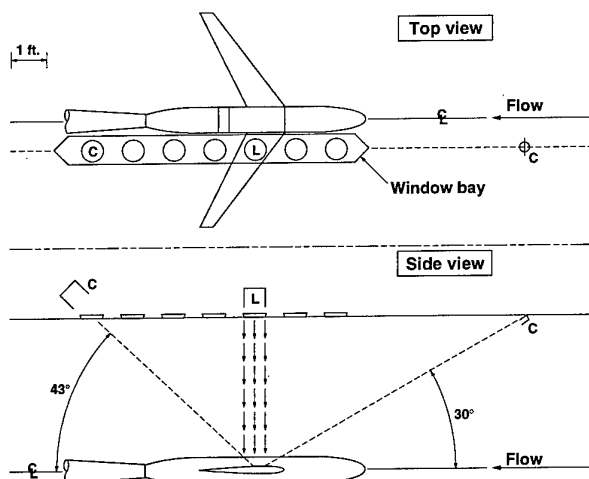
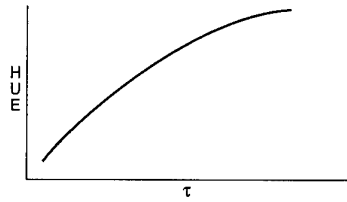
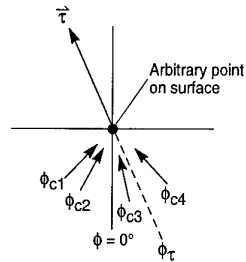


Fig. 5 Schematic of experimental arrangement for shear-vector visualizations in Boeing Transonic Wind Tunnel.

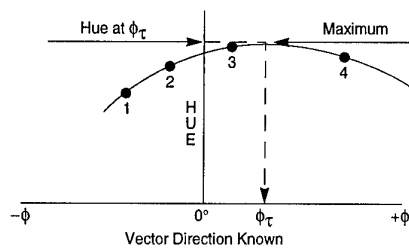
- I** For camera above – plane angle α_c fixed, calibrate color-measurement system for camera and vector aligned, flow away from camera ($\phi_c = \phi_\tau$)



- II** For same α_c , record full-surface color images of liquid crystal coating response to shear from multiple ϕ_c angles encompassing all vector directions



- III** For each surface point, curve fit hue vs. ϕ with a symmetric function to define maximum



- IV** Use calibration of Step I to get vector magnitude

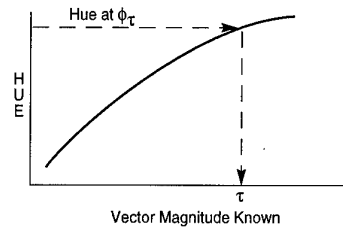


Fig. 8 Full-surface shear stress vector measurement methodology.

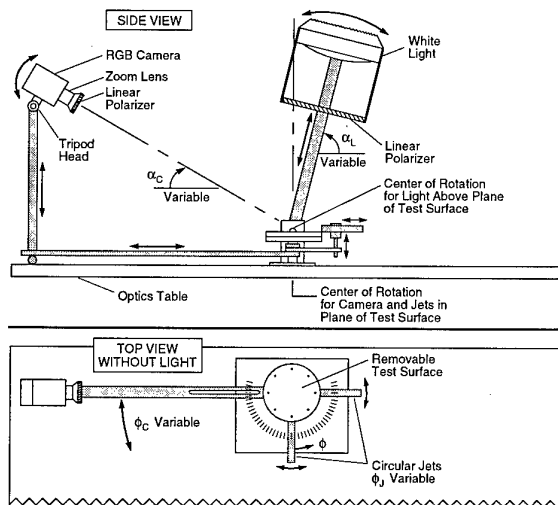


Fig. 9 Schematic of experimental arrangement for measurement of shear vector distribution beneath tangential jet.

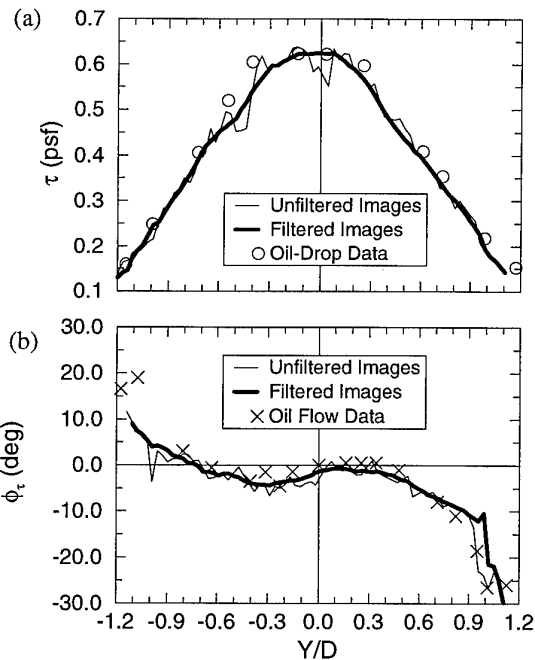


Fig. 11 Cross-stream profiles of shear vector field beneath tangential jet at $X/D = 9$: (a) magnitudes vs. oil-drop data; (b) orientations vs. oil-flow data.

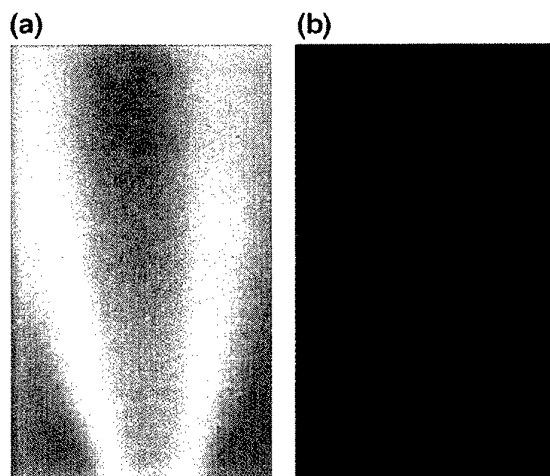


Fig. 1 Color-change response of liquid crystal coating to tangential jet flow, $\alpha_L = 90^\circ$, $\alpha_C = 35^\circ$: (a) flow away from observer, (b) flow toward observer.

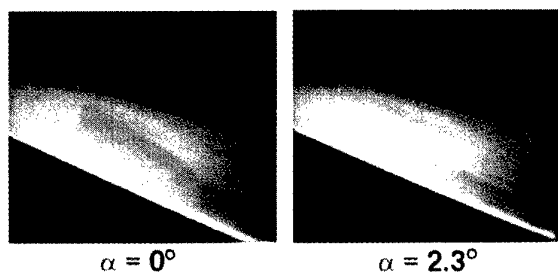


Fig. 6 Transition-front visualizations recorded by downstream-facing camera at $M = 0.4$ and $Re = 2.5 \times 10^6/ft$.

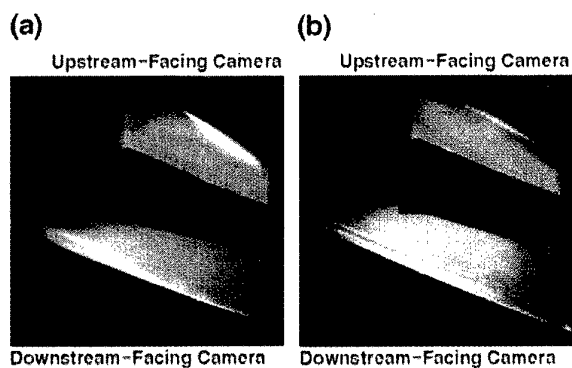


Fig. 7 Color-change responses as recorded by opposing-view cameras: (a) leading edge separation, $\alpha = 8^\circ$, $M = 0.4$, $Re = 2.5 \times 10^6/ft$; (b) normal-shock/boundary-layer interaction, $\alpha = 5^\circ$, $M = 0.8$, $Re = 3.4 \times 10^6/ft$.

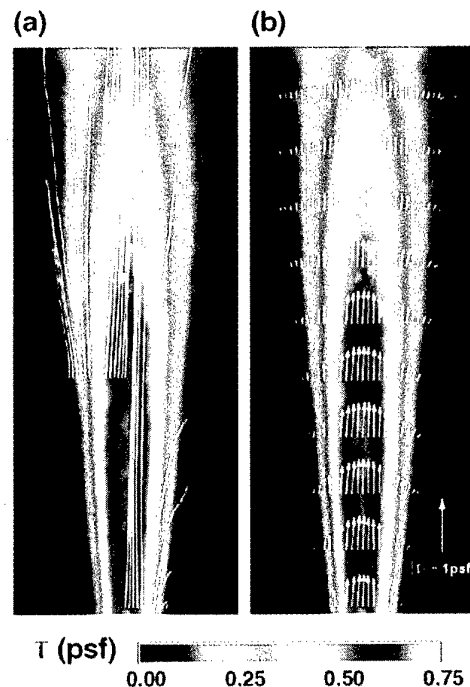


Fig. 10 Measured surface shear stress vector field beneath tangential jet where color contours show vector magnitudes: (a) vector orientations shown by streaklines originating from $X/D = 5$ and 10; (b) vector cross-stream profiles starting at $X/D = 5$, every $\Delta X/D = 1.23$.

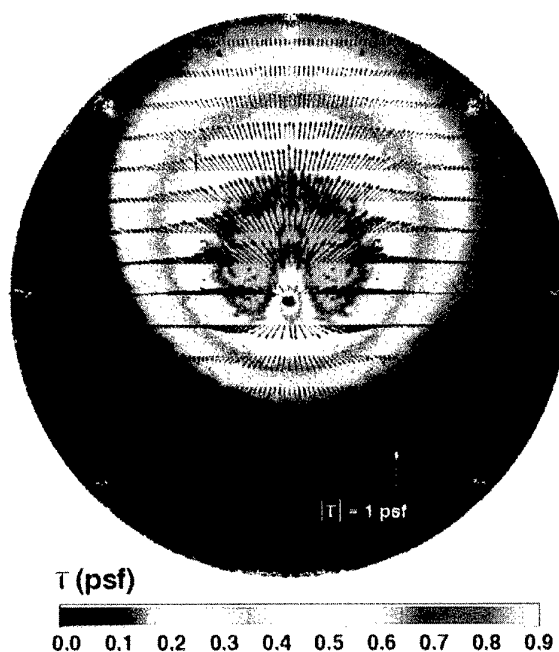


Fig. 13 Measured surface shear stress vector field beneath inclined, impinging jet: color contours show vector magnitudes and vector cross-cut profiles every $\Delta X/D = 1$ show vector orientations.

SHEAR SENSITIVE LIQUID CRYSTALS IN SUBSONIC AND TRANSONIC WIND TUNNEL TESTING

G. Lombardi

Department of Aerospace Engineering, University of Pisa
Via Diotisalvi 2, 56126 PISA, Italy

M. Morelli

D. Waller

Medium Speed Wind Tunnel, CSIR
P.O. Box 395, PRETORIA 0001, South Africa

SUMMARY

The present paper single out the advantages connected with the use of the liquid crystal technique for the visualization of the surface flow phenomena during wind tunnel tests; they appear significant, and can be summarized in reversibility, rapid time response, non-toxicity and low cost. The more significant benefits are that different types of analysis (boundary layer transition, separation and reattachment, shock wave position) can be performed with a single technique, and that the reversibility of the process gives the possibility to analyze several conditions in a single run of the wind tunnel. Therefore, the technique is characterized by low cost and time requirements. In any case, it is important to note that several effects can affect the images and this imply a degree of uncertainty in the interpretation of the results. It is therefore necessary to acquire a high confidence level in the technique in order to assure a good degree of repeatability and accuracy in the analysis of the results. Mainly, the use of the technique is related to the visualization of the main feature of the surface flow. In this regard, several examples showing the determination of the boundary layer transition, separation lines and the shock wave position on the surface, are presented. To enhance the knowledge on the boundary layer conditions a quantitative use of this technique will be a powerful tool. Several attempts to have a quantification of the response of the liquid crystals were carried out and are discussed in the paper. Nevertheless, it is necessary to stress that, at the present state of the research, the technique is probably non precise enough for an absolute determination of the local shear stress, and the indicated procedure seems applicable only for comparative tests.

1. INTRODUCTION

Several techniques are presently available for surface flow visualizations, starting from the classical well-established methods, such as oil film, up to the more recent approaches, such as infrared thermography (see, e.g., Ref. 1). Recently, the use of the Liquid Crystal Coating (LCC) technique for surface flow visualization has significantly increased. The advantages of shear sensitive liquid crystal materials for surface flow visualization are significant (see, e.g., Refs. 2-6); they can be summarized in reversibility, rapid time response, non-toxicity and low cost. Furthermore, they may now be used in conjunction with

color analysis for quantitative measurements, of surface temperature and heat transfer (see, e.g., Refs. 7-10) when a temperature sensitive LCC is used, or of the surface shear stress vector distribution (see, e.g., Refs. 11-17) when a temperature insensitive LCC is used.

In a co-operation between the Department of Aerospace Engineering of the University of Pisa (Italy) and the Aerotek, a division of the Council for Scientific and Industrial Research (CSIR), in South Africa, the capabilities of this technique were investigated by means of experiments on several configurations, carried out in the Medium Speed Wind Tunnel (MSWT) and in the High Speed Wind Tunnel (HSWT), at the Aerotek facilities.

The bases of the specific technique used in the Aerotek Laboratories was preliminary described in Ref. 18. The research singled out the advantages connected with the use of the liquid crystal technique for the visualization of the surface flow phenomena during wind tunnel tests. The more significant benefits are that different types of analysis (boundary layer transition, separation and reattachment, shock wave position) can be performed with a single technique, and that the reversibility of the process gives the possibility to analyze several conditions in a single run of the wind tunnel. Therefore, the technique is characterized by low cost and time requirements.

Mainly, the use of the technique is related to the visualization of the main feature of the surface flow. In this regard, several examples showing the determination of the boundary layer transition, separation lines and the shock wave position on the surface, are presented in the present paper; they indicate that the liquid crystal paint technique can be considered a well established tool for flow visualizations.

To enhance the knowledge on the boundary layer conditions, particularly for the study of friction drag, a quantitative use of this technique will be a powerful tool. Several attempts to have a quantification of the response of the liquid crystals have been carried out. In order to have a quantification of the response of the liquid crystals, a method of analysis of the image, suggested by the relation between the wave length of the reflected color and the local shear stress, is proposed in the paper. This methodology is based on the acquisition of the three basic RGB channels,

coupled with a calibration of the image on white. By means of these data, it is possible to determine the wave length of the reflected color and, therefore, an indication of the shear stress.

2. BASIC PRINCIPLES

A complete background on the basic physical aspects of the liquid crystal materials can be found in Ref. 19. A liquid crystal is defined a substance that share some of the properties of both liquids and crystals. Mechanically, these substances resemble liquids, with viscosity ranging from runny glue to sold glass. Optically, they exhibit many of the properties of the crystals, scattering light in symmetrical patterns and reflecting different colors depending on the view direction. In particular, in a cholesteric liquid crystal the spatial distributions of molecules is liquid like, the molecules are chiral and, therefore, a macroscopic twist is associated with the molecular orientation. Chirality and twist produce a helical structure whose pitch is typically a few wavelengths of visible light. Selective reflection occurs, producing a displacement of the reflected color from the red to the blue increasing the temperature (temperature sensitive liquid crystal) and/or the shear stress (shear stress sensitive liquid crystal).

The mechanism of modification of the reflected color, based on the modification of helical structure of the liquid crystal, suggests a linearly dependence between the shear stress and the dominant wavelength of the reflected light (for temperature non-sensitive liquid crystal). Indeed, a linear relationship between the reflected light wavelength and the applied shear, at least at values of the shear stress typical of wind tunnel tests, has been observed; for instance, Klein and Margozi (Ref. 11) and Parmar (Ref. 13), found that the selective reflection wavelength decrease linearly with an increase in the shear stress.

In any case, it must be stressed that the intensity of the color in a given condition (temperature and/or shear stress) is dependent on several other factors, including the previous history of heating and cooling within the liquid crystal material and the surface on which it is deposited. In particular, for the industrial application, the modification of the crystal liquid response with time, during a wind tunnel run, appear to represent an important problem to solve to obtain a really accurate quantitative analysis.

3. EXPERIMENTAL SET-UP

3.1 The Wind-Tunnels

The tests were performed at the CSIR facilities. The MSWT is a closed circuit, variable density, transonic wind-tunnel, with longitudinally slotted walls for a total porosity of 5%. Its operational speed ranges from $M=0.25$ to $M=1.5$ with stagnation pressure varying from 20 kPa to 250 kPa. The test section has a 1.5m x 1.5m square cross section and is 4.5m in length. The HSWT is a trisonic, open circuit blow-down type tunnel. Its operational speed ranges from $M=0.4$ to $M=4.5$ (set through an automatically controlled flexible nozzle) with stagnation pressure varying from 70 kPa to 1200 kPa. The test section has a 0.45m x 0.45m

square cross section. The run time varies between 10 and 60 seconds depending on the Mach number and stagnation pressure chosen.

3.2 Model preparation

For a higher resolution of the visualization, a dark (preferably black) surface is necessary, thus avoiding undesired reflected light. The light reflecting properties of the liquid crystal are determined by the arrangement of their molecules and any modification of this structure reduces the sensitive of such a properties. These modifications could arise for several reasons, mainly related to pollution from solvents or organic material on the test surface or in the coating. For these reasons the surface preparation is a critical aspect of this visualization technique. During the tests, considerable problems related to the model base painting were found. Usually, stove-enamelled paints or flat black paint are recommended. However, with these painting techniques several problems were encountered during the test. It was found that the liquid crystal had insufficient adherence to the surface, greatly reducing the visualization time during a test. With a model painting technique consisting of a heat treated bi-component paint, 15 minutes of visualization time was available at a Mach number of 0.4. This aspect can be improved by black anodizing the model, which, obviously, must then be manufactured from aluminium alloys. This preparation technique produces a model surface that is free from any organic residual, and represented a notable improvement in the visualization technique in the HSWT at a significantly higher Mach number.

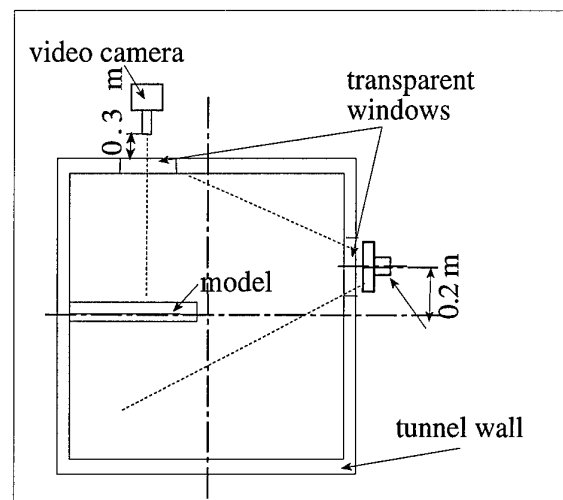
3.3 Application of the liquid crystal coating

In the literature several techniques are described, depending on the specific problem and on the desired thickness of the liquid crystal (see, e.g., Ref. 5). Different types of liquid crystals and several liquid crystal/solvent ratios were analyzed, with different methods of application. The technique applied during these tests was as follows. The liquid crystal (Merck TI-511, 10 ml per m^2 of surface to be "painted") is mixed with a high grade (>99.5%) solvent (1,1,2 trichlorotrifluoroethane), in a 1 to 5 volumetric ratio. The solution is then sprayed onto the model surface to be analyzed (thoroughly cleaned with the same solvent), by means of an air-brush supplied by a pressure slightly higher than the atmospheric (1.2-1.5 bar). The solvent evaporates leaving a thin film of liquid crystal coating, with a thickness of approximately 5 μm . It must be noted that the recommended optimal thickness is approximately 4-6 μm , while larger thickness (10 μm or more) cause the creeping of the liquid crystal as a result of the aerodynamics loads, with a modification in the typology of the colors changes; a typical oil flow visualization is then obtained.

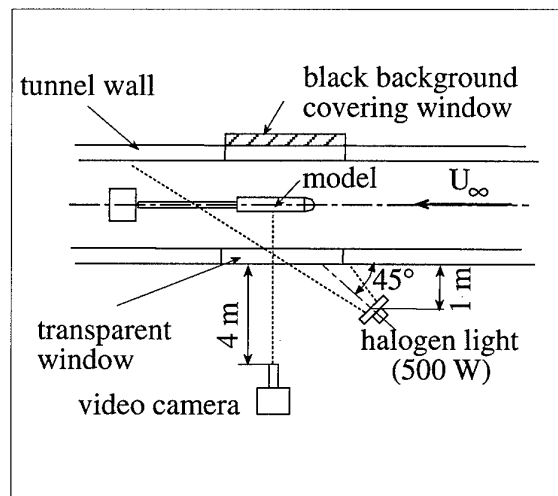
3.4 Lighting and viewing of the model

Several lighting techniques and viewing points combinations were investigated. An important feature for the intensity of the reflected colors is that related to the lighting. General specifications for the lighting are not available, and the optimum lighting technique must be investigated for the specific test. Usually, a good illumination is achieved by aligning the light source with

the view point (for greater detail see again Ref. 5). Furthermore, a diffused light source seems preferable to a concentrated one. A suitable viewing point is that perpendicular to the coated surface to be analyzed; this requirement could represent a significant problem in those areas characterized by large curvature, as, for example, the leading edge of a wing. In this case, a single viewing point is normally not sufficient, and different viewing points, each one dedicated to a specific zone, are necessary. The layouts described in Fig. 1 were used for the tests.



a) MSWT - rear view (not to scale)



b) HSWT - top view (not to scale)

Fig. 1 - Layout of lighting and viewing

4. LIQUID CRYSTAL OR FOR SURFACE FLOW VISUALIZATIONS

4.1 The image analysis

The images of the model surface, acquired by means of a video camera, were recorded on a video tape and subsequently transferred to an image processor. By means of the image processor it was possible to achieve a good definition of the lines at which the changes in the colors

occurred, allowing the transition and separation lines, for each of the analyzed configurations, to be identified.

In particular, a typical application of the image processing is the conversion from a colored image analysis to a gray-level analysis. The advantage of this conversion is a clearer and immediate idea of the boundaries that separate the areas of significant surface stress changes. It is important to note that this conversion is not unique, as it passes from a three parameter definition to a one parameter definition. Furthermore, the conversion is "guided" by the operator. As the white corresponds to the lower limit of the liquid crystal response (the red) and the black to the higher limit (the violet), Fig. 2, it follows that darker is the zone and higher is the stress level. Furthermore, the conversion

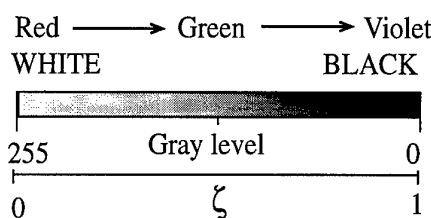


Fig. 2 - The colors/gray-level correspondence

reduces the quantitative information, for each pixel into which the surface is subdivided by the video camera resolution, to only one parameter (the gray level). It is therefore easy to manage this value mathematically by means of isolines, sections, etc. With a 8 bit gray-level resolution, the value 0 corresponds to black and the value 255 to white and it is therefore useful to define a non-dimensional parameter as:

$$\zeta = (255 - \text{value}) / 255 \quad (1)$$

Given the above definition, the parameter ζ ranges from 0 (stress level lower than the minimum observable by the specific liquid crystal) to 1 (stress level higher than the maximum observable by the specific liquid crystal) (see again fig. 2).

Obviously, the information given by the parameter ζ can not be taken as absolute, but only a qualitative analysis can be performed. The "true" information is not the numerical value itself, but the zone in which a change occurs, that indicates a change in the local tangential stress, and, therefore, a modification in the boundary layer condition. There are two reasons why this parameter can only be considered to be a qualitative one. The first is that the specific color reflected by the liquid crystal does not depend merely on the tangential stress, but on many other factors, as well the view direction with respect to the specific zone of the surface, the light, the thickness of the liquid crystal. For instance, during the tests it was observed that the lines at which the changes in colors occurred, for identical flow conditions, remained exactly the same, but the colors reflected were different. The other reason is that a unique correspondence between a color scale and a gray level scale cannot be drawn, bearing in mind that the gray

scale can be described with one parameter, while the color scale needs a minimum of three parameters to uniquely describe a color.

Some example of the present procedure will be show in the following section.

4.2 Examples of results in transonic flow

The configuration, tested in the HSWT, is a hemisphere-cylinder body at a Mach number of 0.9 and an angle of attack of 0° . The results, in terms of the parameter ζ along the longitudinal axis, are shown in Fig. 3.

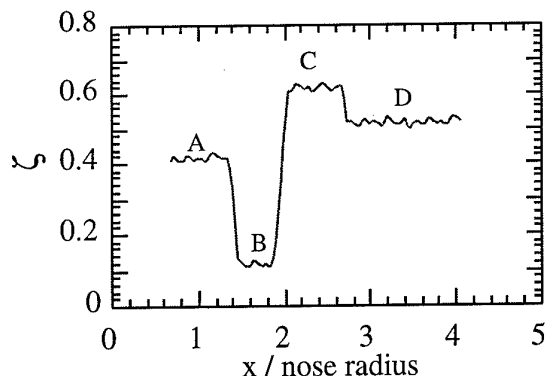


Fig. 3 - hemisphere-cylinder body - $M=0.9$ - $\alpha=0^\circ$
The parameter ζ along the body axis.

It is possible to single out, along the flow direction, a first zone (A) with a certain local stress level, followed by a zone (B) with a lower stress level, than a zone (C) characterized by a significantly increase in the shear stress and, finally, a zone (D) with a shear stress that decreases to a value higher than that present in zone A. In this case, by means of the liquid crystal visualization, it is possible to identify an initial laminar zone in the boundary layer, followed by a separation bubble (in which the shear stress decreases to very low values), followed by a turbulent reattachment (the shear stress increases to higher values than in the laminar zone) and, finally, a decrease in the shear stress, probably due to a sudden increase in the boundary layer thickness, corresponding to the shock wave position. This behavior is confirmed by the Schlieren visualization of the phenomenon (superimposed, in Fig. 4, to the gray-level liquid crystal image).

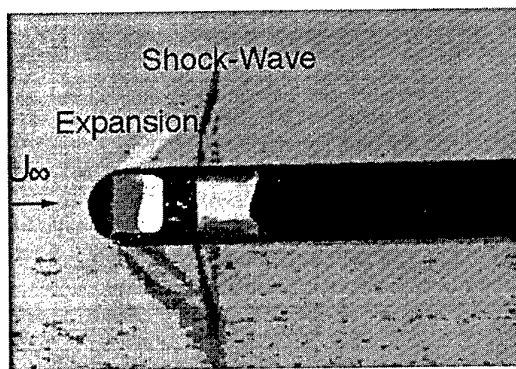


Fig. 4 - Superimposition of the Schlieren and liquid crystal painting photographs

From a comparison of Figs. 3 and 4, it is possible to state that the shock wave position can be identified by the liquid crystal technique. By this example, It is singled out that the interpretation of the liquid crystal visualization (as well as all other visualization techniques) is not always immediate, and a coupling with other experimental techniques or CFD is usually helpful.

4.3 Examples of results in transonic flow

4.3.1 Isolated forward swept wing

A first configuration tested in the MSWT is a 25° forward swept wing, tested at a Mach numbers of 0. For a complete definition of the configuration see Ref. 7. Fig. 5 shows the upper surface patterns (obtained by means of the gray correspondence defined in Fig. 2), for angles of attack of 0° and 8° and a Reynolds number (referred to the mean aerodynamic chord) of 2.8×10^6 (the image is not complete

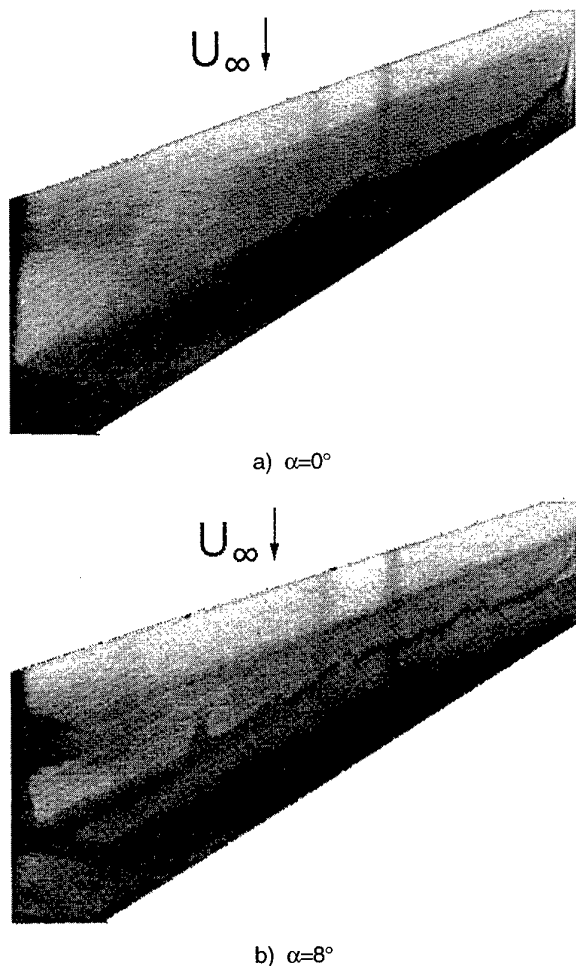


Fig. 5 - Gray level surface representation for a 25° forward swept wing. Mach=0.3, Reynolds 2.8×10^6

in the chordwise direction). It must be pointed out that the leading edge area (approximately 15% of the chord) was not coated, as this area was not considered for the purpose of the analysis (the boundary layer, in the tested conditions, is certainly laminar in that area). In any case, it should be noted that, were the analysis of that zone be required, a different viewing direction should be used. By

analyzing Fig. 5 it is evident that the method used is able to indicate the position of the boundary layer transition line, and, consequently, its shifting caused by the change in the angle of attack.

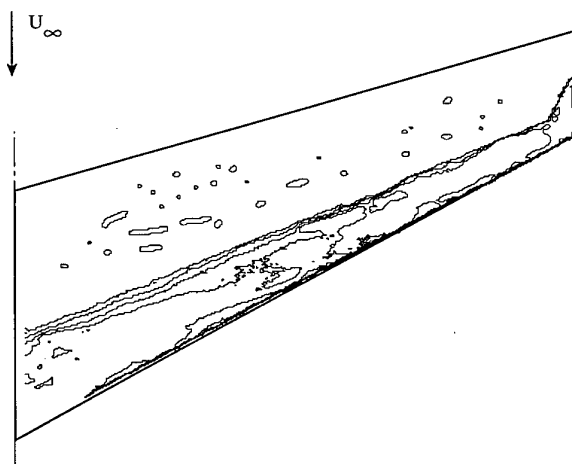


Fig. 6 - Isolines of the parameter ζ .
Mach=0.3, $Re=2.8 \times 10^6$, $\alpha=0^\circ$

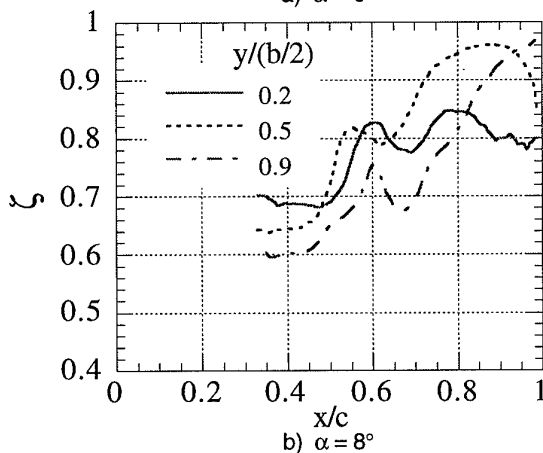
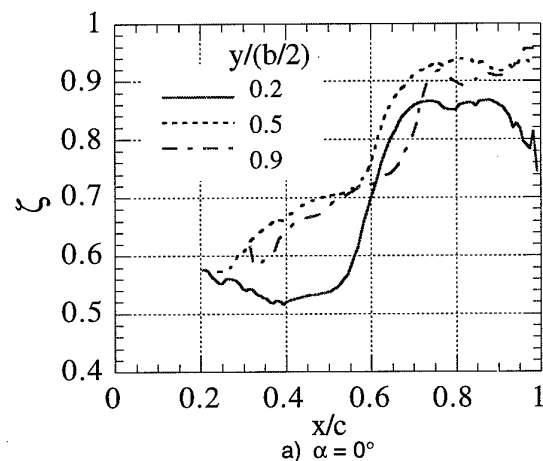


Fig. 7 - The parameter ζ along different spanwise stations. Conditions as in Fig. 5.

More detailed information can be obtained by analyzing the isolines of the parameter ζ , shown, as an example, in Fig. 6 for $\alpha=0^\circ$, and the same behavior is also apparent

from Fig. 7, which shows the parameter ζ along three different spanwise stations. By analyzing this figure it is possible to determine the transition line, corresponding to the maximum gradient. Furthermore, a precise quantitative definition of the region of transition is obtainable by analyzing the chordwise variation the parameter ζ . It can be seen that the transition occurs nearer the leading edge in the region of the wing tip, and that it moves forward as the angle of attack is increased to 8° .

As an example, the transition lines from laminar to turbulent boundary layer, at different angles of attack, are shown in Fig. 8, obtained by analyzing figures similar to Fig. 6.

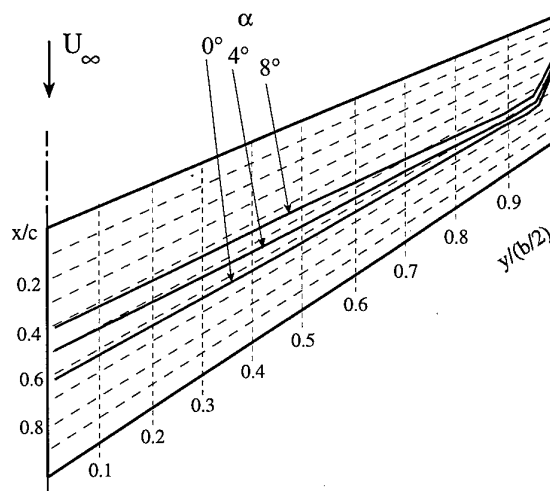


Fig. 8 - Transition lines for a 25° forward swept wing.
Mach=0.3, Reynolds 2.8×10^6

At the considered angles of attack, the transition line is practically straight along the span, except than in a small zone close to the wing tip, characterized by a significant up-stream displacement of the transition line. This displacement, present at all the angles of attack, seems to be related to the turbulence produced by the tip vortex, which originates along the tip in a position between 0.3 to 0.5 chords downstream of the leading edge (Ref. 21). At low angles of attack the transition occurs at almost constant x/c and, therefore, it occurs at the root at a larger distance downstream of the leading edge. Increasing the angle of attack, as expected, transition moves up-stream.

It is interesting to note that this displacement is higher at the root than at the tip; indeed, at the root transition moves from about $x/c=0.63$ at $\alpha=0^\circ$ to about $x/c=0.41$ at $\alpha=8^\circ$, while close to the tip ($y/(b/2)=0.9$) the transition moves from about $x/c=0.67$ at $\alpha=0^\circ$ to about $x/c=0.58$ at $\alpha=8^\circ$. As a consequence, at $\alpha=8^\circ$ the transition occurs at a practically constant distance from the leading edge. This behavior is probably related to the appearance of a cross flow, in the inboard direction for a forward swept wing, which provokes an instability of the traveling waves; on the contrary, at $\alpha=0^\circ$, the cross flow is practically absent for the present wing, and the streamwise instability of the Tollmien-Schlichting waves is probably the cause of transition (see, e.g., Refs. 22-24).

In the following discussion, for clarity, only the transition lines determined from the gradient of the parameter ζ , as reported in Fig. 7, will be reported.

The presence of a lifting canard produces significant down-wash in the inboard zone and up-wash in the outboard zone of the wing. For the specific configuration this results in a reduction of the wing lift at a given angle of attack, while the slope of the C_L - α curve remains approximately the same (see REF. 28).

Fig. 13 shows the transition lines for the configurations with and without canard, for the condition of no global lift acting on the wing, $C_L=0$. As can be seen, the behavior of the two cases is completely different. In the canard configuration the transition is anticipated along all the span, and three different zones can be identified: an inner zone, a middle zone and an outer zone.

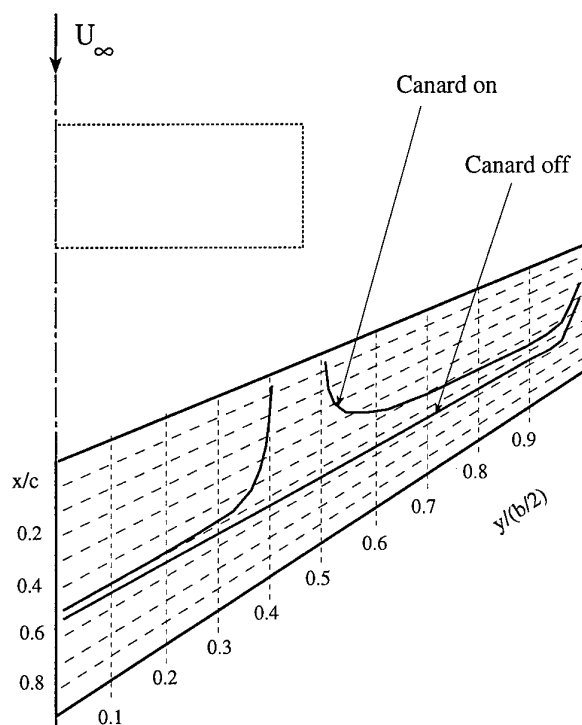


Fig. 13 - Canard effect on the transition lines; $C_L=0$

The middle zone has an extension of about ten per cent of the semi-span, and is characterized by a completely turbulent boundary layer. This zone is interacting directly with the canard tip vortex, which produces, in this zone, a "free-stream" characterized by a very high turbulence level. To analyze the inner and outer zones it is necessary to take into account that, as can be seen from Fig. 14 (derived, with the following Fig. 16, from the results presented in Ref. 28), in the configuration with the lifting canard the spanwise lift distribution on the wing is strongly modified. Indeed, in the canard configuration the spanwise pressure gradients and the cross flow become more important, and probably lead to a cross-flow instability. The appearance of this type of instability, enhanced by the higher amplitude of the perturbation caused by the turbulent flow in the middle zone, causes the flow transition in the boundary layer to occur sooner, both in

the inner and in the outer zones. Moreover, in the outer zone the higher local angles of attack (see again Fig. 14)

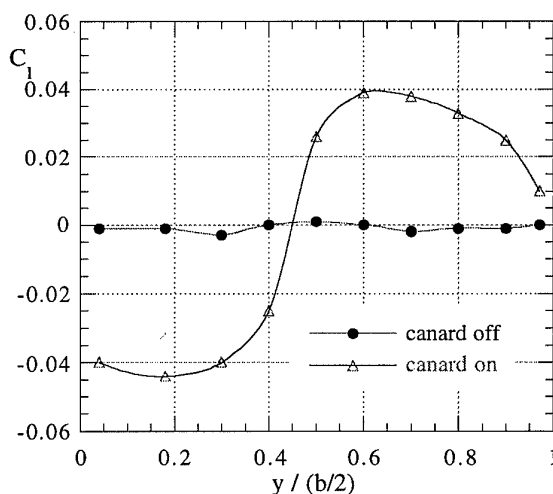


Fig. 14 - Spanwise lift coefficients; $C_L=0$

enhance the fore transition displacement, while in the inner zone the interaction with the canard wake increases the turbulence level of the stream flowing over the wing, with a consequent upstream displacement of the transition. As a conclusion, the transition is displaced upstream over the entire wing span.

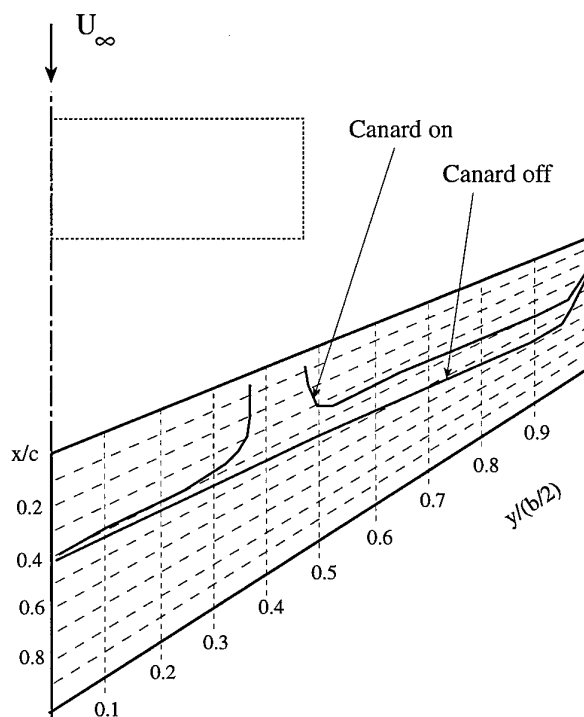


Fig. 15 - Transition lines; $C_L=0.58$

Fig. 15 shows the transition lines for the configurations with and without canard, at a wing lift coefficient $C_L=0.58$, corresponding to an angle of attack of about 8° for the isolated wing and about 9.5° for the canard configuration. Qualitatively, the effect of the canard remains that described previously for the $C_L=0$ case. The transition is again characterized by three different zones. As previously,

in the middle zone the flow is completely turbulent; an inboard displacement of this zone is observed, consequent to the inner displacement of the canard tip vortex when the angle of attack increases. The spanwise extension of this zone remains practically the same, but it is not possible to assume this as a general trend. In fact, two different effects on the extension of this zone can be expected when the angle of attack increases: the increase in the dimension of the canard tip vortex, tends to broaden it, while the higher distance between the canard tip vortex and the wing surface has a narrowing effect. In the specific case a cancellation between these two opposite effects probably occurs.

In the inner zone the transition moves upstream, even though, in the analyzed condition, the local angles of attack in this zone are significantly lower than for the isolated wing, as can be seen by analyzing the spanwise lift distributions shown in Fig. 16.

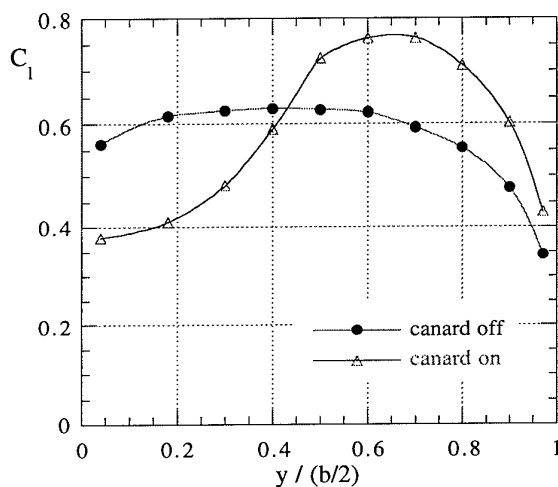


Fig. 16 - Spanwise lift coefficients; $C_L=0.58$

This is probably related to the perturbation incoming from the canard wake and from the turbulent middle zone, and also to the high spanwise pressure gradient and important cross flow, directed in the inboard direction.

In the outer zone the transition occurs more upstream with respect to the isolated wing condition, probably because of the significantly higher local angles of attack (see again Fig. 16). In any case, it is possible to observe that the transition occurs slightly more upstream than in the inner zone, and this can be a confirmation of the importance of the cross-flow type instability in the inner zone of the wing. This type of instability becomes particularly significant in the canard configuration, leading to a remarkable upstream displacement of the boundary layer transition.

5. LIQUID CRYSTAL FOR THE MEASUREMENT OF SURFACE SHEAR STRESS

The measurements of surface shear stress in wind tunnel testing would provide significant information for the aerodynamic design. Conventional methods of measurements such as hot films or Preston tubes are either difficult to interpret and, in any case, provide only local measurements of the shear stress.

Several attempts to have a quantification of the response of the liquid crystals has been carried out. The first work was developed by Klein and Margozi, Ref. 11. Successively, Bonnett et al. developed a technique based on the use of a rotational disk, Ref. 12; further research in this area has recently led to the development of apparatus and methodologies for calibration of shear sensitive LCC (see, e.g. Refs. 14-17).

The calibration procedures involved in the proposed methodologies seem really effective, and probably their efficiency will be largely increased with the improvements in the technology fields of video camera and data/image analysis. In any case, at least at the present state of the art, they seem too complex for an efficient use in industrial application of wind tunnel experiments. Bonnet, for instance, indicate that the method developed in Ref. 12 is only suitable for approximate measurement of shear stress.

As previously indicated in §2, a linear relationship between the reflected light wavelength and the applied shear stress has been observed, at least at values of the shear stress typical of wind tunnel tests. Therefore, following Ref. 11, it is possible to assume:

$$\tau_0 = K_1 \lambda - K_0 \quad (2)$$

where τ_0 is the tangential stress, λ the wavelength of maximum scattering and K_0 and K_1 constant values, to be determined by a calibration procedure.

The dominant wavelength of maximum scattering in a given point and test condition, can be obtained starting from the standard chromatic coordinates (X , Y), as indicated in Refs. 2 and 14, using well stated methods, by extrapolation from the white light through the measured chromaticity coordinates.

In the present application the image is acquired by means of the three channels RGB, then converted into the standard chromatic coordinates, X , Y (see, e.g., Ref. 29).

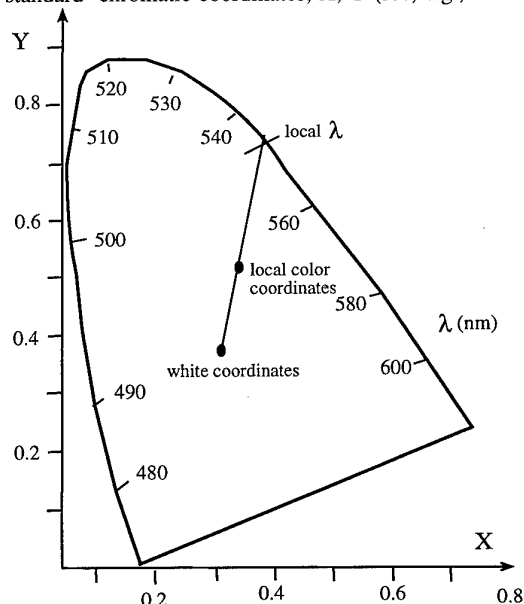


Fig. 17 - the chromaticity diagram (indicative)

By means of the calibration of the video camera on the white and the values X and Y , it is possible to determine the dominant wavelength from the chromaticity diagram, as indicated in Fig. 17. By means of the described procedure, it is possible to have a representation of the surface visualization in terms of dominant wavelength, as shown, for instance in Fig. 18, showing the dominant wavelength at different spanwise stations, for the forward swept wing previously analyzed; it is the corresponding to Fig. 7a (it is necessary to take into account that an increase in the tangential stress produces a decrease in the dominant wavelength).

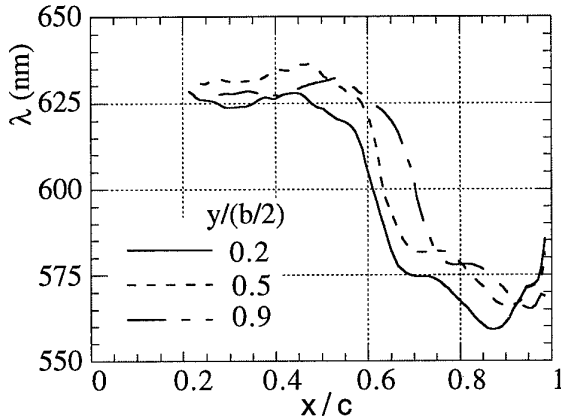


Fig. 18 - The dominant wavelength λ along different spanwise stations for a 25° forward swept wing. Conditions as in Fig. 5, $\alpha=0^\circ$

This procedure appears more accurate of the conversion to gray-level, because the passage from a three parameter representation to a one parameter representation is not guided by the operator, and the information is directly the dominant wavelength λ . However, it is necessary to observe that the procedure is not free from problems, mainly related to the numerical representation of the involved quantity, and to the small differences in λ involved in several problems.

Eq. 2 suggests (Ref. 13) that in order to obtain quantitative information on the flow parameters over a test surface, three reflection spectra are required: one from a white surface and the other two from the liquid crystal surface with and without shear stress, respectively. In this case it is possible to obtain, in a given point A, the dominant wavelength λ for two different values of τ_0 (zero and τ_{0A}) and it is possible to obtain:

$$\Delta\tau = \tau_{0A} = K_{1A} (\lambda_A - \lambda_{Azero}) \quad (3)$$

The quantitative problem, in any case, is not yet solved: in fact a calibration procedure is necessary, in order to settle the values of the sensitivity K_i ; this usually represent a difficult task. Furthermore, it is necessary to take into account that K_0 and K_1 are dependent on both the position and time (depending on the local liquid crystal thickness, view angle, etc.), as previously singled out. In effect, Eq. 2 must be written, also for steady flow:

$$\tau_0(P) = K_1(P, t) \lambda - K_0(P, t) \quad (2')$$

where P identifies the surface point and t the time.

Therefore, it seems that Eq. 3 could be applied only for very short run time, for which not significant dependence on time are introduced.

An example of a partial application of the above procedure (without the calibration) has been shown in Fig. 18. By comparing with the corresponding Fig. 7a, where the parameter ζ was shown, we can observe that the transition from laminar to turbulent flow is indicate in same positions. But from Fig. 18 it is possible to have also some "quantitative" indications. By assuming that the different behavior for different points and time, singled out in Eq. 2', is not significant (for time this is reasonable, because the analyzed image was acquired immediately after the wind tunnel start), the dominant wavelength is directly related to the shear stress. Therefore, it is probable that the shear stress assume values that at the root are higher than at the tip. Naturally, without a specific calibration, it is not possible to have the value of the shear stress, neither in terms of difference between two different points.

From a practical point of view, in industrial applications the identification of the behavior of the liquid crystal by means of preliminary specific calibration appears quite complex. Therefore, at the present state of the research, the technique is probably non precise enough for an absolute determination of the local shear stress, and the indicated procedure seems applicable, in industrial applications, only for comparative tests.

6. CONCLUSION

The present research singled out the advantages connected with the use of the liquid crystal technique for the visualization of the surface flow phenomena during wind tunnel tests. The benefits are that different types of analysis (boundary layer transition, separation and reattachment, shock wave position) can be performed with a single technique, which is characterized by low cost and time requirements (the last feature is essentially related to the reversibility of the liquid crystal coat response). The disadvantages are mainly connected with the important dependence of the response on the lighting sources and viewing point (in particular, for a complete analysis of the entire surface several viewing directions could be necessary) and on the method of application of the liquid crystals.

The various factors mentioned above imply a degree of uncertainty in the interpretation of the results. It is therefore necessary to acquire a high confidence level in the technique in order to assure a good degree of repeatability and accuracy in the analysis of the results. To avoid the possibility of misinterpretations in the analysis of the results, the coupling with other experimental techniques (visualization or CFD), together with a preliminary knowledge of the expected flow behavior, may be extremely useful.

To enhance the knowledge on the boundary layer conditions a quantitative use of this technique will be a powerful tool. Several attempts to have a quantification of the response of the liquid crystals were carried out. The

calibration procedures involved in the proposed methodologies seem really effective, and probably their efficiency will be largely increased with the improvements in the technology fields of video camera and data/image analysis. In any case, at least at the present state of the art, they seem too complex for an efficient use in industrial application of wind tunnel experiments, and it is probably non precise enough for an absolute determination of the local shear stress, while it seems really effective for comparative tests. The present activity is under development at the CSIR Laboratories, and more detailed results will be presented in the future.

ACKNOWLEDGEMENTS

The present investigation was financially supported by the Italian Ministry of University and Scientific and Technological Research and by the South Africa Council for Scientific and Industrial Research.

REFERENCES

- Buresti, G., Carlomagno, G.M., De Luca L., Lombardi, G., "Characterization of Boundary Layer Conditions in Wind Tunnel Tests through Infrared Thermography Imaging," Proc. Int. Meeting on "Applications of Infrared Technology", London, June 1988, SPIE Vol. 918, pp. 23-29.
- Kasagi, N., Moffat, R.J., Hirata, M "Liquid Crystals," in Handbook of Flow Visualization, Wen-Jei Y. Ed., 1989.
- Holmes, B.J., Gall, P.D., Croom, C.C., Manuel, G.S., Kelliher, W.C., "A New Method for Laminar Boundary-Layer Transition Visualization in Flight-Color changes in Liquid-Crystals Coatings," NASA TM-87666, 1986.
- Reda, D.C., "Liquid Crystals for Unsteady Surface Shear Stress Visualization," AIAA Paper 88-3841, 1988.
- Smith, S.C., "Use of Shear-Sensitive Liquid Crystals for Surface Flow Visualization," *Journal of Aircraft*, Vol. 29, No. 2, March-April 1992.
- Reda, D.C., Aeschliman, D.P., "Liquid Crystals Coatings for Surface Shear Stress Visualization in Hypersonic Flows," *Journal of Spacecraft and Rockets*, Vol. 29, No. 2, 1992.
- Schoeler, H., "Application of Encapsulated Liquid Crystal on Heat Transfer Measurements in the Fin-Body Interaction Region at Hypersonic Speed," AIAA Paper 78-0777, 1978.
- Simonich, J.C., Moffat, R.J., "Liquid Crystal Visualization of Surface Heat Transfer on a Concavely Curved Turbulent Boundary Layer," ASME Paper 83-GTJ-7, 1983.
- Akino, N., Kunugi, T., Ichimiya, K., Mitsushiro, K., Ueda, M., "Improved Liquid-Crystal Thermometry excluding human colour sensation," *Journal of Heat Transfer*, No. 111, 1989.
- Farina, D.J., Hacker, J.M., Moffat, R.J., Eaton, J.K., "Illuminant Invariant Calibration of Thermochromic Liquid Crystals," HTD - Vol. 252, Visualization of Heat Transfer Processes, ASME, 1-11, 1993.
- Klein, E.J., Margozzi, A.P., "Apparatus for the calibration of Shear Sensitive Liquid Crystals," *Rev. Sci. Instrum.*, Vol. 612, No. 2, Feb. 1970.
- Bonnet, P., Jones, T.V., McDonnell, D.G., "Shear-Stress Measurements in Aerodynamic Testing Using Cholesteric Liquid Crystals," *Liquid Crystals*, Vol. 6, No. 3, 1989, pp. 271-280.
- Parmar, D.S., "A Novel Technique for Response Function Determination of Shear Sensitive Cholesteric Liquid Crystals for Boundary Layer Investigation," *Rev. Sci. Instrum.*, Vol. 62, No. 6, June 1991.
- Reda, D.C., "Measurement of Surface Shear Stress Vectors Using Liquid Crystal Coatings," *AIAA Journal*, Vol. 32, No. 8, Aug. 1994, pp. 1576-1582.
- Savory, E., Sykes, D.M., Mohan, S.R., Hoang, Q.H., Toy, N., "Calibration and Application of Liquid Crystals for Transition Detection and Skin Friction Measurements in High Speed Flows," 3rd International Symposium on Turbulent Modeling and Measurements, Crete, May. 1996, pp. 401-410.
- Savory, E., Toy, N., Hoang, Q.H., "Investigation of Complex Surface Flow Fields Using Shear Sensitive Liquid Crystals Coatings," 1st Pacific Symposium on Flow Visualization and Image Processing, Honolulu, Feb. 1997.
- Reda, D.C., Wilder, M.C., Farina, D.J., Zilliac, G., "New Methodology for the Measurement of Surface Shear Stress Vectors Distributions," *AIAA Journal*, Vol. 35, No. 4, Apr. 1997, pp. 608-614.
- Lombardi, G., Morelli, M., Waller, D., "Flow Visualization with Shear Sensitive Liquid Crystal - Some Examples and Problems," Proceedings of the 7th Flow Visualization Symposium, Sept. 1995, pp. 526-531.
- Ferguson, J.L., "Liquid Crystals," *Scientific American*, Vol. 211, Aug. 1964, pp. 76-85.
- Manacorda G., "Sull'Uso dei Cristalli Liquidi in Aerodinamica Sperimentale", Report of the Department of Aerospace Engineering of Pisa, ADIA 93-3, Apr. 1993.
- Lombardi, G., Cannizzo, F., "High Aspect Ratio Wings: Tip Vortex Structure And its Numerical Implications," AIAA Paper 96-1961, June 1996.
- Saric, W.S., Reed, H.L., "Stability and Transition of Three-Dimensional Boundary Layer," in AGARD CP 438, Oct. 1988.
- Morkovin, M.V., "Instability, Transition to Turbulence and Predictability," in AGARDograph 236, 1977.
- Dagenhart, J.R., Saric, W.S., Mousseux, M.C., Stack, J.P., "Crossflow-vortex Instability and Transition on a 45-degree Swept Wing," AIAA Paper 89-1892, 1989.
- Lombardi G., "Experimental Study on the Aerodynamic Effects of a Forward Sweep Angle," *Journal of Aircraft*, Vol. 30, No. 5, Sep./Oct. 1993.
- Lombardi, G., Morelli, M., Waller, D., "Canard Influence on the Boundary Layer of a Forward Swept Wing," 20th ICAS Congress, Paper 96-1.3.4, Sept. 1996.
- Lombardi, G., Morelli, M., Waller, D., "Boundary Layer Transition on a Forward Swept Wing in Canard Configuration," *Journal of Aircraft*, Vol. 33, No. 6, Nov.-Dec 1996.
- Lombardi, G., Morelli, M., "Pressure Measurements On A Forward Swept Wing-Canard Configuration," *Journal of Aircraft*, Vol. 31, No. 2, Mar.-Apr. 1994.
- Wyszecky, G., "Colorimetry," Handbook of Optics, McGraw-Hill, New York, 1978.

Applications of Temperature and Pressure Sensitive Paints

Tianshu Liu and John P. Sullivan
School of Aeronautics and Astronautics
Purdue University, 1282 Grissom Hall
West Lafayette, IN 47907-1282, USA

Summary

Luminescent molecular probes imbedded in a polymer binder form a temperature or pressure paint. On excitation by light of the proper wavelength, the luminescence, which is quenched either thermally or by oxygen, is detected by a camera or photodetector. From the detected luminescent intensity, temperature and pressure can be determined. The basic photophysics, calibration, accuracy and time response of a luminescent paints is described followed by applications in low speed, transonic, supersonic and cryogenic wind tunnels and in rotating machinery.

Introduction

The use of luminescent molecular probes for measuring surface temperature and pressure on wind tunnel models and flight vehicles offers the promise of enhanced spatial resolution and lower costs compared to traditional techniques. These new sensors are called temperature-sensitive paint (TSP) and pressure-sensitive paint (PSP). Traditionally, arrays of thermocouples and pressure taps have been used to obtain surface temperature and pressure distributions. These techniques can be very labor-intensive and model/flight vehicle preparation costs are high when detailed maps of temperature and pressure are desired. Further, the spatial resolution is limited by the number of instrumentation locations chosen. By comparison, the TSP and PSP techniques provide a way to obtain simple, inexpensive, full-field measurements of temperature and pressure with much higher spatial resolution. Both TSP and PSP incorporate luminescent molecules in a paint which can be applied to any aerodynamic model surface. Figure 1 shows a schematic of a paint layer incorporating a luminescent molecule.

The paint layer is composed of luminescent molecules and a polymer binder material. The resulting 'paint' can be applied to a surface using a brush or sprayer. As the paint dries, the solvent evaporates and leaves behind a polymer matrix with luminescent molecules embedded in it. Light of the proper wavelength to excite the luminescent molecules in the paint is directed at the model and luminescent light of a longer wavelength is emitted by the molecules. Figure 2 shows the spectra for a typical luminescent ruthenium molecule. Using the proper filters, the excitation light and luminescent emission light can be separated and the intensity of the luminescent light can be determined using a photodetector. Through the photo-

physical processes known as thermal- and oxygen-quenching, the luminescent intensity of the paint emission is related to temperature or pressure. Hence, from the detected luminescent intensity, temperature and pressure can be determined.

The polymer binder is an important ingredient of a luminescent paint used to adhere the paint to the surface of interest. In some cases, the polymer matrix is a passive anchor. In other cases, however, the polymer may affect significantly the photophysical behavior of the paint through a complicated interaction between the luminescent molecules and the macro-molecules of the polymer. A good polymer binder should be robust enough to sustain skin friction and other forces on the surface of an aerodynamic model. Also, it must be easy to apply and repair to the surface in a smooth, thin film. For TSPs, many commercially available resins and epoxies can be chosen serve as polymer binders if they are not oxygen permeable and do not degrade the activity of the luminophore molecules. In contrast, a good polymer binder for a PSP must have high oxygen permeability besides being robust and easy to apply.

Two recent papers (Liu et al 1997) and (Gouterman 1997) provide excellent reviews of the foundations and history of TSP and PSP and contain extensive reference lists.

Measurement Systems

The measurement systems are the same for both TSPs and PSPs. The essential elements of the systems include illumination sources, optical filters, photodetectors and data acquisition/processing units. This section provides a brief description of two measurement systems: the CCD camera system and the laser scanning system. Intensity based measurements are considered first and then lifetime and multi-luminophore systems.

CCD Camera System

The CCD camera system for luminescent paints is the most commonly used in aerodynamic testing. A schematic of this system is shown in Figure 3. The luminescent paint (TSP or PSP) is coated on the surface of the model. The paint is excited to luminesce by the illumination source, such as a lamp or a laser. The luminescent intensity image is filtered optically to eliminate the illuminating light and then captured by a CCD camera and transferred to a computer with a frame grabber board for image processing.

Both wind-on image (at temperature and pressure to be determined) and wind-off image (at a known constant temperature and pressure) are obtained. The ratio between the wind-on and wind-off images is taken after the dark current level image is subtracted from both images, yielding a relative luminescent intensity image. Using the calibration relations, the surface temperature and pressure distributions can be computed from the relative luminescent intensity image.

Selection of the appropriate illumination sources depends on the absorption spectrum of the paint and the optical access of the facility. The source must provide a large number of photons in the wavelength band of absorption. A variety of illumination sources are available. Lasers with fiber-optic delivery systems have been used in wind tunnel tests (Morris et al. 1993b, Crites 1993, Bukov et al. 1992, Engler et al. 1995). Other light sources reported in literature include a xenon arc light with a blue filter (McLachlan et al. 1993a), incandescent tungsten/halogen lamps (Dowgillo et al. 1994) and fluorescent UV lamps (Liu et al. 1995a, 1995b). Morris et al. (1993a) and Crites (1993) discussed the characteristics of some illumination sources. For imaging the surface, scientific grade cooled CCD digital cameras can provide high intensity resolution (12 and 16 bits) and high spatial resolution (up to 2048×2048 pixels). Since the scientific grade CCD camera exhibits good linearity and high signal-to-noise ratio (SNR), it is particularly suitable to quantitative luminescent intensity measurements.

A necessary step in data processing is taking the ratio between the wind-on luminescence image and the wind-off reference image at a known reference temperature and pressure. The image ratio process can eliminate the effects of spatial non-uniformity in illumination light, coating thickness, and luminophore concentration. However, since aerodynamic forces may cause model motion and deformation in high-speed wind tunnel tests, the wind-on image may not align with the wind-off image. The ratio between the non-aligned images leads to considerable errors in calculating temperature and pressure using the calibration relations. Also, some distinct flow characteristics, such as shocks, transition and separation locations, could be smeared. In order to correct this non-alignment, an image registration method was suggested by Bell and McLachlan (1993) and Donovan et al. (1993).

Laser Scanning System

A laser scanning system for TSPs and PSPs is shown in Figure 4. A low power laser is focused to a small point and scanned over the surface of the model using computer controlled mirrors. The laser illumination excites the paint on the model and luminescence is detected by a low noise photodetector (e.g. a PMT). The photodetector signal is digitized with a high resolution A/D converter and processed to obtain temperature and pressure. The mirror

is synchronized to the data acquisition so that the position of the laser spot on the model is accurately known.

Compared with the CCD camera system, it takes longer to obtain full-surface temperature and pressure distributions using the laser scanning system. However, this system has some advantages. (Hamner et al. 1994)

- (i) Luminescence is detected by a low noise photodetector. Before the analog output from the PMT is digitized, filtering and other SNR enhancement techniques are available to improve the measurement resolution. The signal is then digitized with a high resolution (12 to 24 bit) A/D converter. Additional noise reduction can be accomplished by using a lock-in amplifier if the laser intensity is modulated.
- (ii) The laser scanning system can be used for measurement in a facility where optical access is very limited and the CCD camera system is difficult to use.
- (iii) The system provides uniform illumination over the surface by scanning a single light spot.
- (iv) The system can be easily adapted for measurement of luminescent lifetime or phase shift if a pulsed laser or modulated laser is used.

Lifetime-based detection systems

A promising method for making temperature and pressure measurements is to determine the luminescent lifetime of the paint rather than the luminescent intensity. Compared with the intensity-based method, the greatest advantage of this method is that the lifetime-temperature or -pressure relation is not dependent on illumination intensity. Therefore, the calibration relation is intrinsic for a particular paint and the image ratio process is not required. Also, the lifetime measurement is insensitive to luminophore concentration, paint thickness, photodegradation, tubid paint surface and dirty optical surfaces. The temperature and pressure can be directly obtained from the measured lifetime. The lifetime measurement technique in photochemistry is well-developed (Szmecinski and Lakowicz 1995, Papkovsky 1995). The basic configuration of this system is similar to either the CCD camera or the laser scanning system, except a pulsed excitation light is used. After each pulse, the luminescence decay is detected and acquired by a computer. Then, temperature or pressure is obtained by using the calibration relation. Using a lifetime detection system, Davies et al. (1995) measured the pressure distributions on a cylinder in subsonic flow and on a wedge at Mach 2. Comparison with data obtained by conventional pressure taps was favorable.

A frequency-domain method detects the phase angle between the luminescence emission and harmonically modulated excitation light. If the modulation frequency is fixed, the phase angle is a function of the lifetime and hence is dependent on temperature and pressure. The phase angle can be measured using a lock-in amplifier. Campbell et al. (1994) gave a calibration between phase angle and temperature for Ru(bpy)-Shellac paint at 100

kHz modulation frequency. A simple phase detection system using blue LED excitation was used to measure surface temperature on an electrically heated steel foil on which a round air jet impinged (Campbell et al. 1994). Torgerson et al. (1996) measured the pressure distribution in a low-speed impinging jet using a laser scanning system with an optical modulator.

Multi-Luminophore System

Use of the normal CCD camera or laser scanning system requires a ratio between the wind-on and wind-off luminescent images. This image ratio method inevitably causes inaccuracy in determining temperature and pressure because the image registration is never perfect. A two-color luminophore paint would eliminate the need for a wind-off reference image. Two-color luminescent TSP is made by combining a temperature-sensitive luminophore with a temperature-insensitive reference luminophore. Similarly, two-color luminescent PSP consists of a pressure-sensitive luminophore with a pressure-insensitive reference luminophore. The probe luminophore and reference luminophore can be excited by the same illumination. However, there is ideally no overlap between the emission spectra of the probe luminophore and reference luminophore such that two color luminescent images can be completely separated by optical filters. The ratio between these two color images can eliminate effects of spatial non-uniformity in illumination, paint thickness and luminophore concentration. Besides the aforementioned combinations, a temperature sensitive luminophore which is not quenched by oxygen can be combined with an oxygen sensitive luminophore. This dual luminophore temperature/pressure paint can be used for temperature correction in PSP measurement. Furthermore, a multi-color PSP can be developed to correct simultaneously the effects of both temperature variation and non-uniformities in lighting, paint thickness and concentration. Some preliminary experiments indeed indicate that a two-color PSP can correct variations in illumination (Oglesby et al. 1995, Harris and Gouterman 1995). Three pressure sensitive paints with internal temperature sensitive luminophore have also been tested by Oglesby et al. (1996). Their results show that the dual luminophore paint enables point-by-point correction of temperature effects of PSP measurement. Only recently, a two-color PSP was used to measure pressure distribution in a low speed impinging jet (Torgerson et al. 1996).

Temperature Sensitive Paints

This section will describe the photophysics, calibration, accuracy, time response of temperature sensitive paint.

Photophysics

For a TSP, it is assumed that the paint layer is not oxygen-permeable so that $[O_2] = 0$. Hence, the quantum yield is simply given by

$$\Phi = \frac{I}{I_a} = \frac{k_L}{k_L + k_D} = k_L \tau_0 \quad (1)$$

The deactivation term k_D may be decomposed into a temperature-independent part k_0 and a temperature-dependent part k_1 that is related to thermally activated intersystem crossing (i.e. $k_D = k_0 + k_1$). The rate k_1 can be assumed to have an Arrhenius form (Bennett and McCartin 1966, Schanze et al. (1997)

$$k_1 = C \exp(-E/RT) \quad (2)$$

where C is a constant, E is the Arrhenius activation energy, R is the universal gas constant and T is the thermodynamic temperature (in Kelvin).

The relation (1) can be approximately written in the simple Arrhenius form

$$\ln \frac{I(T)}{I(T_{ref})} = \frac{E}{R} \left(\frac{1}{T} - \frac{1}{T_{ref}} \right) \quad (3)$$

Theoretically speaking, the Arrhenius plot of $\ln[I(T)/I(T_{ref})]$ versus $1/T$ gives a straight line of slope E/R . Tests indicate that the simple Arrhenius relation does fit experimental data over a certain temperature range. However, for some paints, the data may not fully obey the simple Arrhenius relation over a wider range of temperature. As an alternative, the relation between the luminescence intensity and temperature can be expressed in a functional form

$$\frac{I(T)}{I(T_{ref})} = F(T/T_{ref}) \quad (4)$$

The empirical expression $F(T/T_{ref})$ could be a polynomial, exponential or other functions to fit the experimental data over a certain temperature range. Both (3) and (4) are operational forms of the calibration relation for a TSP used for data reduction in practical applications.

TSP Calibration

In order to quantitatively measure temperature with the TSP coatings, a calibration relating luminescent intensity or lifetime to temperature is needed. A calibration rig consists of a temperature controlled sample and appropriate illumination source and luminescent detector.

Typical temperature dependencies of luminescent intensity are shown in Figure 5 for some TSPs. Several TSPs have high temperature sensitivity in cryogenic temperature range. Others can be used in a temperature range from -20 to 105 °C. Figure 6 gives a lifetime calibration of two TSP's.

Accuracy

The accuracy of the temperature measurement has been shown to depend primarily on calibration accuracy, but is in the range of 1 degree. (see Liu et al. 1995c for a detailed analysis)

Time Response

There are two characteristic time scales that are related to the time response of the paint. One is the luminescent lifetime which represents an intrinsic physical limit for the achievable temporal resolution of the paint. Luminescent paint usually has a lifetime ranging from 10^{-10} seconds to

milliseconds. Another is the time scale of the thermal diffusion in the TSP layer. In a forced convection-dominated case, the thermal diffusion time can be expressed by $\tau = \rho c \ell / h$, where ρ is the density, c is the specific heat, ℓ is the paint thickness and h is the convection heat transfer coefficient. In general, the diffusion time is much larger than the lifetimes of most luminescent paints. Therefore, the time response of the luminescent paint is mainly limited by the diffusion processes for both TSP and PSP measurements.

Figure 7 shows a the temperature response of the TSP paint subjected to the pulsed laser heating. (Liu et al., 1995c). The surface temperature increases rapidly after the pulsed laser beam is turned on and then gradually decays due to natural convection. By fitting the experimental data with the asymptotic solutions, it is found that $\tau_1 = 0.25$ ms and $\tau_2 = 25$ ms.

Transition Detection

TSP has also been utilized as an approach to flow transition detection (Campbell 1994, McLachlan et al. 1993b). Since convective heat transfer is much higher in turbulent flow than in laminar flow, TSP can visualize the surface temperature difference between turbulent and laminar regions. In low speed wind tunnel tests, the model is typically heated or cooled to enhance temperature variation across the transition line. Using EuTTA-dope paint, Campbell et al. (1992, 1993) visualized transition patterns on a symmetric NACA 654-021 airfoil in a low-speed wind tunnel. (Figure 8). Recently, a cryogenic TSP system have been developed at Purdue, the University of Florida NASA Langley and NAL Japan. Several TSP formulations have been successfully used to detect transition on airfoils in a 0.1m transonic cryogenic wind tunnel at the National Aerospace Laboratory (NAL) in Japan (Figure 9 from Asai et al. 1997) and a 0.3m cryogenic wind tunnel at NASA-Langley (Figure 10 from Popernack et al.).

Quantitative Heat Transfer

Global surface heat transfer mapping on a waverider model in Mach 10 flow has been obtained using EuTTA-dope paint (Liu et al. 1994b, 1995b).

A thin Mylar insulating layer covered the windward side of the model, and EuTTA-dope paint was applied on the insulating layer. The temporal evolution of surface temperature distributions was obtained and then heat flux was calculated using a simple heat transfer model. Figure 11 shows a representative map of heat flux on the windward side of the waverider. The bright and dark regions correspond to high and low heat transfer, respectively. The low heat transfer region near the leading edge corresponds to laminar flow. Transition from laminar to turbulent flow can be easily identified by an abrupt change from low to high heat transfer. Figure 12 shows a typical heat transfer history. The TSP measurement is in good agreement with data obtained by thermocouples.

Pressure Sensitive Paints

This section will describe the photophysics, calibration, accuracy, time response of pressure sensitive paint.

Photophysics

PSP operation is based on the principle that certain fluorescent molecules are quenched by the presence of oxygen. In the molecules of interest, oxygen interacts with the excited molecules and the excess energy is transferred to the oxygen in a collisional process, with no photons being emitted. This process, known as oxygen quenching, is the basis for the pressure sensitive paint method. According to Henry's law, oxygen concentration is proportional to the partial pressure of oxygen, which is proportional to static pressure. The result is that if there is a locally high pressure area, the fluorescent molecules will be quenched by oxygen.

The quenching process is governed by the Stern Volmer equation which can be written as a ratio of intensities in order to remove the effects of concentration, thickness and illumination variations.

$$\frac{I_{\text{ref}}}{I} = A(T) + B(T) \left(\frac{P}{P_{\text{ref}}} \right) \quad (5)$$

I_{ref} = fluorescence intensity at reference condition

P_{ref} = pressure at reference condition

$A(T), B(T)$ = Stern Volmer constants

The result is that an increasing pressure causes the intensity of the paint to decrease. In using equation 5, an intensity map must be acquired at a reference condition, typically a flow off or slow rotation where the pressure is a known constant across the surface.

In this version of the Stern Volmer equation, the constants A and B are written as functions of temperature.

$$A(T) = a_1 \left[1 + \frac{E_{\text{nr}}}{RT_{\text{ref}}} \left(\frac{T - T_{\text{ref}}}{T_{\text{ref}}} \right) \right],$$

$$B(T) = b_1 \left[1 + \frac{E_p}{RT_{\text{ref}}} \left(\frac{T - T_{\text{ref}}}{T_{\text{ref}}} \right) \right]$$

E_{nr} = non-radiative activation energy

E_p = polymer activation energy

R = interaction distance

a_1, b_1 = constants

The temperature dependence of A is due to the thermal quenching as in TSP. The temperature dependence of B is due to the temperature dependence of diffusivity of the polymer binder. (Torgerson 1997, Schanze et al.)

Calibration

Figure 13 shows Stern Volmer curves for various paints at room temperature. A calibration of Ru(ph₂-phen) in GE RTV 118 at several temperatures is given in Figure 14 and for PtTFPP in polystyrene in Figure 15.

Accuracy

To estimate the uncertainty of the PSP measurement with a scientific-grade CCD camera system, Morris et al. (1993a)

conducted a series of calibration experiments focused on a proprietary PSP paint sample in a pressure vessel which controlled both the temperature and pressure. After averaging a 32 sequential images to improve the SNR, they found that the minimum pressure resolution near atmospheric pressure (13 to 16 psia) is about ± 0.05 psid for their system. Note that the above uncertainty estimates do not contain the contributions from some major error sources such as the temperature effects and model displacement. The uncertainty of PSP measurements depends strongly on a systematic error source associated with the temperature dependence of the paint. An analysis by Sajben (1993) indicates that the temperature uncertainty dominates the PSP measurement errors. Another major error source is model motion between the wind on and wind off images. To date, it has been necessary to perform an in-situ calibration of the PSP using standard pressure taps on the model in order to obtain reasonable accuracy.

Time Response

Based on the transient solution of the diffusion equation, the oxygen diffusion time for a thin PSP coating is on the order of $\tau = \ell^2 / D_m$, where ℓ is the coating thickness and D_m is the mass diffusivity of oxygen in the paint layer. Baron et al. (1993) studied the time response to oxygen concentration changes of several PSPs using a pressure jump apparatus. The PSPs that they investigated are PtOEP in GP-197 and MAX-100 polymer binders and H₂TFPP in Silica-W, Silica-B and TLC binders. They found that the response times for GP-197 and MAX-100 binder are 2.45 s and 0.4 s, respectively. The Silica-W and Silica-B show response times of 11 ms and 1.5 ms, respectively. The response time of the TLC is about 25 μ s. Recently, using a similar set-up, Carroll et al. (1996) measured the step response of three PSPs: a proprietary PSP from McDonnell Douglas, PtOEP on a white primer layer, and PtOEP in GP-197. For the McDonnell Douglas paint with thickness ranging from 13 to 35 μ m, the response time varies from 0.042 s to 0.42 s. The response time of PtOEP on a white primer layer is 45 ms. For PtOEP in GP-197, the response times are 1.4 s, 1.6 s and 2.6 s for the paint thickness of 22 μ m, 26 μ m and 32 μ m, respectively. Bukov et al. (1992) reported that a proprietary fast-responding PSP coating developed by TsAGI has a time constant of 5 ms. Clearly, the diverse time constants of various PSPs result from the effects of the different polymer diffusivity, coating thickness and structure of the paint.

PSP Applications

Most of PSP measurements on aerodynamic models have been conducted in transonic and supersonic wind tunnels. Recently, the PSP technique has been used for pressure measurements in low-speed flows and rotating machinery.

Tests in wind tunnels

PSPs have been applied to pressure measurements in wind tunnel tests over a wide range of Mach numbers in order to examine the feasibility of this method. Kavandi et al.

(1990) and McLachlan et al. (1993a) tested a two-dimensional airfoil (NACA-0012) over a Mach number range of 0.3 to 0.66. McLachlan et al. (1995a, 1995b) also tested a large generic transport wing/body configuration in transonic Mach number from 0.7 to 0.9. The PSP data not only provide good quantitative chordwise pressure results, but also show complicated two-dimensional pressure maps that would be difficult to deduce from the usual discrete tap data. Some experiments conducted in the McDonnell Douglas Research Laboratories (Morris et al. 1993b) include pressure measurements on a generic wing/body model (Mach number = 2 and angle of attack = 8 degree), a model of a high performance fighter (Mach number = 1.2), and a two-dimensional converging/diverging nozzle. Sellers and Brill (1994) conducted a demonstration test of a PSP in the Arnold Engineering Development Center transonic wind tunnel for an aircraft model. Using fast-responding PSP coatings developed at TsAGI, Troyanovsky et al. (1993) carried out a semi-quantitative pressure visualization for a shock/body interaction in a Mach 8 shock tube with 0.1 s duration, and Borovoy et al. (1995) determined the pressure distributions on a cylinder at Mach 6 in a shock wind tunnel with about 40 ms duration. In general, the PSP technique works well in high Mach number subsonic flows and supersonic flows since static pressure change is typically large. Morris (1995) and Shimbo et al. (1997) measured the pressure on delta wings at low Mach numbers ranging from 0.05 to 0.2. These results indicate the low pressure regions induced by leading edge vortices.

Figure 16 shows a typical surface pressure map in the interaction of a cylinder mounted normal to a flat floor with a supersonic turbulent boundary layer at a freestream Mach number of 2.5. In this test carried out in the Purdue University supersonic wind tunnel, the incoming boundary layer thickness is 4 mm, the cylinder height is 15 mm, and the cylinder diameter is 4.8 mm. The PSP, Ru(ph₂-phen) in GE RTV 118, was applied to the floor surface for pressure measurement. The pressure map clearly indicates a pressure rise induced by a bow shock ahead of the cylinder and a low pressure region in the turbulent wake behind the cylinder.

Transonic Airfoil - Lifetime Method

The laser scanning method for pressure and temperature sensitive paints was demonstrated in the Boeing Company model transonic wind tunnel. (Torgerson 1997) The airfoil was 10% thick with a sharp leading edge and a small amount of camber. It had 19 pressure taps along the upper surface to compare with the pressures found from the paints. The laser used was a small air-cooled argon-ion laser. The beam was modulated using an electro-optic modulator, enabling the signal to be processed by a two phase lock-in amplifier. Both intensity and phase were recorded during the scan over the airfoil, so that a comparison between intensity and lifetime methods could be made. Results in Figure 17 show both methods compare favorably with the pressure tap data. The phase

measurements have the advantage that wind off data is not required.

Cryogenic Pressure Paint

Recently, Asai et al. 1997 demonstrated the feasibility of using luminescent coatings for surface pressure measurements in a cryogenic wind tunnel. Calibrations of a new anodized layer (Figures 18 and 19) show extremely high oxygen sensitivity. By injecting a small of oxygen (250 ppm) into the NAL transonic cryogenic tunnel excellent comparison between pressure taps and PSP was obtained for flow over a 14% circular-arc bump model.(Figure 20)

Rotating Machinery

The PSP/TSP technique provides a promising tool for measuring surface pressure distributions on a high-speed rotating blade at a high spatial resolution. Instrumentation is particularly difficult in the rotating environment and the pressure taps weaken the structure of the rotating blade. Recently, a test was performed to measure the chordwise pressure distributions on the rotor blades of a high speed axial flow compressor shown in Figure 21 (Liu et al 1996c). TSP (Ru(bpy)-Shellac) and PSP (Ru(ph₂-phen) in GE RTV 118) were applied to alternating blades. The TSP provided the temperature distributions on the blades for temperature correction of the PSP results. A scanning laser system was used for excitation and detection of luminescence. Both the TSP and PSP were excited with an Argon laser and luminescence was detected with a Hamamatsu PMT. The pressure map of Figure 22 shows a strong suction surface shock wave. Comparisons to CFD over a range of rotational speeds (Figure 23) show good correlation but require care in interpretation since the error in the PSP is ~.1 psia because an in-situ calibration was not possible. The same system was on used on an Allied Signal F109 gas turbine engine (Figure 24) giving the suction surface pressure map at 14000 rpm shown in Figure 25.

Conclusion

The fundamentals and applications of the TSP and PSP techniques have been discussed in this paper. The TSP technique has been used not only to visualize surface flow features such as boundary layer transition, shocks and separation, but also to obtain quantitative surface temperature and heat transfer maps with good accuracy. Applications of the PSP technique are focused on surface pressure measurements on airfoils, generic wing-body models aircraft models and turbomachinery over a wide range of Mach numbers. The field mapping capability of the TSP and PSP techniques is able to provide information about complicated flow characteristics that cannot be easily acquired using more conventional methods. Much effort has been made to improve essential elements of the measurement system including paint formulation, illumination, imaging, and data acquisition/processing hardware and software. Many groups are working extend and refine TSP and PSP measurements so they will become a routine procedure in aerodynamics testing.

Acknowledgment:

This work was supported by ONR, AFOSR, NASA Langley, NASA Ames, NASA Lewis and the Boeing Company. The authors would like to thank Dr. Keisuke Asai of the National Aeronautics Laboratory, Japan for his generous cooperation.

REFERENCES

- Asai, K., Kanda, H., Kunimasu, T., Liu, T. and Sullivan, J. (1997), Detection of Boundary-Layer Transition in a Cryogenic Wind Tunnel by Using Luminescent Paint, *J. of Aircraft* Vol. 34, No. 1, 34-42.
- Asai, K., Kanda, H., Cunningham, C., Ebrahimi, R. and Sullivan, J. (1997), Surface Pressure Measurement in a Cryogenic Wind Tunnel Using a Luminescent Coating, 17th Int. Cong. Instrumentation in Aerospace Simulation Facilities (ICIASF), Institute of Electrical and Electronics Engineers, Monterey CA., USA.
- Baron, A. E., Danielson, J. D., Gouterman, M., Wan, J., Callis, J. B. and McLachlan, B. (1993), Submillisecond Response Times of Oxygen-Quenching Luminescent Coatings, *Rev. Sci. Instrum.* 64(12), 3394-3402.
- Bell, J. H. and McLachlan, B. G. (1996), Image Registration for Luminescent Paint Sensors, *EXP FLUIDS* 22: (1) 78-86
- Bennett, R. G. and McCartin, P. J. (1966), Radiationless Deactivation of the Fluorescent State of Substituted Anthracenes, *The Journal of Chemical Physics*, Vol. 44, No. 5, 1969-1973.
- Birch, D. J. S. and Imhof, R. E. (1991), Time-Domain Fluorescence Spectroscopy Using Time-Correlated Single-Photon Counting, *Topics in Fluorescence Spectroscopy*, Volume 1: Techniques, edited by J. R. Lakowicz, Plenum Press, New York, Chapter 1.
- Borovoy, V., Bykov, A., Mosharov, V., Orlov, A., Radchenko, V. and Phonov, S. (1995), Pressure Sensitive Paint Application in Shock Wind Tunnel, *Proc. 16th Int. Cong. Instrumentation in Aerospace Simulation Facilities (ICIASF)*, Institute of Electrical and Electronics Engineers, Wright-Patterson Air Force Base, Dayton, OH, USA, 34.1-34.4.
- Bukov, A., Mosharov, V., Orlov, A., Pesetsky, V., Radchenko, V., Phonov, S., Matyash, S., Kuzmin, M. and Sadovsky, N. (1993), Optical Surface Pressure Measurements: Accuracy and Application Field Evaluation, 73th AGARD Fluid Dynamics Panel Meeting and Symposium on Wall Interference, Support Interference and Flow Field Measurements, Brussels, Belgium.
- Campbell, B., Liu, T. and Sullivan, J. (1994), Temperature Sensitive Fluorescent Paint System, *AIAA Paper* 94-2483.
- Carroll, B. F., Abbitt, J. D., Lukas, E. W. and Morris, M. J. (1996), Step Response of Pressure Sensitive Paints, *AIAA J.* Vol. 34, No. 3, 521-526.
- Crites, B. C. (1993), Measurement Techniques — Pressure Sensitive Paint Technique, *Lecture Series 1993-05*, von Karman Institute for Fluid Dynamics.
- Davies, A. G., Bedwell, D., Dunleavy, M. and Brownjohn, N. (1995), Pressure Sensitive Paint Measurements Using a Phosphorescence Lifetime Method, presented at Seventh International Symposium on Flow Visualization, September 11-14, Seattle, Washington.
- Donovan, J. F., Morris, M. J., Pal, A., Benne, M. E. and Crites, R. C. (1993), Data Analysis Techniques for Pressure- and Temperature-Sensitive Paint, *AIAA Paper* 93-0176.
- Dowgwillo, R. M., Morris, M. J., Donovan, J. F. and Benne, M. E. (1996), Pressure sensitive paint in transonic wind-tunnel testing of the F-16, *J AIRCRAFT* 33: (1) 109-116 *J AIRCRAFT* 33: (1) 109-116.
- Engler, R. H. (1995), Further Developments of Pressure Sensitive Paint (OPMS) for Non Flat Models in Steady Transonic Flow and Unsteady Conditions, *Proc. 16th Int. Cong. Instrumentation in Aerospace Simulation Facilities (ICIASF)*, Institute of Electrical and Electronics Engineers, Wright-Patterson Air Force Base, Dayton, OH, USA, 33.1-33.8.
- Gouterman M. (1997) Oxygen quenching of luminescence of pressure sensitive paint for wind tunnel research, *J Chem Educ* 74: (6) 697-702
- Hamner, M., Campbell, B., Liu, T. and Sullivan, J. (1994), A Scanning Laser System for Temperature and Pressure Sensitive Paint, *AIAA Paper* 94-0728.
- Harris, J. and Gouterman, M. (1995), Referenced Pressure Sensitive Paint, *Flow Visualization VII, Proceeding of the Seventh International Symposium on Flow Visualization*, edited by J. Crowder, Seattle, Washington, p.802.

- Kavandi, J., Callis, J. B., Gouterman, M. P., Khalil, G., Wright, D., Green, E., Burns, D. and McLachlan, B. (1990), Luminescent Barometry in Wind Tunnels, *Rev. Sci. Instrum.* 61(11), 3340-3347.
- Liu, T., Campbell, B. and Sullivan, J. (1994b), Remote Surface Temperature and Heat Transfer Mapping for a Waverider Model at Mach 10 Using Fluorescent Paint, *AIAA Paper* 94-2484.
- Liu, T., Campbell, B. and Sullivan, J. (1995a), Fluorescent Paint for Measurement of Heat Transfer in Shock-Turbulent Boundary Layer Interaction, *Experimental Thermal and Fluid Science* 10, 101-112.
- Liu, T., Campbell, B. and Sullivan, J. (1995c), Accuracy of Temperature-Sensitive Fluorescent Paint for Heat Transfer Measurements, *AIAA Paper* 95-2042.
- Liu, T. and Sullivan, J. (1996a), Heat Transfer and Flow Structures in an Excited Circular Impinging Jet, *Int. J. Heat Mass Transfer* (in press).
- Liu, T., Johnston, R., Torgerson, S., Fleeter, S. and Sullivan, J. (1996c), Rotor Blade Pressure Measurement in a High Speed Axial Compressor Using Pressure and Temperature Sensitive Paint, *AIAA Paper* 97-0162.
- Liu, T., Campbell, T., Burns, S., and Sullivan, J. (1997), Temperature and Pressure Sensitive Luminescent Paints in Aerodynamics, *App Mech. Rev.* Vol 50, No 4.
- McLachlan, B. G., Kavandi, J. L., Callis, J. B., Gouterman, M., Green, E. and Khalil, G. (1993a), Surface Pressure Field Mapping Using Luminescent Coatings, *Experiments in Fluids* 14, 33-41.
- McLachlan, B. G., Bell, J. H., Gallery, J., Gouterman, M. and Callis, J. (1993b), Boundary Layer Transition Detection by Luminescence Imaging, *AIAA Paper* 93-0177.
- McLachlan, B. G. and Bell, J. H. (1995a), Pressure-Sensitive Paint in Aerodynamic Testing, *Experimental Thermal and Fluid Science*, 10, 470-485.
- McLachlan, B. G., Bell, J. H., Park, H., Kennelly, R. A., Schreiner, J. A., Smith, S. C., Strong, J. M., Gallery, J. and Gouterman, M. (1995b), Pressure-Sensitive Paint Measurements on Supersonic High-Sweep Oblique Wing Model, *Journal of Aircraft*, Vol. 32, No. 2, March-April, 217-227.
- Morris, M. J., Benne, M. E., Crites, R. C. and Donovan, J. F. (1993a), Aerodynamics Measurements Based on Photoluminescence, *AIAA Paper* 93-0175.
- Morris, M. J., Donovan, J. F., Kegelman, J. T., Schwab, S. D., Levy, R. L. and Crites, R. C. (1993b), Aerodynamic Applications of Pressure Sensitive Paint, *AIAA Journal*, Vol. 31, No. 3, March, 419-425.
- Morris, M. J. (1995), Use of Pressure-Sensitive Paints in Low-Speed Flows, *Proc. 16th Int. Cong. Instrumentation in Aerospace Simulation Facilities (ICIASF)*, Institute of Electrical and Electronics Engineers, Wright-Patterson Air Force Base, Dayton, OH, USA, 31.1-31.10.
- Oglesby, D. M., Leighty, B. D. and Upchurch, B. T. (1995), Pressure Sensitive Paint With an Internal Reference Luminophore, *Proceedings of the 41st International Instrumentation Symposium*, Instrument Society of America, Denver, CO, 381-395.
- Oglesby, D. M., Upchurch, B. T., Leighty, B. D. and Simmons, K. A. (1996), Pressure Sensitive Paint With Internal Temperature Sensing Luminophore, *Proceedings of the 42nd International Instrumentation Symposium*, Instrument Society of America, San Diego, CA.
- Poernack, T., Owens, L., Hamner, M., Morris, M., (1997) Application of Temperature Sensitive Paint for Detection of Boundary Layer Transition, *17th Int. Cong. Instrumentation in Aerospace Simulation Facilities (ICIASF)*, Institute of Electrical and Electronics Engineers, Monterey CA., USA.
- Papkovsky, D. B. (1995), New Oxygen Sensors and Their Application to Biosensing, *Sensors and Actuators B*, 29, 213-218.
- Sajben, M. (1993), Uncertainty Estimates for Pressure Sensitive Paint Measurements, *AIAA J.*, Vol. 31, No. 11, 2105-2110.
- Schanze KS, Carroll BF, Korotkevitch S, et al., (1997) Temperature dependence of pressure sensitive paints, *AIAA J* 35: (2) 306-310
- Shimbo, Y., Mehta, R. Cantwell, B. (1997), Vortical Flowfield Investigation Using Pressure Sensitive Paint Technique at Low Speed, *AIAA Paper* 97-0388.
- Sellers, M. E. and Brill, J. A. (1994), Demonstration Test of Pressure Sensitive Paint in the AEDC 16-ft Transonic Wind Tunnel Using the TST Model, *AIAA Paper* 94-2481.
- Szmacinski, H. and Lakowicz, J. R. (1995), Fluorescence Lifetime-Based Sensing and Imaging, *Sensors and Actuators B*, 29, 16-24.
- Torgerson, S. D., Liu, T. and Sullivan, J. P. (1996), Use of Pressure Sensitive Paints in Low Speed Flows, *AIAA Paper* 96-2184.
- Torgerson, S. D. (1997), Laser Scanning System for use with pressure and temperature sensitive paint. MS Thesis, Sch of Aero and Astro, Purdue Univ, W. Lafayette IN.

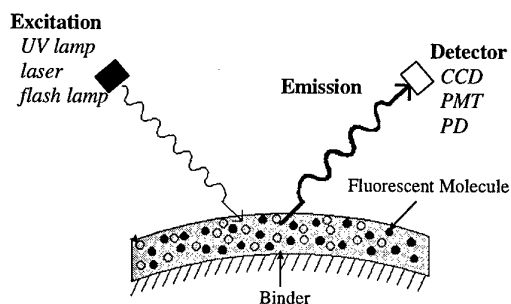


Figure 1: Schematic of TSP/PSP Layer

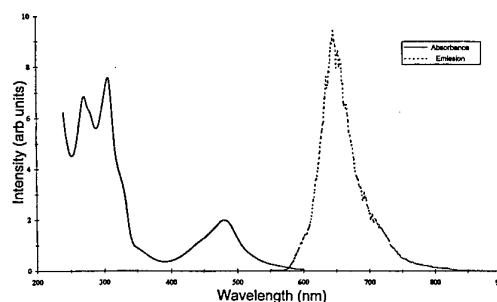


Figure 2: Excitation and Emission spectra of a Ruthenium based molecule

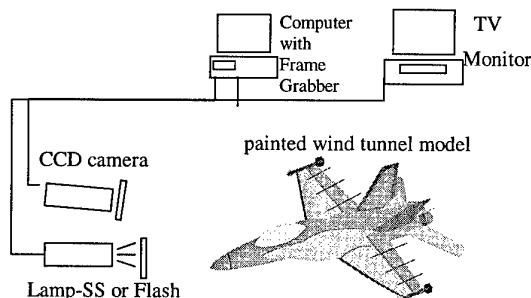


Figure 3: Schematic of CCD camera system

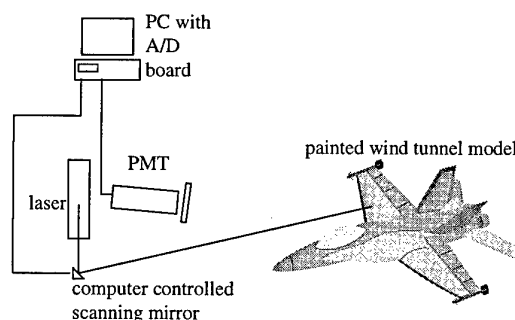


Figure 4: Schematic of laser scanning system

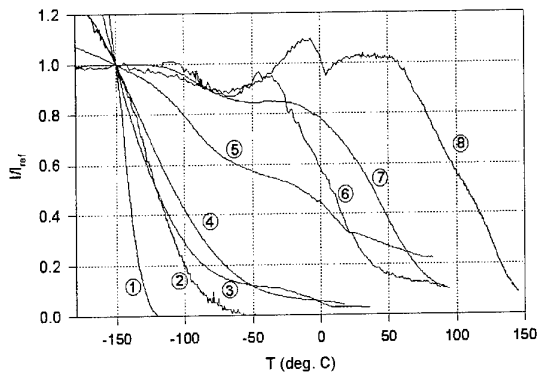


Figure 5. Temperature dependence of luminescence intensity for several TSP formulations: (1) Ru(trpy) in Ethanol/Methanol, (2) Ru(trpy)(phtrpy) in GP-197, (3) Ru(VH127) in GP-197, (4) Ru(trpy) in Du Pont Chroma Clear, (5) Ru(trpy)/Zeolite in GP-197, (6) EuTTA in dope, (7) Ru(bpy) in Du Pont Chroma Clear, (8) Perylenedicarboximide in Sucrose Octaacetate. ($T_{ref} = -150^{\circ}\text{C}$).

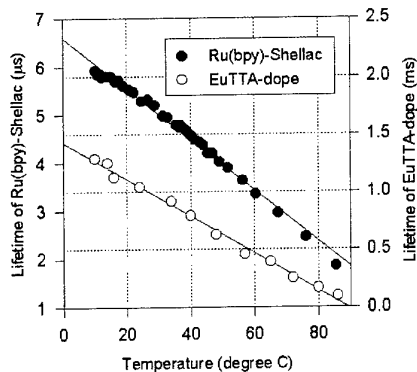


Figure 6 Lifetime-temperature relations for Ru(bpy)-Shellac and EuTTA-dope paints.

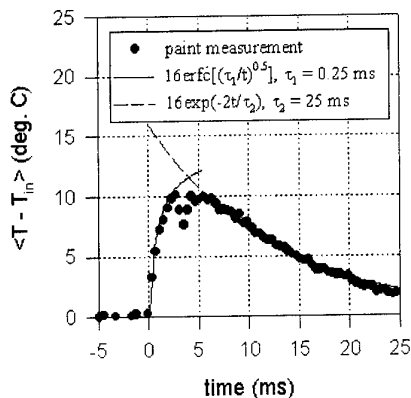


Figure 7 Temperature response of Ru(bpy)-Shellac paint to pulsed laser heating on steel foil.

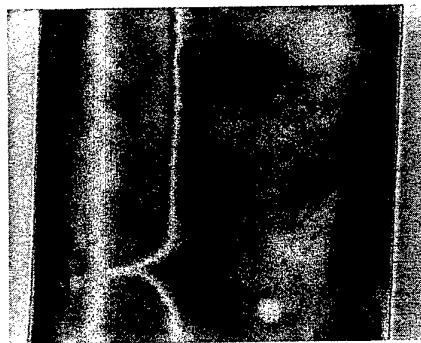


Figure 8. Transition at low speed on a NACA 65-021 Airfoil

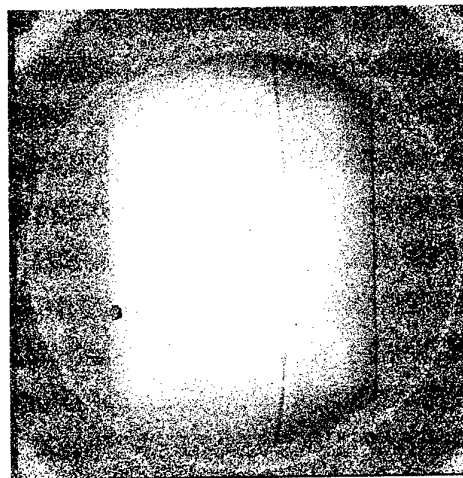


Figure 9. Transition on a NACA 64A021 at $M=.82$ and $T=120 \text{ K}$ in NAL cryogenic wind tunnel.

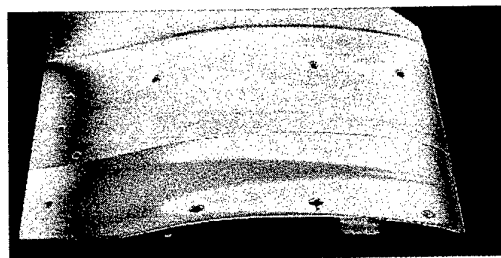


Figure 10. Transition on a HSNLF in the NASA .3 meter cryogenic wind tunnel.

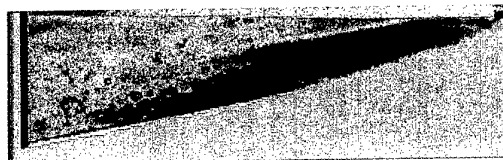


Figure 11. Transition on Waverider at $M=10$.

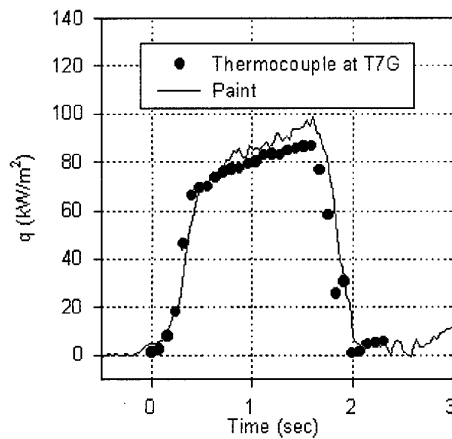


Figure 12 Heat transfer history on a Mach 10 waverider model at location T7G.

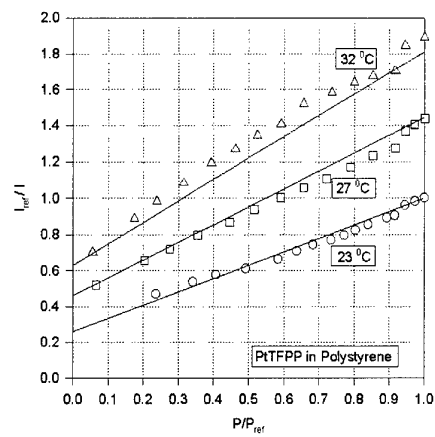


Figure 15. Calibration of PtTFPP pressure paint.

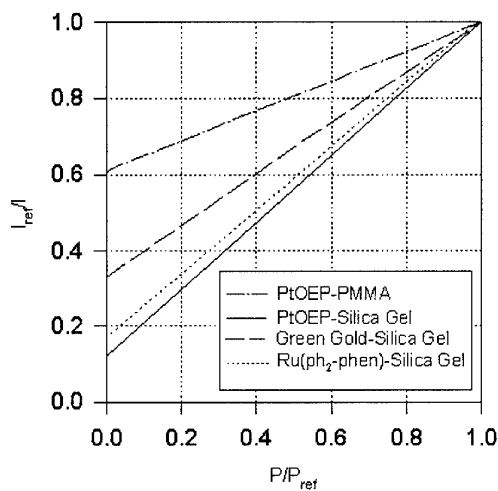


Figure 13 Stern-Volmer plots for several PSPs at ambient temperature (22 °C), where P_{ref} is the ambient pressure and I_{ref} is the luminescence intensity at ambient conditions.

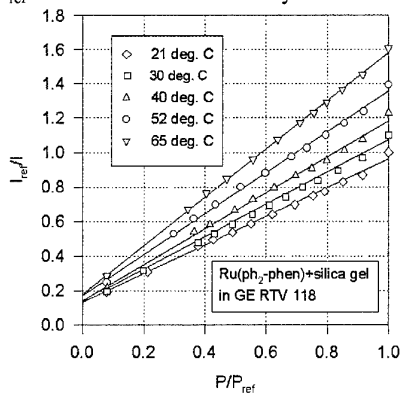


Figure 14. Calibration of Ruthenium based PSP.

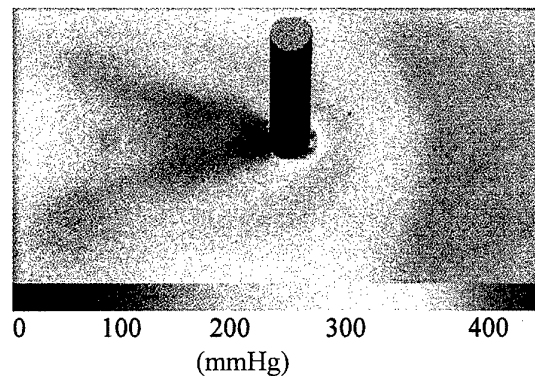


Figure 16. Pressure map for cylinder/BL interaction at $M=2.5$.

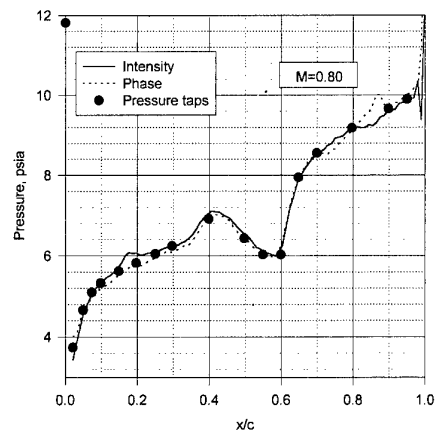


Figure 17. Pressure distribution on a transonic airfoil using both intensity and lifetime based methods.

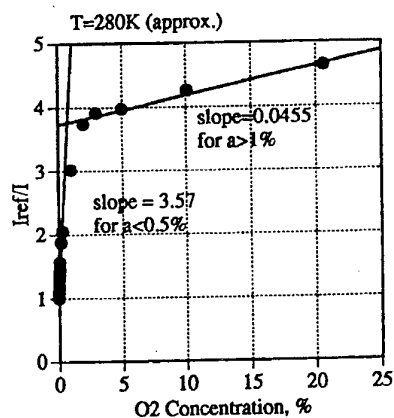


Figure 18. Calibration curve luminescent coating on an anodized surface.

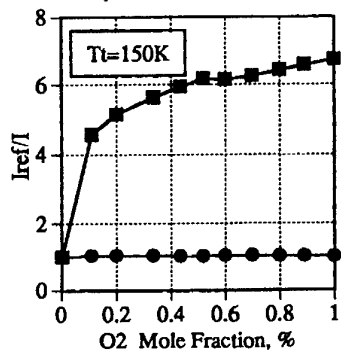


Figure 19. Calibration curve at cryogenic temperature.

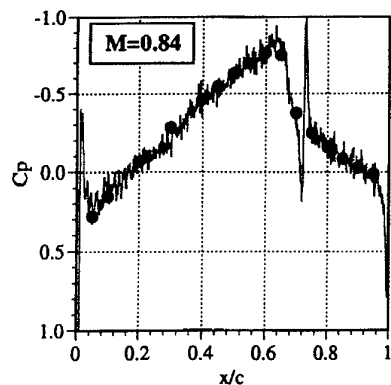


Figure 20. Comparison of luminescent paint and pressure tap data at $T=100K$.

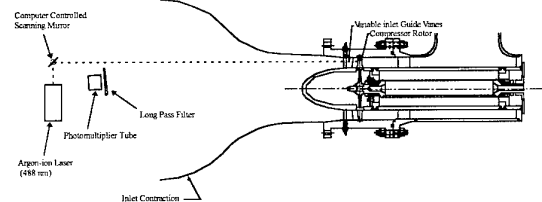


Figure 21. Transonic compressor rig with laser scanning system

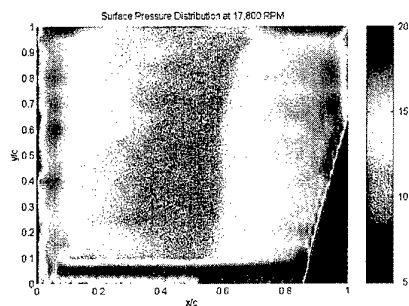


Figure 22. Compressor blade suction surface pressure map at 17,800 rpm (scale in psia).

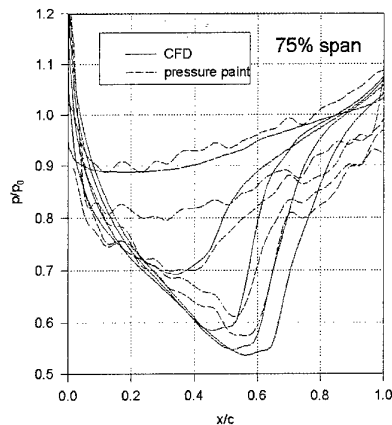


Figure 23. Comparison of PSP data and CFD results.

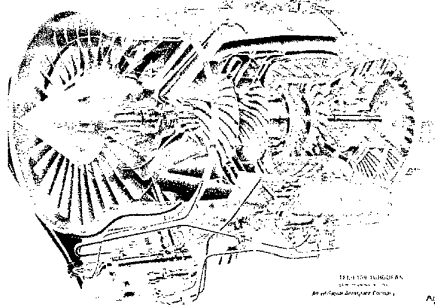


Figure 24. Allied F109 turbofan engine.

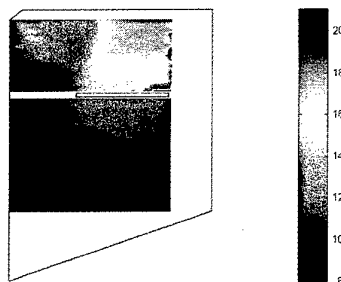


Figure 25. Fan blade pressure distribution at 14,000rpm (scale in psia).

STUDY RESULT FOR THE APPLICATION OF TWO-COMPONENT PSP TECHNOLOGY TO AERODYNAMIC EXPERIMENT

A. Bykov, S. Fonov, V. Mosharov, A. Orlov, V. Pesetsky, and V. Radchenko
Central Aerohydrodynamic Institute (TsAGI), 140160 Zhukovsky Moscow reg., RUSSIA

Abstract. The increase in the PSP measurement accuracy in wind tunnels is related first of all to the application of the two-component PSP technology. Besides the active luminophor the luminescence of which depends on pressure, the two-component PSP formulation also contains an additional luminophor. The simultaneous measurement of the luminescence intensities of the active luminophor and the additional luminophor makes it possible to avoid numerous difficulties characteristic of the one-component PSP technology. Consideration is given to some processes affecting the two-component PSP measurement accuracy. The transonic wind tunnel investigations of the two-component PSP are presented. Also, the first results of investigating the possibility of applying PSP pressure measurements to the helicopter rotor blade using the two-component PSP are given.

INTRODUCTION

The PSP technology to measure air pressure distributions on vehicle model surfaces in wind tunnels is well known to experimental aerodynamicists. Its essence is as follows [1,2]: the model surface is covered with a thin layer of PSP consisted of a binder, for example, a polymer one, and a luminophor (working luminophor) whose luminescence depends on the partial air oxygen pressure. For a chosen wind tunnel flow condition, the model is illuminated by the light which excites the luminophor luminescence. The luminescence intensity distribution on the model surface is registered by, for example, a CCD-camera. Given the calibration characteristics of the PSP layer painted on the model surface, a required pressure distribution is determined proceeding from the measured luminescence intensity distribution.

Although the accuracy of PSP measurements is presently inferior to that of tapping measurements, this accuracy is quite sufficient to solve some aerodynamic problems, among these are, for example:

- visualization of pressure distributions on model surfaces in a wide range of trans- and supersonic flow velocities;

- determination of distributed loads on vehicle model components etc.

However, on the way to the routine application of the PSP technology in experimental aerodynamics it is necessary to solve some additional complicated problems, in particular:

- to reduce the dependence of PSP sensitivity coefficients on temperature;

- to reduce errors caused by time-dependent optical transmission variations in the optical channel and instability of exciting radiation source;

- to reduce errors associated with the necessity of recognizing and identifying the points on the model surface to measure pressure;

- to exclude the effect of the model displacements in a nonuniform exciting radiation field on the measurement error. The solution of this problem is quite obligatorily in order to develop the PSP technology application technique for moving objects, in particular to measure pressure distributions on rotating objects, for example, on helicopter propeller blades, compressor blades etc.

To reduce the effect of unknown parameters, i.e., the active PSP layer temperature, as well as variations in the exciting radiation intensity and in the optical channel transmission, on the pressure PSP measurement accuracy, it is naturally to suggest that, for example, two

additional luminophors should be included into the PSP composition to obtain the additional information on these parameters [3]. We believe, however, that the stated problems can be solved by applying only one additional luminophor [3]. First investigation results for the two-component PSP technology were published in 1995 in [4-5]. At TsAGI, the investigations and application of the two-component (binary) PSP were started in 1990. The present paper contains the laboratory and wind tunnel investigation results for the binary PSP LPS B1 and LPS B12 produced by the OPTROD company.

FOUNDATIONS

Let us consider the PSP composition comprising an active luminophor and an additional (reference) luminophor in the polymer binder. Let these luminophors feature the same absorption spectra and significantly different dependencies of luminescence on air pressure. Also, assume that each luminophor has a certain luminescence sensitivity to temperature. Let the model covered by a thin layer of this composition be illuminated by exciting radiation $I_{ex}(M, t)$, where $M=M(R)$ is any point on the model surface and $R=R(x, y, z)$ is the radius-vector of point M . $Z=z(x, y)$ presents the equation of the model surface in the laboratory coordinate system for which the wind tunnel coordinate system can be used. The PSP luminescence intensity at point M for the homogeneous distribution of both luminophors across the PSP layer thickness is as follows:

$$I_i(M, P, T, t) = I_{ex}(M, t) \theta_i(M, t) \Phi_i(P, T) G(M) \quad (1)$$

where $i = a$ (active luminophor); $i = r$ (reference luminophor); P, T are the air pressure above the PSP layer and the layer temperature at point M , respectively,

$$G(M) = (1 - 10^{-K(M)h(M)}) \frac{\epsilon_i \cdot n_i(M)}{K(M)}$$

$h(M)$ is the PSP layer thickness at point M , $K(M) = \epsilon_a n_a(M) + \epsilon_r n_r(M)$; ϵ_i are the luminophor extinction coefficients; $n_i(M)$ are the luminophor concentrations in the PSP layer at point M ;

$\Phi_i(P, T)$ is the luminophor luminescence quantum efficiency. In this case,

$$\Phi_a(P, T) = \frac{1}{a(T) + b(T) \cdot P + c(T) \cdot P^2} \quad (2)$$

and $\Phi_r(P, T) = \Phi_r(T)$;

$\theta_i(M, t)$ is the optical channel transmission for exciting radiation and luminescence at point M .

The coefficients $a(T)$, $b(T)$ and $c(T)$ are determined during the PSP calibration.

Let us consider a case of practical importance when $\theta_i(M, t)$ is governed by the process of depositing dust particles, which are present in the flow, on the PSP layer surface. It can be assumed that the optical channel transmission variations are described by the Bugger's law:

$$\theta_i(M, t) = \exp \left[- \left(k_{ex} + k_i \right) \delta(M, t) \right] \quad (3)$$

where k_{ex} and k_i are, respectively, the absorption coefficients of exciting radiation and luminescence of both luminophors by the dust layer of the thickness of $\delta(M, t)$.

In practice, it is difficult to provide quite homogeneous distributions of concentrations of the active and reference luminophors in the PSP layer. Therefore, to measure the air pressure at point M on the model surface, the ratio of luminescence intensities of the active (a) and reference (r) luminophors should be found at this point at the time moment t_1 for known values of $P=P_1$ and $T=T_1$ (for example, without the flow) and at the time moment t for unknown P and T in the wind tunnel; then the ratios obtained should be divided. The result of division, taking account of Eqs. (1), (2) and (3), can be written in the form:

$$\beta = \frac{J_1}{J_2} = \frac{\Phi_a(P_1, T_1) \Phi_r(P, T)}{\Phi_r(P_1, T_1) \Phi_a(P, T)} \cdot \exp \Psi, \quad (4)$$

where: $\Psi = -(k_r - k_a)[\delta(M, t_1) - \delta(M, t)]$;

$$J_1 = \frac{I_r(M, P, T, t)}{I_a(M, P, T, t)}; \quad J_2 = \frac{I_a(M, P_1, T_1, t_1)}{I_r(M, P_1, T_1, t_1)}$$

If $k_a = k_r$ or there is no dust deposition, then $\Psi = 0$. Then, by applying Eqs. (2) and (4) we have the required pressure

$$P = A(T) + B(T) \cdot \beta + C(T) \cdot \beta^2 \quad (5)$$

It is seen from Eq. (4) that there is no dependence on I_{ex} and, hence, on the model displacements in the heterogeneous exciting radiation field. Also, it becomes possible to compensate for the temperature dependence of the sensitivity coefficient by choosing a reference luminophor with a respective temperature dependence of luminescence.

To implement the suggested technique, the luminescence of each luminophor should be registered separately. As stated in [], there are two main approaches for this:

1. when active and additional (reference) luminophors have nonintersected luminescence spectra.
2. when luminophors have significantly different luminescence life times, but their luminescence spectra can intersect.

The first approach is implemented in LPS B1 and LPS B12. Figure 1 presents the calibration characteristic for LPS B1 and Figure 2 shows the value of Standard Deviation (SD) for multiple measurements of the calibration characteristic.

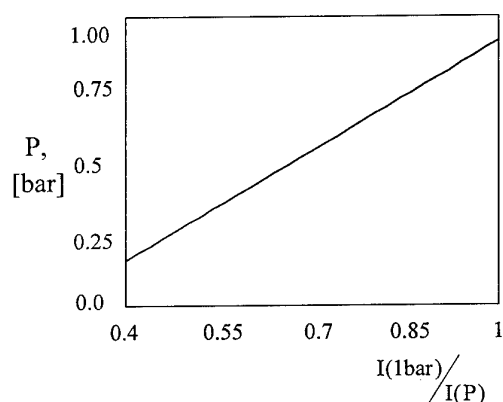


Figure 1. The calibration characteristic for LPS B1.

The temperature dependences $I(T)/I(T_0)$ for LPS B1 and LPS B12 are given in Figure 3. The temperature dependence of the sensitivity coefficient for LPS B12 is less than that for LPS B1 which is achieved by applying the reference luminophor featuring an optimal dependence of luminescence on temperature in the LPS B12 formulation.

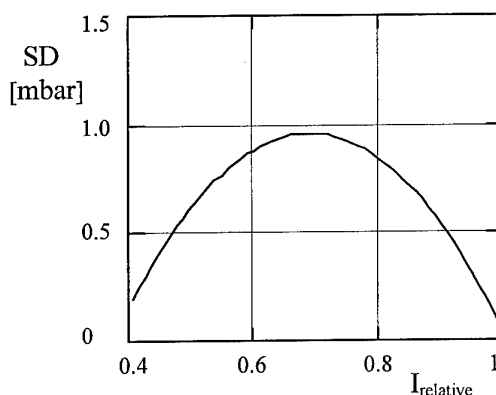


Figure 2. The value of Standard Deviation (SD) for multiple the PSP pressure measurements in calibration chamber.

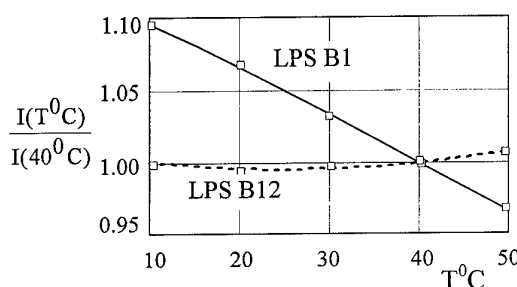


Figure 3. The temperature dependencies $I(T)/I(T_0)$ for LPS B1 and LPS B12 at $P=1$ bar.

PSP PRESSURE MEASUREMENT ACCURACY

Besides temperature, the main factors affecting the accuracy of measuring pressure distributions by the binary PSP are as follows:

- nonuniformity of the PSP calibration characteristic on the model surface;
- heterogeneous distributions of concentrations of the active and reference luminophors in the PSP layer applied to the model surface;
- model displacements and deformations affecting the accuracy of identifying the model surface points to measure pressure;
- time-variation of the optical channel transmission;
- ratio of the useful signal to shot noise of the CCD camera.

Consider these factors.

TEMPERATURE EFFECT

For stationary flows, the PSP layer temperature on the steel model surface is about $0.7-0.8 T_w$ (T_w is the wind tunnel wall temperature). Hence, for moderate transonic velocities, the difference between maximum and minimum temperatures attains 6-7 degrees. In the general case, for the error ΔC_p in measuring C_p to be no more than 0.02 it is necessary that the temperature dependence of the sensitivity coefficient should be within the range of 0.06 - 0.07 %/degr. This condition can be relaxed by measuring the PSP layer temperature at several model surface points and applying corrections to the PSP pressure measurements. An effective approach is also the application of the iteration procedure which implies the calculation of the temperature field using the pressure values measured by the PSP technology and subsequent application of corrections to the PSP pressure measurement results.

NONUNIFORMITY OF THE PSP CALIBRATION CHARACTERISTIC ON THE MODEL SURFACE

The nonuniformity of the PSP calibration characteristic on the model surface results in a decrease in the PSP pressure measurement accuracy. The surface nonuniformity of the LPS B1 calibration characteristic depends on the proper observance of the technology of applying the LPS B1 layer to the model surface, in particular, on humidity level in the room where the LPS B1 layer is applied. If this operation is performed in rooms without humidity control the calibration characteristic of the LPS B1 layer on the model surface becomes surface nonuniform. The maximum absolute PSP pressure measurement error due to this nonuniformity is about ± 5 mbars.

EFFECT OF HETEROGENEOUS DISTRIBUTIONS OF CONCENTRATION OF ACTIVE AND REFERENCE LUMINOPHORS IN THE PSP LAYER

Eq. (1) is written for an ideal case of the homogeneous distributions of concentrations of the active and reference luminophors in the PSP layer. Generally, the concentration distribution is quasihomogeneous. In this case, if the exciting radiation is uniform the luminescence field from each luminophor features a thin (spotty) structure. Figure 4 presents the curve $[I - \text{AVERAGE}(I)] / \text{AVERAGE}(I)$ which illustrates the spotty structure of the luminescence fields from both luminophors in a certain section of the CCD images of the PSP sample.

Some aspects of the influence of the thin structure of the luminescence field for the one-component PSP on the PSP measurement accuracy are first considered in [6]. The binary PSP pressure measurement error due to the phenomenon under study will be assessed for a certain section along the aircraft model wing chord (temperature and other effects are not considered here). Let the pressure distribution $P_{\text{psi}}(x)$ and the exciting radiation intensity distribution, for example,

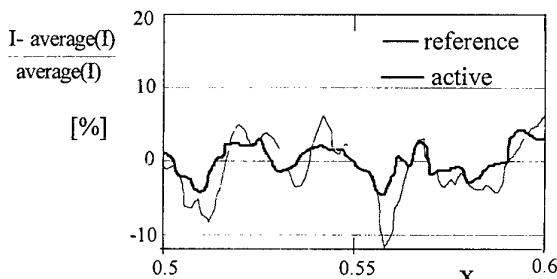


Figure 4. The spotty structure of the PSP luminescence fields in a certain section of the CCD images of the PSP sample.

$I_{\text{ex}}(x) = 10^{-5} \cdot (1 + 10^{-3} \cdot x)$ Wt/cm² be known in a section along the aircraft model wing chord (x is the relative coordinate along the chord). Then the intensity of luminescence from both the reference luminophor $I_{r0}(x)$ and the active luminophor $I_{a0}(x)$ in the absence of the spotty structure in accordance Eq.(1) is:

$$I_{i0}(x) = I_{\text{ex}}(x) \cdot \Phi_i \cdot G \quad (6)$$

where $i = a, r$ just as in Eq.(1); $G = G(M)$.

The intensity of luminescence with the spotty structure $I_i(x)$ of both luminophors can be written in the form:

$$I_i(x) = I_{i0}(x) + \delta I_i(x) \cdot \frac{I_{i0}(x)}{\max(I_{i0}(x))} \quad (7)$$

$\delta I_i(x) = I_{i\text{Sample}}(x) - \text{average}[I_{i\text{Sample}}(x)]$ is the real spotty luminescence structure obtained using a 95-mm PSP sample. Figure 5 shows the distributions of intensities (7) in a given wing section.

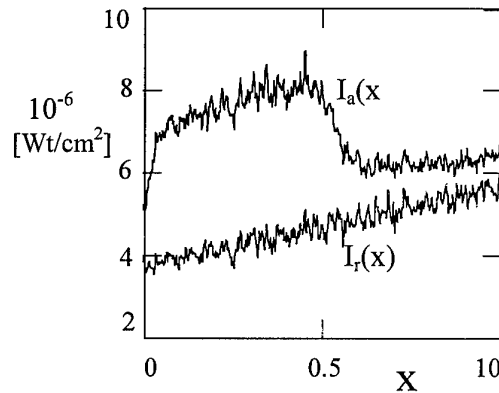


Figure 5. The distributions of intensities $I_r(x)$ and $I_a(x)$ in a given wing section.

The sizes of the PSP sample image are 512x512 pixels. Thus, 0.23mm on the PSP sample corresponds to 1 pixel on the PSP sample image. The pressure distribution $P_{\text{psi}}(x)$ in a certain wing section is taken from the real experiment carried out in a wind tunnel having the 1.95m x 1.95m test section. In this experiment, $\Delta x = 0.9$ mm on the wing corresponds to 1 pixel in this section of the wing image. The CCD camera lens is capable of resolving about 0.5mm on the wing surface. Therefore, the intensities (7) are filtered by a Gaussian filter with a dispersion $\sigma = 0.46$ mm. Then the filtered intensities are discretized in the same way as the CCD array does:

$$E_i(x) = \int_{x-0.5\Delta x}^{x+0.5\Delta x} I_i(x') dx' \quad (8)$$

Then in accordance with Eq. (5) we derive from Eqs.(8) the required PSP-measured pressure in a given section of wing:

$$P_{\text{PSP}}(x) = A + B \cdot E_{\text{rel}}(x) + C \cdot (E_{\text{rel}}(x))^2 \quad (9)$$

where:

$$E_{\text{rel}}(x) = \frac{E_{0a}(x)}{E_{0r}(x)} \cdot \frac{E_r(x)}{E_a(x)}$$

$E_i(x)$ for "wind on" condition, and $E_{0i}(x)$ for "wind off" condition is calculated.

As a result, after each operation we have the following PSP pressure distributions:

$P_{i0}(x)$ is derived from luminescence intensities (6);

$P_{i0}(x)$ is $P_{i0}(x)$ after the Gaussian's filtration;

$P_i(x)$ is derived from luminescence intensities (7);

$P_{i0}(x)$ is $P_i(x)$ after the Gaussian's filtration;

P_{PSP} is obtained in accordance with Eq.(9).

Figure 6 shows the above PSP pressure distributions in a certain fragment of a chosen wing section, as well as P_{PSI} distribution for comparison.

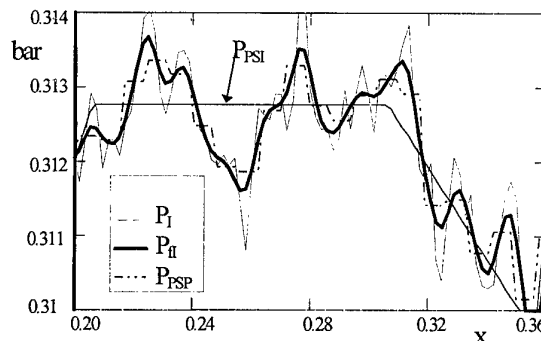


Figure 6. P_i , P_{i0} , P_{PSP} , P_{psi} pressure distributions in a certain fragment of a chosen wing section.

$$\Delta P_I = \frac{P_I - P_{PSI}}{P_{PSI}}; \quad \Delta P_{fI} = \frac{P_{fI} - P_{PSI}}{P_{PSI}}$$

$$\Delta P_{PSP} = \frac{P_{PSP} - P_{PSI}}{P_{PSI}}; \quad \Delta P_{fPSP} = \frac{P_{fPSP} - P_{PSI}}{P_{PSI}} \quad (10)$$

The relative deviations of the above PSP pressure distributions from PSI pressure distribution in the region of the shock wave location on the wing surface in a chosen section where P_{fPSP} is the P_{PSP} after the Gaussian's filtration are given in Figs. 7a,b,c in the form of plots.

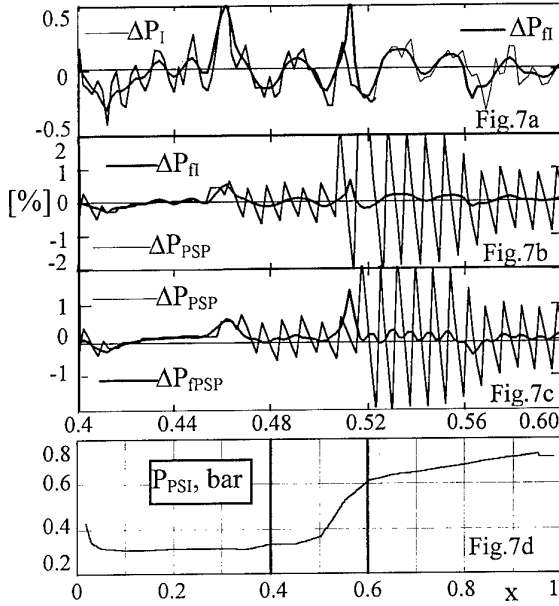


Figure 7a,b,c,d. The relative deviations (10) in the region of the shock wave location on the wing surface in a chosen section (this region is indicated (the bold line) in Fig. 7d). Fig. 7d shows the PSI pressure distributions in a chosen wing section.

The region of the shock wave location on the wing surface is indicated in Figure 7d. It is seen in Figure 7c that in all filtration operations there occurs a deviation of the obtained PSP pressure with respect to the true values, i.e., P_{PSI} . These deviations are caused by both the spotty component and the pressure-determined component of the luminescence field. Now we estimate the contribution of the pressure-determined component of the luminescence signal to the PSP pressure measurement accuracy. To do this, we consider the following ratios (relative deviations):

$$\Delta P_{fI0} = \frac{P_{fI0} - P_{PSI}}{P_{PSI}}; \quad \Delta P_{fPSP}$$

ΔP_{fI0} is found using the pressure distribution $P_{fI0}(x)$, obtained from intensities (6) (i.e., in the absence of the spotty luminescence structure). The ratio ΔP_{fPSP} includes both components of the luminescence field. Figure 8a presents both ratios in the form of the plots. Figure 8b gives the relative deviation $(P_{fPSP} - P_{fI0}) / P_{fI0}$ which illustrates the estimate of the PSP measurement error due to the noise component of the luminescence field plots. It is seen from Figure 8a that the contribution of the pressure-determined component of the luminescence field to the PSP measurement accuracy is the greatest in the regions of large pressure gradients on the wing surface (wing leading edge, shock wave locations etc.).

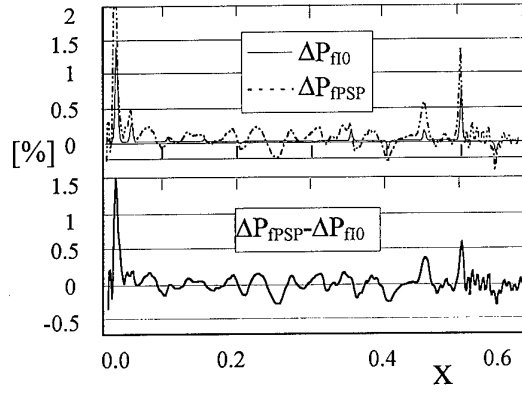


Figure 8a,b. The relative deviations ΔP_{fI0} and ΔP_{fPSP} (8a). The relative deviations $(\Delta P_{fPSP} - \Delta P_{fI0})$ the estimate of the PSP measurement error due to the noise component of the luminescence field (8b).

In these regions, this contribution exceeds the contribution of the noise component. The latter does not exceed 0.3%, except from the leading edge and shock wave location (Figure 8b).

The PSP pressure distributions are obtained using the luminescence field images at different time moments. For various reasons, these images can have shifts and deformations relative to each other and, accordingly, the measurement accuracy can reduce. Figure 9 shows relative deviations of the PSP pressure distributions from PSI pressure distributions obtained without the relative shift of the luminescence fields

$$\Delta P_{fPSP}(x) = \frac{P_{fPSP}(x) - P_{PSI}(x)}{P_{PSI}(x)}$$

and in the case of the shift $\delta x = 0.26\text{mm}$ (this shift corresponds to the accuracy of mapping the luminescence field images of 0.25 pixel.)

$$\Delta P_{fPSP}(x + \delta x) = \frac{P_{fPSP}(x + \delta x) - P_{PSI}(x)}{P_{PSI}(x)}$$

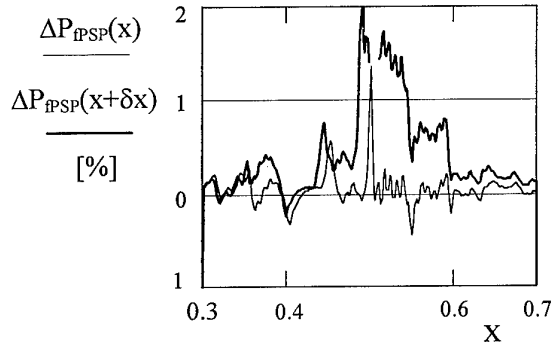


Figure 9. Relative deviations of the PSP pressure distributions from PSI pressure distributions in dependence from the relative shift of the luminescence fields ($\delta x = 0.26\text{mm}$)

It is seen that even rather a small relative shift of the luminescence fields results in a considerable decrease in the PSP measurement accuracy. The greatest contribution to the PSP measurement error is made by the pressure-determined component of the luminescence field in the case of a relative shift of the luminescence fields in regions of large pressure gradients on the wing surface. Figure 10 illustrates the contribution of the noise component of the luminescence fields to the PSP

measurement accuracy. On the Figure present the relative deviation $\Delta P_{\text{PSP}}(x + \delta x) - \Delta P_{\text{PSP}}(x)$ and $\Delta P_{\text{fl}}(x + \delta x) - \Delta P_{\text{fl}}(x)$.

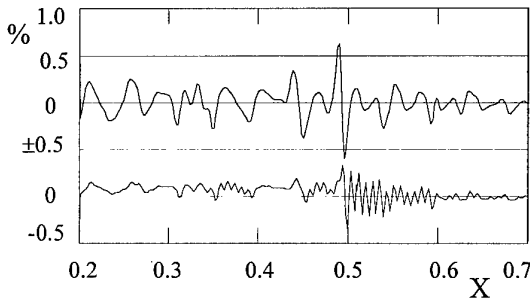


Figure 10.

The relative deviation $\Delta P_{\text{fl}}(x + \delta x) - \Delta P_{\text{fl}}(x)$ (upper curve) и $\Delta P_{\text{PSP}}(x + \delta x) - \Delta P_{\text{PSP}}(x)$ (lower curve).

It is seen that this contribution depends less on the shift of each luminescence field than the contribution of the pressure-determined component of the luminescence field from the active luminophor not to exceed, as a whole, 0.3%. Besides, the noise contribution depends on the sizes of spots of the spotty luminescence field structure. The spots whose image sizes are less or comparable with the sizes of pixel are well averaged by CCD discretization operations and filtering of different than the size of pixel make a considerable contribution to the PSP measurement accuracy.

The final contribution of the spotty structure of the luminescence fields to the PSP measurement accuracy depends on their amplitude and sizes which, in turn, depend on PSP formulation and the technology of applying the PSP layer on the model surface.

VARIATIONS IN THE OPTICAL CHANNEL TRANSMISSION ARE CAUSED BY THE DUST DEPOSITION ON THE PSP LAYER

In this case, it is already impossible to assume that $k_r = k_a$ because the dust can be colored and $\Psi \neq 0$ in Eq.(4). If, however, condition (3) is valid the following procedure of determining the unknown multiplier $\exp \Psi$ can be suggested:

- the luminescence distribution on the model surface covered by the PSP layer is registered prior to the wind tunnel start $t=t_1$, for chosen regimes during the wind tunnel operation $t=t$ and after the wind tunnel stop $t=t_2$ for the same model positions:

$$I_i(M, P_1, T_1, t_1); I_i(M, P, T, t); I_i(M, P_2, T_2, t_2) \quad (11)$$

Combining these expressions with Eqs.(1), (3) and (4) it is possible to obtain the formula to determine the function Ψ :

$$\Psi = \frac{\ln[\alpha_1 \cdot \xi_1 \cdot \eta_1]}{\ln[\alpha_2 \cdot \xi_2 \cdot \eta_2]} \ln[\beta_1 \cdot \frac{\Phi_r(T_2) \cdot \Phi_a(P_1, T_1)}{\Phi_a(P_2, T_2) \cdot \Phi_r(T_1)}]; \quad (12)$$

where:

$$\begin{aligned} \beta_1(M) &= \frac{I_r(M, T_2, t_2)}{I_a(M, P_2, T_2, t_2)} \cdot \frac{I_a(M, P_1, T_1, t_1)}{I_r(M, T_1, t_1)} \\ \eta_1 &= \frac{I_{\text{ex}}(t_1)}{I_{\text{ex}}(t)}; \quad \eta_2 = \frac{I_{\text{ex}}(t_1)}{I_{\text{ex}}(t_2)} \\ \xi_1 &= \frac{\Phi_r(T_1)}{\Phi_r(T)}; \quad \xi_2 = \frac{\Phi_r(T_1)}{\Phi_r(T_2)} \end{aligned} \quad (13)$$

$$\alpha_2 = \frac{I_r(M, P_2, T_2, t_2)}{I_r(M, P_1, T_1, t_1)}; \quad \alpha_1 = \frac{I_r(M, P, T, t)}{I_r(M, P_1, T_1, t_1)}$$

The procedure (11)-(13) was verified experimentally using binary PSP LPS B12 having luminescence in blue and red spectrum portions. The LPS B12 layer was applied to a metal plate. Rust applied twice successively to the same half of the plate served as dust. The images (10) were obtained, respectively, before the dust deposition (time moment t_1), after the first and second (moments t_1 and t_2) operations of dust deposition, the air pressure and temperature being unvaried. Figure 11 shows the distributions $\beta_1(M)$; $\beta(M)$; $\beta(M) \times \exp \Psi$ in a certain plate section.

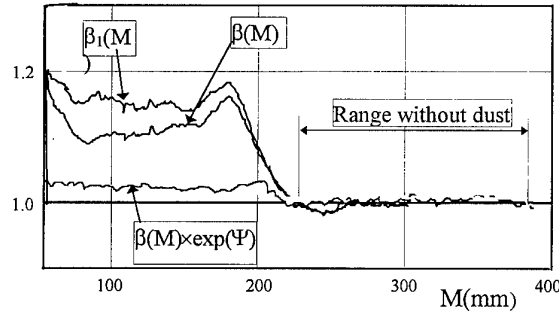


Figure 11. The distributions $\beta_1(M)$; $\beta(M)$ and $\beta(M) \times \exp \Psi$ in a certain test plate section.

It is seen that the application of the suggested procedure allows a significant decrease in the influence of dust deposition on the active layer of the binary PSP on the PSP pressure measurement results. The procedure (11-13) makes it possible to obtain quite satisfactory results if variations in the luminescence intensity of both luminophors due to the model dust deposition during the tests are greater than those due to variations in the exciting radiation. Note, however, that for the correct application of the procedure (11)-(13) it is necessary to have a stable source of exciting light or to measure ratios η_1 and η_2 .

EFFECT OF THE RATIO OF USEFUL SIGNAL / SHOT NOISE OF THE CCD CAMERA.

The modern CCD cameras have a great dynamic range at small dark-current noise levels. The dynamic range is usually expressed in a maximum quantity of photoelectrons produced by the CCD array for a maximum exposition when the linear relationship between them still retains. Then, if W is the dynamic range of the used CCD camera and W_{PSP} is the working range in PSP measurements, the minimum rms error of PSP pressure measurements can be estimated as $\Delta P/P = 1/(W_{\text{PSP}})^{-0.5}$. If, for example, $W = 3 \times 10^5$ photoelectrons $W_{\text{PSP}} = W/3$ then $\Delta P/P \sim 0.3\%$.

A MATH PROCEDURE OF THE LUMINESCENT IMAGES AND IDENTIFYING THE POINTS ON THE MODEL SURFACE TO MEASURE

All the above relationships are obtained for any point M on the model surface. We deal, however, with the luminescence field images on the CCD camera array and, in particular, with images M of the point M . Therefore, because we consider the luminescence field images registered at different time moments t_1 , t , and t_2 , the question arises how to follow one and the same point M using the luminescence field images. The solution of this geometric problem is described, in particular, in [9] where the method of optical markers is applied. The optical marker is a circle 2-3mm in diameter on which there is no PSP layer. This method implies the following operations;

- the model surface is covered with a certain quantity of optical markers;
- the coordinates of images of these optical markers are determined in the CCD array coordinate system;
- the coordinates of the image M of the point M at each time moment under consideration are determined proceeding from the coordinates of images of these optical markers;
- the coordinates of all or a portion of optical markers are measured on the model surface in the model coordinate system;
- the coordinates of the point M on the model surface are determined using the coordinates of optical markers on the model surface and the coordinates of images of these optical markers;
- 3-D PSP pressure distribution is found using the equations for the model surface.

Note that in order to solve the problem of identification of model surface points at which the pressure is measured using a sufficient quantity of optical markers and when the center of each marker is identified rather accurately there is no need to know a priori the objective aberrations, model surface geometry etc.

WIND TUNNEL TESTS OF BINARY LPS B1-TYPE OF PSP

As stated above, the laboratory investigations of binary LPS B1-type PSP show that the absolute accuracy (99% Confidence interval) of the PSP pressure measurements due to the error of the LPS B1-type PSP itself is no less than 5-6 mbar. It is known that when the PSP technology is applied to measure pressure distributions in a real aerodynamic experiment there are many other causes deteriorating the accuracy of these measurements. Nevertheless, it follows from the laboratory investigation results that it is quite reasonable to conduct further studies in eliminating or decreasing the effect of some of them.

WIND TUNNEL T-128 TsAGI INVESTIGATIONS OF LPS B1

For a clarification purpose of the causes deteriorating the accuracy of these measurements the investigations of LPS B1 were carried out, in particular, in the T-128 2.75m×2.75m transonic wind tunnel. The LPS B1 layer was applied to the upper surface of a symmetric wing (right half). 5 tapping orifices were provided at 5 wing sections. In order to ensure the geometric coincidence of the "wind-off" frame with the "wind-on" frame and a subsequent identification, 30 optical markers were placed on the test surface. The tests were carried out at $M=0.6$; 0.85 ; and 0.95 and angles of attack varying from -6° to 6° . Figure 12,a,b show the investigation results for LPS B1.

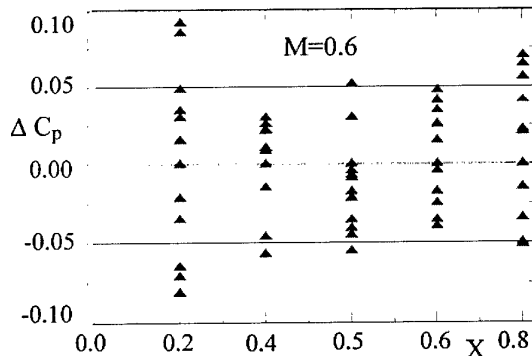


Figure 12a. The deviation of value $\Delta C_p = C_p(\text{PSP}) - C_p(\text{PSI})$ on a section of wing at different angle attacks ($M=0.6$).

At $M=0.6$, the standard deviation of value $\Delta C_p = C_p(\text{PSP}) - C_p(\text{PSI})$ at different angle attacks is 0.036,

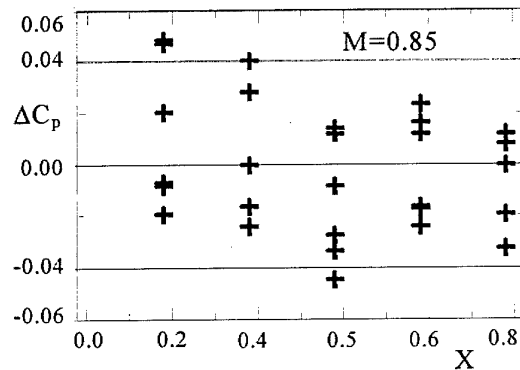


Figure 12b. The deviation of value $\Delta C_p = C_p(\text{PSP}) - C_p(\text{PSI})$ on a section of wing at different angle attacks ($M=0.85$).

and average $\text{AVERAGE}[C_p(\text{PSP}) - C_p(\text{PSI})] = 0.001$. At $M=0.85$, the standard deviation of value ΔC_p is 0.024, and average $\text{AVERAGE}[C_p(\text{PSP}) - C_p(\text{PSI})] = 0.0004$. These results show that a greater part of the contribution to the deterioration of the PSP pressure measurement accuracy in this test was due to errors of the measuring system, flow quality in the wind tunnel and errors in solving geometric problems.

BINARY PSP APPLICATION FOR ROTATING OBJECTS

Below are given the results of another investigation aimed at evaluating the possibility of applying the binary PSP to measure pressure distributions on the helicopter propeller blade. The first PSP applications for rotating objects are recently made at TsAGI [7] and at the Purdue University [8].

A first specific feature of this test type is that when the propeller is rotated in a free-stream flow the blade makes considerable displacements normally to the propeller rotation plane and in the rotation plane. Therefore, it is essentially impossible to provide the same position of the blade and its shape in obtaining reference and active images. This results in some difficulties in ensuring the same distributions of the exciting radiation intensity in obtaining "rotation-off" and "rotation-on" condition images. Variations in the exciting light distributions of the light source are also noted.

The second specific feature important for rotor blades is that the rotation is a periodic process having the frequency of about $3 \div 10 \text{ Hz}$. Pressure in any point is changed periodically but non-harmonically during the rotation cycle. To measure accurately the pressure distribution on the rotating blade in the airflow, PSP must to transfer a few harmonics (about ten) from non-harmonic pressure. Theoretical estimation of Amplitude-Frequency and Phase-Frequency Characteristics of the blade rotation [8] shows that for the pressure measurement on rotating blades, the PSP with response time less than 5 msec should be used. The response time of LPS B1 is about 40 msec (for the active layer thickness of 15 mkm and 70% transition level) [9]. Thus, the pressure field registered in this experiment is a distribution averaged in the azimuth angle range of about 60° for the rotation velocity 256RPM.

The above investigations were carried out in the subsonic T-101 $24 \text{ m} \times 14 \text{ m}$ wind tunnel.

Experimental Setup in T-101 wind tunnel.

A three-blade rotor 13m in diameter was chosen for investigations. The general view of the experimental setup in the T-101 wind tunnel is presented in Figure 13. The prototype of the blade rotor luminescence pressure measurement system consist of three parts: a registration Head, a Illumination system and a Optical Synch Unit. The Registration Head was installed on the hub of the

9. Mosharov V., Orlov A., Radchenko V., Kuzmin M., Sadovskii N., "Luminescent Pressure Sensors for Aerospace Research: Diffusion-Controlled Characteristics", 2nd European conference on optical chemical sensors and biosensors, Firenze, Italy, 19-21 April 1994.

The two- component PSP investigation on a civil aircraft model in S2MA wind tunnel.

Marianne Lyonnet, Bruno Deléglise, Gérard Grenat ONERA Modane

B.P. 25 73500 MODANE, FRANCE

A. Bykov, V. Mosharov, A. Orlov, S.Fonov TsAGI

Zhukovsky, Moscow region, RUSSIA

1. Summary

Pressure sensitive paint (PSP) is a technology of major interest to wind tunnel operators. As part of the cooperation programme between ONERA and TsAGI an evaluation test of the optical pressure measurement system developed by TsAGI was performed in the transonic test section of the S2MA wind tunnel at the Modane centre.

The tests were carried out on an Airbus model loaned by Aérospatiale. The left wing was instrumented with 240 pressure taps, the right wing was covered by a two-component PSP, developed by the Russian firm OPTROD.

Experimental set-up, characteristics of the two-component paint and data processing are described. Comparisons between results from conventional and PSP measurements are presented, and the effects of incidence, Mach number, pressure and temperature are discussed.

2. Introduction

Pressure measurements on the surface of a wind tunnel model play an important role in the development of wing design. Aspects of interest include, structural loading distributions, aerodynamic efficiency and the validation of CFD codes.

In most cases such pressures are measured using conventional measurements through pressure ports. These conventional measurements are very accurate but are limited to several hundred pressure taps. Furthermore, for some models these methods are difficult to use, for example on thin section surfaces or in more complex areas such as a wing engine pylon junction.

Pressure sensitive paint, on the other hand, is a new pressure measurement technique. In this technique, the pressure distribution on the model surface is determined optically, measuring the luminescence of a special kind of paint applied on the model. The

painted surface is illuminated by a light source of a particular wavelength and the luminescence of the paint is measured as a light intensity field ; this intensity field is related to the pressure field. One of the most important features of the pressure sensitive paint technique is that it is a continuous pressure field measurement system. Pressure information is available wherever the pressure paint is applied as long as optical access to the relevant area is available. Therefore, with the advent of PSP technology, the potential exists for a considerable saving in time and cost of model manufacture while offering an excellent spatial resolution.

Newskey and Pervushin, from TsAGI were among the first to use luminescence quenching for pressure measurements on aerodynamic models. The TsAGI team began to work on pressure sensitive paints in the middle of the eighties and following cooperation with Moscow University a set of pressure sensitive paints were developed. The following studies were for the purpose of extending the field of PSP use : new formulations allowing the use of PSP for non stationary flows as in shock tube, or near oscillating wings were obtained [1]. More recently research has been carried out to improve the accuracy of pressure sensitive paint : the definition of a two component paint able to take the illumination field changes into account is the most impressive result of this research.

At ONERA, studies on PSP are more recent ; however, ONERA benefits from the experience acquired over many years in the field of Temperature Sensitive paint and imaging. Therefore, it was natural to include PSP in the cooperation programme between ONERA and TsAGI. As part of this programme, it was first decided to perform an evaluation test of the optical pressure measurement system developed by TsAGI.

The evaluation of this device was performed in the transonic test section of the S2MA wind tunnel at the Modane Centre. The model used was an Airbus

model, equipped with an A300 wing type, kindly placed at ONERA's disposal by Aérospatiale.

The left wing was instrumented with 240 pressure taps, measured by electronic scanned pressure multisensors (ESP), located inside the model. The right wing was covered by the two-component pressure sensitive paint. These tests were for the purpose of evaluating the influence of various parameters on the measurement accuracy obtained with this new technique, by comparison with conventional pressure measurements taken on the opposite wing of the model. The effects of incidence, Mach number, temperature and pressure were studied.

3. Advantages of a two-component paint

The active compound used in the PSP is a photoluminescent organic molecule. The absorption of an energetic photon (ultraviolet or blue light), modifies its electronic state : the molecule jumps to an excited energy level. If nothing else happens to this molecule, it will emit a photon of red or yellow light and return to its ground state. However, if an oxygen molecule collides with the excited molecule, the oxygen absorbs the excess energy and the molecule returns to its ground state without photon emission. In addition other non radiative processes corresponding to conversion of energy into heat can occur. A complete description of this phenomena is given by Lumb[2].

Luminescence intensity of PSP coating is inversely proportional to the pressure p and directly proportional to excitation light intensity and to the thickness of the paint. To exclude the influence of excitation light and thickness, the pressure field is computed from the ratio of 2 luminescence intensity images, one recorded wind-off at known conditions, the other recorded wind-on at unknown conditions. The pressure field can be expressed as

$$P(x) = a(t, t_0) \left(\frac{I_0(x)}{I(x)} \right)^2 + b(t, t_0) \left(\frac{I_0(x)}{I(x)} \right) + c(t, t_0).$$

I_0 is the intensity of the considered point in the reference image, taken wind-off at known pressure and temperature values, I is the intensity emitted by the same physical point in the wind-on image.

During tests performed in wind tunnels, the model location changes under aerodynamic loads and it is necessary to realign the wind on and the wind off images to obtain accurate results. This operation is carried out through specific points on the model. For this purpose, markers are glued on the model before application of the PSP coating and removed after. As there is no paint, these markers appear as dark spots on the images. The positions of the 2 sets of markers are used to realign the wind-on image onto the reference image.

However, although this step is essential it doesn't enable the effects due to model shift to be completely corrected. In fact, due to this shift, the illumination field is modified and the same physical point doesn't receive the same excitation light intensity during the 2 images. Excitation light distribution can not be absolutely uniform, so any model displacement modifies light distribution on the model surface. On the other hand, displacement of the model in relation to the light source, changes the excitation light intensity on the model surface. As the light intensity at a given distance of the light source is inversely proportional to the square of this distance, a 1% change in the distance from the light source causes 2% change in excitation light intensity. Furthermore, as the distance to each point of the model changes differently, the mean value and the distribution of light intensity are modified.

One way to take this point into account is to place the model in the same position for the wind-on and the wind-off images, using a 6 degrees of freedom support [3]. The implementation of such a system is very complex and can not be considered for an industrial wind tunnel, where a variety of test set-ups are used.

Another method, more promising, is to use a binary paint. The paint LPS-B1 developed by OPTROD is made up of 2 luminophores. The luminescence of the first component depends significantly on the air pressure, while that of the second component does not show this dependence and can be used as a reference channel to compensate the variations of the excitation light intensity.

4. Paint LPS-B1

The selected components are excited by the same ultraviolet light (here 337 nm) and show good spectrum separation between reference and measurement channels : the pressure sensitive component emits in blue region around 450 nm, while the insensitive one emits in red region, over 620 nm (Fig 1).

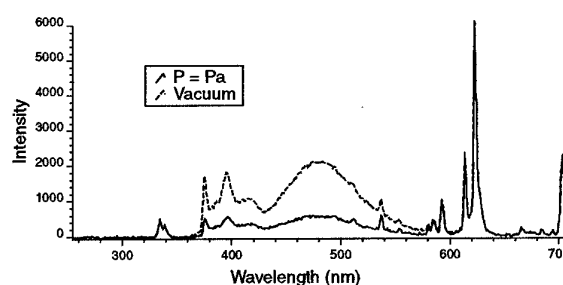


Fig. 1 : Pressure level effect on LPS B1 spectrum.

The paint calibration is done using the ratio I_{blue}/I_{red} . The curves presented in figure 2 show the sensitivity to pressure at different temperature values, from $t = 15^\circ\text{C}$ to $t = 37^\circ\text{C}$. These curves were obtained in the calibration chamber on samples painted at the same time as the model.

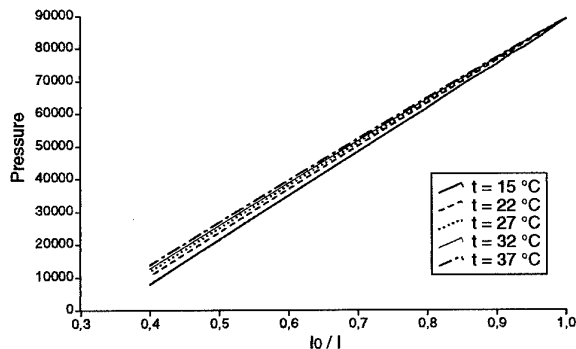


Fig. 2 : Calibration curves.

The sensitivity to temperature at different pressure levels is shown in figure 3.

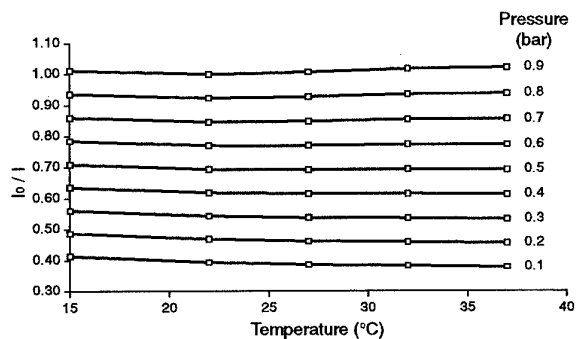


Fig. 3 : Temperature sensitivity

The two components have comparable sensitivities and the use of the ratio I_{blue}/I_{red} enables the temperature sensitivity to be reduced to 0.1% per degree between 15°C and 37°C . This is the second interesting feature of the LPS-B1 paint.

5. Experimental Set-Up

A prototype pressure measurement system, developed by TsAGI, was assembled to demonstrate the capability to obtain quantitative results in a production wind tunnel environment.

General layout of the Optical Pressure Measurement System is presented in figure 4.

A Nitrogen impulse laser was installed on the ceiling of the plenum chamber. During the test, a shutter enables the illumination to be switched off except during the measurement points in order to minimize photodegradation of the paint. That laser is coupled to a beam splitter so that several optical fibers can be used. An AT200 digital CCD camera from Photometrics company, with 512×512 pixel spatial resolution, and 2 illuminators, were installed on the test section ceiling. A CCD camera controller and water circulation cooling system were placed near the CCD camera in the test section plenum. The CCD camera was equipped with a switchable red/blue filter. Data acquisition and operation control were performed through a 486 PC located in the wind tunnel control room. The images acquired during 0.5 s were digitized on 12 bits. An additional analog CCD camera coupled with a video recorder was used for flow field visualization.

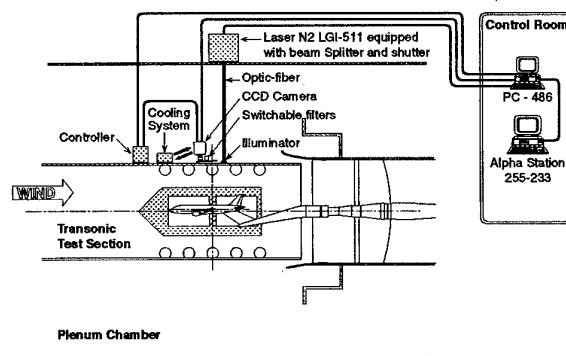


FIG. 4 : General layout of the experimental set-up.

To compare PSP results with standard pressure tap measurement, the upper surface of the right wing was painted with the LPS-B1, and left wing was instrumented with standard pressure taps connected to electronic scanned pressure multi sensors EPS.

In order to provide better spatial resolution, only part of the painted surface was illuminated and acquired during the tests. With the selected lens, one pixel corresponds to about 0.7 mm on the model. In order to allow accurate realignment and 3D reconstruction, 18 marker points were implemented on the model surface.

For each measurement point, 2 images are acquired : one with the blue filter, the other with the red filter. The use of the color parameter I_{blue}/I_{red} allows the change in the illumination field to be corrected. However the relative concentration of the two components can change with the point under consideration. To take this effect into account, it is necessary to normalize this ratio by the value I_{blue}/I_{red} obtained in the wind off image (figure 5).

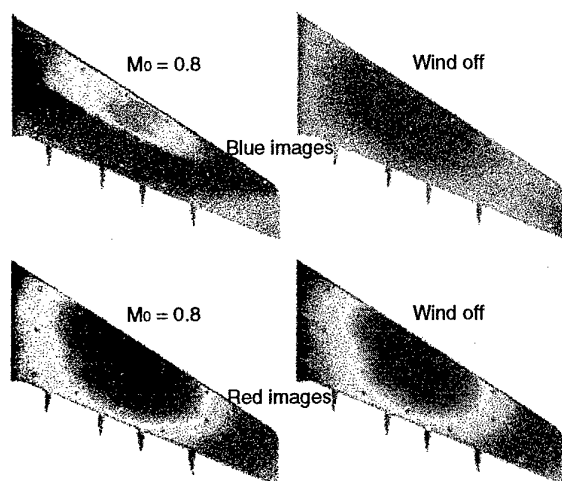


Fig. 5 : Data acquisition with 2 component paint ($\alpha = 2^\circ$).

6. Data processing

Data processing was first performed directly on PC computer by TsAGI team. After the test, ONERA decided to develop its own software: the choice was made to conduct acquisition on PC computer and data processing on Alpha Station working under UNIX environment. ONERA already had at its disposal efficient image processing software, developed over many years by Aerodynamic Directorate and used in the field of temperature imaging and heat transfer measurements. New software was written jointly by the Aerodynamic and the Large testing Facilities Directorates to improve the data processing methods and to provide the wind tunnel teams with a specific tool compatible with the requirements of industrial tests. This software is described below.

All the images acquired on PC are transferred to the Alpha station : dark images, reference images, run images (for blue and red channel).

Data processing then comprises the following steps performed on the Alpha station :

- for each channel the dark image subtraction is performed for reference and run image ;
- the reference and run image are normalized, which means that the blue image is divided by the red image ;
- the marker points in the reference image are manually detected in interactive mode. Each marker point is approximatively located on the screen, a zoom of this area is then displayed on the screen and the location of the marker center can be adjusted ;
- the marker points in the run image are automatically extracted, using a dedicated image processing software. This software detects all contrasted area of a given radius; the coordinates of these points are then compared with the coordinates

of the marker points in the reference image in order to eliminate false marker points;

- the coordinates of the marker points in the reference and in the run image are then used to realign the 2 images. The transformation is expressed as follow :

$$x = \sum_{i,j=0}^2 a_{ij} X^i Y^j$$

$$y = \sum_{i,j=0}^2 b_{ij} X^i Y^j \text{ with } (i + j \leq 2)$$

where x,y are the coordinates in the reference image and X,Y are the coordinates in the run image.

The coordinates of the 18 marker points are used in conjunction with the least-squares technique to determine the coefficients $a_{i,j}$ and $b_{i,j}$;

- the normalized reference image is then divided by the normalized run image. After marker points elimination some image filtering can be applied ;
- determination of the C_p image (figure 6), taking into account the temperature image, usually calculated using the recovery temperature on a flat adiabatic wall ;

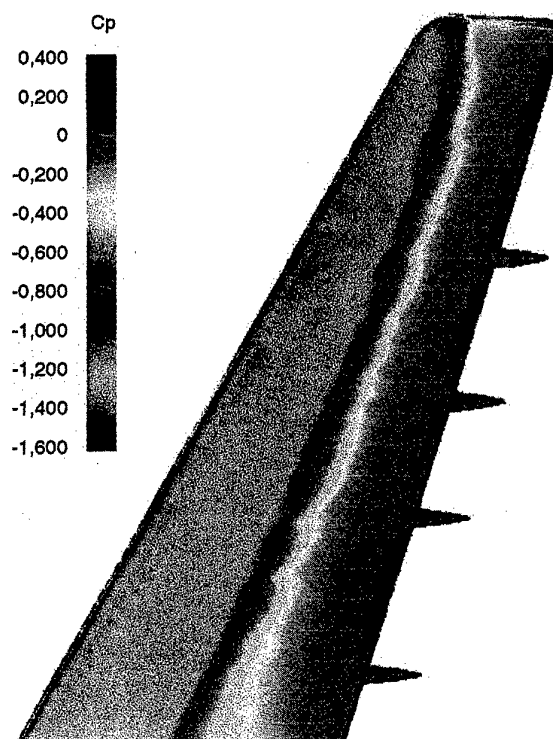


Fig. 6 : Pressure field image ($Mach = 0,8 - \alpha = 2^\circ$).

- extraction of results :

Real coordinates x_m and y_m of the marker points are directly measured on the wing surface and real

zm coordinate is calculated using the model representation.

The camera optical system is modelled using the optical center hypothesis. 3 rotations and 3 translations are then used to define the camera attitude and location (CAL parameters). The software computes the image points corresponding to the real markers using initial values of the 6 parameters and calculates an error function as the root-mean-square value of the discrepancy between the computed image points and the markers. This error function is then minimized to obtain the correct values of the six parameters. It is then possible to display the image on the screen with the computed and real marker points. If a grid of the model is available it can also be displayed to check the transformation. The standard deviation on marker location is about 0.5 pixel. After camera attitude and location determination it is then possible from a real point to associate an image point. This is used to extract the values of C_p coefficients corresponding to the instrumented sections of the model.

- virtual images

However to relate an image pixel to a real point on the model, the grid representation must be available. This grid is constructed with triangular meshes. There is no special requirement for the mesh size, except that the grid has to provide an accurate model description. Each mesh is projected onto the image plane using the 6 parameters. The projected mesh is also a mesh and the included pixels are closely related to points inside the physical mesh. By computing the projected mesh within the whole grid in this way, each image pixel becomes related to a point on the model. This method can be used for 3D reconstruction. A virtual image can be computed from an initial image, an initial CAL and a virtual CAL. The description of the basic software package for CAL determination and 3D reconstruction is given in [4].

7. Test Results

The main goal of the evaluation test, performed in S2MA, was to investigate influence of flow parameters (temperature, total pressure, Mach number) and PSP measurement system parameters (camera position, in situ vs. Laboratory calibration) on the output results obtained with PSP technology.

Calibration check

Calibration curves obtained in the calibration chamber on a small sample, having square form with sides of about 20 mm, are used for the total surface of the model.

To estimate the uncertainty induced by this assumption, a check of calibration laws was performed directly on the model in the wind tunnel test section, where it is possible to set different pressure levels.

Figure 7 shows the distribution of the deviation between the applied and the calculated pressure, obtained with a pressure level of about 0.2 bar inside the test section.

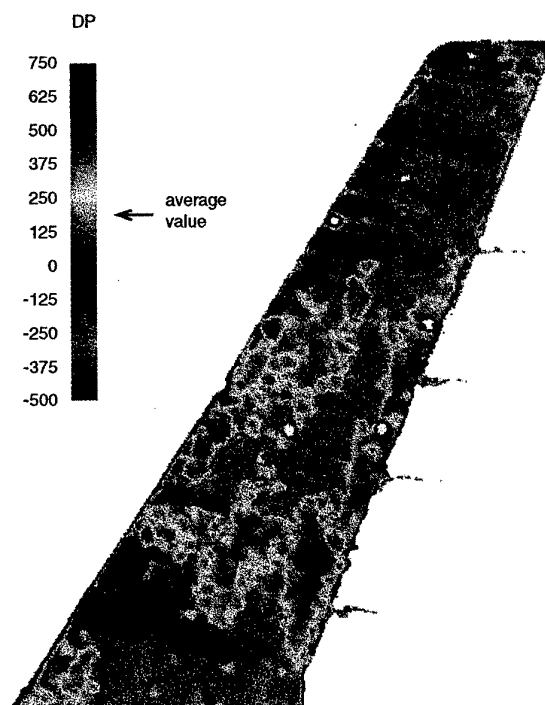


Fig. 7 : Calibration check inside the test section ($P = 0.2$ bar).

The pressure was calculated using the calibration law determined for 27°C (temperature of the model about 25°C) ; the mean discrepancy between the applied pressure and the calculated pressure is about 250 Pa ; the local discrepancies around this average value are about ± 700 Pa. The origin of this spread can be explained by the way the paint is applied on the model : thickness variation of the PSP layer, evaporation velocity of the solvent ...

Repeatability

First of all it was necessary to determine the repeatability that can be obtained with PSP technology. The nominal point : $Mo = 0.8$, $\alpha = 2^\circ$, $P_{io} = 1.1$ bar, $T_{io} = 300$ K was investigated in all runs. Figure 8 shows the spread of the PSP results ; these results come from 4 different runs. Three selected sections, called 65, 67 and 69, located respectively at 52.3%, 75.3% and 95.3% of the half span are shown.

The standard deviation from the mean C_p value is less than 0.02 before the shock, and less than 0.05 after the shock. It should be noticed that the pressure tap data hasn't been used to obtain this result and that no offset correction has been applied.

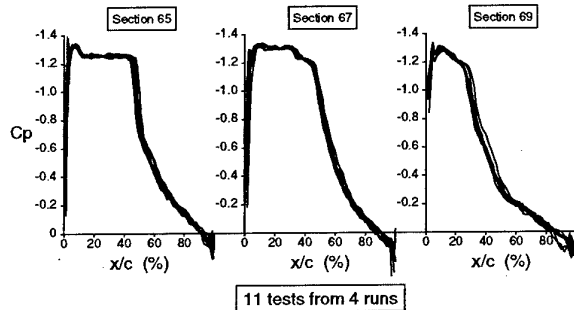


Fig. 8 : Repeatability of PSP results ($M_0 = 0.8$ - $\alpha = 2^\circ$).

Cp distribution in comparison with ESP values

Figure 9 shows the C_p distribution from PSP results in comparison with ESP values at cruise conditions ($M_0 = 0.8$, $\alpha = 2^\circ$).

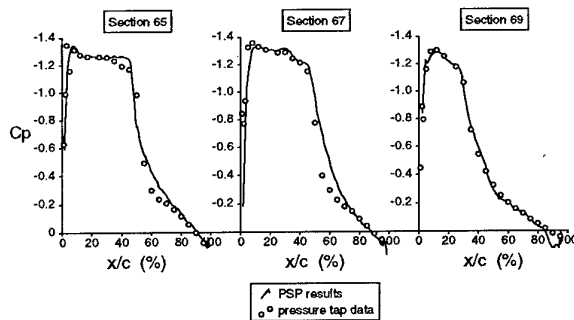


Fig. 9 : C_p distribution in comparison with ESP values ($M_0 = 0.8$ - $\alpha = 2^\circ$).

The results coming from the 2 measurement methods, conventional pressure taps and PSP, are in good agreement. The discrepancies on the C_p value in the supersonic area are about 0.02 in C_p . For the section 67, the location of the shock is slightly different. It should be noticed that PSP results are measured on the right half wing while ESP results come from the left half wing. As these tests were performed without boundary layer tripping, the location of the transition on the 2 wings can be slightly different, due to the PSP coating. This can induce a slight difference in the shock location.

Incidence effect

Figure 10 shows the C_p distribution extracted from PSP image compared with the ESP values, on the section 65 located at 52.3%, for 3 different values of incidence.

The angle of attack was set at -2° , 0° and 3° respectively.

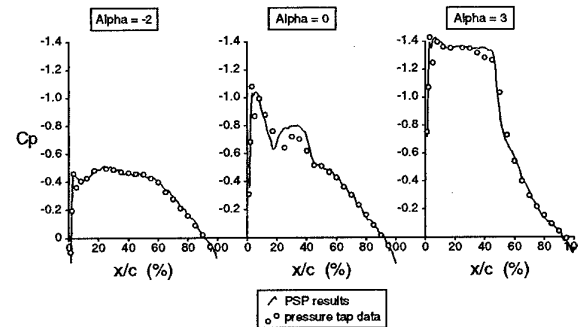


Fig. 10 : C_p distribution in comparison with ESP values (Incidence effect - $M_0 = 0.8$ - section 65).

Pressure level effect

The pressure level effect was investigated at $M_0 = 0.8$ and $\alpha = 2^\circ$, through a change in stagnation pressure, from $P_{i0} = 0.5$ bar to $P_{i0} = 1.1$ bar.

The results were first computed using the calibration law obtained at $t = 27^\circ\text{C}$ corresponding to the stagnation temperature value. Figure 11.a shows the results obtained in these conditions. The results from the pressure taps are plotted on the left part, the results from PSP images are plotted on the right part. It is clear that the discrepancies with PSI values increased when the stagnation pressure decreased.

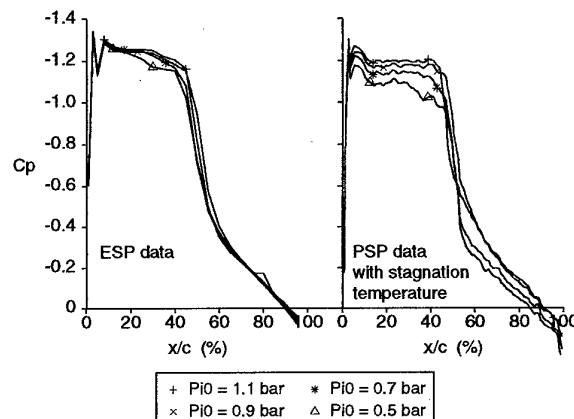


Fig. 11a : C_p distribution in comparison with ESP values (Pressure level effect - $M_0 = 0.8$ - $\alpha = 2^\circ$ - Section 65).

This behaviour was related to the temperature effect ; this effect, negligible at ambient pressure, increases at low pressure and becomes important due to the scale factor of the C_p values.

In order to check this assumption, the results were computed again, using an estimated value of the local temperature for each pixel, calculated as the temperature of an adiabatic flat wall.

Figure 11.b shows the results of the stagnation pressure effect, computing the data with the local temperature.

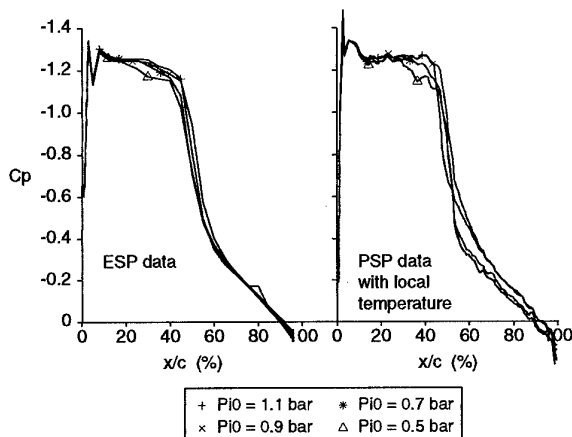


Fig. 11b : CP distribution in comparison with ESP values (Pressure level effect - $Mo = 0.8$ - $\alpha = 2^\circ$ - Section 65).

Taking the local temperature into account enables the right absolute level to be found for all stagnation pressure values.

After this experiment the calculation of local temperature was included in the software and all the results presented in this paper were computed using the local temperature.

Temperature effect

The temperature effect was investigated in the range allowed by the wind tunnel. At $Mo = 0.8$, the temperature range goes from $T_{io} = 295$ K to $T_{io} = 310$ K. These values correspond to local temperatures from 13°C to 27°C for the supersonic area. Figure 12 shows the spread of the results obtained at different T_{io} values, over the curve obtained with conventional measurements (there is no T_{io} effect on pressure tap results).

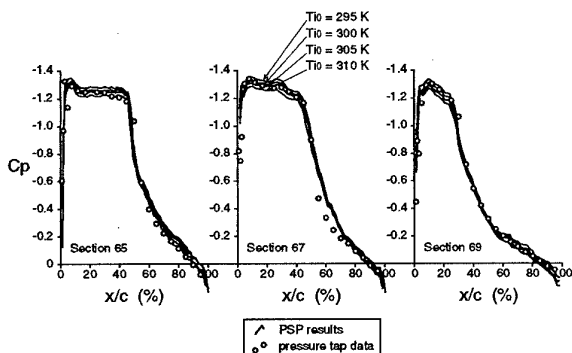


Fig. 12 : CP distribution in comparison with ESP values (Temperature effect - $Mo = 0.8$ - $\alpha = 2^\circ$).

The spread of the different results is about ± 0.03 in C_p value. To reduce this spread it would be necessary to determine the local temperature more accurately.

Two ways are going to be studied in the near future to reduce the uncertainty due to thermal effects: the first way is to measure the temperature simultaneously using infrared camera, the second way is to use a third channel paint with 2 color parameters, one for the pressure, the other for the temperature.

Mach number effect

Mach number effect was investigated at $\alpha = 0^\circ$, from $Mo = 0.6$ to $Mo = 0.84$. In this Mach number range and for this value of α , no particular effect of the Mach number was found.

Reference image effect

Initial research on two-component paints was conducted with the hope that using such a paint would avoid the need for a wind-off image and suppress the realignment step. In fact, a wind-off image is still necessary to take into account the spread of relative concentration on the model surface. However, it is not necessary to repeat this reference image for all incidences studied during the run. Figure 13 compares the results obtained when computing the run image acquired at $Mo = 0.8$ and $\alpha = 2^\circ$ with 3 different reference images, one taken at $\alpha = 2^\circ$, the others taken at $\alpha = 0^\circ$ and 4° . The spread of the results is the same as that observed during a simple repeatability test. Obviously, this procedure requires an high performance realignment programme.

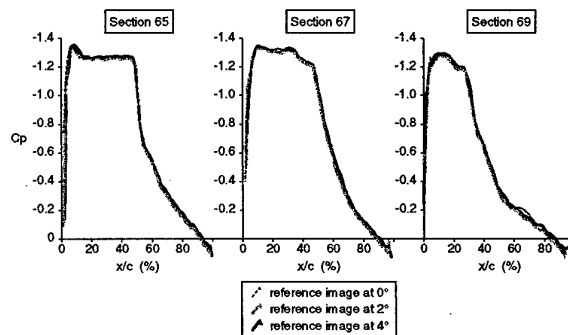


Fig. 13 : Reference image effect ($Mo = 0.8$ - $\alpha = 2^\circ$).

8. Conclusion

The evaluation results of the prototype measurement system developed by TsAGI in the transonic test section of the S2MA wind tunnel show that the PSP technology can be used in an industrial environment.

The acquisition times are short, about 1.5 s for each measurement point, and no degradation effect is observed after a one hour run.

The two-component paint LPS-B1 enables the illumination field changes on the model surface between the reference and run images to be taken into account. This point is particularly useful in large industrial wind tunnels where important model displacements are observed. Moreover, the sensitivity of LPS-B1 paint to temperature is very low : under 0.1% per degree between 15°C and 40°C at ambient pressure. These two features allow the accuracy obtained with PSP technology to be improved.

The repeatability obtained on the pressure coefficient is about ± 0.02 at $Mo = 0.8$ and $Pio = 1.1$ bar.

Furthermore, the comparison with pressure tap data shows an acceptable accuracy without the use of these pressure taps for any offset correction.

From now on, the PSP technology can be used in industrial tests and ONERA is offering this opportunity to its clients. The accuracy obtained with this technology can still be improved. Further improvements should include a better correction of temperature effects and a better correction of the spread of the calibration curves from one point of the model to another.

9. References

- [1] S.Fonov, V.Mosharov, A.Orlov, V. Pesetsky, V. Radchenko, A.Bukov, S.Matyash " Optical surface pressure measurements : Accuracy and application field evaluation" *73th AGARD Fluid dynamics symposium . Brussels 1993.*
- [2] Lumb M.D. "Organic luminescence" published in *Luminescence Spectroscopy, Academic Press, New-York, 1978, pp94-146*
- [3] R.H. Engler, C. Klein "First results using the new DLR PSP system, Intensity and lifetime measurement" *CEAS Cambridge 1997*
- [4] Y. Le Sant, M.C. Merienne "An image resection method applied to mapping techniques" *16th International Congress on Instrumentation in Aerospace Simulation Facilities. ICIASF'95.*

Low-Speed Flow Studies Using the Pressure Sensitive Paint Technique

O.C. Brown

Stanford University Department of Aeronautics and Astronautics
120 East Creek Dr. #8, Menlo Park, CA 94025, USA

R. D. Mehta

NASA Ames Research Center

B. J. Cantwell

Stanford University Department of Aeronautics and Astronautics

1. SUMMARY

Optical pressure measurements have been made on a NACA 0012 airfoil coated with Pressure Sensitive Paint (PSP) at very low flow speeds (≤ 50 m/s). Angle of attack was limited to 5° for most measurements. Effects of temperature gradients and mis-registration errors on PSP response have been established and minimized. By reducing measurement error caused by these effects, PSP sensitivity has been enhanced. Acceptable aerodynamic data at flow speeds down to 20 m/s have been obtained and valid pressure paint response was observed down to 10 m/s. Measurement errors (in terms of pressure and pressure coefficient) using PSP with pressure taps as a reference are provided for the range of flow speeds from 50 m/s to 10 m/s.

2. LIST OF SYMBOLS

α	Airfoil angle of attack
A	Linearized image intensity calibration intercept coefficient
A'	Linearized pressure ratio calibration intercept coefficient
B	Linearized image intensity calibration slope coefficient
B'	Linearized pressure ratio calibration slope coefficient
Cp	Pressure Coefficient
I	Wind-on image PSP intensity
Iref	Reference image (wind-off) PSP intensity
P	Wind-on image surface pressure
Pref	Reference image (wind-off) surface pressure

3. Introduction

Optical pressure measurement systems using PSP's are gaining acceptance in the aerospace community for use as an effective and efficient instrumentation tool. PSP response is good at higher flow speeds (typically $M=0.3$ and above), but at lower flow speeds ($M=0.1$ and below), where pressures and pressure differences are relatively small, paint sensitivity

begins to be affected by external factors which can limit, and sometimes, invalidate paint response. These factors are:

- 1) Temperature induced intensity changes: Intensity of light emitted by PSP is proportional to oxygen concentration, which makes the paint pressure sensitive. Intensity of light emitted by PSP is also (unfortunately) temperature sensitive. Thus, changes in temperature on a model being monitored can potentially corrupt PSP pressure evaluations.
- 2) Mis-registration effects: In the calibration process described here, images taken during tunnel tests are divided into a reference image taken with the wind tunnel turned off. In this ratioing, both images should be perfectly aligned. When the wind tunnel is running, the model will almost always move and deform. Software must correct for this movement with a registration process. Any uncorrected movement will result in mis-aligned images and errors in the ratioed results.
- 3) Shot Noise: The CCD electronic array of the digital camera used for imaging has an inherent electronic noise component associated with the photonic shot noise. This shot noise serves as the ultimate limit in PSP resolution.

PSP research has been conducted at NASA Ames on a NACA 0012 airfoil within the speed range of 50 m/s ($M=0.15$) and 10 m/s ($M=0.03$). This research has begun to quantify the effects of temperature and mis-registration on paint response and sensitivity at these low speeds. Corrective actions have been applied to experimental procedures in an attempt to limit these effects. The present study will explain these corrective actions and their impact on PSP accuracy. Limiting pressure changes (and hence limiting flow speeds for the 0012 airfoil) have now been identified at which reasonable data can be obtained using PSP. Paint response, in terms of calibration error, has been quantified in terms of equivalent error in Cp for each speed measured.

4. EXPERIMENTAL METHOD

4.1 Experimental Arrangement

A NACA 0012 2-D solid steel airfoil, with a 7.5 cm chord and 25 cm span was spray painted on the top surface with a white basecoat and "Fib-07" PSP supplied by the University of Washington. After application, the PSP was buffed to reduce the surface roughness, giving a total paint thickness of about 45 μm and surface roughness of about 1.0 μm . This same airfoil was used for early PSP experiments at higher speeds ($M > 0.3$) by McLachlan (Ref. 1) and Kavandi (Refs. 1 and 2).

The airfoil was tested in a small return-circuit wind tunnel at NASA Ames Research Center. This tunnel has a contraction ratio of 6.25:1 and test section size of 30.5 x 30.5 x 45.5 cm. It has a radiator which receives a cooled water supply from a small cooling tower. This cooling tower does not have the capacity to fully maintain wind tunnel temperature at a desired (near ambient) level at speeds above 10 m/s. However, after approximately 30 minutes, an equilibrium temperature can be reached at which the settling chamber temperature does not change by more than approximately 1.5°C/hr. Tunnel temperature is monitored in the settling section via a thermocouple wired to a digital temperature gage.

4.2 Data Collection

In-situ pressures were recorded using a Setra digital pressure transducer receiving signals from a series of 16 pressure taps located along the center span of the NACA 0012 wing. The manufacturer quotes the RSS accuracy of the transducer as ± 4.2 Pa.

The PSP was excited by two Electro-Lite UV lamps producing blue light at 365 nm. Images were obtained using a Photometrics CH250 14-bit CCD camera with a 650 ± 10 nm filter attached to a 50 mm lens. Data were collected on a PC using PMIS imaging software. While recording pressure tap data, a total of 16 images were taken and averaged, thus increasing signal to noise ratio (this imaging process takes about three minutes). Dark field images were then subtracted. A similar series of images were taken with the wind tunnel turned off, immediately before, or immediately after, the wind-on image (the consequences of which particular strategy is employed are discussed below).

Once wind-on and wind-off images had been acquired, they were transferred to a Silicon Graphics workstation running PSP software, "Greenboot". This program has been written by NASA Ames and Boeing (McDonnell Douglas) especially for PSP data reduction. Images were first flat-fielded: this process

eliminates any gain variations among individual pixels in the CCD array, as well as normalizing overall radial-wise gain asymmetry due to the camera shutter operation. Wind-on and wind-off images were then registered: a series of 10 registration marks placed on the wing surface serve as reference points for the registration (in most cases, pressure taps were used as additional registration points). The registration process is similar to that detailed by Bell and McLachlan (Ref. 3). Once registered, the images were then ratioed. It is this ratioing technique that acts as a normalization to offset any variations in paint concentration and thickness, as well as UV lighting differences on the wing. The recorded pressure data are then used to create a least square fit of adjacent image ratio data (an average of a 7 x 7 ring of pixels around each pressure tap is used in this fit). The result is the formation of a linear response curve relating pressure and intensity ratio on the wing (See Refs. 1 and 2 for the details of this relationship):

$$I_{\text{ref}}/I = A(T) + B(T) * P/P_{\text{ref}} \quad (\text{Eq. 1})$$

Here, both constants A and B are temperature dependent. Assuming both wind-on and wind-off images are taken with the wing at the same (spatially uniform) temperature, $A+B = 1$. If temperatures of wind-on and wind-off measurements are not the same, but uniform about the wing, Eq. 1 is not invalid, but A and B will change to accommodate the accompanying intensity changes with temperature. Tests at the University of Washington have shown that the Fib-07 PSP intensity will increase by 0.7% per 1°C temperature decrease. So, for example, if wind-off temperature is greater than wind-on, the curve given by Eq. 1 will shift downward. Both constants (A and B) will decrease to accommodate this temperature shift.

Eq. 1 can be inverted to give a calibrated pressure ratio curve:

$$P/P_{\text{ref}} = A' + B' * I_{\text{ref}}/I \quad (\text{Eq. 2})$$

Intensity ratio data obtained from the CCD images were calibrated to pressure using this relation, thus producing a surface pressure map for the 0012 wing.

5. EXPERIMENTAL RESULTS

5.1 Results: Phase I

In the first phase of the present investigation, runs were conducted at 10 to 50 m/s in 10 m/s increments, with $\alpha = 5^\circ$ for all cases. In these runs, a wind-off average image was taken and then the wind tunnel was turned on. For the run at 10 m/s the tunnel temperature remained stable at initial ambient conditions. For higher speeds the tunnel cooler was turned on. Images were taken at the higher speeds

after the tunnel temperature was allowed to come to equilibrium for each case (in all cases, the tunnel temperature increased about 0.1°C during the data collection process). The resultant images for 50 m/s and 20 m/s are shown in Figures 1 and 2 respectively. Flow is from right to left in these and all subsequent PSP image figures.

The image quality for both cases is quite poor. The large chord-wise streak at the bottom of each image was caused by a scratch in the Plexiglas of the wind tunnel test section. Striation patterns nearly perpendicular to the flow direction are also evident in both images. These striation patterns are believed to have been caused by mis-registration exacerbating paint non-uniformities. The uniform series of lines extending from the top of the image to each pressure tap are the result of detection of the machined gutters used to connect pressure lines to the taps. A large degree of spatial noise is also evident throughout both images.

Figure 3 shows the intensity ratio versus pressure ratio curve and the pressure ratio versus chord (x pixel location) for the 50 m/s run. The former plot shows tap data, as well as the least square fit of the tap data corresponding to Eq. 1. The latter uses Eq. 2 to create pressure ratios based on intensity ratios measured in the chord-wise direction at center span. Tap data is shown for comparison in this plot as well. Note that in the intensity ratio versus pressure ratio plot, data from left to right correspond to pressure tap data from leading edge to trailing edge. In the pressure ratio versus chord plot, data from left to right correspond to pressure tap data from trailing edge to leading edge. Figure 4 is a similar set of plots for the 20 m/s run. Noise which can be associated with the visible striation patterns previously noted is visible in each calibrated pressure versus chord plot. Note also from Figure 3 that the 50 m/s intensity ratio falls off unexpectedly from the least square fit of tap data for the last two data points (corresponding to the last two pressure taps at the trailing edge). These last two taps were not used in the image calibration because of this deviation. The RMS error in the calibrated pressure ratio versus chord curve is a good measure of the resolution of the paint system. In the 50 m/s and 20 m/s cases, this RMS error was 0.226 Cp units and 0.479 Cp units, respectively (or equivalently 342.0 Pa and 116.0 Pa, respectively). Such large errors are unacceptable for use in assessment of the aerodynamic properties of this or any other airfoil.

It was assumed that for this initial phase of runs, temperature effects and image registration errors contributed to the poor image quality and unacceptable noise levels. Since the tunnel temperature changed when turned on, it was suspected that spatial temperature gradients may have developed on the model surface. The model (and to a similar

degree the test section) does move between wind-on and wind-off measurements. As discussed previously, data reduction software accounts for this motion by aligning registration marks between wind-on and wind-off images. Unfortunately, this alignment process is not exact, nor does it account for changes in lighting conditions about the model due to movement relative to the UV lamps.

5.2 Observations and Corrective Actions

During the previous runs, UV lamps and the CCD camera had been mounted to a test stand that was bolted to the tunnel facility floor. To reduce the amount of movement of this imaging equipment in relation to the 0012 model, both lamps and the camera were mounted firmly to the tunnel test section (which in turn serves as the mount for the 0012 wing). Table 1 notes the results of this new stabilization technique, showing that model motion was noticeably reduced.

Method	X pixel Shift	Y Pixel Shift
1. System mounted to floor	2.41	1.90
2. System mounted to tunnel	0.43	0.00

Table 1. Average pixel shift of model between wind-on (50 m/s) and wind-off measurements using different stabilization techniques.

It was believed that some error was also induced by temperature effects. Temperature differences in the tunnel settling chamber between wind-on and wind-off imaging were on the order of 5°C . As noted previously, such a temperature difference, if it indeed exists on the painted surface, will not impact the linearity and accuracy of the calibration as long as a uniform (or at least similar) temperature variation exists for both wind-on and wind-off conditions.

When taking the wind-on image, it is possible that a temperature gradient existed on the surface of the wing, especially since the model has a chord-wise varying thickness and the tunnel temperature changes between runs at different speeds. Such a temperature gradient could have affected calibration results since a uniform profile existed on the wind-off image which was taken before the tunnel was started. It was therefore believed that taking a wind-off image immediately after a run at a given tunnel speed would be more appropriate since the temperature gradient on the wind-on image could possibly be maintained for the wind-off image. This would then, hopefully, eliminate or at least minimize temperature induced calibration errors.

The tunnel test section Plexiglas on the imaging side was also replaced for the subsequent runs, to eliminate the interference due to the scratch noted in the previous images.

The wing was repainted and buffed with more intense scrutiny.

5.3 Results: Phase II

With the improved stabilizing mechanism in place, and the decision made to use the strategy of taking wind-off images immediately after a wind-on image, a new series of data runs was conducted. Figures 5 through 8 show images taken at 50, 40, 20, and 10 m/s. Figures 9 through 12 show the image ratio versus pressure ratio and pressure ratio versus chord plots. From these figures, the following observations are made:

1. The image quality for the new images (Figures 5 through 8) is improved significantly from the previous images (Figures 1 and 2).
2. Pressure response is evident at flow speeds down to 10 m/s; response at this speed had not been previously observed on this wing with the old setup and procedures.
3. At 40 m/s, and to a lesser degree at 50 m/s, image ratios still fall below the expected linear trend near the trailing edge of the airfoil (because of this inconsistency, in the 40 m/s case we only used taps 1-12 to calibrate the image data to the pressure data).

Response at 30 m/s (not shown) was acceptable.

The reason for the unexpected and unacceptable image ratio deviation on the 40 m/s image was examined. During the 40 m/s run, tunnel settling section temperature had decreased from 21.9°C while taking wind-on images to 21.7°C during the wind-off imaging. This relatively small drop in temperature was not expected to affect the data. The tunnel had been run for about 20 minutes prior to initial data collection for this run.

Several experiments were run to determine the sensitivity of image response to imposed temperature gradients. In the first experiment, a wind-off image was taken prior to running the tunnel (the tunnel had not been run previously for a period in excess of 24 hours). The tunnel temperature was at ambient room conditions of 25.3°C. The tunnel was then run for a time period in excess of one hour and then stopped. A wind-off image was then taken immediately after tunnel airflow had ceased. Temperature during this data acquisition had cooled to about 19.7°C. The ratio of the first wind off image to the second was then taken (I wind-off initial/I wind-off post run). The ratioed profile is shown in Figure 13. Ideally, since the pressures for the two cases were equal

(atmospheric), a uniform intensity ratio profile below one (since the tunnel and the model had cooled) would be expected. With a thinner trailing edge one would expect the trailing edge to have cooled faster than the rest of the wing during the run. However, this figure shows the temperature of the trailing is higher than the rest of the wing, thus indicating a warm-up of this section after the wind tunnel was turned off. This result demonstrates that temperature gradients on the wing can change even in the very short time period it takes to turn the wind tunnel off and acquire wind-off data.

The second experiment attempted to show the change in temperature gradients on the wing as a function of tunnel running time. During this experiment, an initial wind-off image was taken (tunnel temperature was at ambient - the tunnel had not yet been operated that day). Then, the tunnel was run at 50 m/s for approximately 20 minutes with the cooler turned off. During this time, temperature increased from 28.1°C to 38.1°C. A series of four averaged images were taken at 2°C intervals during the warm-up period. The cooler was then turned on, and a fifth image captured. During this acquisition period, the temperature decreased from 30.7°C to 27.8°C. This series of ratioed images is shown in Figure 14. The following observations are made:

1. During the warm-up period, a slight increase in image ratio slope is noted from leading edge to trailing edge for each consecutive run (less the last run), thus indicating that trailing edge temperatures are increasing faster. During the last run with the cooler off, the rate of temperature increase in the tunnel began to level off, and thus the temperature gradient began to decrease, giving a near equilibrium condition.
2. During the cool-down period, the image ratio shows a negative slope near the trailing edge, very similar to previous results for ratioed images obtained at 50 m/s and 40 m/s. This shows that the trailing edge now cooled faster than the rest of the wing.

Given the above experimental results, it is apparent that temperature gradients indeed can be induced on this wing at both wind-on and wind-off conditions, and that such temperature gradients can adversely impact image results at these low speeds. The fact that the wing develops temperature gradients is not really surprising. However, it was startling to note that even very small temperature changes that occurred during the short time it took to turn the wind off and obtain the wind-off images had significant effects on the calibration.

In order to estimate how the wing temperature may have changed after stopping the tunnel for the 40 m/s run, a "forced" calibration procedure was followed. By first extrapolating the image ratio to pressure ratio

curve fit to a pressure ratio of 1.0 (where the image ratio would ideally be 1.0 for equal wind-on and wind-off run temperatures), the overall average change (reduction) in wind-off temperature can be determined. Then, assuming all deviations about the linear fit are temperature induced, the temperature gradient can be inferred. The results are presented in Figure 15, which shows that the overall temperature decreased by approximately 1.0°C , while a nearly linear temperature gradient appeared at mid-chord, with the trailing edge warming to near wind-on conditions. The temperature change of 1°C is of the same order of magnitude as the temperature change monitored in the tunnel during this data run.

It should be noted that at the higher speeds typically used for PSP data acquisition, similar temperature gradients to those just discussed exist, but their impact may go unnoticed. For example, assuming (1) $M=0.3$, (2) a C_p profile identical to the 40 m/s case, (3) an image ratio to pressure ratio curve fit identical to the 40 m/s case, and (4) an identical wind-on minus wind-off temperature profile across the wing, Figure 16 was generated. This image ratio versus pressure ratio plot shows that the fall-off in image ratio data is barely detectable for this hypothetical case with a higher flow speed (recall that for the 40 m/s case that the image ratios had actually begun to decrease at the higher pressure ratios).

Similar effects have been noted in previous PSP studies. Ref.'s 1, 4, and 5 all note the existence of two calibration curves for image ratio versus pressure ratio data. As Ref. 1 states correctly, these curves exist because of the presence of temperature gradients on the wing. As long as such gradients are very discrete (i.e. stepwise) and image intensity ratios increase monotonically with pressure, use of two or more calibration curves is appropriate, but not ideal.

Based on the above findings, a second run at 40 m/s was conducted in an attempt to produce a quality image not influenced by temperature. During this run, the tunnel was allowed to run for approximately one hour prior to wind-on data collection. A wind-off image was taken after running the tunnel. Figures 17 through 18 display results, which are greatly improved from the previous 40 m/s case.

It is believed that the good results produced in this run were greatly influenced by the extended tunnel run time prior to data acquisition. Temperature gradients most probably existed across the wing (both chord-wise and span-wise) during all runs. Extending the tunnel run time at a given speed allows the internal wing temperatures to come to an equilibrium condition. Equilibrium core wing thermal conditions will act as a stabilizing influence for the surface temperatures of the wing. Basically, heat transfer due to conduction effects will be minimized, and this

probably helps to maintain the wind-on temperature distribution.

To demonstrate the capabilities of this PSP data acquisition system, data were also collected with the 0012 wing at 50 m/s and $\alpha = 7^{\circ}$ (the maximum α before separation at this flow speed). Results are shown in Figures 19 and 20. Note the goodness of fit in both plots. At this speed and α , the larger pressure signal has enabled this precise and relatively noise-free signal to be created.

5.4 Review of Phase II Results

From each image ratio versus pressure ratio curve fit, an RMS error was obtained which measured the deviation between pressure tap data and calibrated image data at the tap. This error has been converted into equivalent units of pressure and C_p for the best case runs from 10 to 50 m/s. The results are shown in Figure 21.

As indicated, results are very good at 50 m/s and 7° angle of attack. The large signal available produced an excellent calibration. It should be noted that Mendoza (Ref.6) has recently identified PSP results with a C_p error of ≤ 0.04 as acceptable for "aerodynamic assessment". Mendoza has further calculated that such accuracy can be obtained by a "state of the art PSP system" at $M \geq 0.15$. The C_p error of 0.026 obtained in the research at 50 m/s (or $M=0.15$) and $\alpha = 7^{\circ}$ is slightly better than the value given by Mendoza.

Also note that data down to 20 m/s appear reasonable (maximum C_p at this speed was -2.65, equivalent to a change of 638 Pa from the reference pressure). An error of 0.12 in C_p at the rather low speed of 20 m/s is encouraging, and believable response to pressure at 10 m/s is quite intriguing. It should be noted that such speeds and associated pressure changes are typical of an automobile traveling at just under highway speed limits. Thus, valid PSP measurements can indeed be made in the realm of automotive aerodynamics.

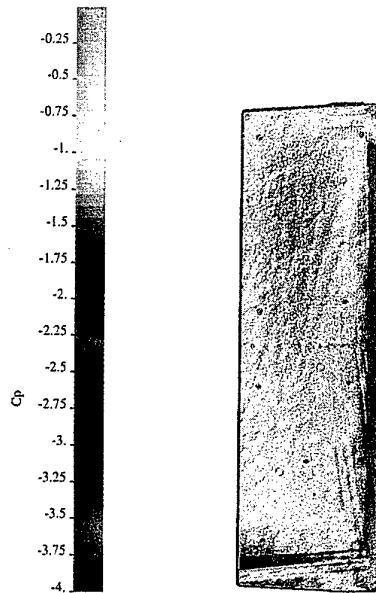
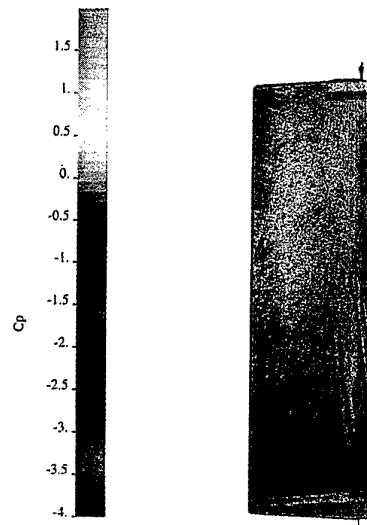
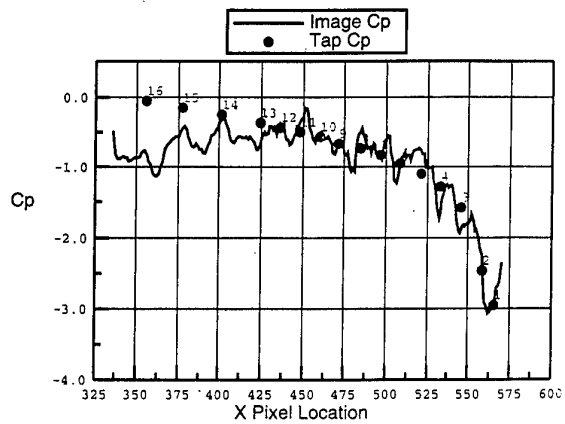
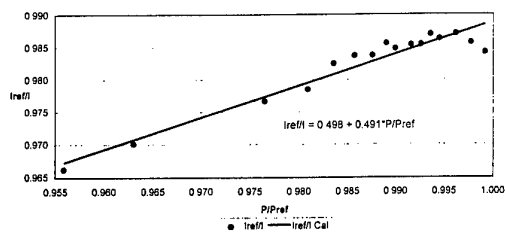
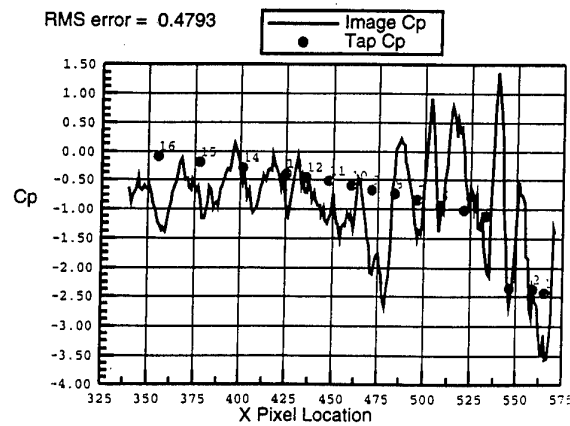
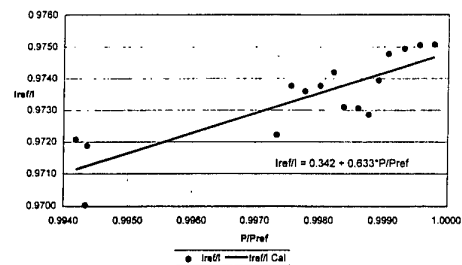
6. CONCLUSIONS

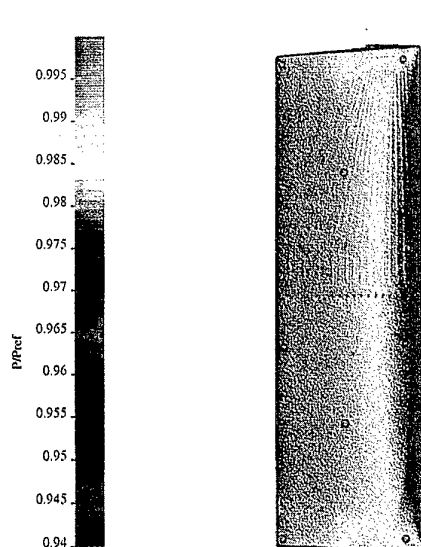
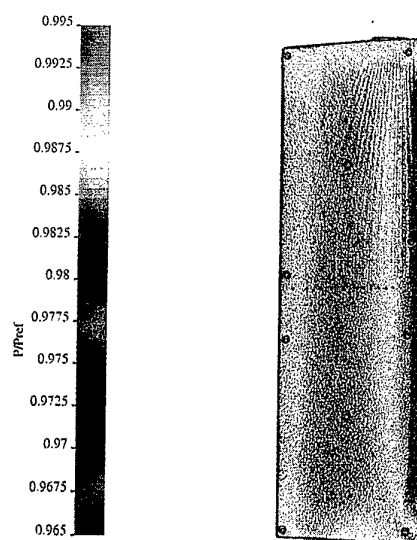
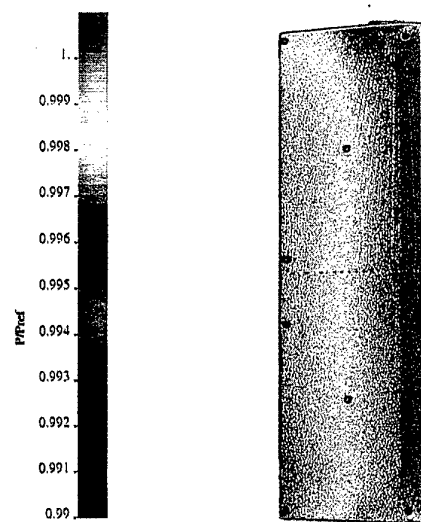
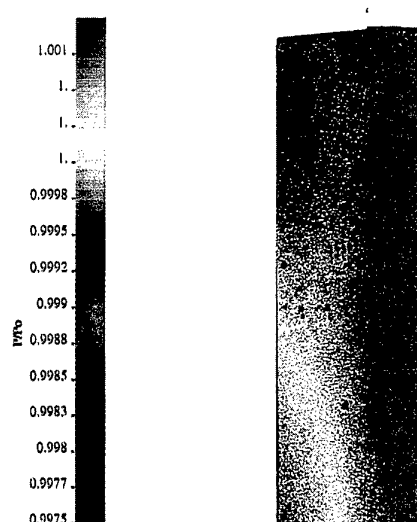
Valid aerodynamic data at very low speeds can be obtained via optical pressure measurements using Pressure Sensitive Paints. As shown in this work, reasonable pressure data can be measured at speeds as low as 20 m/s on an airfoil with a common pressure profile using PSP. Errors in PSP calibration are influenced most by temperature gradients appearing on the model surface. To reduce such effects, wind-tunnel temperature must be controlled as well as possible, ideally at ambient conditions. If this is not possible, the tunnel and the painted model must be allowed to come to a stable equilibrium temperature distribution. When using the ratio method, it is best to

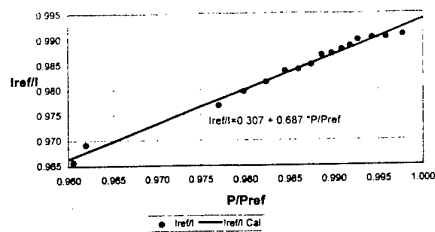
take wind-off reference images immediately after the wind-on image. Finally, registration errors play a large role in PSP measurement accuracy at low speed. When possible, it is best to stabilize imaging and lighting systems to the same surface which also stabilizes the model. Shot noise will always be the ultimate limitation in PSP resolution at low speed, but will never compare to those effects caused by temperature and mis-registration induced errors.

References

1. McLachlan, B.G., Kavandi, J.L., Callis, J.B., Gouterman, M., Green, E., Khalil, G., and D. Burns, "Surface pressure field mapping using luminescent coatings", *Experiments in Fluids* 14, pp 33-41, 1993.
2. Kavandi, J.L., "Luminescence Imaging for Aerodynamic Pressure Measurements", Ph.D. Thesis, University of Washington, 1990.
3. Bell, J.H. and B.G. McLachlan, "Image registration for pressure-sensitive paint applications", *Experiments in Fluids* 22, pp 78-86, 1996.
4. Shimbo, Y., Mehta, R. and B. Cantwell, "Application of Pressure Sensitive Paint Technique to Steady and Unsteady Flow", *JIAA TR* 115, June 1996.
5. Reda, D.C., Wilder, M.C., Mehta, R., and G. Ziliac, "Measurement of the Continuous Pressure and Surface Shear Stress Vector Distributions Beneath an Inclined, Impinging Jet Using Coating and Imaging Techniques", *AIAA paper* 97-2489.
6. Mendoza, D.R., "Limiting Mach Number for Quantitative Pressure-Sensitive Paint Measurement", *AIAA Journal*, 35, 7, pp 1240-1241, 1997.

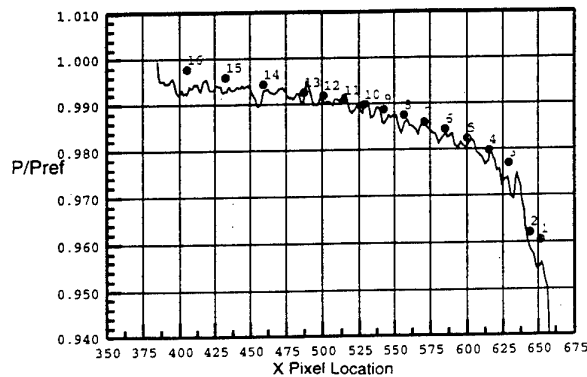
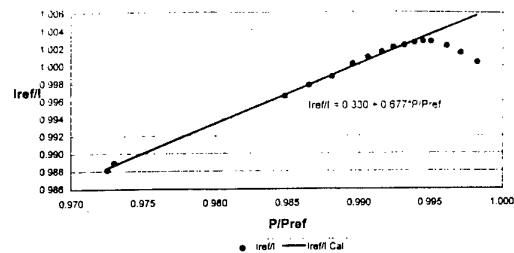
Figure 1. Initial PSP image at 50 m/s, $\alpha = 5^\circ$.Figure 2. Initial PSP image at 20 m/s, $\alpha = 5^\circ$.Figure 3. Initial PSP intensity and pressure ratio plots at 50 m/s, $\alpha = 5^\circ$.Figure 4. Initial PSP intensity and pressure ratio plots at 20 m/s, $\alpha = 5^\circ$.

Figure 5. Improved PSP image at 50 m/s, $\alpha = 5^\circ$.Figure 6. PSP image at 40 m/s, $\alpha = 5^\circ$.Figure 7. Improved PSP image at 20 m/s, $\alpha = 5^\circ$.Figure 8. PSP image at 10 m/s, $\alpha = 5^\circ$.



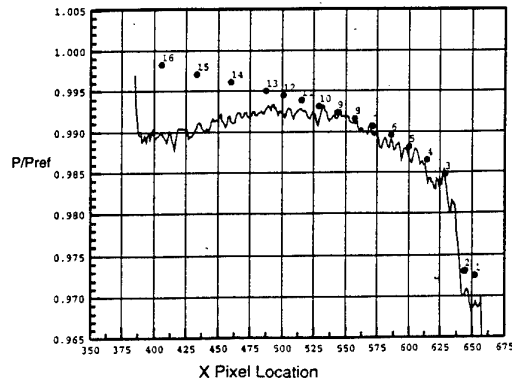
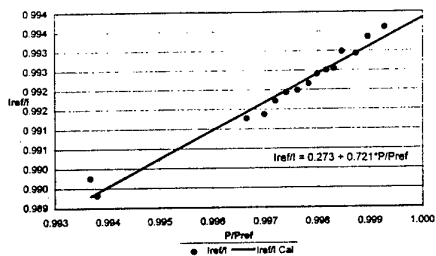
RMS error = 0.001196

— Image Pressure Ratio
● Tap Pressure Ratio

Figure 9. Improved PSP intensity and pressure ratio plots at 50 m/s, $\alpha = 5^\circ$.

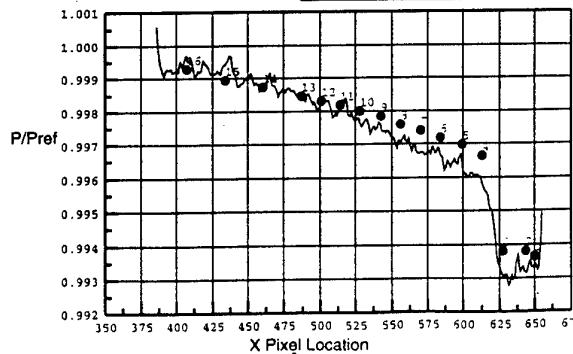
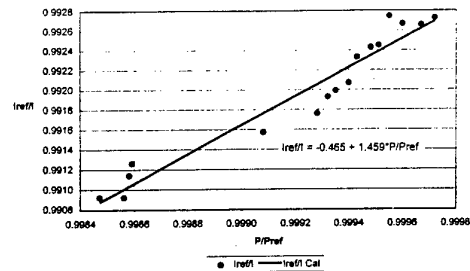
RMS error = 0.002619

— Image Pressure Ratio
● Tap Pressure Ratio

Figure 10. PSP intensity and pressure ratio plots at 40 m/s, $\alpha = 5^\circ$.

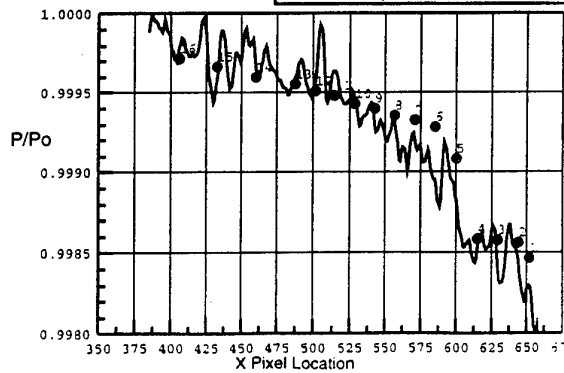
RMS error = 3.658E-04

— Image Pressure Ratio
● Tap Pressure Ratio

Figure 11. Improved PSP intensity and pressure ratio plots at 20 m/s, $\alpha = 5^\circ$.

RMS error = 1.456E-04

— Image Pressure Ratio
● Tap Pressure Ratio

Figure 12. PSP intensity and pressure ratio plots at 10 m/s, $\alpha = 5^\circ$.

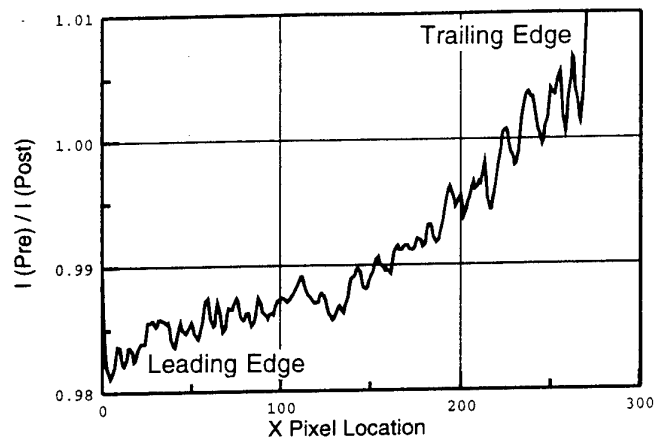


Figure 13. Intensity ratio plot of two wind-off images showing creation of temperature gradient on wing during wind-off conditions.

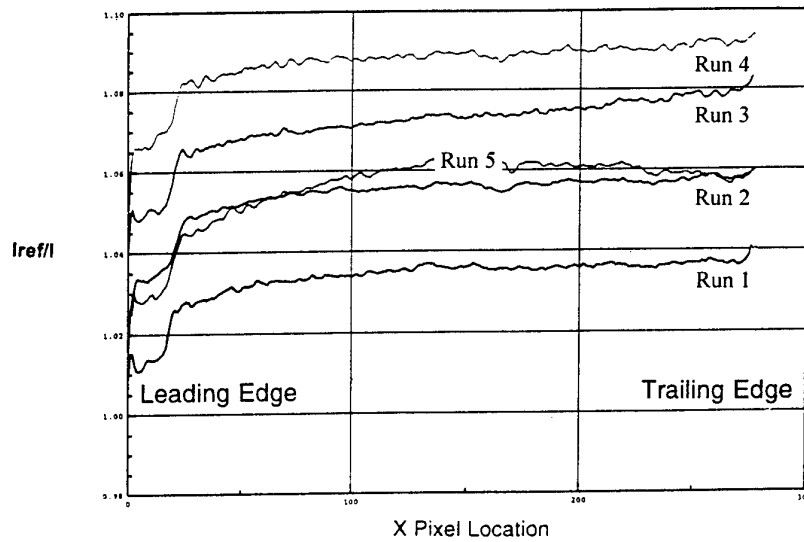


Figure 14. Series of ratioed images taken at 50 m/s, $\alpha = 5^\circ$.
Runs 1-4 taken during tunnel warmup. Run 5 taken during tunnel cooldown..

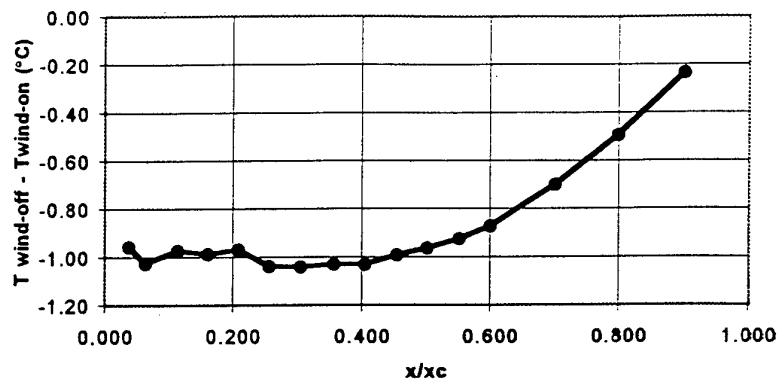


Figure 15. Plot of temperature change on 0012 airfoil between wind-on and wind-off conditions for 40 m/s run.

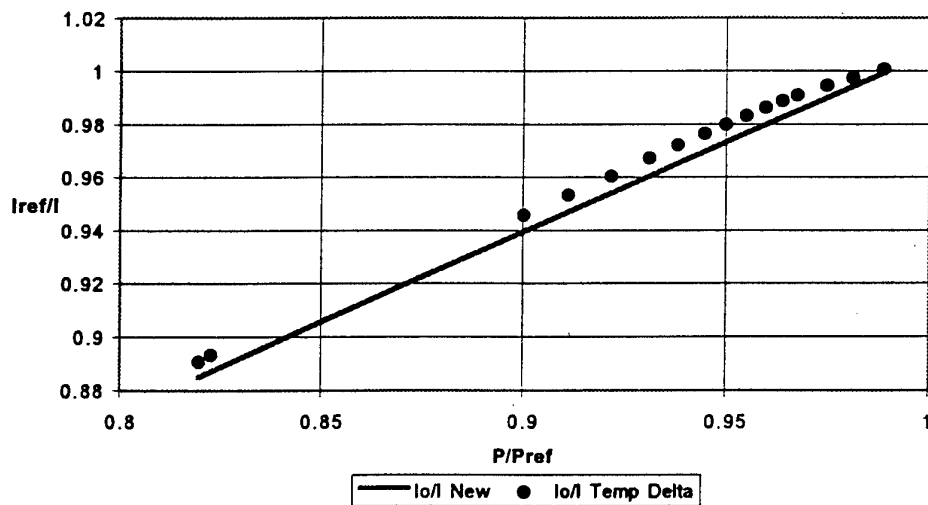
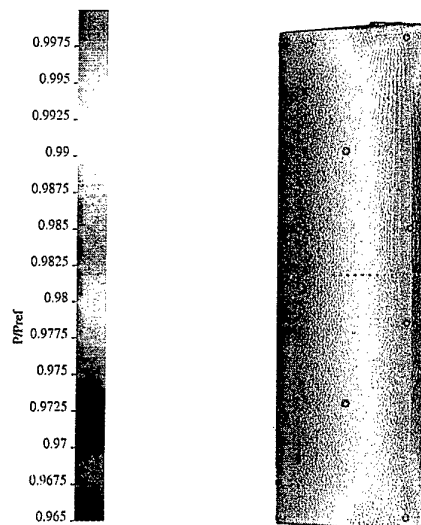
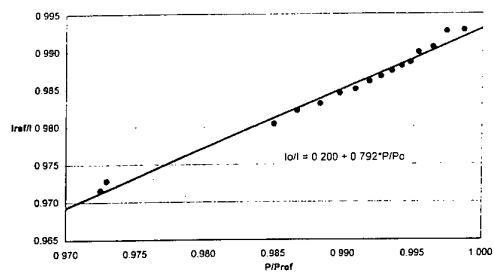
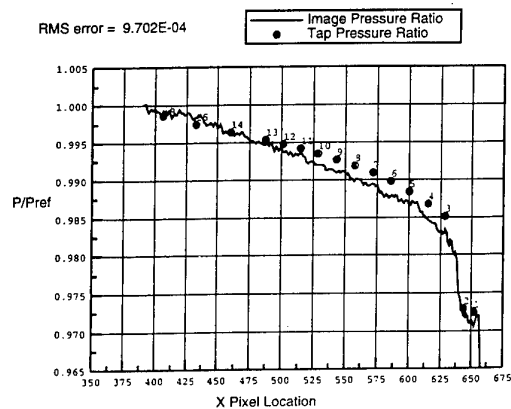
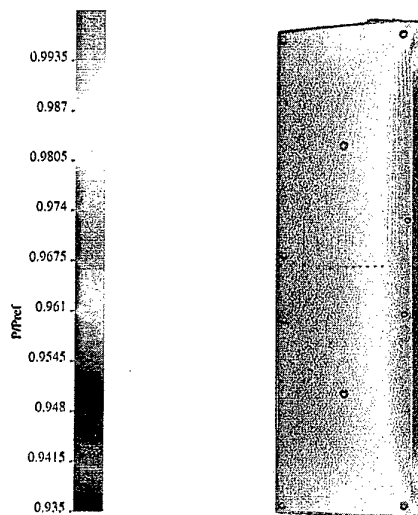
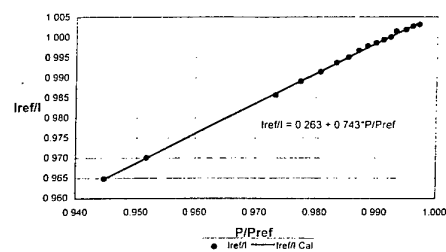


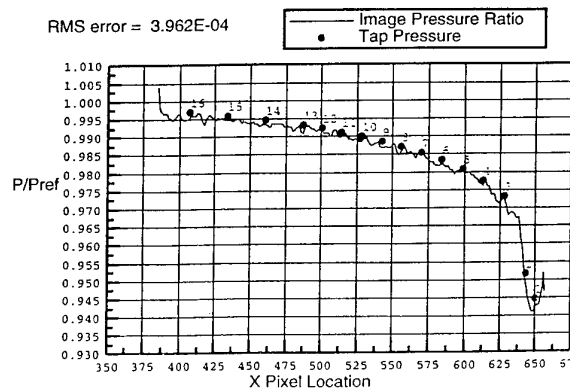
Figure 16. Hypothetical image ratio vs. Pressure ratio plot for 0012 wing at $M=0.3$.

Figure 17. Improved PSP image at 40 m/s, $\alpha = 5^\circ$.

RMS error = 9.702E-04

Figure 18. Improved PSP intensity and pressure ratio plots at 40 m/s, $\alpha = 5^\circ$.Figure 19. PSP image at 50 m/s, $\alpha = 7^\circ$.

RMS error = 3.962E-04

Figure 20. PSP intensity and pressure ratio plots at 50 m/s, $\alpha = 7^\circ$.

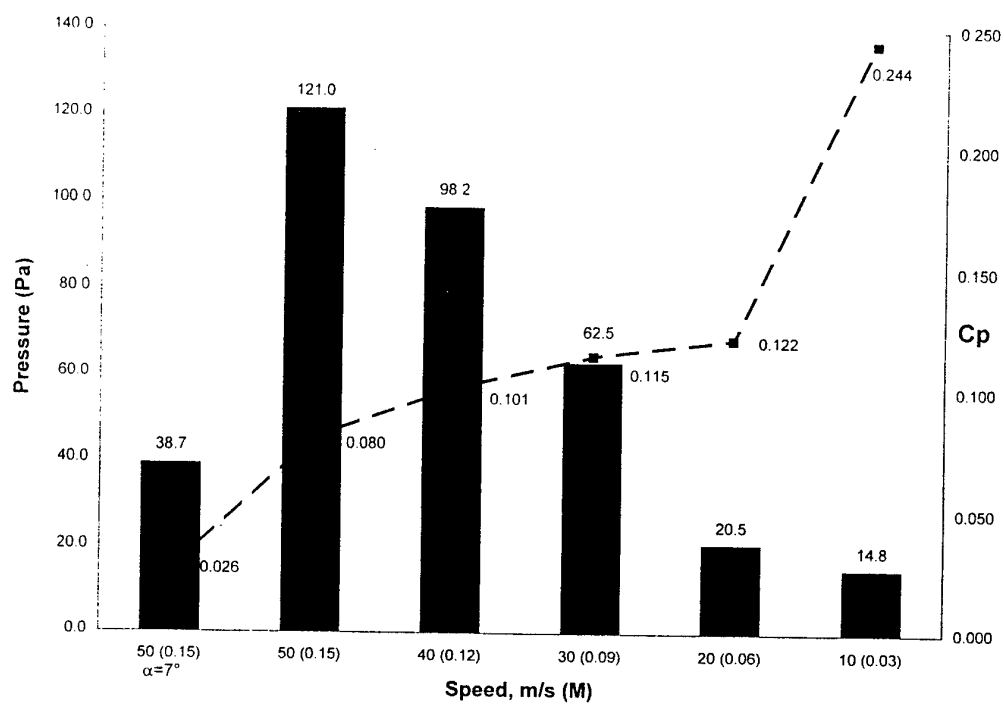


Figure 21. Best case Cp and pressure RMS calibration error for various low speed data runs. Actual values of pressure error appear over bar graphs. Actual Cp error values appear next to block.

The Status of Internal Strain Gage Balance Development for Conventional and for Cryogenic Wind Tunnels

(Invited Paper)

Prof. Dipl. Ing. B. Ewald
Darmstadt University of Technology
Petersenstrasse 30, D-64287 Darmstadt
Germany

1. Summary

The measurement of the aerodynamic forces is still the most important task in the wind tunnel at least for aircraft development work. Accuracy and reliability of the balance are key factors in this test technology. The urgent requirement for more and more accurate force testing leads to a demand for more and more balance accuracy. The most urgent demand in this field comes from the Cryogenic Tunnels like the NTF and the new European Wind Tunnel. Funding from the German Ministry for Research and Technology made possible about 12 years of uninterrupted research in internal wind tunnel balances, especially in cryogenic balances, at the Darmstadt University of Technology in co-operation with Daimler Benz Aerospace Airbus GmbH. The outcome of this effort is not only a cryogenic balance technology, which allows transport performance measurements in the ETW with a repeatability of less than one drag count with variable tunnel temperature but also a considerable improvement of balances for conventional tunnels. For this result all aspects of the balance technology had to be treated.

- For the balance design a computerised method was developed, which allows an optimisation of the structural design in a short time. Principal aspects of the design were studied with Finite Element analysis for optimised solutions.
- The technique of the electron beam welded balance was established successfully. This construction method gives considerable advantages with respect to design for optimum structure stiffness and low interference.
- The difficult problem of strain gaging and wiring for cryogenic environment with severe moisture conditions was solved as a result of lengthy efforts.
- For cryogenic balances a novel axial force measurement system was developed, which solves the problem of temperature gradient induced error signals. For residual errors of this type numerical correction methods are proven.
- For balance calibration a new strategy is used. A novel mathematical algorithm extracts a third order measuring matrix (no matrix inversion necessary) from the calibration data set. In a mathematical sense this is the best possible closed solution. In co-operation with Deutsche Airbus and the Carl Schenck Company a fully automatic calibration machine was developed for ETW. A smaller and simplified version of this machine is under construction at the Darmstadt University of Technology.

- **Finite element** analysis turned out to be a powerful tool in the development of optimised balance structures. Novel balance structures with minimised linear and non-linear interference and with minimised sensitivity against temperature gradients have been developed.
- For **half model testing**, which is a more and more important technique in transport development, compact half model balances have been developed and constructed. The crucial problem of temperature sensitivity of such balances was successfully solved by FEM optimisation.

In October 1996 an „International Strain Gage Balance Conference“ was organised by NASA Langley. Some comments on this conference will be given in this paper.

2. Introduction

The successful design and development of commercial transport aircraft depends (among many other problems !) on excellent aerodynamics. Especially the flight performance reacts very sensitively on aerodynamics. Since flight performance must be guaranteed to the customer long before the first flight of the prototype, the success of the aircraft depends heavily on wind tunnel tests with the utmost accuracy. This ever rising requirement for accuracy in wind tunnel testing and especially the challenge of precise force testing in cryogenic wind tunnels gave a strong impetus for strain gage balance research in the recent past. Since accuracy limits for conventional strain gage balances are set mainly by thermal effects, the target to achieve at least the same or possibly even better accuracy with cryogenic balances in cryogenic tunnels is an extremely difficult task. For the research work on cryogenic balances a target of one drag count repeatability for transonic transport performance testing was set.

To achieve considerable improvements compared to balances known and used today, a single clever idea respectively a single successful detail improvement is not sufficient. A systematic search through all parts and aspects of balance technology and the improvement of all details of this technology to the limits of the available technology is necessary. The important parts of the technology are :

- Design philosophy
- Design computation and optimisation
- Balance joints
- Selection of spring material for the balance body
- Material heat treatment
- Balance fabrication methods

- Strain gage selection and wiring method
- Moisture proofing respectively cryogenic environment proofing
- Data acquisition electronics
- Mathematical calibration algorithm
- Calibration equipment
- Strategy of balance use in the wind tunnel

The aim of the balance research at the Darmstadt University of Technology was to improve each of these partial aspects of balance technology to the scientific limits available today. Due to this research in Cryogenic Balances many improvements also for balances for conventional wind tunnels resulted.

In this paper only some of the topics mentioned above are described in detail :

- Design philosophy
- Design computation and optimisation
- Balance joints
- Balance fabrication methods
- Mathematical calibration algorithm
- Calibration equipment
- Cryogenic balances
- Half Model Balances

For more details on the other topics see the references.

3. Design Philosophy

For a successful balance design some essentials must be fulfilled :

1. *Choose the balance ranges as close as possible to the actual measuring task. In defining the ranges include the consideration, that ranges of the balances may be overloaded, if other components are not fully used in the tests. This overload capacity of a balance normally is defined by the 'load rhombus'.*
2. *Choose the geometric dimensions of the balance as large as allowed by the available space in the model.*
3. *Design the balance structure for maximum stiffness.*

The first essential requires the design of dedicated and tailored balances for the different tasks of a wind tunnel. As an example for a typical transport configuration development model matched in scale to the test section dimensions in a transonic wind tunnel at least three different balances are required for high accuracy testing:

- Very sensitive balance for cruise condition L/D optimisation work.
- Less sensitive balance for cruise condition work including buffet tests, maximum lift tests and M_{DIVE} tests.
- Envelope balance for stability and control tests up to M_{NE} including full control surface deflections and large angles of attack and yaw.

This requirement results in a numerous and expensive balance equipment for a wind tunnel but improves tunnel accuracy very much.

The maximum load capacity of a balance design within a fixed diameter is limited even if an ultra high tensile strength steel (High Grade Maraging Steel) is used. In our balance design method we introduced a balance load capacity parameter S , which is defined as

$$S = \frac{Z \cdot l^* + M_y}{D^3} \quad [N / cm^2]$$

The characteristic length l^* of the balance is defined as the distance from the reference centre to the end of the active part of the balance, see Figure 1. So this „Balance Capacity Parameter“ is a simplified measure of the bending stress in the balance body close to the balance connection to model or sting, which may be a cone or a flange. In most balance designs this is the critical position with respect to stress.

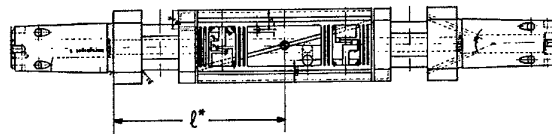


Figure 1 Characteristic Length

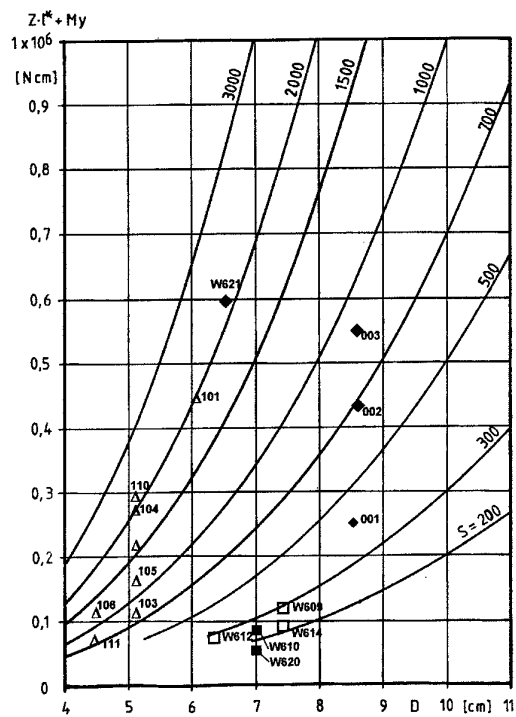


Figure 2 : Balance Load Capacity Diagram

Figure 2 shows a load capacity diagram for a range of balances with diameters between 40 and 110 mm. A group of curves of constant load capacity parameter S is plotted in the diagram. The messages of this figure are :

- Beyond a value of $S = 2000 \text{ N/cm}^2$ the design of a precise balance including an axial force system is not possible.
- For a transport performance high precision balance the load capacity parameter should not exceed $S = 500 \text{ N/cm}^2$.

Even lower load capacity parameters are recommended for optimum precision in drag measurement, if the space in the model allows for the larger diameter.

The third essential mentioned above - high stiffness of the balance body - is difficult to achieve with the conventional balance fabrication process by EDM (Electric Discharge Machining). With this method all internal cuts in the balance body must be accessible for the electrode from the outer side of the balance body. This compromises the stiffness requirement. So the fulfilment of the stiffness requirement is mainly a question of the fabrication method.

The ultimate solution of this problem is the Electron Beam Welded Balance concept, which was developed by the author at VFW (now Daimler Benz DASA, Bremen) more than twenty years ago. The balance is fabricated from four pieces, which are prefabricated to the final dimensions of all internal surfaces and welded together by electron beam welding. All external machining including opening of the flexure systems is done after welding. The production steps are clarified by the Figures 3.

Provided that a proper material is selected and a sophi-

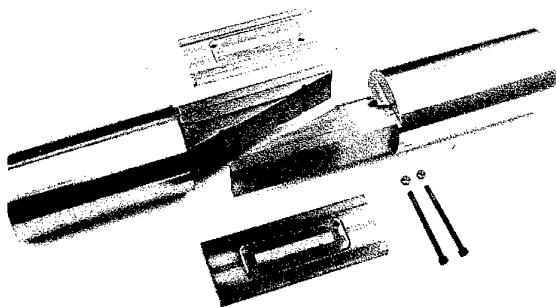


Figure 3a. Prepared Balance Parts

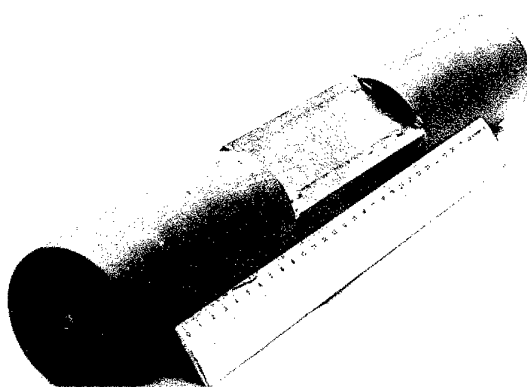


Figure 3b. Welded Balance Body



Figure 3c. Finished Balance Body

sticated heat treatment after the welding process is done, full material strength is restored in the welding zone and the finished balance is a one piece balance and - with respect to strength and hysteresis - definitively behaves like a one piece balance. In a polished cut of the welding seam the welding zone is hardly visibly.

The concept of the Electron Beam Welded Balance turned out to be highly successful and was used since the invention for all balances constructed by the Deutsche Airbus GmbH and by the Darmstadt University of Technology. This fabrication method gives complete freedom in the internal design of the balance structure and allows a much stiffer design of the balance.

4. BALANCE DESIGN COMPUTATION AND OPTIMISATION

A strain gage balance is a complicated piece of structure with a very large number of dimensions. So the balance design can not be achieved as a closed solution from the external dimensions and the required component ranges.

At the Technical University of Darmstadt the design computation is done with the interactive computer programme „SEKOWA“. With each step this programme completely computes the stress situation at all critical positions of the balance body and some additional characteristic parameters. All results are printed. The user checks the results and according to his experience with the design process he modifies one or several geometric dimensions. Each step is designated as a "RUN". An experienced balance designer needs about 40 to 60 runs for a final satisfying result or for the understanding, that a good balance with the specified ranges can not be designed within given dimensions. This work can easily be done in 2 or 3 hours. The computation is based on basic stress and strain formula for short bending beams and short torsion beams. Provision is made in the programme for notch stress concentration. The computer programme also creates overload diagrams similar to the conventional overload rhombus.

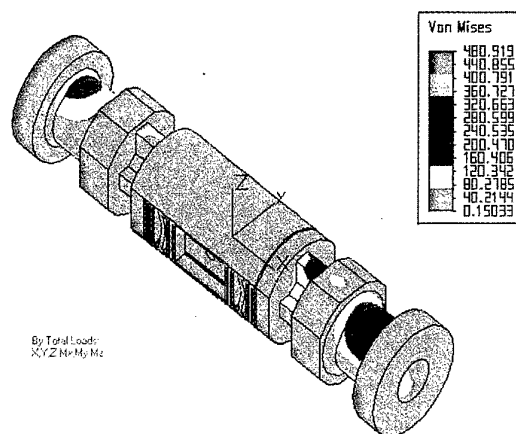


Figure 4. Balance W617, FE Computation

The use of finite element analysis for routine balance design is not possible, since the discretisation of the complicated structure with many modifications for the

optimised design is to laborious. Nevertheless for principal optimisation of strain gage balance designs finite element analysis proved to be an extremely valuable and strong tool, this was demonstrated by the work of Junnai Zhai [22] at the Technical University of Darmstadt. Work on balance optimisation with the instrument of finite element analysis is continued at the Technical University of Darmstadt. Figure 4 shows the stress distribution of the balance W 617 under full combined loads computed by finite element analysis.

The analysis of balance structures by the Finite Element Method demonstrated, that the computation and the minimisation of linear and non-linear interference effects is possible by this method. For more details on this work see reference [28].

5. Balance Joints

An internal balance is interfaced to the model at the front end and to the tail sting at the rear end. These joints shall

- carry large loads
- have an absolute positive fit
- be self-adjusting
- be easy to assemble and to disassemble

Efforts for standardisation of joints were unsuccessful up to now. There are at least as many different joint designs

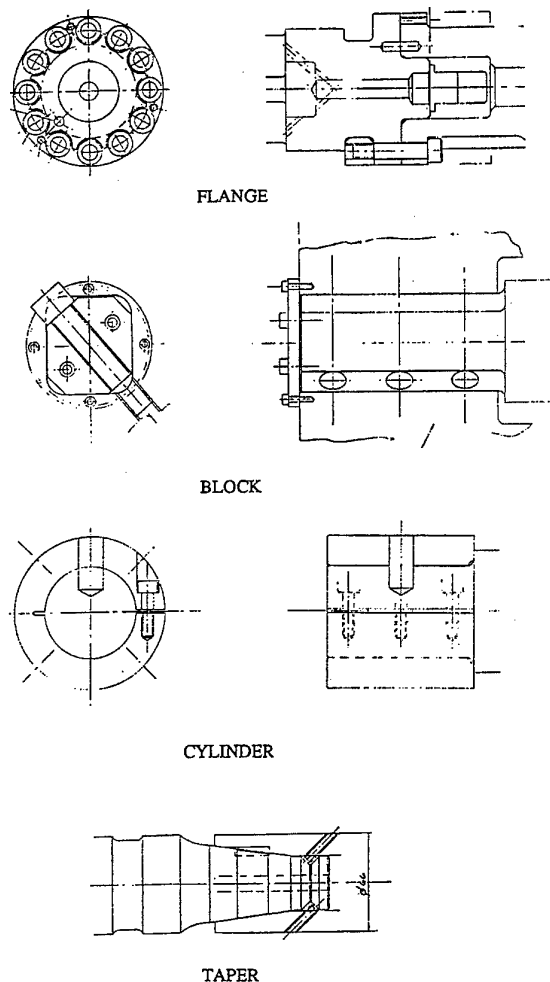


Figure 5 : Conventional Balance Joints

as there are balance designers over the world.

Figure 5 demonstrates some conventional balance joints. The most common joint is the taper joint since it transfers the largest loads. Nevertheless there are serious problems with this joint. For an optimum fit the taper is difficult to machine. With slender cones the taper joint is difficult to disassemble and with a more steep cone this joint needs large forces from the bolts or keys for a reliable fit.

The flange joint has a lower load capability but otherwise is superior in any respect. Fabrication is simple. The joint is self centring and very easy to assemble and to disassemble. With correct pre-tightening of the screws this is a very reliable joint with positive fit. For transport configuration measurements even in pressurised transonic tunnels the load capability is sufficient and this joint should be the first choice. It is well proven in the DNW and also in the cryogenic ETW.

Block and cylinder joints are sometimes used for the balance-model joints. Nevertheless at least for transport configuration models also for the balance-model joint the flange is the superior solution.

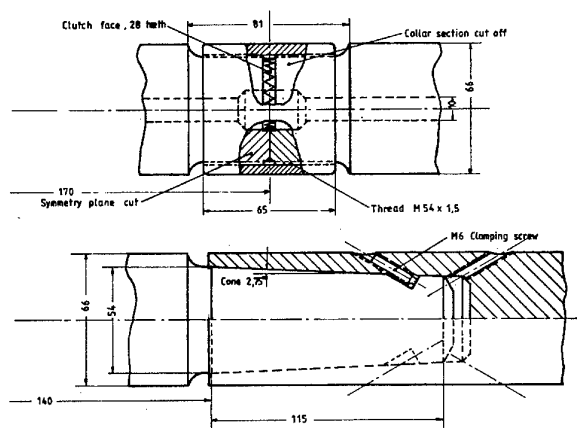


Figure 6 : Comparison of clutch joint and taper joint

Figure 6 gives a comparison of the taper joint with the more unconventional clutch joint. An analysis done during the Balance Pre-Design Study for the ETW demonstrated a load capacity of about 80 to 90 % of the taper joint. The clutch joint offers very simple assembly and disassembly with excellent self centring. A separate roll key is not required. We recommend this joint for highly loaded balances.

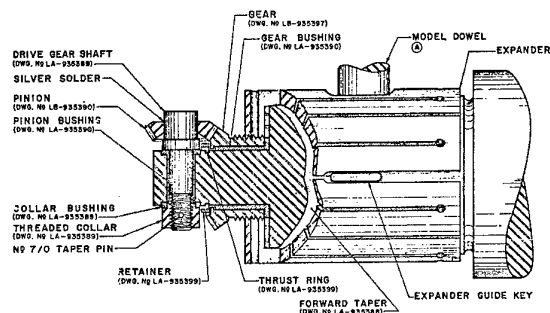


Figure 7 : NASA LaRC Expanding Sleeve Joint

A very interesting solution for the balance-model joint is shown in Figure 7. This joint is operated by an expanding sleeve with a cylindrical outer surface. So in the model only a cylindrical bore is required, which simplifies model manufacture. Figure 7 demonstrates, that even an assembly from outside the fuselage is possible with the bevel gear. This joint may not give the absolute maximum of load capability but is comfortable for the tunnel engineer.

The main problem of the balance joints is the total absence of any standardisation. Here is a most fruitful working field for balance designers, wind tunnel engineers and model designers.

6. Balance Fabrication Methods

A main feature of our balance fabrication methods was outlined already in Figure 3 (see above, chapter 3). The Electron Welded Balance concept used since about 20 years was highly successful. Nevertheless the success of this concept depends on the availability of top class welding equipment and experience.

Another important part of the balance fabrication methods is heat treatment. Hysteresis, which is a common feature of maraging steel, can be reduced to a very low level by proper heat treatment, see [17]. Also the degree of the final ageing process has a large influence on hysteresis.

Proper selection of strain gage types, treatment of gages, gage application and gage wiring may have a large influence on the final balance quality. Thermal zero shift can be reduced very much by matching the gages used in one bridge for harmonised thermal behaviour. This successful method was first proposed by Judy Ferris from NASA Langley. Another method to reduce thermal zero shift is the use of Poisson gages whenever possible. This allows a close concentration of the gages wired in one bridge. Utmost care and a long experience of the gage application operator is a matter of course in high quality balance fabrication.

Moisture protection is most important for long term balance reliability. In this field improvements are still welcome. Sputtering of the completely applied and wired balance may be a future solution but is still in development.

7. Mathematical calibration algorithm

Balance Calibration is still the field with the largest improvement potential for balance accuracy. Improvements may be realised as well due to improved calibration algorithms as due to improved calibration equipment.

The first problem of balance calibration is the choice of the mathematical description of the balance behaviour. For a long time the second order calibration was the standard method :

$$S_i = R0_j + \sum_{j=1}^6 A_{ij} F_j + \sum_{j=1}^6 \sum_{k=1}^6 B_{ijk} F_j F_k$$

where S_i is the signal of the strain gage bridge dedicated to the component „i“. With a complete calibration for all load combinations this results in a calibration matrix

with 168 coefficients. Since a long time we changed this description to a third order matrix :

$$S_i = R0_j + \sum_{j=1}^6 A_{ij} F_j + \sum_{j=1}^6 \sum_{k=1}^6 B_{ijk} F_j F_k + \sum_{j=1}^6 C_{ij} F_j^3$$

Only the third order description is able to describe symmetrical non-linearities in the positive and negative load direction. Recently this method was also adopted by other balance engineers. The third order matrix has 204 coefficients.

During the International Strain Gage Balance Conference at Langley even higher order matrixes for the description of the balance were considered. The author of this paper is pessimistic with respect to such considerations. The extraction of the much higher number of coefficients from the calibration data set calls for much larger data set and hence for a much more lengthy calibration.

The optimum accuracy is achieved from the calibration, if the calibration covers no load conditions outside of the load ranges achieved during a specific wind tunnel test, provided, that inside this load range a sufficient number of calibration points are available. So after completion of a test campaign an additional OFF LINE evaluation can be made with a balance matrix extracted from calibration load conditions only which are inside the load conditions of the test.

An even more promising idea is to evaluate a special balance matrix for any data point recorded during the wind tunnel test. For this evaluation the available calibration data points are weighted with a factor which is inversely proportional to the „distance“ of the calibration point from the actual balance condition. This idea calls for a very fast balance computer. Feasibility studies are under work at our University.

Another mathematical problem of balance calibration is the method to extract the balance matrix from the calibration data set. Most balance engineers use the principle idea, that from the calibration data set a „calibration matrix“ is evaluated in the form :

$$\text{Signals} = \text{Function of Loads}$$

This matrix is inverted to the form required for the evaluation of measurements :

$$\text{Loads} = \text{Function of Signals}$$

Since for a non-linear matrix an inverted matrix does not exist, for the inversion approximations have to be used with a resulting loss of accuracy.

In principle there is no mathematical difference between loads and balance signals in the calibration data set of a balance. So we changed the method completely and deduce directly a matrix

$$\text{Loads} = \text{Function of Signals}$$

from the calibration data set. This evaluation is possible also from a calibration data set, where the load conditions are mixed loadings of all components. This occurs with some types of automatic calibration machines, where the desired components or component combinations are superimposed by small loads in the other components. For more details see [20], [26].

8. Calibration Equipment

The modern alternative to the well known conventional calibration rig with calibration force generation by dead-weights is the Automatic Calibration Machine. Several designs have been fabricated up to now; a very successful one is the ETW Automatic Balance Calibration Machine designed by the Darmstadt University of Technology and the Schenck Company at Darmstadt.

Nevertheless also the conventional Calibration Rig got some development. Figure 8 shows a relatively small rig for Normal Force ranges up to 4000 N which was designed recently by the Darmstadt University of Technology. The most modern part of this machine is the balance signal acquisition hardware and the machine's software. This software guides the operator through the calibration process, so also operators with little training in balance calibration are able to perform professional calibrations. For more details see [29].

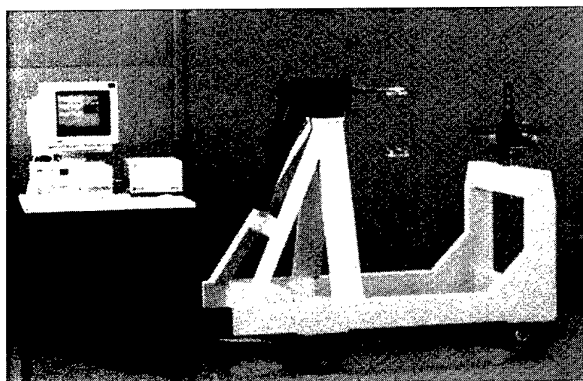


Figure 8 : Conventional calibration rig with data system

A careful manual calibration, especially for a high capacity balance, consumes a lot of man power and lasts up to several weeks. The appearance of the cryogenic tunnel at the latest rose the requirement for an automatic balance calibration process since the temperature as an additional balance calibration parameter multiplied the amount of work for a balance. So after a careful pre-design study the ETW machine was developed. Figure 9

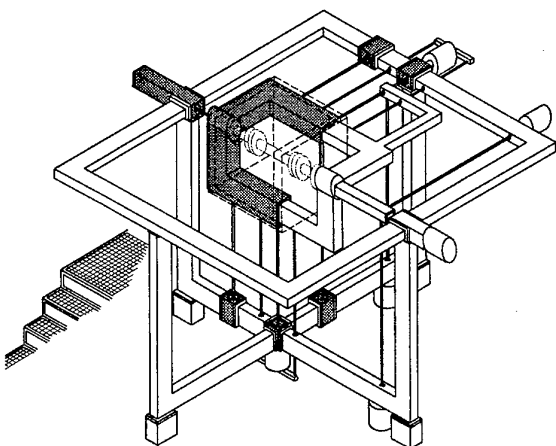


Figure 9 : Measuring part of ETW Calibration Machine

demonstrates the functional principle of the machine.

With this machine the functions '*calibration load generation*' and '*calibration load measurement*' are totally separated. The Internal Balance is connected with its model end to a six component force measuring device similar to an external wind tunnel balance. This device (the '*measuring machine*') measures the calibration loads applied to the balance precisely in the axis system of the model end of the balance. The '*Master Calibration Matrix*' of this measuring machine allows for the small misalignment resulting from the elasticity of the connection between balance and measuring machine. In Figure 9 the elements of the measuring machine are accentuated by dots on the left side; the force generating system is located on the right side of the Internal Balance. The perfect separation of calibration load generation and measurement of the component loads contributes largely to the excellent accuracy of the machine.

The loads are generated by push-pull pneumatic load generators acting on a loading frame connected to the sting end of the balance. Since the loads are measured precisely at the model end, load generation can be done rather crude and fast. When loads are generated due to its elasticity the loading frame becomes misaligned and one gets a mixed loading, where the desired loads generated by one or more pneumatic cylinders are superimposed by small loads in the other components. This poses no problems, since all components are measured by the measuring machine precisely. Of course the software algorithm must be able to evaluate the calibration loads from these mixed loading data sets.

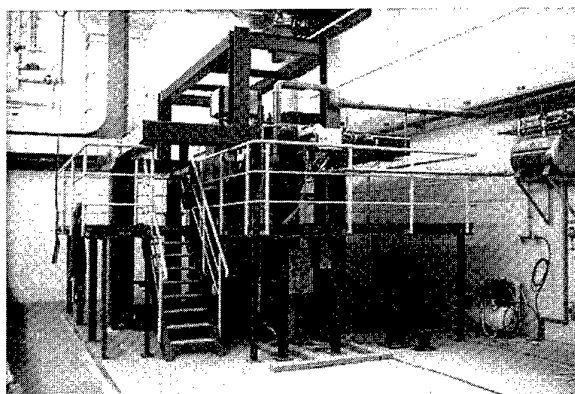


Figure 10 : ETW Automatic Calibration Machine

Figure 10 shows the „ABCM“ in the ETW Calibration Lab. The Normal Force capacity of the ETW machine is 25 000 N.

The calibration of cryogenic balances asks for a full force calibrations at several temperature levels between ambient and 100 K. So the machine must allow to condition the balance through the total temperature range of the cryogenic tunnel. For a high precision calibration the balance must be conditioned also at low temperatures without any spatial temperature gradients in the balance structure. Nearly all balance designs react with false signals on temperature gradients. So a force calibration must be done without any gradients and a gradient calibration must be done separately.

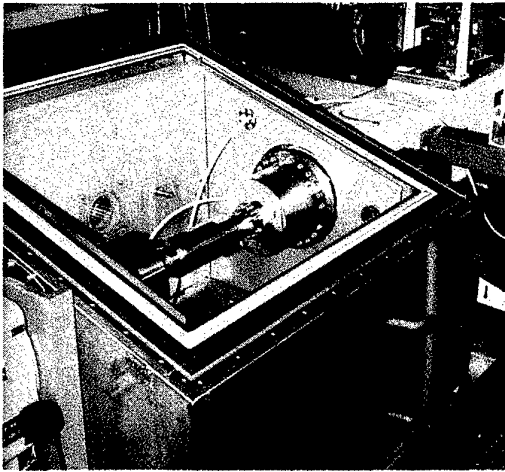


Figure 11 : Climate Chamber of ETW Machine

Figure 11 shows a balance installed in the sophisticated climate chamber of the ETW Machine. Much development was necessary for the joints between balance and machine to get a near perfect temperature isolation and a high stiffness and rigidity for the calibration loads. The climate chamber temperature is controlled by liquid nitrogen injection.

The ETW machine allows a complete force calibration including all single loads and all combination of two components in one working shift.

According to all experiences with the ETW machine a second generation machine was designed at the Darmstadt University of Technology. Figure 12 shows the design principle.

The main difference to the ETW Machine is the arrangement of the loading frame and the load generators. This new arrangement allows less

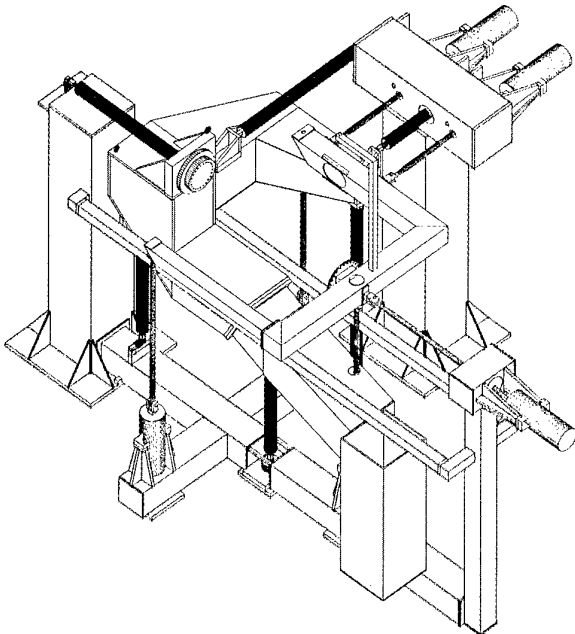


Figure 12 : Second Generation Calibration Machine

interference between the different load generators and so an even faster operational speed. The design of the load generators is much simplified.

A second generation machine with a Normal Force capacity of 6 000 N, which will be equipped with a climate chamber for cryogenic balances, is presently under construction at the Darmstadt University of Technology. This machine will be available on a commercial basis also in other load ranges.

9. Cryogenic Balances

Engineers familiar with strain gage balances know pretty well, that the accuracy of these instruments normally is limited by thermal effects. So the design of a cryogenic balance, which may be used in a tunnel environment between ambient temperature and 100 K and in an appreciable part of this range even during a single tunnel run, is a terrific challenge. Since the available balance space in most wind tunnel models does not allow the installation of a sophisticated climate chamber for the balances, unheated balances are normally used.

The designer of a cryogenic balance has to fight with the following problems :

- Avoidance or correction of zero and sensitivity shift of the strain gage bridges over large temperature ranges.
- Insensitivity of strain gage application and wiring against the cryogenic environment down to 100 K.
- Moisture proofing
- Avoidance or correction of false signals caused by spatial temperature gradients in the balance body.

When we started cryogenic balance development for the Tunnels KKK and ETW, we were especially frightened by the last effect of this list. With conventional balances we experienced large false signals due to temperature gradients. The operational concept of the ETW asked for up to 40 degrees tunnel temperature change in a 20 minute run, so temperature differences of up to 5 degrees centigrade could be expected over the active balance length.

A special arrangement of the axial force elements was developed, which solved this problem satisfactorily. Figure 13 shows the balance W 617, which we constructed for transport configuration measurements in ETW.

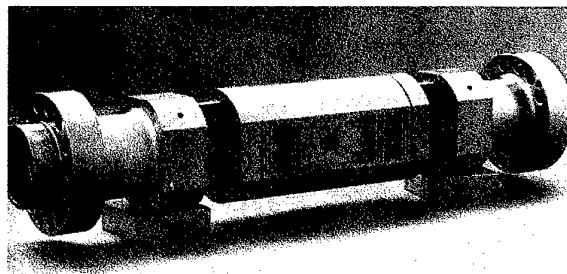


Figure 13 : ETW Transport Balance W 617

There are two axial force elements placed in the middle of the flexure groups. An axial force bends the axial force bending beams in the same direction, while a

temperature difference between the upper and the lower outrigger beam results in an opposite bending of these beams. So if the signals of the front elements and the aft elements are added, the effect of the temperature difference is deleted. Fortunately temperature differences of the upper and the lower outrigger beams are the overwhelming effect of temperature gradients at all. This idea worked very successful. Small residual sensitivities against temperature gradients can be reduced even further by trimming the individual sensitivity of the front and aft axial force system.

Another measure against temperature gradients is also demonstrated by the balance W 617 (see above). This balance is fabricated entirely from Copper Beryllium alloy. This alloy is not only famed as an excellent spring material with extremely low hysteresis; its thermal conductivity is higher than that of maraging steel by a factor of six. So temperature differences in the balance body vanish much faster.

With respect to the zero and sensitivity shift valuable preparatory work was done by Judy Ferris from NASA LaRC [13]. She introduced the idea of gage matching. This means, that the thermal behaviour of the individual gages are measured before final application and that only closely matched individual gages are used in one bridge. We did further work on this method and found it to be very successful. Also the successful use of gages especially trimmed for Young's Modulus / K-factor correction in the cryogenic range was initiated by Judy Ferris.

The sensitivity of gage application (bonds!) and wiring posed no real problem, the gage manufacturer offered satisfying materials and methods for the cryogenic range with one exception only, and that is moisture proofing.

In cryogenic operations and especially when the cold balance comes into contact with humid air, a lot of moisture develops on the balance. The moisture proofing materials offered by the gage manufacturers are not sufficient for these hard conditions. Extremely careful multiple and very thin coatings with nitril rubber is the best method we found up to now. Further improvements by new developments are welcome in this field.

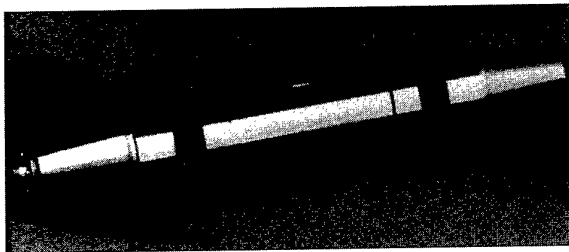


Figure 14 : ETW High Capacity Balance W 621

Figure 14 shows another cryogenic balance fabricated for the ETW. The balance W 621 offers the maximum possible load ranges in the given dimensions. With this very compact balance the twin axial element design demonstrated in Figure 13 was not possible. Correction of temperature gradient induced false axial signals is done with this balance by a temperature measurement

with platinum elements along the upper and lower outrigger beam.

10. Half Model Balances

For transport aeroplane wind tunnel development half model testing becomes more and more attractive. In a given wind tunnel the half model technology allows an increase of the Reynolds Number by a factor of two with reduced model costs. The half model method is unable to produce accurate total forces and moments, especially the drag force accuracy is reduced. Since most of the wind tunnel test are evaluated on an incremental basis, the reduced accuracy of the total forces is no real disadvantage.

In the past half model balances have been built in different technologies. Some examples have been designed like a very compact external balances built up from elements like rods, levers and load cells, other half model balances follow the design principle of internal balances fabricated from a single piece of metal. Recently the latter design principle was used nearly exclusively. We designed half model balances following this principle only.

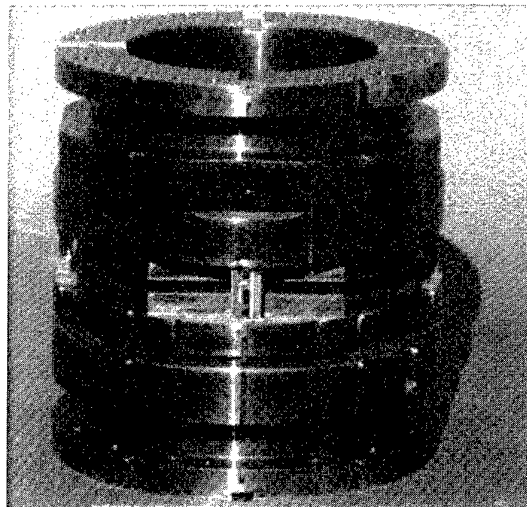


Figure 15 : Half Model Balance W 519 for the KKK

Figure 15 shows a half model balance designed and fabricated for the cryogenic Low Speed Tunnel KKK at Cologne. The Normal Force capacity of this balance W 519 is 3500 N and the diameter is 250 mm. In Figure 15 the balance is shown just ready for gaging.

Past experience showed, that balances of this type are very sensitive against temperature gradients. So obviously there was no chance to use this balance as an unheated balance and let its temperature float with the tunnel temperature. From the very beginning we decided together with the KKK staff to install this balance in an isolated and heated environment. The installation of the balance is shown in Figure 16, this installation was designed and fabricated by the DLR.

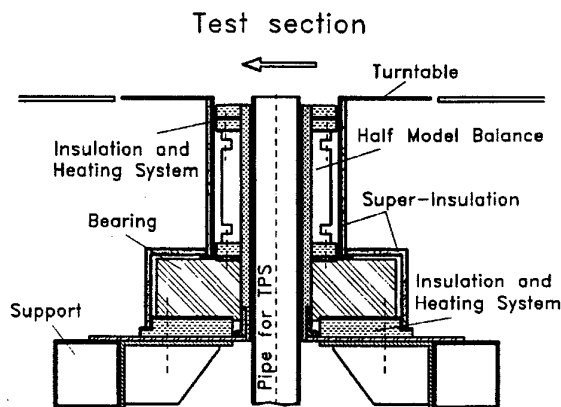


Figure 16 : Half Model Balance Installation in KKK

We found out, that we underestimated the temperature gradient sensitivity of the balance as well as the difficulty to avoid any temperature gradients by isolating and heating. Very sophisticated development work on the isolation and conditioning system was necessary to get this balance into satisfactory operation.

For future half model balances we performed a detailed finite element study on the temperature problem of such balances. We found a special design of the connection between the active balance block and the end flanges, which keeps all distortions away from the active balance block and thus reduces the temperature gradient sensitivity by at least one order of magnitude. A second half model balance for the KKK with different load ranges and a half model balance for the Indonesian Transonic Speed Tunnel will be fabricated according to this design. The details of this design are still a matter of patent pending.

11. Future Development

The never ending search for improved performance and better economy of transport aeroplanes requires improvements of all development tools, including wind tunnel balances. So we should look into the future of internal balances.

For about half a century the basic principle of internal balances did not change, they are still a metallic spring element and the distortions caused by the forces are measured with strain gages. Up to now no other basic force measuring principle turned out to be a promising alternative. So at the moment there is no other way for internal balance improvement than patient and careful work on all items of balance design, fabrication and calibration like stated in the introduction.

The most important improvement potential may be found in the fields of calibration theory and calibration equipment. The other promising field is to design the balances for less sensitivity against temperature gradients.

One should well bear in mind, that vast experience with balances and permanent work in this field is necessary to create progress. Internal wind tunnel balances are fabricated in many organisations in the world, but in most of these places the work on balances is subcritical, that means not intensive enough to create technological

progress. A concentration of balance development and fabrication at a few places would improve this situation very much.

Another deficiency is the lack of literature on internal balances. Neither for the information of the average wind tunnel engineer on balance utilisation and calibration nor for the further education of balance designers really useful literature on the subject is available. The author proposed to the Fluid Dynamics Panel of AGARD to collect all the available know how on internal balances in an AGARDograph. Hopefully this proposal will be approved by AGARD.

REFERENCES

- [1] E. Graewe, "Development of a Six-Component Balance for Cryogenic Range". Forschungsbericht W 84-022 BMFT 1984
- [2] Prof. B. Ewald, "Grundsatzuntersuchung zum Temperatur-Verhalten von DMS-Axial-Kraftteilen", BMFT LVW 8420 10, Nr. 10/85 1985
- [3] B. Ewald, "Development of Electron Beam Welded Strain-Gage Wind Tunnel Balances", Journal of Aircraft Volume 16, May 1979
- [4] Prof. B. Ewald, G. Krenz, "The Accuracy Problem of Airplane Development Force Testing in Cryogenic Wind Tunnels", AIAA Paper 86-0776, Aerodynamic Testing Conference, March 1986
- [5] Prof. B. Ewald, E. Graewe, "Entwicklung einer 6-Komponenten-Waage für den Kryo-Bereich", 3. BMFT-Status-Seminar, Hamburg, May 1983,
- [6] Prof. B. Ewald, E. Graewe, "Development of Internal Balances for Cryogenic Wind Tunnels", 12th ICIASF, Williamsburg, VA, June 1987,
- [7] Prof. B. Ewald, "Balance Accuracy and Repeatability as a Limiting Parameter in Aircraft Development Force Measurements in Conventional and Cryogenic Wind Tunnels", AGARD FDP Symposium, Neapel, September 1987
- [8] Prof. B. Ewald, P. Giesecke, E. Graewe, T. Balden, "Feasibility Study of the Balance Calibration Methods for the European Transonic Wind Tunnel" Report TH Darmstadt A 37/88, January 1988
- [9] Prof. B. Ewald, Th. Balden, "Balance Calibration and Evaluation Software", Proc. Second Cryogenic Wind Tunnel Technology Meeting, ETW, Cologne, June 1988
- [10] Prof. B. Ewald, T. Preusser, L. Polanski, P. Giesecke, "Fully Automatic Calibration Machine for Internal Six Component Wind Tunnel Balances Including Cryogenic Balances", ISA 35th International Instrumentation Symposium, Orlando, Florida, May 1989
- [11] Prof. B. Ewald, P. Giesecke, E. Graewe, TH. Balden, "Automatic Calibration Machine for Internal Cryogenic Balances", Proc. Second

- Cryogenic Wind Tunnel Technology Meeting, ETW, Cologne, June 1988
- [12] Prof. B. Ewald, T. Preusser, L. Polanski, P. Giesecke, *"Fully Automatic Calibration Machine for Internal Six Component Wind Tunnel Balances Including Cryogenic Balances"*, ICIASF Congress, September 1989, Göttingen
- [13] Alice T. Ferris, *"Cryogenic Strain Gage Techniques used in Force Balance Design for the National Transonic Facility"*, NASA TM 87712, May 1986
- [14] Prof. B. Ewald, L. Polanski, E. Graewe, *"The Cryogenic Balance Design and Balance Calibration Methods"*, AIAA "Ground Testing Conference" July 1992, Nashville, Bericht A 99/92
- [15] Prof. B. Ewald, K. Hufnagel, E. Graewe, *"Internal Strain Gage Balances for Cryogenic Wind Tunnels"*, ICAS-Congress, Sept. 92, Peking
- [16] Prof. B. Ewald, E. Graewe, *"The Development of a Range of Internal Wind Tunnel Balances for Conventional and Cryogenic Tunnels"*, European Forum on Wind Tunnels and Wind Tunnel Test Techniques, Sept. 92, Southampton
- [17] H.F. Rush, *"Grain Refining Heat Treatment To Improve Cryogenic Toughness of High-Strength Steels"*, NASA TM 85816, 1984
- [18] Schnabl, *"Entwicklung eines numerischen Algorithmus und eines Rechnerprogramms zur Auswertung der Eichversuche an 6-Komponenten-DMS-Waagen."*, Technical University of Darmstadt, Diploma-Thesis A-D-69/87
- [19] Dipl.Ing. T. Balden, *"Ein neues Konzept zur Kalibration von Kry-Windkanal-Waagen"*, Deutsche Airbus Bremen, Proceedings of DGLR Jahrestagung 1993, Göttingen
- [20] B. Ewald, *"Theory and Praxis of Internal Strain Gage Balance Calibration for Conventional and Cryogenic Tunnels"*, 18 AIAA Ground Testing Conference, June 1984, Colorado Springs
- [21] G. Viehweger, B. Ewald, *"Half Model Testing in the Cologne Cryogenic Tunnel (KKK)"*, 18th AIAA Ground Testing Conference, June 1984, Colorado Springs
- [22] Junnai Zhai, Bernd Ewald, Klaus Hufnagel, *"An Investigation on the Interference of Internal Six-Component Wind Tunnel Balances with FEM"*, ICIASF '95, Dayton, Ohio
- [23] Prof. B. Ewald, *"Advanced Force Testing Technology for Cryogenic and Conventional Wind Tunnels"*, ICAS Congress 1994, Anaheim, California
- [24] Prof. B. Ewald, *"The Development of Advanced Internal Balances for Cryogenic and Conventional Tunnels"*, NASA International Symposium, October 1996, Langley, VA, USA)
- [25] Prof. B. Ewald, *"The Half Model Balance for the Cologne Cryogenic Tunnel (KKK)"*, NASA International Symposium, October 1996, Langley, VA, USA)
- [26] Prof. B. Ewald, *"Development and Construction of Fully Automatic Calibration Machines for Internal Balances"*, NASA International Symposium, October 1996, Langley, VA, USA)
- [27] Prof. B. Ewald, *"Design and Construction of Internal Balances for the German/Netherlands Winds Tunnel (DNW)"*, NASA International Symposium, October 1996, Langley, VA, USA)
- [28] M. Sc. Junnai Zhai, *"Optimization of Internal Strain Gage Wind Tunnel Balances with Finite Elements Computation"*, NASA International Symposium, October 1996, Langley, VA, USA)
- [29] Dipl.-Ing. M. Quade, Dr.-Ing. K. Hufnagel, *"The Development of a Modern Manual Calibration and Measuring System for Internal Balances"*, NASA International Symposium, October 1996, Langley, USA)

Summary Report of the First International Symposium on Strain Gauge Balances and Workshop on AoA/Model Deformation Measurement Techniques

John S. Tripp*, Ping Tcheng*,
Alpheus W. Burner#, and Tom D. Finley#

Mail Stop 238
NASA Langley Research Center
Hampton, Virginia 23681
USA

1. SUMMARY

The first International Symposium on Strain Gauge Balances was sponsored under the auspices of the NASA Langley Research Center (LaRC), Hampton, Virginia during October 22-25, 1996. Held at the LaRC Reid Conference Center, the Symposium provided an open international forum for presentation, discussion, and exchange of technical information among wind tunnel test technique specialists and strain gauge balance designers. The Symposium also served to initiate organized professional activities among the participating and relevant international technical communities.

The program included a panel discussion, technical paper sessions, tours of local facilities, and vendor exhibits. Over 130 delegates were in attendance from 15 countries. A steering committee was formed to plan a second international balance symposium tentatively scheduled to be hosted in the United Kingdom in 1998 or 1999.

The Balance Symposium was followed by the half-day Workshop on Angle of Attack and Model Deformation on the afternoon of October 25. The thrust of the Workshop was to assess the state of the art in angle of attack (AoA) and model deformation measurement techniques and to discuss future developments.

2. INTRODUCTION

The concept of an international strain gauge balance symposium was advocated in a technology assessment entitled "A White Paper on Internal Strain Gauge Balances." This internal document, published by LaRC staff members in March 1995, was based on an international survey of internal strain gauge balances conducted under contract in 1994-1995 (ref. 1). The conclusions of the white paper were presented to a peer review panel on wind tunnel testing technology, composed of selected leaders from major commercial and government aeronautical facilities, held in July 1995 at LaRC. The panel strongly endorsed the proposed international strain gauge balance symposium, which is the first of its kind.

Over 130 delegates from 15 countries were in attendance, including Australia, Canada, China, Finland, France, Germany, India, Indonesia, Israel, the Netherlands, Russia, South Africa, Sweden, United Kingdom, and the United States. The program opened with a panel discussion, followed by technical paper sessions, and guided tours of the National Transonic Facility (NTF) wind tunnel, a local commercial

balance fabrication facility, and the LaRC balance calibration laboratory. Vendor exhibits were also available.

The opening panel discussion addressed "Future Trends in Balance Development and Applications." The nine panel members included eminent balance users and designers representing eight organizations and five countries. Formal presentation of papers in technical sessions followed the panel discussion. Forty-six technical papers were presented in 11 technical sessions covering the following areas: calibration, automatic calibration, data reduction, facility reports, design, accuracy and uncertainty analysis, strain gauges, instrumentation, balance design, thermal effects, finite element analysis, applications, and special balances. A general overview of the past several years' activities of the AIAA/GTTC (Ground Testing Techniques Committee) Internal Balance Technology Working Group was presented. The group's activities has prompted sufficient interest among the foreign Symposium attendees, that a separate Euro-Asian International Internal Balance Working Group was contemplated. At the conclusion of the Symposium, a steering committee representing most of the nations and several US organizations attending the Symposium was established to initiate planning for a second international balance symposium, to be held within 2 or 3 years in the UK.

The Workshop on Angle of Attack and Model Deformation Measurement Techniques was held immediately following the Symposium for assessment of the state of the art in AOA and model deformation measurement techniques and to discuss future developments. Twelve presentations from industry and government in the United States, Europe, and Asia covered various AOA and model deformation measurement techniques, applications, and concerns. The Workshop concluded with an open panel discussion.

The following summaries of the panel discussion and selected technical papers were obtained orally and from video tape recordings of the presentations. The authors of this report disclaim responsibility for accuracy of the transcribed notes and regret any misinterpretations of the panelists' and symposium authors' intentions. Panelists and symposium authors should be contacted directly for further elaboration; contact information is available from NASA LaRC representatives.

* Co-Chairs of the International Balance Symposium

Authors of comments on Workshop on AoA/Model Deformation Measurement Techniques

3. PANEL DISCUSSION

The Symposium opened with a panel discussion entitled "Future Trends in Balance Development and Applications." The panel consisted of the following members:

Ron D. Law, Defense Research Agency (DRA), Bedford, UK, Panel Chair

Maurice Bazin, Office National D'Études et de Recherches Aéropatiales (ONERA), France

David M. Cahill, Sverdrup Technology Inc./AEDC Group, USA

Prof. Bernd Ewald, Technische Hochschule Darmstadt (TUD), Germany

Pieter H. Fuykschot, Nationaal Lucht-En Ruimtevaartlaboratorium (NLR), the Netherlands

Steven Hatten, Boeing Commercial Airplane Group, USA

James G. Mitchell, Microcraft, Inc., USA

Lawrence E. Putnam, NASA Langley Research Center (LaRC), USA

Paul W. Roberts, NASA Langley Research Center, USA.

Each panelist briefly presented his views regarding future trends in balance development and applications. Important areas covered included materials, temperature compensation, gauging, analysis methods, and calibration efficiency. The panel members agreed that the existing balance technology will continue to prevail in the foreseeable future, with only evolutionary improvements possible. No radically new basic technologies such as fiber optics techniques are expected to offer any competition in terms of accuracy and reliability. It was agreed that international standards for nomenclature, calibration procedures, accuracy reporting methods, etc. should be adopted in the future following the precedent of the North American Internal Balance Working Group, although agreement is not presently feasible. However, this Symposium is an important first step in establishing formal international discussions about these concerns, especially in regard to agreement on terminology. After the individual presentations a group discussion followed.

Selected observations from the panel discussion follow.

Ron D. Law, DRA Bedford, UK, Panel Chair

Stiffer balances are needed for tests at high angles of incidence under unstable flow conditions. Since the balance forms part of the spring system of the model and its supporting structure, unwanted dynamic oscillations within the balance itself will corrupt test data. Although an infinitely stiff balance would eliminate this problem, it is unrealizable. Stiffer balances are especially needed for half-models and for heavy models. Replacement of strain-gauged flexures with sensitive piezo-electric cells provides greatly increased stiffness with good signal output. The use of high-output platinum strain gauges provides high sensitivity for stiff designs although temperature sensitivity is greater. Composite materials, such as carbon-fiber layered flexures, have been suc-

cessfully tested in lighter weight balances used for low speed testing. Improved semiconductor strain gauges also offer increased sensitivity. Finite element analysis can be employed during design to predict balance dynamic behavior.

Maurice Bazin, ONERA, France

ONERA has developed balances which provide good drag-count resolution for all wind tunnel applications including cryogenic testing. Future trends are difficult to predict at present. Advanced technology may offer better ways of measuring strain, such as the use of doped materials or micro-laser techniques

David M. Cahill, Sverdrup Technology Inc./AEDC Group.

Analysis of elastic and anelastic hysteresis, and study of fabrication and heat treatment techniques for metallic and non-metallic materials are areas where additional emphasis is needed. Development of alternative techniques for strain measurement would be beneficial. Hardware as well as software compensation techniques for temperature effects are recommended. Calibration techniques need to be examined, including: the number of loadings required for calibration, application of combination loadings including third order and above, and the inclusion of calibration uncertainty analysis. Standardization is needed in the following areas: terminology for forces and moments, and the axis systems; the calibration matrix and the matrix format; treatment of calibration tares; data reduction to forces and moments by the non-iterative mathematical model and the iterative mathematical model; and inclusion of model weight as part of the tares during data reduction.

Prof. Bernd Ewald, TUD, Germany.

TUD has developed a new single-piece balance from copper-beryllium alloy for the European Wind Tunnel (ETW). Although copper-beryllium imposes some inconvenient manufacturing requirements, it is an excellent spring material, has very low hysteresis, and has very high heat conductivity. Tests of titanium alloy at TUD disclosed no detectable hysteresis indicating that it is a promising material for future balance fabrication. Machine calibration is seen as becoming mandatory because of its accuracy and reliability, and because of the excessive manpower requirements for manual calibration. The maximum resolution of the conventional strain gauge is on the order of 25×10^{-9} mm or approximately 1/20000 of the wavelength of visible light. It is unlikely that potential strain measurement alternatives can match this resolution at present. Electric and pneumatic lines bridging the balance in the test model produce measurement bias errors due to unknown residual forces. TUD has considered integrating these lines into the balance structure. The resulting effects of residual forces would then be removed by calibration.

Pieter H. Fuykschot, NLR, the Netherlands.

No major revolution, rather evolution, is seen in balance technology. Two major problem areas are interactions and temperature effects. Balances should be designed for minimum interactions and maximum linearity, rather than using calibration to remove their effects. Nonlinearity can cause bias errors due to rectification effects during dynamic test conditions, which cannot be corrected by calibration. Materials with a low coefficient of thermal expansion, such as titanium, should be considered. Compensation for tempera-

ture gradients is important. Balance convection screens can be installed within the model to reduce heat transfer within the flexures. Dynamic modeling should be done during the design phase to minimize resonant vibrations during tests. Standardized model-to-balance couplings should be adopted for inter-laboratory compatibility. Automatic calibration is an important future trend. The balance should be calibrated through zero load to attain positive and negative loadings rather than by mechanical inversion as usually done during manual calibration. The balance should be calibrated with couplings identical to those used during tests.

Steven Hatten, Boeing Commercial Airplane Group.

Corporate concerns have resulted in an emphasis on reducing the development cycle times for both production aircraft and for test models. Simplified designs and procedures are emphasized, such as parametric spreadsheet design tools. Parametric finite element models are employed to analyze stiffness and dynamic behavior. Older balances in the inventory are being recycled for new testing. External balance calibration is being automated. Balance users at Boeing are demanding improved balance measurement accuracy, especially in drag. Ways to increase drag accuracy are being investigated. Uncertainty due to mechanical hysteresis is being reduced via a redesigned model attachment interface. Effort is also being applied to thermal gradient correction methods for improved accuracy.

James G. Mitchell, Microcraft, Inc.

Progress in strain gauge balances has been slow, with 40-50 year-old strain gauge and design methodology still in use. The strain gauge balance design community should exploit new technology in related fields such as optics, microelectronics, and smart structures. Balance customers, i.e., test facilities and test engineers, are asking for "better, faster, and cheaper." The response is as follows: Better: Uncertainties can be reduced through study of calibration practices, increased load per unit diameter, increased stiffness, improved math models, and calibration using combined loadings. Faster: While balance design, fabrication, and gauging can be accelerated, the large opportunity is in the area of calibration with automated machines. Balance calibration times are reduced from days and weeks to a few hours. Cheaper: Reduced cycle times result in lower costs.

Lawrence E. Putnam, NASA LaRC, USA.

Comments were made from a wind tunnel user's point of view. LaRC balances must function over test environments ranging from cryogenic conditions at the NTF wind tunnel to high temperatures at the eight-foot high temperature structures tunnel. Drag uncertainty provided by LaRC balances, based on calibration laboratory data, is on the order of 0.6 drag counts, which is adequate for customer requirements. However, operational accuracy in the wind tunnel is worse. Temperature gradients during tests are a major source of uncertainty. Multiple calibrations are needed to estimate precision uncertainties which are not currently done with manual calibration. This is feasible only with automated calibration equipment. Improved balance robustness is needed to reduce down time during tests. Problem areas include strain gauges, cement, and moisture proofing.

Paul W. Roberts, NASA LaRC, USA.

Future improvements in balance design and performance can be expected in a number of areas. Areas in calibration include the experimental design, estimation of separate precision and bias uncertainties, and custom calibration for specific wind tunnel tests. The mathematical model will be extended to include higher order interactions. Although interactions and nonlinearities should be minimized, balance physical size constraints dictated by the test facility may preclude this. More complete uncertainty analysis than is now provided will be available. Real-time compensation for thermal gradients and other effects are being developed. More sensitive strain measurement sensors, although not presently feasible, can be expected over the long term. New fabrication methods with shortened production time are possible. Finally, automatic balance calibration systems are an essential need for the future.

4. OVERVIEW OF TECHNICAL PRESENTATIONS

The majority of the three-and-one-half-day symposium was devoted to 46 papers delivered in 11 technical sessions. A list of the scheduled paper presentations and authors is given in the Appendix. Several papers were not presented due to the authors' inability to attend the Symposium. Brief summaries of selected topics representing important areas of the balance technology are now presented.

4.1 Balance Design

Nearly half of the technical papers presented described unique balance design techniques. Several innovative axial section designs for improved sensitivity and reduced thermal effects were discussed. Finite element analysis methods have disclosed unexpected local stress concentrations, approaching yield limits of the material in some cases, which could not be readily predicted by conventional design methods. Varied techniques for thermal gradient characterization and compensation were described. State-of-the-art methods in strain gauge manufacturing and application were described. Other papers were given on conventional and unique balance applications, including unusual balance designs for special applications.

4.1.1 J. Zhai, TUD, Germany, discussed optimization of internal strain gauge balance design using finite element computation. The aim of the TUD study was to improve accuracy by reducing interferences (interactions) and by increasing stiffness. Sources of linear interactions include the structure, strain gauges, and manufacturing tolerance errors. Strain gauge effects include gauge factor, position, and direction. Product interactions result primarily from deformation of the material. Quadratic and cubic interferences arise from nonlinearity of the material. These effects can be reduced by structural redesign. The linear interaction on drag can be reduced by decreasing the stiffness of the measuring spring, decreasing spacing between measuring beams, and increasing the slope of the main beam. The shape of the drag sensing element can be changed to provide additional decoupling. TUD attained a 38% reduction in drag interaction by choosing suitable dimensions and a 92% reduction in drag interaction by use of a point-symmetrical configuration. Low stiffness causes large nonlinear interactions and a lower natural frequency of the model-balance-sting system which, in turn, increases measurement errors during dynamic test conditions. Stiffness in the X direction was increased 60% by changing the drag-sensing element from a bending beam to a

shear spring. Similarly, stiffness in the Z direction was increased 65% by changing the bending moment measuring system from a bending beam to a shear spring. Additionally, stiffness in the Z direction was increased 21% through the use of combined main beams.

4.1.2 Prof. Bernd Evald, TUD, Germany, discussed advanced internal balances for cryogenic and conventional wind tunnels. Only gradual improvements based on careful research and development are anticipated. Three general rules for balance users and designers include the following: selection of the load range to match the test requirements as closely as possible; employment of geometric dimensions as large as possible; and design of the balance structure to be as stiff as possible. Three types of balances are generally needed for industrial aircraft development: very sensitive balances for cruise optimization; less sensitive balances for buffet, maximum lift, and dive testing; and an envelope balance for stability and control, control surface deflection, and large AoA and yaw angle tests. Balances with high stiffness are difficult to fabricate with conventional electric-discharge machining techniques. Now, electron beam welding technology gives the balance designer complete freedom to fabricate any desired internal structure. TUD employs an interactive software package for design via fundamental stress and strain analysis methods. Research and optimization are done via FEA software. Maraging steels, which are good for electron beam welding, are used for cryogenic and conventional balances. Special heat treatment methods are applied to reduce hysteresis. Although some authorities advocate the use of heated balances for cryogenic use, Prof. Evald prefers balance designs which tolerate thermal gradients by mechanical cancellation methods and by electrical compensation. He proposes future development of a "black box" plug-and-play balance concept in which all necessary parameters would be stored in a memory chip integrated into the balance structure. The balance identification, calibration matrix, and electrical connection information would be stored on-board. The proper electrical connections and data reduction would be automatically configured by wind tunnel data systems. Future developments would also provide an optical telemetry link from the balance to the wind tunnel data acquisition system to eliminate mechanical bridging caused by strain gauge conductors.

4.1.3 The design philosophy of a high-quality balance at NASA LaRC is briefly presented. All LaRC balances are custom designed to meet the load ranges, physical size, thermal environment, and accuracy requirements for given research projects. Single-piece construction techniques using high-quality maraging steel are employed whenever possible. Most LaRC balances are of the direct-reading type; moment-type balances are typically used in extreme thermal conditions such as the cryogenic environment at the National Transonic Facility (NTF). All LaRC balances employ modulus compensated transducer quality strain gauges. Where extreme thermal environments are anticipated, a patented apparent-strain gauge-matching technique is used. Thermal compensation is provided by pure nickel wire placed in the Wheatstone bridge circuit to reduce temperature effects on the bridge output to less than 0.005 percent full scale per degree Fahrenheit. Balance temperatures and gradients are measured by means of resistance temperature detectors (RTD). These temperature measurements allow linear cor-

rections to be applied for thermal sensitivity shifts and second-order corrections for apparent strain.

4.2 Automatic Balance Calibration

Presentations were given describing four different automatic calibration machines at DRA-Bedford, CARDC, IAI, and TUD. Significant advantages of automatic calibration include manpower savings, decreased calibration time, expanded experimental loading schedules, the ability to apply multiple loadings, and improved calibration accuracy. However, differing results with respect to loading accuracy and repeatability were reported. Primary sources of calibration inaccuracy are load vector misalignment, force measurement sensor inaccuracy, and precise repeatability of the balance mechanical position within test fixtures. Highlights of reported experience with automatic calibration are summarized

4.2.1 China Aerodynamics Research and Development Center (CARDC)

CARDC reports the best calibration accuracy although verification data were not available. It is possible that the cited Chinese calibration accuracy is estimated based on the accuracy of the load cells used and the assumption that the system is perfectly realigned after each load application.

4.2.2 Israel Aircraft Industries (IAI)

Michael Levkovitch, IAI, gave an unscheduled presentation describing the IAI automatic calibration machine. He indicated that a new machine with a larger load capacity is under development. The presentation indicated that the IAI machine does not reposition to correct loading deflections, but rather measures deflections. Thus, inaccuracies in measurement of angular alignment may dominate the total machine uncertainty. The authors note that since the machine is not designed to function as a repositioning servomechanism, machine accuracy could be improved with better displacement measurement sensors. Without improved positioning measurement accuracy, the use of expensive highly accurate load cells would produce only marginal improvements in overall calibration machine accuracy at present.

4.2.3 Technische Hochschule Darmstadt (TUD)

A first generation automatic calibration machine was designed by TUD and manufactured by Schenk for the European Wind Tunnel (ETW.) A second generation prototype is being developed at TUD. The needs for machine calibration include manpower costs, reduced calibration time, avoidance of human errors, and convenient inclusion of temperature as a calibration parameter. The machine is able to generate loadings in any order in all possible component combinations up to sixth order, thus allowing estimation of third and higher order coefficients. Zero readings are obtained automatically. Loads are generated by actuators and measured independently by load cells, such that the actual applied loads are determined. The balance may be enclosed in a temperature-controlled chamber for cryogenic calibration. The design avoids thermal gradients during temperature-controlled calibration.

4.2.4 DRA Bedford

DRA recently developed a six-component precision automatic balance calibration machine for in-house use. Forces are applied using pneumatic actuators and are measured using sensors. Forces are applied such that the need for reposition-

tioning is avoided. An example was given of calibration of a balance to be installed away from its virtual center. Since the measured outputs depend on the moment arm length in this configuration, the balance must be calibrated at two positions to permit correction for positioning at any displacement from center during tests. The automatic machine facilitates the multiple calibrations necessary for this application. A second example illustrated static calibration of a dynamic balance by automatic machine where loads must be applied and removed quickly.

4.2.5 IAI Balance Calibration Consortium

In 1995 Microcraft established a consortium to calibrate selected balances using the IAI automatic calibration machine at the San Diego, California facility. Two papers related to this effort were given. A paper containing some of the calibration results is summarized in Section 4.3. A summary of the other paper is now presented.

4.2.6 IAI Machine Calibration of NASA LaRC Balance

Ping Teheng, NASA LaRC, presented a comparison of machine calibration accuracy versus manually loaded calibration accuracy. The paper contained a general discussion covering primarily data reduction and uncertainty analysis. Uncertainty analyses of eight sets of machine calibration data indicated that its calibration accuracy is adequate for many applications, providing better than 0.5 percent full-scale accuracy. The authors believe that manual calibration, albeit time consuming and labor intensive, is necessary to attain the best calibration accuracy at present. The IAI machine was user-friendly, easy to operate, with sophisticated supporting software providing immediate data reduction following calibration.

Inconsistencies noted among the eight calibration data sets were traced to poor repeatability of the balance center position caused by slack in the balance-to-test-fixture attachments following removal and re-installation of the balance. It was of interest to note that comments were received describing "spatial relocation error" problems with the Schenk automatic calibration machine at ETW similar to those observed by LaRC during IAI automatic machine calibrations at San Diego.

4.2.7 Comments by Participants in IAI Calibration Consortium

Additional comments were received from other Consortium participants regarding the consistencies of the automatic calibration machine. It was agreed by all participants that further improvements would be desirable. Boeing indicated that, in hindsight, a balance with larger interactions should have been selected for test calibration on the IAI machine. This would have better discriminated between the performance of the machine calibration and that of manual calibration. Moreover, the performance of higher order mathematical models and expanded loading schedules could have been better investigated and evaluated. In addition, during the consortium tests, LaRC engineers attempted to evaluate an enhanced calibration experimental design and mathematical model intended for balances experiencing significant third order interactions. Inasmuch as the test balance possessed only second order interaction effects with no apparent third order effects at all, the test of the enhanced calibration design and

expanded mathematical model was not well-posed. Therefore, the results were inconclusive.

4.3 Mathematical Modeling

Several presentations covered the interdependent areas of mathematical modeling, calibration experimental design, and calibration uncertainty analysis. It is clear that potentially significant improvements in balance accuracy lie in improved mathematical modeling and in the calibration experimental design. Additional resources may be profitably allocated to further development effort in this area.

4.3.1 Richard S. Crooks, Microcraft San Diego, presented a paper on the limitations of balance calibration mathematical models. This paper, of a general philosophical nature, was illustrated by comparative studies of the robustness, or predictive accuracy, of various polynomial-based mathematical models for three differently sized calibration experimental designs. The calibration data sets were obtained using the IAI automatic machine to calibrate a single balance. It was seen that the largest and most comprehensive experimental design (1322 points) produced the lowest calibration residuals and, consequently, the least overall standard error.

In order to investigate balance model robustness Crooks has taken advantage of the "proof-load" technique. He found that proof-load residuals were significantly reduced by the addition of a single third-order cross-interaction (non-cubic) term to the standard second-order polynomial model. The particular third-order term was selected by trial and error balance coefficient estimation with proof-load test data appended to the normal calibration data set. However replicated calibrations had not yet been conducted to estimate the uncertainty of the significant third-order term and to verify that it is not merely a spurious effect due to random errors, i.e., fitting data to measurement noise.

4.3.2 The authors believe that the practice of attaching proof-load data to calibration data prior to coefficient estimation invalidates subsequent tests for calibration design and model robustness based on proof-load data. Indeed, predictive validation of the model should be based on independent proof-load data acquired at loading combinations and levels absent from the calibration experimental design.

4.4 Uncertainty Analysis

Frank L. Wright, Boeing, discussed how balance accuracy requirements are specified by balance designers and users. In the past accuracy has been imprecisely defined in widely varying ways. Now AGARD Standard 304 is coming into use wherein bias and precision uncertainties, and their combined uncertainty are specified at a given confidence level. The user must clearly state the factors such as test conditions, the coordinate system being used, units, etc. at which the accuracy is being quoted. In the commercial aircraft industry the most important wind tunnel quantity is drag coefficient. Customers now ask for $\frac{1}{2}$ drag count uncertainty at a 95 percent confidence level. Computations for a typical wind tunnel test show that uncertainties of $\pm 0.002^\circ$ in angle-of attack, ± 2.5 lb in normal force, and ± 0.8 lb in axial force are necessary to attain this requirement, which is probably not currently possible. Normal force and axial force precision uncertainties during tunnel tests may be estimated from balance calibration data by the following rules of thumb: tunnel re-

peat-point uncertainty is estimated from repeated back-to-back component calibrations; uncertainty within a Mach number run is estimated from multiple component calibrations interspersed over a five-day calibration; uncertainty over a complete test is estimated from the overall calibration standard error at the desired confidence level; and long term balance bias shift is estimated from zero shifts observed over a four-year period.

John S. Tripp, NASA LaRC, presented an overview of strain gauge balance uncertainty analysis techniques developed at LaRC. A second-order multivariate polynomial direct model is employed; i.e., balance voltage outputs are represented as functions of the applied input loads in accordance with the physical process being modeled. A Newton-Raphson iterative inversion method is employed for data reduction. The uncertainty analysis employs a global regression technique for least-squares estimation of the polynomial coefficient matrix. Equations are obtained therefrom for computation of calibration confidence intervals and prediction intervals as functions of the applied loadings. This is an extension of the previous method of reporting balance uncertainty as simple percentages of the full scale per component. It is noted that the calibration confidence intervals become fossilized bias errors subsequent to calibration. Additional sources of calibration bias uncertainties include calibration standard errors and mathematical modeling errors. Concepts for selection of calibration experimental design based on analytic methods developed by G. E. P. Box were presented for minimization of overall precision uncertainty and overall bias uncertainty. Statistical techniques for detection and estimation of calibration bias errors have been developed. It was pointed out that present procedures of lumping calibration bias and precision errors together in a single computation may significantly underestimate total calibration uncertainty. If the contributions of highly-correlated systematic errors are additive, then for the large calibration experimental designs typically used for balance calibration the usual RMS standard error underestimates the total uncertainty. Methods for separate estimation of bias and precision uncertainties are being developed.

Mark E. Kammeyer, formerly of the Naval Surface Weapons Center, Dahlgren Division, Silver Spring, MD presented an uncertainty analysis for force testing in production wind tunnels. It is an overview of a complete uncertainty analysis to provide bias and precision limits for computed model attitude and force coefficients inferred from measurements in Hypervelocity Wind Tunnel 9 at Dahlgren. Calibration and measurement uncertainties were propagated through the data reduction equations in accordance with the standard procedures specified by ASME, AIAA, and IOS. A jitter approach using computer software rather than analytical computation was used to propagate the bias and precision limits into the inferred reduced data in order to keep the computational requirements manageable. Results using actual test data show that balance load uncertainties are by far the dominant contributors to overall uncertainties in the reduced parameters. It was also found that precision errors in balance axial force measurements are dominant, whereas bias errors in the other balance components are dominant. These results are helpful in pinpointing areas wherein balance measurement accuracy improvements are needed.

The Dahlgren approach is similar to that reported in an uncertainty study conducted by Batill of Notre Dame (ref. 2) for the NTF wind tunnel in 1993. However, Dahlgren's analysis was more manageable because of the lower complexity of the Dahlgren facility compared to NTF.

4.5 Finite Element Analysis

Three agencies reported activities in finite element analysis (FEA): LaRC, NLR, and TUD. Notable progress in the application of FEA to balance stress analysis has been made recently. The technique is especially suited to determination of stress concentrations, to which conventional stress analysis techniques are not generally applicable. TUD reported using the technique for optimizing stress beam design as described above in Section 4.1.1. The consensus seems to be, however, that FEA is not yet sufficient to replace conventional stress analysis techniques. None of the above agencies report temperature effect analysis using FEA techniques. However, papers have previously been published at ONERA, France, on this topic by Bazin, et al. (ref 3).

Michael C. Lindell, NASA LaRC, presented an FEA study of an existing LaRC cryogenic balance. The purpose was to correlate FEA predicted strain levels with experimental values obtained from loadings, and to identify high-stress concentrations within the balance structure. The FEA software, which is adaptive, does not require prior knowledge of stress concentrations. Strain levels for a single full-scale load in each of the six components were computed and compared with measured values. Differences varied from 0.2% in predicted normal force to 11% in yawing moment. Maximum predicted stress was as large as 40% of yield under a full-scale normal force load, and 50% of yield under a full-scale pitching moment load. The analysis predicted maximum stress on the order of 100% of yield under simultaneous full-scale six-component loading. It was planned to verify this result experimentally. The study concluded that stress levels are predicted accurately by FEA and that stress concentrations can be predicted. Thus, FEA can improve the balance design cycle, and can be used to optimize the design to accommodate higher loads with lower weight and higher safety factors.

4.6 Thermal Gradient Compensation

Maurice Bazin, ONERA, France, discussed methods for balance thermal compensation. ONERA follows multiple approaches, namely bridge resistive compensation, mechanical design to minimize thermal effects, and numerical correction. Mechanical design methods to minimize thermal gradient effects are emphasized since error correction is very difficult compared to error prevention. Design methods to reduce temperature gradient effects include a traction-compression push-pull arrangement and a bending push-pull arrangement. Conventional gauging methods are used.

4.7 Facility Reports

Several presentations provided general descriptions of internal balance development and applications at major facilities.

Henk-Jan Alons, NLR, the Netherlands, gave a presentation co-authored with H. B. Vos describing balance development at NLR. NLR has investigated the performance of model-to-balance and balance-to-sting attachments. A hysteresis angle of 0.01° produces a 0.17% FS error in normal force, which is

excessive. In an effort to minimize attachment hysteresis NLR investigated taper joint, cylindrical tap, and end face flange attachments. The hysteresis angle of each of these attachments was measured under load by means of a precision inclinometer. The advantage of the taper joint is its small dimension in comparison to its high bending moment capacity. Its disadvantage is hysteresis under bending due to the unavoidable mating between the sting and the attachment socket. Typical taper joint angle hysteresis of $\pm 0.05^\circ$ was measured. The cylindrical tap, previously thought to exhibit lower hysteresis, was found to be comparable to the taper joint. The tests disclosed, however, that the end face flange exhibits minimal hysteresis. Currently NLR employs the end face flange on the model end of the balance. Integral Wheatstone bridge strain gauges are provided to insure correct installation pre-stress levels. A taper joint is still employed on the balance sting end to maintain compatibility with existing wind tunnel stings.

5. STATUS REPORT ON NORTH AMERICAN INTERNAL BALANCE USERS WORKING GROUP

David M. Cahill, Sverdrup/AEDC, presented a general overview of the past several years' activities of the AIAA/GTTC Internal Balance Technology Working Group. Numerous areas of progress were cited: an increased willingness to exchange information freely among the participants; a survey of members' balance usage and methods of engineering practice; preliminary agreement on definitions of technical terms; and a 6×96 generalized matrix representation of balance calibration parameters. It was noted that a standardized method of computing and reporting balance measurement uncertainties will be developed and accepted soon.

6. FUTURE ACTIVITIES OF THE STRAIN GAUGE BALANCE COMMUNITY

6.1 Second International Symposium on Strain Gauge Balances

A steering committee representing most of the nations and several US organizations attending the Symposium was established to initiate planning for a second international balance symposium. Ron D. Law, DRA-Bedford, announced that DRA might be able to host a second symposium within 3 years. It was agreed that steering committee meetings in the interim should be scheduled in conjunction with other international aerospace conferences to enable as many members as possible to participate. Such an opportunity will arise at the Supersonic Tunnel Association (STA) meeting scheduled to be hosted by ARA and DRA in 1999. It was agreed that Japan should be invited to participate in future symposia. Additional discussion is needed to select a theme for the second Symposium.

6.2 International Round-Robin Balance Calibration

R. W. Galway, National Research Council, Canada, discussed the inter-facility balance calibration project proposed within STA in the fall of 1992. A round-robin test of a single balance by participating facilities had been suggested to provide an opportunity for comparison of different calibration techniques, experimental loading procedures, equipment, data reduction methods, and accuracy reporting methods. It would also provide some insight into the contribution of balance calibration uncertainty in tunnel-to-tunnel comparisons. The round-robin test results would be assembled into a

data set to allow investigation of the effects of the various calibration experimental loading designs used by the participants. This data set would be closely controlled in terms of what was measured and how.

STA contains approximately 45 participating organizations of whom about 25 were interested in the round-robin test, and of those about 15 were definitely interested. The Boeing #661 balance had been selected for testing. The STA proposal has remained inactive since the inception of the AIAA/GTTC North American Balance Working Group, the 1995 IAI automatic balance calibration consortium at Microcraft, San Diego, and this Symposium. Galway inquired whether the Symposium delegates considered a round-robin calibration of a single balance to be a "useful exercise." He volunteered to serve as the point of contact through which interested parties may register their interest in participation.

6.3 Euro-Asian Internal Balance Working Group

David M. Cahill proposed the establishment of a separate Euro-Asian Inter-Nation Balance Working Group as a result of interest indicated by several European Symposium attendees in participating in the North American Internal Balance Working Group. He also proposed that the Euro-Asian group should be established under the auspices of AIAA. He suggested that the solidarity of the new group should become established before its eventual merge with the North American Internal Balance Working Group. The feasibility of establishing a Euro-Asian group would depend upon its reception by the proposed membership.

7. CONCLUDING REMARKS ON STRAIN GAUGE BALANCES

The Symposium was very successful in the free open exchange of information, in establishing an international community for future communication on balance usage and technology, and in setting a precedent for future Symposia. It is expected that the professional relationships established during the Symposium pave the way for future international cooperation in the strain gauge balance field. The Symposium provided a previously unavailable technical forum for the exchange of information for users, designers, and manufacturers of strain gauge balances.

The Symposium augmented and extended the results gleaned from the international balance users survey conducted by LaRC in 1995. It is clear that no aerospace agency holds a commanding lead in all technical areas. NASA LaRC is the world's major strain gauge balance user in terms of existing inventory, the number of units used in tests annually, and the number of new balances fabricated annually. Automatic calibration machines, although not yet equivalent to manual calibration with respect to loading accuracy, are an increasingly significant factor in realizing time and manpower savings. They are also an important tool for developing improved mathematical models and calibration experimental designs, and for establishing balance calibration and measurement uncertainties.

The symposium proceedings scheduled for publication in spring 1997 have been delayed due to shifted priorities at NASA LaRC.

8. BALANCE SYMPOSIUM REFERENCES

Contractor Reports

- 1 Kilgore, R. A.: *Internal Strain-Gage Balances: An International Survey*. VigYAN, Inc., Hampton, VA 23666, March 1995.
- 2 Batill, S. M.: *Experimental Uncertainty and Drag Measurements in the National Transonic Facility*. NASA Contractor Report 4600, June 1994.

Other Reports

- 3 Bazin, M.; Blanche, C.; and Dupriez, F.: *Instrumentation for Cryogenic Tunnels*. ONERA, France.

9. WORKSHOP ON ANGLE OF ATTACK AND MODEL DEFORMATION

A workshop on angle of attack (AoA) and model deformation measurement techniques was held on the afternoon of the last day of the Symposium. Short review papers were requested covering AoA and model deformation requirements and needs, thoughts for the future, and problem areas, in addition to papers covering actual applications and developments. The thrust of the workshop was to assess the state of the art in AoA and model deformation measurement techniques and discuss future developments in an informal but informative atmosphere. A panel discussion on AoA and model deformation was held in conjunction with the Workshop. Co-chairs of the Workshop were Tom D. Finley and Alpheus W. Burner, NASA LaRC.

9.1 Presentations

Twelve presentations were made at the Workshop. The presenters, affiliation, country, and presentation titles are listed below.

Tom D. Finley, NASA LaRC, USA: "AoA Overview"

Alpheus W. Burner, NASA LaRC, USA: "Model Deformation Overview"

Frank L. Wright, Boeing, USA: "Comparison of Model Attitude systems: Active Target Photogrammetry, Precision Accelerometer, and Laser Interferometry"

Maurice Bazin, ONERA, France: "AoA and Model Deformation at ONERA"

Peter Bauman, DLR, Germany: "DLR Model Deformation Measurement System"

Peiter H. Fuykschot, NLR, the Netherlands: "Vibration Compensation of Gravity Sensing Inclinometers in Wind Tunnels"

J. R. Hooker, McDonnell Douglas, USA: "Static Aeroelastic Analysis of Transonic Wind Tunnel Models Using Finite Element Methods"

YuFu Liu, CARDC, China: "The Model Real Time Angle of Attitude Measurement in 4m X 3m Low Speed wind Tunnel"

Sergi Fonov, TsAGI, Russia: "Model Deformation Measurements in TsAGI's T-128 Wind Tunnel by Videogrammetry System"

Gregory M. Buck, NASA LaRC, USA: "In-Situ Calibration of Sting Bending Using Optical Measurements"

Anton R. Gorbushin, TsAGI, Russia: "Angular, Linear Model Displacements, and Model Deformation During Wind Tunnel Tests"

Ralph D. Buehrle, NASA LaRC, USA: "Summary of Inertial Model Attitude Correction Techniques"

9.2 Panelists

The panel included the following members:

Frank L. Wright, Boeing, USA, Moderator

Pieter Fuyschot, NLR, the Netherlands

Tom D. Finley, NASA LaRC, USA

Richard A. Wahls, NASA LaRC, USA

Alpheus W. Burner, NASA LaRC, USA

John S. Tripp, NASA LaRC, USA

9.3 Summary of Presentations

Tom D. Finley, NASA LaRC, USA, opened the Workshop with an overview of angle of attack (AoA) measurement. He described the history of AoA measurement at LaRC, which has been based primarily on the use of precision accelerometers. He described the current state of the art of LaRC inertial AoA measurement systems including components and implementation. Specially selected high performance sensors are obtained from the manufacturer. Each unit is packaged with special output temperature compensation circuitry and mechanical isolation pads to reduce the effects of high frequency vibration.

Alpheus W. Burner, NASA LaRC, USA, presented an overview of the development of model deformation measurement capability at the Langley Research Center. Aeroelastic model deformation in wind tunnels was defined. Some fundamental questions and concerns about model deformation measurements in general were presented. The approach, described as a single camera, single view video photogrammetric technique, used to make model deformation measurements at three NASA LaRC facilities, was described. An example of the change in wing twist induced by aerodynamic loading as a function of angle-of-attack at the National Transonic Facility at various dynamic pressures was presented as a typical data example.

Frank L. Wright, Boeing, USA, presented a wind-on comparison among three independent model attitude measurement systems: the traditional inertial accelerometer measurement system, a Boeing designed and built laser interferometer system, and a commercially available photogrammetric system. Test data for the three systems, obtained at various Mach numbers, showed prediction intervals lying between 0.005 and 0.01 degrees. Two other applications of the photogrammetric system were described: flap position measurement during an aircraft flight test, and wing twist measurement of a wind tunnel model.

Maurice Bazin, ONERA, France, described developments at ONERA in AoA and model deformation measurement techniques. Precision accelerometers are used for AoA as well as the MAMS system due to Bertin (AGARD VKI-1996) which is somewhat similar to the Boeing Laser Angle of Attack (LAM) system. Potentiometers and encoders are used as well. Model deformation measurements have been made with stereo observation with the RADAC (ONERA T.P. n° 1990-57) and ROHR (ONERA Activities 1996). The RADAC system uses special cameras that contain crossed linear arrays. The ROHR system employs two conventional cameras. The uses of optical fibers and quadrant light detectors and a polarization torsionometer for model attitude and deformation measurements are described in ONERA T.P. n° 1982-91.

Peter Bauman, DLR, Germany, discussed the use of moiré interferometry for the measurement of model deformation and hinge moments. DLR selected moiré interferometry as the technique with greatest potential over others such as coded light, holographic interferometry, and speckle interferometry. The technique currently requires diffusely reflecting surfaces that may necessitate the painting of highly polished models. Bending and twist measurements have been made in wind tunnels. Expected accuracies are 0.01° for flap angles, 0.03° for twist, and 0.1 mm for bending. Future applications in the automotive industry and for laboratory measurements on helicopter rotor blades are anticipated.

Peiter H. Fuykschot, NLR, the Netherlands, described a correction technique given in a paper presented at an Instrument Society of America conference in May 1996. The technique reduces bias errors in model AoA measurements due to centrifugal forces developed during high tunnel dynamic test conditions. He showed that this inertial error, termed a "sting whip" error, is corrected by measuring the model's linear and angular velocities and multiplying them together. The technique, which requires multiple sensors for correction in both pitch and yaw planes, provides a real-time correction without knowledge of the vibrational modes of the model. He instrumented a model and demonstrated the ability of the technique at two single frequency modes and one multi-frequency mode.

J. R. Hooker, McDonnell-Douglas, USA, discussed the use of experimental measurements to calibrate computational methods used to predict wind tunnel model aeroelastic deformations. A wind-off static loading experiment conducted in the National Transonic Facility (NTF) test section was used to calibrate both the optical technique and the finite element analysis (FEA) technique. Optical wing twist data from the NTF were presented, which were used to calibrate the FEA results with wind on. It was found that one-dimensional FEA analyses are sufficient to generate wind tunnel model jig wing definition, but that advanced three-dimensional solid FEA analyses may be required to generate wing definition suitable for computational fluid dynamic (CFD) analyses. Hooker recommended utilization of CFD methods to define the required accuracy of model deformation measurements for a given configuration and noted that the required accuracy may vary from configuration to configuration. Generally a 5% variation in wing twist is expected to result in acceptable accuracy for low wing transport configurations.

YuFu Liu, CARDC, China, described real-time attitude measurement and side-slip angle measurement systems used in the CARDC 4 by 3 meter low-speed wind tunnel. The pitch measurement system employs a QFlex accelerometer with an added temperature sensor which corrects the accelerometer output as a function of temperature. This system, used over a range from -30 degrees to 110 degrees by offsetting the accelerometer, provides a measurement precision of 0.005 degrees. The side-slip system employs a laser and dual CCD linear scanning camera to measure yaw from -2.5 degrees to 2.5 degrees with a measurement precision of 0.005 degrees.

Sergi Fonov, TsAGI, Russia, presented examples of wing twist and bending measurements as functions of lift force and AoA at the T-128 wind tunnel using a CCD camera and reference targets with the single camera, single view videometric technique. He also presented results of flap torsion and displacement for which fluorescent strips were illuminated with a nitrogen laser. A prototype deformation measurement system was described for a full-scale helicopter rotor blade using a camera in the rotating hub with connection to the recording system by slip rings. Deformation measurements using projection moiré were also mentioned.

Gregory M. Buck, NASA LaRC, USA, presented results of tests conducted to study sting bending and model injection during wind-on and wind-off conditions at the 20-Inch Mach 6 CF₄ Tunnel. Angle and displacement measurements were made on a small section of the model that was in the field of view of a camera when the model is fully injected into the test section. A back illuminated ground glass view screen was placed in the field of view of the camera to yield a very high contrast edge from which the slope angle and intercept can be found by least squares estimation.

Anton R. Gorbushin, TsAGI, Russia, briefly discussed angle measurements using accelerometers that are manufactured in Russia. He also described a research and development project based on the development of a magnetic system to measure angular and linear model displacements and model deformations during wind tunnel tests. The purpose is to develop a prototype system for the simultaneous measurements of full angular orientation, coordinates, and deformations of a model, including wings, control surfaces, etc., during wind tunnel testing. High-sensitivity three-axis magnetometers on one-domain film structures will serve as transducers for navigation and orientation in an artificial low-frequency electromagnetic field.

Ralph D. Buehrle, NASA LaRC, USA, summarized several sting whip correction techniques proposed over the last few years. Time-domain and frequency-domain methods were not successful in extracting the small signals necessary to determine error. A modal correction technique was tested with limited success. This method requires measurement of all model vibration modes in pitch and yaw prior to wind tunnel testing. The model must be excited in both vertical and lateral directions; modal analysis of the acquired vibration data provides corrective information. During tests corrections at each mode are summed to provide a total correction. This technique requires considerable pre-test and post-test computation. The linear-angular technique of Pieter H.

Fuyschot described above has the ability to provide real time corrections without modal analysis.

9.4 Panel Discussion

Frank L. Wright, Boeing, USA, served as panel moderator. He opened the discussion with comments on the need to properly define AoA measurement accuracy requirements. Force measurement using internal strain gauge balances requires accurate AoA measurement to properly resolve normal and axial force to obtain lift and drag forces. However, Wright stressed that AoA measurement accuracy requirements vary depending on the test configuration. For instance AoA accuracy requirements are better defined at cruise conditions and are more stringent for climb-out than for approach conditions. The AoA accuracy requirements at maximum lift are also not well defined. Although $\pm 0.01^\circ$ AoA accuracy may not be required for every test, better than $\pm 0.1^\circ$ accuracy is probably always necessary. A comment from the audience noted that the wind tunnel user often requests "the best accuracy you can give me". Wright also stressed that repeatability is of the greatest importance during increment testing at a fixed AoA. The point was made that the confidence level is often not specified when stating a numerical accuracy requirement.

The topic turned to aeroelastic model deformation. Measurement of aerodynamic twist is needed for comparison with CFD results. As model size increases, wall interference effects become more significant while deformations may increase as well. Both effects must be accounted for. It was asked when $\pm 0.05^\circ$ experimental wing twist measurement accuracy would be available in wind tunnels. It was pointed out that such measurement accuracies are now possible at the LaRC Unitary Plan Wind Tunnel and are also possible at the NTF wind tunnel at somewhat reduced accuracy. The required accuracy for measurement of the change in wing twist induced by aerodynamic loading is still an open question.

Uncertainty issues in general were then discussed. The uncertainty of CFD results is needed along with the uncertainty of experimental results. The CFD community is just starting to assess uncertainty.

The discussion then returned to AoA where it was stated that AoA should be separated from angle of incidence. To obtain drag, the AoA is needed, not angle of incidence. This led to the question of how well flow angularity can be measured. It was recommended that uncertainty analyses be conducted on the computation of flow angularity from upright and inverted tests. A question was then asked about the Optotrak system in use at Boeing and several other aeronautical establishments. Wright stated that the number of and position of optical markers required for wind tunnel testing with the Optotrak system had not been optimized.

The effect of high-pressure tunnel operation on testing was raised. Wright stated that drag data taken at 4 atm in the NTF wind tunnel was as accurate as data taken at 1 atm in the Boeing wind tunnel; in addition, the 4 atm drag data was as useful for predicting flight behavior as the 1 atm data.

The fragility of precision quartz flexure accelerometers was discussed. Tom D. Finley stated that the typical lifetime of quartz accelerometers is five years. Most problems with

accelerometers are due to mishandling rather than excessive model vibration during tests. It was also stated that the quartz flexure is not subject to loss of response as with metal flexures. It was recommended from the audience that accelerometers be powered during transit for protection. Finley pointed out that such protection would occur only in the axial direction. Several people commented that accelerometer manufacturer's specifications are reliable and that they therefore perform no additional calibration. Frank L. Wright stated that accelerometer output data corrected for temperature using manufacturer-furnished data agrees well with temperature-controlled accelerometer output data, as commonly used at the NTF. Pieter H. Fuyschot recommended the use of precision wedges to spot-check angle measurement accuracies. The importance of the use of the local value of the gravitational constant was mentioned.

The discussion turned to the problem of setting the model to zero angle in the facility. Leveling fixtures and tooling balls combined with a bubble level may possibly be used to level horizontal models; however, fundamental leveling problems exist with floor-mounted half models. The importance of the reference surface on which the accelerometer is mounted was also mentioned.

An AGARD uncertainty document published in 1982 was mentioned as an excellent reference. However, Wright cautioned that the individual uncertainty values cited in that reference, which are associated with one drag-count uncertainty, account for the entire one drag-count error. If all of the component uncertainties are combined, approximately 2.8 drag-count uncertainty results as opposed to one drag count. A member of the audience suspected that load resistor variation caused accelerometer output drift. Finley noted that LaRC employs precision load resistors located in the AoA signal conditioning electronics package rather than resistors installed in the accelerometer package. With this arrangement no significant output drift has been observed.

The panel discussion ended with a brief discussion on the problem of measuring yaw. There appears no clear solution. However, the Optotrak system offers promise in solving the yaw measurement problem.

APPENDIX: STRAIN GAUGE BALANCE PAPER TITLES AND AUTHORS

Session 1 CALIBRATION & DATA REDUCTION		
Authors	Title	Organization
V. Crivoruchenko & I. Panchenko	Calibration of Multi-Component Aerohydrodynamic Balances with Application of Optimal Planning Tests Methods	TsAGI, Russia
M. Quade & K. Hufnagel	The Development of a Modern Manual Calibration and Measuring System for Internal Balances	Technical University of Darmstadt, Germany
I. N. Panchenko	Transformation of Aerodynamic Balances Formulas to the Resolved Respecting To Loading Form	TsAGI, Russia
R. S. Crooks	Limitations of Internal Balance Calibration Math Models for Simulating Multicomponent Interactions	Micro Craft Technology, San Diego, USA
Session 2 FACILITY REPORTS		
E. Graewe, B. Ewald, & D. Eckert	Design and Development of Internal Balances for the German/Netherlands Low Speed Wind Tunnel (DNW)	Technical University of Darmstadt, Germany
D. X. He, & X. R. Gu	Recent Advances in Strain-gage Balances at CARDC	CARDC, China
D. Cahill	AIAA/GTTC Internal Balance Technology Working Group	Sverdrup/AEDC, USA
H. B. Vos	Strain Gauge Balance Development at NLR	NLR, the Netherlands
P. W. Roberts	NASA LaRC Force and Strain Measurement Capabilities	NASA LaRC, USA
Session 3 SPECIAL BALANCES I		
B. Ewald, K. Hufnagel, G. Viehweger, & R. Rebstock	The Half Model Balance for the Cologne Cryogenic Low Speed Tunnel (KKK)	Technical University of Darmstadt, Germany
K., Fristedt	Internal Bending Beam Strain-Gauge Wind-Tunnel Balances	AKTIEBOLAGET ROLLAB, Sweden
K. K. Guo	Hinge Moment Balance for Complete Models	Beijing Institute of Aerodynamics, China
A. Kuzin, G. Shapovalov, & N. Prohorov,	Strain-Gage Balance for Magnetic Suspension and Balance System	Moscow Aviation Technological Institute, Russia
Session 4 ACCURACY AND UNCERTAINTY ANALYSIS		
A. J. Day, & N. Corby	Developments to Improve the Accuracy of Half-Model Balance Measurements in the AEA 9ft x 8ft Transonic Wind Tunnel	Aircraft Research Association, Ltd., UK
P. H. Fuykschot	Looking for the Last Drag Count: Model Vibrations Vs Drag Accuracy	NLR, the Netherlands
M. E. Kammeyer	Uncertainty Analysis for Force Testing in Production Wind Tunnels	Naval Surface Weapons Center, USA
F. L. Wright	Experiences Relative to the Interaction Between the Balance Engineer and the Project Engineer with Regard to Measurement Uncertainty	Boeing Commercial Airplane Group, USA
J. S. Tripp	Strain Gauge Balance Uncertainty Analysis at NASA Langley - A Technical Overview	NASA LaRC, USA
Session 5 AUTOMATIC CALIBRATION		
Ewald K., Hufnagel, L. Polansky, & L. Badet	Development and Construction of Fully Automatic Calibration Machines for Internal Balances	Technical University of Darmstadt, Germany
R. D. Law	The Application of an Automatic Precision Balance Calibration Machine to the Calibration of Wind Tunnel Strain-gauged Balances	DRA-Bedford, UK
Y. P. Zhang	Fully Automatic Calibration System of the Six Component Balance for High Speed Wind Tunnels	CARDC, China
P. Tchong & J. S. Tripp	Statistical Analysis of the NASA LaRC Evaluation of the IAI Automatic Balance Calibration Machine	NASA LaRC, USA

Session 6 APPLICATIONS		
Authors	Title	Organization
D. Booth	Development of a Six Component Unitized Flexured Force Balance	Micro Craft Technology, USA
V. Lapygin	Typical Balance Test tasks for Aerodynamic Facilities of TSNIMASH	TSNIMASH, Russia
D. Levin & M. Ringel	Accurate Axial Force Measurement with Small Diameter Balances under High Normal Loads	Technion, Israel
A. R. Gorbushin	Some Peculiarities of Balance Tests in the Transonic TsAGI T-128 Wind Tunnel	TsAGI, Russia
T. C. Moore	Strain Gages in Service at NASA Langley - A Technical Review	NASA LaRC, USA
Session 7 SPECIAL BALANCES II		
L. X. Liao & Y. Tao	A Water-cooled Six-Component Internal Balance	Beijing Institute of Aerodynamics, China
G. S. Liu, Z. G. Lu, & X. Q. Qi	Single Load and Multicomponent Balance Calibration System (SL&MBCS) of Piezoelectric Balance in Shock Tunnel	CARDC, China
P. Parker	Free Oscillation Dynamic Stability Balance System	Modern Machine & Tool Company Inc., USA
Session 8 BALANCE DESIGN		
G. Drouin, B. Girard, & K. Mackay	A Stiff Monopiece Wind Tunnel Balance	Defence Research Establishment, Canada
G. I. Johnson	A New Master Balance for the MK15 Calibration Rig at FFA	FFA, Sweden
N. R. Patel	Development of A Five-Component Balance As an Integral Part of a Control Surface	Modern Machine & Tool Company Inc., USA
M. A. Ramaswamy	Design Features of Some Special Strain Gage Balance	India Institute of Science, India
R. D. Rhew	NASA LaRC Strain Gage Balance Design Concepts	NASA LaRC, USA
Session 9 INSTRUMENTATION, STRAIN GAUGES, & THERMAL EFFECTS		
B. Fagerstrom & P. Kempainen	An Easy-to-use Calibration and Readout System for Small Internal Beam-Type Wind Tunnel Balances	Helsinki University of Technology, Finland
X. R. Gu & J. Q. Hu	Development of BFH-series Strain Gages	CARDC, China
A. T. Ferris	Strain Gauge Balance Calibration and Data Reduction at NASA Langley Research Center	NASA LaRC, USA
W. Liu	Temperature Effect Research on Strain-gage Balances in a Conventional Wind Tunnel	CARDC, China
M. Bazin	ONERA Balances and Dynamometers	ONERA, France
Session 10 FINITE ELEMENT ANALYSIS & NEW TECHNOLOGY		
M. Lindell	Finite Element Analysis of a NASA National Transonic Facility Wind Tunnel Balance	NASA LaRC, USA
J. Zhai & K. Hufnagel	Optimization of the Internal Strain Balances with Finite Elements Computation	Technical University of Darmstadt, Germany
V. Lagutin	New Design of Tubular Type Strain-gage Balances	TSNIMASH, Russia
B. Ewald, K. Hufnagel, & E. Graewe	The Development of Advanced Internal Balances for Cryogenic and Conventional Tunnels	Technical University of Darmstadt, Germany
V. Bogadanov & V. S. Volobuev	The Status and Prospects for the Further Development of Load Measuring Devices for Wind Tunnel Tests	TsAGI, Russia
Session 11 SPECIAL BALANCES III		
G. Rajendra, H. S. Murthy, & G. V. Kumar	A New Balance Calibration Methodology for Long Slendered Bodies in a Blowdown Tunnel	National Aerospace Laboratories, India
C. J. Suarez, & G. N. Malcolm	Development of a 5-component Strain Gage Balance for Water Tunnel Application	Edidetics Corporation, USA
Z. G. Tang	Development of Microbalance in Low Density Wind Tunnel	CARDC, China
B. Vasudevan & M. A. Ramaswamy	Novel Oil Filled Bellow Type Internal Strain Gauge Balance for Water Tunnel Applications	India Institute of Science, India

Model Deformation Measurements at NASA Langley Research Center

A. W. Burner
 NASA Langley Research Center
 MS 236
 Hampton, Virginia 23681-0001
 United States
 A.W.Burner@Larc.nasa.gov

1. SUMMARY

Only recently have large amounts of model deformation data been acquired in NASA wind tunnels. This acquisition of model deformation data was made possible by the development of an automated video photogrammetric system to measure the changes in wing twist and bending under aerodynamic load. The measurement technique is based upon a single view photogrammetric determination of two dimensional coordinates of wing targets with a fixed third dimensional coordinate, namely the spanwise location. A major consideration in the development of the measurement system was that use of the technique must not appreciably reduce wind tunnel productivity. The measurement technique has been used successfully for a number of tests at four large production wind tunnels at NASA and a dedicated system is nearing completion for a fifth facility. These facilities are the National Transonic Facility, the Transonic Dynamics Tunnel, and the Unitary Plan Wind Tunnel at NASA Langley, and the 12-FT Pressure Tunnel at NASA Ames. A dedicated system for the Langley 16-Foot Transonic Tunnel is scheduled to be used for the first time for a test in September. The advantages, limitations, and strategy of the technique as currently used in NASA wind tunnels are presented. Model deformation data are presented which illustrate the value of these measurements. Plans for further enhancements to the technique are presented.

2. INTRODUCTION

Model deformation may be defined as the change in shape of a wind tunnel model (particularly the wings and control surfaces) under aerodynamic load. This change in the design geometry can cause differences between the acquired and expected wind tunnel results if the expected results are based upon rigid body assumptions. Differences can also occur between acquired wind tunnel data and computational predictions based upon rigid body assumptions. These differences can lengthen and degrade the aircraft design process. The measurement of model deformation has thus been of interest for over 20 years¹.

The accurate prediction, as well as the measurement, of model static aeroelastic deformations is becoming increasingly important, especially for transonic transports. It is essential to accurately predict deformations in the wind tunnel in order to duplicate the desired CFD configuration. Deformations must often be taken into account when comparing CFD predictions to experimental measurements at off-design conditions. Increased reliance is being placed on high Reynolds number testing for configuration development and CFD validation, making accurate predictions of static aeroelastic deformations very important, since deformations increase significantly at the higher dynamic pressures associated with

high Reynolds number testing. Computational methods such as the finite element method (FEM) need to be calibrated and validated with wind tunnel model deformation measurements in order to ensure accurate predictions².

The two fundamental techniques used to measure model deformation are photogrammetry and projection moiré interferometry (PMI). The rapid development of relatively low cost electronic imaging, driven largely by the consumer video market, coupled with improvements in low cost computing have enabled the development of video photogrammetric and PMI techniques for model deformation. However, turnkey systems are generally not suitable for incorporation into a wind tunnel data acquisition system because of the user interaction required. In addition, limited view ports, illumination, and targeting options often contribute to the requirement for custom measurement systems for large wind tunnels. An exception to this is the commercially available photogrammetric system made by Northern Digital known as Optotrak, which has been successfully used by Boeing for both wind tunnel and flight aeroelastic and angle of attack measurements^{3,4}.

The history of the development of a model deformation measurement capability for the National Transonic Facility is presented in reference 5 which includes the rationale for the single camera, single view photogrammetric technique with emphasis on the measurement of the change of wing twist due to aerodynamic load. Examples of the measurement of wing twist in non-automated mode along with error considerations are also presented in reference 5. A description of the automation of the video photogrammetric model deformation technique, experimental procedure and data reduction, description of software, and targeting considerations are given in reference 6. Examples of variations of the model deformation technique used for the measurement of angle of attack, sting bending, and the effect of varying model injection rates are presented in reference 7. A brief description of the Aeronautics Design / Test Environment Program, a NASA program to improve the productivity of and amount of knowledge extracted from existing wind tunnels, is also presented in reference 7. Reference 7 also discusses the unification of several wind tunnel instrumentation techniques, including model attitude and deformation, pressure sensitive paint (PSP), Doppler global velocimetry (DGV), and phased microphone array technology (PMAT).

A major consideration in the recent development of an automated test technique for model deformation was that the productivity of wind tunnel testing should not be appreciably reduced while providing useful and accurate deformation information. The determination of the change in wing twist

due to aerodynamic loading is the primary concern, while wing deflection (bending) is of secondary importance. Angular measurements such as model pitch are common in wind tunnel testing. Thus, with wind-off, the measurement of the change in pitch angle at various stations along the wing can be used for in situ calibration. Deflection measurements, however, are not a common part of wind tunnel testing, making in situ calibrations more difficult. For these reasons the emphases in the development of a model deformation capability has been on the accurate, repeatable, and routine measurement of the change in wing twist due to aerodynamic load. Less emphasis has been placed on the measurement of wing bending.

2.1 Additional Model Deformation Developments

There have been several in-flight measurements of model deformation besides the Optotrak measurements made by Boeing mentioned above. An electro-optical deflection measurement system was developed by Grumman⁸ and used at NASA Dryden for flight tests⁹. The Grumman system uses synchronized LED's in a manner similar to the Optotrak system.

Rotating blade deformation measurements have been made and additional studies are planned. A nonintrusive optical method has been used to measure propeller blade deflections at NASA Lewis¹⁰. The basic system consisted of a photodiode and a single laser used to illuminate the leading and trailing edges of the blade. The photodiode output was recorded on tape for later reduction. The Army is currently investigating the deformation measurement of helicopter rotor blades on a test stand at NASA Ames¹¹. A camera will be located on the rotating hub to view a single blade. The single camera, single view photogrammetric technique is currently under consideration for data reduction.

Model deformation measurements have been made with stereo observations with the RADAC¹² and ROHR¹³ measurement systems at ONERA in France. The RADAC system uses special cameras that contain crossed linear arrays. The ROHR system employs two conventional cameras. Optical fibers and quadrant light detectors in addition to a polarization torsionometer have also been used in the past at ONERA for model attitude and deformation measurements^{14,15}.

Projection moiré interferometry (PMI) has been investigated by DLR in Germany for the measurement of hinge moments and model deformation¹⁶. (PMI is also being investigated at NASA Langley. See section 6 below.) PMI was chosen by DLR over techniques such as coded light, holographic interferometry, speckle interferometry, and different moiré techniques because PMI is easy to set up and use and can be easily adapted to measure the deformation of a wide range of model geometries. Flap bending angles due to aerodynamic load have been measured by DLR at the transonic wind tunnel (TWG) up to Mach 1.15. An average deviation of $\pm 0.01^\circ$ from strain gauge measurements was achieved. Wing twist and bending for a transport model at the Deutsch-Niederländischer-Windkanal (DNW) have been measured with a standard deviation of 0.1 mm and 0.03° respectively. A special implementation of the system for routine wing twist and bending measurements has recently been commissioned¹⁷ under cryogenic conditions and worked satisfactorily at the European Transonic WindTunnel (ETW). Further

improvements to the system for ETW are currently underway.

Further discussions of model deformation measurement developments and applications can be found in reference 18, which summarizes a workshop on AoA and model deformation held at NASA Langley last year. The workshop was held in conjunction with the International Strain Gauge Balance Symposium. The thrust of the workshop was to assess the state of the art in AoA and model deformation measurement techniques and discuss future developments.

3. EXPERIMENTAL PROCEDURE

The optical technique used to determine the change in wing twist and bending due to aerodynamic loading is based upon the recording and analysis of digitized video images with the single camera, single view photogrammetric approach. A video signal from a standard RS-170 solid state camera with 752 horizontal by 240 vertical pixels per field is routed to a frame grabber controlled by a PC which records a predetermined number of video fields into the frame grabber memory. The adjustable field integration time of the charge-coupled device (CCD) video camera is set to 1/250 sec or less in order to reduce the effects of dynamics on image recording. Fixed focal length lenses have been used at the TDT, UPWT, and 12-Ft. A 10 to 100 mm focal length remotely controlled zoom lens is currently used for imaging at the NTF and UPWT. Considerations when calibrating zoom lenses for wind tunnel use are discussed in reference 19.

Image plane coordinates of wing targets are automatically measured and used to determine the X, Z coordinates (X is in the flow direction, Y points out the right wing, and Z is up) as outlined in reference 6. Reference 6 more fully describes the relations for the single camera, single view photogrammetric approach and the automated image processing software. The slope angle and offset in planes parallel to the X, Z plane are determined at each spanwise target location. Angular corrections are made based on wind-off polars. The change in wing twist at each span location is then computed as the difference between the wind-on wing angle (zeroed at 0° angle of attack with the wind-off polars) and the body angle of attack.

3.1 Calibration

The initial pre-test calibration procedure determines those camera parameters necessary for conversion from pixels to corrected image plane coordinates. The photogrammetric principal point is found using a laboratory laser illumination technique²⁰. The point of symmetry for distortion is determined in situ from the point of image symmetry of the zoom lens¹⁹ or laboratory laser illumination technique. In cases where the video camera cannot be taken back to the lab, the principal point is taken to coincide with the point of symmetry for distortion if a zoom lens is used. In such cases for a fixed focal length lens, a previous value (or center of image plane if previous value is not available) is used for the principal point. The need for extensive camera calibration is lessened somewhat by on-line calibration using the model pitch angle for wind-off reference at the tunnel total temperature and pressure test conditions. The pointing angles and location of the camera in the tunnel coordinate system are determined at the start of the test by photogrammetric resection on a target plate that is aligned to the coordinate system of the tunnel. A target plate consists of a flat black aluminum or

hard foam plate with an array of flat white targets or retroreflective targets with locations measured by a 3-D coordinate measurement machine. For sting mounted models, the X -axis of the calibration plate is aligned parallel to the body axis by contact with a leveled V-block placed on the body. The V-block also serves as a convenient way to establish the distance of the calibration plate zero Y -reference from the body axis. The target plate is translated a known amount along an optical rail to several Y locations where resections are made. Provided the alignment is correct, the three pointing angles and X and Z of the camera will be nearly equal at each location of the plate whereas the Y value for the camera will follow the change in location. A technique is then used to determine the photogrammetric principal distance that causes best agreement with the changing Y values of the target plate if necessary. This technique for determining the principal distance is described in reference 7.

Once the three Euler angles and position of the camera are established relative to the tunnel coordinate system, measurements can then be made on the target plate for an in situ check of the technique by comparing measured and known Z values. Providing the Z value determinations are reasonable, a pitch polar can then be taken with wind-off to ensure that the measured change in pitch angles at each semispan location on the wing track with the onboard accelerometer angle. An alternate technique to the above for determining the pointing angles and location of the camera in the tunnel coordinate system is by photogrammetric resection of a wind-off reference run. A known set of targets for resection are established by merging wind-off points at several angles into a single reference target field based on knowledge of the center of rotation and the rotation angle from the onboard accelerometer.

The final calibration step requires a wind-off pitch sweep at run temperature and pressure over the range of angles expected during the subsequent wind-on testing. A wind-off polar in the middle and at the conclusion of a set of runs is helpful to verify system stability, especially at the NTF during cryogenic operation.

3.2 Additional Wind Tunnel Considerations

Targets must be placed on the wing at the semispan locations where change in wing twist and bending are required. The Y coordinates of the targets in the spanwise direction are determined from pressure tap and other reference locations on the wing to be used in the computation of X in the streamwise and Z in the vertical direction. High contrast targets are required on the wing in order for the image processing routines to automatically locate the targets reliably, without ambiguity, and with no user interaction. These wing targets are either white diffuse circular targets on a dark background, or ideally, retroreflective tape targets such as have been used at all the facilities except the NTF. A light source placed near the camera will yield a very high contrast image when the retroreflective tape targets are used. It was recently demonstrated at a test at the Ames 12-Ft Tunnel that it is possible to use PSP reference targets and existing test section lighting, in place of the usual high contrast wing targets, with the next generation video photogrammetric system currently under development. Tests at Ames with UV illumination and PSP targets, while encouraging, were not entirely successful.

Retroreflective tape targets have not yet been used at the NTF due to difficulties in locating a light source sufficiently close to the camera and concerns about the aerodynamic effects due to the thickness of the tape. Instead, a polished paint technique has been used at the NTF to produce high contrast white dot targets allowing the first automated measurements of wing twist at the facility. A black background surrounding the white targets is produced by reflection of a black test section wall from the highly reflective wing surface. A typical target set at a given semispan station consists of a row of 4 white circular targets with a diameter of 8 mm aligned along the streamwise direction.

Target rows are generally located at three or more semispan stations along the wing in addition to the body. The body targets are used to determine the pitch angle for comparison to the onboard inertial sensor. In cases where the two results differ and model dynamics are low enough not to perturb the results from the inertial sensor, the body data can be used for correction of data along the wing span. If model dynamics are high, causing the accelerometer angle measurement to be suspect, the body angle results can be used as an alternate source for the angle of attack measurement itself. The subtraction of the body angle data from the outboard wing angles has generally been found to reduce data scatter when comparing repeat runs taken throughout a test.

Currently the final data reduction, requiring just a few minutes, using wind-off polars for correction does not occur until the end of a series of runs. The data reduction procedure is written in MATLAB and executed in the MATLAB environment. In the future it is expected that raw angles and Z values for each semispan location will be transferred to the facility data acquisition system for final reductions in order to reduce operator requirements for the model deformation system.

4. WIND TUNNEL EXAMPLES

Aeroelastic deformation measurements have been made for a number of tests at four large production wind tunnels at NASA and a dedicated system is nearing completion for a fifth facility. These facilities are the National Transonic Facility (NTF), the Transonic Dynamics Tunnel (TDT), and the Unitary Plan Wind Tunnel (UPWT) at NASA Langley, and the 12-FT Pressure Tunnel at NASA Ames. The first scheduled test for the dedicated system for the Langley 16-Foot Transonic Tunnel is in September.

The location of the data-recording camera varies with the tunnel due to window location constraints, competition with other instrumentation for viewing ports, and ease of mounting. The experimental camera locations at the various NASA facilities are depicted in figure 1. Usually only one wing and the body are viewed in order to increase resolution. However, the capability exists at the NTF to view both wings simultaneously. Measurements on both wings have been made during only one test at the NTF in order to compare the right and left wing deformations since there were differences in the pressure tube routings between the two wings. Sting mounted horizontal models are viewed at the NTF, UPWT, and 16-Ft. A sting mounted vertical model was viewed for one test at the UPWT in order to allow for PSP measurements to be made in conjunction with the deformation measurements, but translations while pitching the model in the

horizontal plane make such arrangements more difficult to properly interpret displacements. Wall mounted semi-span models are viewed at the TDT. Floor mounted semispan and Bipod supported full models are viewed at 12-Ft.

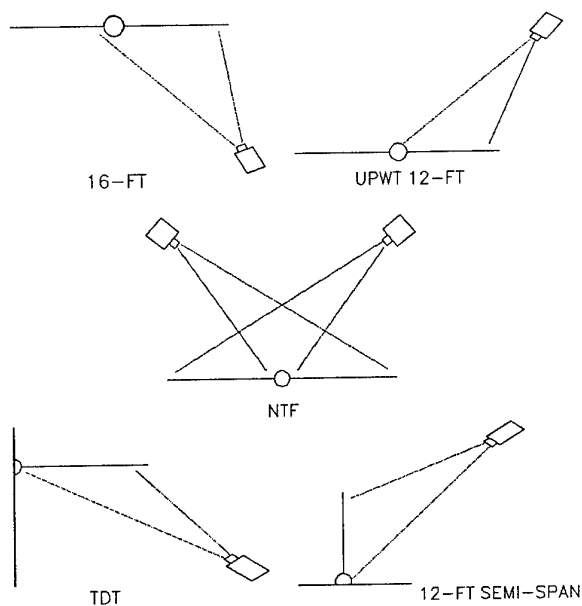


Figure 1. Sketch of camera locations at NASA facilities.

4.1 National Transonic Facility

The National Transonic Facility (NTF) is a fan-driven, closed circuit, continuous-flow pressurized wind tunnel²¹. The 8.2 x 8.2 x 25-ft long test section has a slotted-wall configuration. The wind tunnel can operate in an elevated temperature mode up to $T = 140^\circ\text{F}$, normally using air, and in a cryogenic mode, using liquid nitrogen as a coolant, to obtain a test temperature range down to about -250°F . Thermal insulation inside the pressure shell minimizes energy consumption. The design total pressure range for the NTF is from 15 psia to 130 psia. The combination of pressure and cold test gas can provide a maximum Reynolds number of 120,000,000 at Mach 1.0, based on a chord length of 9.75 inches. These characteristics afford full-scale Reynolds number testing for a wide range of aircraft. Three types of investigations are possible: Reynolds number effects at constant Mach number and dynamic pressure; model aeroelastic effects at constant Reynolds number and Mach number; and Mach number effects at constant dynamic pressure and Reynolds number. The constraints imposed by operation in a high-pressure environment over such a wide range of temperatures have had a significant impact on the continuing development, improvement, and optimization of instrumentation at the facility. A major instrumentation challenge at the National Transonic Facility is the requirement to make measurements over the wide range of temperature from 140°F down to -250°F .

Aeroelastic deformation measurements have been made at the NTF for both High Speed Research (HSR) and Advanced Subsonic Technology (AST) models. As an example of the demand for deformation measurements, the last four tests before the recently scheduled tunnel enhancement shutdown

at the NTF all had a requirement for deformation measurements. High demand for such measurements is expected to continue when the NTF returns to full operations after the scheduled shutdown.

Examples are presented below of wing twist data from the NTF at low Reynolds number. A model of a generic transport wing/body configuration was tested with and without an outboard aileron deflected. Aerodynamically induced changes in model wing twist were measured at 95% semispan. Test results are presented at both subsonic and transonic Mach numbers below. Positive aileron deflection, $\delta_{a,OB}$, is defined as positive for the trailing edge down. The changes in wing twist due to aerodynamic load, θ , are plotted versus lift coefficient, C_L , and angle of attack, α . Figures 2, 3, and 4 show Mach 0.5, 0.82, and 0.85 wing twist data respectively. As expected, positive deflections increased the lift outboard and, consequently, increased the static aeroelastic deformations at the measured 95% semispan location.

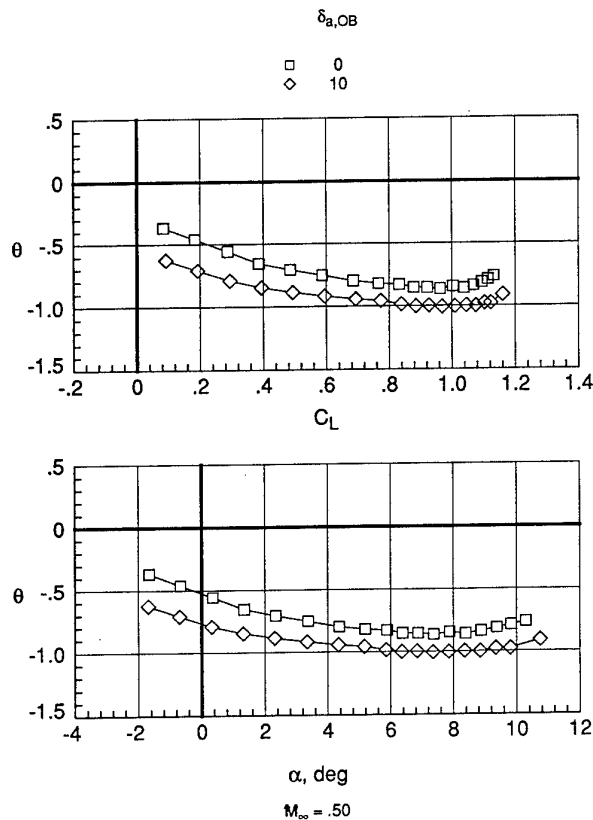


Figure 2. Effect of outboard aileron deflection on the model aeroelastic deformation at Mach 0.5 at the NTF.

4.2 Transonic Dynamics Tunnel

The Langley Transonic Dynamics Tunnel (TDT) is a unique "national" facility that is used almost exclusively for performing aeroelastic research and for conducting flutter-clearance and other aeroelastic-verification tests of Department of Defense, industry, and NASA fixed-wing and rotary-

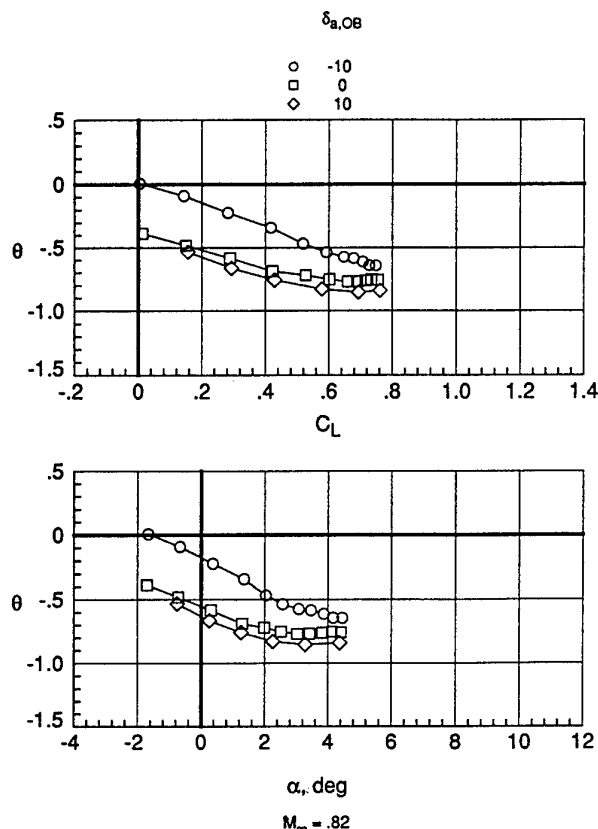


Figure 3. Effect of outboard aileron deflection on the model aeroelastic deformation at Mach 0.82 at the NTF.

wing flight vehicles and launch vehicles²¹. Semispan side-wall-mounted vehicles and full-span sting-mounted or cable-mounted models can be used. In addition, a rotorcraft test-bed is available for rotor-blade loads research. The TDT is a continuous-flow, variable-pressure wind tunnel with a 16-ft by 16-ft test section. The tunnel uses either air or a heavy gas as the test medium and can operate at Mach numbers up to about 1.2 while obtaining Reynolds numbers per foot of approximately 3×10^6 in air and 10×10^6 in heavy gas.

The first automated videometric measurements of wing twist and bending at NASA Langley were made at the TDT in 1994 where the application of high contrast targets on the wing made possible the use of image processing techniques to automatically determine the image coordinates of the targets. A frame grabber with a large onboard memory of 64 Mbytes has been used to record and analyze up to 8 sec of video images per data point taken at a 60 Hz rate for dynamic studies. The system at the TDT has been used for a number of tests of semispan models, both rigid and flexible. Static laboratory wing loading tests have been conducted with the automated system with a worst case agreement of 0.3 mm compared with dial gauges.

Measurements have also been made on the DARPA/Wright Labs/Northrop Grumman Smart Wing that had variable twist

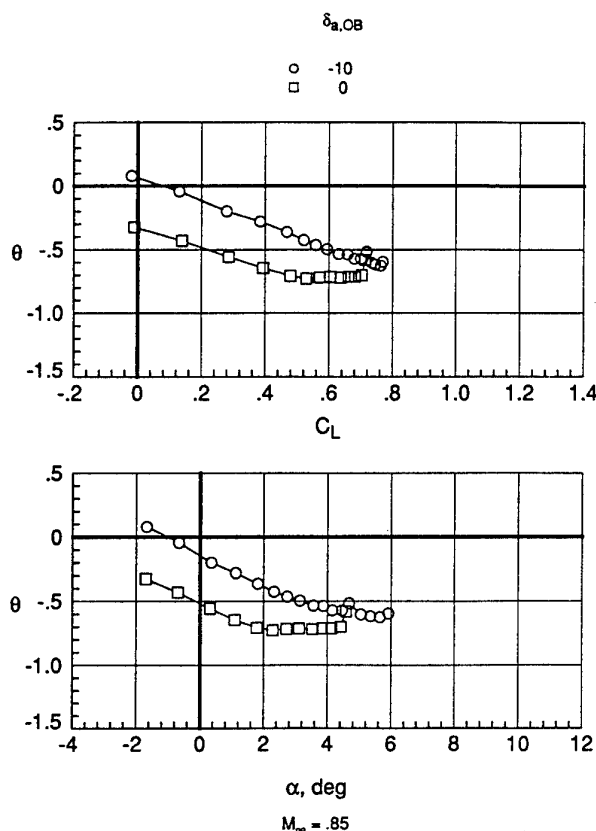


Figure 4. Effect of outboard aileron deflection on the model aeroelastic deformation at Mach 0.85 at the NTF.

and adaptive control surfaces to provide continuous wing contour and variable camber²². Tests were first conducted on a conventional wing model without smart structures for comparison to the Smart Wing and to validate the model deformation system. The system was used to determine the trailing edge deflection angles of the Smart Wing, which were embedded with shape memory alloy (SMA). The system was also used to measure model wing twist when the SMA torque tubes were activated. The system provided near real time model control surface deflections and twist. Additional measurements are planned for the Smart Wing in January 1998, which is the first scheduled test when TDT resumes operations after a lengthy maintenance and enhancement shutdown.

The measurement system at the TDT has also been adapted for displacement measurements during a test of a piezoelectric wafer actuator to alter the upper surface geometry of a subscale airfoil to enhance performance. Results showed that the piezoelectric actuator can be used to alter the camber of a small airfoil under aerodynamic load^{23, 24}. Fluorescent paint on the wafer edge illuminated by UV light sources provided a high contrast image suitable for automated measurements in a small-scale wind tunnel setup at 15 locations along the edge of the wafer. Deflection measurements at various angles of attack at a 30 Hz rate in bursts up to 1 minute (or at a 10 Hz

rate for continuous operation) were possible with the modified automated measurement system.

4.3 Unitary Plan Wind Tunnel

The Langley Unitary Plan Wind Tunnel (UPWT) is a closed circuit, continuous-flow, variable-density tunnel with two 4-ft by 4-ft by 7-ft test sections²¹. One test section has a design Mach number range from 1.5 to 2.9, and the other has a Mach number range from 2.3 to 4.6. The tunnel has sliding-block-type nozzles that allow continuous variation in Mach number while the facility is in operation. The maximum Reynolds number per foot varies from 6×10^6 to 11×10^6 , depending on Mach number. Types of tests include force and moment, pressure distribution, jet effects, dynamic stability, and heat transfer. The model deformation measurement system at the UPWT has sufficient automation that facility personnel now fully operate the system, including calibration and validation, for tests in either test section. The measurement system has been used for aeroelastic studies to assess Mach number and Reynolds number effects in addition to comparisons of models with flapped and solid wings.

The model deformation measurement system at the UPWT has also been used in a special test to assess the "modern design of experiments" approach. The advantages of the modern design of experiments approach to wind tunnel testing were compared with the conventional pitch-polar "classical" design to identify the relative costs and benefits of each approach in actual wind tunnel test conditions. "Modern" designs seek to minimize resources by simultaneously changing independent variables to assess their joint impact on response variables. Because "classical" designs change only one variable at a time, they can be more costly than modern designs. The modern design can also help in data analysis in discovering effects that might be overlooked in a classical design.

The comparison test between modern and classical designs at the UPWT consisted of the measurement of aerodynamically induced wing twist at five semispan locations on the wing of a slender wing/body/tail configuration over selected ranges of Mach number, Reynolds number, and angle of attack. For this test, a savings in wind-on minutes of approximately 60% was achieved when Modern Design methods were used in place of the conventional pitch-polar (classical) method. The resource comparison is shown in figure 5 that compares the number of data points and wind-on minutes for the modern and classical approaches.

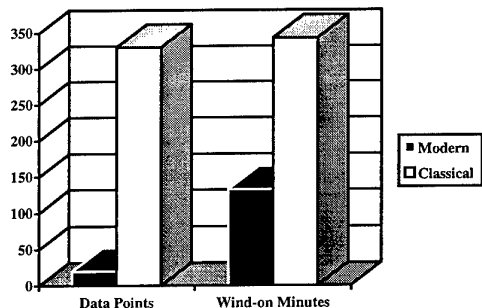


Figure 5. Resource comparison of classical and modern experimental designs.

Figure 6 plots the change in wing twist due to aerodynamic load versus angle of attack for one of the semispan locations. The classical data are plotted as solid rectangles with the corresponding 95% prediction interval plotted as the jagged line. The 95% prediction interval results from the modern design are plotted as the smoothly varying lines that are noted to agree very well with the classical data. An important point to note regarding this data is that the classical data consists of

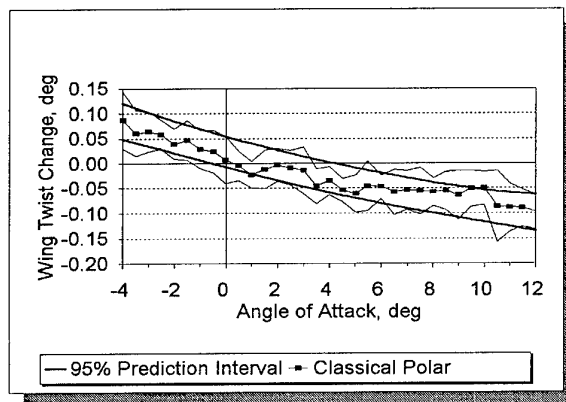


Figure 6. Comparison of classical data and prediction intervals to those found with the modern approach.

32 data points, while for the modern design results, **not a single data point was taken at the particular Mach number and semispan location where the classical data were taken**. The curve fit that represents the modern results for this plot was obtained from the wing twist response surface generated as part of the modern design analysis. The results of the comparison test were considered very encouraging and have led to additional tests of the modern method using more common aerodynamic variables at other NASA facilities²⁵.

4.4 Ames 12-Ft Pressure Tunnel

The restored 12-Foot Pressure Tunnel at NASA Ames is a closed-return, variable-density tunnel with a continuously variable Mach number from 0.05 to 0.60. Maximum Reynolds number is 12 million per foot. The twelve-foot diameter, 28.5-foot long test section has 4-foot wide flats on the ceiling, floor and sidewalls. The entire test section rotates to permit installation or removal of fully assembled models, which reduces model access time by 2/3 from the original tunnel. The 12-Foot tunnel is the only large scale, pressurized, very low turbulence, subsonic wind tunnel in the United States. It provides unique capabilities in high Reynolds number testing for the development of high-lift systems for commercial transport and military aircraft and high angle of attack testing of maneuvering aircraft.

A variety of model support systems are available, including bipod, semispan floor mounting, rear sting, and high angle of attack support. To date, aeroelastic model deformation measurements have been made for two tests, a full model supported on the bipod and a semispan model floor mounted vertically. For the bipod supported model the deformation system viewed retroreflective targets placed at various

semispan locations along the right wing and body. The CCD camera was installed for protection in a pressure vessel with window. An incandescent lamp was placed near the camera in the same viewport in order to illuminate the retroreflective targets. Part of the wing had to be painted flat black to eliminate specular reflections where the surface normal bisected the camera and light source locations.

The second model deformation test at 12-Foot was conducted in conjunction with pressure sensitive paint (PSP) measurements for the first time in a joint Ames-Langley wind tunnel experiment under the Aeronautics Design / Test Environment (ADTE) program. The emphasis of the ADTE program, which is managed from NASA Ames Research Center, is to improve the productivity of existing wind tunnels, improve the quality and extent of knowledge extracted and radically change the role of wind tunnels in the aircraft development process. A subelement of the ADTE program is the unification of production instrumentation systems to allow the capture of as much data as possible at a given test condition. This would eliminate the need to run multiple tests with different instrumentation systems, would facilitate the combining of multi-disciplines eliminating multiple test runs, and provide real time data containing a greater impact on the design process. Unification would include development of common software for cameras, common containment vessels, etc. The production instrumentation systems to be unified include pressure sensitive paint (PSP), model position and deformation, Doppler global velocimetry (DGV), and phased microphone array technology (PMAT). NASA Langley, the lead for model position and deformation, is currently collaborating with NASA Ames in the unification effort. A major component of this effort is the unification of model deformation with PSP and temperature sensitive paints (TSP).

The next-generation model deformation system was used for the first time in the semispan test to make aeroelastic wing twist and bending measurements on a 7.25% MD-11 semispan model using PSP reference targets. For this high lift PSP and model deformation test, Mach number ranged from 0.23 to 0.3, dynamic pressure ranged from 140 to 328 psf, Reynolds number ranged from 2.9 to 6.7 million per foot, and angle-of-attack ranged from -6° to 23° . The model deformation data from this test was especially needed since finite element methods were not used to predict aeroelastics due to the complicated nature of the high lift configuration. The new deformation measurement system employed an optimization method for determination of the exterior and interior orientation parameters of a camera to simplify and reduce the time required for calibration. In addition, the new system employed a target tracking technique for robustness with non-optimum targets and background such as occurs when viewing PSP reference targets. These reference targets are placed on a model surface during PSP for image registration to correct the effects of non-uniformity of illumination, paint thickness and luminophore concentration. The increase in robustness for non-optimum target contrast is considered a major improvement over the current version, which could not locate the PSP reference targets reliably in automated mode.

4.5 16-Foot Transonic Tunnel

The Langley 16-Foot Transonic Tunnel is a single-return atmospheric wind tunnel with a slotted transonic test section and a Mach number range of 0.2 to 1.25.²¹ The octagonal test

section measures 15.5 ft across the flats. The tunnel is used for force, moment, pressure, flow visualization, and propulsion-airframe integration studies. Models are mounted in the test section by sting, sting-strut, or semispan support arrangements.

The dedicated model deformation system for the facility is suitable only for sting mounted models at present. The CCD camera, light source and power supply are currently mounted on a movable flat of the test section which must be compensated for with wind-off polars at the various flat angular settings. The compensation scheme for the movable flat remains to be tested. A flat mirror is used to direct the light from a 150-watt lamp around the camera and out the same window. The light output is variable from the control room. A vortex cooler requiring a pressurized air supply is used to reduce the temperature near the camera, which may reach 170° F without cooling. The model center of rotation is located near to the wing area, which enables a smaller field of view in order to increase resolution.

The first test at 16-Ft with the recently installed dedicated system is currently scheduled for September 1997. The next-generation deformation measurement system will also be used for this test for evaluation while viewing PSP reference targets that will be on the upper wing surface while the current version views retroreflective targets on the lower wing surface. The PSP and model deformation measurement systems, while still separate systems, will be installed with the intent to take PSP and deformation as close to the same time as practical.

5. NEXT-GENERATION VIDEO MODEL DEFORMATION MEASUREMENT SYSTEM

The next-generation model deformation system currently under development will exploit advances in video and computer hardware while incorporating lessons learned from using the model deformation system in actual wind tunnel testing as described earlier. One of the important recent developments is the shift to high-performance 32-bit peripheral buses, such as PCI, in personal computers. This has led to the development of inexpensive video-acquisition boards for PCs which greatly improve system throughput without resorting to the use of on-board memory or signal processors. The increased processing speed can be used in several ways. By using more fields of video data per wind-tunnel data point (for example, 30 or 60 fields in a second instead of the current 15), the new system will be more immune to anomalies related to model dynamics by providing better statistics in the measured angular data. Increased system speed also makes practical the use of higher-resolution video cameras, which can help with operational details, such as the required speed of targets on the model. Most importantly, the increased speed opens the door to more sophisticated solutions to the complicated problems of target-detection and sorting, while maintaining the goal of near-real-time performance. By using a combination of active target tracking (instead of passive searching in each field) and pattern recognition, the robustness of the model deformation system will be greatly improved by reducing its sensitivity to extraneous bright areas in the image. This will allow highly automated operation, and will improve the flexibility of the targeting and lighting options for the system. This is highly desirable in sensitive environments such as the NTF, and will increase the prob-

ability of successful integration with other optical measurements. With these improvements, the system will be able to function more like a traditional instrument, returning current data on demand for wing twist or model attitude.

The new system will also use an upgraded version of the model deformation software that requires less user intervention. This will permit unattended operation for extended periods, with model deformation results delivered automatically to the wind tunnel data system. As part of the ADTE program, the new system will interface with the advanced DARWIN²⁶ and ServIO systems. These systems allow for real-time sharing of data between cooperating instrumentation systems, storage of data using standardized file formats, and data searching based on selected metadata parameters.

6. OTHER NASA LANGLEY MODEL DEFORMATION MEASUREMENT DEVELOPMENTS

Projection Moiré Interferometry (PMI), a second method for measuring wind tunnel model deformation, has been under development at NASA Langley²⁷. PMI is a simple, yet powerful technique that has been used since the early 1900's for surface topology and shape characterization. Past efforts to use PMI for wind tunnel model deformation measurements revealed limitations in the technique - particularly directional ambiguity. Recent advances in electronic image acquisition and image processing have overcome these limitations, and have made PMI a viable instrument capable of measuring whole field, 3-component displacement vectors of any visible point on the model surface.

A single component PMI system consists of an illumination source, Ronchi ruling, CCD camera, and frame grabber. Using the illumination source and ruling, a series of equispaced, parallel lines are projected onto the object surface. A reference image is acquired in a non-deformed (or wind off) condition to digitally record the projected line pattern. Under load, the model will have moved, and the projected lines will appear to lie in different spatial locations. When subsequent images of the deformed state are acquired and subtracted from the reference image, moiré fringes are formed. The geometric configuration of the instrument and projected line pitch dictate the moiré fringe spacing. Using this relation and fringe counting via image processing, the displacement field can be determined. With commercial hardware and generic RS-170 video cameras, fringe sensitivities of 0.5 mm are common. Advanced image processing and fringe interpolation techniques can extend this resolution to 1/10 to 1/20 of a fringe.

In contrast to video photogrammetry, PMI requires no surface preparation or registration targets to be placed on the model. The off-line deformation analysis is done whole field, rather than by curve fitting between targets. Moiré fringes can be observed in real time providing the test engineer immediate video feedback regarding model position. If desired, this capability allows the engineer to reposition the model to account for differences between wind-off and wind-on body AoA before acquiring aerodynamic data. With the proper illumination source, both PMI and video photogrammetry can be used with other optical wind tunnel instrumentation systems simultaneously. At NASA Langley, PMI systems are being designed with high power, 800-810 nm laser diodes as the illumination source. When selectively filtered, this per-

mits simultaneous operation with such techniques as Pressure Sensitive and Temperature Sensitive Paint (PSP and TSP), conventional laser velocimetry, and Doppler global velocimetry (DGV).

Because PMI is still under development as a wind tunnel instrument, video photogrammetry remains the predominant model deformation tool used at Langley. PMI is currently being investigated for measuring dynamic rotor blade deflection, and for unification with other instrumentation systems. Towards these goals, two proof-of-concept tests have been planned: (1) a combined PMI/DGV rotor craft test in the Langley 14- x 22- foot tunnel to investigate rotor blade / wake vortex interaction, and (2) a unified instrumentation test in the Langley Unitary Plan Wind Tunnel comprised of PMI, video photogrammetry, DGV, and PSP. Long term PMI applications include measuring deformation profiles of active feedback controlled rotor blades in simulated flight conditions.

ACKNOWLEDGMENTS

Lewis Owens and Dr. Richard Wahls have been associated with a number of model deformation tests at the NTF. The advocacy of Owens and Wahls for model deformation measurements was instrumental to the development of dedicated systems for the UPWT and 16-Ft tunnels. Dr. Ray Mineck supplied the low Reynolds number wing twist plots from the NTF and has collaborated on a number of model deformation tests at the NTF. Gary Erickson has collaborated on several tests at the UPWT, including the comparison of modern and classical experimental designs. Richard DeLoach has designed model deformation experiments to minimize the expenditure of resources while maximizing information obtained using modern design of experiment techniques and supplied the two data plots from UPWT illustrating the comparison of modern and classical experimental designs. Gary Fleming supplied the description of NASA Langley developments with the PMI technique and the comparison of PMI to the video photogrammetric technique. W. K. Goad is acknowledged for his continuing developments of the video system at the NTF and for his many contributions to the dedicated systems at the TDT, UPWT, and 16-Ft. Harriett Dismond and Kenneth Cate are acknowledged for continuing support in installations, calibration, and operations. Dr. Tianshu Liu and Dr. Ron Radeztsky, High Technology Corporation, are acknowledged for their ongoing development of the next-generation model deformation system and applications under the ADTE program in cooperation with John Schreiner and Dr. James Bell at NASA Ames and the Experimental Testing Technology Division at NASA Langley. Finally, the operations and research staff at the NASA Langley NTF, TDT, UPWT, 16-Ft, the Experimental Testing Technology Division, and the NASA Ames 12-Ft Tunnel are acknowledged for assistance and support in developments and applications at their facilities.

REFERENCES

1. Brooks, J. D. and Beamish, J. K., "Measurement of Model Aeroelastic Deformations in the Wind Tunnel at Transonic Speeds Using Stereophotogrammetry", NASA TP 1010, Oct. 1977.
2. Hooker, J. R., Burner, A. W., Valla, R., "Static Aeroelastic Analysis of Transonic Wind Tunnel Models Using Finite

- Element Methods", *Presented at the AIAA Applied Aerodynamics Conference*, Atlanta, GA, AIAA paper 97-2243, June, 1997.
3. Watzlavick, R. L., Crowder, J. P., Wright, F. L., "Comparison of Model Attitude Systems: Active Target Photogrammetry, Precision Accelerometer, and Laser Interferometer", *presented at the 19th AIAA Advanced Measurement and Ground Testing Technology Conference*, AIAA 96-2252, June 17-20, 1996.
 4. Willard, P., Hardin, J. D., Whitehead, J. H., "Determination of In-Flight aeroelastic Deformation of a Transport High-Lift System Using Optical Position Measurement Technology", *presented at the 1st AIAA Aircraft Engineering, Technology, and Operations Congress*, Los Angeles, CA September 19-21, 1995.
 5. Burner, A. W., Wahls, R. A., and Goad, W. K., "Wing Twist Measurements at the National Transonic Facility", NASA TM 110229, Feb. 1996.
 6. Burner, A. W. and Martinson, S. D., "Automated Wing Twist and Bending Measurements Under Aerodynamic Load", *presented at the 19th AIAA Advanced Measurement and Ground Testing Technology Conference*, AIAA 96-2253, June 17-20, 1996.
 7. Burner, A. W., "Videometric Applications in Wind Tunnels", *presented at the SPIE International Symposium on Optical Science, Engineering, and Instrumentation, Videometrics V*, paper # 3174-24, 30-31 July 1997.
 8. DeAngelis, V. M., Fodale, R., "Electro-Optical Flight Deflection Measurement System", *presented at the Society of flight Test Engineers Conference*, 1987, 14 pages.
 9. Lokos, W. A., "Predicted and Measured In-Flight wing Deformations of a Forward-Swept-Wing Aircraft", NASA TM 4245, Nov. 1990, 21 pages.
 10. Kurkov, A. P., "Optical Measurement of Propeller Blade Deflections", NASA TP 2841, 1988, 28 pages.
 11. Wadcock, A. and Lillie, M., NASA Ames, *private communication*, 1997.
 12. Lamiscare, B., Sidoruk, B., Castan, E., and Bazin, M., "Dispositif RADAC de Mesure des Deformations de Maquette. Premiers Resultats Obtenus dans la Soufflerie F1", ONERA T.P. n° 1990-57, 17 pages.
 13. ONERA Activities 1996.
 14. Surget, J., "Model Attitude and Deformation Measurement in wind Tunnels", ONERA T.P. n° 1982-91, 15 pages.
 15. Charpin, F., Armand, C., Selvaggini, R., "Measurement of Model Deformation in Wind Tunnels", ONERA T.P. n° 1986-126, 20 pages.
 16. Baumann, P. H. and Butefisch, K. A., "Measurement of hinge moments and model deformations in wind tunnels by means of Moire interferometry", *presented at the SPIE Optical Techniques in Fluid, Thermal, and Combustion flow*, SPIE vol. 2546, pp. 16-32, San Diego, CA, July 1995.
 17. ETW News, Issue No. 6, April 1997, pp. 4.
 18. Tripp, J. S., Tchong, P., Burner, A. W., Finley, T. D., "Report on the First International Symposium on Strain Gauge Balances and Workshop on AOA/Model Deformation Measurement Techniques", *presented at the RTO (NATO) Advanced Aerodynamic Measurement Technology Meeting*, Seattle, Washington, Sept. 22 - 25, 1997.
 19. Burner, A. W., "Zoom Lens Calibration for Wind Tunnel Measurements", *Proc. of Videometrics IV*, Philadelphia, Pennsylvania, SPIE Vol. 2598, pp. 19 - 33, Oct. 25-26, 1995.
 20. Burner, A. W., Snow, W. L., Shortis, M. R., and Goad, W. K., "Laboratory Calibration and Characterization of Video Cameras", *presented at ISPRS Symposium: Close-Range Photogrammetry Meets Machine Vision*, Zurich, Switzerland, Sept. 1990; published in SPIE Proceedings 1395 pp. 664-671.
 21. *Research and Technology Highlights 1994*, NASA TM-4708, Dec 1995.
 22. Scherer, L. B., Martin, C. A., Appa, K., Kudva, J., and West, M. N., "Smart Wing Wind Tunnel Test Results", *presented at the SPIE Fourth Annual Symposium on Smart Structures and Materials*, San Diego, CA, 1997, paper NO. 3044-05.
 23. Pinkerton, J. L., McGowan, A. R., Moses, R. W., Scott, R. C., Hegg, J., "Controlled Aeroelastic Response and Airfoil Shaping Using Adaptive Materials and Integrated Systems", *presented at the SPIE 1996 Symposium on Smart Structures and Integrated Systems*, San Diego, CA Feb 26-29, 1996.
 24. Pinkerton, Jennifer L. and Moses, Robert W., "A Feasibility Study to Control Airfoil Shape Using THUNDER," NASA TM-4767, *Publication pending*.
 25. DeLoach, R., "Application of Modern Experimental Design to Wind Tunnel Testing", *to be presented at the Ground Test Techniques session of the AIAA Aerospace Sciences Conference*, Reno, NV, Jan 12-15, 1998.
 26. Schreiner, J. A., Trosin, P. J., Pochel, C. A., and Koga, D. J. "DARWIN - Integrated Instrumentation and Intelligent Database Elements", *presented at the 19th AIAA Advanced Measurement and Ground Testing Technology Conference*, AIAA Paper 96-2251, 1996.
 27. Antcliff, R. R., "Advanced Measurement Technology at NASA Langley Research Center", *presented at the RTO (NATO) Advanced Aerodynamic Measurement Technology Meeting*, 22 - 25 Seattle, Washington, Sept. 1997.

MEMS Applications in Aerodynamic Measurement Technology

E. Reshotko and M. Mehregany

Case School of Engineering
Case Western Reserve University
Cleveland, Ohio 44106 U.S.A.

C. Bang

Advanced MicroMachines, Incorporated
11000 Cedar Avenue
Cleveland, Ohio 44106 U.S.A.

1. INTRODUCTION

Microelectromechanical systems (MEMS)¹ embodies the integration of sensors, actuators, and electronics on a single substrate using integrated circuit fabrication techniques and compatible bulk and surface micromachining processes. Silicon and its derivatives form the material base for the MEMS technology. MEMS devices, including microsensors and microactuators, are attractive because they can be made small (characteristic dimension about 100 microns), be produced in large numbers with uniform performance, include electronics for high performance and sophisticated functionality, and be inexpensive.

For aerodynamic measurements, it is preferred that sensors be small so as to approximate measurement at a point, and in fact, MEMS pressure sensors, wall-shear-stress sensors, heat flux sensors and micromachined hot wires are nearing application.^{2,3} For the envisioned application to wind tunnel models, MEMS sensors can be placed on the surface or in very shallow grooves. MEMS devices have often been fabricated on stiff, flat silicon substrates, about 0.5 mm thick, and therefore were not easily mounted on curved surfaces. However, flexible substrates are now available and heat-flux sensor arrays have been wrapped around a curved turbine blade. Electrical leads can also be built into the flexible substrate. Thus MEMS instrumented wind tunnel models do not require deep spanwise grooves for tubes and leads that compromise the strength of conventionally instrumented models. With MEMS, even the electrical leads can potentially be eliminated if telemetry of the signals to an appropriate receiver can be implemented.

While semiconductor silicon is well known for its electronic properties, it is also an excellent mechanical material for MEMS applications. However, silicon electronics are limited to operations below about 200

C, and silicon's mechanical properties start to diminish above 400 C. In recent years, silicon carbide (SiC) has emerged as the leading material candidate for applications in high temperature environments and can be used for high-temperature MEMS applications. With SiC, diodes and more complex electronics have been shown to operate to about 600 C, while the mechanical properties of SiC are maintained to much higher temperatures.

Even when MEMS devices show benefits in the laboratory, there are many packaging challenges for any aeronautics application. Incorporating MEMS into these applications requires new approaches to packaging that goes beyond traditional integrated circuit (IC) packaging technologies. MEMS must interact mechanically, as well as electrically with their environment, making most traditional chip packaging and mounting techniques inadequate. Wind tunnels operate over wide temperature ranges in an environment that is far from being a "clean-room." In flight, aircraft are exposed to natural elements (e.g. rain, sun, ice, insects and dirt) and operational interferences (e.g. cleaning and deicing fluids, and maintenance crews). In propulsion systems applications, MEMS devices will have to operate in environments containing gases with very high temperatures, abrasive particles and combustion products. Hence deployment and packaging that maintains the integrity of the MEMS system is crucial.

This paper presents an over view of MEMS fabrication and materials, descriptions of available sensors with more details on those being developed in our laboratories, and a discussion of sensor deployment options for wind tunnel and flight applications.

2. FABRICATION TECHNOLOGY

MEMS devices are fabricated by a combination of IC fabrication processes and micromachining techniques. Silicon micromachining represents the fashioning of microscopic mechanical parts from or on a silicon substrate, and is an extension of the IC fabrication technology. Micromachining has been used, for example, to fabricate beams, diaphragms, grooves, orifices, sealed cavities, pyramids, needles, springs, gears, linkages, and motors. With integrated electronics, these microstructures acting as transducer elements have been used to realize a gamut of microsensors and microactuators.⁴

Some of the key silicon micromachining techniques are surface and bulk micromachining, substrate bonding, and micromolding.¹ In surface micromachining, micromechanical devices are fabricated on the surface of the substrate by consecutive deposition and patterning of thin films of structural and sacrificial materials, with the wafer acting as a mechanical carrier. The structural parts of the device are encased by the sacrificial layers during fabrication. At the end, the sacrificial layers are dissolved in a chemical etchant that does not remove the structural parts. Polysilicon and silicon dioxide are common examples of structural and sacrificial materials, respectively, used in a process known as polysilicon surface micromachining, which is the process used to fabricate the shear stress sensor described later in this paper. Surface micromachining can be used to fabricate conventional beams, diaphragms, and suspensions, as well as more complex mechanical structures such as gears, turbines, and linkages.¹

Bulk micromachining uses wet and dry silicon etching techniques, with etch masks and etch stops, to sculpt mechanical devices from the silicon wafer.¹ Certain chemicals, such as KOH, etch the (100) and (110) silicon crystal planes much faster than the (111) planes. This property can be used to create desired shapes/structures by utilizing etch masks and etch stops to selectively expose areas of the silicon wafer to the anisotropic wet etchant. Silicon dioxide and silicon nitride generally have very slow etch rates in the silicon anisotropic wet etchants and make good etch masks. Etch stop regions are created by manipulating the doping concentration to make desired regions resistive to the wet chemical etchant. Silicon pressure sensors, for example, commonly rely at least in part on bulk micromachining technology to create the pressure sensitive diaphragm. Since the geometries that may be fabricated by bulk micromachining are generally limited by the silicon crystal plane orientations (e.g., generally Manhattan planar shapes and sloped side walls) when using wet anisotropic etchants, dry plasma etching of silicon

using a reactive ion etcher has been used to define more complex geometries with curved planar features and deep vertical side walls into a silicon wafer.⁵

Bonding techniques permit a silicon substrate to be attached to another substrate, usually glass or silicon, to provide added design flexibility, mechanical support, electrical connection, and/or thermal sink/isolation.¹ Since the silicon fabrication techniques are generally planar in nature, bonding extends design flexibility in the thickness direction. Electrostatic bonding of silicon to glass substrates and silicon-fusion bonding - bonding of two wafers at high temperature (near 1000°C) in an oxygen or nitrogen ambient - in tandem with bulk machining has been used to fabricate a variety of other MEMS devices (e.g., accelerometers, flow sensor, microvalves, micropumps, etc.).⁴

The aforementioned micromachining techniques are augmented by the capabilities of micromolding, a process in which a photolithographically-defined mold is used to plate up metallic microstructures.⁶ The mold is dissolved away subsequent to plating to release the metal microstructures. Techniques, such as x-ray photolithography, allow mold features with height-to-width aspect ratios over 100; features a few microns wide and several hundred microns deep with vertical side walls are possible.⁷

3. MATERIALS BASE

Single-crystalline silicon is generally the basic material for MEMS devices. While semiconductor silicon is well-known for its electronic properties, it is also an excellent mechanical material (e.g., modulus ~190GPa) for MEMS applications. However, silicon electronics are limited to operations below ~200 C, and silicon's excellent mechanical properties start to diminish over ~400 C. In recent years, silicon carbide (SiC) has emerged as the leading material candidate for applications in high-temperature environments and can complement silicon for high-temperature MEMS applications. With SiC, diodes and more complex electronics have been shown to operate up to ~600 C, while the excellent mechanical properties of SiC are maintained to much higher temperatures.⁸

In addition to single-crystal silicon, polysilicon, silicon dioxide, and silicon nitride are widely used in MEMS. Other materials which have been or are being experimented with include shape-memory alloy (SMA) metals, tungsten, diamond-like films, piezoelectrics, piezoceramics, polyimides, magnetic or ferrous materials such as nickel, and high-temperature superconductors. While all materials that can be processed with thin film technology can be incorporated into MEMS devices, limitations arise from IC and process compatibility. The former becomes important when an IC facility is used for

MEMS fabrication. The latter arises from the fact that a given device fabrication process is a composite of many fabrication steps, all of which must be compatible with respect to materials and processing requirements.

Mechanical properties, such as residual stresses, elastic modulus, fracture stress, adhesion, fatigue, creep, friction, and wear, of thin film materials are important in MEMS development. These properties have been and are being studied to varying degrees. MEMS devices typically have larger surface-to-volume ratio, higher smoothness of the contact surfaces, and smaller contact forces. As a result, conventional wisdom does not always explain the observed behaviors.

4. SENSOR EXAMPLES

MEMS devices, including both sensors and actuators, are increasingly being studied for aerodynamic applications. The sensor developments are more mature since actuator applications are generally more challenging. And it is in fact the sensors that are relevant to the theme of this conference.

4.1 Microfabricated Wall-Shear-Stress Sensors

Many boundary-layer control schemes (discussed later) require knowledge of the surface shear stress. However, the direct measurement of surface shear stress has been elusive. Conventional devices were simply too large or not sensitive enough for practical measurements. Simple and inexpensive direct measurement of surface shear stress can be made using MEMS technology. Two types of such sensors have been developed - one is a floating element design and the other is based on a surface mounted hot film sensor.

Floating Element Design: Microfabricated shear stress sensors based on a floating element balance design, as first demonstrated by Schmidt,⁹ are under development in our laboratory.¹⁰ Both active and passive designs have been demonstrated, and integration of the sensors with on-chip electronics is pursued. Furthermore, in a collaboration between CWRU and Analog devices, Inc., Waltham, MA, integrated shear stress sensors have been produced which combine surface micromachining with a 2 μm CMOS process. These sensors have the transducer element and electronics for signal amplification and conditioning integrated on the same chip.

An SEM photograph of a CWRU active shear stress sensor is shown in Fig. 1. The sensor is fabricated using polysilicon surface micromachining techniques and consists of a rectangular sense plate, 100 μm x 100 μm , suspended by 100 μm -long folded beams. The beams are flexible in the plane parallel to the surface and relatively inflexible in the direction normal to the substrate. The plate and beams are fabricated from

2.2 μm -thick phosphorous-doped polysilicon. Comb finger structures located on opposite sides of the plate are electrostatic actuators capable of moving the rectangular plate by electrostatic force when a voltage is applied across the outer comb finger pairs.

As gas flows over the chip, the surface shear stress produces a force on the floating element that causes the element to deflect. The deflection of the element is related to the shear force F and spring constant k by $\delta = F/k$. As the plate moves, the overlap area between the rectangular plate and a pair of underneath sense electrodes changes, producing a change in capacitance which can be measured with on-chip electronics. Differential pair and charge amplifiers are currently fabricated on-chip in a NMOS process which is combined with the polysilicon surface micromachining process needed to fabricate the transducer element. The electrostatic comb actuators may be used in a feedback control loop to maintain the plate at a null position for improved dynamic range and linearity. The actuators also provide the capability for self-test. Since the cavity below the plate is exposed to the environment, steady ambient pressure changes have no effect.

To calibrate the sensors, a flow calibration channel is designed.^{10,11} The sensor chip is flush-mounted in a recessed groove and subjected to a well-defined isothermal compressible two-dimensional channel flow. The gas enters one end of the flow channel, and travels a length sufficient for full flow development before reaching the sensor chip. Pressure ports along the channel allow the pressure gradient of the flow to be characterized. The deflection of the suspended plate is measured under a microscope and the relationship between flow and deflection is determined. It is also possible to monitor the element deflection electronically. The shear stress in the flow channel is calculated based on the measured pressure gradient and Mach number at the sensor location. The channel height is determined by the thickness of a thin shim stock bolted in between the upper and lower flow channel plates. The calibration relation is derived from the momentum theorem of fluid mechanics and so is independent of whether the flow in the channel is laminal, transitional or turbulent.

The graph in Fig. 2 shows test results for a sample of shear stress sensors.¹⁰ Sensors with 100 μm and 120 μm folded beams were tested, illustrating that the sensitivity of the sensor can be tailored by varying the stiffness of the suspended support structure. The suspended plate with the longer support beams is more compliant, exhibiting a higher sensitivity to shear stress. Separate data points indicate test results of different sensors, showing that a similar response is achieved from one sensor to the next. The devices have resonant frequencies of ~13KHz, but the current electronics have a flat response only to ~3KHz.

Clearly, capturing the high-frequency structures in a turbulent flow would require a new mechanical design and new electronics.

Surface Hot-Film Design: Hot film surface shear stress sensors are commonly used¹² but are subject to error because of heat loss to the substrate. At the micro scale, because of the large surface to volume ratio, these losses are prohibitive. However, by etching away a sacrificial layer underneath a silicon nitride diaphragm (Fig. 3), a vacuum chamber can be placed underneath the heating element thus significantly reducing the heat loss and enabling a functioning, sensitive sensor.^{13,14,15} The heating element is made of a uniformly doped polysilicon resistor and aluminum metalization forms the metal leads. Fig. 4 is a calibration curve showing a linear relation between the square of the output voltage and the one-third power of the shear stress. The typical cut-off frequency of the sensor is 10 kHz when operating in the constant temperature mode. These sensors can be assembled in closely packed large arrays and can also be mounted on flexible substrates.

4.2 Micro Pressure Sensors

Micro pressure sensors consist of a diaphragm with a piezoresistor patterned on it for strain measurement or else a capacitive readout of the diaphragm deflection. The majority of silicon pressure sensors are made for automotive and medical applications, however, silicon pressure sensors for aerospace instrumentation have been available for years from suppliers such as Kulite. Technology advances in micro pressure sensors are making available pressure sensors which are smaller, faster, and provide signal conditioning electronics. Frequency responses as high as 2 Mhz have been demonstrated for dynamic pressure measurements,¹⁶ although natural frequencies under 100 kHz are more typical. Micro pressure sensors are commonly available in pressure ranges from 0-5 PSI up to 0-500 PSI. Passive devices exhibit outputs up to 100 mV over the full scale span. Sensors with on-chip conditioning electronics are available with amplified output up to 5 V over the full scale span and temperature compensation.

4.3 Conformal Sensor Arrays in a Smart Skin Technology

In many applications, distributed sensors, actuators, and electronics acting over a large surface (larger than typical IC chip dimensions) with arbitrary shapes are desired. For example, it may be desirable to place an array of sensors, actuators, and electronics on the curved surface of an aircraft wing. MEMS devices are generally fabricated on rigid substrates that are not suitable for mounting on curved surfaces, making many applications impractical. In the case of the aircraft wing, small recesses would need to be machined in the wing along with wire through-holes at each distributed point. To solve this problem, suppose that a thin, flexible, large area sheet could be

manufactured containing arrays of MEMS, including electronics. Such a sheet could be manufactured separately in bulk and applied directly to an arbitrary structural surface, providing a convenient means for sensing, signal processing, and actuation for a wide variety of structures. An example of this smart skin technology is the heat flux sensor array for measuring heat transfer on a turbine blade has been developed at Advanced MicroMachines Incorporated (AMMi), Cleveland, OH. The concept is outlined in Fig. 5. An array of heat flux sensors is contained in a flexible surface that is sized to conform over a turbine blade or other test article. Electrical connections are made by metal lines microfabricated in the flexible material, eliminating the need for external wires. At one end of the array, which may be extended before the base of the turbine blade and away from the turbine gases, an interface chip is directly mounted to contact pads in the flexible material, eliminating the need for external wiring. The interface chip provides signal amplification and substantially reduces the number of output lines required through multiplexing. The sensing array is bonded to the surface of the turbine blade, conforming to its shape and providing multiple sensor locations distributed across the surface. The skin sensor array will allow a detailed area profile of surface heat flux to be measured, providing valuable data about unsteady heat transfer phenomenon in turbomachinery.

A cross section of an individual heat flux sensor is shown in Fig. 6. The sensor is comprised of temperature sensitive metal resistors sputtered and patterned on a flexible substrate. The insulating materials are spin-coated and patterned. During processing, the flexible substrate is mounted on a silicon wafer to provide rigidity and semiconductor material handling compatibility. After the sensors are completed, the flexible substrate is removed from the silicon wafer. The sensor employs a bridge arrangement of four temperature sensitive resistors. One resistor pair has a thin coating of insulation, while the other has a thick coating. As heat flows through the sensors into the test article, there is a slight temperature difference between the resistor pairs due to the larger thermal resistance over the resistors with thicker insulation. This temperature difference is proportional to the heat flux. The temperature change in the resistors produces a change in resistance that imbalances the bridge. If a current flows through the bridge, there will be a voltage between the output nodes that is proportional to the heat flux.

AMMi has developed a conformal pressure sensor array technology. A thin, flexible sheet containing multiple pressure sensing elements can be custom designed for the requirements of a particular test application. The pressure sensor array can be mounted onto an arbitrarily shaped test article to provide static and dynamic pressure measurements. Pressure ranges from 0-5 PSI up to 0-50 PSI are

currently available. The array contains interface electronics, including signal multiplexing and amplification. The sensor array provides over 4 V output over the full scale range.

Aside from the heat flux and pressure sensing applications described here, a wide range of MEMS devices could be employed in a smart skin for a wide variety of surface sensing and actuation applications. Incorporation of such devices into a smart skin array would further extend the capabilities of sensor technologies by providing a convenient means of sensor placement on an arbitrary (developable) surface.

5. APPLICATION ISSUES

Aerospace applications typically require MEMS devices to operate in hostile environments, possibly subjected to high Mach numbers, high temperatures, or excessive vibration. In many applications, high accuracy and high reliability are required. The suitability of MEMS for a particular application depends not only on device selection but also on how the device is packaged and installed. Specialized packaging is often required for rugged and reliable operation. Sensor packaging and installation can significantly affect the sensor performance, so that calibration must be done after packaging and in some cases after installation. Sensor accuracy may be improved through on-chip or hybrid electronics which provide temperature compensation and other signal conditioning functions. Self-test features are available for some MEMS devices. In cases where the sensor must be flush mounted to measure a surface flow, such as with shear stress sensors, backside contacts may be required to allow electrical interconnection without flow interference from wires. Because most MEMS research has been focused more on device demonstration than implementation in applications, the packaging technology is generally less mature than the device technology. Furthermore, the sensor packaging can substantially increase the cost of a MEMS device. Efforts to incorporate MEMS devices in applications should consider carefully the environment in which the device must operate, the performance requirements, and how the device will be packaged and calibrated in a given application. Paying attention to these issues from the onset will allow the end user to make better decisions in matching MEMS technology with application requirements for successful results.

5.1 Durability, Robustness, Drift

By and large, the questions of durability, robustness, drift, etc. have not been addressed. MEMS devices however may not be as delicate as they seem. The silicon has high strength and high Young's modulus. Those few tests that have been done so far show that MEMS sensors do survive in ordinary testing environments.

A CWRU/ADI shear stress sensor was recently tested in a shock tube at NASA-Lewis Research Center.¹⁷ The shock waves were intentionally weak because the objective of the tests was to see if the sensor could remain functional after being subjected to the starting shock system of supersonic wind tunnels. A working sensor gave repeatable traces after successive passes of a shock wave of strength $p_2/p_1 \approx 1.4$ ($\Delta p \approx 0.4$ psi). SEM inspection of the sensor before and after the tests revealed no structural damage.

Nevertheless, issues of durability, robustness and drift will have to be seriously addressed before there will be any meaningful use of MEMS sensors.

5.2 Deployment of Sensors or Sensor Systems

As stated at the very beginning of this paper, MEMS embodies the integration of sensors, actuators and electronics on a single chip. However, the decision as to what gets packaged on a single chip is very much application dependent. So far, there are no protocols established. Some possibilities are as follows:

Wind tunnel applications: MEMS technology can provide a very dense packaging of pressure and/or shear-stress sensors over a small area to give detailed information about local distributions. The signals can be multiplexed to minimize the number of lead wires needed (as in the case of the pressure sensor arrays and heat flux sensor arrays described earlier). However, this task is already being accomplished to a major extent by pressure sensitive paint and shear sensitive paint. Alternatively, one can package sensor combinations (pressure, shear-stress, heat-flux) on one chip with appropriate electronics. This enables readings of these disparate quantities at approximately a point. This is indicative of the many possibilities that could be thought of and implemented.

Flight applications: Shear stress sensors positioned near the trailing edge of a wing can be used as indicators of trailing edge separation, thus indicating the need for trim. If we dream further, the on chip electronics can cause the trim to be done automatically. Also, an array of shear stress sensors wrapped around the leading edge could be a way to quite precisely locate the attachment line. For these applications, the sensors could even be uncalibrated. Another flight application would be icing detectors. These are small diaphragms (1mm x 1mm to 3mm x 3mm) that are capacitively vibrated. Icing significantly changes the vibrational response of the sensor and gives a quantitative measure that is independent of the pilot's eyesight. Again, there are likely many other possible applications that can be developed.

Telemetry: In principle, telemetry is possible. If the transmitter is on the sensor chip or close to the sensor chip, then a transmitting antenna and power supply are needed near the chip. At present, battery

power supplies are quite large by MEMS standards (of the order of a number of square centimeters), and the receivers must be fairly close to the transmitters. So telemetering may lend itself only to special circumstances.

The eventual use of MEMS sensors in the wind tunnel or flight environment will require extensive dialog between the testing community and the sensor developers and packagers - the testing community to find out what is possible, and the MEMS community to find out what is desired. Without this dialog, it is unlikely that satisfactory MEMS systems can be delivered.

6. CONCLUSIONS

MEMS signifies the integration of sensors, actuators, and electronics on a single substrate. Because of their small size, low cost, high performance, and sophisticated functionality, MEMS sensors and actuators offer exciting opportunities for aerodynamics applications. MEMS sensor development for aerodynamic applications is becoming mature. While laboratory demonstrations of MEMS devices are often promising, significant packaging challenges must be overcome for practical use. It is important that the MEMS and user communities join in defining the implementable packages.

ACKNOWLEDGEMENT

This paper includes results from research contracts sponsored by ARO, AFOSR, and NASA at CWRU and AMMi. The most recent work is supported under AFOSR Grant F49620-96-1-0482.

REFERENCES

1. Mehregany, M., "Microelectromechanical Systems," IEEE Circuits and Devices, July 1993, pp.14-22.
2. Jiang, F., Tai, Y-C, Ho, C.-M., and Li, W., "A Micromachined Polysilicon Hot-Wire Anemometer," in Technical Digest, IEEE Solid State Sensor and Actuator Workshop, Hilton Head, SC, June, 1994, pp.264-267
3. Mehregany, M., DeAnna, R.G. and Reshotko, E., "Microelectromechanical Systems for Aerodynamics Applications, AIAA Paper 96-0421, January, 1996
4. Technical Digests, International Conferences on Solid State Sensors and Actuators, 1983, 1985, 1987, 1989, 1991, 1993, and 1995.
5. Klaassen, E., Petersen, K., Noworolski, J., Logan, J., Maluf, N., Brown, J., Storment, C., McCulley, W. and Kovacs, G., "Silicon Fusion Bonding and Deep Reactive Ion Etching; A New Technology for Microstructures," in Technical Digest, The 8th Int. Conf. on Solid State Sensors and Actuators, Stockholm, Sweden, June 1995.
6. Miyajima, H. and Mehregany, M., "High-Aspect-Ratio Photolithography for MEMS Applications," J. of Microelectromechanical Systems, vol.4, pp.220-229, Dec.1995.
7. Guckel, H., Christenson, T., Skrobis, K., Klein, J. and Karnowsky, M., "Design and Testing of Planar Magnetic Micromotors Fabricated by Deep X-ray Lithography and Electroplating," in Technical Digest, The 7th Int. Conf. on Solid State Sensors and Actuators, Yokohama, Japan, June 1993.
8. Krotz, G., Legner, W., Wagner, C., Moller, H., Sonntag, H. and Muller, G., "Silicon Carbide as a Mechanical Material," in Technical Digest, The 8th Int. Conf. on Solid State Sensors and Actuators, Stockholm, Sweden, June 1995.
9. Schmidt, M., Howe, R., Senturia, S. and Haritonidis, J., "Design and Calibration of a Micro-fabricated Floating-Element Shear-Stress Sensor," IEEE Trans. Elect. Dev., vol. 35, pp.750-757, June 1988.
10. Pan, T., Hyman, D., Mehregany, M., Reshotko, E. and Willis, B., "Characterization of Microfabricated Shear Stress Sensors," in Technical Digest, The 8th Int. Conf. on Solid State Sensors and Actuators, Stockholm, Sweden, June 1995.
11. Reshotko, E., Pan, T., Hyman, D. and Mehregany, M., "Characterization of Microfabricated Shear Stress Sensors," Proc. Eighth Beer-Sheva International Seminar on MHD and Turbulence, Jerusalem, Israel, February 1996
12. Hanratty, T.J. and Campbell, J.A., "Measurement of Wall Shear Stress," in Goldstein, R.J., Fluid Mechanics Measurements, 2nd ed., Chapt. 9, pp. 575-648, Taylor & Francis, 1996
13. Liu, C., Tai, Y-C, Huang, J. and Ho, C-M, "Surface-Micromachined Thermal Shear Stress Sensor," in Application of Microfabrication to Fluid Mechanics, FED-Vol. 197, pp. 9-16, ASME, 1994

14. Huang, J., Ho, C-M, Tung, S., Liu, C. and Tai, Y-C, "Micro Thermal Shear Stress Sensor With and Without Cavity Underneath," Proc. IEEE Instrumentation and Measurement Technology Conference, Waltham, MA, 1995.
15. Huang, J., Tung, S., Ho, C-M, Liu, C. and Tai, Y-C, "Improved Micro Thermal Shear Stress Sensor," IEEE Transactions on Instrumentation and Measurement, Vol. 45, No. 2, April 1996
16. Eaton, W.P., and Smith, J. H., "Characterization of a Surface Micromachined Pressure Sensor Array", Micromachining and Microfabrication Symposium, Oct. 23-24, 1995, Austin, TX, Proceedings of the IEEE, Vol. 2642, pp. 256-264.
17. Frate, F., "Dynamic Response of MEMS Shear Stress Sensors Within a Shock Tube," private communication (senior project report, Dept. of Mechanical and Aerospace Engineering, CWRU), May 1997

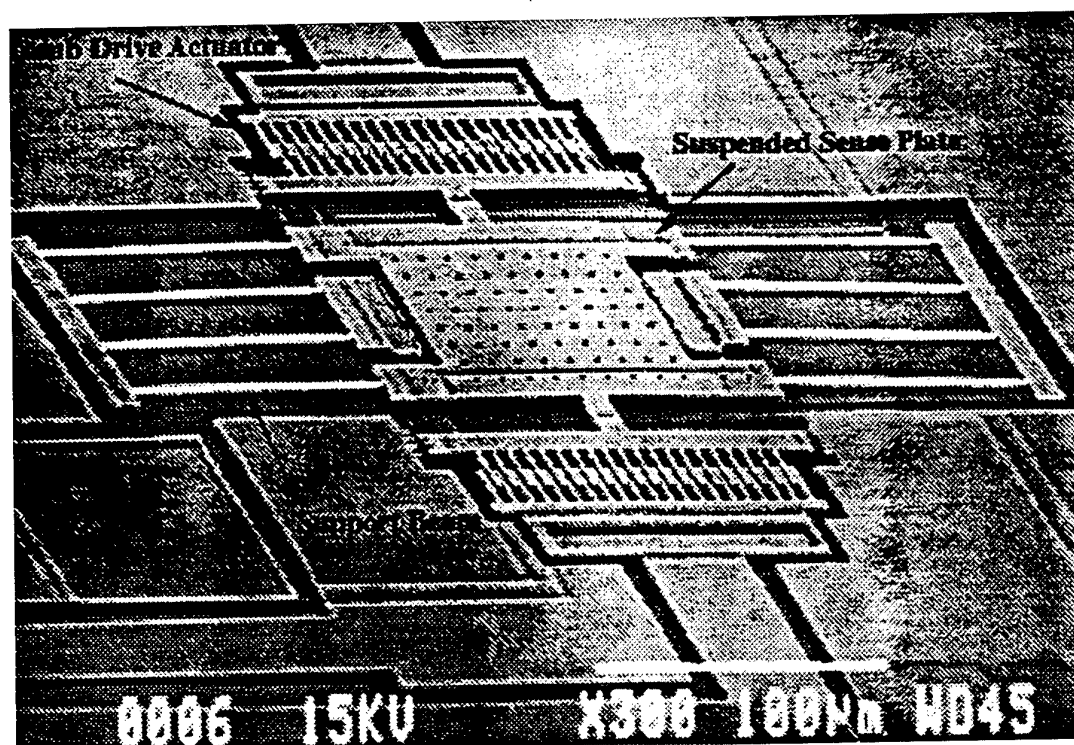


Figure 1: SEM photo of the CWRU shear stress microsensor.

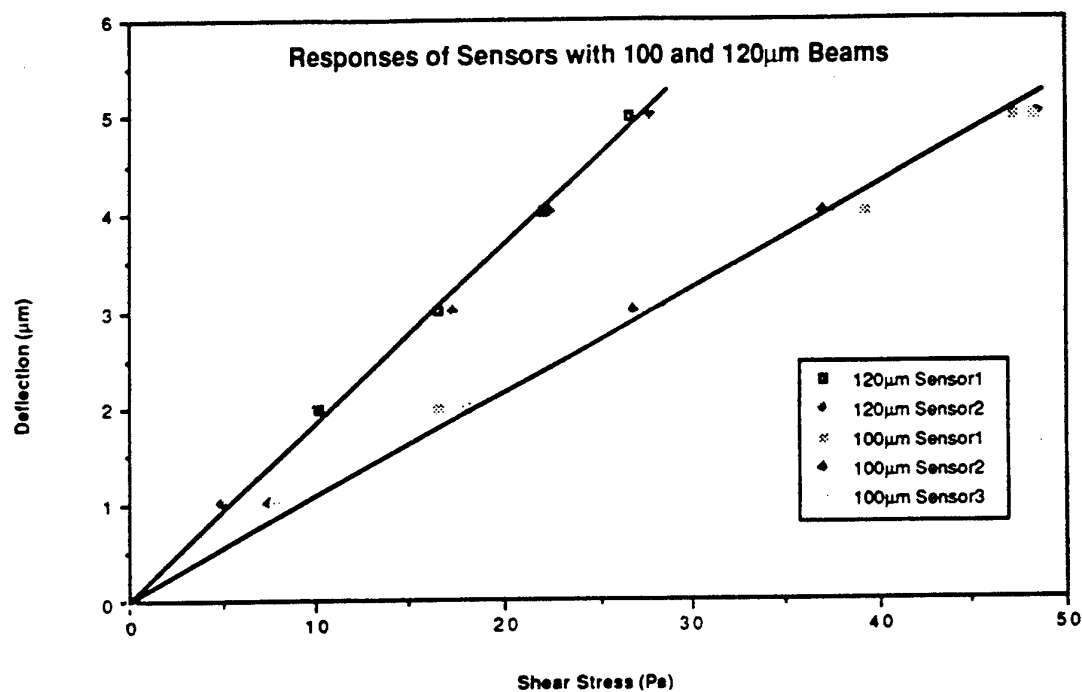


Figure 2: The element deflection as a function of applied shear stress is indicated for three sensors with 100µm-long and two sensors with 120µm-long support beams. The sensors with longer beams are more compliant, resulting in a greater sensitivity.

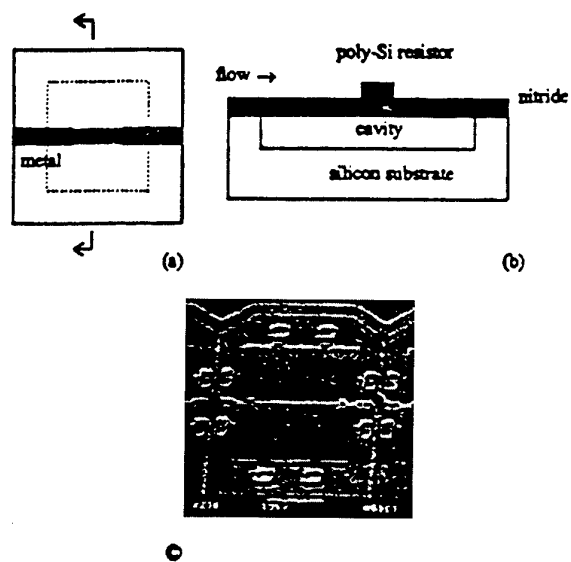


Fig. 3. Schematic of the top (a) and cross-sectional, (b) views of the micro shear-stress sensor, (c) SEM picture of the micro shear-stress sensor.

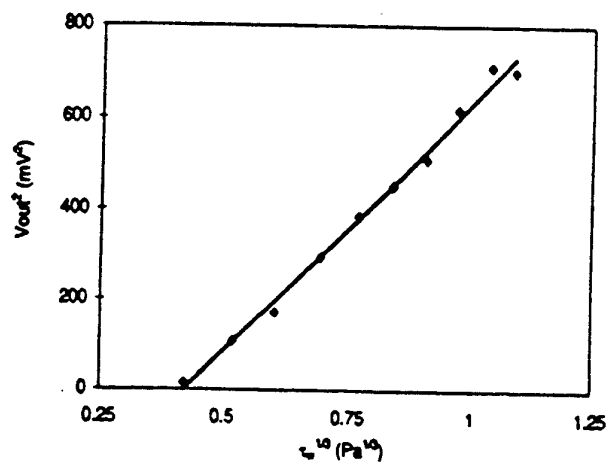


Fig. 4 Micro surface shear stress sensor output versus shear stress at constant temperature mode.

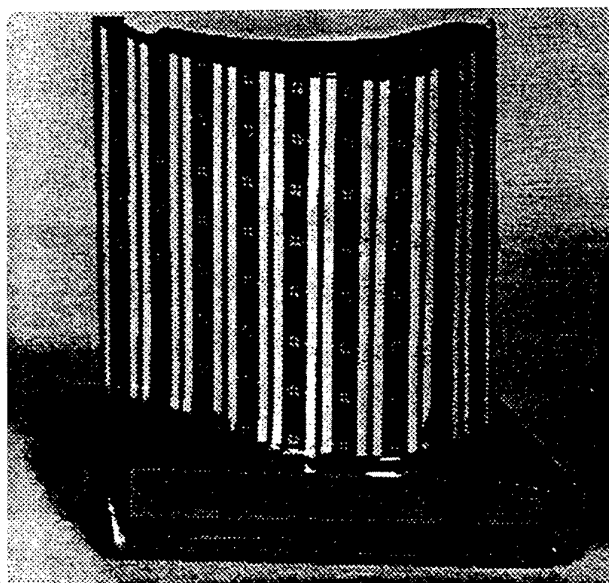
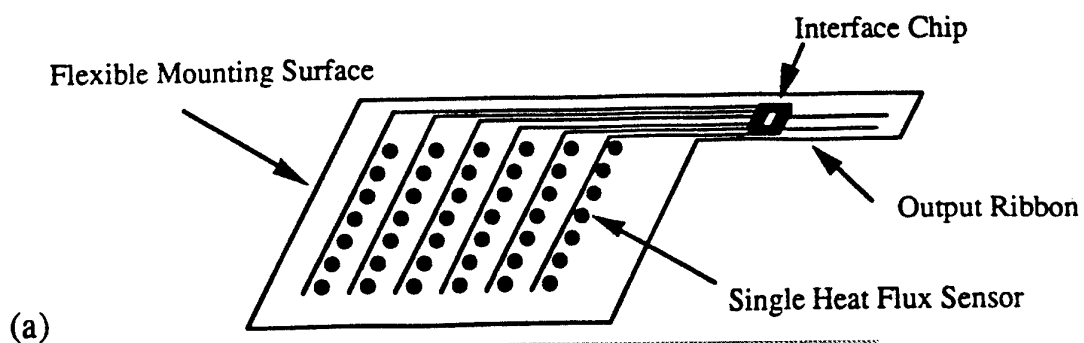


Figure 5: Heat flux sensor array system on a flexible skin: (a) schematic; and (b) actual.

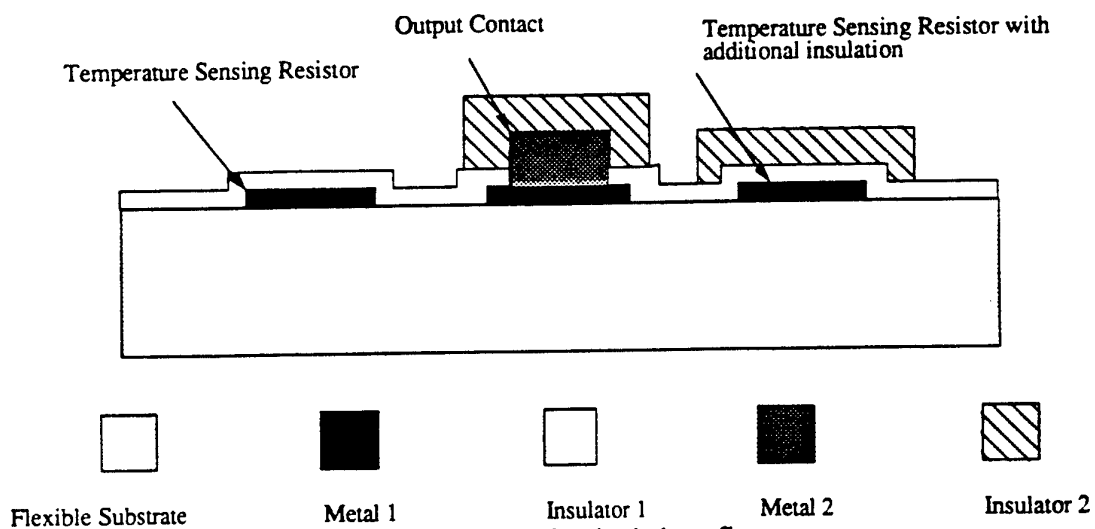


Figure 6: Cross section of a single heat flux sensor.

GENERAL DISCUSSION

FDP Fall Symposium in Seattle, USA, 22-25 September 1997

Ir. B. Elsenaar, NLR Netherlands:

This ends the Session on Specific Special Topics, and since I am standing here I might as well introduce Jim Crowder, the Technical Evaluator of this Conference. He had a very difficult job of sitting here in the lecture room, listening to all the talks, evaluating them and putting them together. Jim doesn't need much introduction, but I can just say one reason why we wanted him here to evaluate this Conference. He is a very innovative thinking man with good ideas about wind tunnel measurements, and he is working in the environment of an industrial company like Boeing and this combination makes him excellent, I think, for the evaluation of this Conference.

J. Crowder, Boeing, USA:

The 'Technical Evaluator': it is almost operatic; like the 'Grand Inquisitor' or the 'Lord High Executioner'. It is with some range of feelings that I am approaching this task. Originally proposed to me by my ex-boss, Ron Bengelink, I had a natural reaction to say yes. He said, "it is an easy thing". You heard the last comment, that it is a real difficult job. I am satisfied that the extent to which I am supposed to be prepared today is limited by the calendar. So, I am going to ask that you all contribute comments, opinions, etc., so that the final result will be a bit more complete and fleshed out. I sat around the house last night banging my head on the keyboard and realized that when you don't have a lot to say, maybe the first thing you do is resort to statistics. That will get us warmed up a little bit. By the way, I have been noticing that the audience throughout this Conference has been a little inhibited, so loosen up a little bit and I will try to provoke some conversation.

We had 35 papers. Excluding the review papers there are 32 application papers. So, what are the topics? Incidentally, this single session format is unique to my experience and I quite appreciate it. We all sit together and review all of the papers and presentations rather than go off to our specialities - hypersonics in one room and low speed in another room. So, one of my first comments is that I am a little conflicted about how that should be managed. I am not particularly interested in hypersonic rarefied flow, but I guess I can appreciate the problem. Maybe there will be an exchange which is synergistic, to use a common phrase. Flow field: I was reading from the original literature of the Fluid Dynamics Panel and was a little surprised to see that originally it was intended for wind tunnel application of flow field measurements. In talking to some other people with a history of the organization, they said we haven't focused on flow fields. There are a lot of things going on on the surface that are of interest. I think that this year we are really focusing on flow fields, or at least paying a lot more attention to flow field measurements. The other prominent region is the surface reactions. I would like to divide these. The flow field is distinctly separate from surface reactions. Filling out the program were topics of balance technology, geometry deformation measurements and MEMS. Of course, don't forget

rainbow thermometry, I may be a little facetious here, but I was surprised to realize that there is a rainbow thermometry. No disrespect intended.

Of the flow field topics, we can see the breakdown of optical velocimeters into Particle Image Velocimetry (PIV) and Doppler Global Velocimetry (DGV). By the way, is it going to be Doppler Global or Planar Doppler Velocimetry? Then come optical transmission methods: holography, interferometry, schlieren and some very interesting evolutionary applications. The topic of interest to me, pressure probe surveys, comes in dead last. Of the surface reaction topics, skin friction and transition is one and pressure sensitive paint is the other. Now, I didn't mean to exclude or dismiss the review papers. These are my comments. Feel free to contribute.

Paper No. 1 by Heyes and Whitelaw - I thought it was generally a good and complete description of optical velocimeters and the paints: pressure and temperature sensing paints for surface reactions. Paper No. 2 is a very informative summary of NASA Langley activities. I really am impressed by the long-range inflight solar schlieren and I think it is a fantastic accomplishment and should be extremely useful in supersonic transport research and sonic boom studies. The third review paper I find is a welcome reminder of the need for cryogenic capable measurement systems. A lot of the things we would like to do are shut off from the cryogenic environment, or at least it seems like it. Maybe we should keep an open mind on that.

Regarding cryogenic flow visualization, I am going to quickly assert my prerogative here and discuss two topics that were not presented here, but that I thought would be of interest in the area of cryogenic measurement systems and flow visualizations. These results are not widely known.

Fluorescent mini tufts are tufts made of very small fibre, 50 microns, nearly invisible except when you image them with fluorescent illumination. They can be attached to a model surface with glue. I have conducted in the last year or so a convincing demonstration in the NTF of their non-intrusiveness. That was one of the original applications. You could leave these things on the model for the whole test program and get free visual data about separation. The NTF has extremely stringent surface roughness requirements, so one immediate reaction was that you can't put those on the model because you will feel them with your fingertips. You can in some situations apply them with no adverse effect. We had a 767 running at 65 million Reynolds number, full cryogenic conditions. Careful back-to-back force measurements were made to compare tufts on and tufts off, with 8 repeat runs, which is a luxury in NTF. The difference between the tufts on and off is less than 0.3 of a drag count, which is the confidence interval. In that case, you can leave them on. Now, I have to say, we only had 160 tufts applied near the trailing edge in two rows. It is worth remembering that I think there is generally a single roughness requirement applied to the entire model, but it shouldn't be. The leading edge is sensitive to such roughness. The trailing edge is a completely different kind of flow. Evidently, you can put lots of things on the trailing edge and not feel a disturbing effect.

Cryogenic flow visualization for separation and direction streaks on the surface can, in principle, be conducted with liquids, but it is not going to be with oil. It is going to be something like propane, which is gas at room temperature but quite a friendly liquid at cryogenic conditions. I have demonstrated that propane will accept a fluorescent dye in low concentrations. You can see it with UV light. All you need is a way to put it on the model, wind-on.

Flow field comments:

The optical velocimeters occupy a fairly well established sensor type these days. I note that they are often described and even defended as being non-intrusive, in that there is no probe in the flow. In my paper, I pointed out that there are lots of ways of measuring intrusiveness and that includes dollars, man hours and difficulty, so I guess that I would suggest that non-intrusiveness in that sense, may not be a particularly important attribute. Some flows require no physical presence. A vortex that is about to burst will completely change if you try to stick anything in it.

However, in my experience, most flows do not have that sensitivity, at least flows relating to commercial transports. So there are many applications where a physical presence is not a serious disadvantage. The other prominent attribute of these optical velocimeters is an instantaneous capture of the flow field. I guess I would like to raise the question, and maybe this would be a good time for you to respond, "Is this a productivity issue or an accuracy of depicting the unsteady nature of the flow?". If you say I can capture a complete flow field in a second compared to a microsecond, there is a million times increase in productivity. However, there really is a diminishing return when we talk about time in this sense. A one second measurement in a continuous running tunnel is hardly any more advantageous than a 10 second or maybe even a 100 second measurement. Somewhere around there there is a break point where the productivity really benefits.

I note in Paper No. 5 that Dr. Kooi showed unexpected unsteady flow in the regions where I wouldn't have expected it. In a case like that, the instantaneous capture is essential. Certainly there are cases where instantaneous capture of the flow field is essential, and there are cases where no physical presence is essential. We should keep in mind the balance of these situations. Any comments.

N. Malmuth, Rockwell Center, USA:

I am particularly interested in the capability of the pressure probes in connection with porous walls and ventilated walls in wind tunnels. Just from an overview point of view I am very concerned about their invasiveness and intrusiveness. I am wondering in connection with this whole idea what the opportunities are to deal with that, even with the amount of work that is going on with this kind of pressure probes, what is our latest assessment of how they could work in that kind of environment near ventilated walls?

J. Crowder, Boeing, USA:

That is a good question. If you just build a fixed bracket and bolt a rack of probes to the wall with a 1 inch thick flange with square corners, you are probably going to suffer the effects you mentioned. I think it is a detailed engineering problem to reduce the probe size. Certainly, the response of a flow field to a 1 inch diameter probe ought to be different than to a 0.1 inch diameter probe, or the probe size needs to be scaled to the characteristic length of the flow. Reducing the probe size and providing a more carefully engineered support system, using long tapered elements that are distributed over a fairly long length of the wind tunnel, I believe, is a practical approach, and similar to what I have been demonstrating in our wind tunnel measurements.

I should also point out again that one of my other favorite subjects is the so-called Flying Strut system. For some classes of flows, I believe that system is readily available now. It is discussed in my paper, but it is a way of supporting probes, a physical object in the flow with very low disturbance by aerodynamically trimming the support system.

N. Malmuth, Rockwell Center, USA:

That became a very challenging problem when we were trying to explore the pressure field in the model in the TSAGI wind tunnel. We had a lot of difficulty making that compromise by making the support sufficiently rigid, to protect the high q , and then you had the problem that you had a very invasive strut that was in there that was completely compromising your ability to get accurate measurements. It seemed to me at the time, not being a specialist in instrumentation, how challenging that problem really is. Maybe somebody in the audience can make other comments.

B. Elsenaar, NLR, Netherlands:

One remark I would like to make about productivity versus accuracy and the capturing of the whole flow fields. Our experience is that as soon as you have equipment available to map the complete flow field, it is used because it gives you so much more information. When we started with the 5-hole probe rake (it's intrusive, I agree with you but we didn't consider that to be a problem) one out of two customers wanted to use it just to get the good view of what the flow was all about. You are willing to do this because you can do it very easily and it doesn't cost you a lot of time. If you need half a day to scan the whole flow, nobody will use it. If you can do it in 5 minutes or 2 minutes, it is excellent and you are willing to do it even if you lose some accuracy. That is my comment.

J. Crowder, Boeing, USA:

I agree with that quite a bit, and I would say you are to be congratulated in developing a system that has that attribute. I have to confess that in my work at Boeing I have struggled and suffered because some of our early traversing probe systems were not obviously non-intrusive and required extensive installation time. In that setting, it was completely unsatisfactory and of no interest to the customers. Now we are making up for lost time developing more practical traversing systems and smaller probe systems, and expect to see a similar reaction with our user community. One other comment regarding specifically the TSAGI wind tunnel is that I have worked for the last several years with Professor Amiryants of the Dynamics Group there. He has developed a flying strut which was demonstrated last year in the T-128 wind tunnel at a Mach number 0.95 and two atmospheres. This apparatus has a total reach of 2.4 meters and is highly swept forward to distribute the volume over some length. So there are ways of doing it. There are probably ways of doing it that are not on hand yet. I think we need to keep those prospects in mind before concluding that a particular method is the way to go. From my perspective, the PIV appears to be better developed than DGV. Is there controversy over that? Do the results say that?

T. Beutner, Wright Patterson AFB, USA:

I think PIV is certainly better developed, which is representative of perhaps the age of the technique. DGV is relatively new in comparison to PIV.

J. Crowder, Boeing, USA:

My impression is that they are fairly contemporary. When did these methods become more readily available?

T. Beutner, Wright Patterson AFB, USA:

Perhaps somebody else can comment on PIV. I think PIV was commercially available by the time the first literature reference to DGV came out which was around 1991.

J.W. Kooi, DNW, Germany:

I am wondering what will be the future when we go from 2D to 3D, and I am wondering if DGV is not the better way to go. Although I am an advocate for PIV, for the 3D, maybe the DGV is the better solution.

J. Crowder, Boeing, USA:

I agree with that if the PIV is limited in that respect.

T. Beutner, Wright Patterson AFB, USA:

I think that we may see these techniques being complementary and even used simultaneously in some tests, if for no other reason than that it is difficult to make an error estimate without an independent measurement. Many of the classical error estimation techniques are somewhat unsuitable for both of these techniques for reasons that I think are addressed quite well in the papers. They have different seeding requirements as well, and they are limited ultimately by different aspects of the optical sensors. In PIV we are limited by the spatial resolution of the camera; in DGV we are limited by the intensity resolution, not the spatial resolution. So, we have competing interests in terms of having a scientific grade camera versus a large number of pixels for these two techniques. In fact, the preferred technique may depend more on camera technology development and camera affordability than it does ultimately on physics.

J. Crowder, Boeing, USA:

I guess it is well known or readily acknowledged that seeding remains a weak link in most of these optical velocimeter applications. Is there any feeling or opinion about the relative difficulty between PIV and DGV in terms of producing a sufficient quantity and sufficiently uniform distribution?

J. Fulker, Defence Research Agency, UK:

Can I say one thing. Are we sure that we can actually get the seeding into the area that is of real interest? The second point is, what is the problem for shadowing on all these techniques, can we genuinely get into the parts of the field that we want to see?

T. Beutner, Wright Patterson AFB, USA:

I have done a back-to-back PIV and DGV test in a vortical flow field. I will tell you with either of them it is very difficult to get the seeding that you need in a vortex core. You get neither condensation nor smoke seeding into an annular region of the vortex core and that is a challenge with both techniques. The shadowing issue that you point out is a good one, too. The out-of-plane velocity components are very challenging for PIV in the center of the core even if you do get seeding in there. It is difficult to get a valid sample, or a good cross-correlation where you have a high through-plane component and where you are measuring an in-plane velocity component. That is a problem that DGV does not suffer from. On the other hand, the frequency shift that you see across the whole flow field is challenging; so in the outer flow where the velocities are relatively small, it can be challenging for DGV to see enough velocity change whereas PIV can handle the smaller velocities. I think with PIV in some of these flow fields you almost need to take multiple images with different spacing between the pulses. With DGV, again, we may be forced to use different absorption profiles to cover the velocity range - one profile expanded by introducing nitrogen into it. So, all of these techniques may ultimately require multiple images of the same flow field in order to cover the whole dynamic range of the velocities.

J. Crowder, Boeing, USA:

The location of the seed dispenser is an important point. It seems that most users have some means of locally seeding a small part of the wind tunnel with a traversing apparatus that will move the small local seed plume to the region of interest. This proves another kind of intrusiveness. If you have to introduce an object like the seed, and the seed dispenser into the flow field, that is another form of intrusiveness. In terms of smoke flow visualization, where I have experience, I found that the flying strut apparatus is very effective in introducing a small smoke plume anywhere in the flow except the vortex cores, where it gets excluded all the time.

Another point about capturing flow field data: I wonder how much of this is used beyond qualitative judgements of locating a vortex core. I suggest that kind of a simple application is probably not as valuable as higher order functions such as deriving vorticity distributions or even the lift and induced drag distributions. I have a lot of trouble looking at a vortex vector plot. My eyes go to the back of my head. I think that there are probably better ways of displaying these raw data. We should think about not focusing on those raw measurements so much as reducing them down to some higher order functions that could be more readily compared and correlated with forces and CFD solutions. Do the customers like the vector plots?

T. Beutner, Wright Patterson AFB, USA:

It seems to me that if we come up with this sort of detailed flow field information for the simple purpose of integrating it to come up with a single number, there must be easier ways to get our induced drag. The purpose of these techniques seems to be to give us that insight that comes from the whole field mapping, and I resist the temptation to try to reduce that to very simple numbers, although it certainly can be done. There has been work, (see SAE Technical Papers 901935, 901934 and 901933 by van Dam, Brune, Kroo and co-authors) which has looked at getting induced drag directly from a 5 hole probe survey of the Trefftz plane. If up have sufficient confidence in your velocity measurements to get the vorticity field out of them, you can get the induced drag directly. You can get that if you want it, but to reduce the whole field measurement to that seems counterproductive.

J. Crowder, Boeing, USA:

I guess I challenge that. Our opinion at Boeing is that induced drag is an important parameter that has never been directly measured in the past without these flow field data. We have relatively high confidence in the accuracy and utility of induced drag measurements as well as the spatial distributions of lift. We can measure the lift with the balance, but we don't have a good way of looking at the fine detailed spatial distribution. We can't put in enough pressure tap rows.

I guess this is going into a long discussion and we do have a limited time. Let me counter your comment that you would like to see the detail and not reduce it to a single number. I agree with that, but I think that there are better ways of doing that than with a complex multi-component velocimeter system. We shouldn't lose sight of simple total pressure maps. This relates back to some of the data presentations of the vector plots. In that kind of a presentation, I miss the details that I come to expect in the wake surveys with small thin wakes that balloon out into characteristic regions. It is true that there is no vector pointing in the direction of the vortex. It doesn't take much intellect to assign these various blob shapes to certain types of vorticity, so I urge that consideration.

Let's finish up with a few more comments. Technical diversity is great. We should resist the temptation to adopt or defend one particular method to the exclusion of others. It has been my experience that some organizations, bureaucracies or managers have the opposite trend. They see this parallel development as being wasteful; that it is not too difficult to identify the best ones to support and let the other ones wither. I don't believe that at all.

Not to pick on any one organization, but I do see published material from NASA that suggests interest in developing an integrated instrumentation package. They go so far as to identify specific methods or reactions that would be included in this integration package. Hopefully, they are not really committed to just one velocimeter and just one deflection method because we would miss out on a lot of valuable diversity. Another comment - somebody mentioned, "better, faster, cheaper", and I have to confess I react to that. "Better, faster, cheaper" is what I always try to do. I don't need to be told that. Also, when you see "better, faster, cheaper", I think that

there is a pressure to maybe knock off the "better" and reduce it down to "faster and cheaper". Let's resist that.

It is kind of traditional in conferences to elect a "best paper", but usually there are hundreds of papers, and we would need the Committee sitting in judgement and so forth. That is a luxury we don't have. I invite nominations for a best paper: no big deal, no prize. From my own perspective, pressure paint is the most exciting and valuable methodology that is coming along. I would call it a breakthrough technology. All we have to do is make it work. Even in that methodology there are valuable applications that can rely on the qualitative visualization of pressure. A simple paint that can be put on without any preparation using cheap imaging and illumination systems that would allow these things to be quickly implemented can be quite valuable. I think we seriously need to keep looking at all the ways of measuring these pressures photochemically. Professor Sullivan in Paper No. 28 lists those. Don't necessarily think in terms of intensity measurements. Back to my comment about the best paper, I would suggest that Paper No. 30 by Lyonnet is the best. It shows the immediacy of this application, with an unusually high data quality. The data are startling in their resolution. It is extremely valuable to see the effects of all the potential noise sources. If anyone else has suggestions about which paper might be best, please comment.

I have taken enough time. Thanks for participating. We had some comments going. Back to the session chairman.

B. Elsenaar, NLR Netherlands:

There is still time for more questions and for more discussion. Any more questions or comments?

Prof. Meier, DLR, Germany:

I would like to make a more general comment on the Conference. We had a lot of very good papers and progress was shown especially in the optical techniques. Also, the classical techniques have been represented very well in this Conference. But one point which seems to be important for me has not been mentioned up to now. The classical technique of force measurement accounts for 90% of the business in development and research. This is the usual way to do measurements under the present conditions. Why do we really enforce the optical techniques? One aspect has been mentioned already. We would like to have a better impression on the spatial distribution of velocities of pressures in the field and get a better knowledge about the flow. But is this really needed? Is this really the right way to go? For my feeling, this question has not been answered or tackled in the Conference. Maybe it is a question which is not really the topic here, but I think we have to consider this question because the cost of the application of this modern technique cannot be neglected any more compared to the cost of wind tunnels. The laser equipment is fairly expensive and also the time which is used to develop these techniques is not negligible. We have to find good reasons that we should use these techniques in the future in R & D work. These are not only that we would like to have a better view on the flow or better comparisons with numerical results for validation. I believe that the further

development of aircraft and other aerospace applications really needs more detailed knowledge of the flow field and not only in space but also in time. We need more information about the unsteady flows: the reasons for the generation of noise or for fatigue effects have to be detected, and this is only achievable if we really use these modern optical or other techniques with a fast time response. From my point of view, we have to advance good arguments to go this way and I think we have to convince our boards that we have to continue this way like AGARD should continue also in the future.

J. Crowder, Boeing, USA:

I second your comment. I thought it was very well put. I agree with that to a considerable extent. In my experience, when I first developed these qualitative methods, I was very excited. Obviously, everybody is going to want information like that about their particular configuration, I thought. Then I ran into the comment that, "It is just a pretty picture. What do you do with it? You can't link that to the airplane's performance". I responded by saying that you can identify types of flows, separation of flows. You can identify, semi-quantitatively, the location of some of these features. It was a hard sell. Eventually user interest dropped off. The people who were paying the money for the wind tunnel didn't see the value until recently. We had not made a more important case that hard numbers can be derived which are extremely beneficial. Recently, there was a little emergency on an airplane configuration. There was a disagreement in the wave drag distribution, so we implemented these mapping methods and could specifically identify the areas of their concern. Highly spatial resolution distributions of lift and profile drag can be, and I believe will increasingly be, depended on as we try to refine and optimize our configuration. Regarding the unsteady nature, I have regarded all these flow fields as essentially stationary, at least up to a certain frequency domain. Maybe there are some surprises there, but in the mappings that I have done which have never been able to measure the high frequency response, one can detect and observe reactions that indicate whether or not there are high frequency flow components. The feature shown here is a separation and distinctly recognizable with a fluffy edge and apparently intermittent boundaries. This other feature is much different. It is apparently stable over a long period of time. The sensor is not filtered but the data are sort of averaged over time and space with a fast acting sensor. My view of these flow fields is that, in the area outside there is an all inviscid field where total pressure is constant everywhere except here in the wake. You can make judgements about which parts of the wake profile or distribution are stationary or semi-steady and which ones are not being depicted correctly. Another point that I specially wanted to raise is the difference between a pressure probe-based flow field measurement and an optical velocity-based flow field measurement. As I see it, and as it has been explained to me by the people who developed the numerical methodology, measurement of the total pressure deficit, which defines the wake, is essential for deriving profile drag. The profile drag is a very important part of the entire airplane performance. I don't see how velocity, by itself, can yield that parameter. So, is there is any comment about the utility of velocity measurements alone?

N. Malmuth, Rockwell Center, USA:

I am not addressing your question specifically, but I would like to relate back to Prof. Meier's comment because it stimulated some recent experience I had where we were interested at looking at a new concept in reducing transition. I won't mention the facility, but it was a large facility and we wanted to get not just a transition locus, but the evolution of the transition and all the types of stabilities and unstabilities. The only way traditionally we used to do that is with hot wires. If we could get three axis fluctuation measurements with that it would greatly enhance the information that you can get only in a very skeletal way using infrared to look at the locus. The problem that we face is the incredible cost, the setup time to put this all together. We had an enormous bill in terms of our planning to do that experiment. I still am impressed with that challenge, I don't know if we are there yet, to set up a test like that where we can get, even on a simple shape, a good set of hot wire measurements or equivalent to the velocity fluctuation measurements to give us insight into the mechanisms of transition. I think that is a real challenge for us today. I don't know if that is controversial, but it is my personal perspective.

J. Crowder, Boeing, USA:

You picked a good one. Solve that one and you will be, not rich, but famous. I agree with you. I don't have anything to suggest for that except that all the various capabilities and attributes have to be examined and applied with cleverness. It should be noted that these optical methods are very limited in their ability to measure near a solid surface.

B. Elsenaar, NLR, Netherlands:

I would like to terminate the discussion at this point due to the time. One final remark I would like to make, and you said it yourself already, many methods are complementary to each other. It is really bad to pick out only one for application in the future. It depends very much what kind of problem you are dealing with and what kind of information you want to get out of it. That makes it interesting to compare and to use different methods. I would like to thank Jim very much for his evaluation. He is an experimentalist, it was an experiment to run the discussion and the technical evaluation at the same time, but I think it made things more vivid. I thank you very much.

Professor C. Ciray, Chairman FDP, Middle East Technical University, Turkey:

Good afternoon. We have come to the end of the Symposium we started on Monday. In my estimation, it was a successful meeting. I will talk to you for about 10 minutes or so. First, I would like to express our appreciation for all those who have contributed. I would like to mention their names. After, I will take a few minutes to give you information about the future prospects and programs.

This Symposium was conceived something like two years ago in the Panel and the U.S. delegation was very kind to invite us to hold the meeting in the U.S. in Seattle. The invitation of

the U.S. delegation was translated by the contributions of three important agencies of the U.S. They are the United States Air Force, NASA and the Boeing Company. They made handsome contributions and we thank and appreciate very much their contributions. We also appreciate very much the tour to Boeing. I would like to invite you to express our appreciation to the delegation, to the United States Air Force, to NASA and to Boeing.

These institutions have asked our good friends and Panel Members Dave Selegan and Ron Bengelink to organize this meeting, to be the hosts of this meeting. Dave Selegan, who is at the same time the U.S. National Coordinator in the Panel, acted as the Local Coordinator in hosting us here. On the other hand, Ron Bengelink, also a Panel Member, was responsible for all the local arrangements and for the Boeing tour. Of course, many of you appreciated the baseball tickets and also the organization at the Conference Center. They have worked diligently and whatever they have done, they have done it always with a smiling face. Having the experience of being a host myself (and many of you, too) in the past, I am sure you appreciate very much what these two gentlemen have done for us. I would like again to ask your appreciation. Thank you very much.

Both of them were seconded by two people. One of them, Miss Cresh from Universal Technology Corporation, who is a subcontractor for the U.S. Air Force, handled the administration of registration and the logistical arrangements with the Conference Center. Also, Miss Sandy Henderson from the U.S. Air Force, Wright Patterson Air Force Base, who is the secretary to Dave Selegan, helped with the administration and registration. I would like to ask you to show your appreciation to these ladies.

A very important part of our activities is the companions' program. There were two ladies who were behind the companions program. They were Mrs. Nicky Selegan and Mrs. Ann Bengelink. Both of them have tried to do their best in order to keep the companions happy and to give them a good time while we were working in this hall. On behalf of the companions and of all the participants, we would like to extend to Ann Bengelink and Nicky Seragan our appreciation and our thanks.

The reason we came here was the technical meeting, the Symposium. It was conceived in the Panel, as I said before some two years ago, but of course the way we are working in the Panel is that we form a Technical Program Committee who is responsible for the technical organization of the program. As you might have seen in the Symposium announcement, there are 12 panel members with their Chairman, Dr. Louis Chan from Canada. I wish I had prepared a vu-graph to show their names here; but since you have the green sheet, you can have a look at it. They have done a very good job. They have made a good selection from all the papers submitted to them. To do this they have spent hours and hours in a number of meetings. I think that the outcome was a very, very high level technical program, and I also think that you concur in judging that it was a successful program. So if you find this successful, please show your appreciation to the Technical Program Committee.

The other group of people involved, perhaps the most important contributors, are those who have prepared these papers, i.e., the authors, and those who have come here to present the papers. I think that they have done a very good job. I didn't have personally many occasions to attend the sessions, but in those sessions where I had a possibility to listen to them, I can say that the expositions were very good, the presentations very neat. To my judgement the discussions were not so lively; I interpret this as the papers were presented concisely, neatly and completely.

I would like to thank the authors and also those who have come here to present the papers. Of course, I have noticed one thing, that the number of ladies who started to present papers in these meetings started to increase. I would like to pay a special tribute to the ladies who have made representations. Thank you young ladies for the presentations.

There are some people who were behind the scenes in the booths who were trying to translate the presentations. These are Miss Van Damme and Miss Caplan. They have done a very difficult job, and if you have benefited and understood some papers which were not in your own language, then you owe this to their excellent interpretations and translations of the papers.

We owe also thanks to Mr. Crowder for his kindness to accept the responsibility as Technical Evaluator and, to my estimation, he has very ably led the Technical Evaluation Session.

We had some other people who have helped us with the audio-visual system, and I would like to mention the name of Mr. Lance Cobena and Mr. Jeremy Young. Also, in the convention services we have had the help of Ms. Lorri Young who is one of the Conference Center staff. We thank them all for their help in running this Conference.

This meeting was a responsibility of the RTO/AGARD Fluid Dynamics Panel, and there are two people who are always behind the scenes, so that everything is done according to the standards of the Panel. These are the Executive Officer of the Panel Dr. Jack Molloy, and the Secretary Miss Danielle Pelat. We thank you both very much for your expert work.

There is one group of people that we owe thanks; and it is the audience. Because they have cared for this meeting; they have found the meeting important and they have travelled perhaps long distances to come to attend this meeting. Also, they have contributed to the discussions and they made this meeting more meaningful. Without the audience, any Symposium does not mean too much. We had a good Symposium and we thank you for your interest in this meeting.

I have completed the first part of my comments and now I would like to show you something about the future.

Many of you during this meeting, presumably, have heard that AGARD is ending, the Fluid Dynamics Panel is finished and the future is not very clear and so on. I would like to throw a bit of light to this point. We are not at the end of anything; we are starting a new life. This new life is going to bear the spirit of AGARD, if old Agardians and you, the audience, are going to continue to show your interest. NATO has undergone a certain change. As a consequence of it, the research organization of NATO had to go through a certain change, and finally, we have a new organization and a new name, The Research and Technology Organization. The Research

and Technology Organization has six Panels. You can see the names here. The first one is Studies Analysis and Simulation Panel. This is a kind of continuation of the Applied Aeronautical Studies Committee of the previous AGARD. The second one is SCI, which is System Concepts and Integration Panel. This has the relation to the combination of Mission Systems Panel and Flight Vehicles Panel (FVP) of AGARD. The third one is SEP which stands for Sensors and Electronics Technology Panel and this is again, a kind of continuation of the SPP which was the Sensors and Propagation Panel of AGARD. The fourth, ISP is an entirely new panel and its name is Information System Technology Panel. The sixth one is HFM, Human Factors and Medicine Panel and this Panel has a relation to the AMP, Aeromedical Panel of AGARD. So, you see that AGARD is there. The AVT, the Applied Vehicle Technology Panel, is a combination of the three oldest panels of AGARD: these are Fluid Dynamics Panel, the Propulsion and Energetics Panel and the Structure and Materials Panel, so this Panel has a large scope of technical interests, but nevertheless I think that with time that this question is going to be handled in a better way. You see that all these six Panels have a relation to AGARD.

Of course, with respect to AGARD, there is one important difference and this difference is in the scope of the areas of interest. Within AGARD, we were interested only in aviation, in aerospace problems. Now, RTO is not only interested in aerospace, but at the same time in the naval problems and at the same time in land force problems. However, this structure is going to evolve, but what I want to try to show to you is that AGARD is there. Now as a token of this, you can see our near future activities of for example, the Fluid Dynamics Panel. Of course, from now on we will not be named Fluid Dynamics Panel. But whenever you see the word AVT you understand that it is at the same time the Fluid Dynamics Panel.

In 1998, we are going to have two symposia. The first one is the Symposium on Missile Aerodynamics in Sorrento, Italy. The second one is the Symposium of Fluid Dynamics Problems of Vehicles Operating Near or in the Air-Sea Interface. So, you see that we have already started to get our hands in naval problems or in the problems at the interface. This Symposium is going to take place in Amsterdam, the Netherlands. You see that the special courses, the VKI responsibilities, continue. The course on Turbulence in Compressible Flows has already taken place at VKI and will also be repeated at NASA Langley. We have a special course on Higher Order Discretization Methods in CFD and a third one, Fluid Dynamic Research on Supersonic Aircraft. Therefore, the way that the FDP and AGARD was contributing to aerospace sciences will continue.

Finally, I have come to the end of my paper. I am very grateful to you all that you have made the trip to come here to attend this meeting. Starting from this afternoon, the participants will go back to their countries or to their next destinations. I hope that each of you will have a safe trip back home. I would like to see you in other conferences, symposia, and other activities of the Organization.

Thank you, good bye and have a nice trip back home. God bless you all.

REPORT DOCUMENTATION PAGE

1. Recipient's Reference	2. Originator's Reference AGARD-CP-601	3. Further Reference ISBN 92-836-0056-8	4. Security Classification of Document UNCLASSIFIED/ UNLIMITED		
5. Originator Advisory Group for Aerospace Research and Development North Atlantic Treaty Organization 7 rue Ancelle, 92200 Neuilly-sur-Seine, France					
6. Title Advanced Aerodynamic Measurement Technology					
7. Presented at/sponsored by The 81st Fluid Dynamics Panel Symposium held in Seattle, United States, 22-25 September 1997.					
8. Author(s)/Editor(s) Multiple			9. Date May 1998		
10. Author's/Editor's Address Multiple			11. Pages 420		
12. Distribution Statement There are no restrictions on the distribution of this document. Information about the availability of this and other AGARD unclassified publications is given on the back cover.					
13. Keywords/Descriptors <table style="width: 100%; border: none;"> <tr> <td style="width: 50%; vertical-align: top;"> Wind tunnels Measurement Measuring instruments Flow visualization Velocity measurement Diagnostic equipment Holography Interferometers Flow distribution Fluid dynamics </td> <td style="width: 50%; vertical-align: top;"> Temperature measurement Skin friction Pressure measurement Pressure sensitive paints Wind tunnel models Deformation Strain gages Balancing Cryogenics </td> </tr> </table>				Wind tunnels Measurement Measuring instruments Flow visualization Velocity measurement Diagnostic equipment Holography Interferometers Flow distribution Fluid dynamics	Temperature measurement Skin friction Pressure measurement Pressure sensitive paints Wind tunnel models Deformation Strain gages Balancing Cryogenics
Wind tunnels Measurement Measuring instruments Flow visualization Velocity measurement Diagnostic equipment Holography Interferometers Flow distribution Fluid dynamics	Temperature measurement Skin friction Pressure measurement Pressure sensitive paints Wind tunnel models Deformation Strain gages Balancing Cryogenics				
14. Abstract <p>The papers prepared for the AGARD Fluid Dynamics Panel (FDP) Symposium on "Advanced Aerodynamic Measurement Technology" which was held 22-25 September, 1997 in Seattle, Washington, USA, are contained in this Report. In addition, a Technical Evaluator's Report aimed at assessing the success of the Symposium in meeting its objectives, and an edited transcript of the General Discussion held at the end of the Symposium are also included.</p> <p>Measurement techniques were presented for flows from subsonic to hypersonic Mach numbers and environments from cryogenic to high-enthalpy reacting flows. Papers presented during the sessions addressed the following subjects:</p> <ul style="list-style-type: none"> - Particle Image Velocimetry - Doppler Global Velocimetry - Molecular Diagnostic Techniques - Holographic Interferometry - Skin Friction Measurements - Pressure Sensitive Paints - Balance and Model Deformation Measurements 					

L'AGARD détient un stock limité de certaines de ses publications récentes. Celles-ci pourront éventuellement être obtenus sous forme de copie papier. Pour de plus amples renseignements concernant l'achat de ces ouvrages, adressez-vous à l'AGARD par lettre ou par télécopie à l'adresse indiquée ci-dessus. *Veuillez ne pas téléphoner.*

Des exemplaires supplémentaires peuvent parfois être obtenus auprès des centres de diffusion nationaux indiqués ci-dessous. Si vous souhaitez recevoir toutes les publications de l'AGARD, ou simplement celles qui concernent certains Panels, vous pouvez demander d'être inclus sur la liste d'envoi de l'un de ces centres.

Les publications de l'AGARD sont en vente auprès des agences de vente indiquées ci-dessous, sous forme de photocopie ou de microfiche. Certains originaux peuvent également être obtenus auprès de CASI.

CENTRES DE DIFFUSION NATIONAUX

ALLEMAGNE

Fachinformationszentrum Karlsruhe
D-76344 Eggenstein-Leopoldshafen 2

BELGIQUE

Coordonnateur AGARD - VSL
Etat-major de la Force aérienne
Quartier Reine Elisabeth
Rue d'Evere, B-1140 Bruxelles

CANADA

Directeur - Gestion de l'information
(Recherche et développement) - DRDGI 3
Ministère de la Défense nationale
Ottawa, Ontario K1A 0K2

DANEMARK

Danish Defence Research Establishment
Ryvangs Allé 1
P.O. Box 2715
DK-2100 Copenhagen Ø

ESPAGNE

INTA (AGARD Publications)
Carretera de Torrejón a Ajalvir, Pk.4
28850 Torrejón de Ardoz - Madrid

ETATS-UNIS

NASA Center for AeroSpace Information (CASI)
Parkway Center, 7121 Standard Drive
Hanover, MD 21076

FRANCE

O.N.E.R.A. (Direction)
29, Avenue de la Division Leclerc
92322 Châtillon Cedex

GRECE

Hellenic Air Force
Air War College
Scientific and Technical Library
Dekelia Air Force Base
Dekelia, Athens TGA 1010

ISLANDE

Director of Aviation
c/o Flugrad
Reykjavik

ITALIE

Aeronautica Militare
Ufficio Stralcio AGARD
Aeroporto Pratica di Mare
00040 Pomezia (Roma)

LUXEMBOURG

Voir Belgique

NORVEGE

Norwegian Defence Research Establishment
Attn: Biblioteket
P.O. Box 25
N-2007 Kjeller

PAYS-BAS

Netherlands Delegation to AGARD
National Aerospace Laboratory NLR
P.O. Box 90502
1006 BM Amsterdam

PORTUGAL

Estado Maior da Força Aérea
SDFA - Centro de Documentação
Alfragide
P-2720 Amadora

ROYAUME-UNI

Defence Research Information Centre
Kentigern House
65 Brown Street
Glasgow G2 8EX

TURQUIE

Millî Savunma Başkanlığı (MSB)
ARGE Dairesi Başkanlığı (MSB)
06650 Bakanlıklar - Ankara

AGENCES DE VENTE

NASA Center for AeroSpace Information (CASI)

Parkway Center, 7121 Standard Drive
Hanover, MD 21076
Etats-Unis

The British Library Document Supply Division

Boston Spa, Wetherby
West Yorkshire LS23 7BQ
Royaume-Uni

Les demandes de microfiches ou de photocopies de documents AGARD (y compris les demandes faites auprès du CASI) doivent comporter la dénomination AGARD, ainsi que le numéro de série d'AGARD (par exemple AGARD-AG-315). Des informations analogues, telles que le titre et la date de publication sont souhaitables. Veuillez noter qu'il y a lieu de spécifier AGARD-R-nnn et AGARD-AR-nnn lors de la commande des rapports AGARD et des rapports consultatifs AGARD respectivement. Des références bibliographiques complètes ainsi que des résumés des publications AGARD figurent dans les journaux suivants:

Scientific and Technical Aerospace Reports (STAR)

STAR peut être consulté en ligne au localisateur de ressources uniformes (URL) suivant:
<http://www.sti.nasa.gov/Pubs/star/Star.html>
STAR est édité par CASI dans le cadre du programme NASA d'information scientifique et technique (STI)
STI Program Office, MS 157A
NASA Langley Research Center
Hampton, Virginia 23681-0001
Etats-Unis

Government Reports Announcements & Index (GRA&I)

publié par le National Technical Information Service
Springfield
Virginia 2216
Etats-Unis
(accessible également en mode interactif dans la base de données bibliographiques en ligne du NTIS, et sur CD-ROM)



AGARD holds limited quantities of some of its recent publications, and these may be available for purchase in hard copy form. For more information, write or send a telefax to the address given above. *Please do not telephone.*

Further copies are sometimes available from the National Distribution Centres listed below. If you wish to receive all AGARD publications, or just those relating to one or more specific AGARD Panels, they may be willing to include you (or your organisation) in their distribution.

AGARD publications may be purchased from the Sales Agencies listed below, in photocopy or microfiche form. Original copies of some publications may be available from CASI.

NATIONAL DISTRIBUTION CENTRES

BELGIUM

Coordonnateur AGARD - VSL
Etat-major de la Force aérienne
Quartier Reine Elisabeth
Rue d'Evere, B-1140 Bruxelles

CANADA

Director Research & Development
Information Management - DRDIM 3
Dept of National Defence
Ottawa, Ontario K1A 0K2

DENMARK

Danish Defence Research Establishment
Ryvangs Allé 1
P.O. Box 2715
DK-2100 Copenhagen Ø

FRANCE

O.N.E.R.A. (Direction)
29 Avenue de la Division Leclerc
92322 Châtillon Cedex

GERMANY

Fachinformationszentrum Karlsruhe
D-76344 Eggenstein-Leopoldshafen 2

GREECE

Hellenic Air Force
Air War College
Scientific and Technical Library
Dekelia Air Force Base
Dekelia, Athens TGA 1010

ICELAND

Director of Aviation
c/o Flugrad
Reykjavik

ITALY

Aeronautica Militare
Ufficio Stralcio AGARD
Aeroporto Pratica di Mare
00040 Pomezia (Roma)

LUXEMBOURG

See Belgium

NETHERLANDS

Netherlands Delegation to AGARD
National Aerospace Laboratory, NLR
P.O. Box 90502
1006 BM Amsterdam

NORWAY

Norwegian Defence Research Establishment
Attn: Biblioteket
P.O. Box 25
N-2007 Kjeller

PORTUGAL

Estado Maior da Força Aérea
SDFA - Centro de Documentação
Alfragide
P-2720 Amadora

SPAIN

INTA (AGARD Publications)
Carretera de Torrejón a Ajalvir, Pk.4
28850 Torrejón de Ardoz - Madrid

TURKEY

Millî Savunma Başkanlığı (MSB)
ARGE Dairesi Başkanlığı (MSB)
06650 Bakanlıklar - Ankara

UNITED KINGDOM

Defence Research Information Centre
Kentigern House
65 Brown Street
Glasgow G2 8EX

UNITED STATES

NASA Center for AeroSpace Information (CASI)
Parkway Center, 7121 Standard Drive
Hanover, MD 21076

SALES AGENCIES

NASA Center for AeroSpace Information (CASI)

Parkway Center, 7121 Standard Drive
Hanover, MD 21076
United States

The British Library Document Supply Centre

Boston Spa, Wetherby
West Yorkshire LS23 7BQ
United Kingdom

Requests for microfiches or photocopies of AGARD documents (including requests to CASI) should include the word 'AGARD' and the AGARD serial number (for example AGARD-AG-315). Collateral information such as title and publication date is desirable. Note that AGARD Reports and Advisory Reports should be specified as AGARD-R-*nnn* and AGARD-AR-*nnn*, respectively. Full bibliographical references and abstracts of AGARD publications are given in the following journals:

Scientific and Technical Aerospace Reports (STAR)

STAR is available on-line at the following uniform resource locator:

<http://www.sti.nasa.gov/Pubs/star/Star.html>

STAR is published by CASI for the NASA Scientific and Technical Information (STI) Program
STI Program Office, MS 157A
NASA Langley Research Center
Hampton, Virginia 23681-0001
United States

Government Reports Announcements & Index (GRA&I)

published by the National Technical Information Service
Springfield
Virginia 22161
United States
(also available online in the NTIS Bibliographic Database or on CD-ROM)



Printed by Canada Communication Group Inc.
(A St. Joseph Corporation Company)
45 Sacré-Cœur Blvd., Hull (Québec), Canada K1A 0S7